INNOVATIONS IN MR HARDWARE FROM ULTRA-LOW TO ULTRA-HIGH FIELD

EDITED BY: Elmar Laistler, Jean-Christophe Ginefri, Lionel Marc Broche, Mark E. Ladd, Mathieu Sarracanie, Roberta Frass-Kriegl, Sigrun Roat and Simone Angela S. Winkler

PUBLISHED IN: Frontiers in Physics

frontiers Research Topics

ISSN 1664-8714
ISBN 978-2-83250-297-6
DOI 10.3389/978-2-83250-297-6

About Frontiers

Frontiers is more than just an open-access publisher of scholarly articles: it is a pioneering approach to the world of academia, radically improving the way scholarly research is managed. The grand vision of Frontiers is a world where all people have an equal opportunity to seek, share and generate knowledge. Frontiers provides immediate and permanent online open access to all its publications, but this alone is not enough to realize our grand goals.

Frontiers Journal Series

The Frontiers Journal Series is a multi-tier and interdisciplinary set of open-access, online journals, promising a paradigm shift from the current review, selection and dissemination processes in academic publishing. All Frontiers journals are driven by researchers for researchers; therefore, they constitute a service to the scholarly community. At the same time, the Frontiers Journal Series operates on a revolutionary invention, the tiered publishing system, initially addressing specific communities of scholars, and gradually climbing up to broader public understanding, thus serving the interests of the lay society, too.

Dedication to Quality

Each Frontiers article is a landmark of the highest quality, thanks to genuinely collaborative interactions between authors and review editors, who include some of the world's best academicians. Research must be certified by peers before entering a stream of knowledge that may eventually reach the public - and shape society; therefore, Frontiers only applies the most rigorous and unbiased reviews.
Frontiers revolutionizes research publishing by freely delivering the most outstanding research, evaluated with no bias from both the academic and social point of view. By applying the most advanced information technologies, Frontiers is catapulting scholarly publishing into a new generation.

What are Frontiers Research Topics?

Frontiers Research Topics are very popular trademarks of the Frontiers Journals Series: they are collections of at least ten articles, all centered on a particular subject. With their unique mix of varied contributions from Original Research to Review Articles, Frontiers Research Topics unify the most influential researchers, the latest key findings and historical advances in a hot research area! Find out more on how to host your own Frontiers Research Topic or contribute to one as an author by contacting the Frontiers Editorial Office: frontiersin.org/about/contact

INNOVATIONS IN MR HARDWARE FROM ULTRA-LOW TO ULTRA-HIGH FIELD

Topic Editors:
Elmar Laistler, Medical University of Vienna, Austria
Jean-Christophe Ginefri, Laboratoire d'imagerie biomédicale Multimodale Paris-Saclay (BioMaps), France
Lionel Marc Broche, University of Aberdeen, United Kingdom
Mark E. Ladd, German Cancer Research Center (DKFZ), Germany
Mathieu Sarracanie, University of Basel, Switzerland
Roberta Frass-Kriegl, Medical University of Vienna, Austria
Sigrun Roat, Medical University of Vienna, Austria
Simone Angela S. Winkler, Cornell University, United States

Citation: Laistler, E., Ginefri, J.-C., Broche, L. M., Ladd, M. E., Sarracanie, M., Frass-Kriegl, R., Roat, S., Winkler, S. A. S., eds. (2022). Innovations in MR Hardware From Ultra-Low to Ultra-High Field. Lausanne: Frontiers Media SA.
doi: 10.3389/978-2-83250-297-6

Table of Contents

frontiers | Frontiers in Physics

TYPE Editorial
PUBLISHED 09 September 2022
DOI 10.3389/fphy.2022.1015289

OPEN ACCESS

EDITED AND REVIEWED BY
Federico Giove,
Centro Fermi—Museo storico della fisica e Centro studi e ricerche Enrico Fermi, Italy

*CORRESPONDENCE
Roberta Frass-Kriegl,
roberta.frass@meduniwien.ac.at

SPECIALTY SECTION
This article was submitted to Medical Physics and Imaging, a section of the journal Frontiers in Physics

RECEIVED 09 August 2022
ACCEPTED 22 August 2022
PUBLISHED 09 September 2022

CITATION
Frass-Kriegl R, Broche LM, Ginefri J-C, Ladd ME, Roat S, Sarracanie M, Winkler SAS and Laistler E (2022), Editorial: Innovations in MR hardware from ultra-low to ultra-high field. *Front. Phys.* 10:1015289. doi: 10.3389/fphy.2022.1015289

Editorial: Innovations in MR hardware from ultra-low to ultra-high field

Roberta Frass-Kriegl[1]*, Lionel Marc Broche[2], Jean-Christophe Ginefri[3], Mark E. Ladd[4], Sigrun Roat[1], Mathieu Sarracanie[5], Simone Angela S. Winkler[6] and Elmar Laistler[1]

[1]Center for Medical Physics and Biomedical Engineering, Medical University of Vienna, Vienna, Austria, [2]Aberdeen Biomedical Imaging Centre, University of Aberdeen, Aberdeen, United Kingdom, [3]Université Paris-Saclay, CEA, CNRS, Inserm, BioMaps, Service Hospitalier Frédéric Joliot, Orsay, France, [4]Medical Physics in Radiology, German Cancer Research Center (DKFZ), Heidelberg, Germany, [5]Center for Adaptable MRI Technology, Department of Biomedical Engineering, University of Basel, Allschwil, Switzerland, [6]Weill Cornell Medicine, New York, NY, United States

KEYWORDS

magnetic resonance imaging (MRI), ultra-low field (ULF) MRI, ultra-high field MR, MR hardware, radio frequency coils, magnet technology

Editorial on the Research Topic
Innovations in MR hardware from ultra-low to ultra-high field

Magnetic Resonance Imaging and Spectroscopy (MRI, MRS) have become indispensable diagnostic tools in numerous medical applications, providing anatomical, functional, and chemical information non-invasively with ever increasing sensitivity and specificity. However, many performance challenges are present in connection with improving the sensitivity, safety, and accessibility of these modalities. In this context, a traditional strategy to improve sensitivity is to develop ultra-high field scanners, but this gives rise to numerous technical hurdles, physics related concerns, and safety issues in addition to increased exclusiveness. More recently, the development of ultra-low field MR systems has also resurfaced in an effort to focus on accessibility, inherently, avoiding safety issues and wave propagation-related image distortions most typical of high fields. However, their inherently low MR signal amplitude comes at the cost of poor sensitivity.

Both the ultra-high and ultra-low field domains, consequently, call for scientific innovations that pave the way for the next generation of MR hardware systems. Today's challenges in the development of MR instrumentation arise from the different requirements and limitations faced at different magnetic fields strengths, and all innovations target the improvement of image quality, safety, and/or diagnostic value of MR.

Consequently, this Research Topic has invited submissions on all innovative developments in MR hardware over the entire range of static magnetic field strengths.

The resulting collection of articles thus covers a large variety of topics, ranging from ultra-low to ultra-high field MR, including intermediate field strengths, spanning work on radio frequency components, magnet and gradient design, as well as complete MR systems. The Research Topic consists of mostly Original Research articles, augmented by a Perspective and a Mini Review article, as well as a paper in the category Technology and Code.

At ultra-high field strengths, the strongest unmet need concerns the improvement of radiofrequency (RF) transmission systems regarding homogeneity of the RF excitation, efficiency, decoupling strategies, and patient safety with respect to the associated specific absorption rate (SAR) limitations. In this sense, Wenz and Gruetter investigate the impact of quasi-transverse electric modes on the transmit field distribution using dipole-fed rectangular dielectric resonator antennas at 7 T. Also, Williams et al. propose a nested 8-channel transmit array with an open-face concept for human brain imaging at 7 T. In her Mini Review article, Irena Zivkovic discusses available interelement decoupling strategies for ultra-high field MR coils. Van Leeuwen et al. discuss a potential reduction in peripheral local SAR for a birdcage body coil at 3 T using a magnetic shield.

At ultra-low field, but also for MR of X-nuclei (i.e., other than ^{1}H), the most challenging task is to increase the sensitivity of the RF detection system, driven by the need to overcome the sensitivity-based limitation of image quality and spatio-temporal resolution set by the various noise sources present in the MR experiment. To this end, several strategies employing new coil geometries, new materials, or cryogenic devices are pursued.

The investigation of novel RF coil element types is an active domain of hardware development for MRI, with the ultimate goal of improving sensitivity. Labbé et al. present their results on high-temperature superconducting RF coils, exploiting the intrinsically low coil noise of such devices. New RF coil shapes are reported by Nowikow et al. in their contribution about Koch Snowflake fractal geometry coils for ^{23}Na MRI.

The need for innovative electronics for ultra-low field MR is evidenced by Harper et al. in their work about an unmatched RF chain for low field MRI. In addition, the trend towards portability and ease of use of MR instrumentation calls for other features that increase usability and accessibility but imposes novel technological challenges, on the one hand regarding magnet design for portable MRI systems, and on the other hand flexible, lightweight or wireless RF devices. De Vos et al. introduce an improved portable and sustainable low-field MRI system, complemented by B_0 shimming methodology for affordable and compact low-field MRI magnets as described by Wenzel et al. In a computational and phantom study at ultra-low field MRI, Höfner et al. investigate the feasibility of 3D neuronal current imaging, relying on the measurement of the minuscule phase perturbation generated by the neuronal magnetic fields.

Regardless of field strength, the development of improved gradient designs enables novel applications of MRI and increases imaging performance. In their Technology and Code article, Littin et al. present an intuitive open-source collection that can be employed to find new gradient coil designs. In an endeavor to reduce acoustic noise and heat in gradient coils, Motovilova and Winkler review existing techniques and present solutions for quiet operation and efficient gradient cooling.

Finally, in a Perspective article, Galuppini et al. discuss the key challenges of field-frequency lock in fast field cycling MRI and define possible research directions in the field.

We, the editors of this Research Topic, hope that the readers will derive added value from the presented collection of articles. We are convinced that innovative hardware concepts and technological development, such as the works presented here, will be highly beneficial for MR research at all field strengths in the future. By combining papers on seemingly very disparate sub-topics in MR hardware development into a single collection, we aim at establishing stronger links within the community, so as to foster unconventional and creative solutions for the upcoming challenges in the development and improvement of MR systems.

Author contributions

All authors have made a substantial, direct and intellectual contribution to the work, and approved it for publication.

Conflict of interest

Topic Editor EL is co-founder and shareholder of ALSIX GmbH, a spin-off company from the Medical University of Vienna, dedicated to RF coil development. Topic Editor MS is a co-founder and shareholder of Hyperfine Research, a company developing low-field mobile MRI scanners. Topic Editor LB holds two patents related to low-field MRI systems (US20180031667 and 102019000007647). SW is the Owner and CEO of inGenuyX LLC.

The remaining authors declare that the research was conducted in the absence of any commercial or financial relationships that could be construed as a potential conflict of interest.

Publisher's note

frontiers in Physics

ORIGINAL RESEARCH
published: 26 April 2021
doi: 10.3389/fphy.2021.647376

Computational and Phantom-Based Feasibility Study of 3D dcNCI With Ultra-Low-Field MRI

*Nora Höfner[1], Jan-Hendrik Storm[1], Peter Hömmen[1], Antonino Mario Cassarà[2] and Rainer Körber[1]**

[1] Physikalisch-Technische Bundesanstalt, Berlin, Germany, [2] Foundation for Research on Information Technologies in Society (IT'IS), Zurich, Switzerland

The possibility to directly and non-invasively localize neuronal activities in the human brain, as for instance by performing neuronal current imaging (NCI) via magnetic resonance imaging (MRI), would be a breakthrough in neuroscience. In order to assess the feasibility of 3-dimensional (3D) NCI, comprehensive computational and physical phantom experiments using low-noise ultra-low-field (ULF) MRI technology were performed using two different source models within spherical phantoms. The source models, consisting of a single dipole and an extended dipole grid, were calibrated enabling the quantitative emulation of a long-lasting neuronal activity by the application of known current waveforms. The dcNCI experiments were also simulated by solving the Bloch equations using the calculated internal magnetic field distributions of the phantoms and idealized MRI fields. The simulations were then validated by physical phantom experiments using a moderate polarization field of 17 mT. A focal activity with an equivalent current dipole of about 150 nAm and a physiologically relevant depth of 35 mm could be resolved with an isotropic voxel size of 25 mm. The simulation tool enabled the optimization of the imaging parameters for sustained neuronal activities in order to predict maximum sensitivity.

Keywords: ultra-low-field magnetic resonance imaging, neuronal current imaging, current dipole phantom, MEG, simulation

OPEN ACCESS

Edited by:
Mathieu Sarracanie, University of Basel, Switzerland

Reviewed by:
Angelo Galante, University of L'Aquila, Italy
Per Magnelind, Los Alamos National Laboratory (DOE), United States

***Correspondence:**
Rainer Körber
rainer.koerber@ptb.de

Specialty section:
This article was submitted to Medical Physics and Imaging, a section of the journal Frontiers in Physics

Received: *29 December 2020*
Accepted: *18 March 2021*
Published: *26 April 2021*

Citation:
Höfner N, Storm J-H, Hömmen P, Cassarà AM and Körber R (2021) Computational and Phantom-Based Feasibility Study of 3D dcNCI With Ultra-Low-Field MRI. Front. Phys. 9:647376. doi: 10.3389/fphy.2021.647376

1. INTRODUCTION

The realization of ultra-low-field (ULF) magnetic resonance imaging (MRI), i.e., MRI in the μT-regime, was possible when new, very sensitive superconducting quantum interference devices (SQUID) sensors could be used to detect nuclear spin precession [1, 2], and, within a few years, several ULF scanners have been developed [3–7]. As the magnetization of the examined volume scales with the surrounding magnetic field, ULF MRI has to cope with a lower signal-to-noise ratio (SNR) compared to high-field MRI—typically employing fields on the order of 1 T and above. Despite different measures to mitigate this low SNR, e.g., pre-polarization, only comparably large voxel sizes in the mm-range could be reached until now in *in vivo* applications. However, the possibility of using ULF MRI for functional imaging is promising motivating the development effort albeit with some compromises regarding spatial resolution. Consequently, imaging of neuronal magnetic fields via their interaction with the spin population, coined neuronal current imaging (NCI), was soon investigated by attempting to directly detect the influence of biomagnetic signals on the phase and relaxation of the nuclear spin precession in the ultra-low-field regime [8].

The successful implementation of NCI would be of particular significance, as currently available non-invasive methods for imaging brain function, such as functional MRI (fMRI), magnetoencephalography (MEG), or electroencephalography (EEG) suffer from either poor temporal resolution or error-prone spatial localization accuracy [9]. The possibility of NCI via high-field MRI was studied intensively applying different approaches [10–12]. Unfortunately, the results were either inconclusive due to a lack of sensitivity of the MRI signal to evoked neuronal activity [13] or irreproducible because of the dominating blood oxygen level-dependent (BOLD) effect [14]. In contrast, owing to the low magnetic field, ULF MRI has the advantage that the BOLD effect becomes negligible [15].

Several phantom studies have explored possible implementations of NCI using ULF MRI, and have highlighted the necessary technical and methodical improvements [16–19]. These studies suggest two different approaches. The so-called *AC* or *resonant mechanism* proposes the use of the magnetic field generated by the neuronal currents itself to manipulate the spin dynamics. This condition would be best met by tuning the Larmor frequency to match the main frequencies of the neuronal activity (resonant condition) [16–18, 20] and the MR signal would be produced exclusively by the proton spins in close proximity to the source. The second approach, called the *DC mechanism*, aims at measuring the minuscule phase perturbation generated by the very weak neuronal magnetic field [16–18]. One possible implementation is based on the acquisition of MR images in the presence and absence of evoked activity. A difference image would then reveal the effect of the neuronal magnetic field. The effectiveness of the two approaches has been demonstrated in multiple phantom studies; however, a fundamental lack of sensitivity has to be overcome for *in vivo* applications. Körber et al. [18] showed that for sufficiently long-lasting neuronal activities, the *DC mechanism* could feature larger contrast-to-noise ratio (CNR) than the *AC mechanism*. As different simulation studies on NCI using high-field MRI showed, the specific spatial and temporal characteristics of the neuronal currents affect the measurable phase and relaxation changes [20–25].

Motivated by this, and expanding on our earlier phantom experiments [17, 18, 26], we developed a computational framework that can be used to simulate 3-dimensional (3D) dcNCI sequences based on ULF MRI. It is centered on our low-noise ULF-MRI hardware and on a well-characterized long-lasting, monophasic neuronal activity which can be evoked by median nerve stimulation. We strove for current dipole phantoms, which could be manufactured with a well-defined geometry facilitating the simulation of their internal and external fields. Measuring their far-field distribution using a multi-channel SQUID system allowed the determination of their equivalent current dipole (ECD) strength for a given applied current. The simulated internal field distributions served as input to an analytic MR solver to characterize the dcNCI signature of the phantoms for multiple configurations and to optimize the imaging sequence for the existing experimental 3D ULF-MRI setup. The validated framework was then used to assess the feasibility and requirements toward *in vivo* dcNCI.

2. MATERIALS AND METHODS

2.1. 3D Ultra-Low-Field MRI Hardware

The experimental phantom study was performed using low-noise ULF-MRI hardware [27] at the Physikalisch-Technische Bundesanstalt (PTB), Berlin, as shown in **Figure 1A**. The system deploys resistive room temperature MRI coils and is located inside a moderately magnetically shielded room (MSR) which features a residual field of <1.5 nT after degaussing [28].

Helmholtz coils generate the homogeneous detection field $\boldsymbol{B}_0$ along x and the $\pi/2$-pulse ($\boldsymbol{B}_{\pi/2}$) along the y-direction, while a Maxwell coil provides the frequency encoding gradient $G_F = dB_x/dx$ and two orthogonal biplanar gradient coils generate the phase encoding gradients $G_{Ph} = dB_x/dy$ and dB_x/dz. A

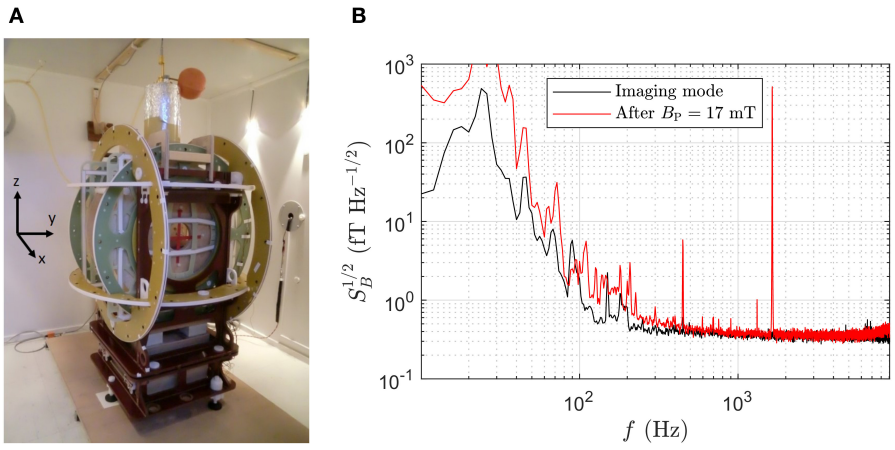

FIGURE 1 | (A) ULF-MRI setup inside magnetically shielded room. **(B)** Field noise (referred to the bottom pick-up loop) of the 3D ULF-MRI setup in imaging mode and after a polarizing pulse of $B_P = 17$ mT. The signal at 1,645 Hz was obtained with $B_0 = 38.6\ \mu$T and $dB_x/dx = 2.4\ \mu$T/m. Data were captured 25 ms after initiating B_P turn-off (compare to validation measurement shown in **Figure 4**).

self-shielded coil provides the homogeneous polarizing field $\boldsymbol{B}_P$ along x while simultaneously reducing transient effects from the MSR. The coils, with the parameters given in **Table 1**, are powered by low-noise current sources placed outside the MSR that are disconnected during data acquisition, if possible.

For signal detection we use our single-channel ultra-low-noise SQUID system that is operated inside the low intrinsic noise dewar LINOD2 [29]. A SQUID current sensor is inductively coupled to a superconducting pick-up coil designed as an axial second-order gradiometer with an overall baseline of 125 mm and a diameter of 45 mm. Since a longitudinal gradient is applied for frequency encoding, this configuration and a very low-noise current source with 470 pA $Hz^{-1/2}$ driving the G_F coil (active during data acquisition) are necessary to reduce noise contributions to a negligible level. A transverse gradient can be used to relax these requirements. The gradiometer dimensions also maximize the SNR with respect to the sustained neuronal source, which was estimated to have a distance of about 50 mm (source-scalp distance 35 mm, see below) to the lower pick-up coil of the gradiometer [30]. When the single-channel SQUID system is operated within the 3D ULF-MRI setup in imaging mode, i.e., with B_0 and G_F coils powered, the total field noise (referred to the bottom pick-up loop) is about 380 aT $Hz^{-1/2}$ for frequencies above 1 kHz and does not increase after application of the polarizing pulse (see **Figure 1B**).

TABLE 1 | Coil parameters of the PTB ULF-MRI system.

Coil	B/I or G/I
B_0 (x), μT/A	48
$B_{\pi/2}$ (y), μT/A	4.8
B_P (x), mT/A	1.0
G_F (dB_x/dx), μT/(Am)	242
G_{Ph} (dB_x/dy), μT/(Am)	65.8
G_{Ph} (dB_x/dz), μT/(Am)	61.4

B/I and G/I denote the field-to-current and gradient-to-current ratio, respectively.

2.2. Current Dipole Phantoms

Current dipole phantoms mimic the underlying focal neuronal activity, which is a sustained, monophasic response following electrostimulation of the median nerve. Its characterization was carried out in previous MEG studies, as shown in **Figure 2A** [18]. The activity is located at a depth of about 35 mm to the scalp surface within the somatosensory cortex SII with a maximum ECD_{max} of about 50 nAm. A time-stable dipolar field indicates a focal activity which decays over about 1 s after stimulation. The derived waveform of variable length, depending on the dcNCI parameters, starts after the last stimulus which excludes artifacts in a potential *in vivo* experiment.

In **Figure 2B**, the phantom positioned below the ULF-MRI SQUID system is shown with the dipole at a depth of 35 mm corresponding to the depth of the physiological model. The NCI phantom with an 80 mm diameter is filled with a $CuSO_4$ and NaCl solution featuring the conductivity $\sigma_{Sol} = 0.325$ S/m and the ULF-MR parameters of brain tissue with $T_1 = T_2 = 100$ ms [31]. A gap of 10 mm between the phantom and the dewar simulates the skull which has a negligible MR signal.

The scalable current dipole concept is based on commercially available printed-circuit-boards (PCBs), allowing a precise fabrication of various arrangements and numbers of current dipoles. The electrodes are made from insulated Pt wire (diameter 125 μm) with a total length of 9.5 mm. At both wire-ends 1 mm of the insulation is removed. Two phantoms were fabricated: a single current dipole consisting of two electrodes pointing apart, as shown in **Figure 2C**, and a dipole grid with 5 × 5 current dipoles arranged in a square lattice with a dipole spacing of 2 mm, as shown in **Figures 2D,E**. If the grid dipoles were mounted on a solid, continuous plate, a slightly higher current would flow in the outside electrodes, since the shorter return path through the conducting medium leads to a lower resistance. Therefore, the mounting plate of the grid was assembled with holes to minimize this effect. Simulations described below also confirmed that this suppresses cross currents between electrodes on each side of the grid. The minute additional potential drop from the base to the tip of the electrode due to the current is practically identical for all individual electrodes.

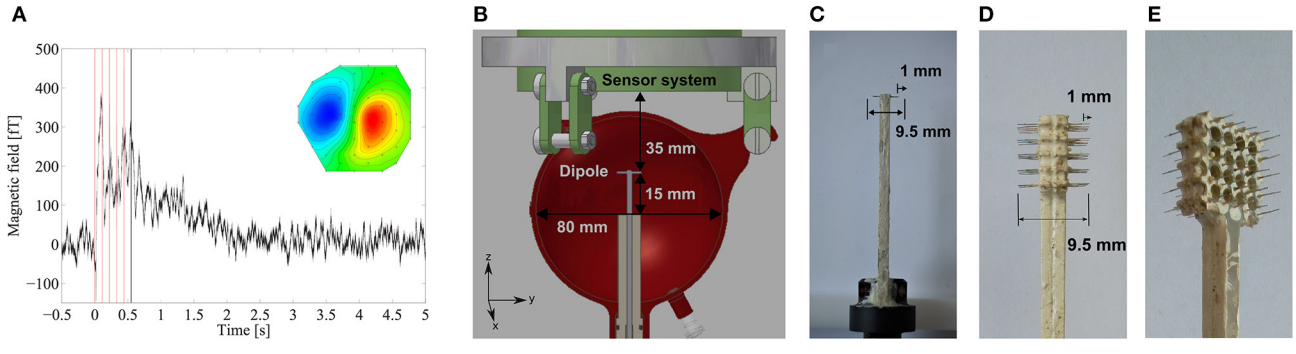

FIGURE 2 | (A) MEG field trace of sustained activity after five electrostimuli of the median nerve (red lines) and the field map averaged from 0.5 to 1.0 s (inset), adapted with permission from Körber et al. [18]. The waveform of variable length (dependent on dcNCI parameters) starts at 0.55 s, as indicated by the black line. **(B)** Head phantom positioned below the dewar with the integrated single current dipole within a conducting solution. **(C)** Single current dipole. **(D)** 5 × 5 dipole grid simulating an extended source. **(E)** Extended source phantom showing the array of holes facilitating the flow of return currents to avoid cross currents.

Currents of up to 80 μA were applied using a home-built, battery-powered, voltage-controlled current source enabling a faithful reproduction of arbitrary waveforms. The phantoms were calibrated by measuring the external magnetic field map for a known drive current with 97 sensors of the 304-channel SQUID system of PTB [32]. Those were close to the phantom and more distant sensors were not used, since they would contain mostly noise and hence negligible signal information. Performing an equivalent current dipole reconstruction allowed the determination of the effective dipole length.

2.3. 3D Ultra-Low-Field MRI Pulse-Sequence

The 3D ULF-MRI sequence was a gradient echo sequence and is displayed in **Figure 3**. The polarizing field B_P of 17 mT, applied for 500 ms (t_P) including a 150 ms ramp, is turned off adiabatically over 15 ms (t_{Off}) until it is aligned with the permanent detection field B_0 of 38.6 μT. A $\pi/2$-pulse of length 2.43 ms (t_{RF}) initiates the precession of the magnetization $\boldsymbol{M}$. Then, one frequency encoding gradient G_F (dB_x/dx) and two phase encoding gradients G_{Ph} (dB_x/dy), G_{Ph} (dB_x/dz) are applied for the spatial encoding of the three dimensions (k-space filling). For anatomical imaging, t_{Ph} should be as short as possible to minimize signal loss due to relaxation. A t_{Ph} of 30 ms was used, as in our previous *in vivo* imaging [27]. Detecting up to four consecutive echoes leads to an overall measurement time of about 800 ms, including the polarization period. A pause of 2 s between the individual measurements avoids overheating of the uncooled polarizing coil. **Table 2** summarizes the imaging parameters.

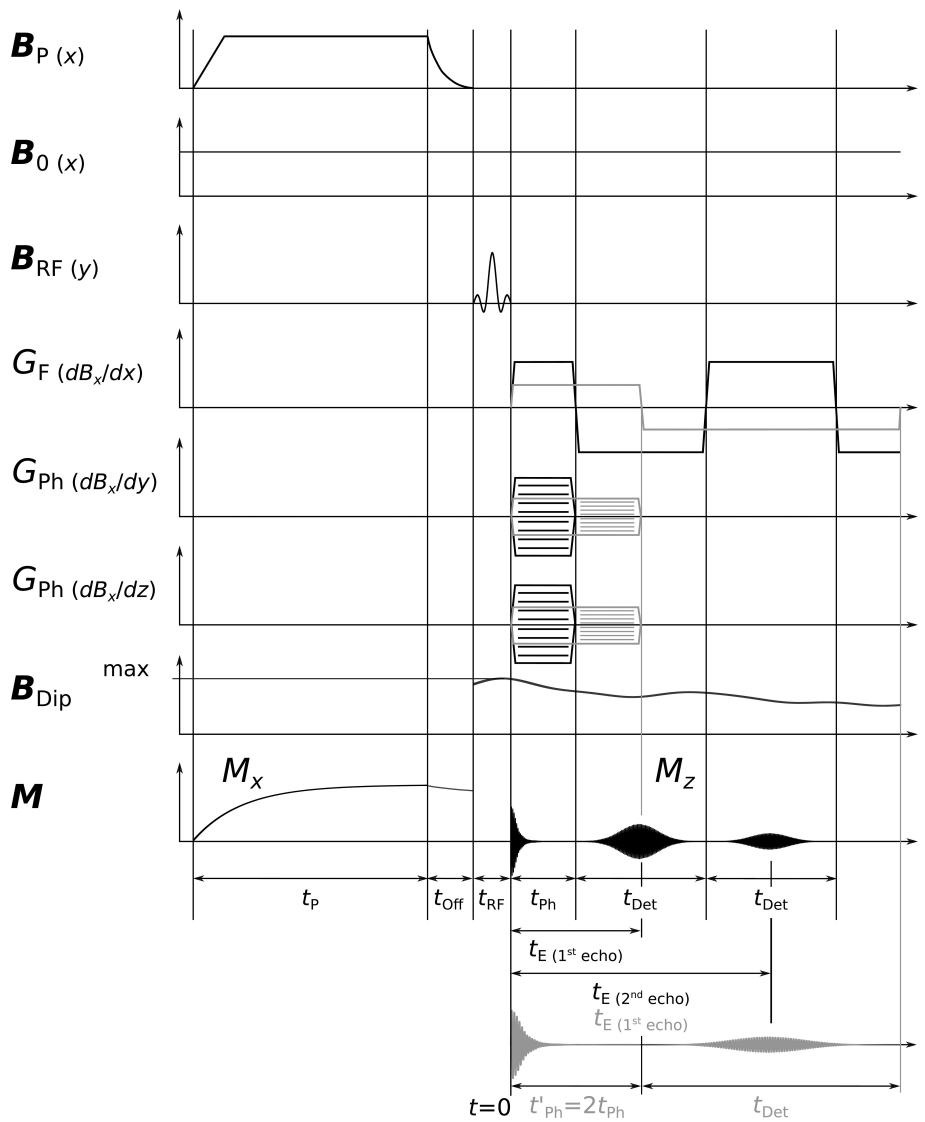

FIGURE 3 | Schematic 3D ULF-MRI sequence. After adiabatic turn-off of $\boldsymbol{B}_P$ and a subsequent $\pi/2$-pulse, phase encoding gradients G_{Ph} and a frequency encoding gradient G_F are utilized and echoes are generated by reversing G_F. The dipole field $\boldsymbol{B}_{Dip}$ is applied permanently during the entire encoding period. Exemplary echoes are shown for phase times t_{Ph} and $t'_{Ph} = 2t_{Ph}$ (gray color). In the latter, the gradient strengths are halved giving the same k-space coverage. Time periods t are differently scaled.

TABLE 2 | Imaging parameters for a phase time $t_{Ph} = 30$ ms and sampling frequency of 20 kHz resulting in isotropic voxel sizes.

Voxel size (mm)	Phase steps $N_y \times N_z$	$FOV_{y,z}$ (cm)	G_F (μT/m)	$G_{Ph,max}$ (μT/m)
5	20 × 20	10	78.2	74.7
10	20 × 20	20	39.1	37.2
15	10 × 10	15	26.1	23.5
20	10 × 10	20	19.6	17.6
25	10 × 10	25	15.6	14.1

All voxel sizes were used for the simulation and 25 mm for the experimental study. $FOV_{y,z}$ denotes the field-of-view in the y or z-direction, respectively.

In order to guarantee maximum phase accumulation, and therefore the largest detectable signal, the dipoles are oriented perpendicularly to $\boldsymbol{B}_0$. In this way, $\boldsymbol{B}_{\mathrm{Dip}}$ are parallel and anti-parallel to $\boldsymbol{B}_0$ just above and below the dipole, respectively. The applied dipole field, as shown in **Figure 3**, was derived from the measured temporal amplitude profile of a somatosensory evoked long-lasting activity. $\boldsymbol{B}_{\mathrm{Dip}}$ affects the precession during the spatial encoding and the readout of the echo signal causing phase and frequency shifts. The expectedly small frequency changes in the millihertz range [33] are visualized using a difference image technique. During one measurement the dipole field $\boldsymbol{B}_{\mathrm{Dip}}$ is active (on). A second measurement serves as a reference in which the dipole is not driven and $B_{\mathrm{Dip}} = 0$ (off). Subtracting the two data sets (on−off) in the time domain reveals the affected ^{1}H-spins in the difference image. An additional reference measurement (off′) allows screening for artifacts by calculating a difference image (off−off′) which should not show a residual above the noise level.

The measurement of the very small B_{Dip} of several hundred pT imposes high demands on the 3D ULF-MRI setup, requiring a high SNR, as well as a high stability of the applied magnetic fields. In order to reduce the influence of magnetic field drifts due to current drifts in the detection field coil or changes of the background field within the magnetically shielded room, we alternate the order of the measurements with and without the applied dipole field. Nevertheless, low-frequency drifts mainly from the current source driving the detection coil lead to measured equivalent frequency shifts of up to ±27 mHz for successive measurements. This causes artifacts in the difference image, masking the influence of the dipole field. To correct for these, the current through the detection coil was simultaneously measured by acquiring the voltage across a precise sense resistor, R_S =1Ω, for subsequent phase correction. At a Larmor frequency of 1,645 Hz the maximum frequency shifts correspond to ∼16 ppm (parts per million), which translate to a current change of 13 μA in the detection coil or 13 μV over the sense resistor. After a ground isolation stage, this voltage is acquired with a 24-bit digitizer. The noise of 65 nV $\mathrm{Hz}^{-1/2}$ is dominated by the isolation stage and would result in 5.8 μV_{rms} given the 8 kHz measurement bandwidth. Therefore, digital low-pass filtering with $f_c = 50$ Hz is applied to allow sub-μV resolution.

The number of measurements per setting, i.e., dipole on or dipole off, was 400 so that for voxel sizes of 15, 20, and 25 mm averaging could be implemented to increase sensitivity. The overall measurement time amounted to ∼40 min (on and off) and to ∼60 min if the additional reference off′ was taken, respectively.

2.4. Data Post-Processing

The magnetic flux changes during the data acquisition t_{Det} result from the induced echo signal $M_z(t)$ (see **Figure 3**), as well as interfering field changes of various sources. Starting the data analysis, we apply first a fitting routine and subtract low-frequency transients. These result from transient responses of the shielded room, background field changes or small vibrational movements of the sensor system within the gradient field. A truncation to remove filter artifacts leads to a ∼10% larger voxel size in the x-direction.

The Hilbert-Transformation is applied to the real-valued measured data to derive the analytical signal $s_a(t_n)$, with t_n denoting a discrete step of time t. This is then demodulated using two synthetic waveforms c_1 and $c_2(t_n)$ according to:

$$s(t_n) = s_a(t_n) \cdot c_1 \cdot c_2(t_n) \tag{1}$$

$$c_1 = \exp\left(-i\Delta\phi_0\right) = \exp\left(-i2\pi\,\frac{t_{\mathrm{Ph}}}{N}\sum_{k=1}^{N}\Delta f_{\mathrm{L}}(t_k)\right) \tag{2}$$

$$c_2(t) = \exp\left(-i\Delta\phi(t)\right) = \exp\left(-i2\pi\int_{t_{\mathrm{Ph}}}^{t}\Delta f_{\mathrm{L}}(\tau)d\tau\right) \tag{3}$$

$$c_2(t_n) \approx \exp\left(-i2\pi\,\frac{t_n - t_{\mathrm{Ph}}}{2n}\sum_{k=1}^{n-1}\left(\Delta f_{\mathrm{L}}(t_k) + \Delta f_{\mathrm{L}}(t_{k+1})\right)\right), \tag{4}$$

where c_1 adjusts the initial phase, accumulated during the phase encoding period t_{Ph}, and, $c_2(t_n)$ takes time varying phase changes during data acquisition into account, and, f_{L} is the Larmor frequency. A further phase correction is applied, in order to adjust the boundary between two slices to the position of the current dipole in the phantom, thus avoiding signal loss due to signal cancellation within one voxel reducing the difference signal amplitude.

Subsequently, performing the 3D Fourier transform of the time-domain difference signal $\Delta s = s_{\mathrm{on}} - s_{\mathrm{off}}$ and calculating its amplitude image ΔS, the highest possible CNR and reduced influence of the detection field instabilities can be achieved. For further analysis, the voxel with the largest amplitude ΔS_{max} is identified and the maximum CNR calculated according to:

$$\mathrm{CNR} = \frac{\Delta S_{\mathrm{max}}}{\mathrm{SD}}. \tag{5}$$

Here, the image noise is given by the standard deviation SD of the complex Gaussian noise $\mathcal{N}(0, \mathrm{SD}^2)$. It is obtained using $\mathrm{SD} = \langle \Delta S_N \rangle / \sqrt{(\pi/2)}$ where $\langle \Delta S_N \rangle$ is the mean of the Rayleigh distributed amplitude noise of the difference image ΔS. For the simulations, $\langle \Delta S_N \rangle$ can be evaluated using the entire (off−off′) images. For the experiments, it is evaluated over the central

x-region of the difference images to take effects of residual artifacts into account (see **Appendix** for details).

2.5. Computational Models of the Phantoms

The magnetic field internal and external to the phantom is generated by the sum of the primary current in the dipole electrodes and the return volume currents within the solution. It was calculated using commercial software (COMSOL Multiphysics) in the quasi-static regime after the geometry of the phantom and the electric sources were carefully digitized. In the quasi-static approximation, the electric field $\boldsymbol{E}$ satisfies $\nabla \times \boldsymbol{B} = 0$ both inside and outside the phantom volume and one can use the electrostatic potential V leading to the Laplace equation $\Delta V = 0$. Since the currents can only flow parallel to surfaces other than the electrodes, the boundary condition for the inner phantom surface, including the PCB mounting, is $E_\perp = 0$. For the calculation, the potential was set to $+V$ on one electrode base and to 0 on the counter electrode base. As $\sigma_{\mathrm{Pt}} = 9.43 \times 10^6\,\mathrm{S/m} \gg \sigma_{\mathrm{Sol}}$, $\boldsymbol{E}$ is essentially perpendicular to the uninsulated Pt conductor surface.

The volume current density $\boldsymbol{J}$ was obtained by solving $\boldsymbol{J} = \sigma \boldsymbol{E}$ and used to determine the magnetic flux density $\boldsymbol{B}$ per unit current using $\nabla \times \boldsymbol{B}/\mu_0 = \boldsymbol{J}$. The magnetic field inside the phantom mimics the neuromagnetic field in the proximity of the source. After normalization by unit current and multiplication by the shape of the long-lasting MEG-derived activity, it served as the input to the Bloch equation solver to investigate the impact of the source parameters on the dcNCI signal.

The magnetic field outside the phantom was calculated at all the coordinates of the 304 channel SQUID system of PTB [32] for comparison with experimental measurements and calibration purposes. In the model, the phantom was placed with its center 70 mm below the bottom of the sensor array. The simulated data allowed the estimation of the ECD of the phantoms which was compared to the ECD of the built phantoms, as estimated from direct measurements.

2.6. Analytical MR Solver for 3D dcNCI

A Matlab-based (The MathWorks, Inc.) NMR solver was created to execute virtual NCI, ULF-NMR, and MRI experiments. For arbitrary time varying fields $\boldsymbol{B}(t)$, the solution of the Bloch equation can usually only be obtained by numerical methods. However, if the spatial direction of the total magnetic field $\boldsymbol{B}$ experienced by the sample is constant, the problem simplifies immensely and one can determine the evolution of the magnetization for any time dependent field using an analytical expression.

Since the dipole phantoms are central in the MRI coil system, we assume ideal MRI fields solely along the x-direction and neglect concomitant gradients. In this case, the instantaneous Larmor frequency, determined by $B_x(\boldsymbol{r}, t)$, can be evaluated directly provided accumulative phase adjustment is taken into account. With $t_0 = 0$ and $\boldsymbol{M}_0$ assumed to be constant throughout the volume due to the homogeneous $\boldsymbol{B}_{\mathrm{P}}$, the precession of the complex magnetization $\boldsymbol{M}(\boldsymbol{r}, t_n) = M_y(\boldsymbol{r}, t_n) + iM_z(\boldsymbol{r}, t_n)$ of a volume element dV and a given time step t_n is calculated as:

$$\boldsymbol{M}(\boldsymbol{r}, t_n) = \boldsymbol{M}_0 \exp\left(i\gamma B_x(\boldsymbol{r}, t_{n-1}) t_n - i\gamma \sum_{k=2}^{n} \Big(B_x(\boldsymbol{r}, t_{k-1}) - B_x(\boldsymbol{r}, t_{k-2}) \Big) t_{k-1} \right) \exp(-t_n/T_2), \tag{6}$$

where γ is the gyromagnetic ratio of the proton. In case of the dipole field $\boldsymbol{B}_{\mathrm{Dip}}(\boldsymbol{r}, t)$, only the x-component parallel to the much larger imaging fields is considered. The solver was verified against a numerical solution of the Bloch equation and found to be in very good agreement with differences below the parts-per-million level.

For the phantom volume, anisotropic discretization was implemented with a minimum spacing of 0.1 mm close to the dipoles. The time-domain signal $s(t_n)$ of the SQUID output is then computed according to:

$$s(t_n) = \int \boldsymbol{C}(\boldsymbol{r})^{\mathsf{T}} \boldsymbol{M}(\boldsymbol{r}, t_n)\, dV, \tag{7}$$

where the coupling field of the sensor $\boldsymbol{C}(\boldsymbol{r})$ was obtained using the principle of reciprocity. A validation via an NMR experiment with an 80 mm diameter spherical sample of distilled water found excellent agreement both in the amplitude and the shape of the free induction decay (FID), but also small frequency changes in the measured data, as shown in **Figure 4**. By evaluating the phase difference $\Delta\phi$ between the simulated and measured FID (see **Appendix**), we determined the corresponding field drift ΔB_x within the first 50 ms to ∼15 nT and identify transient fields following the fast turn-off of the x-directional B_{P} of 17 mT as the

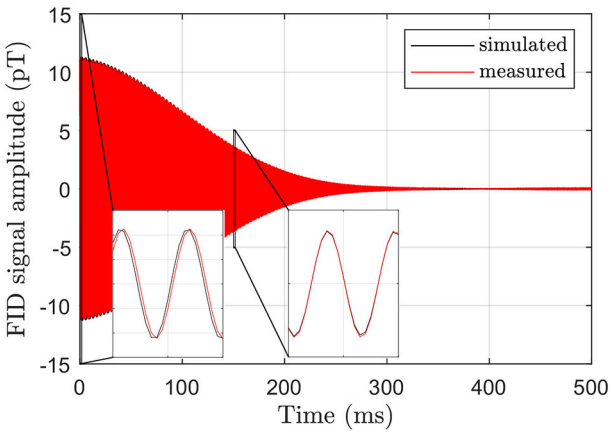

FIGURE 4 | Comparison of simulated and measured FID signals for dephasing in the static field $B_0 = 38.6\ \mu$T and the gradient $dB_x/dx = 2.4\ \mu$T/m. The insets show close ups from 0 to 1 ms and from 150 to 151 ms, respectively, and reveal a small field drift of ∼15 nT in the measured FID compared to the simulation which assumes a constant $B_x(\boldsymbol{r})$.

likely origin. However, we found that this transient response and additional frequency shifts are very reproducible and removed by the subtraction method described in section 2.4.

Phantom dcNCI experiments were then simulated for dipole depths of 15 and 35 mm representing a shallow and a deep cortical source, respectively. The voxel sizes were isotropic ranging from 5 to 25 mm.

3. RESULTS

3.1. Simulated Magnetic Field Distributions

We first present the results of the FEM calculations of the internal and external fields. In **Figure 5**, the magnetic field generated by the single dipole and the dipole grid within the phantom are shown for an applied current of 5 μA. Compared to the single dipole, the maximum field per unit current produced by the extended dipole is significantly smaller due to cancellation effects within the array. The simulations also show that cross currents in the grid phantom are effectively suppressed by the holes in the mounting plate facilitating the current flow across the grid.

3.2. Calibration of Physical Phantoms

The calibration of the phantoms was carried out using the simulated and measured field distributions B_z/I outside the phantoms, as illustrated in **Figure 6**. The field generated by the extended dipole per unit current is 5% larger compared to the single dipole. The ECD reconstruction assumes a point-like dipole within a homogeneous conducting sphere. In case of the simulated data, the center of the sphere was set to -70 mm (with respect to the bottom of the sensor array) and the position of the dipole to 15 mm above it, as given by the geometry of the computational models.

For the measured maps, five fitting parameters were used: the coordinates of the sphere center relative to the bottom plane of the sensor array and the ECD components in x- and y-direction (zero z-component was imposed, as the alignment was defined by the phantom geometry). The estimated uncertainty of the ECD's vertical position of 0.5 mm was taken into account by performing source reconstructions for fixed distances in the range of (15 $\pm$ 0.5) mm. The resulting effective dipole lengths (ECD normalized by applied current) are shown in **Table 3**. The uncertainties are derived from the standard deviation of the fit parameters combined with the uncertainty of the dipole distance to the sphere center, as shown in **Figure 6F**.

The simulated effective lengths of the dipoles were found to be about 10% smaller than the physical dimension of the dipole electrodes. This is in line with expectations, as the current in the electrodes flows into the solution as soon as it reaches the uninsulated element of the Pt wire. Also, the effective length of the extended dipole is slightly larger than the single dipole both in the simulation and the measurement. The disagreement of about 30% compared to the actual values arises from an insufficient electric insulation of the current feeds on the PCB immersed in the aqueous solution. Due to this shunting, some of the current does not flow over the electrodes resulting in a reduced effective length of the physical dipoles.

3.3. Simulations and Experiments of 3D dcNCI

We next present the results of the simulated noise-free dcNCI experiments considering 35 mm deep dipoles. In **Figure 7A**, the amplitude image together with the difference images are shown for the single dipole and the dipole grid for an $\mathrm{ECD}_{\mathrm{max}}$ of 41 and 43 nAm, respectively. Also shown are experiments for a voxel size of 25 mm in **Figure 7B**, which were obtained for a dipole current of 80 μA corresponding to an $\mathrm{ECD}_{\mathrm{max}}$ of 418 and 497 nAm for the single dipole and the dipole grid, respectively. The images have been phase adjusted to obtain the maximum difference signal ΔS_{max}. While the original location of the single dipole and the dipole grid center was $z = 0$ for all voxel sizes, this adjustment shifts the dipole positions toward the voxel edge along $+z$. In this way, signal loss due to cancellation effects within one voxel is minimized.

The maximum amplitude of the difference image ΔS_{max} is about 1,000 times smaller than the maximum amplitude image itself in agreement with previous NMR phantom studies [18]. As expected from the simulations of the phantom's internal field, ΔS_{max} of the single dipole is about a factor of 1.7 larger

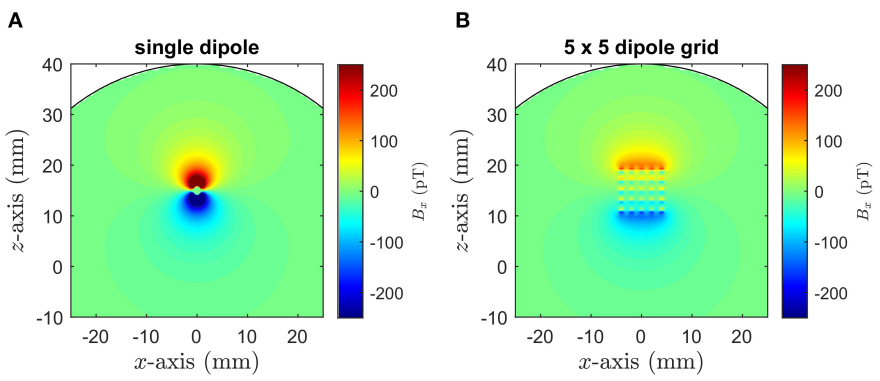

FIGURE 5 | FEM simulation of the internal B_x field maps obtained for an applied current of 5 μA for **(A)** the single dipole and **(B)** the 5 $\times$ 5 dipole grid. The electrodes are parallel to the y-direction with the single dipole and the center of the dipole grid 15 mm above the spherical phantom center.

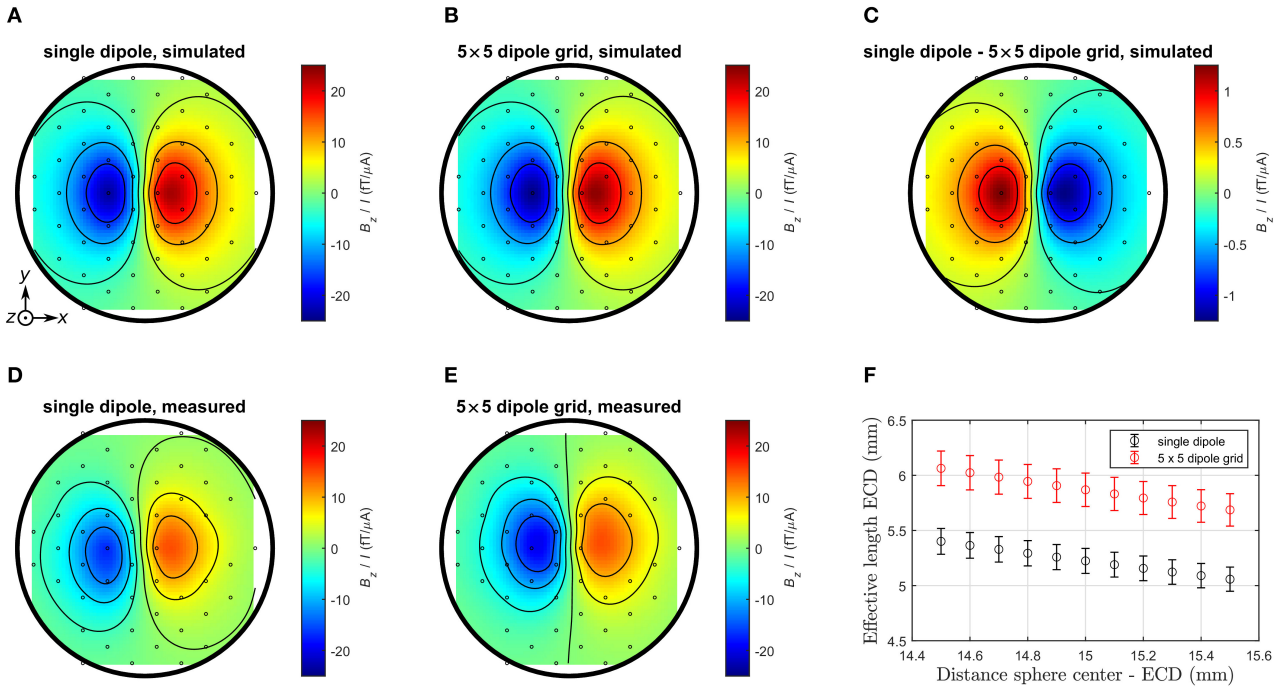

FIGURE 6 | Comparison of simulated and averaged measured field maps obtained for the bottom sensor array of the 304-channel system. **(A)** Simulation single dipole. **(B)** Simulation 5 × 5 dipole grid. **(C)** Simulation single dipole − 5 × 5 dipole grid. **(D)** Measurement single dipole. **(E)** Measurement 5 × 5 dipole grid. **(F)** Fitted effective length of each dipole source for different distances ECD—sphere center. Circles denote the coordinates of the *z*-sensors. For the simulated data, all 304 channels were used for the reconstruction. For the measured data, 97 channels were deployed and complete coverage of the bottom *z*-plane was not possible, as some were malfunctioning.

TABLE 3 | Simulated and measured effective dipole lengths of the two phantoms.

Phantom	Effective length simulated (mm)	Effective length measured (mm)
Single dipole	8.25	5.22 ± 0.30
5 × 5 dipole grid	8.70	5.87 ± 0.34

The physical length of an individual current dipole is 9.5 mm with 1 mm insulation removed at each electrode.

compared to the dipole grid for the 5 mm voxel size. The effect is most pronounced around the dipole where B_{Dip} is largest and the difference image appears smoother and more extended for the dipole grid. This effect disappears for voxel sizes larger than 10 mm and very similar ΔS_{max} are determined. Clearly, larger voxel sizes cannot reflect the detailed structure of the internal fields between the single dipole and the dipole grid. The phantom experiments for 25 mm voxel size reasonably reproduce the simulations with a twice as large expected ΔS_{max} for the single dipole. Good agreement is found for the dipole grid in this particular measurement. However, also visible are residual artifacts that could not be removed by the post-processing procedure (see **Appendix** for details).

The dependency of ΔS_{max} on the voxel size for dipole depths of 15 and 35 mm, as determined by the simulations, is displayed in **Figure 8A**. ΔS_{max} decreases with larger depth according to the sensitivity profile of the sensor system. In addition, ΔS_{max} increases linearly with voxel size up to about 15 mm and then levels off, which is particularly clear for the 35 mm deep dipoles. Also included is the image noise which reflects the sensitivity of the MRI setup for the image sequence using a phase encoding time of 30 ms. **Figure 8A** suggests that a 15 mm deep dipole with a maximum strength of 50 nAm could be theoretically detected by the low-noise MRI setup using the defined imaging sequence for voxel sizes >20 mm. In contrast, a 35 mm deep dipole would be unresolvable even for the largest voxel sizes, and we note that there is no significant difference between the single and the extended dipole source. Only for voxel sizes comparable to the physical dimensions of the dipolar source does the single dipole show a larger ΔS_{max} compared to the dipole grid, as already mentioned before.

Figure 8B shows the dependence of ΔS_{max} on the applied $\mathrm{ECD}_{\mathrm{max}}$ for dipoles at a fixed depth of 35 mm and a voxel size of 25 mm. The simulations predict, that the amplitude of the difference signal decreases linearly with a decreasing current dipole strength in line with previous NMR phantom studies [18]. For the experimental data, ΔS_{max} and the SD are factor of ∼2 larger than predicted by the simulations. We attribute both effects to the aforementioned residual artifacts and discuss this in more detail later.

The results of the simulations and measurements indicate that a 35 mm deep dipole with an $\mathrm{ECD}_{\mathrm{max}}$

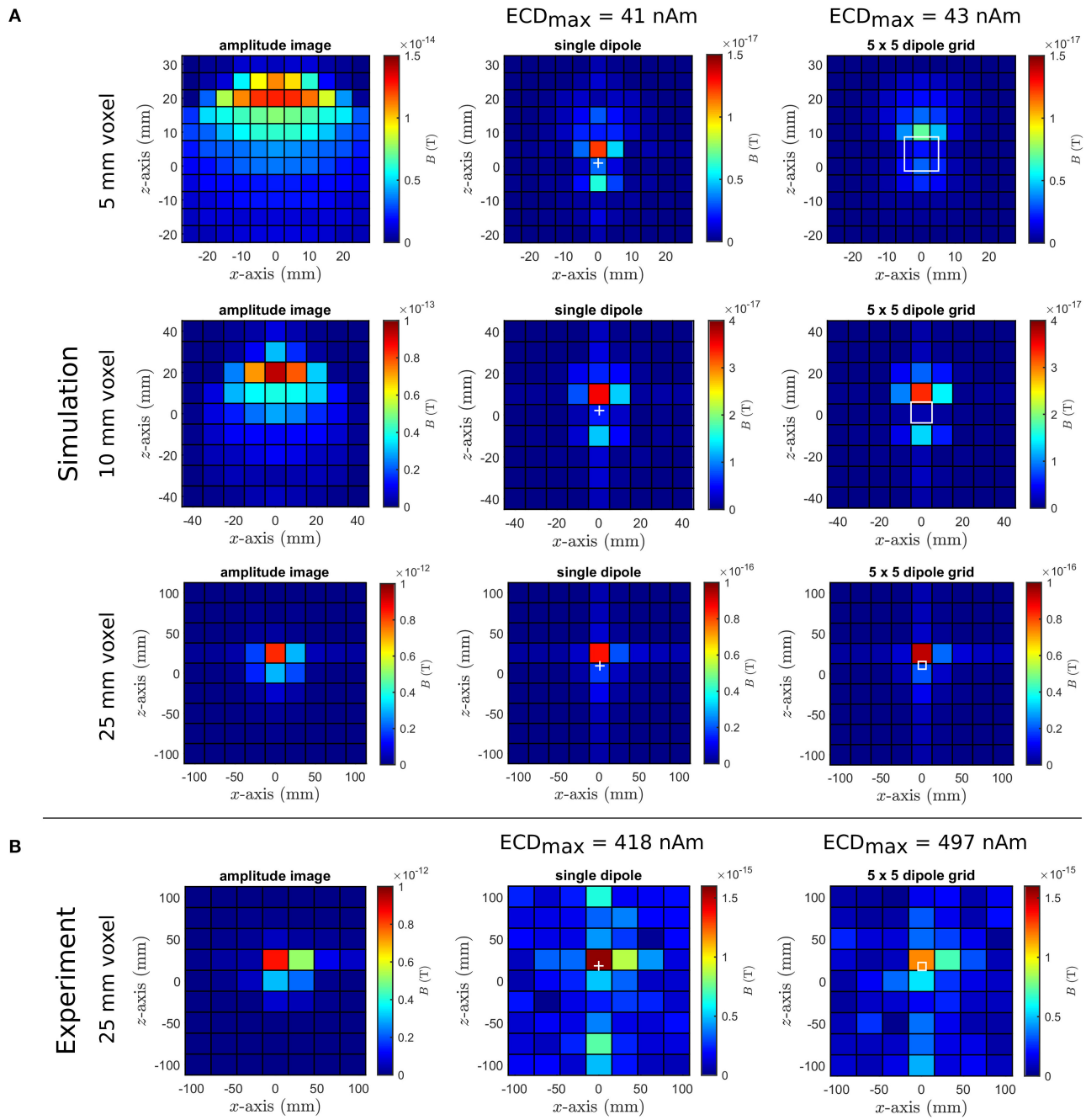

FIGURE 7 | (A) Noise-free dcNCI simulations with voxel size of 5 mm (top), 10 mm (middle), and 25 mm (bottom) for 35 mm deep dipoles. Images were phase adjusted to obtain maximum ΔS_{max} which increases with voxel size; only for 5 mm is there a significant difference between the single dipole and the dipole grid. **(B)** Phantom experiments with nearly isotropic voxel size of 25 mm ($\Delta x \approx 28$ mm) and $\sim 10\times$ stronger ECD_{max} to enable clear identification of dipole activity in the presence of noise and artifacts. In all cases, amplitude images of the phantoms are shown on the left, difference amplitude images of the single dipole in the middle and of the dipole grid on the right. The cross and square denote the position of the single dipole and the dipole grid, respectively.

of about 150 nAm could be resolved using voxel sizes not smaller than 25 mm. Therefore, the detection of a realistic current dipole strength of 50 nAm requires an improvement of the experimental sensitivity by at least a factor of 3.

3.4. Optimization of 3D dcNCI Sequence

In order to identify optimal dcNCI sequence parameters for maximum CNR, multiple images were simulated varying the phase time t_{Ph} from 15 to 100 ms corresponding to echo times t_E of 30 to 200 ms for the 1st echo. The gradients G_F and $G_{Ph,max}$

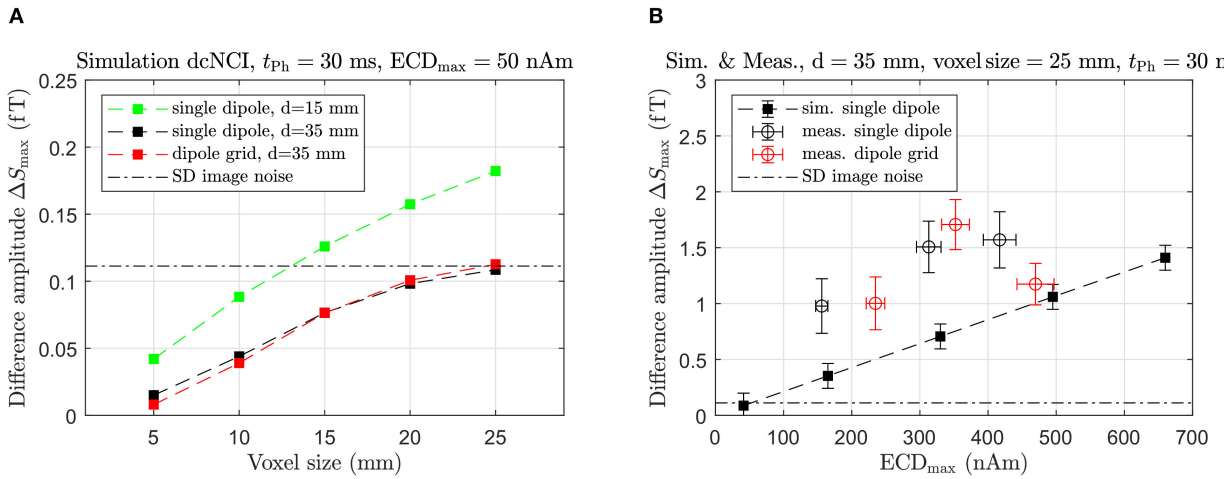

FIGURE 8 | (A) Noise-free simulation of dcNCI showing ΔS_{max} in dependence of voxel size for the single dipole and the dipole grid with an ECD$_{max}$ of 50 nAm and different depths. **(B)** Comparison between simulated and measured ΔS_{max} vs. ECD$_{max}$.

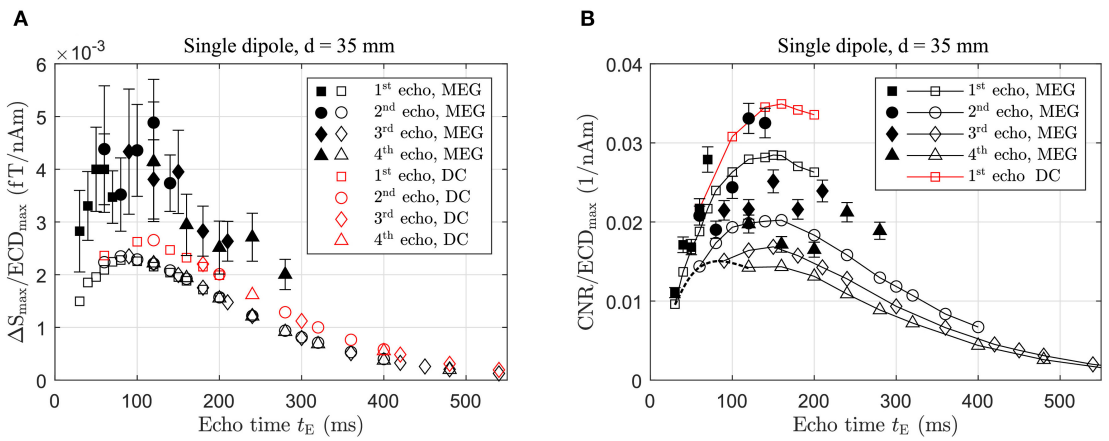

FIGURE 9 | (A) Dependency of ΔS_{max}/ECD$_{max}$ and **(B)** CNR/ECD$_{max}$ for varying echo times t_E and a voxel size of 25 mm. Open markers represent noise-free simulations and filled markers phantom experiments using 80 μA. Results are grouped according to echo number and an example for data belonging to t_{Ph} = 15 ms are connected by the dashed black line in **(B)**.

were adjusted accordingly to obtain a voxel size of 25 mm, as illustrated in **Figure 3**, while the number of phase encoding steps was fixed with $N_y = N_z = 10$ retaining the FOV$_{y,z}$ of 25 cm. Since the sampling frequency was kept constant and t_{Det} depends on t_{Ph}, the FOV$_x$ varied, but was in the meter-range in all cases.

An optimum sequence is expected, as two competing mechanisms occur. A longer t_E allows B_{Dip} to cause larger frequency shifts, but, on the other hand, spin relaxation leads to a signal decrease. As B_{Dip} is not constant and derived from an actual MEG measurement, comprehensive simulations are required to determine an optimal t_{Ph}. For comparison, the optimization was also carried out for a true DC activity, which may be elicited for instance by auditory stimulation [34]. We reiterate that this is in contrast to conventional imaging where t_{Ph} should be as short as possible to obtain maximum image SNR. We also limit this optimization to an inverted frequency encoding gradient G_F during echo formation so that $t_{Det} = 2t_{Ph}$ as this is implemented in our hardware. Application of a different G_F during this period would allow one to vary t_{Det} independently from t_{Ph}.

In **Figure 9**, the dependencies of ΔS_{max} and the CNR, both normalized by ECD$_{max}$, on the echo time t_E are illustrated. The normalization allows the comparison of the predictions between the realistic sustained MEG activity and a constant DC signal. Since four echoes were simulated for each phase time, different t_{Ph} result on occasion in an identical t_E for different echoes. As shown in **Figure 3**, for example, the 2nd echo of a sequence with t_{Ph} is formed at the same time as the 1st echo when $t'_{Ph} = 2t_{Ph}$ resulting in equal echo peak amplitudes. Hence, the values for ΔS_{max} collapse for separate echoes provided the echo times are

the same. The DC signal results in a larger normalized ΔS_{max} and the maximum values are observed for an echo time of ∼90 and 120 ms for the MEG and the DC signal, respectively.

The experimental results were obtained with a dipole current of 80 μA. Again, they show values for $\Delta S_{max}/ECD_{max}$ about a factor of 2 larger than the predictions; however, they also clearly demonstrate the maximum at $t_E \sim 100$ ms in line with the simulations.

The CNR, on the other hand, shows an optimum at $t_E \sim 150$ ms both for the sustained MEG and the constant DC signal, respectively (see **Figure 9B**). In explaining this result, we refer again also to **Figure 3**. In our sequence we always have $t_{Det} = 2t_{Ph}$ and for a given echo, an increase in t_{Ph}, and correspondingly t_E, leads to a longer acquisition time t_{Det}. For the 1st echo, for instance, this gives $t_{Det} = t_E$. Since the sampling frequency is kept constant, the noise is then distributed over more frequency bins resulting in $\mathcal{N} \propto t_E^{-1/2}$. Beyond t_E resulting in maximum ΔS_{max}, the image noise decreases more strongly compared to ΔS_{max} pushing the optimum for CNR to longer echo times. The maxima are rather broad and, as $\Delta S_{max}/ECD_{max}$ is smaller for the MEG-derived signal, its CNR is correspondingly decreased. The maximum CNR for each echo occurs at the same echo time but decreases for consecutive echoes as t_{Det} gets successively shorter and consequently the noise larger, as discussed above. This is not shown for the true DC signal which exhibits the same behavior. For large t_E, spin relaxation dominates causing ΔS_{max} and CNR to approach zero eventually.

The enhancement in CNR compared to the experimental setup when using a t_E of 60 ms is a factor of 1.5 for the MEG signal improving the detection limit from ∼150 to 100 nAm. A true DC activation in comparison to the MEG-derived activity results in an even better improvement of 1.85 provided it has the same ECD_{max}. The phantom experiments confirm this picture and, within the accuracy of the measurement, the maximum in CNR at $t_E \sim 150$ ms is also observed. It is worth pointing out that increasing t_E from 60 to 150 ms has only a secondary effect on the total measurement time, since this is dominated by the polarizing time t_P, in particular if only the 1st echo is acquired.

4. DISCUSSION

4.1. Experimental Validation

A comparison between simulated and measured 3D dcNCI phantom experiments show an approximately 2-fold larger ΔS_{max} for the experimental case. In the simulation model, we used independently determined quantities, e.g., SQUID conversion factor, and the actual geometry of the phantom within idealized MRI fields without any freely adjustable parameter. The very good agreement in the validation measurement of the solver (see **Figure 4**) confirms the accuracy of the computational model. However, with this in mind, the generally larger effect in the 3D dcNCI phantom experiments deserves a closer inspection. It is possibly related to the increased uncertainty due to residual artifacts, which—as pointed out in the **Appendix**—are likely due to field drifts of environmental origin within the moderately shielded MSR that are undetectable by the sensing circuit. This might introduce a bias toward an overestimation of ΔS_{max}. Clearly, the residual artifacts after subtraction represent an experimental issue and a more strongly shielded environment may provide a possible solution. As a further comment, we consider an erroneous determination of the ECD_{max} of the phantoms unlikely, since the observed shunting during the calibration proved to be stable in time. Further studies are required to determine the origin of the larger experimental ΔS_{max}. Nevertheless, we consider the agreement adequate and the results of the simulations form the basis for further discussions below.

4.2. Theoretical Sensitivity Limits of 3D dcNCI

As we have shown, the theoretical CNR of 3D dcNCI using voxel sizes in the cm-range and an optimized sequence applied to our low-noise ULF-MRI setup is only slightly larger than unity. In addition, compared to the phantoms, the water content of brain tissue is lower and heterogeneous ranging from 70.6% for white matter, 84.3% for gray matter and 97.5% for cerebrospinal fluid (CSF) [35]. Partial volume effects may then be present as large voxel sizes are likely to include multiple tissues. Consequently, one can expect a reduction in CNR in an *in vivo* experiment which depends on the size and the location of each voxel and for the present discussion, we assume a worst case value of 70.6%. However, improvements are possible on the instrumental side. We performed the study for a moderate B_P of 17 mT, the maximum achievable field of our setup. A much larger B_P of up to 150 mT has been demonstrated in *in vivo* imaging of the human brain [3] corresponding to an increase in M_0 and consequently in ΔS_{max} of a factor 9.

With respect to the noise performance, the application of a large B_P has been shown to lead to an excess low-frequency noise due to flux trapping in the superconducting pick-up coil [36]. However, it may be avoided by operation at a sufficiently large Larmor frequency [37], a suitable B_P ramp down [38] or rapid thermal cycling of the pick-up coil [39]. Consequently, the noise performance is ultimately limited by Johnson noise of the human body which was recently measured at 55 aT $Hz^{-1/2}$ [40]. Improvements in SQUID performance, e.g., by use of sub-micron-sized Josephson junctions, lead us then to the conclusion that a noise level of about 100 aT $Hz^{-1/2}$, although being quite challenging, is nevertheless feasible [41, 42]. Of course, this discussion requires instrumental factors, such as noise generated by the field and gradient supplies to be negligible, as should be the case for our ULF-MRI setup. In addition, the occurrence of artifacts will have to be addressed. The projected CNR for the MEG-derived sustained activity with $ECD_{max} = 50$ nAm and all these factors taken into account is shown in **Figure 10**.

An overall improvement of ∼35 in CNR for the optimized dcNCI setup appears possible. With CNR ∼ 10, a 15 mm deep, shallow focal cortical source should be well resolvable with a voxel size of ∼5 mm. For deeper sources, such as the exemplary somatosensory evoked sustained activity, the voxel size for CNR ∼ 10 is about 10 mm. Voxel sizes in the range of 5 mm

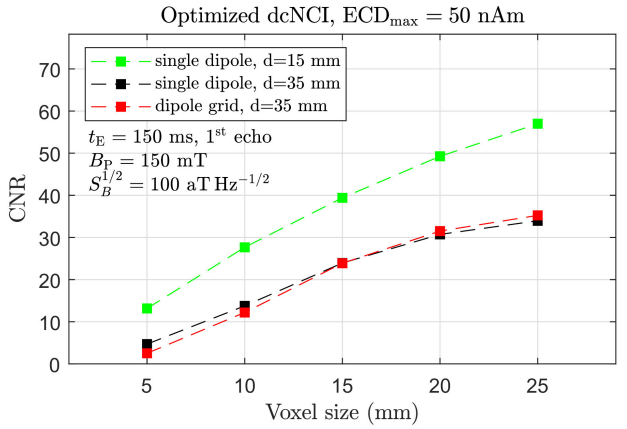

FIGURE 10 | Projected CNR for optimized dcNCI of the MEG-derived sustained activity with an ECD_{max} of 50 nAm taking $t_E = 150$ ms (1st echo), $B_P = 150$ mT, and $S_B^{1/2} = 100$ aT Hz$^{-1/2}$. Signal reduction by 0.706 due to reduced spin density was taken into account.

result again in CNR close to unity and represent in our opinion the theoretical limit of 3D dcNCI.

4.3. Toward *in vivo* 3D dcNCI

The development of a validated computational framework, able to execute virtual dcNCI experiments, was motivated by multiple needs. The identification of the required technological improvements of ULF-MR hardware and the identification of optimized dcNCI sequence parameters being the most prominent. In particular, a sound knowledge of the impact of the neuronal source spatial distribution, timing and orientation on the MR signals permits the identification of optimal strategies for detection. Hardware measures, such as increase of B_P and the reduction of system noise, are rather obvious means to improve the CNR for the realization of dcNCI.

In assessing the relevance of the experimental and computational phantom study for *in vivo* dcNCI, several issues are worth discussing. dcNCI using ULF MRI, as presented here, is limited to evoked and sustained, ideally monophasic, neuronal activities. In addition, the emphasis is on focal activation which can be approximated, at least from an MEG point of view, by a dipolar source and parameterized by an ECD. In this case, the simulation studies show that for voxel sizes larger than 10 mm there is no significant difference between the single dipole and the extended dipole grid in sensitivity even though the internal fields are markedly different. This suggests, that the detailed spatial structure of the neuronal field in an *in vivo* experiment cannot be resolved by 3D dcNCI for voxel sizes larger than 10 mm and voxels in the low mm-range are needed to possibly achieve this.

The dependence on sustained activities of dcNCI has also bearing on the temporal resolution which is of the order of the echo time t_E, the time during which the long-lasting activity is present. For the somatosensory evoked and a true DC activation, this amounts to 120 ms for the optimized sequence which is significantly longer than in MEG but superior to fMRI. Note that this comparison relates to the time needed to acquire one line in *k*-space and not the entire image, which is much longer. This emphasizes again the limitation to evoked activities that can be elicited reliably. By reducing t_E, an improvement of the temporal resolution at the expense of CNR is possible.

A further point which deserves attention is the requirement of parallel alignment between $\boldsymbol{B}_{Dip}$ and $\boldsymbol{B}_0$ in order to result in a maximum CNR. However, this condition is less restrictive than it might first appear. As long as $B_0 \gg B_{Dip}$, which is certainly fulfilled even for dcNCI using ULF MRI, the component of $\boldsymbol{B}_{Dip}$ parallel to $\boldsymbol{B}_0$ is of significance. As this scales as $\cos\phi$, where ϕ is the angle between $\boldsymbol{B}_0$ and $\boldsymbol{B}_{Dip}$, even a substantial misalignment by $\phi = 30°$, for example, results in a reduction of the CNR by only ∼13%. As a corollary we note that a radial dipole, although silent in MEG, will show the full effect in dcNCI as long as the dipole is perpendicular $\boldsymbol{B}_0$.

Finally, the above estimation of the sensitivity limit was based on the assumption of a homogeneous distribution of white-matter-like tissue within the MRI voxel. However, as already mentioned, single voxel signals are expected to be largely influenced by partial volume effects due to the presence of multiple tissues with different proton densities and relaxation times, such as white matter, CSF, bone, dura, and blood vessels. This and many other concomitant factors, related to the complex anatomical and neuroelectric complexity of the human head, have not been investigated in this work. This could be done replacing simplified phantom models with high-resolution anatomical human head models, such as the ones of the Virtual Population (IT'IS Foundation, Zurich, Switzerland) [43] or the MIDA head model [44], combined with realistic electrophysiological models of neuronal networks.

5. CONCLUSION

In conclusion, we illustrated the elements of a validated computational framework allowing virtual experiments with the aim to assess the feasibility of 3D dcNCI. The simulations provide a controllable basis which allows the evaluation for a best-case scenario. To this end, we considered idealized MRI fields and magnetic field distributions generated by current dipole phantoms mimicking neuronal activities. The source models consisted of a single dipole and an extended dipole grid with well-defined phantom geometry enabling accurate FEM simulations of the internal and the external fields. The latter were validated with MEG-type measurements, which served as a calibration of the fabricated phantoms. An MR solver based on an analytical solution to the Bloch equation was developed and used to simulate the dcNCI experiment based on our low-noise 3D ULF-MRI setup. The framework was verified via phantom experiments and allowed the assessment of the detection limit. This experimental part was equally important, since it highlights the technical challenges which need to be addressed.

We found that with our current technology and an optimized dcNCI sequence minimal voxel sizes of 20 mm are required to detect a 35 mm dipole deep dipole with an ECD of about

100 nAm, which is a factor of 2 larger than the physiological value. In addition, we used this tool to project a possible 35-fold increase in CNR due to hardware improvements. The framework should be combined with field simulations of a realistic neuronal network embedded inside a cortical structure. This is highly desirable, as it would ultimately allow the optimization of *in vivo* dcNCI based on ULF MRI which remains a formidable challenge.

DATA AVAILABILITY STATEMENT

The raw data supporting the conclusions of this article will be made available by the authors, without undue reservation.

AUTHOR CONTRIBUTIONS

NH, AC, and RK contributed to the conception of the study. J-HS developed the dipole phantoms and performed the FEM simulations. NH performed the dcNCI phantom experiments, analyzed the dcNCI data, and wrote the first draft of the manuscript. RK developed the MR solver and revised the manuscript based on the annotations of the co-authors. PH contributed to system performance. All authors contributed to manuscript revision, read, and approved the submitted version.

FUNDING

This project has received funding from the DFG under Grant KO 5321/1-1, the SNF under project No 200021E-166809, and from the European Union's Horizon 2020 research and innovation programme under grant agreement No 686865.

SUPPLEMENTARY MATERIAL

The Supplementary Material for this article can be found online at: https://www.frontiersin.org/articles/10.3389/fphy.2021.647376/full#supplementary-material

REFERENCES

1. Greenberg YS. Application of superconducting quantum interference devices to nuclear magnetic resonance. *Rev Modern Phys*. (1998) 70:175–222. doi: 10.1103/RevModPhys.70.175
2. de Souza RE, Schlenga K, Wong-Foy A, McDermott R, Pines A, Clarke J. NMR and MRI obtained with high transition temperature dc SQUIDs. *J Brazil Chem Soc*. (1999) 10:307–12. doi: 10.1590/S0103-50531999000400009
3. Inglis B, Buckenmaier K, SanGiorgio P, Pedersen AF, Nichols MA, Clarke J. MRI of the human brain at 130 microtesla. *Proc Natl Acad Sci USA*. (2013) 110:19194–201. doi: 10.1073/pnas.1319334110
4. Zotev VS, Matlashov AN, Volegov PL, Savukov IM, Espy MA, Mosher JC, et al. Microtesla MRI of the human brain combined with MEG. *J Magn Reson*. (2008) 194:115–20. doi: 10.1016/j.jmr.2008.06.007
5. Lee SJ, Shim JH, Kim K, Yu KK, Hwang Sm. Magnetic resonance imaging without field cycling at less than earth's magnetic field. *Appl Phys Lett*. (2015) 106:103702. doi: 10.1063/1.4914973
6. Vesanen PT, Nieminen JO, Zevenhoven KCJ, Dabek J, Parkkonen LT, Zhdanov AV, et al. Hybrid ultra-low-field MRI and magnetoencephalography system based on a commercial whole-head neuromagnetometer. *Magn Reson Med*. (2013) 69:1795–804. doi: 10.1002/mrm.24413
7. Hilschenz I, Körber R, Scheer HJ, Fedele T, Albrecht HH, Cassará AM, et al. Magnetic resonance imaging at frequencies below 1 kHz. *Magn Reson Imaging*. (2013) 31:171–7. doi: 10.1016/j.mri.2012.06.014
8. Espy M, Volegov P, Matlachov AN, George J, Kraus RH Jr. Simultaneously detected biomagnetic signals and NMR. *Neurol Clin Neurophysiol*. (2004) 2004:12.
9. Babiloni C, Pizzella V, Del Gratta C, Ferretti A, Romani GL. Fundamentals of electroencefalography, magnetoencefalography, and functional magnetic resonance imaging. *Int Rev Neurobiol*. (2009) 86:67–80. doi: 10.1016/S0074-7742(09)86005-4
10. Singh M. Sensitivity of MR phase shift to detect evoked neuromagnetic fields inside the head. *IEEE Trans Nucl Sci*. (1994) 41:349–51. doi: 10.1109/23.281521
11. Song AW, Takahashi AM. Lorentz effect imaging. *Magn Reson Imaging*. (2001) 19:763–7. doi: 10.1016/S0730-725X(01)00406-4
12. Witzel T, Lin FH, Rosen BR, Wald LL. Stimulus-induced Rotary Saturation (SIRS): a potential method for the detection of neuronal currents with MRI. *Neuroimage*. (2008) 42:1357–65. doi: 10.1016/j.neuroimage.2008.05.010
13. Parkes LM, de Lange FP, Fries P, Toni I, Norris DG. Inability to directly detect magnetic field changes associated with neuronal activity. *Magn Reson Med*. (2007) 57:411–6. doi: 10.1002/mrm.21129
14. Chu R, de Zwart JA, van Gelderen P, Fukunaga M, Kellman P, Holroyd T, et al. Hunting for neuronal currents: absence of rapid MRI signal changes during visual-evoked response. *Neuroimage*. (2004) 23:1059–67. doi: 10.1016/j.neuroimage.2004.07.003
15. Mößle M, Han SI, Myers WR, Lee SK, Kelso N, Hatridge M, et al. SQUID-detected microtesla MRI in the presence of metal. *J Magn Reson*. (2006) 179:146–51. doi: 10.1016/j.jmr.2005.11.005
16. Kraus RH, Volegov P, Matlashov AN, Espy M. Toward direct neuronal current imaging by resonant mechanisms at ultra-low field. *Neuroimage*. (2007) 39:310–7. doi: 10.1016/j.neuroimage.2007.07.058
17. Höfner N, Albrecht HH, Cassará AM, Curio G, Hartwig S, Haueisen J, et al. Are brain currents detectable by means of low-field NMR? A phantom study. *Magn Reson Imaging*. (2011) 29:1365–73. doi: 10.1016/j.mri.2011.07.009
18. Körber R, Nieminen JO, Höfner N, Jazbinšek V, Scheer HJ, Kim K, et al. An advanced phantom study assessing the feasibility of neuronal current imaging by ultra-low-field NMR. *J Magn Reson*. (2013) 237:182–90. doi: 10.1016/j.jmr.2013.10.011
19. Kim K, Lee SJ, Kang CS, Hwang Sm, Lee YH, Yu KK. Toward a brain functional connectivity mapping modality by simultaneous imaging of coherent brain waves. *Neuroimage*. (2014) 91:63–9. doi: 10.1016/j.neuroimage.2014.01.030
20. Cassarà AM, Hagberg GE, Bianciardi M, Migliore M, Maraviglia B. Realistic simulations of neuronal activity: a contribution to the debate on direct detection of neuronal currents by MRI. *Neuroimage*. (2008) 39:87–106. doi: 10.1016/j.neuroimage.2007.08.048
21. Konn D, Gowland P, Bowtell R. MRI detection of weak magnetic fields due to an extended current dipole in a conducting sphere: a model for direct detection of neuronal currents in the brain. *Magn Reson Med*. (2003) 50:40–9. doi: 10.1002/mrm.10494
22. Xue Y, Gao JH, Xiong J. Direct MRI detection of neuronal magnetic fields in the brain: theoretical modeling. *Neuroimage*. (2006) 31:550–9. doi: 10.1016/j.neuroimage.2005.12.041
23. Park TS, Lee SY. Effects of neuronal magnetic fields on MRI: numerical analysis with axon and dendrite models. *Neuroimage*. (2007) 35:531–8. doi: 10.1016/j.neuroimage.2007.01.001
24. Blagoev KB, Mihaila B, Travis BJ, Alexandrov LB, Bishop AR, Ranken D, et al. Modelling the magnetic signature of neuronal tissue. *Neuroimage*. (2007) 37:137–48. doi: 10.1016/j.neuroimage.2007.04.033
25. Luo Q, Jiang X, Chen B, Zhu Y, Gao JH. Modeling neuronal current MRI signal with human neuron. *Magn Reson Med*. (2011) 65:1680–9. doi: 10.1002/mrm.22764

26. Körber R, Storm JH, Seton H, Mäkelä JP, Paetau R, Parkkonen L, et al. SQUIDs in biomagnetism: a roadmap towards improved healthcare. *Supercond Sci Technol*. (2016) 29:113001. doi: 10.1088/0953-2048/29/11/113001
27. Hömmen P, Storm JH, Höfner N, Körber R. Demonstration of full tensor current density imaging using ultra-low field MRI. *Magn Reson Imaging*. (2019) 60:137–44. doi: 10.1016/j.mri.2019.03.010
28. Voigt J, Knappe-Grüneberg S, Gutkelch D, Haueisen J, Neuber S, Schnabel A, et al. Development of a vector-tensor system to measure the absolute magnetic flux density and its gradient in magnetically shielded rooms. *Rev Sci Instrum*. (2015) 86:055109. doi: 10.1063/1.4921583
29. Storm JH, Hömmen P, Drung D, Körber R. An ultra-sensitive and wideband magnetometer based on a superconducting quantum interference device. *Appl Phys Lett*. (2017) 110:072603. doi: 10.1063/1.4976823
30. Körber R. Ultra-sensitive SQUID instrumentation for MEG and NCI by ULF MRI. In: *EMBEC & NBC 2017*. Singapore: Springer Singapore (2017). p. 795–8. doi: 10.1007/978-981-10-5122-7_199
31. Zotev VS, Matlashov AN, Savukov IM, Owens T, Volegov PL, Gomez JJ, et al. SQUID-based microtesla MRI for *in vivo* relaxometry of the human brain. *IEEE Trans Appl Supercond*. (2009) 19:823–6. doi: 10.1109/TASC.2009.2018764
32. Schnabel A, Burghoff M, Hartwig S, Petsche F, Steinhoff U, Drung D, et al. A sensor configuration for a 304 SQUID vector magnetometer. *Neurol Clin Neurophysiol*. (2004) 2004:70.
33. Burghoff M, Albrecht HH, Hartwig S, Hilschenz I, Körber R, Sander Thömmes T, et al. SQUID system for MEG and low field magnetic resonance. *Metrol Meas Syst*. (2009) 16:371–6.
34. Keceli S, Inui K, Okamoto H, Otsuru N, Kakigi R. Auditory sustained field responses to periodic noise. *BMC Neurosci*. (2012) 13:7. doi: 10.1186/1471-2202-13-7
35. Mansfield P. Imaging by nuclear magnetic resonance. *J Phys E Sci Instrum*. (1988) 21:18–30. doi: 10.1088/0022-3735/21/1/002
36. Storm JH, Drung D, Burghoff M, Körber R. A modular, extendible and field-tolerant multichannel vector magnetometer based on current sensor SQUIDs. *Supercond Sci Technol*. (2016) 29:094001. doi: 10.1088/0953-2048/29/9/094001
37. Espy MA, Magnelind PE, Matlashov AN, Newman SG, Sandin HJ, Schultz LJ, et al. Progress toward a deployable SQUID-based ultra-low field MRI system for anatomical imaging. *IEEE Trans Appl Supercond*. (2015) 25:1–5. doi: 10.1109/TASC.2014.2365473
38. Al-Dabbagh E, Storm JH, Körber R. Ultra-sensitive SQUID systems for pulsed fields—degaussing superconducting pick-up coils. *IEEE Trans Appl Supercond*. (2018) 28:1–5. doi: 10.1109/TASC.2018.2797544
39. Matlashov A, Magnelind P, Volegov P, Espy M. Elimination of 1/*f* noise in gradiometers for SQUID-based ultra-low field nuclear magnetic resonance. In: *2015 15th International Superconductive Electronics Conference (ISEC)*. Nagoya (2015). p. 1–3. doi: 10.1109/ISEC.2015.7383455
40. Storm JH, Hömmen P, Höfner N, Körber R. Detection of body noise with an ultra-sensitive SQUID system. *Meas Sci Technol*. (2019) 30:125103. doi: 10.1088/1361-6501/ab3505
41. Körber R, Kieler O, Hömmen P, Höfner N, Storm J. Ultra-sensitive SQUID systems for applications in biomagnetism and ultra-low field MRI. In: *2019 IEEE International Superconductive Electronics Conference (ISEC)*. Riverside, CA (2019). p. 1–3. doi: 10.1109/ISEC46533.2019.8990912
42. Storm JH, Kieler O, Körber R. Towards ultrasensitive SQUIDs based on submicrometer-sized Josephson junctions. *IEEE Trans Appl Supercond*. (2020) 30:1–5. doi: 10.1109/TASC.2020.2989630
43. Gosselin MC, Neufeld E, Moser H, Huber E, Farcito S, Gerber L, et al. Development of a new generation of high-resolution anatomical models for medical device evaluation: the Virtual Population 3.0. *Phys Med Biol*. (2014) 59:5287–303. doi: 10.1088/0031-9155/59/18/5287
44. Iacono MI, Neufeld E, Bonmassar G, Akinnagbe E, Jakab A, Cohen E, et al. A computational model for bipolar deep brain stimulation of the subthalamic nucleus. *Annu Int Conf IEEE Eng Med Biol*. (2014) 2014:6258–61. doi: 10.1109/EMBC.2014.6945059

Conflict of Interest: The authors declare that the research was conducted in the absence of any commercial or financial relationships that could be construed as a potential conflict of interest.

frontiers in Physics

ORIGINAL RESEARCH
published: 15 June 2021
doi: 10.3389/fphy.2021.675509

Dipole-Fed Rectangular Dielectric Resonator Antennas for Magnetic Resonance Imaging at 7 T: The Impact of Quasi-Transverse Electric Modes on Transmit Field Distribution

Daniel Wenz[1,2]* *and Rolf Gruetter*[3]

[1]CIBM Center for Biomedical Imaging, Lausanne, Switzerland, [2]Animal Imaging and Technology, Ecole Polytechnique Federale de Lausanne (EPFL), Lausanne, Switzerland, [3]Laboratory of Functional and Metabolic Imaging (LIFMET), Ecole Polytechnique Federale de Lausanne (EPFL), Lausanne, Switzerland

Shortened dipole antennas based on rectangular dielectric blocks play an important role in ultrahigh field magnetic resonance imaging (UHF-MRI) radio frequency (RF) coil design. However, the generally assumed direct contact with the subject is difficult to maintain in typical *in vivo* settings. We have previously observed that certain dielectrically shortened dipole antennas can produce a substantially altered transmit field distribution with a very low transmit efficiency when the block and the sample are physically separated. Therefore, the aim of this study was to determine a) why certain designs of dielectrically shortened dipole antennas can produce an inefficient transmit field when the block and the sample are physically separated and b) how this depends on key parameters such as rectangular block geometry, dielectric constant, loading geometry, and RF feeding. In this work, two main types of quasi-transverse dielectric modes were found in different rectangular block geometries and interpreted as $TE^{z}_{11\delta}$ (MR efficient) and $TE^{y}_{1\delta\delta}$ (MR inefficient), and their impact on *in vivo* MRI experiments involving the human head, calf, and wrist was explored. This study shows, for the first time, why certain antennas preserve their transmit field efficiency despite physical separation from the sample. We conclude that the proposed approach has the potential to provide new insights into dipole antenna design for UHF-MRI.

Keywords: dielectric resonator antenna, dipole antenna, dielectric mode, radio frequency coil, ultrahigh field magnetic resonance imaging, 7 Tesla

OPEN ACCESS

Edited by:
Elmar Laistler,
Medical University of Vienna, Austria

Reviewed by:
Andrew Webb,
Leiden University, Netherlands
Arthur W. Magill,
German Cancer Research Center (DKFZ), Germany

***Correspondence:**
Daniel Wenz
daniel.wenz@epfl.ch

Specialty section:
This article was submitted to Medical Physics and Imaging, a section of the journal Frontiers in Physics

Received: *03 March 2021*
Accepted: *10 May 2021*
Published: *15 June 2021*

Citation:
Wenz D and Gruetter R (2021) Dipole-Fed Rectangular Dielectric Resonator Antennas for Magnetic Resonance Imaging at 7 T: The Impact of Quasi-Transverse Electric Modes on Transmit Field Distribution. Front. Phys. 9:675509. doi: 10.3389/fphy.2021.675509

1 INTRODUCTION

Ultrahigh field magnetic resonance imaging (UHF-MRI) in humans (magnetic field strength $B_0 \geqq 7$ T) can be challenging due to the short wavelength (about 12 cm) and increased radio frequency (RF) power deposition in the tissue [1]. Multichannel RF coil arrays, which are widely used to address these issues, allow for transmit field (B_1^+) shimming to optimize the B_1^+ homogeneity, thereby providing significant signal-to-noise ratio (SNR) gains and higher acceleration factors in parallel MRI [2–5]. Such multichannel arrays are typically built with loop elements. However, in recent years, it has been shown that dipole antennas can lead to significant B_1^+ efficiency gains in deeper anatomical regions [6–9], and they also support curl-free current patterns that are crucial to

approach the ultimate intrinsic SNR in UHF-MRI [10]. Increasing the number of channels in dipole antenna arrays requires modification to the single dipole antenna element geometry because the length of dipole antennas in free space (~50 cm at 297.2 MHz) is not suitable for most *in vivo* MR applications.

Since the wavelength is inversely proportional to the square root of dielectric permittivity ε_r, one promising approach to shorten dipole antennas is to use a high ε_r medium [6, 11–13]. Unfortunately, the dimensions of dielectric blocks used in previous investigations were rather large, which made it difficult to use them as building blocks in very large dipole antenna arrays (e.g., 32, 64, or 128 elements). Most of the studies followed what Raaijmakers et al. suggested in their study [6], that is, the height should be at least ¼ of wavelength λ. Later, Ipek et al. [14] found that the optimal transmit field efficiency can be achieved for a block with 150 mm × 50 mm × 50 mm and ε_r between 90 and 110. Recently, Eigentler et al. [15] developed a self-grounded bowtie antenna, which was immersed in a small volume filled with deuterium oxide (D_2O), but they used quite a large water bolus to ensure a direct contact with a cuboid phantom.

All these reports [6, 13–15] assumed there was a direct contact between the dielectric block and the human body (or a phantom with a flat surface). Yet, such a contact is rather difficult to achieve for a solid, rectangular geometry, and it may not always be feasible in clinical settings. The curvature of the human head, for example, makes meeting this condition particularly difficult. Therefore, it is reasonable to assume that the dielectric block and various anatomical structures are physically separated. A detailed study, dedicated to this particular, realistic scenario, has not been conducted yet.

In a previous study, we observed that certain types of dielectrically shortened dipole antennas produced an efficient transmit field in the presence of a small air gap, while others did not [16]. We hypothesized that different dielectric modes can be induced within the rectangular block, thereby affecting the antenna performance; if a rectangular dielectric block is sufficiently large, dielectrically shortened dipole antennas can be interpreted as dipole-fed rectangular dielectric resonator antennas. Rectangular dielectric resonator antennas can be characterized by quasi-transverse electric modes [17–20], and UHF-MRI can be an excellent tool to visualize them if water is used as the dielectric medium [21, 22].

Therefore, the aim of this study was to determine: a) why certain dipole-fed dielectric resonator antennas preserve (and others do not) the transmit field distribution and efficiency when the block and the object are physically separated, b) which parameters play a critical role in this context, and c) to what extent different quasi-transverse electric modes can influence *in vivo* human MRI at 7 T.

2 METHODS

Numerical electromagnetic field and specific absorption rate (SAR) simulations were performed using the finite-difference time-domain solver of Sim4Life (Sim4Life, Zurich, Switzerland). Copper elements were modeled as perfect electrical conductors. The excitation signal was of Gaussian type (center frequency = 297.2 MHz and bandwidth = 300 MHz). The grid was manually adjusted for all the components in the simulation. For conductors, dielectric blocks and ports, the smallest mesh cell was 2 mm (1 mm when the effect of the block/phantom physical separation was investigated; 0.2 mm for 0.5 mm gap for $\varepsilon_r = 200$), while for the phantoms it was 4 mm. The RF shield in the magnet and polymethylmethacrylate (PMMA) boxes were not included in the simulations. Two types of phantoms were used in the electromagnetic field simulations: a spherical one, which mimics the human head (radius = 85 mm, $\varepsilon_r = 50.6$, $\sigma = 0.66$ S/m), and a cuboid one (300 mm × 300 mm × 300 mm, $\varepsilon_r = 34$, $\sigma = 0.47$ S/m), which is more relevant for body applications, with dimensions identical to those used in previous studies [6, 13]. Moreover, both phantoms represent two different levels of curvature: a flat (cuboid) and a rounded one (spherical). For all the elements in the work, we used the transmit field efficiency defined as $B_1^+/\sqrt{P}$, where P is the input power, and the SAR efficiency defined as $B_1^+/\sqrt{SAR_{10g}}$, where SAR_{10g} is the maximum SAR averaged over 10*g*. The simulation results obtained using Sim4Life were normalized to 1 W input power.

The transmit field distribution within the spherical phantom was studied for different rectangular block geometries and different values of dielectric permittivity (ε_r = 35, 50, 80, 100, 150, 200, 300, and 500), assuming a 5-mm air gap between the block and the phantom. A constant conductivity value, close to

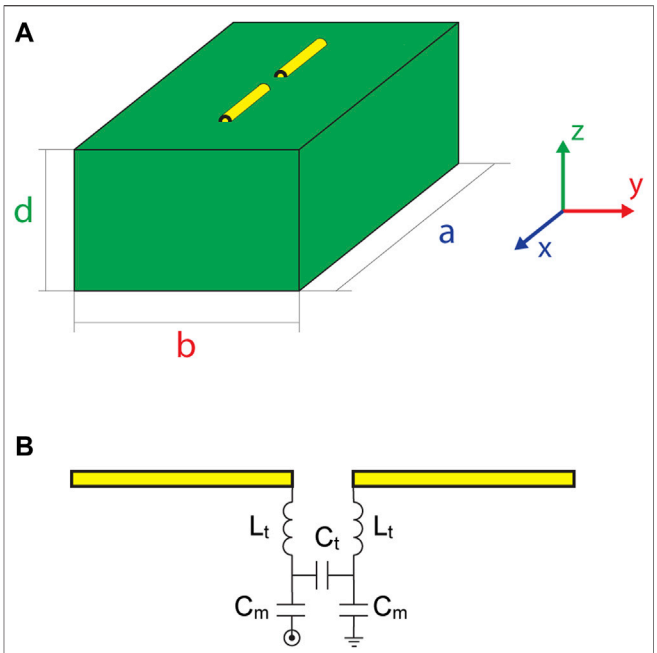

FIGURE 1 | (A) The frame of reference used to calculate the cutoff frequency and to determine the type of the dielectric mode that propagates across dielectric blocks. The following transformation from this system to the system of coordinates in MRI environment would have to be made: x = z, y = x, z = y). **(B)** Matching network diagram.

TABLE 1 | The dimensions of rectangular blocks (in millimeters) used in simulations from **Figure 2**. The dimension *a* (a_0) was constant for each ε_r value: 35 (242 mm), 50 (202 mm), 80 (160 mm), 100 (144 mm), 150 (118 mm), 200 (102 mm), 300 (84 mm), and 500 (64 mm). Four variations of *b* (b_0, 0.75, 0.5b_0, and 0.25b_0) and for each *b* four *d*/*b* (0.75, 0.5, 0.25, and 0.125) ratios were investigated.

b	*d*/*b*	Dielectric permittivity ε_r							
		35	**50**	**80**	**100**	**150**	**200**	**300**	**500**
$b = b_0$	0.75	121/90.7	101/75.7	80/60	72/54	59/44.25	51/38.2	42/31.5	32/24
	0.5	121/60.5	101/50.5	80/40	72/36	59/29.5	51/25.5	42/21	32/16
	0.25	121/30.2	101/25.2	80/20	72/18	59/14.75	51/12.7	42/10.5	32/8
	0.125	121/15.1	101/12.1	80/10	72/9	59/7.37	51/6.3	42/5.25	32/4
$b = 0.75b_0$	0.75	90.7/68	75.7/56.8	60/45	54/40.5	44.2/33.1	38.2/28.6	31.5/23.6	24/18
	0.5	90.7/45.3	75.7/37.5	60/30	54/27	44.2/22.1	38.2/19.1	31.5/5.7	24/12
	0.25	90.7/22.6	75.7/18.75	60/15	54/13.5	44..2/11	38.2/9.5	31.5/7.87	24/6
	0.125	90.7/11.3	75.7/9.3	60/7.5	54/6.75	44.2/5.5	38.2/4.7	31.5/3.93	24/3
$b = 0.5b_0$	0.75	60.5/45.3	50.5/37.8	40/30	36/27	29.5/22.1	25.5/19.1	21/15.7	16/12
	0.5	60.5/30.2	50.5/25.2	40/20	36/18	29.5/14.7	25.5/12.7	21/10.5	16/8
	0.25	60.5/15.1	50.5/12.6	40/10	36/9	29.5/7.3	25.5/6.3	21/5.2	16/4
	0.125	60.5/7.5	50.5/6.3	40/5	36/4.5	29.5/3.6	25.5/3.1	21/2.6	16/2
$b = 0.25b_0$	0.75	30.2/22.6	25.25/18.9	20/15	18/13.5	14.7/11	12.7/9.5	10.5/7.8	8/6
	0.5	30.2/15.1	25.25/12.6	20/10	18/9	14.7/7.3	12.7/6.3	10.5/5.2	8/4
	0.25	30.2/7.5	25.25/6.3	20/5	18/4.5	14.7/3.6	12.7/3.1	10.5/2.6	8/2
	0.125	30.2/3.7	25.25/3.1	20/2.5	18/2.25	14.7/1.8	12.7/1.6	10.5/1.3	8/1

the one for D_2O ($\sigma = 0.065$ S/m) [11], was used for all the blocks explored in this work. To identify the dielectric modes excited in a dipole-fed rectangular antenna, we used a coordinate system consistent with the commonly used convention (**Figure 1**). Note that in this work, we refer to the frame of reference from **Figure 1** and not to the one typically used in MRI. Converting from the antenna frame of reference to the one for MRI requires the following transformation: x→z, y→x, and z→y.

Each dielectric mode was described by three subscripts: *m*, *n*, and *l*. Additionally, one superscript (x, y, or z) was used to indicate the direction of propagation for a given quasi-transverse electric (TE) mode. The fraction δ means that the given index was equal to 0 (see [19]). The geometry of each rectangular block and each ε_r value was determined as follows: first, we found the dimensions of the smallest possible square geometry for which the $TE_{11\delta}$ mode was allowed to propagate according to the following formula [19]:

$$f_{cutoff} = \frac{c}{2\pi\sqrt{\epsilon_r}}\sqrt{\left(\frac{\pi m}{a}\right)^2 + \left(\frac{\pi n}{b}\right)^2 + \left(\frac{\pi l}{d}\right)^2} \quad (1)$$

where *c* is the velocity of light; *m*, *n*, and *l* are the dielectric mode indices (δ means that there is a fraction of a field half-cycle in the given direction); and *a*, *b*, and *d* are the block dimensions according to the coordinate system in **Figure 1**. For instance, to calculate the cutoff frequency using **Eq. 1** for $TE_{11\delta}$ and $TE_{1\delta\delta}$ modes, the indices *mln* would be defined as 110 and 100, respectively. Note that if $l = 0$ (or if $l = 0$ and $n = 0$), Eq. 1 corresponds to the calculation of waveguide modes TE_{11} (or TE_{10}) rather than the 3D resonance TE_{111}. Next, dimension *a*, which was critical to ensure that $TE_{11\delta}$ was allowed to propagate, was multiplied by a factor of 2. By doing so, we obtained initial values of *a* and *b* (a_0 and b_0), which were different for each ε_r (**Table 1**). The dimension *a* (a_0) was constant for each ε_r value: 35 (242 mm), 50 (202 mm), 80 (160 mm), 100 (144 mm), 150 (118 mm), 200 (102 mm), 300 (84 mm), and 500 (64 mm). Then, dimension *b* was varied as follows: b_0, 0.75b_0, 0.5b_0, and 0.25b_0. For these dimensions of *b*, we investigated the following *d*/*b* ratios: $d/b = 1$, 0.75, 0.25, and 0.125. According to **Eq. 1**, for $b = b_0$ and $b = 0.75b_0$, the cutoff frequency for $TE_{21\delta}$ was lower than the resonance frequency. However, the $TE_{21\delta}$ mode was not observed in any of the investigated blocks regardless of the ε_r value. For each ε_r value, the relative wavelength was calculated $\left(\lambda_r \sim {}^1/_{\sqrt{\varepsilon_r}}\right)$, and the length of each dipole antenna was accordingly chosen: 42, 35, 28, 25, 20, 18, 14, 11, and 8 mm per dipole arm (5-mm distance between both arms) for $\varepsilon_{r\ \text{from 35}}$ to 500. Half of the dipole antenna (copper wire, radius = 1 mm) was immersed in the dielectric medium, while the other half was in contact with air (**Figure 1**). Each antenna was tuned to 297.2 MHz and matched to 50 Ω using an LCC tuning/matching network (L-series, C-parallel, C-series).

The transmit field efficiency in the spherical phantom could not be compared between all the blocks from **Table 1** in a fair manner because higher ε_r values resulted in smaller blocks and shorter dipole antennas. For this purpose, a constant block geometry ($a = 160$ mm, $b = 60$ mm, and $d = 7.5$ mm) and dipole antenna length (28 mm per arm) was defined for all analyzed ε_r values. The dimensions were chosen so that such a block could be used as one of the elements in a close-fitting 8-channel transmit/receive array for brain imaging [11].

The effect of an air gap on the transmit field distribution in a cuboid phantom was studied for one larger block (0.75b_0, $d/b = 0.75$) for each ε_r value. The cuboid phantom was chosen for this purpose because it provided good coupling (flat surface) to the rectangular dielectric block; the transmit field distribution in the cuboid phantom was also benchmarked against the results obtained for the spherical phantom (rounded surface). Five different air gaps were studied: 1, 2, 3, 4, and

5 mm for all ε_r values. These simulations were extended by investigating the y-component of the magnetic field $\vec{H}$ (H_y) for one larger air gap (20 mm) for two low-ε_r blocks (35, 50) and one smaller air gap (0.5 mm) for one high-ε_r block (200). These results were compared to the ones obtained for the spherical phantom (5-mm air gap). The reason why the H-field was considered instead of the B-field was to refer to the previous study conducted by Ipek et al. [14], which focused on the case when there is a perfect direct contact between the block and a large cuboid phantom.

Plane wave simulations were conducted for six different wave number and electric field vector configurations with the following parameters: number of mesh cells = 681,000, excitation signal = Gaussian, center frequency = 297.2 MHz, and bandwidth = 300 MHz, amplitude = 1 V. The dielectric block (160 mm × 70 mm × 52.5 mm) was defined as the wave source according to the approach provided by Sim4Life, which is based on total-field/scattered-field (TF/SF) formulation (also called the plane-wave injector). In this method, only a certain region of the calculation domain, the total field region (the dielectric block in our case), propagates the plane wave.

Two dielectrically shortened dipole antennas (ε_r = 80) were designed, built, and evaluated in MR experiments: 160 mm × 70 mm × 52.5 mm ($0.75b_0$, d/b = 0.75) and 160 mm × 70 mm × 17.5 mm ($0.75b_0$, d/b = 0.25). The prototypes were built of a PMMA shell (wall thickness = 3 mm). The geometries were chosen so that different dielectric modes can be excited within the blocks. The reason for using ε_r = 80 was that water has an ε_r value close to 80 at 297.2 MHz. Water is readily available and easily imaged by MRI [22]. To visualize the dielectric modes within the different block geometries, deionized water was used, and the dipole antenna was tuned to 297.2 MHz and matched to 50 Ω.

MR experiments were conducted with a 7.0-T 68-cm bore scanner (Magnetom, Siemens Healthineers, Erlangen, Germany). A shielded cable trap, consisting of a capacitor soldered to the shield of the coaxial cable, was connected to each element and used in every experiment. MRI experiments were performed in one male subject (age = 29 years, BMI = 28.5 kg/m^2), who had signed written consent approved by the local ethics committee, in three different regions of interest: head, calf, and wrist. It was not feasible to conduct additional experiments for other anatomical structures because the scanner used is dedicated to the human head. The goal was to investigate how different dielectric modes could propagate across various anatomical structures (with different loading geometries), given our prior knowledge on the differences between cuboid and spherical phantoms [16]. To visualize the magnetic field distribution within both blocks, standard gradient echo (GRE) imaging was used with the following parameters: repetition time (TR) = 8.6 ms, echo time (TE) = 4.0 ms, field of view (FOV) = 250 × 250 mm^2, slice thickness = 7.0 mm, number of averages = 2, FA = 15°, and reference transmit voltage = 5 V. For *in vivo* experiments, deionized water, which produced a very-high-intensity signal, compromising the *in vivo* image quality, was replaced by heavy water (D_2O, Sigma Aldrich, Germany), and a 2-mm acrylonitrile butadiene styrene board was placed between the block and the subject. *In vivo* images were acquired by 3D-GRE imaging with the following parameters: TR/TE = 6.5/2.82 ms, FOV = 256 × 240 mm^2, slice thickness = 1.0 mm, number of averages = 1, FA = 4°, and reference transmit voltage = 100 V. The acquisition parameters of the RF pulse sequence were used to scan each body part.

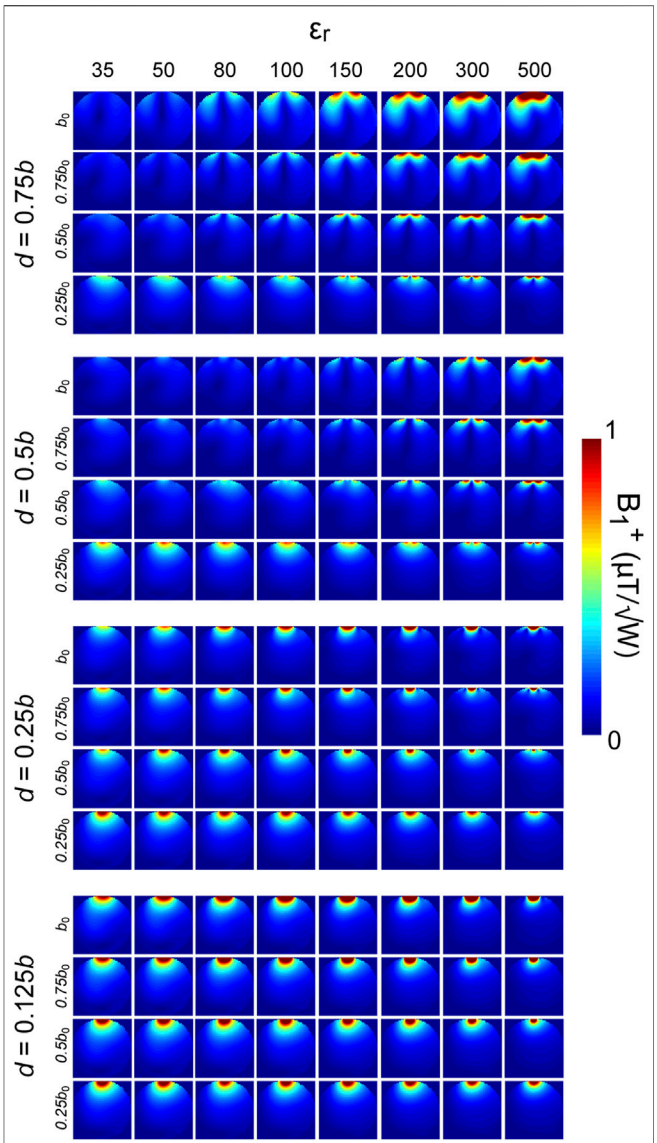

FIGURE 2 | Transmit field distribution in the spherical phantom for various geometries (**Table 1**) of dipole-fed rectangular dielectric resonator antennas and dielectric permittivity ε_r (35, 50, 80, 100, 150, 200, 300, and 500). The distance between the bottom of the block and the phantom was 5 mm. Each column depicts different ε_r values. The figure was divided into four groups (starting from the top): d/b = 0.75, 0.5, 0.25, and 0.125. Each group consists of four rows: $b = b_0$, $0.75b_0$, $0.5b_0$, and $0.25b_0$. Substantial differences in the transmit field pattern and efficiency can be observed between different geometries for a given ε_r, as well as for the same $a/b/d$ ratio, but different ε_r values.

TABLE 2 | Maximum local SAR_{10g} values in W/kg provided for the simulations from **Figure 2**. The exact dimensions of the blocks can be found in **Table 1**. In general, for lower b values ($0.5b_0$ and $0.25b_0$), the thicker blocks yielded lower was the SAR_{10g} than their thinner counterparts. This trend changed for d/b = 0.75 for higher-ε_r blocks (300 and 500). For $b = b_0$, SAR_{10g} values for higher-ε_r blocks (200, 300, and 500) were found to be significantly higher for d/b = 0.75 than for d/b = 0.125.

b	d/b	Dielectric permittivity ε_r							
		35	50	80	100	150	200	300	500
$b = b_0$	0.75	0.04	0.07	0.21	0.34	0.71	1.12	1.85	3.07
	0.5	0.05	0.05	0.06	0.07	0.12	0.22	0.44	1.02
	0.25	0.23	0.27	0.32	0.33	0.61	0.33	0.33	0.37
	0.125	0.55	0.68	0.85	0.91	0.94	0.98	0.93	0.73
$b = 0.75b_0$	0.75	0.04	0.05	0.12	0.19	0.39	0.65	1.11	2.09
	0.5	0.07	0.08	0.10	0.11	0.17	0.27	0.46	0.93
	0.25	0.29	0.34	0.40	0.41	0.42	0.46	0.48	0.59
	0.125	0.64	0.76	0.90	0.93	0.96	1.03	1.01	1.17
$b = 0.5b_0$	0.75	0.08	0.09	0.15	0.20	0.33	0.50	0.76	1.29
	0.5	0.17	0.18	0.23	0.26	0.33	0.43	0.57	0.86
	0.25	0.31	0.52	0.63	0.65	0.72	0.79	0.83	0.95
	0.125	0.78	0.90	1.07	1.11	1.21	1.31	1.35	1.31
$b = 0.25b_0$	0.75	0.28	0.35	0.45	0.48	0.56	0.64	0.73	0.86
	0.5	0.46	0.54	0.67	0.70	0.78	0.84	0.87	0.95
	0.25	0.79	0.91	1.06	1.09	1.18	1.25	1.27	1.18
	0.125	1.18	1.26	1.47	1.61	1.99	2.12	2.09	2.55

3 RESULTS

To determine the effect of block geometry and dielectric permittivity on the transmit field distribution and efficiency within the spherical phantom, electromagnetic field simulations were performed (**Figure 2**). The transmit field distribution within the spherical phantom for $d = 0.125b$ was the most consistent regardless of the combination of b/b_0 and ε_r. Moreover, $d = 0.125b$ (for $b = 0.5b_0$ and $b = 0.75b_0$) resulted in the highest transmit field efficiency in the center of the phantom for all ε_r values. The most apparent change in the transmit field distribution (two-side lobes and almost no transmit field along the z-axis) and decrease in the transmit field efficiency was observed for $d = 0.75b$ ($b = b_0$, $b = 0.75b_0$, and $b = 0.5b_0$) for all ε_r values (**Figure 2**). For $d = 0.75b$ ($b = 0.25b_0$), that effect was still present, but for the higher-ε_r blocks ($\varepsilon_r \geq 200$). A similar change in the transmit field pattern as for $d = 0.75b$ was also observed for thinner blocks with $d = 0.5b$. This was especially prominent for higher ε_r ($\varepsilon_r \geq 150$). Local SAR_{10g} values for each block are summarized in **Table 2**. Higher d/b ratios yielded lower SAR_{10g} values for narrower blocks ($b = 0.25b_0$ and $b = 0.5b_0$), excluding d/b = 0.75, for the highest-εr values ($\varepsilon_r \geq 200$). For wider blocks ($b = 0.75b_0$ and $b = b_0$), SAR_{10g} was the highest for the thickest blocks (d/b = 0.75) excluding the lowest-ε_r values, 35 and 50 (the latter only for d/b = 0.5).

To determine which ε_r provided the highest transmit field and SAR in the center of the spherical phantom, electromagnetic field simulations were performed using a constant block geometry and dipole antenna length (**Figure 3**). The electric field distribution was found to depend on ε_r of the block (**Figure 3**), and it was significantly different for higher-ε_r blocks ($\varepsilon_r \geq 200$). The highest transmit field efficiency in the center of the phantom was obtained with ε_r = 300 (0.21 $\mu T/\sqrt{W}$) and ε_r = 200 (0.197 $\mu T/\sqrt{W}$), but at the cost of reduced SAR efficiency (0.103 $\mu T/\sqrt{W/kg}$ and 0.126 $\mu T/\sqrt{W/kg}$). The highest SAR efficiency in the center was obtained with lower ε_r values: 0.149 $\mu T/\sqrt{W/kg}$ for ε_r = 80, and 0.148 $\mu T/\sqrt{W/kg}$ for ε_r = 50. The transmit efficiency (center of the phantom) with ε_r = 300 was higher by 33%, and the SAR efficiency was lower by 31% than with ε_r = 80. The transmit efficiency (center of the phantom) with ε_r = 200 was higher by 29%, and the SAR efficiency was lower by 15.5% than with ε_r = 80.

To investigate how physical separation between the dielectric block and the cuboid phantom can influence the transmit field pattern and efficiency, an air gap (1–5 mm) between the block and the phantom was assumed for one block geometry ($b = 0.75b_0$, $d = 0.75b$) for all ε_r (**Figure 4**). The larger block was chosen because it produced a highly inefficient transmit field in the spherical phantom (**Figure 2**, second row). It was found for lower ε_r values (35 and 50) that, despite the air gap, the transmit field pattern was very similar to the one obtained with a direct contact between the block and the cuboid phantom, albeit with slightly lower efficiency. For higher ε_r values ($\varepsilon_r \geq 80$), a significant difference in the transmit field pattern and efficiency could be observed. For ε_r = 80, the effect was present with a 3-mm air gap, while for higher ε_r values ($\varepsilon_r \geq 200$), a 1-mm air gap was already sufficient, and the observed effect was much more prominent.

The impact of block/phantom physical separation and phantom geometry was further investigated by simulating the y-component of the magnetic field (H_y). Increasing the distance between the phantom and the block by 20 mm for the two lower-ε_r (35, 50) blocks resulted in H_y being mostly contained within the blocks (**Figure 5A**). For higher ε_r (200), the effect was already prominent with a 0.5-mm air gap, showing that the distance between the block and the phantom for the given ε_r value significantly influenced the transmit field distribution. The results were compared to those obtained previously for the spherical phantom (5-mm air gap; **Figure 5B**): H_y was mostly contained within the low-ε_r blocks (ε_r = 35 and 50) for the spherical phantom, while for the cuboid phantom, H_y propagated toward the phantom despite the 5-mm air gap.

To investigate the transmit field distribution within different rectangular block geometries, PMMA boxes were filled with deionized water and imaged by gradient-recalled echo at low-flip angles. Based on the analysis of the simulated transmit field patterns and MR experiments (**Figure 6**), we interpreted the mode excited in the larger block ($d = 0.75b$) as $TE^{y}_{1\delta\delta}$. Using the same approach, we identified the mode in the smaller block ($d = 0.25b$). Our results indicated that two modes ($TE^{z}_{11\delta}$ and $TE^{y}_{1\delta\delta}$) were adjacent to each other and could be switched by changing the ratio of the block dimensions (d in this case).

To understand the impact on an MRI experiment of the different dielectric modes that can be excited by a dielectrically shortened dipole antenna, *in vivo* studies were performed with one male subject. Two block geometries were investigated: $d = 0.25b$, $d = 0.75b$. *In vivo* images of the head, calf, and wrist were obtained (**Figure 7**).

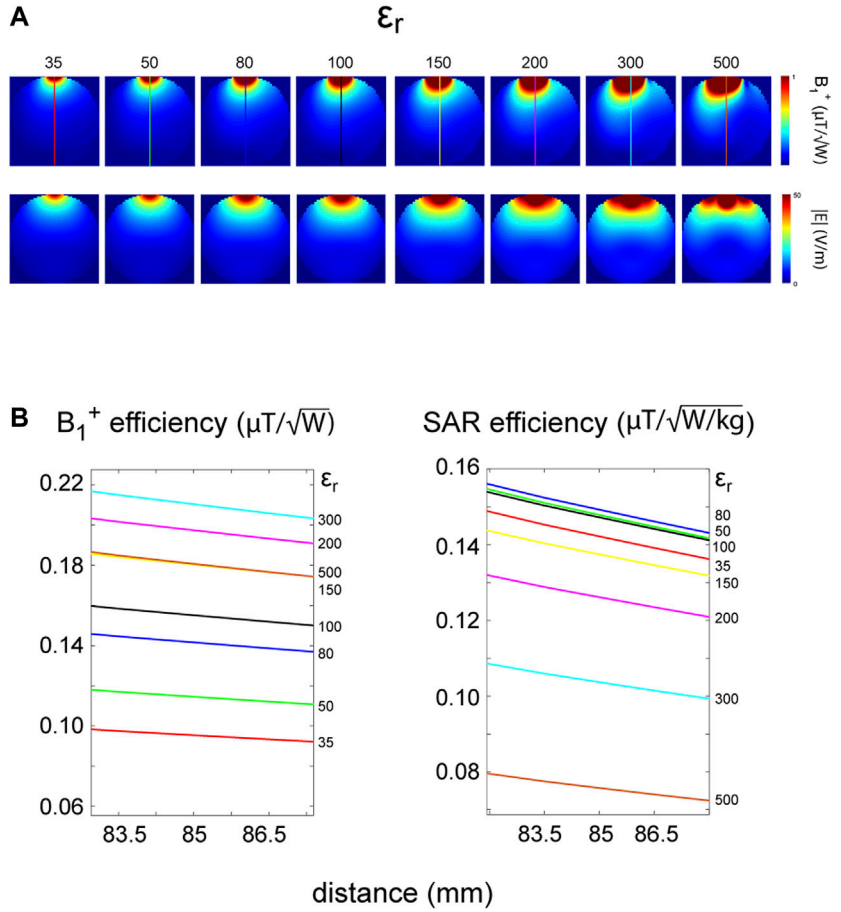

FIGURE 3 | (A) Transmit field and electric field distribution within the spherical phantom for the constant block geometry (160 mm × 60 mm × 7.5 mm) and dipole antenna length as a function of dielectric permittivity ε_r (35, 50, 80, 100, 150, 200, 300, and 500). The air gap was 5 mm. **(B)** Transmit and SAR efficiency as functions of distance. The plots were zoomed in (85 mm on the *x*-axis corresponds to the center of the phantom) to better distinguish the differences between the blocks. The highest transmit field efficiency in the center of the phantom was obtained for ε_r = 300 (0.210 μT/√W) and ε_r = 200 (0.197 μT/√W) but at the cost of a reduced SAR efficiency (0.103 and 0.126 μT/√W/kg). The highest SAR efficiency in the center was obtained for lower ε_r values: 0.149 μT/√W/kg for ε_r = 80 and 0.148 μT/√W/kg for ε_r = 50. Note that in higher-ε_r blocks (300, 500), a higher-order mode ($TE^z_{12\delta}$) was excited.

The thinner block provided highly superior image quality for all tissues compared to its thicker counterpart, which yielded very noisy images (very low to no SNR) for the brain, calf, and wrist. However, qualitative differences were apparent among the images obtained using the larger block, and the best image quality was obtained with the wrist, which provided a flatter surface. Significantly, lower image quality was noted for the calf while the lowest was for the head, the body part with the highest level of curvature in this study.

To determine whether the larger block (160 mm × 70 mm × 52.5 mm) could still be used as an efficient RF antenna, plane-wave simulations for six different orientations of the magnetic field vector $\vec{H}$, the electric field vector $\vec{E}$, and the wave number vector $\vec{k}$ were performed (**Figure 8**). Different mutual orientations of these three vectors led to different magnetic field patterns in the spherical phantom. The mutual orientation of $\vec{H}$ and $\vec{E}$: E_z-k_x was consistent with dipole excitation and yielded a transmit field pattern similar to that in **Figure 2**. There were also other excitation schemes (E_y-k_x, E_x-k_y, and E_x-k_z) that, unlike E_z-k_x, provided efficient magnetic field in the spherical phantom.

4 DISCUSSION

This study demonstrates for the first time why certain dipole-fed rectangular dielectric resonator antennas for MRI at 7 T can preserve (and others do not) the transmit field distribution and efficiency when the dielectric block and the sample are physically separated. We showed that different types of quasi-transverse electric modes, which were induced in the analyzed block geometries by dipole antennas, played the most critical role in this context: $TE^z_{11\delta}$ and $TE^y_{1\delta\delta}$. The approach used in this study constitutes an important extension of prior work [14], which focused on the analysis of the special case where there is a direct contact between a rectangular block and a large cuboid phantom: first, such a condition may not always be realistic: for example, human heads and other body parts have different curvatures, and

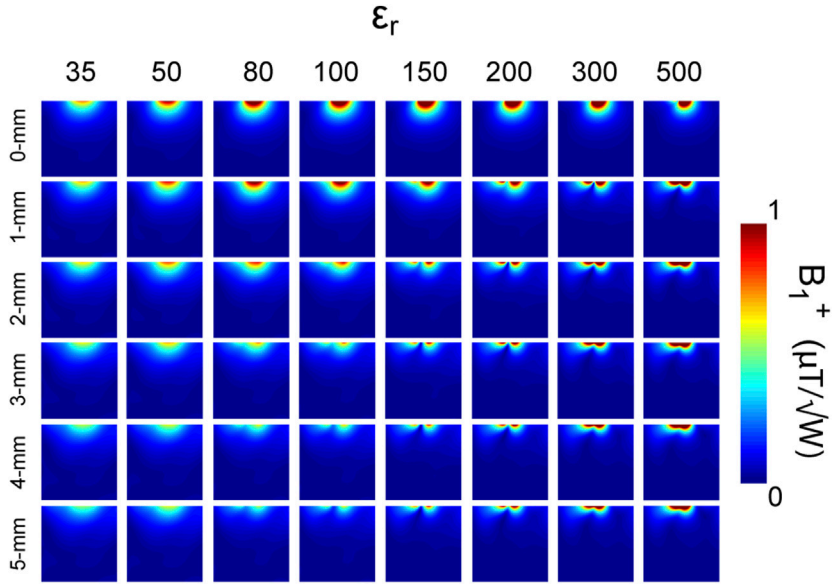

FIGURE 4 | Transmit field distribution in the cuboid phantom as a function of dielectric permittivity of the block and the block/phantom physical separation. The geometry of one of the larger blocks was chosen ($b = 0.75b_0$, $d/b = 0.75$—**Table 1**). The effect of five different sizes of an air gap (1, 2, 3, 4, and 5 mm) was investigated for all ε_r values (35, 50, 80, 100, 150, 200, 300, and 500). No significant change was noted in the transmit field pattern for lower ε_r values (35, 50) when the antenna was moved 5 mm away from the phantom. The transmit field changed significantly for higher ε_r values. The higher the ε_r value of the block, the lower the "threshold" size of the air gap, for which the transmit field pattern changed along with a decreased efficiency.

therefore, a perfect direct contact between the body and a rectangular block is difficult, if not impossible, to achieve in general. Thus, instead of assuming a perfect contact between the dielectric block and phantom, the presence of air gaps is a more realistic consideration.

By using the term "quasi-*TE* modes", we have referred to Pan et al. [20], who reported on a negligibly weak E-field component which can be observed in the direction of propagation for *TE* modes in rectangular dielectric resonator antennas. Moreover, the prefix "quasi" refers to a larger group of rectangular geometries which were studied in this work but not optimized to excite "pure" *TE* modes. In such cases, a nonzero E-field component in the direction of propagation may be observed. The same applies to the distinction between $TE^z_{11\delta}$ and $TE^y_{1\delta\delta}$ modes. These modes can be identified based on the electromagnetic field patterns within a dielectric block (in principle, simulated vector fields are preferable to discern the intricacies between different geometries). To determine m, we looked into the magnetic field variation along the x-axis (**Figure 6**, coronal slice), and we found that a full-field maximum is contained within the block (indicating a sharp change in the magnetic field direction at the dielectric boundaries along the x-axis), yielding $m = 1$ for both blocks. To find n, we looked at the magnetic field variation along the y-axis (**Figure 6**, coronal slice). In the case of the $TE^z_{11\delta}$ mode, the field maximum was fully contained within the thinner block, that is, there was a sharp change in the magnetic field direction at the block boundaries along the y-axis. This resulted in no magnetic field leaking through the dielectric boundaries along the y-axis, and the field decreased to nearly zero at the edge of the block, resulting in $n = 1$. In this case, the magnetic field propagates along the z-axis through the dielectric wall, and the upper index z was used to better describe this mode. By increasing the dimension d of the block, decreased magnetic field variation along the y-axis can be observed, due to an increased contribution of the $TE^y_{10\delta}$ mode ($n = 0$ stands for no magnetic field variation in the y-direction), and a similar magnetic field pattern is found in rectangular waveguides for the TE_{10} mode. In the case of the $TE^y_{10\delta}$ mode, the magnetic field is not contained within the block along the y-axis, that is, there is no change of magnetic field direction at the boundaries, and the magnetic field leaks through the dielectric walls in both directions along the y-axis and propagates down toward the sample. The upper index y therefore serves to indicate the change in the direction of magnetic field propagation for thicker blocks. This change of magnetic field pattern between thinner block and its thicker counterpart is similar to the transition between TE_{11} and TE_{10} in rectangular waveguides (see the subchapter "Rectangular waveguide" in "Transmission lines and waveguides" in Pozar's [19] book). In this work, different, semi-arbitrarily chosen rectangular geometries were analyzed, and $TE^y_{10\delta}$ is considered to be a subcomponent of a larger group of $TE^y_{1\delta\delta}$ modes. We have introduced index δ to indicate that certain modes have insufficient purity to be interpreted as $TE^y_{10\delta}$ and contributions from both modes $TE^z_{11\delta}$ and $TE^y_{10\delta}$ can be very apparent (see **Figure 1**). None of the blocks analyzed in this study had index l equal to 1; however, it is clear (**Figure 6**, axial slice) that a fraction of magnetic field variation can be observed along the z-axis for both blocks, and we therefore assigned $l = \delta$ for both blocks.

Dipole-fed rectangular dielectric resonator antennas, in which the $TE^z_{11\delta}$ mode was excited, preserved their transmit field distribution and efficiency regardless of (a) any block/sample physical separation and (b) any level of curvature of the sample (for both phantom and

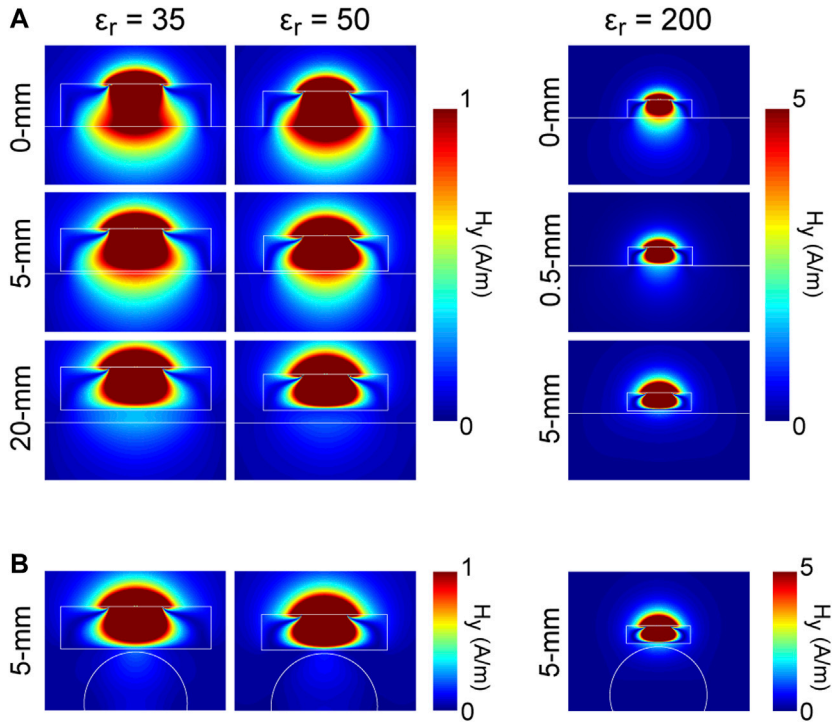

FIGURE 5 | (A) The distribution of the y-component (in x–z plane) of the magnetic field (H_y) as a function of dielectric permittivity, phantom geometry, and block/phantom physical separation. White lines depict the boundaries of the blocks and the phantoms. For the direct contact case (cuboid phantom) as well as for smaller air gap (5-mm), H_y for lower-ε_r blocks (35, 50) coupled well to the phantom enabling the propagation of H-field in the z-direction. For the cuboid phantom (20-mm air gap) and lower-ε_r blocks, H_y was mostly confined within the blocks, especially for $\varepsilon_r = 50$. In the case of $\varepsilon_r = 200$, a similar effect was observed even with a 0.5-mm air gap. **(B)** H_y distribution in the cuboid phantom (5-mm air gap) was benchmarked against H_y distribution in the spherical phantom (5-mm air gap). The results showed that H_y distribution within the block (and therefore the transmit field efficiency) was significantly dependent on the loading geometry.

in vivo experiments). Rectangular dielectric resonator antennas, in which the $TE^y_{1\delta\delta}$ mode was induced, performed poorly when the block was separated from the sample: a significantly altered transmit field distribution and low efficiency was observed. When $TE^y_{1\delta\delta}$ was excited, there were two general cases in which it produced an efficient transmit field: (a) a direct contact with the cuboid phantom (flat surface) regardless of the ε_r value of the block and (b) a fairly small block/phantom separation but only for low-ε_r blocks (35, 50). Here, condition (b) remains valid as long as the surface of the sample is flat: the resulting transmit field will be a function of the level of curvature of the sample, and it can substantially change when the surface approaches a rounded one (**Figure 5B**). *In vivo* experiments showed that the $TE^y_{1\delta\delta}$ mode, unlike $TE^z_{11\delta}$, led to substantially degraded image quality, highlighting the influence of dielectric block geometry and propagation of dielectric modes on the performance of dielectrically shortened dipole antennas. Further discussion on how different parameters can influence the antenna performance is given below.

The propagation of quasi-transverse dielectric modes depends mainly on the ratio of the block dimensions (**Figure 1**): a, b, and d (if the feeding type did not change; **Figure 2**) and on the feeding type (if the dimensions were constant; **Figure 8**). Our results show that when d was sufficiently smaller than b, a quasi-TE^z mode was expected to propagate. However, when dimension d approaches b (even for $d = 0.5b$), the dominant mode shifts toward a quasi-TE^y mode (**Figure 2**). The main dielectric modes observed in our experiments were interpreted as $TE^z_{11\delta}$ (MR efficient) and $TE^y_{1\delta\delta}$ (MR inefficient; **Figure 6**). There was a striking difference in performance between these modes, which had a major impact on *in vivo* experiments (**Figure 7**). This observation differs from the work of Ipek et al. [14], who reported only one type of mode ($TE^y_{1\delta1}$): this was possible due to the substantially different boundary conditions (perfect direct contact between the block and the cuboid phantom) in their experiments, leading to the situation in which electromagnetic wave is guided across different dielectric media (no high-/low-ε_r interface and less reflection). However, for the geometries studied here, $TE^y_{1\delta1}$ was not allowed to propagate (only for the geometries with $d/b = 0.75$, the cutoff frequency was very close to 297.2 MHz (see **Eq. 1**).

We found that a relatively small d/b ratio ($d = 0.5b$ and $d = 0.75b$; for $\varepsilon_r = 500$ even when $d = 0.25b$) results in an inefficient transmit field in the spherical phantom (**Figure 2**): high-ε_r blocks ($\varepsilon_r \geq 200$) can produce an inefficient transmit field for much smaller d/b ratios than low-ε_r blocks (35, 50). This indicates that $TE^y_{1\delta\delta}$ can be excited using smaller $a/b/d$ ratios with higher ε_r values, and block dimensions optimized for low ε_r values should not be linearly scaled for high-ε_r blocks because an inefficient dielectric mode can become more prominent, compromising the antenna performance. Using very "thin" blocks ($d = 0.125b$) can be advantageous in the context of

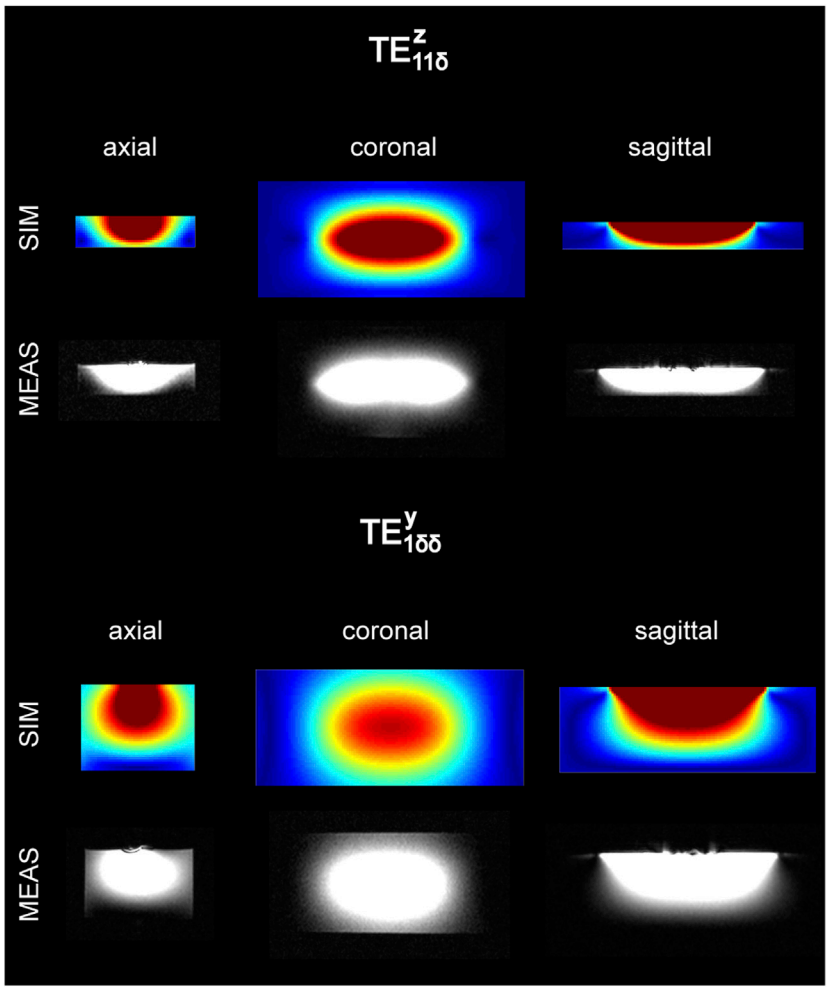

FIGURE 6 | Visualization of dielectric modes: the comparison between the electromagnetic field simulations and magnetic resonance measurements for two elements: thinner one ($d = 0.25b$) and thicker one ($d = 0.75b$). The polymethylmethacrylate boxes were filled with deionized water, and their volumes were matched to the dimensions of the dielectric blocks described in the Methods section. Low-flip-angle gradient echo imaging was used. The simulations are in an excellent agreement with the measurements and show significantly different magnetic field distribution between the blocks. The mode that propagates within the thinner block was interpreted as $TE^{z}_{11\delta}$ and within the thicker one as $TE^{y}_{1\delta\delta}$. SIM stands for "Simulation" and MEAS for "Measurement".

transmit efficiency (**Figure 2**) in contrast to the previous report in which $d = b$ for the case of a direct contact between the block and the cuboid phantom [14]. This is possible because the dimension d does not play a key role in excitation of the $TE^{z}_{11\delta}$ mode and can be significantly reduced. This finding can have important practical implication due to substantial space constraints within the MRI scanner bore and the general need for the "miniaturization" of dielectric blocks.

Note, however, that decreasing d can result in needing larger inductors to tune the antenna, which has an impact on the transmit field efficiency. Thinner blocks are also expected to yield higher SAR values than their thicker counterparts, excluding the wider blocks with $b = b_0$ and $b = 0.75b_0$, especially for higher ε_r values ($\varepsilon_r \geq 200$). Therefore, certain tradeoffs would have to be considered and accepted depending on the application. If the block dimension d is properly chosen for a given a and b, the latter two play the key role in overall antenna performance. With $d = 0.125b$, the most efficient transmit field was observed with $b = 0.5b_0$ and $b = 0.75b_0$ (for $d = 0.125b$) for all ε_r values. The transmit field efficiency for $b = 0.5b_0$ was slightly higher (~2.5%) than $b = 0.75b_0$. However, on average, 20% higher inductance was needed to tune the antennas with $b = 0.5b_0$. Losses associated with higher inductance were not included in the simulations, and they are expected to affect the transmit field efficiency. Moreover, the SAR efficiency for $b = 0.5b_0$ was ~7.2% lower than that for $b = 0.75b_0$. Interestingly, according to **Eq. 1**, the cutoff frequency for the $TE^{z}_{11\delta}$ mode was almost identical to the resonance frequency of protons at 7.0 T for blocks with $0.75b_0$.

Transmit field patterns for $d = 0.75b$ (**Figure 2**) should not be confused with the pattern that would be expected for a standalone loop coil at 297.2 MHz. A transmit field pattern similar to the one for the loop coil can be obtained by replacing the dipole-with a loop-type excitation (see E_y-k_x excitation from **Figure 8**). Note that for the ratio $d = 0.75b$, the TE^{z} mode turns into the TE^{y} mode. The upper index indicates that the magnetic field propagates across the dielectric

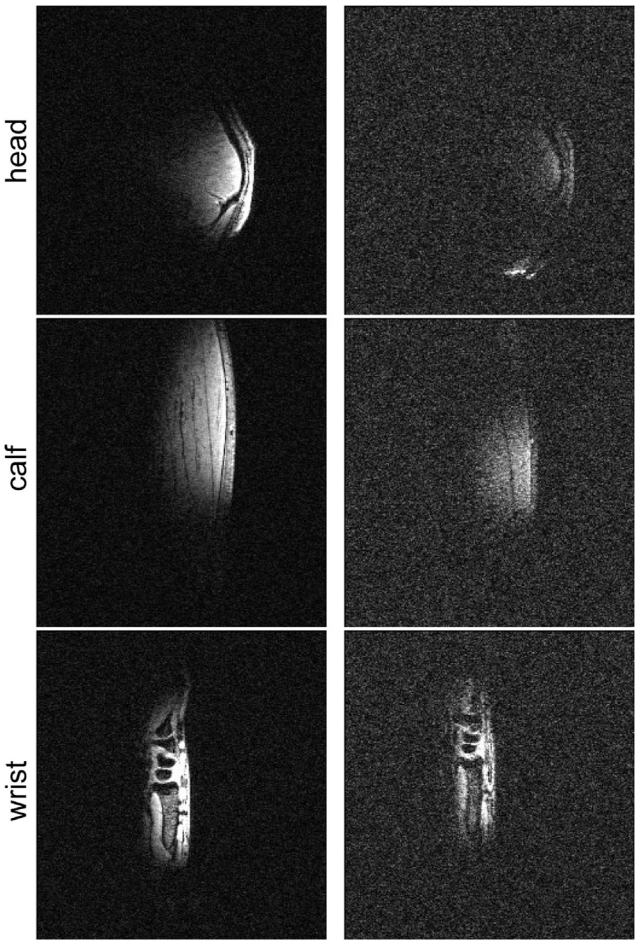

FIGURE 7 | *In vivo* MRI experiments in one human male subject using two blocks: thinner (d/b = 0.25) and thicker one (d/b = 0.75). Three different regions of interest (head, calf, and wrist) were investigated. The quality of all the images was significantly compromised for the larger block (very noisy). The images obtained using the smaller block were superior, and all the tissues can be clearly delineated. Even though the quality of images (larger block) was very low, it can be observed that the quality of the image of the wrist (low level of curvature and almost flat surface) was the highest. The worst quality was noticed for the image of the head (high level of curvature). These results can be benchmarked against the ones obtained for the cuboid (wrist, **Figure 5**) and the spherical phantom (head, **Figure 5**). The images have the same absolute intensity.

boundaries along the *y*-axis (almost no propagation along the *z*-axis; see **Figure 6**, axial view) and partially couples to the phantom placed below the block (the resulting transmit field will also strongly depend on the loading geometry; **Figure 7**). This applies to all the ε_r values ($d = 0.75b$) from **Figure 2**. The reason why the transmit field pattern for $d = 0.75b$ in **Figure 2** appears to be different for different ε_r values is due to the colorbar with a maximum value of 1 $\mu T/\sqrt{W}$ chosen as the maximum value. For higher-ε_r values, the magnetic field concentration is higher within and in the vicinity of the block, resulting in a substantially higher transmit field in the peripheral regions of the phantom (note that we used a different scale for the simulations for $\varepsilon_r = 200$ in **Figure 5**). In the case of thinner blocks (e.g., $d = 0.125b$), the transmit field pattern in the phantom can be considered similar to the one for a standalone dipole antenna. However, in the blocks with $d = 0.125b$, according to **Eq. 1**, the $TE_{11\delta}$ mode can still be excited, and the electromagnetic field pattern within the block for $d = 0.125b$ looks very similar to the one for $d = 0.25b$ (see **Figure 6**, axial view).

The above considerations provide additional evidence why dielectric modes are critical in dielectrically shortened dipole antennas, given the fact that the particular b/b_0 and d/b ratio increments used in our study were chosen in an arbitrary fashion. Our data also suggest that the propagation of dielectric modes can become a limiting factor in miniaturization of rectangular dielectric blocks in UHF-MRI. We observed that a more efficient transmit field for dielectrically shortened dipole antennas can be achieved when, for a given geometry and ε_r, the cutoff frequency for the $TE^z_{11\delta}$ mode was lower (or close to) the Larmor's frequency.

The effect of the dielectric permittivity of the block on the transmit field performance was analyzed by keeping the distance between the block and the spherical phantom constant (5 mm) along with the geometry of the block ($a/b/d$ ratio) and dipole antenna (wire) length (**Figure 3**). The geometry was chosen such that it could be used as a building block of an 8-channel array [11]. Our data showed that as expected for higher ε_r values, the electromagnetic field is more concentrated near the block [23]. This led to higher transmit efficiency in the periphery for higher-ε_r blocks (especially for ε_r = 300 and 500, in which the $TE^z_{12\delta}$ mode was excited). However, the best performance in terms of transmit field efficiency among all the analyzed permittivity values in the center of the spherical phantom was found for ε_r = 300 and 200, which are ~3× and ~2× higher than those reported for the case of a direct contact between the block and the cuboid phantom [14]. This increase, however, was accompanied by a decreased SAR efficiency with higher ε_r values (**Figure 3**). The block with the best overall performance would therefore represent a trade-off between transmit and SAR efficiency. For example, with $\varepsilon_r = 200$, the transmit efficiency was higher by 29% and the SAR efficiency was lower by 15.5% than with $\varepsilon_r = 80$. The observed SAR increase for $\varepsilon_r \geq 300$ is associated with the higher-order $TE^z_{12\delta}$ mode. This mode had a critical impact on the E-field pattern which was found in the spherical phantom (**Figure 3**). The lowest transmit efficiency was observed for the lowest ε_r values (35, 50). Note that these geometries were too small to allow propagation of efficient dielectric modes, indicating that dielectric modes play a critical role in the transmit field efficiency of dielectrically shortened dipole antennas. We further note that the observed higher transmit efficiency for higher-order modes ($TE^z_{12\delta}$) has, to our knowledge, not been reported to-date for dielectrically shortened dipole antennas for UHF-MRI, and this aspect could be further investigated in the future.

The electromagnetic field simulations also showed that the larger rectangular dielectric block, which was coupled to the $TE^y_{1\delta\delta}$ mode using dipole feed placed on the top, could be still used as an efficient RF antenna (**Figure 8**). One way to couple to a different mode is to change the geometry of the block, and another solution is to change the feeding type. By conducting plane-wave simulations, we found other possible excitation schemes (different mutual orientations of the vectors $\vec{H}$, $\vec{E}$, and $\vec{k}$) that provided an efficient transmit field without any geometrical modifications of the block. Different modes could

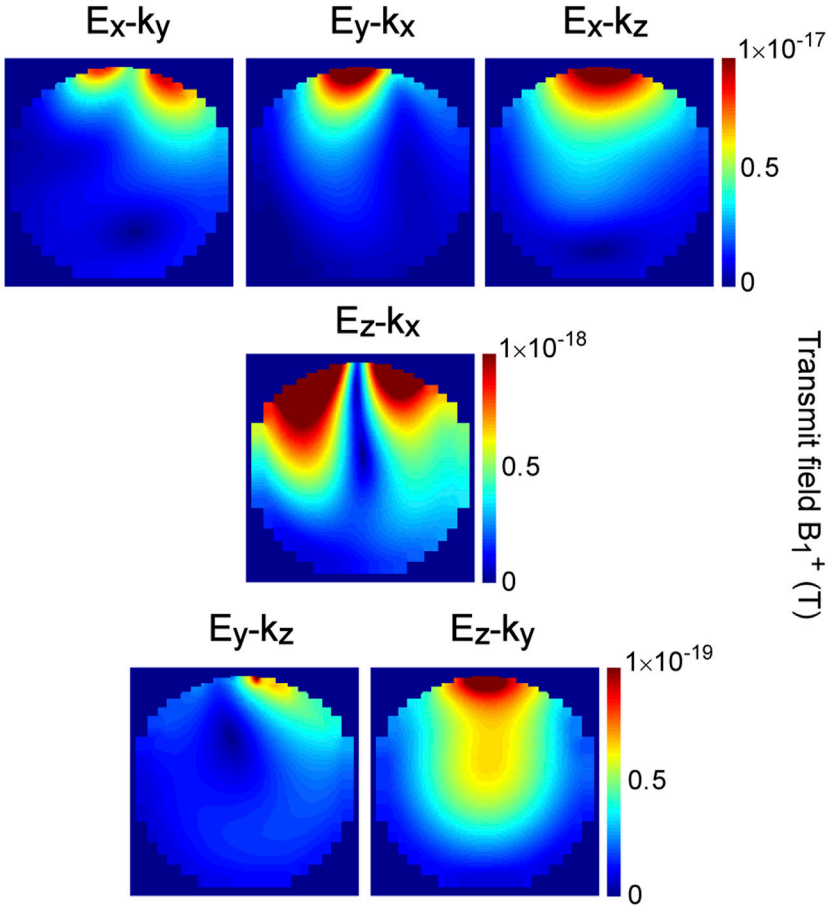

FIGURE 8 | Plane-wave simulations: the transmit field distribution in the spherical phantom (5-mm air gap) for one dielectrically shortened dipole antenna (ε_r = 80, 160 mm × 70 mm × 52.5 mm). Six different transmit field patterns arise from six different orientations of the $\vec{H}$, $\vec{E}$, and $\vec{k}$ vectors: E_x-k_y, E_x-k_z, E_y-k_x, E_y-k_z, E_z-k_x, and E_z-k_y. We see that different coupling schemes can lead to the excitation of different (MR efficient or MR inefficient) dielectric modes for a given dielectric block. Different modes could propagate, for example, by coupling with a small loop coil (E_y-k_x), instead of a dipole antenna (E_z-k_x). Note that different color scales were assigned to each row of the figure.

propagate for example by coupling with a small loop coil (E_y-k_x), instead of a dipole antenna (E_z-k_x; **Figure 8**). If a dipole antenna is the desired coupling mechanism, the geometry of the block should be designed according to the guidelines presented in this work, that is, to avoid geometries in which the $TE^{y}_{1\delta\delta}$ mode could propagate. However, as shown in **Figure 8**, this does not exclude certain block geometries from being used as an efficient RF antenna. We note that there could be other efficient feed mechanisms (or their combinations, given the fact that some of them are orthogonal) which could be used, for example, E_x-k_z (**Figure 8**) and should be investigated in the future [23–28].

The analysis of the transmit field produced within the cuboid phantom by bigger blocks (b = 0.75b_0, d = 0.75b) with ε_r values ranging from 35 to 500 showed that the distance between the block and the phantom for a given ε_r is critical for the transmit field pattern and efficiency (**Figure 4**). For each ε_r value, five different air gaps (1–5 mm) were investigated, and, despite the air gap, the transmit field pattern for lower ε_r values (35 and 50) was very similar to the one obtained with a direct contact between the block and the phantom, albeit with a slightly lower efficiency. For higher ε_r values ($\varepsilon_r \geq 80$), we observed a significant difference in the transmit field pattern and efficiency dependent on the air gap size. For ε_r = 80, an altered transmit field pattern along with a decreased efficiency was present with a 3-mm air gap, while for higher ε_r values ($\varepsilon_r \geq 200$) a 1-mm air gap was already sufficient, and the observed effect was much more prominent. This can be explained by the different ε_r values of the block. The higher the ε_r value, the higher the concentration of the electromagnetic field within the block and therefore the lower the coupling to the phantom (H_y remains well confined within the block).

Additional simulations demonstrated that a change in the transmit field pattern and efficiency (with H_y mostly confined within the block) can be still observed with lower ε_r values but requires larger air gaps (**Figure 5**). In general, the lower the ε_r value, the greater the "threshold" air gap size required to have H_y confined within the block and not significantly present in the phantom. In the case of higher ε_r values (200), the effect was even observed for smaller air gap (0.5 mm). The latter highlights the importance of this study because the "perfect direct contact" condition seems to be difficult to achieve in practice because even such tiny air gaps can influence antenna performance. Note that even with a direct contact for ε_r = 500, a slight change in the transmit field pattern can be already observed

(**Figure 4**). The results obtained with the cuboid phantom (5-mm air gap) were compared to the data obtained with the spherical phantom (**Figure 5**). All the blocks included in the comparison supported the $TE^{y}_{1\delta\delta}$ mode and produced a very inefficient transmit field along with a substantially altered field pattern in the spherical phantom for each ε_r value. However, this was not the case for the cuboid phantom for ε_r = 35 and 50. This indicates that the geometry of loading can substantially affect block/phantom coupling and influence the transmit field of dielectrically shortened dipole antennas, as discussed further below.

As spherical and rectangular phantom geometries can be considered ideal experimental conditions that may not mimic the practical situation, we performed preliminary *in vivo* experiments involving one male subject, focusing on three different organs: the head, calf, and wrist (**Figure 7**). All the investigated anatomical structures had different levels of curvature: human head (high), calf (medium), and wrist (low, almost flat). Dielectric blocks with d = 0.25b and 0.75b were used. All the images obtained when using the thicker block were substantially inferior to the ones when using the thinner block. We observed subtle differences between the images obtained using the thicker block: the image of the wrist had the highest quality, while the image of the head was very noisy, with almost no anatomical details visible, and the calf image quality was intermediate. *In vivo* data can be compared with our simulations using spherical and cuboid phantoms; the wrist was similar to the flat surface of the cuboid phantom, and the head was obviously more rounded like the spherical phantom. Note that the thicker block used in the *in vivo* experiments was very close to the optimal design described by Ipek et al. [14], yet its performance was very low. To summarize, when anatomical structures can be considered flat with respect to the bottom surface of the rectangular block, such as the wrist, they can couple better to the antenna's $TE^{y}_{1\delta\delta}$ mode than organs with curvature such as the head (or even the calf).

An arbitrarily chosen conductivity σ (constant for each block) can be considered one of the study's limitations because σ is expected to increase with ε_r of the block. Therefore, the authors recommend to interpret with caution the results concerning transmit efficiency. This, however, is not expected to significantly influence the data obtained in the context of different dielectric modes and transmit field patterns which were affected by them. Also, we would like to point out that expected σ increase with ε_r should have a rather limited impact on future developments, given the fact that there are available technologies which enable manufacturing ceramic blocks with a very high ε_r value (range of thousands) along with a very low σ value of 0.001 S/m (roughly 60 times lower than the one used in this study).

In the context of our study, previous work can be divided into two groups: (a) reports in which different, mainly loop-coupled, dielectric structures were used with a clear motivation to induce desired dielectric modes [23–26, 28] and (b) reports in which dielectric structures were used solely for the purpose of shortening dipole antennas [6, 11, 13, 15, 29, 30]. In the case of (a), different types of dielectric modes were investigated, while in the case of (b), even if dielectric modes and their impact on antenna performance were considered by the authors, it was not mentioned in any of those reports. Based on our results, we believe that (a) and (b) should not be considered separately, and this is particularly apparent when the cutoff frequency for a given block geometry and ε_r is below the NMR frequency. In this study, we showed that dielectric modes play a key role in the antenna's overall performance when the block is separated from the sample. Therefore, by treating such an element as a dipole-fed dielectric resonator antenna rather than dielectrically shortened dipole antenna, we highlight the impact of dielectric modes on overall performance of a dipole antenna. This aspect could be further investigated by looking into transmit field patterns produced by combinations of different dipole antenna geometries with different dielectric structures. We have already conducted a study [16], in which we investigated the elements developed by Winter et al. [11], Sanchez-Heredia et al. [13], and a scaled-version of Raaijmakers et al. [6], and we found that exactly the same types of modes demonstrated in this work were excited.

We conclude that the approach presented in this study can offer guidance and new insights into the design of rectangular dielectric resonator antennas for MRI at 7 T, given the growing number of such antenna designs for UHF-MRI [29–31]. These findings should also be relevant for geometries other than the rectangular ones and for higher Larmor frequencies than the one investigated in this study.

DATA AVAILABILITY STATEMENT

The original contributions presented in the study are included in the article/Supplementary Material, and further inquiries can be directed to the corresponding author.

ETHICS STATEMENT

The studies involving human participants were reviewed and approved by the Swiss cantonal ethics committee. The patients/participants provided their written informed consent to participate in this study. Written informed consent was obtained from the individual(s) for the publication of any potentially identifiable images or data included in this article.

AUTHOR CONTRIBUTIONS

DW designed the study, performed all of the numerical simulations, designed and built the prototypes used in *in vivo* experiments, analyzed and interpreted the data, prepared the figures, and wrote the manuscript. RG analyzed and interpreted the data and revised the manuscript.

ACKNOWLEDGMENTS

The authors wish to thank Hikari Yoshihara (EPFL) for proofreading the manuscript, Lijing Xin (CIBM and EPFL) for helping with *in vivo* experiments, and Andre Kuehne (MRI.TOOLS, Berlin, Germany) for a helpful discussion. They acknowledge access to the facilities and expertise of the CIBM Center for Biomedical Imaging, a Swiss research center of excellence founded and supported by Lausanne University Hospital (CHUV), University of Lausanne (UNIL), Ecole polytechnique fédérale de Lausanne (EPFL), University of Geneva (UNIGE), and Geneva University Hospitals (HUG).

REFERENCES

1. Ladd ME, Bachert P, Meyerspeer M, Moser E, Nagel AM, Norris DG, et al. Pros and Cons of Ultra-high-field MRI/MRS for Human Application. *Prog Nucl Magn Reson Spectrosc* (2018) 109:1–50. doi:10.1016/j.pnmrs.2018.06.001
2. Roemer PB, Edelstein WA, Hayes CE, Souza SP, and Mueller OM. The NMR Phased Array. *Magn Reson Med* (1990) 16:192–225. doi:10.1002/mrm.1910160203
3. Sodickson DK, and Manning WJ. Simultaneous Acquisition of Spatial Harmonics (SMASH): Fast Imaging with Radiofrequency Coil Arrays. *Magn Reson Med* (1997) 38:591–603. doi:10.1002/mrm.1910380414
4. Pruessmann KP, Weiger M, Scheidegger MB, and Boesiger P. SENSE: Sensitivity Encoding for Fast MRI. *Magn Reson Med* (1999) 42:952–62. doi:10.1002/(sici)1522-2594(199911)42:5<952:aid-mrm16>3.0.co;2-s
5. Griswold MA, Jakob PM, Heidemann RM, Nittka M, Jellus V, Wang J, et al. Generalized Autocalibrating Partially Parallel Acquisitions (GRAPPA). *Magn Reson Med* (2002) 47:1202–10. doi:10.1002/mrm.10171
6. Raaijmakers AJE, Ipek O, Klomp DWJ, Possanzini C, Harvey PR, Lagendijk JJW, et al. Design of a Radiative Surface Coil Array Element at 7 T: the Single-Side Adapted Dipole Antenna. *Magn Reson Med* (2011) 66:1488–97. doi:10.1002/mrm.22886
7. Raaijmakers AJE, Italiaander M, Voogt IJ, Luijten PR, Hoogduin JM, Klomp DWJ, et al. The Fractionated Dipole Antenna: A New Antenna for Body Imaging at 7 T Esla. *Magn Reson Med* (2016) 75:1366–74. doi:10.1002/mrm.25596
8. Ertürk MA, Raaijmakers AJE, Adriany G, Uğurbil K, and Metzger GJ. A 16-channel Combined Loop-dipole Transceiver Array for 7 T Esla Body MRI. *Magn Reson Med* (2017) 77:884–94. doi:10.1002/mrm.26153
9. Clément J, Gruetter R, and Ipek Ö. A Combined 32-channel Receive-loops/8-channel Transmit-dipoles Coil Array for Whole-brain MR Imaging at 7T. *Magn Reson Med* (2019) 82:1229–41. doi:10.1002/mrm.27808
10. Lattanzi R, Wiggins GC, Zhang B, Duan Q, Brown R, and Sodickson DK. Approaching Ultimate Intrinsic Signal-To-Noise Ratio with Loop and Dipole Antennas. *Magn Reson Med* (2018) 79:1789–803. doi:10.1002/mrm.26803
11. Winter L, Özerdem C, Hoffmann W, Santoro D, Müller A, Waiczies H, et al. Design and Evaluation of a Hybrid Radiofrequency Applicator for Magnetic Resonance Imaging and RF Induced Hyperthermia: Electromagnetic Field Simulations up to 14.0 Tesla and Proof-Of-Concept at 7.0 Tesla. *PLoS One* (2013) 8:e61661. doi:10.1371/journal.pone.0061661
12. Oezerdem C, Winter L, Graessl A, Paul K, Els A, Weinberger O, et al. 16-channel bow Tie Antenna Transceiver Array for Cardiac MR at 7.0 Tesla. *Magn Reson Med* (2016) 75:2553–65. doi:10.1002/mrm.25840
13. Sanchez-Heredia JD, Avendal J, Bibic A, and Lau BK. Radiative MRI Coil Design Using Parasitic Scatterers: MRI Yagi. *IEEE Trans Antennas Propagat* (2018) 66:1570–5. doi:10.1109/TAP.2018.2794400
14. Ipek O, Raaijmakers A, Lagendijk J, Luijten P, and van den Berg C, Optimization of the Radiative Antenna for 7-T Magnetic Resonance Body Imaging, *Concepts Magn Reson* (2013) 43B. p. 1–10. doi:10.1002/cmr.b.21224
15. Eigentler TW, Winter L, Han H, Oberacker E, Kuehne A, Waiczies H, et al. Wideband Self-Grounded Bow-Tie Antenna for Thermal MR. *NMR Biomed* (2020) 33:33. doi:10.1002/nbm.4274
16. Wenz D, and Gruetter R. Dielectrically-Shortened Dipole Antennas for MRI at 7.0 T: Thick or Thin? *Proc Intl Soc Mag Reson Med* (2020) 28:4087.
17. Mongia RK, and Bhartia P. Dielectric Resonator Antennas-A Review and General Design Relations for Resonant Frequency and Bandwidth. *Int J Microw Mill-Wave Comput-Aided Eng* (1994) 4:230–47. doi:10.1002/mmce.4570040304
18. Keyrouz S, and Caratelli D. Dielectric Resonator Antennas: Basic Concepts, Design Guidelines, and Recent Developments at Millimeter-Wave Frequencies. *Int J Antennas Propagation* (2016) 2016:1–20. doi:10.1155/2016/6075680
19. Pozar DM. *Microwave Engineering*. 4th ed. Hoboken, NJ: Wiley (2012).
20. Pan YM, Leung KW, and Lu K. Study of Resonant Modes in Rectangular Dielectric Resonator Antenna Based on Radar Cross Section. *IEEE Trans Antennas Propagat* (2019) 67:4200–5. doi:10.1109/TAP.2019.2911198
21. Wen H, Jaffer FA, Denison TJ, Duewell S, Chesnick AS, and Balaban RS. The Evaluation of Dielectric Resonators Containing H2O or D2O as RF Coils for High-Field MR Imaging and Spectroscopy. *J Magn Reson Ser B* (1996) 110:117–23. doi:10.1006/jmrb.1996.0019
22. Webb AG. Visualization and Characterization of Pure and Coupled Modes in Water-Based Dielectric Resonators on a Human 7T Scanner. *J Magn Reson* (2012) 216:107–13. doi:10.1016/j.jmr.2012.01.013
23. O'Reilly TPA, Ruytenberg T, and Webb AG. Modular Transmit/receive Arrays Using Very-High Permittivity Dielectric Resonator Antennas: Very-High Permittivity DRA Arrays. *Magn Reson Med* (2018) 79:1781–8. doi:10.1002/mrm.26784
24. Aussenhofer SA, and Webb AG. Design and Evaluation of a Detunable Water-Based Quadrature HEM11 Mode Dielectric Resonator as a New Type of Volume Coil for High Field MRI. *Magn Reson Med* (2012) 68:1325–31. doi:10.1002/mrm.24451
25. Aussenhofer SA, and Webb AG. An Eight-Channel Transmit/receive Array of TE01 Mode High Permittivity Ceramic Resonators for Human Imaging at 7T. *J Magn Reson* (2014) 243:122–9. doi:10.1016/j.jmr.2014.04.001
26. Ruytenberg T, and Webb AG. Design of a Dielectric Resonator Receive Array at 7 Tesla Using Detunable Ceramic Resonators. *J Magn Reson* (2017) 284:94–8. doi:10.1016/j.jmr.2017.09.015
27. Ruytenberg T, O'Reilly TP, and Webb AG. Design and Characterization of Receive-Only Surface Coil Arrays at 3T with Integrated Solid High Permittivity Materials. *J Magn Reson* (2020) 311:106681. doi:10.1016/j.jmr.2019.106681
28. Moussu MAC, Glybovski SB, Abdeddaim R, Craeye C, Enoch S, Tihon D, et al. Imaging of Two Samples with a Single Transmit/receive Channel Using Coupled Ceramic Resonators for MR Microscopy at 17.2 T. *NMR Biomed* (2020) 33:e4397. doi:10.1002/nbm.4397
29. Oberacker E, Kuehne A, Oezerdem C, Nadobny J, Weihrauch M, Beck M, et al. Radiofrequency Applicator Concepts for thermal Magnetic Resonance of Brain Tumors at 297 MHz (7.0 Tesla). *Int J Hyperthermia* (2020) 37:549–63. doi:10.1080/02656736.2020.1761462
30. Woo MK, DelaBarre L, Lagore R, Jungst S, Yang Q, Zhang B, et al. Improved B1+ Efficiency of a Dipole Antenna Equipped with High Dielectric Constant (HDC) Materials at 10.5T. *Proc Intl Soc Mag Reson Med* (2019) 27:1498.
31. Sadeghi-Tarakameh A, Jungst S, Wu X, Lanagan M, Adriany G, Metzger GJ, et al. A New Coil Element for Highly-Dense Transmit Arrays : An Introduction to Non-uniform Dielectric Substrate (NODES) Antenna. *Proc Intl Soc Mag Reson Med* (2019) 27:0732.

Conflict of Interest: The authors declare that the research was conducted in the absence of any commercial or financial relationships that could be construed as a potential conflict of interest.

frontiers in Physics

PERSPECTIVE
published: 22 June 2021
doi: 10.3389/fphy.2021.688479

The Field-Frequency Lock for Fast Field Cycling Magnetic Resonance: From NMR to MRI

G. Galuppini[1]*, *L. Magni*[1] and *G. Ferrante*[2]

[1]Identification and Control of Dynamic Systems Lab, Department of Civil Engineering and Architecture, University of Pavia, Pavia, Italy, [2]Stelar s.r.l., Mede, Italy

Magnetic field stability plays a fundamental role in Nuclear Magnetic Resonance (NMR) and Magnetic Resonance Imaging (MRI) experiments, guaranteeing accuracy and reproducibility of results. While high levels of stabilization can be achieved for standard NMR techniques, this task becomes particularly challenging for Fast Field Cycling (FFC) NMR and MRI, where the main magnetic field is switched to higher or lower levels during the pulse sequence, and field stabilization must be guaranteed within a very short time after switching. Recent works have addressed the problem with rigorous tools from control system theory, proposing a model based approach for the synthesis of magnetic field controllers for FFC-NMR. While an experimental proof of concept has underlined the correctness of the approach for a complete FFC-NMR setup, the application of the novel, model based Field-Frequency Lock (FFL) system to a FFC-MRI scanner requires proper handling of field encoding gradients. Furthermore, the proof of concept work has also stressed how further advances in the hardware and firmware could improve the overall performances of the magnetic field control loop. The main aim of this perspective paper is then discussing the key challenges that arise in the development of the FFL system suitable for a complete MRI scanner, as well as defining possible research directions by means of preliminary, simulated experiments, with the final goal of favoring the development of a novel, model based FFL system for FFC-MRI.

Keywords: FFC-NMR, FFC-MRI, field-frequency lock, stability, magnetic field

OPEN ACCESS

Edited by:
Lionel Marc Broche, University of Aberdeen, United Kingdom

Reviewed by:
Harish Kittur, VIT University, India
Duarte Mesquita Sousa, University of Lisbon, Portugal

***Correspondence:**
G. Galuppini
giacomo.galuppini01@ateneopv.it

Specialty section:
This article was submitted to Medical Physics and Imaging, a section of the journal Frontiers in Physics

Received: *30 March 2021*
Accepted: *08 June 2021*
Published: *22 June 2021*

Citation:
Galuppini G, Magni L and Ferrante G (2021) The Field-Frequency Lock for Fast Field Cycling Magnetic Resonance: From NMR to MRI. Front. Phys. 9:688479. doi: 10.3389/fphy.2021.688479

1 INTRODUCTION

Fast Field Cycling (FFC) Nuclear Magnetic resonance (NMR) and Magnetic Resonance Imaging (MRI) are two high-end techniques that exploit the dependence of the spin-lattice relaxation rate $R_1 = 1/T_1$ on the B_0 magnetic field experienced by the sample, to highlight information about molecular dynamics otherwise invisible to standard NMR or MRI. This eventually allows a more complete characterization of the sample and a better classification of healthy and diseased tissues.FFC experiments are characterized by a fast switching of the B_0 field, whose magnitude cycles over three levels [1, 2]:

- a high *polarization* field $B_0 = B_{pol}$, to pre-polarize the sample;
- a low *relaxation* magnetic field $B_0 = B_{rel}$, whose intensity is changed at every repetition to observe relaxation at different field strengths;

- an *acquisition* field $B_0 = B_{acq}$, to guarantee a sufficient Signal-to-noize Ratio (SNR) for signal acquisition;

As magnetic resonance techniques, FFC-NMR and MRI require a very precise and stable acquisition field. Due to the tight bound between magnetic field strength and resonance frequency, each magnetic field disturbance results in a perturbation of the resonance frequency and, ultimately, in noise affecting the experimental data. In addition, the FFC experimental design requires the desired level of field accuracy to be guaranteed as soon as possible, after the relaxation/acquisition magnetic field switch. As a matter of fact, the later the actual signal acquisition starts after the magnetic field reaches the acquisition value, the less information about the dependence of the spin-lattice relaxation rate on the magnetic field magnitude is encoded in the acquired signal [1, 2].

1.1 The Challenge of Field Stabilization in Fast Field Cycling Magnetic Resonance

In standard FFC setups, a magnetic field control loop, based on direct magnetic field measurements, takes care of the tracking of the field reference profile, but may not provide the desired field regulation and disturbance rejection performances during the acquisition phase [3, 4]. The main issue of this approach resides in the lack of a proper magnetic field sensor, which should be able to provide high resolution and quick response over a wide range of measured values, while being sufficiently compact and suitable to be placed very close to (*virtually inside*) the measured NMR sample [5, 6]. Furthermore, the need for field cycling capabilities does not allow for the application of the typical approaches adopted to generate stable magnetic fields, such as the use of permanent or superconducting magnets [7, 8]. The NMR Field-Frequency Lock (FFL) is another common approach to reduce magnetic field oscillations in NMR experiments [5, 6, 9, 10, 11, 12, 13, 14]. FFL systems exploit the dependence of the NMR signal on the magnetic field, and obtain an indirect but very precise measurement of magnetic field fluctuations from a parallel NMR experiment, called the *lock experiment*. To avoid cross-talk between main and lock experiments, the two are performed targeting different nuclear species. Very often, it is possible to construct samples containing the nuclei of interest for both the main and the lock experiments, obtaining measurements of the magnetic field at the exact position of the sample [9, 15, 16, 17]. The standard implementation of the FFL is the phase Locked Loop (PLL) [8, 10, 18]: the lock signal is first processed to extract its main frequency, which is compared with the reference one to generate an error signal. The error eventually feeds into a regulator that computes the necessary magnetic field adjustment to steer the field error, and thus the frequency error, to zero. However, the PLL control scheme is only effective for the compensation of slow magnetic field drifts, such as thermal drift effects, and does not allow for the rapid field stabilization [5] required in the FFC context. A reliable estimation of the frequency of the lock signal requires in fact a sufficient number of samples, as well as a sufficient Signal to Noise (SNR) ratio. Consequently, the control action can be computed and applied to the system only at a relatively low frequency, resulting in long closed-loop settling times and poor high frequency disturbance rejection capabilities [19, 20].

1.2 State-of-the-Art Solutions for Field Stabilization in Fast Field Cycling Magnetic Resonance

To overcome the above limitation, the FFL approach can be adapted as discussed in some recent works. References [5, 6] demonstrate that a series of low power, high repetition rate Radio Frequency (RF) pulses, which bring the sample in a *Steady State Free Precession* (SSFP) regime ([15, 21, 22, 23, 24]), generate a continuous NMR signal measuring the field deviation from the resonant one. In the reminder of this work, the SSFP NMR signal will be denoted as $M_y(t)$; the magnetic field deviation from the value resulting in perfect resonance will be denoted as $\Delta B(t)$. The $M_y(t)$ signal can be effectively adopted as feedback signal in a continuous-time control loop [5, 6, 11]. Furthermore, [5, 6], characterize the lock experiment as a *sensor*, both in term of static and dynamic response, by means of simulations and real experiments. The analysis underlines that the static response of the sensor is linear and bijective in a symmetric interval centered in $\Delta B(t) = 0$, with $\Delta B = 0$ corresponding to $M_y = 0$ at steady state. Moreover, the analysis underlines that the sensor dynamic response can be approximated in this region as that of a linear dynamic system. In addition, both works stress the impact of field homogeneity on both static and dynamic responses, and provide further insight on how the sample spin-lattice and spin-spin time constants, T_1 and T_2, could affect the sensor dynamics. Finally, [6, 25], propose a methodology for the synthesis of a linear regulator, based on the linear model of the NMR lock experiment, providing robust field regulation to the desired value within a specified time deadline, as well as field disturbance rejection capabilities. Reference [25] also demonstrates the effectiveness of the approach by means of experiments performed on a complete FFC-NMR setup, based on Stelar [26] (magnets, probes, firmware and software) and IECO [27] equipment (power supplies) [27]. The FFL setup tested in [25] provides regulation of magnetic field to the setpoint in about $0.015\,s$, while the effects of sinusoidal disturbances at $10\,Hz$, $25\,Hz$ and $50\,Hz$ can be reduced by $14\,dB$, $8\,dB$, and $2\,dB$, respectively. The effect of the FFL system on the main FFC-NMR experiment (S1P sequences, generating a standard decay) is quantified as the power of the imaginary NMR signal component, which should be null when the experiment runs in perfect resonance. The best FFL setup tested in [25] allows reduction of the imaginary signal power to 24% and 63% of the original, open-loop values in presence of $10\,Hz$ and $50\,Hz$ current sinusoidal disturbances, respectively.

While delivering promising results, a more specific analysis of the experiments presented in [25] can highlight a series of issues that may act as limiting factors for the FFC-FFL performances. Therefore, this perspective paper aims at discussing such issues and proposing possible research directions, based on preliminary simulated experiments. Moreover, the final goal of this research is the integration of a FFL into a novel FFC-MRI scanner, as the one

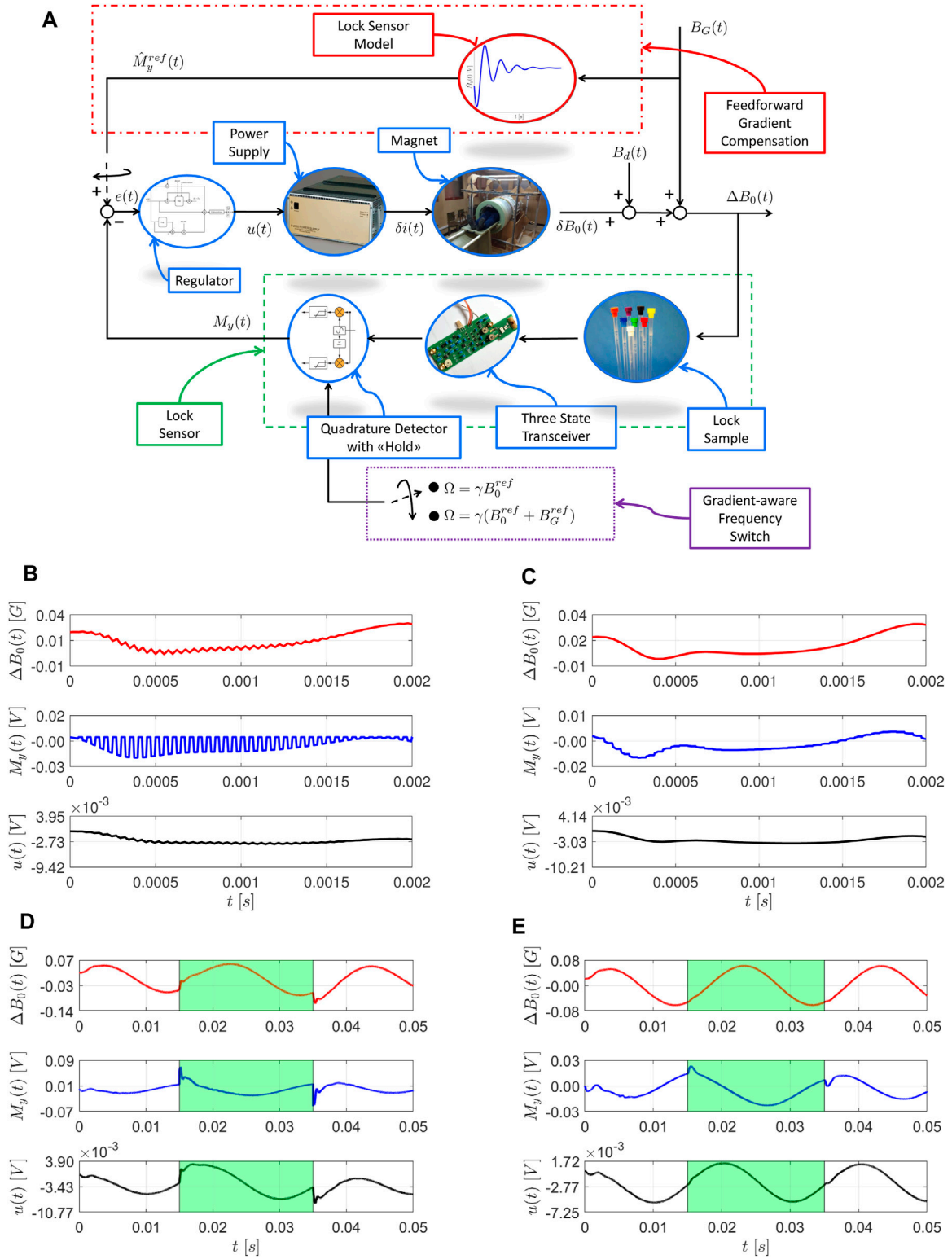

FIGURE 1 | Enhanced FFL control scheme for MRI and preliminary closed-loop simulations. Simulations are performed with a virtual version of the Copper Sulfate sample from [25]. **(A)** The control loop, including power supply, magnet, lock sample, three state transceiver, quadrature detector with hold procedure and a linear regulator. The cascade sample-transceiver-detector plays the role of lock magnetic field sensor (green, dashed box). The main signals in the loop are the voltage control action $u(t)$, the current correction $\delta i(t)$, the magnetic field correction $\delta B_0(t)$, the magnetic field disturbance $\Delta B_d(t)$, the overall magnetic field deviation $\Delta B_0(t)$, the

(*Continued*)

FIGURE 1 | gradient magnetic field contribution $B_G(t)$, the measured lock signal $M_y(t)$, the error signal $e(t) = 0 - M_y(t)$. Additionally, two different field encoding gradient compensation strategies can be implemented, according to the gradient intensity in the lock sample volume. When the gradient intensity is small, a Feedforward Gradient Compensation strategy (red, dotted-dashed box) exploits a dynamical model of the lock sensor to compute and adapt in real time the closed-loop reference $\widehat{M}_y(t)$ and require regulation to the correct field intensity. With high intensity gradients, a Gradient-Aware Frequency Dwitch policy (purple, dotted box) adapts the receiver working frequency to account for the presence of the gradient, thus obtaining a lock signal measuring the field deviation from the new resonance condition. **(B)** Closed-loop simulation with sinusoidal field disturbance: a standard receiver *gate* procedure during the receiver blank time $T_{rb} = 20\,\mu s$ (repetition time $T = 100\,\mu s$) results in chattering of the control action and, in turn, in chattering of the magnetic field. **(C)** Closed-loop simulation with sinusoidal field disturbance: the proposed receiver *hold* procedure during the receiver blank time $T_{rb} = 20\,\mu s$ (repetition time $T = 100\,\mu s$) avoids chattering and helps improving the FFL regulation performances. **(D)** Closed-loop simulation with sinusoidal field disturbance and high intensity field gradient active from $t = 15\,ms$ to $t = 35\,ms$: the GAFS procedure restores the correct FFL operation after a short transient phase characterized by underdamped oscillations. **(E)** Closed-loop simulation with sinusoidal field disturbance and low intensity field gradient active from $t = 15\,ms$ to $t = 35\,ms$: the FGC procedure quickly restores the correct FFL operation with almost no oscillations after gradient switch on and off.

described in [28]. Field stabilization of standard MRI scanners represents a great challenge itself, due to the spatial distribution of the magnetic field and the presence of field-encoding gradients. Only few works address this problem, adopting both feedforward [29, 30, 31, 32] or feedback control methods [13, 33, 34, 35]. However, none of them is currently examining solutions for FFC-MRI scanners. Therefore, this work also aims at discussing possible approaches to adapt the state-of-the-art field stabilization strategies for FFC to handle the presence of field-encoding gradients characterizing FFC-MRI scanners, thus moving a step forward toward the design of a suitable FFL system for FFC-MRI.

2 DISCUSSION

The Discussion section of this work addresses the key issues in the implementation of a FFL system for FFC-NMR and MRI, as well as possible ways to face them. In particular, **Figure 1A** depicts the overall FFL scheme for FFC-MRI proposed in this work. The main enhancements to its components are analyzed in the reminder of this Section, by means of simulated experiments. The simulation environment models all the main components of the NMR lock experiment, consisting of magnet and power supply, NMR physics, transmission and acquisition chains, linear regulator. The simulation environment is discussed in detail in [6, 25].

2.1 Field Frequency Lock Hardware and Firmware Improvements

The proposed FFL can benefit from the hardware and firmware enhancements described in the reminder of this Section, in case of application to both FFC-NMR and MRI setups.

2.1.1 Receiver *Hold* Procedure

As previously introduced, the main step allowing to overcome the use of PLLs and improve the FFL performance is the generation of a continuous NMR signal, acting as magnetic field disturbance measure. To this end, the lock sample must be stimulated with low power RF pulses, with a repetition time T such that $T < T_2^*$. In this way, a SSFP is enforced [15, 21, 22, 23, 24], and the resulting NMR signal provides high sensitivity to magnetic field disturbances [5, 6]. However, it must be noted that the signal is not actually acquired during the RF pulse (with a receiver *gate* procedure, the signal is typically set to zero), as well as immediately before and after it, to avoid measuring noise related to transmitter operations (polarization, transmission and discharge) [9, 15, 16, 17]. This interval of time will be denoted as *receiver blank time*, T_{rb}. The temporary lack of significant lock signal represents a (typically high frequency) measurement disturbance acting on the FFL closed-loop. While linear regulators can be tuned to provide rejection of high frequency measurement noise [19, 20], as well as some degree of robustness, the temporary lack of feedback signal inevitably results in chattering of the control action and in degraded regulation performance. Simulations (as an example, see **Figures 1B,C**) suggest that, when the receiver is not operating, *holding* the last meaningful lock signal sample during T_{rb} represents a simple but effective improvement with respect to setting the missing samples to zero. This modification can be implemented in the firmware or hardware receiver chain in a straightforward way.

2.1.2 Three-State Transceiver Design

Even when applying low power pulses, due to field inhomogeneity, the sample T_2^* limit may require the RF pulse repetition time T to be so short that T_{rb} may constitute a significant portion of T. In this scenario, the *hold* procedure described above may not be sufficient to guarantee correct and effective operation of the lock control loop. The analysis performed in [5, 6] suggests that a longer T may results in poor sensitivity of the lock signal to field disturbances. On the other hand, improving the field homogeneity, e.g, by means of a local shimming setup, has the effect of increasing the lock signal sensitivity, but, at the same time, shrinking the field disturbance region where the lock signal response is approximately linear. The proposed linear regulator can guarantee robust field regulation and disturbance rejection, provided that the magnetic field deviation from the resonance condition does not exceed the linear region characterizing the lock experiment [6, 25]. Therefore, local shimming may not be a viable solution.The design of a high-power RF transmitter would allow reducing the time needed to deliver the required energy, but may require a much longer time for discharge, thus delaying the start of signal acquisition. To overcome this trade-off, a novel transceiver design is proposed in this work, with the goal of combining high power transmission capabilities, fast damping of the associated spurious, discharge signal, and high SNR during signal acquisition. In addition, the new transceiver should be compact and shielded

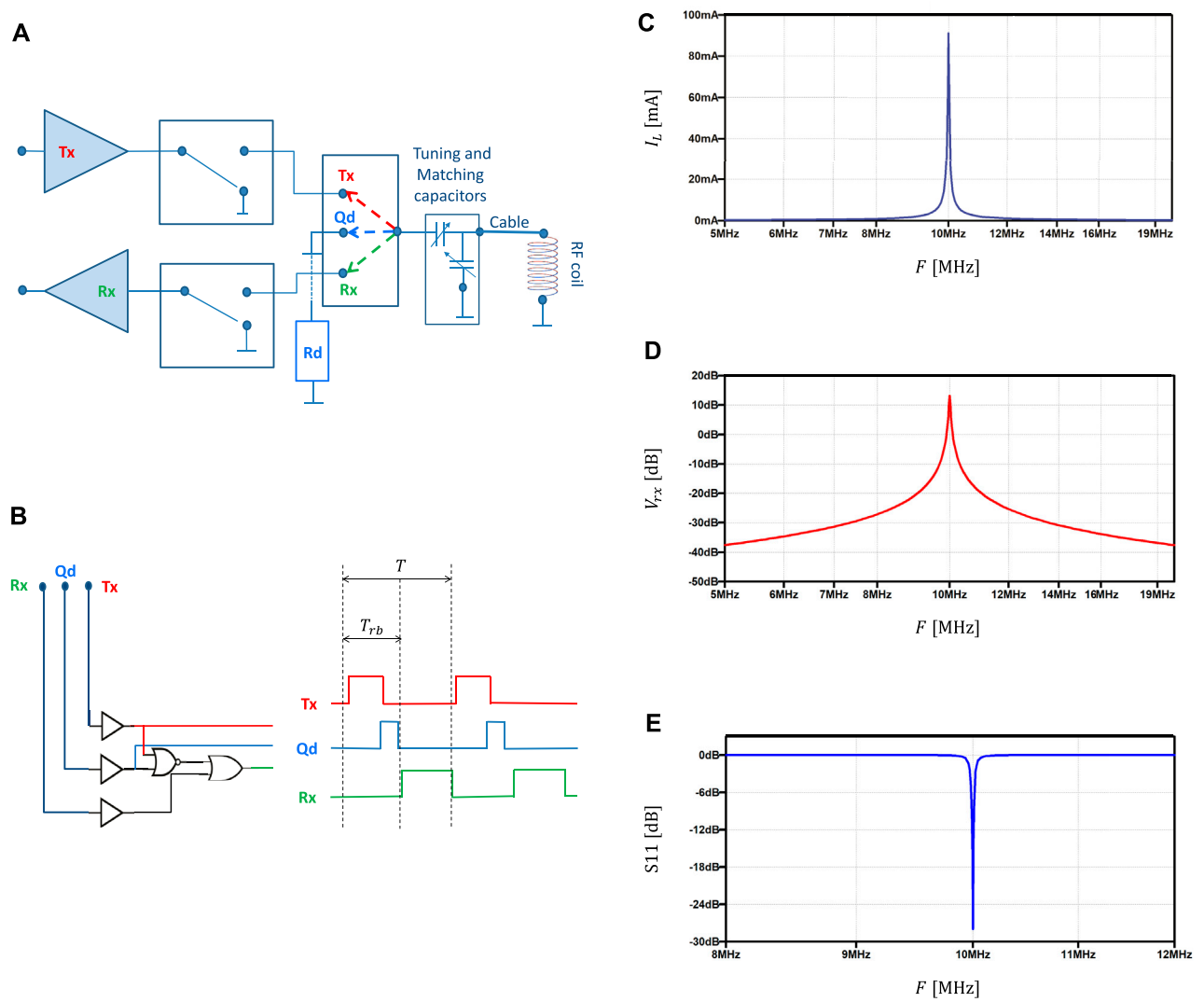

FIGURE 2 | Three state transceiver. **(A)** Conceptual block scheme including transmitter, receiver, Q damping resistor, three way switch, tuning and matching capacitors and RF coil. **(B)** Example of logic circuit (three command lines) driving the three state transceiver over transmit, Q-damping and receive states at each RF pulse repetition time T. The receiver blank time T_{rb} spans over transmit and Q-damping states. **(C)** Current through the RF coil I_L [mA] for a 1 V, AC input, as function of the working frequency F [MHz]. **(D)** Voltage gain of the LC network during receive operation V_{rx} [dB], as function of the working frequency F [MHz]. **(E)** Return loss $S11$ [dB], in case of impedance matching with 50 Ω, as function of the working frequency F [MHz].

against external RF pulses, since it must be included in an existing NMR/MRI instrument. The proposed design is based on the online adaptation of the probe Q factor, according to three operating states on the transceiver:

1. transmit: a high Q factor is engaged to handle high transmission power ($>$ 1 W);
2. *Q-damping*: a low Q factor is engaged to quickly discharge the coil;
3. *receive*: a high Q factor is engaged again to provide high SNR.

As depicted in **Figure 2A**, online adaptation of the probe Q factor is obtained by connecting the probe to a damping resistor during the Q-damping state. The three-state transceiver operation state is determined by a three-way switch that connects the probe to the transmitter, the damping resistor and the receiver, respectively. An example of logic circuit to control the state of the transceiver is depicted in **Figure 2B**. Note that, while in the example the logic circuit is designed to be driven by three lines, it can be straightforwardly adapted to a two lines framework. Finally, to protect the receiver during the high power transmission, the circuit includes protection diodes and preamp disabling during transmit and Q damping states. The proposed three-state transceiver design allows for impedance matching and adjustable gain, and provides filtering of out-band noise and overall low noise amplification, as underlined by preliminary simulations performed with models of commercially available

discrete components. In particular, the plots reported in **Figures 2C–E**, which depict the current through the RF coil for a 1 V, AC input, the voltage gain of the LC network during receive oration and return loss (S11 in dB), in case of impedance matching with 50 Ω, respectively.

2.2 Handling of MRI Field Encoding Gradients

Despite the enhancements discussed in the previous section, the application of the FFL system to a FFC-MRI scanner unavoidably requires explicit handling of field gradients. From the FFL perspective, each magnetic field moving the resonance condition from the original, resonance one represents a disturbance to be rejected. In case of field gradients, the lock sensor would detect a field disturbance and try to restore the resonance condition corresponding to no gradient active, possibly spoiling the results of the encoding procedure. In a worst case scenario, this may spoil the results of the whole experiment. Preliminary simulations suggest two possible ways to mitigate this problem, and retain some of the benefits of the FFL system during the application of field gradients: the *Gradient-Aware Frequency Switch* (GAFS) and the *Feedforward Gradient Compensation* (FGC) procedures. Both techniques are based on the hypothesis that the field deviation introduced with gradients is known (with sufficient precision) at the lock sensor site. Since gradient generation is controlled by the MRI equipment, this hypothesis is typically reasonable.

2.2.1 Gradient-Aware Frequency Switch Procedure

The GAFS procedure, depicted in **Figure 1A**, consists in the online switch of the lock sensor receiver frequency, Ω, from its original value $\Omega = \gamma B_0^{ref}$, to the gradient dependent value $\Omega = \gamma (B_0^{ref} + B_G^{ref})$, with γ the gyromagnetic ratio of the lock target nucleus, B_0^{ref} the magnetic field value corresponding to perfect resonance without gradients, and B_G^{ref} the magnetic field value corresponding to perfect resonance with the current gradient configuration. This approach requires a preliminary, offline phase to determine the value of B_G^{ref} for each possible gradient configuration and construct a look-up table for online consultation, at the benefit of negligible online computational effort. Simulations (see **Figure 1D** for an example) suggest that GAFS can effectively restore the FFL functioning after a short time transient, where the magnetic field may undergo some oscillations. The duration of the transient is related to the closed-loop settling time of the main FFL control loop. This behavior can also be interpreted as a step change in the closed-loop reference.

2.2.2 Feedforward Gradient Compensation Procedure

The FGC procedure, depicted in **Figure 1A**, aims at reducing the impact of such sudden reference change, by dynamically adapting the closed-loop reference according to a dynamic model of the lock sensor response. Note that, as a first approximation, this model can coincide with the linear model used for the model based tuning of the FFL regulator, and is therefore available at no additional effort. While preliminary simulations (see **Figure 1E** for an example) highlight the benefit of the approach, it must be remarked that, due to the use of a linear model for the dynamic lock sensor response, FGC can only be applied for gradients whose intensity, B_0^{ref}, allows the lock sensor to work in its linear operating region [25]. On the contrary, the GAFS procedure can be straightforwardly applied regardless of the gradient intensity, therefore the two solutions can be considered as complementary, rather than alternatives.

2.3 Concluding Remarks and Open Issues

Based on the results presented in the recent literature regarding FFL systems for FFC-NMR, this perspective article highlighted and discussed some key problems and possible ways to improve the FFC-FFL performances, and allow its implementation on a FFC-MRI scanner. Since preliminary simulations suggested that the proposed approaches can provide promising results, the future work will focus on their practical implementation and experimental evaluation. Moreover, while this work focused more on issues related to hardware and firmware enhancements, it is worth mentioning in this concluding section that room for further improvement can also be found in the engineering of a control sample whose characteristic time constants and dynamic behavior could allow for even faster regulation of the magnetic field [5, 25]. Finally, the tuning of the regulator could be optimized and automatized, by adapting optimization-based procedures suitable to handle systems characterized by very complex high frequency behavior [36].

DATA AVAILABILITY STATEMENT

The original contributions presented in the study are included in the article/supplementary material, further inquiries can be directed to the corresponding author.

AUTHOR CONTRIBUTIONS

Conceptualization: GG, LM and GF; writing—original draft preparation: GG writing—review and editing: LM and GF All authors have read and agreed to the published version of the manuscript.

FUNDING

This project has received funding from the European Union's Horizon 2020 research and innovation program under grant agreement No 668119 (project "IDentIFY").

ACKNOWLEDGMENTS

The Authors would like to thank the whole Stelar group for providing great insight and expertize in the development of this research.

REFERENCES

1. Ferrante G, and Sykora S. Technical Aspects of Fast Field Cycling. *Adv Inorg Chem* (2005) 57:405–70. doi:10.1016/s0898-8838(05)57009-0
2. Kimmich R. *Field-cycling NMR Relaxometry: Instrumentation, Model Theories and Applications*. London, UK: Royal Society of Chemistry) (2018).
3. Roque A, Maia J, Margato E, Sousa DM, and Marques G. Control and Dynamic Behaviour of a Ffc Nmr Power Supply. In: IECON 2013-39th Annual Conference of the IEEE Industrial Electronics Society (IEEE), 10-13 November, Vienna, Austria (2013). p. 5945–50.
4. Roque A, Sousa DM, Sebastião P, Margato E, and Marques G. Ffc Nmr Relaxometer with Magnetic Flux Density Control. *Jlpea* (2019) 9:22. doi:10.3390/jlpea9030022
5. Samra J. *A Field-Frequency Lock Implemented with a Sampled-Data Feedback Control Algorithm Derived from a Small-Signal NMR Model*. Master's thesis. University Park, PA: The Pennsylvania State University (2008).
6. Galuppini G, Toffanin C, Raimondo DM, Provera A, Xia Y, Rolfi R, et al. Towards a Model-Based Field-Frequency Lock for Nmr. *IFAC-PapersOnLine* (2017) 50:13020–5. doi:10.1016/j.ifacol.2017.08.1999
7. Maly T, Bryant J, Ruben D, and Griffin RG. A Field-Sweep/field-Lock System for Superconducting Magnets-Application to High-Field EPR. *J Magn Reson* (2006) 183:303–7. doi:10.1016/j.jmr.2006.09.012
8. Hoult DI, Richards RE, and Styles P. A Novel Field-Frequency Lock for a Superconducting Spectrometer. *J Magn Reson (1969)* (1978) 30:351–65. doi:10.1016/0022-2364(78)90106-3
9. Keeler J. *Understanding NMR Spectroscopy*. Hoboken, NJ: John Wiley & Sons (2011).
10. Jiang D, Chen H, Chen Z, and Zheng Z. The Digital Field-Frequency Lock System of High-Resolution Nmr Spectrometer. In: Electrical and Control Engineering (ICECE), 2010 International Conference on IEEE, 25-27 June, Wuhan, China (2010). p. 2328–31.
11. Li M, Schiano JL, Samra JE, Shetty KK, and Brey WW. Reduction of Magnetic Field Fluctuations in Powered Magnets for Nmr Using Inductive Measurements and Sampled-Data Feedback Control. *J Magn Reson* (2011) 212:254–64. doi:10.1016/j.jmr.2011.05.010
12. Yanagisawa Y, Nakagome H, Hosono M, Hamada M, Kiyoshi T, Hobo F, et al. Towards Beyond-1 GHz Solution NMR: Internal 2H Lock Operation in an External Current Mode. *J Magn Reson* (2008) 192:329–37. doi:10.1016/j.jmr.2008.03.015
13. Henry P-G, van de Moortele P-Fo., Giacomini E, Nauerth A, and Bloch G. Field-frequency Locked *In Vivo* Proton Mrs on a Whole-Body Spectrometer. *Magn Reson Med* (1999) 42:636–42. doi:10.1002/(sici)1522-2594(199910)42:4<636::aid-mrm4>3.0.co;2-i
14. Chen S, Xu L, Wang H, and Dai S. Field-frequency Lock Approach for 21.3-mhz High-Performance Nmr Relaxation Analyzer. *AIP Adv* (2018) 8:075327. doi:10.1063/1.5038138
15. Elster A. *Questions and Answers in Magnetic Resonance Imaging*. Maryland Heights, Missouri: Mosby Inc (1994).
16. Hornak JP. *The Basics of NMR*. Rochester, NY: Rochester Institute of Technology, Center for Imaging Science (1997).
17. Jacobsen NE. *NMR Spectroscopy Explained: Simplified Theory, Applications and Examples for Organic Chemistry and Structural Biology*. Hoboken, New Jersey: John Wiley & Sons (2007).
18. Kan S, Gonord P, Fan M, Sauzade M, and Courtieu J. Automatic NMR Field-frequency Lock-Pulsed Phase Locked Loop Approach. *Rev Scientific Instr* (1978) 49:785–9. doi:10.1063/1.1135615
19. Seborg DE, Mellichamp DA, Edgar TF, and Doyle FJ, III. *Process Dynamics and Control*. Hoboken, NJ: John Wiley & Sons (2010).
20. Magni L, and Scattolini R. *Advanced and Multivariable Control*. Bologna, Italy: Pitagora (2014).
21. Carr HY. Steady-state Free Precession in Nuclear Magnetic Resonance. *Phys Rev* (1958) 112:1693–701. doi:10.1103/physrev.112.1693
22. Patz S. Some Factors that Influence the Steady State in Steady-State Free Precession. *Magn Reson Imaging* (1988) 6:405–13. doi:10.1016/0730-725x(88)90477-8
23. Gyngell ML. The Steady-State Signals in Short-Repetition-Time Sequences. *J Magn Reson (1969)* (1989) 81:474–83. doi:10.1016/0022-2364(89)90083-8
24. Bagueira de Vasconcelos Azeredo R, Colnago LA, and Engelsberg M. Quantitative Analysis Using Steady-State Free Precession Nuclear Magnetic Resonance. *Anal Chem* (2000) 72:2401–5. doi:10.1021/ac991258e
25. Galuppini G, Toffanin C, Raimondo D, Provera A, Xia Y, Rolfi R, et al. Towards a Model-Based Field-Frequency Lock for Fast-Field Cycling Nmr. *Appl Magn Reson* (2019) 1–23.
26. [Dataset] *Stelar Website*. Available from: https://www.stelar.it/ (Accessed 14 June 2021).
27. [Dataset] *Ieco Website*. Available from: http://www.ieco.fi/ (Accessed 14 June 2021).
28. Broche LM, Ross PJ, Davies GR, MacLeod MJ, and Lurie DJ. A Whole-Body Fast Field-Cycling Scanner for Clinical Molecular Imaging Studies. *Sci Rep* (2019) 9:10402–11. doi:10.1038/s41598-019-46648-0
29. Juchem C, Nixon TW, Diduch P, Rothman DL, Starewicz P, and De Graaf RA. Dynamic Shimming of the Human Brain at 7 T. *Concepts Magn Reson* (2010) 37B:116–28. doi:10.1002/cmr.b.20169
30. Bhogal A, Versluis M, Koonen J, Siero JCW, Boer VO, Klomp D, et al. Image-based Method to Measure and Characterize Shim-Induced Eddy Current fields. *Concepts Magn Reson* (2013) 42:245–60. doi:10.1002/cmr.a.21290
31. Fillmer A, Vannesjo SJ, Pavan M, Scheidegger M, Pruessmann KP, and Henning A. Fast Iterative Pre-emphasis Calibration Method Enabling Third-order Dynamic Shim Updated fMRI. *Magn Reson Med* (2016) 75:1119–31. doi:10.1002/mrm.25695
32. Vannesjo SJ, Dietrich BE, Pavan M, Brunner DO, Wilm BJ, Barmet C, et al. Field Camera Measurements of Gradient and Shim Impulse Responses Using Frequency Sweeps. *Magn Reson Med* (2014) 72:570–83. doi:10.1002/mrm.24934
33. Sinanna A, Bermond S, Donati A, Gros P, Hugon C, Jacquinot J-F, et al. Field Stabilization of an Mri Magnet Operating in Driven Mode. *IEEE Trans Appl Supercond* (2009) 19:2301–4. doi:10.1109/tasc.2009.2018105
34. Dürst Y, Wilm BJ, Dietrich BE, Vannesjö S, and Pruessmann KP. *Real-time Shim Feedback for Field Stabilization in Human Mri Systems*. Melbourne, Australia: Scientific Meeting of the International Society for Magnetic Resonance in Medicine (2012).
35. Duerst Y, Wilm BJ, Dietrich BE, Vannesjo SJ, Barmet C, Schmid T, et al. Real-time Feedback for Spatiotemporal Field Stabilization in Mr Systems. *Magn Reson Med* (2015) 73:884–93. doi:10.1002/mrm.25167
36. Galuppini G, Creaco E, and Magni L. Bi-objective Optimisation Based Tuning of Pressure Control Algorithms for Water Distribution Networks. *Control Eng Pract* (2020) 104:104632. doi:10.1016/j.conengprac.2020.104632

Conflict of Interest: Author GF is company director of Stelar s.r.l.

The remaining authors declare that the research was conducted in the absence of any commercial or financial relationships that could be construed as a potential conflict of interest.

frontiers in Physics

ORIGINAL RESEARCH
published: 20 July 2021
doi: 10.3389/fphy.2021.705438

Recent Advances and Challenges in the Development of Radiofrequency HTS Coil for MRI

Aimé Labbé[1], Gilles Authelet[2], Bertrand Baudouy[2], Cornelis J. van der Beek[3], Javier Briatico[4], Luc Darrasse[1] and Marie Poirier-Quinot[1]**

[1]Université Paris-Saclay, CEA, CNRS, Inserm, Laboratoire d'Imagerie Biomédicale Multimodale Paris Saclay, Orsay, France, [2]Université Paris-Saclay, CEA, Département des Accélérateurs, de Cryogénie et de Magnétisme, Gif-sur-Yvette, France, [3]Université Paris-Saclay, CNRS, Centre de Nanosciences et de Nanotechnologies, Palaiseau, France, [4]Unité mixte de physique, CNRS, Thales, Université Paris-Saclay, Palaiseau, France

OPEN ACCESS

Edited by:
Simone Angela S. Winkler,
Cornell University, United States

Reviewed by:
Michael D. Noseworthy,
McMaster University, Canada
Sigrun Roat,
Medical University of Vienna, Austria
Elizaveta Motovilova,
Weill Cornell Medicine, United States

***Correspondence:**
Aimé Labbé
aime.labbe@universite-paris-saclay.fr
Marie Poirier-Quinot
marie.poirier-quinot@universite-paris-saclay.fr

Specialty section:
This article was submitted to Medical Physics and Imaging, a section of the journal Frontiers in Physics

Received: 05 May 2021
Accepted: 24 June 2021
Published: 20 July 2021

Citation:
Labbé A, Authelet G, Baudouy B, van der Beek CJ, Briatico J, Darrasse L and Poirier-Quinot M (2021) Recent Advances and Challenges in the Development of Radiofrequency HTS Coil for MRI. Front. Phys. 9:705438. doi: 10.3389/fphy.2021.705438

Radiofrequency (RF) coils fashioned from high-temperature superconductor (HTS) have the potential to increase the sensitivity of the magnetic resonance imaging (MRI) experiment by more than a dozen times compared to conventional copper coils. Progress, however, has been slow due to a series of technological hurdles. In this article, we present the developments that recently led to new perspectives for HTS coil in MRI, and challenges that still need to be solved. First, we recall the motivations for the implementations of HTS coils in MRI by presenting the limits of cooled copper coil technology, such as the anomalous skin effect limiting the decrease of the electric resistance of normal conductors at low temperature. Then, we address the progress made in the development of MRI compatible cryostats. New commercially available low-noise pulsed-tube cryocoolers and new materials removed the need for liquid nitrogen-based systems, allowing the design of cryogen-free and more user-friendly cryostats. Another recent advance was the understanding of how to mitigate the imaging artifacts induced by HTS diamagnetism through field cooling or temperature control of the HTS coil. Furthermore, artifacts can also originate from the RF field coupling between the transmission coil and the HTS reception coil. Here, we present the results of an experiment implementing a decoupling strategy exploiting nonlinearities in the electric response of HTS materials. Finally, we discuss the potential applications of HTS coils in bio-imaging and its prospects for further improvements. These include making the technology more user-friendly, implementing the HTS coils as coil arrays, and proposing solutions for the ongoing issue of decoupling. HTS coil still faces several challenges ahead, but the significant increase in sensitivity it offers lends it the prospect of being ultimately disruptive.

Keywords: high temperature superconductor, magnetic resonance imaging, MRI compatible cryostat, nonlinear properties of superconductors, HTS coil, cryogenics, imaging artefact

INTRODUCTION

The discovery of high-temperature superconductivity (HTS) by [1], paved the way for the application of superconductor-based technologies at temperatures above that of boiling nitrogen. Simultaneously, powerful, low vibration, reliable cryocoolers have been developed for applications at temperatures close to 90 K, the critical temperature of high-temperature superconducting $YBa_2Cu_3O_7$ (YBCO) which is the technologically most useful HTS material. In microwave technology, HTS has allowed the design of detectors and filters of unmatched sensitivity/selectivity and noise figures, suitable for satellite telecommunications [2]. A down-to-earth application of HTS materials is Magnetic Resonance Imaging (MRI). Here, the use of HTS materials can be envisioned both as magnet coils and as probes for the detection of the radiofrequency (RF) MR signal. The vanishing electric resistance of the superconducting MRI coil brings electric noise levels within reach that are unachievable with more traditional copper coils, even if the latter are cooled to much lower temperatures than the HTS coil; typically, the signal-to-noise ratio (SNR) can be increased more than a dozen times [3]. In spite of the promise held, the development of HTS radiofrequency MRI coils, starting from early prototypes in the 90s [4], has been slow. Interest in this technology faded in the 2000s due to technological deadlocks that seemed insurmountable at the time. These included drawbacks such as having to employ wet cryostats (e.g. using liquid nitrogen or LN_2), as well as the necessary decoupling of the RF detection coil (fashioned from a HTS material) from the (copper) RF transmission coil. Both issues induce important artifacts in MR images. Recently, however, a number of hurdles have been lifted, heralding new possibilities for HTS coils in MRI. In this paper, we review recent progress and challenges ahead.

First, we review the limitations of copper coils. Cryogenic RF coils become relevant when the dominant noise source in MRI is the RF coil used to collect the signal, *i.e.* in the case of nonconductive samples, or when conductive samples are probed with "small" surface antennas. With copper coils, noise reduction is readily limited by the intrinsic properties of the material. This limit can be significantly pushed by using superconductors, justifying the implementation for HTS coils in MRI with small samples or small RF coils.

We next present the progress made in the design of MRI compatible cryostats. Such cryogenic systems face the key challenges of ensuring full electromagnetic compatibility in DC and RF domains and user-friendly integration for routine practice in MR exams.

A recent study [5] has led to a much better understanding of how the static field (B_0)-inhomogeneities induced by magnetic flux expulsion in the HTS coil can be mitigated. In addition to their low intrinsic resistivity, HTS materials also present strong diamagnetism that can induce significant B_0-artifacts in MR images, such as localized signal loss and continuous phase shifts. Under the right circumstances, however, these can be avoided.

We then address the subject of the RF (B_1) coupling between the transmission coil (volume coil) and the HTS reception coil (surface coil). In the absence of magnetic coupling, the HTS coil acquires the MR signal with high sensitivity during reception and does not perturb the homogeneous RF excitation emitted by the transmission coil during transmission. This represents the targeted operational mode for HTS coils. In presence of coupling, however, the HTS coil picks up and locally amplifies the B_1^+-field generated by the transmission coil, possibly inducing important B_1^+-homogeneity artifacts in the MR images. These include large-scale signal amplitude modulations and localized π-phase shifts. To avoid the B_1^+-artifacts, a decoupling strategy must be implemented so as to deactivate the HTS coil during transmission. To illustrate this issue and its implications, this section will present the original results of an experiment implementing a decoupling strategy based on non-linearities in the RF response of the HTS material.

Finally, we discuss the perspectives for further improvements of HTS coil technology in view of novel MRI applications.

LIMITS OF COPPER COILS IN MAGNETIC RESONANCE IMAGING

Cooling the RF coil circuit at cryogenic temperatures to improve the sensitivity of nuclear magnetic resonance (NMR) detection has been an early idea [6]. From the fluctuation-dissipation theorem, the noise spectral density generated by a linear dissipative medium is proportional both to its temperature and to its power dissipation rate. A drastic reduction of the coil noise is thus expected as a result of drop of the coil resistance as the temperature is lowered. Conversely, neither the sample temperature nor its equivalent damping resistance into the coil are affected, so that the noise from the sample will eventually limit the improvement in sensitivity [7]. The earliest proofs of concept have been established with copper coils cooled to 4.2 K using liquid helium (LHe) and at 77 K with liquid nitrogen, respectively, to increase the sensitivity in ^{13}C high-resolution spectroscopy [8], and in low-field clinical MRI [9]. A dramatic improvement in sensitivity was reported in NMR spectroscopy, whereas for MRI the gain was rather modest due to the large noise induced by the human body. A few years later, the potential of HTS ceramics for replacing copper had been demonstrated with prototypes of RF coils, at 77 K for low-field MRI [10], 10 K for MR microscopy at high field [4] and 25 K for ^1H detection in a 400 MHz spectrometer [11]. Electrical losses of more than two orders of magnitude below that of copper were reported. Since these early achievements, however, the cooled-copper RF coil technology has spread widely in the markets of high-resolution NMR spectroscopy [12] and preclinical micro-MRI [13]. The replacement of copper by HTS materials, on the other hand, has remained a research topic in industrial and academic labs [3,14–18]. The objective of this section is to provide guidelines to assess the coil material performance in terms of ultimate SNR performance and report the limits achievable with copper.

Using the reciprocity principle [7], the contribution of the RF coil to the final signal-to-noise ratio in MR images can be expressed by the RF sensitivity factor S_{RF}:

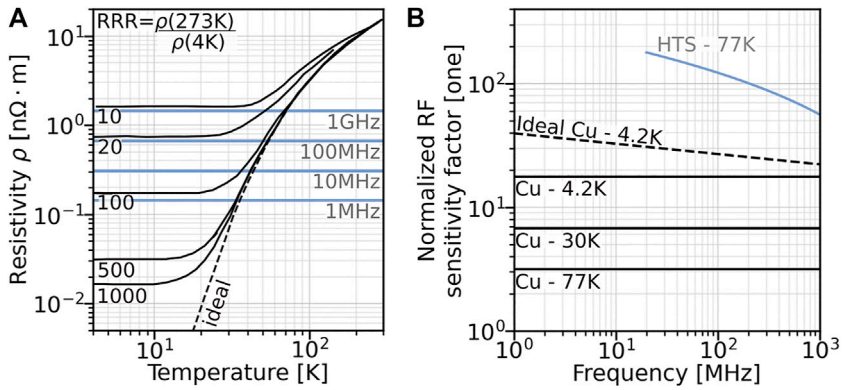

FIGURE 1 | (A) Expected resistivity ρ of copper at low temperature theoretically computed from [20], (black) and expected frontiers, i.e. $\alpha(\rho, \omega) = 1$, (blue) below which the anomalous skin effect is no longer negligible compared to the skin effect. **(B)** Corresponding RF sensitivity factor, in the case of a lossless sample, using a cooled copper coil (black) with RRR = 20 at different temperatures or a HTS coil (blue) at 77 K {data interpolated from [21]}, normalized by the sensitivity factor of the same copper coil at room temperature. The dashed line corresponds to the ultimate surface resistance achievable with absolutely pure copper, accounting for the anomalous skin effect [$\alpha(\rho, \omega) \to \infty$]. The effect of the static magnetic field on the HTS coil, not taken into account here, can significantly reduce these performances.

$$S_{RF} = \frac{\omega\left(\frac{B_1^-}{I}\right)}{\sqrt{4k_B\left(R_{\text{coil}}T_{\text{coil}} + R_{\text{sample}}T_{\text{sample}}\right)}} \tag{1}$$

that represents the time-domain SNR available from the coil per unit magnetic moment and unit acquisition bandwidth [19] at the Larmor frequency ω, assuming noiseless electronics. The RF coil circuit is modeled by a self-inductance L in series with the NMR electromotive force and with a sum of equivalent loss resistances. The term B_1^-/I, with B_1^- the transverse magnetic field amplitude generated by a RF current I in the circuit during reception, evaluates the interaction between the coil and a nuclear magnetic moment at a given position in the sample volume. The equivalent resistances R_{coil} and R_{sample} are weighted by the temperatures T_{coil} and T_{sample} to quantify the power spectral density of the noise sources in the coil and in the sample, respectively (with k_B the Boltzmann constant). By defining the quality factor Q as the ratio between the coil reactance and resistance, with respective unloaded and loaded values $Q_u = \omega L/R_{\text{coil}}$ and $Q_l = \omega L/(R_{coil} + R_{sample})$, S_{RF} is reformulated as:

$$S_{RF} = \frac{B_1^-}{I\sqrt{L}}\sqrt{\frac{\omega Q_l}{4k_B T_{eff}}} \quad with \quad T_{eff} = T_{sample}\left(1 - \frac{Q_l}{Q_u}\right) + T_{coil}\frac{Q_l}{Q_u} \tag{2}$$

where T_{eff} is the effective noise temperature of the equivalent loaded circuit. Assuming a negligible deformation of the electromagnetic field by the conduction and displacement currents inside the sample (quasistatic approximation), B_1^-/I and L do not vary significantly upon sample loading and thus only depend on the coil geometry. The measurement of Q_l and Q_u with a vector network analyzer (VNA) then allows a quick assessment of the noise sources and a comparison of sensitivity between RF coils of similar geometries operated at different temperatures and loading conditions [3].

In the case of lossless samples (i.e. when $R_{sample} \approx 0$ in **Equation 1**, or $Q_l = Q_u$ in **Equation 2**), an RF coil with a given geometry reaches an ultimate SNR performance that depends only on its temperature T_{coil} and on its resistance R_{coil}. In the following, we consider the RF regime in which the electromagnetic field only penetrates a thin layer of the conducting material. Then, R_c is directly related to the intrinsic surface resistance Ω by:

$$R_{coil} = n^2\xi\frac{a}{r}\Omega \tag{3}$$

with n the number of turns, a the average coil radius, and r the wire radius. The proximity factor ξ accounts for the concentration of the AC current along the minimum energy path in bent or parallel wires. Assuming that the term $\xi a/r$ only depends on aspect ratios of the coil geometry, then R_{coil} only depends on Ω considering homothetic scaling.

Figure 1 displays the ultimate sensitivity gain for RF coils at different cooling temperatures as compared to copper at room-temperature. For normal metals, the resistivity ρ drops almost linearly for decreasing temperatures: inelastic scattering of conduction electrons arises mainly from lattice vibrations until it reaches a temperature-independent plateau given by the residual resistance ratio (RRR) [20]. The latter is due to residual scattering by impurities and lattice defects. The screening of the metal by conduction electrons in a normal conductor leads to the RF surface resistance Ω_{nc}:

$$\Omega_{nc} = \frac{\rho}{\delta} = \sqrt{\frac{\mu_0\omega\rho}{2}} \tag{4}$$

with δ the RF skin depth and $\mu_0 = 4\pi \cdot 10^{-7}\ 4\pi\ \text{Hm}^{-1}$ the magnetic permeability of the vacuum. Actually, at extremely low ρ,Ω_{nc} can be much larger than expected from **Equation 4** because δ decreases as $\rho^{1/2}$ while the electronic mean free path λ increases as ρ^{-1} (anomalous skin effect). Since a part of the accelerated electrons tends to leave the conducting skin layer, the effective surface resistance [21] increases significantly when

$$\alpha = \frac{3}{2}\left(\frac{\lambda}{\delta}\right)^2 = \frac{3}{4}\mu_0(\rho\lambda)^2\omega\rho^{-3} \tag{5}$$

becomes comparable or greater than 1, as showcased in **Figure 1A** (grey curves). The factor $(\rho\lambda)$ is an intrinsic constant for a conductor, close to $7.2 \cdot 10^{-16}\ \Omega.m^2$ for copper. When α increases well above 1,Ω_{nc} tends to a low asymptotic limit of about $3.4 \cdot 10^{-10}\omega^{2/3}$. Thus, the anomalous skin effect only affects by a few percent the data at highest frequencies of **Figure 1B**, which relies on a RRR of 20, an order of magnitude for the RRR value of copper used in MRI probes. However, due to the fast decrease of α with ρ, it represents a severe limit for copper with larger RRR values.

Figure 1B also displays the normalized RF sensitivity factor expected for a typical HTS material at 77 K. A first key feature of HTS is the partition of the conduction electrons between a coherent Cooper pair state that carries the lossless supercurrent, and a dissipative contribution from excited quasiparticle states. A second is that the electromagnetic field is extinguished over a surface layer, the thickness of which corresponds to the frequency-independent London penetration depth λ_L; in HTS, typically $\lambda_L \approx 150$ nm). The kinetic energy of the Cooper pairs is concentrated within this layer. Electrical losses are zero only for DC currents, when the Cooper pair supercurrent shorts the quasiparticle current. However, AC electric fields accelerate (and decelerate) both the Cooper pairs and the quasiparticles contained in the surface layer. Assuming that $\mu_0\omega \gg 1/2\rho_{qp}$, with ρ_{qp} the quasiparticle resistivity, the theoretical surface resistance Ω_{sc} is given by [2]:

$$\Omega_{sc} \approx \frac{1}{2}\mu_0^2\omega^2\frac{\lambda_L^3}{\rho_{qp}}. \tag{6}$$

The depth λ_L increases rapidly as the temperature or magnetic field approach the critical values T_c or H_c above which the superconducting state disappears totally. Inversely, for "perfect" superconductors, the dissipative quasiparticle contribution is supposed to progressively vanish $(\rho_{qp} \to 0)$ far below the critical limits. In HTS materials in particular, supplementary losses occur due to the motion of magnetic flux vortices, weak-link effects at grain boundaries, and the unconventional d-wave Cooper pairing mechanism, leading to complex and strongly anisotropic dependences of dissipation on the magnetic field and RF current [2]. In spite of fundamental limitations, much of the performance of a HTS material relies on its fabrication process though. For applications at 77 K, the best technology to date is that of thin-film YBCO epitaxially grown on single-crystal dielectric substrates such as lanthanum aluminate or sapphire, that exhibit extremely low tangent losses. Systematic measurements from 20 MHz to 20 GHz with temperatures between 30 and 77 K [22] show that the ω^2 dependence expected from **Equation 6** is only approached in the GHz range and is closer to a ω^1 in the low-end frequency range up to a few hundred MHz, with a typical Ω_{sc} of 0.5 μΩ at 100 MHz. Wafers of up to 20 cm in diameter are currently available from manufacturers and can be accurately etched to elaborate monolithic resonators using the substrate as capacitance. Thin-film HTS coils with quality factors from a few 1,000 to several 100,000 have been reported for MR imaging applications [19].

Another consideration with cryogenic probes comes from the thermal insulation wall inserted between the sample and the low temperature RF coil. To preserve the field-of-view accessible with the coil, the thickness of the insulator needs to be accommodated with a larger coil radius. Consequently, looking back at **Equation 1**, this tends to mitigate the sensitivity gains predicted above by reducing the B_1^-/I factor. Indeed, from the Biot-Savart volume integral and considering coils with constant aspect ratios the B_1^-/I amplitude of surface coils is expected to decrease as $1/a$ when the coil radius is adjusted to optimize the sensitivity at a target depth below the sample surface. The same $1/a$ law also applies at the center of volume coils. Considering a volume copper coil as a typical example, the ultimate SNR gain at 30 K is about seven when compared to room temperature (**Figure 1**). For a nominal sample diameter of 5 mm and a realistic thickness of 2 mm for thermal insulation, a 30 K copper coil with a mean diameter of 9 mm would thus achieve a net gain of about four over a tightly adjusted RF coil at room temperature. Coping with even smaller samples would require an improved insulation to accommodate the larger surface-to-volume ratios, which intrinsically limits the advantages of cooled RF coils over room-temperature ones below a critical sample size. Since they offer a much larger ultimate SNR performance than copper, HTS materials can significantly alleviate this limit and bring substantial SNR improvements over conventional probes even with millimetric samples [17]. More generally, far more complex rules have to be considered with large conductive samples, with a general trend to limit the SNR gain reachable with cryocooling. In any case, however, HTS materials that provide much lower losses than their copper counterparts offer a promising perspective to design novel RF coil geometries such as actively screened or meta-structured configurations.

PROGRESS IN MAGNETIC RESONANCE IMAGING COMPATIBLE CRYOSTATS

The need for cryogenic means has long been seen as a serious bottleneck to the dissemination of cooled RF coil technology in MR applications. Many advances have been made during the last 20 years in the emerging field of superconductive electronics where the requirement for low-cost, compact, secure, and easy-to-use cryogenic devices has been a strong motivation [23]. However, MR detection meets severe additional constraints of compatibility with the presence of RF as well as of large static magnetic fields: no metallic parts can be present near the RF coil and no magnetic materials nor moving metallic parts can be in proximity to the magnet bore. Specific materials such as PVC, fiberglass composites, polystyrene or polyurethane foams, quartz, glass, or ceramics are generally involved in the cryostat body. Thus, initial developments [19] mostly relied on homemade cryogenic designs. First trials involved immersion of the coil circuit in LHe (4.2 K) or LN_2 (77 K) [8,9], allowing intrinsically uniform and temperature-stabilized cooling of volume coils or large surface coils. To reduce mechanical and electrical instabilities due to boil-off and bubbling, the trend was then to replace the direct liquid immersion by a flow of cold

nitrogen [24] or helium [25] gas, or by a cold finger made of high-performance dielectric material such as sapphire [11,26].

Another particular constraint that arises during the study of human subjects, animal models and biological samples is to maintain the living system at room temperature all the while keeping a small separation from the cooled RF coil. This can be provided either by a plain insulating wall [10], by a double-wall vacuum layer [25], or by a single-wall evacuated cryostat containing the RF coil [27]. The latter allowed the reduction of the insulator thickness to less than 1 mm, which is particularly suitable for high-resolution surface imaging such as that of the human skin and rodents in a preclinical setting. Nevertheless, using conventional superinsulation with metallized layers to block thermal radiation through the insulating window does not fit the requirement for RF transparency, so an amount of thermal leakage still occurs. Thus, insufflation of a warm stream of an inert gas such as N_2 into a reserved space along the outer cryostat surface has been applied to preserve the temperature stability of small living samples [24]. As pointed out in the previous section, the requirement for a minimized insulation thickness is not as severe with HTS coils as with copper coils since the formers offer much higher ultimate SNR gains.

More than 15 years after the early demonstrations of RF coils cooled by direct fluid immersion in the academic world, more elaborated closed-cycle cooled RF probes [28] have become available as standard accessories for analytical NMR spectroscopy [29]. In the new probes, typically, circulating helium gas transfers the cooling power from a distant two-stage Gifford–McMahon refrigerator to the RF coil, through heat exchangers at a regulated temperature ranging between 20 and 30 K. Temperatures of 20–30 K are low enough to improve the sensitivity of copper RF probes by a ratio of four when compared to room temperature, which enables 16 times faster acquisitions at constant SNR. Moreover, an integrated preamplifier cooled to below 80 K by the first stage of the Gifford-McMahon machine ensures a low noise contribution from the receiver, even with noiseless samples. Such new technology has been expanding rapidly since the late 1990s to face the high throughput demand in analytical chemistry. Its impact is tremendous in large scientific domains such as genomics, proteomics, and drug discovery, where the structural and dynamic analysis of large proteins is very time consuming, only small amounts of the substance under study are available, and less sensitive nuclei such as ^{13}C and ^{15}N must be investigated [12].

Based on the closed-cycle technology already developed for NMR probes, cryocooled surface probes designed for high-resolution imaging of the mouse brain [30–32] have become commercially available for routine operation on micro-MRI systems up to 15.2 T. This has given rise to growing numbers of cutting-edge structural and functional imaging applications [13]. Typically, the probes are made of 15–20 mm circular or rectangular copper coil elements bent onto a cold finger. Their half-cylindrical shell packaging leaves a large access to the animal head and offers a warm contact with a temperature-controlled ceramic wall, ensuring a minimum coil-sample distance of about 1 mm. Compared to a similar probe operating at room temperature, *in vivo* image acquisition with a 30 K quadrature surface probe at 9.4 T exhibited a SNR gain of about 2.5 when averaged over the mouse brain [31].

The rather high temperature range targeted with the new closed-cycle technology allows a much more robust operation than achievable with the early cryostats operating at 10 K and below. Notably, the new technology offers a fully automated control and does not require to refill the system with cryogenic fluids. However, designs until now were not versatile enough to allow for a change of RF coil configuration or orientation. The set-up is expensive and cumbersome because a high cooling power is required from the Gifford-McMahon unit, the rotary valve of which has to be located a few meters away from the MRI magnet for electromagnetic compatibility issues. Moreover, while cooling to 30 K is needed to take the most out of copper RF coils, HTS materials already exhibit sufficient performances at temperatures above 50 K. Thus, research activity is still ongoing in academic labs with simple all-in-bore 77 K static cryostats offering some flexibility and sufficient autonomy for acquisition times of several hours [3,33–36].

In order to optimize the handling of HTS coils, cryogenic systems providing intermediate temperature control above 50 K [15,37–40], and variable temperature set-ups for frequency tuning [39,41] have been proposed. Along with a higher working temperature, an important trend to alleviate the charge on closed-cycle cryocoolers is to drastically reduce the distance between the refrigerator machine and the cooled RF coil. Pulsed tube refrigerators without moving parts close to the cold finger have been used at close proximity to the MRI magnet, i.e. on the patient bed [42], or even inside the magnet within the RF coil cryostat [37]. The latter solution was designed to allow a variable orientation of the RF coil with a very compact design; however, it actually needs to be operated in a downward orientation (i.e. upright for the pulse tube) because of gravity issues for ensuring an efficient flow cooling.

The use of a refrigerant was eliminated in the cryogen-free system proposed by [40], later described by [42], and displayed in **Figure 2**. The cold source, provided by a commercial single-stage pulse tube cryocooler connected to a remote motor, is located directly on the non-magnetic cryostat vessel. The cold head is thermally coupled to the HTS coil by a series of high-conductivity pure aluminum flexible straps used in combination with copper and sapphire supports, as depicted in **Figure 2B**. This solution allows the transfer of sufficient cooling power to the RF coil; offers great adaptability to the RF coil bedding geometry; minimizes static and RF magnetic field perturbations induced by the system; and minimizes the transfer of mechanical vibrations to the HTS coil. Moreover, a non-magnetic heat exchanger tip anchored to the coil bed and a fully automated control system enable the control of the coil temperature to within 0.1 K, [41,42]. Thus, the coil frequency can be tuned through temperature as a parameter. These aforementioned characteristics, as well as the reasonable weight (70 kg) and compact nature of the cryostat, allow an installation as close as possible to the measurement zone of the MRI scanner. In fact, this system is cryogenist-free—i.e. no cryogenic knowledge is required to use it -, autonomous, and adaptable to any MRI structure that stays in the examination room during the experiments.

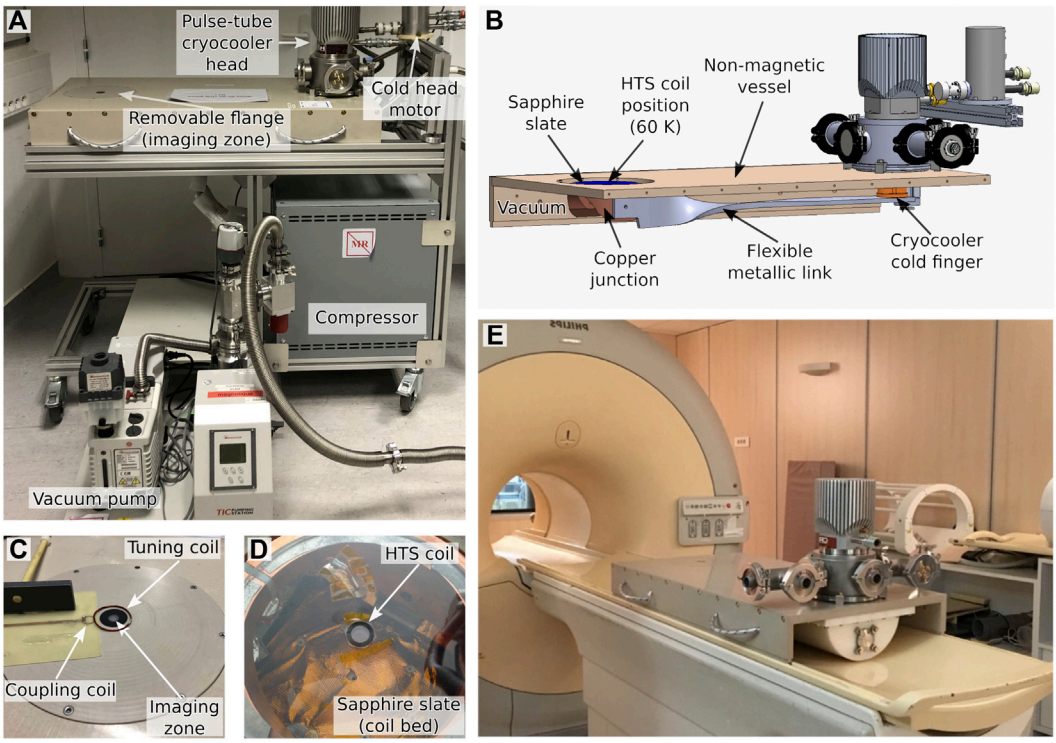

FIGURE 2 | Images of the cryogen-free cryostat. **(A)** The cryostat and associated equipment. **(B)** Detailed 3D drawing of the general layout and cryogenic scheme of the system. **(C)** The HTS coil signal is probed by inductive coupling via the coupling coil. Matching and tuning of the HTS coil to the acquisition chain of the MRI scanner is performed with the coupling coil and the tuning coil, respectively. Fine tuning is also achieved via temperature control of the HTS coil. **(D)** Position of the HTS coil inside the cryostat, approximately 1.7 mm under the imaging zone. **(E)** Cryostat on the patient bed which can be inserted in the bore of the 1.5 T MRI scanner. This system was fully described in [42].

MITIGATING THE EFFECTS OF HIGH-TEMPERATURE SUPERCONDUCTING COIL DIAMAGNETISM

Another recent advance was made by better understanding the interaction between the HTS coil and the static magnetic field B_0 used in MRI. In the presence of a magnetic field, superconductors spontaneously generate screening currents on their edges and surfaces to expel the magnetic flux. This induces static field (B_0)-inhomogeneities in the vicinity of the superconductor, which can result in B_0-artifacts in the MR images. In type-II superconductors, which include all HTS materials, magnetic flux can be readmitted in the form of quantized flux lines, or "vortices" [43]. Consequently, the magnetic properties of HTS materials are typically temperature dependent and hysteretic. Depending on the magnetic history of the material, notably whether it was cooled in the presence (field cooled) or the absence (zero-field cooled) of a magnetic field, it can display perfect or imperfect diamagnetism. As presented in the previous section, HTS coils for MRI applications have mostly been used at LN_2 temperature, i.e. sufficiently close to the superconducting transition temperature T_c of the HTS material for its diamagnetism to be negligible. However, with better-controlled experimental parameters and new cryostats achieving lower temperatures (~ 60 K) this becomes an issue producing major B_0-artifacts on MR images in the vicinity of the HTS coil.

The static field inhomogeneity artifacts due to static field expulsion from HTS coil were recently investigated [5] for different cooling conditions and temperatures of the HTS coil. This was done by measuring the MR signal at 1.5 T of a water sample in the vicinity of a HTS coil: a 12 mm multi-turn Transmission Line Resonator [44] (MTLR) with a pair of six-turn YBCO spirals (T_c = 86 K) on both sides of a Al_2O_3 substrate. In the aforementioned study, the HTS coil was non-resonant to avoid RF B_1^+-artifacts while keeping intact the diamagnetic response of the superconductor. The coil was used in the cryostat described in **Figure 2**, and the normal to its surface was kept perpendicular to the static field B_0 during the whole experiment. A whole-body RF coil was used in transceiver mode. Standard 3D gradient-echo MR images were acquired after zero-field cooling (outside the MRI scanner), field cooling (inside the MRI scanner) and for different temperatures varying from 60 to 90 K.

In **Figure 3**, we present the main results of this study. Images acquired after zero-field cooling displayed important signal losses and phase perturbations (**Figure 3A**). The observed artifacts were predominant closer to the HTS coil and shared the same

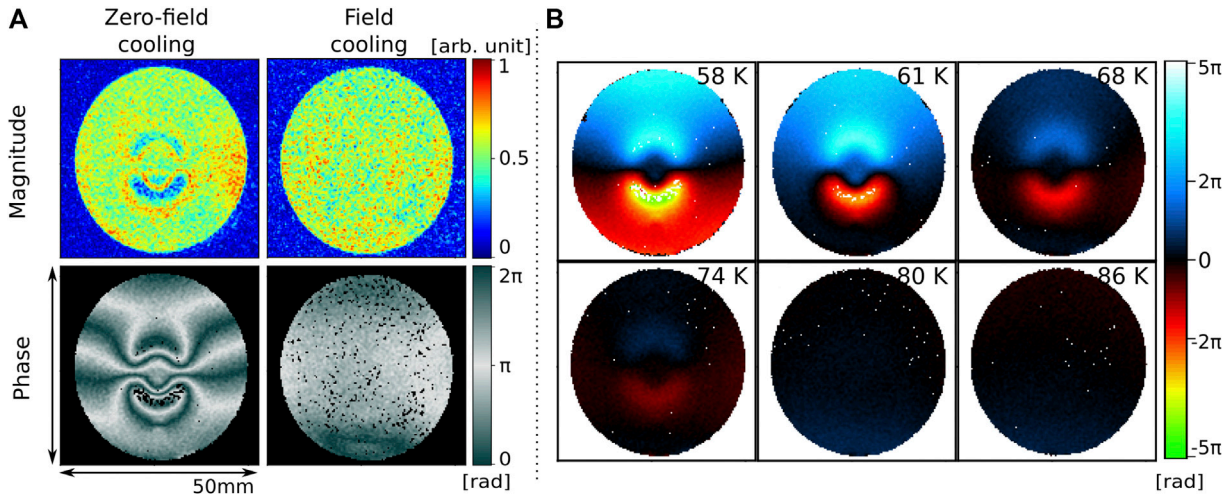

FIGURE 3 | MR images of a water sample in the vicinity of a HTS coil **(A)** after different cooling conditions of the coil (at 58 K), and **(B)** for different temperatures of the coil after zero-field cooling. The slice shown is parallel to the HTS coil plane, ~4.2 mm above. $\vec{B}_0$ is oriented towards the vertical axis of the images. In **(B)**, the phase data were unwrapped, resolving the 2π-jumps. Data taken from [5].

characteristic dimensions. In comparison, images acquired after field-cooling the coil in the MR scanner were unaltered. The phase perturbation was also shown to have a strong temperature dependence (**Figure 3B**); the amplitude of the perturbation was continuously reduced as the temperature increased. Using a phenomenological model of the coil superconducting diamagnetism, it was shown that these artifacts were caused by a small yet unavoidable misalignment, less than 1°, of the HTS coil in the static field B_0, and that their temperature dependence mirrored the temperature dependence of the in-plane critical current of YBCO measured in comparable conditions [45].

Two important conclusions can be drawn from these results. 1) The B_0-artifacts are linked to a low working temperature of the coil when compared to its T_c, and 2) they can be mitigated at low temperature by field-cooling the HTS coil in B_0 at its working position in the MRI scanner.

DECOUPLING THE HIGH-TEMPERATURE SUPERCONDUCTING COIL DURING TRANSMISSION

Another possible source of artifacts comes from the magnetic coupling between the HTS surface coil and the volume coil used during transmission. Copper coil technology typically relies on diodes to deactivate the reception coil during transmission. Unfortunately, these standard techniques cannot be implemented with HTS materials, as the physical connections required for incorporating discrete components in the coil circuit degrade its quality factor and add too much noise. Decoupling is hence a major technological challenge for HTS coils. A solution can be found through the highly nonlinear electrical properties presented by HTS materials [46]. The quality factor Q of HTS coils depends on the power of the incident RF magnetic signal. Their Q of a few thousand during reception (low power stage), typically collapses to a few dozen during transmission (high power stage) [47,48]. These nonlinear properties, which can be tailored by fine engineering of the superconducting track composing the coil, can be exploited as a means to deactivate the HTS coil during transmission [49]. Here we present a study of these nonlinear properties. In a first step **(Setup 1)**, we will present results of a RF characterization of a HTS coil realized in a low field environment (Earth magnetic field). These results will provide insight into the physical mechanism behind the

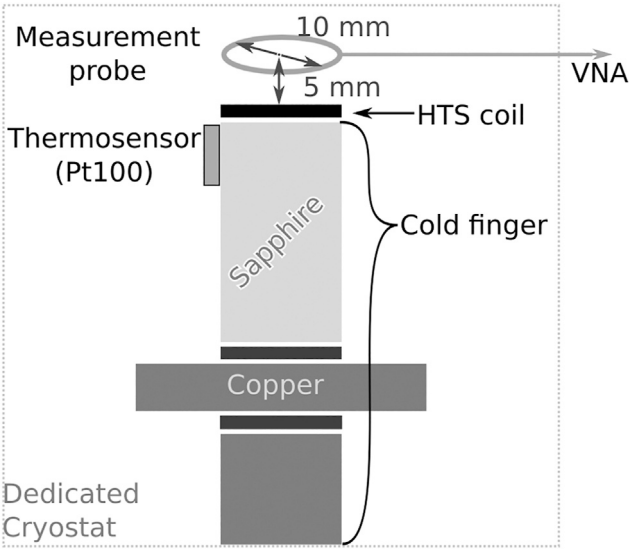

FIGURE 4 | Schematic drawing of the interior of the dedicated cryostat used in Setup 1.The VNA is connected to a measurement probe inductively coupled to the HTS coil, which is secured on a cold finger. The temperature is monitored using a thermosensor (Pt100). The system was fully described by [50].

TABLE 1 | Acquisition parameters of the 3D gradient-echo MRI sequence used in Setup 2.

	HTS coil	Copper coil (Reference)
Pixel receiver bandwidth	217 Hz/pixel	217 Hz/pixel
Echo time/Repetition time	6 ms/25 ms	3 ms/13 ms
Spatial resolution	250 µm × 250 µ × 250 µm	300 µm × 300 µm × 1,000 µm
Field of view	36 mm × 36 mm × 36 mm	20 mm × 20 mm × 20 mm

collapse of the coil quality factor Q. In a second step **(Setup 2)**, we present this decoupling approach implemented in an MRI environment (**Figure 2**), allowing the material to pass from a zero-resistance state to a dissipative state during transmission [49]. In both setups, the experiments were conducted with a resonating (ω = 63.5 MHz at 70 K) HTS surface coil of identical design as the one described in the previous section [5].

Setup 1—The HTS surface coil is used in a dedicated cryostat [50] shown schematically in **Figure 4**, cooled in Earth's magnetic field and characterized with a VNA and a method inspired from [47]. The electrical parameters of the HTS coil are obtained through the measurement of its RF response using an inductive coupling approach involving a measurement probe overcoupled with the HTS coil. The measurement probe is a 10 mm diameter copper loop placed in front of the HTS coil at a 5 mm distance. The incident power produced by the VNA and transmitted to the HTS coil *via* the measurement probe is then converted in equivalent B_1^+ or B_1^- values, depending on the RF amplitude with this experimental geometry. The HTS coil was left resonating at its own resonant frequency, different from the Larmor frequency, for the experiments involving Setup 1.

First, this setup simulates an MRI sequence. A high amplitude pulse with $B_1^+ \in [0.02\,\mu T, 0.4\,\mu T]$ is applied with the measurement probe to mimic the RF pulse used during spin excitation (transmission). Then, a low amplitude pulse corresponding to $B_1^- = 0.02\,\mu T$ is applied to reproduce the NMR signal during reception. The switch time between the two power levels is 12 µs. The HTS coil quality factor Q was extracted as a function of B_1^+ (during the excitation pulse) for three temperatures T = 60, 70, and 80 K.

Secondly, the setup performs a swept-frequency analysis where the modulus and phase of the compensated reflection coefficient $\rho_{comp}(\omega)=\rho(\omega)-\rho_0(\omega)$, are measured with the VNA as a function of the frequency ω for different incident $B_1^+ \in [0.05\,\mu T, 0.35\,\mu T]$ and temperatures T = 60, 70 and 80 K. Here, ρ_0 corresponds to a reference data set taken in the absence of the HTS coil, whereas ρ integrates its contribution [47].

Setup 2—Then, the HTS coil is cooled inside the MR compatible cryostat [42] integrated into a 1.5 T clinical MRI (Achieva, Philips) shown in **Figure 2**. Fine frequency tuning of the HTS coil at ω_0 is performed using a tuning coil [3], while impedance matching is obtained with a coupling coil (**Figure 2D**). The same coupling coil is then used to pick up the HTS coil signal during the experiment. The MRI sequence is a standard 3D gradient-echo using the parameters listed in **Table 1**. During transmission, a volume (whole-body) coil is used to generate rectangular RF pulses with nominal amplitude $B_1^+ \in [0.08, 27\,\mu T]$ and pulse durations $t \in [6.4\,\mu s, 4.0\,ms]$. The pulse duration τ is calculated consequently to keep the flip angle constant ($\alpha = \gamma B_1^+ \tau$). Also, the imaging sample (**Figure 5A**) is filled with a 1 ml solution of water with a gadolinium-based contrast agent (Dotarem, $C = 2.5 \cdot 10^{-3}$ mmol/ml).

With this second setup, we first connected the coupling coil to the MRI acquisition RF channel to acquire the HTS coil signal during reception. A reference measurement was obtained using a room temperature copper coil of similar dimensions (**Figure 5A**). Then, the imaging sample was removed and the coupling coil signal V was connected to an oscilloscope to measure the response of the HTS coil during transmission as a function of B_1^+ at different temperatures $T \in [62\,K, 80\,K]$. A reference measurement was also acquired with the coupling coil only (i.e. without the HTS coil). The ratio V/B_1^+ was then used to track the evolution of the HTS coil quality factor Q. In addition to these measurements, the quality factor Q of the HTS coil was also measured in this configuration using a VNA and an incident power producing a $B_1^+ \sim 0.05\,\mu T$.

Figure 6 presents the results obtained with Setup 1. **Figure 6A** displays the dependance between the Q value of the HTS coil and B_1^+ for three working temperatures of 60, 70 and 80 K. We observe a transition from a superconducting state ($Q \sim 50000$) to a dissipative state ($Q \sim 100$) for B_1^+ values that are temperature dependent. At lower temperature (60 and 70 K), this transition occurs at $B_1^+ \sim 0.2\,\mu T$ whereas at 80 K (closer to T_c), B_1^+ is reduced by almost an order of magnitude to 0.04 µT. Also, we mention that the transition time (not shown here) between the two states was faster than 12 µs.

The effects of the RF power on the HTS material are shown in **Figures 6B–G**, which displays the modulus and phase of ρ_{comp}, noted respectively $|\rho|$ and ϕ thereafter, for different incident B_1^+ and working temperatures. First, at low B_1^+, $|\rho|$ and ϕ display the expected behavior for classical RF coils, except for the temperature dependence of the resonance frequency; at 60 and 70 K, the coil resonates close to 63.5 MHz, which decreases to 63.1 MHz at 80 K. This frequency shift, which is due to the temperature-induced increase of the kinetic inductance of the superconductor, is predominant when T_c = 86 K is approached. Secondly, at higher B_1^+, we observe a collapse of $|\rho|$ and a deformation of ϕ that are also temperature dependent. At 80 K, $|\rho|$ and ϕ simply flatten as B_1^+ increases. This is to be compared with the behaviour observed at 60 and 70 K, where $|\rho|$ becomes strongly deformed at $B_1^+ = 0.35\,\mu T$ and ϕ showcases a discontinuity (inset of **Figures 6C,E**).

In **Figure 5**, we present the results acquired with Setup 2. The spatial inhomogeneities observed in the MR images of **Figures 5B–C** are due to a non-uniform flip angle of the spins over the

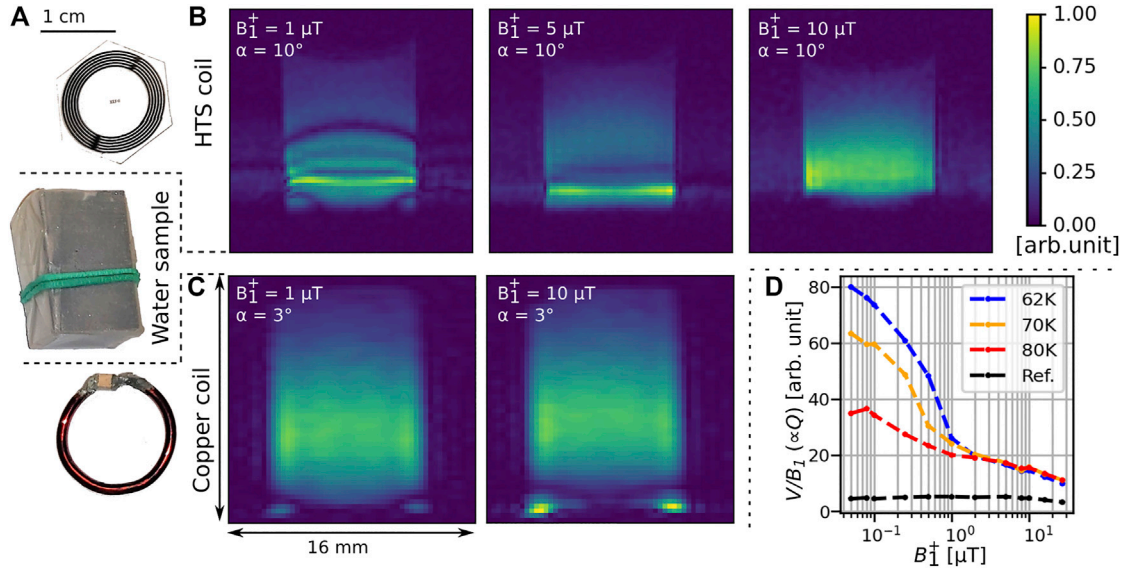

FIGURE 5 | (Setup 2)–**(A)** Pictures of the HTS coil, water sample and copper coil. MR acquisitions obtained with **(A)** the HTS coil at 60 K and **(B)** the copper coil at room temperature for different B_1 varying from 1 to 10 µT at constant spin flip angle α. **(C)** V/B_1^+ ratios ($\propto Q$) as a function of the RF magnetic field B_1^+ transmitted by the volume coil.

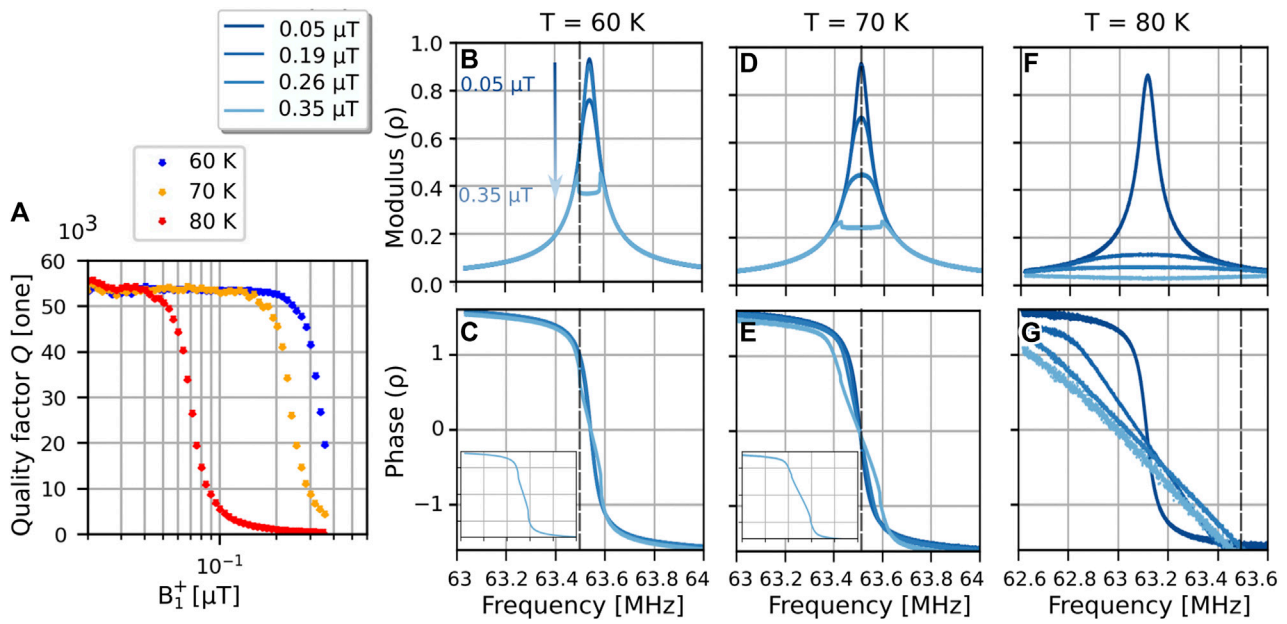

FIGURE 6 | (Setup 1)–**(A)** Measured quality factor Q of the HTS coil as a function of the RF magnetic field B_1 for different temperatures and **(B–G)** swept-frequency analysis of the nonlinear HTS coil for different temperatures and B_1. The top **(B,D,F)** and bottom **(C,E,G)** rows respectively display the modulus and phase of the compensated reflection coefficient ρ_{comp}. The dashed line at 63.5 MHz provides a visual guideline to highlight the temperature drift of the resonance frequency. The insets in **(C)** and **(E)** highlight the phase discontinuity observed for B_1 = 0.35 µT.

sample. This is produced during transmission by the re-emission of the spatially non-uniform B_1^+ field generated by the surface coil, the amplitude of which is proportional to its quality factor Q. In the absence of artifacts, the MR signal would appear relatively uniform over the sample. For a copper coil presenting linear electrical properties (**Figure 5C**), the magnitude of the artifacts does not depend on the value of B_1, as expected at a given flip angle α. For the HTS coil, however, the artifacts in **Figure 5B** are more important at lower B_1^+. This indicates that increasing B_1^+ increases the resistance of the coil, and consequently reduces its quality factor Q during transmission. This behaviour is well observed when we measure the signal of the coupling coil

during transmission. As shown in **Figure 5D**, the ratio V/B_1^+, which is proportional to Q, decreases as a function of B_1^+ of almost one order of magnitude between 0.05 and 10 μT at 62 K. In comparison, this coefficient is almost constant for all B_1^+ values without the HTS coil (ref. curve in black on **Figure 5D**). For values of B_1^+ below 1 μT, Q displays a strong temperature dependence, which is not the case anymore for higher B_1^+. This dependence was also observed with the Q measurement of the HTS coil inside the magnet performed with the VNA, typically with $Q \sim 3000$ at 60 K and $Q \sim 2560$ at 70 K.

These two setups studied the nonlinear electrical properties of the HTS coil in Earth's magnetic field (Setup 1) and in a field of 1.5 T (Setup 2). We observed differences between the behavior of Q in Earth's field and at 1.5 T, in agreement with a previous study (Lambert RSI 2008). This difference can be explained by vortex dynamics, which we assume to be the principal dissipation mechanism in our experiment [51]. The AC current circulating in the HTS coil, depending on $(B_1^+)^2$, is responsible for energy dissipation in the HTS material and leads to the increase of its electrical resistivity (i.e. its surface impedance). In Earth's field, vortex penetration is weak and does not, unless the temperature closely approaches T_c, affect the HTS material response much. At low B_1^+, the vortices remain pinned and the RF current is not strong enough to induce large vortex displacements. Consequently, the surface impedance of the coil remains constant, leading to $Q \approx 50000$ for all working temperatures, in good agreement with precedent measurements {Lambert RSI 2008 [3]}. At higher B_1^+, the effect of hysteretic vortex motion in the HTS material becomes significant, inducing an increase of the electrical resistance, and a decrease of the Q values that amounts to one order of magnitude between 60 and 70 K. This is even more pronounced with an increase of temperature: we observe a decrease of two orders of magnitude of Q. At 1.5 T, the critical current density is lower, and the vortices are more easily set in motion by RF currents even at low B_1^+. This phenomenon becomes more pronounced as the temperature of the HTS material is increased. Consequently, Q is halved between 60 and 80 K. In contrast, for $B_1^+ \geq 1$ μT, Q does not depend on the temperature anymore. This is most probably due to a complete penetration of the material by the vortex lines carrying B_1^+; once the RF field completely penetrates the material, there is no further change in field contrast associated with B_1^+, so that all related artifacts are now independent of temperature. In the experimental results, we observed that the value of B_1^+ at which the superconducting material transits from the superconducting state to the dissipative state depends on temperature, but also on the value of the static field. This can be explained by the temperature, field, and field-orientation dependence of the critical current density of the HTS material, as studied by [45], in comparable conditions.

DISCUSSION

In this work, we reviewed some of the challenges and recent advances made in the implementation of HTS coil in MRI. The key feature of HTS coils is that they do not share the lower limit on resistivity experienced by copper coils, although the ω^2 proportionality law between their electrical noise and working frequency limits their potential for applications in high-field MRI. HTS coils do, however, share the same extrinsic limitations as cryogenic copper coils. To take full advantage of their benefits, the necessity for the sample to be non-conductive, or at least not to overload the coil (c.f. **Equation 2**), restrains the imaging volume to small dimensions for *in vivo* applications at standard medical imaging fields (i.e. up to a few milliliters at 1.5 and 3 T), as discussed in the literature [19]. As for cryogenic copper coils, this limits the prospects of implementations of HTS coils as volume coils. For larger samples, they could nevertheless be implemented as coil arrays, which would allow HTS coils to image far greater fields-of-view while keeping advantageous SNRs. The issue of decoupling the array elements from each other entails substantial work, but a solution could be based on the work of [52], or that of [14]. Considering the small dimensions of HTS coils, they could only be used for surface imaging in clinical MRI for skin [53] or extremities imaging, for instance. In preclinical MRI, they will probably come as a natural successor to cryogenic copper coils, as they are well suited for weakly conductive small biological samples such as mice and rats, or *ex-vivo* biological samples [54]. The high sensitivity of HTS coils also opens up the way to high-resolution MRI (<100 μm) at relatively low fields (<3 T) when compared to the more usual high fields used in preclinical MRI (4.7 T and higher). Since the MR relaxation times depend on B_0, there is a strong motivation to investigate animal models directly in clinical magnetic fields, since this approach greatly facilitates the transfer of MR protocols from preclinical to clinical imaging. Hence, this limits the need for additional investments.

In order for these applications to be developed, the HTS coil must be integrated into a cryostat that achieves both MRI compatibility and good thermal insulation between the cryogenic probe and the room temperature imaging subject. Although this has proven to be an important technological challenge, recent years have seen the design of new and more robust cryostats, with the notable development of the cryogen-free and autonomous system that we described [42]. While we focused our attention primarily on closed-cycle technology, onboard open-cycle cooling approaches dedicated to small RF coils show promising perspectives to address the challenge of cooling high-density flexible HTS coil arrays, i.e. arrays where the relative positions of the coil elements can be modified. Such individual onboard cooling units or, alternatively, distributed refrigerant streams, could be implemented respectively with a compact N_2 Joule-Thomson refrigerator [55] or a microfluidic LN_2 exchanger [56]. The actual challenges of such a device are improving the compactness and reducing the cooling time while keeping a standalone, user-friendly, and cryogen-free solution. Compactness will be achieved by reducing the dimensions, and therefore the weight of the device. Consequently, this will reduce the heat stored in the system at room temperature as well as the thermal resistance between the cooling system and the coil, allowing for faster cooling or less cooling power. This cannot be accomplished without a fine optimization of the thermal capacity of the thermal link with the cooling power of the cryocooler at all stages of cooling. These improvements will

bring the device even closer to the MRI measurement zone and impose having even more non-magnetic material entering its composition. Using new polymeric materials—robust, lighter, and compatible with vacuum and MRI scanners–, will fulfill both requirements.

The question of the optimal working temperature for HTS coils remains open. On the one hand, we have seen that working at temperatures significantly lower than T_c may be associated with circumstantial static field inhomogeneity artifacts caused by the superconducting diamagnetism of the coil; these could be avoided by field cooling the coil in the MRI magnet at its working position. On the other hand, working at lower temperatures should lead to a better sensitivity factor (S_{RF}) of the HTS coil. Therefore, regarding superconducting diamagnetism, working at a lower temperature can be envisioned if these artifacts are consistently avoided. For most applications, this implies frequent temperature cycling of the coil in-between experiments or after a change in geometry. This requires a practical implementation involving quick, localized and uniform heating of the HTS coil inside the cryostat. Such a heating system could work by radiative, resistive, or conductive heating but without any interference with the MRI experiment, and would solve an important issue in the implementation of HTS coils by providing the experimental conditions required to obtain better images with this technology.

The issue of tuning and decoupling of the HTS coil also comes into play for the selection of its working temperature. Until now, our studies were conducted using HTS coils working at around 80 K in transceiver mode. As stated earlier, the HTS coil design is chosen so as to resonate close to the Larmor frequency, and a fine tuning of its resonance frequency is achieved by positioning a closed-circuit copper loop [3]. Thanks to the new cryostat, this fine tuning can now be performed by a fine control of the temperature, as proposed by [42], since the coil resonance frequency depends on the temperature [39]. Also, matching the HTS coil to the source impedance was achieved by a contactless matching technique using an inductive pick-up loop tuned at the Larmor frequency. The coupling coefficient is manually adjusted, modifying the distance between the pick-up loop and the HTS coil, to reach the optimal 50 Ω presented at the input preamplifier. This matching step can be made more user-friendly by the integration of an automated system based on piezoelectric motors inside the cryostat [57].

In parallel, until the issue of the magnetic coupling between the HTS coil and the transmission volume coil is solved, the former can still be used in transceiver mode (i.e. as the transmitter and receiver) Typically, the transmit level of the coupled volume coil is manually adjusted to account for the presence of the HTS coil, which effectively becomes the source of the RF excitation flipping the sample magnetization during transmission. From the perspective of the volume coil, this leads to flip angle values of one to two orders of magnitude smaller than the ones currently used in MR protocols in order to achieve a real π/2-flip angle in the region of interest (ROI) These precautions are necessary to limit the B_1^+-artifacts caused by the HTS coil non-uniform magnetic field. Although this corresponds to a suboptimal implementation of HTS coil, high quality MR images can still be obtained in this operational mode [3]. However, the presented investigations were all based on gradient-echo protocols, and imaging a larger area was realized at the cost of a nonuniformly weighted T1 contrast. Many of the sequences requiring a uniform flip angle to assess a quantitative T1 or T2 contrast, for instance, are not usable in this condition. Consequently, achieving decoupling with HTS coil will open up a new world of applications for this technology.

To that end, the approach illustrated in our experimental results exploits the non-linear electrical response of HTS materials to minimize the quality factor during transmission. Although the coil under study did not reach resistance levels sufficient to achieve proper decoupling, it did provide a proof of concept for this technique. To go further, the HTS coil have to reach its dissipative state for lower RF B_1^+ field values which implies finding ways for the coil current to reach the critical current density of the HTS material sooner. This must be accomplished without degrading the coil sensitivity during reception. This objective can be achieved either by reducing the critical current density notably through temperature, as seen in **Figure 5** and providing another argument for working at higher temperature, or by increasing the current density in the coil by a fine engineering of the superconducting track [49]. This can be performed by adding constrictions of various geometries in the coil design and modifying the HTS material thickness.

CONCLUSION

HTS coil for MRI has come a long way in the last 30 years. Cryogenics have advanced sufficiently to allow the design of MRI compatible cryostats that allow one to reliably operate HTS coils. In addition, we now better understand how HTS coils interact with the superposed magnetic fields B_0 and B_1 used in MRI, allowing for a better integration of the superconducting coil in the MR environment. This technology still faces several challenges before it is ready for practical applications in bio-imaging. However, the significant increase in sensitivity it offers lends it the prospect of being ultimately disruptive.

DATA AVAILABILITY STATEMENT

The raw data supporting the conclusion of this article will be made available by the authors, without undue reservation.

AUTHOR CONTRIBUTIONS

AL: coordinated the writing of the paper; was involved in the redaction of many sections of the article; and acquired parts of the data shown. GA and BB: designed the MRI compatible cryostat shown in the paper; and both were involved in the writing of the section "Progress in MRI compatible cryostats" which displays their work. JB and CvdB: helped design the experiment—Setup 2—shown in the paper; were involved in the writing of the section "Decoupling the HTS coil during transmission;" provided expertise during the discussion of the experimental results LD:

wrote the state-of-the-art sections for "Limits of copper coils in MRI" and "Progress in MRI compatible cryostats" MPQ: coordinated the research project; involved in the design of the experiments shown in this work; main writer of the section "Decoupling the HTS coil during transmission." All authors actively contributed to the writing of this paper.

FUNDING

Experiments were performed on the 1.5 T MRI platform of CEA/SHFJ, affiliated to the France Life Imaging network and partially funded by the network (Grant ANR-11-INBS-0006), under Grant No. ANR-14-CE17-0003 (SupraSense project) and LabeX LaSIPS (ANR-10-LABX-0040-LaSIPS).

ACKNOWLEDGMENTS

The authors thank Dr. Jean-Christophe Ginefri for his contribution to the development of HTS coils within our research group. The authors also thank Rose-Marie Dubuisson for her help with the 1.5 T MRI scanner platform, and Georges Willoquet for his work on the electronics implemented in both cryostats used in this work, as well as Isabelle Saniour and Michel Geahel for their past contributions to this project.

REFERENCES

1. Bednorz JG, and Müller KA (1986) Possible highT C Superconductivity in the Ba-La-Cu-O System. *Z für B - Condens Matter* 64, 189–93. doi:10.1007/BF01303701
2. Lancaster MJ (1997, Passive Microwave Device Applications of High-Temperature Superconductors). *Passive Microwave Device Applications of High-Temperature Superconductors*. United Kingdom: Cambridge University Press doi:10.1017/CBO9780511526688
3. Poirier-Quinot M, Ginefri J-C, Girard O, Robert P, and Darrasse L (2008) Performance of a Miniature High-Temperature Superconducting (HTS) Surface Coil for *In Vivo* Microimaging of the Mouse in a Standard 1.5T Clinical Whole-Body Scanner. *Magn Reson Med* 60, 917–27. doi:10.1002/mrm.21605
4. Black RD, Roemer PB, Mogro-Campero A, Turner LG, and Rohling KW (1993) High Temperature Superconducting Resonator for Use in Nuclear Magnetic Resonance Microscopy. *Appl Phys Lett* 62, 771–3. doi:10.1063/1.108574
5. Labbé A, Dubuisson R-M, Ginefri J-C, Van Der Beek CJ, Darrasse L, and Poirier-Quinot M (2020) Static Field Homogeneity Artifacts Due to Magnetic Flux Expulsion by HTS Coils for High-Resolution Magnetic Resonance Imaging. *Appl Phys Lett* 117, 254101. doi:10.1063/5.0033894
6. Hoult DI, and Richards RE (1976) The Signal-To-Noise Ratio of the Nuclear Magnetic Resonance experiment. *J Magn Reson (1969)* 24, 71–85. doi:10.1016/0022-2364(76)90233-X
7. Hoult DI, and Lauterbur PC (1979) The Sensitivity of the Zeugmatographic experiment Involving Human Samples. *J Magn Reson (1969)* 34, 425–33. doi:10.1016/0022-2364(79)90019-2
8. Styles P, Soffe NF, Scott CA, Crag DA, Row F, White DJ, et al. (1984) A High-Resolution NMR Probe in Which the Coil and Preamplifier Are Cooled with Liquid Helium. *J Magn Reson (1969)* 60, 397–404. doi:10.1016/0022-2364(84)90050-7
9. Hall AS, Barnard B, McArthur P, Gilderdale DJ, Young IR, and Bydder GM (1988) Investigation of a Whole-Body Receiver Coil Operating at Liquid Nitrogen Temperatures. *Magn Reson Med* 7, 230–5. doi:10.1002/mrm.1910070211
10. Hall AS, Alford NM, Button TW, Gilderdale DJ, Gehring KA, and Young IR (1991) Use of High Temperature Superconductor in a Receiver Coil for Magnetic Resonance Imaging. *Magn Reson Med* 20, 340–3. doi:10.1002/mrm.1910200218
11. Anderson WA, Brey WW, Brooke AL, Cole B, Delin KA, Fuks LF, et al. (1995) High-sensitivity NMR Spectroscopy Probe Using Superconductive Coils. *Bull Magn Reson* 17, 98–102.
12. Kovacs H, Moskau D, and Spraul M (2005) Cryogenically Cooled Probes-A Leap in NMR Technology. *Prog Nucl Magn Reson Spectrosc* 46, 131–55. doi:10.1016/j.pnmrs.2005.03.001
13. Niendorf T, Pohlmann A, Reimann HM, Waiczies H, Peper E, Huelnhagen T, et al. (2015) Advancing Cardiovascular, Neurovascular and Renal Magnetic Resonance Imaging in Small Rodents Using Cryogenic Radiofrequency Coil Technology. *Front Pharmacol* 6, 255. doi:10.3389/fphar.2015.00255
14. Wosik J, Xue L, Xie L-M, Kamel MR, Nesteruk K, and Bankson JA (2007) Superconducting Array for High-Field Magnetic Resonance Imaging. *Appl Phys Lett* 91, 183503. doi:10.1063/1.2801384
15. Nouls JC, Izenson MG, Greeley HP, and Johnson GA (2008) Design of a Superconducting Volume Coil for Magnetic Resonance Microscopy of the Mouse Brain. *J Magn Reson* 191, 231–8. doi:10.1016/j.jmr.2007.12.018
16. Lin I-T, Yang H-C, and Chen J-H (2012) Enlargement of the Field of View and Maintenance of a High Signal-To-Noise Ratio Using a Two-Element High-T C Superconducting Array in a 3T MRI. *PLoS One* 7, e42509. doi:10.1371/journal.pone.0042509
17. Ramaswamy V, Hooker JW, Withers RS, Nast RE, Brey WW, and Edison AS (2013) Development of a 13C-Optimized 1.5-mm High Temperature Superconducting NMR Probe. *J Magn Reson* 235, 58–65. doi:10.1016/j.jmr.2013.07.012
18. Laistler E, Poirier-Quinot M, Lambert SA, Dubuisson R-M, Girard OM, Moser E, et al. (2015) *In Vivo* MR Imaging of the Human Skin at Subnanoliter Resolution Using a Superconducting Surface Coil at 1.5 Tesla. *J Magn Reson Imaging* 41, 496–504. doi:10.1002/jmri.24549
19. Darrasse L, and Ginefri JC (2003) Perspectives with Cryogenic RF Probes in Biomedical MRI. *Biochimie* 85, 915–37. doi:10.1016/j.biochi.2003.09.016
20. Matula RA (1979) Electrical Resistivity of Copper, Gold, Palladium, and Silver. *J Phys Chem Reference Data*, 8(4), 1147–298. doi:10.1063/1.555614
21. Sondheimer EH (1952) The Mean Free Path of Electrons in Metals. *Adv Phys* 1, 1–42. doi:10.1080/00018735200101151
22. Wang Y, Su HT, Huang F, and Lancaster MJ (2007) Measurement of YBCO Thin Film Surface Resistance Using Coplanar Line Resonator Techniques from 20 MHz to 20 GHz. *IEEE Trans Appl Supercond* 17, 3632–9.
23. Anders S, Blamire MG, Buchholz F-I, Crété D-G, Cristiano R, Febvre P, et al. (2010) European Roadmap on Superconductive Electronics - Status and Perspectives. *Physica C: Superconductivity* 470, 2079–126. doi:10.1016/j.physc.2010.07.005
24. McFarland EW, and Mortara A (1992) Three-dimensional NMR Microscopy: Improving SNR with Temperature and Microcoils. *Magn Reson Imaging* 10, 279–88. doi:10.1016/0730-725X(92)90487-K
25. Black R, Early T, Roemer P, Mueller O, Mogro-Campero A, Turner L, et al. (1993) A High-Temperature Superconducting Receiver for Nuclear Magnetic Resonance Microscopy. *Science.* 259, 793–5. doi:10.1126/science.8430331
26. Miller JR, Zhang K, Ma QY, Mun IK, Jung KJ, Katz J, et al. (1996) Superconducting Receiver Coils for Sodium Magnetic Resonance Imaging. *IEEE Trans Biomed Eng* 43, 1197–9. doi:10.1109/10.544344
27. Ginefri J-C, Darrasse L, and Crozat P (2001) High-temperature Superconducting Surface Coil for *In Vivo* Microimaging of the Human Skin. *Magn Reson Med* 45, 376–82. doi:10.1002/1522-2594(200103)45:3<376::aid-mrm1049>3.0.co;2-r
28. Marek D. RF Receiver Coil Arrangement for NMR Spectrometers. US Patent 5247256A, 25 April 1990.
29. Hill HDW (1997) Improved Sensitivity of NMR Spectroscopy Probes by Use of High-Temperature Superconductive Detection Coils. *IEEE Trans Appl Supercond* 7, 3750–5. doi:10.1109/77.622233

30. Ratering D, Baltes C, Nordmeyer-Massner J, Marek D, and Rudin M (2008) Performance of a 200-MHz Cryogenic RF Probe Designed for MRI and MRS of the Murine Brain. *Magn Reson Med* 59, 1440–7. doi:10.1002/mrm.21629
31. Baltes C, Radzwill N, Bosshard S, Marek D, and Rudin M (2009) Micro MRI of the Mouse Brain Using a Novel 400 MHz Cryogenic Quadrature RF Probe. *NMR Biomed.* 22, 834–42. doi:10.1002/nbm.1396
32. Junge S (2012) Cryogenic and Superconducting Coils for MRI. *eMagRes* 1, 505–14.
33. Ginefri J-C, Poirier-Quinot M, Girard O, and Darrasse L (2007) Technical Aspects: Development, Manufacture and Installation of a Cryo-Cooled HTS Coil System for High-Resolution Iin-Vvivo Imaging of the Mouse at 1.5T. *Methods* 43, 54–67. doi:10.1016/j.ymeth.2007.03.011
34. Hu B, Varma G, Randell C, Keevil SF, Schaeffter T, and Glover P (2012) A Novel Receive-Only Liquid Nitrogen ($\Hbox{LN}_{2}$)-Cooled RF Coil for High-Resolution *In Vivo* Imaging on a 3-Tesla Whole-Body Scanner. *IEEE Trans Instrum Meas* 61, 129–39. doi:10.1109/TIM.2011.2157575
35. Lin I-T, Yang H-C, and Chen J-H (2013) A Temperature-Stable Cryo-System for High-Temperature Superconducting MR Iin-Vvivo Imaging. *PLoS One* 8, e61958. doi:10.1371/journal.pone.0061958
36. Sánchez-Heredia JD, Baron R, Hansen ESS, Laustsen C, Zhurbenko V, and Ardenkjaer-Larsen JH (2020) Autonomous Cryogenic RF Receive Coil for 13 C Imaging of Rodents at 3 T. *Magn Reson Med* 84, 497–508. doi:10.1002/mrm.28113
37. Vester M, Steinmeyer F, Roas B, Thummes G, and Klundt K (1997) High Temperature Superconducting Surface Coils with Liquid Nitrogen or Pulse Tube Refrigeration (Abstr). in Vancouver, BC: ISMRM 5th Scientific Meeting and Exhibition, doi:10.4095/219009
38. Darrasse L, Chiron L, Ginefri J-C, Poirier-Quinot M, Trollier T, Ravex A, et al. (2004) Cryosonde IRM : antenne IRM supraconductrice pour la microscopie des régions superficielles du corps humain et des petits modèles animaux. *ITBM-RBM* 25, 254–9. doi:10.1016/j.rbmret.2004.09.003
39. Lambert S, Ginefri J-C, Poirier-Quinot M, and Darrasse L (2013) High-temperature Superconducting Radiofrequency Probe for Magnetic Resonance Imaging Applications Operated below Ambient Pressure in a Simple Liquid-Nitrogen Cryostat. *Rev Scientific Instr* 84, 054701. doi:10.1063/1.4802947
40. Authelet G, Poirier-Quinot M, Ginefri J-C, Bonelli A, and Baudouy B (2017) Conceptual Design of a Cryogen-free μMRI Device. in *IOP Conf Ser Mater Sci Eng*, 12122.
41. Authelet G, Bonelli A, Poirier-Quinot M, Ginefri JC, Saniour I, and Baudouy B (2019) All Polymer Cryogen Free Cryostat for μ-MRI Application at Clinical Field. in *IOP Conf Ser Mater Sci Eng*, 12156.
42. Saniour I, Authelet G, Baudouy B, Dubuisson R-M, Jourdain L, Willoquet G, et al. (2020) A Temperature-Controlled Cryogen Free Cryostat Integrated with Transceiver-Mode Superconducting Coil for High-Resolution Magnetic Resonance Imaging. *Rev Scientific Instr* 91, 055106, doi:10.1063/1.5143107
43. Tinkham M (1996) *Introduction to Superconductivity*. 2nd ed. eds. J Shira and E Castellano New-York: McGraw-Hill.
44. Serfaty S, Haziza N, Darrasse L, and Kan S (1997) Multi-turn Split-Conductor Transmission-Line Resonators. *Magn Reson Med* 38, 687–9. doi:10.1002/mrm.1910380424
45. Díez-Sierra J, López-Domínguez P, Rijckaert H, Rikel M, Hänisch J, Khan MZ, et al. (2020) High Critical Current Density and Enhanced Pinning in Superconducting Films of YBa2Cu3O7−δ Nanocomposites with Embedded BaZrO3, BaHfO3, BaTiO3, and SrZrO3 Nanocrystals. *ACS Appl Nano Mater* 3, 5542–53. doi:10.1021/acsanm.0c00814
46. Shen ZY (1994) High-temperature Superconducting Microwave Circuits. Boston, MA: Artech House Publishers.
47. Girard O, Ginefri J-C, Poirier-Quinot M, and Darrasse L (2007) Method for Nonlinear Characterization of Radio Frequency Coils Made of High Temperature Superconducting Material in View of Magnetic Resonance Imaging Applications. *Rev Scientific Instr* 78, 124703. doi:10.1063/1.2825241
48. Geahel M (2018) *Découplage de détecteurs radiofréquences supraconducteurs à très haute sensibilité pour la micro-imagerie par résonance magnétique*. https://tel.archives-ouvertes.fr/tel-01880203/document (Accessed March 20, 2021).
49. Saniour I, Authelet G, Baudouy B, Dubuisson RM, van der Beek CJ, Darrasse L, et al. (2019) *Novel Passive Decoupling Approach for High Resolution HTS RF Coils Based on the Nonlinear Electrical Properties of Superconductors*. Rotterdam: ESMRMB 2019. in *36th Annual Scientific Meeting. Springer*.
50. Saniour I, Geahel M, Briatico J, Beek CJvan der, Willoquet G, Jourdain L, et al. (2020) Versatile Cryogen-free Cryostat for the Electromagnetic Characterization of Superconducting Radiofrequency Coils. *EPJ Tech Instrum* 7, 1–11. doi:10.1140/epjti/s40485-020-00055-2
51. Clem JR, and Sanchez A (1994) Hysteretic AC Losses and Susceptibility of Thin Superconducting Disks. *Phys Rev B* 50, 9355, 62. doi:10.1103/physrevb.50.9355
52. Frass-Kriegl R, Laistler E, Hosseinnezhadian S, Schmid AI, Moser E, Poirier-Quinot M, et al. (2016) Multi-turn Multi-gap Transmission Line Resonators - Concept, Design and First Implementation at 4.7 T and 7 T. *J Magn Reson*, 273, 65–72. doi:10.1016/j.jmr.2016.10.008
53. Ginefri J-C, Durand E, and Darrasse L (1999) Quick Measurement of Nuclear Magnetic Resonance Coil Sensitivity with a Single-Loop Probe. *Rev Scientific Instr* 70, 4730–1. doi:10.1063/1.1150142
54. Poirier-Quinot M, Frasca G, Wilhelm C, Luciani N, Ginefri J-C, Darrasse L, et al. (2010) High-resolution 1.5-Tesla Magnetic Resonance Imaging for Tissue-Engineered Constructs: a Noninvasive Tool to Assess Three-Dimensional Scaffold Architecture and Cell Seeding. *Tissue Eng C: Methods* 16, 185–200. doi:10.1089/ten.tec.2009.0015
55. Wright AC, Song HK, Elliott DM, and Wehrli FW (2005) Use of a Joule-Thomson Micro-refrigerator to Cool a Radio-Frequency Coil for Magnetic Resonance Microscopy. *Rev Scientific Instr* 76, 014301. doi:10.1063/1.1824340
56. Koo C, Godley RF, Park J, McDougall MP, Wright SM, and Han A (2011) A Magnetic Resonance (MR) Microscopy System Using a Microfluidically Cryo-Cooled Planar Coil. *Lab Chip* 11, 2197–203. doi:10.1039/c1lc20056a
57. Li Z, Willoquet G, Guillot Gv., Hosseinnezhadian S, Jourdain L, Poirier-quinot M, et al. (2016) Study of Two Contact-Less Tuning Principles for Small Monolithic Radiofrequency MRI Coils and Development of an Automated System Based on Piezoelectric Motor. *Sensors Actuators A: Phys.* 241, 176–89. doi:10.1016/j.sna.2016.02.008

Conflict of Interest: The authors declare that the research was conducted in the absence of any commercial or financial relationships that could be construed as a potential conflict of interest.

frontiers in Physics

ORIGINAL RESEARCH
published: 26 July 2021
doi: 10.3389/fphy.2021.701157

Design, Characterisation and Performance of an Improved Portable and Sustainable Low-Field MRI System

*Bart de Vos[1], Javad Parsa[1,2], Zaynab Abdulrazaq[1], Wouter M. Teeuwisse[1], Camille D. E. Van Speybroeck[1], Danny H. de Gans[3], Rob F. Remis[4], Tom O'Reilly[1] and Andrew G. Webb[1,4]**

[1]C.J. Gorter Center for High Field MRI, Department of Radiology, Leiden University Medical Center, Leiden, Netherlands, [2]Percuros BV, Leiden, Netherlands, [3]Dienst Elektronische en Mechanische Ontwikkeling (DEMO), Delft University of Technology, Delft, Netherlands, [4]Circuits and Systems, Delft University of Technology, Delft, Netherlands

Low-field permanent magnet-based MRI systems are finding increasing use in portable, sustainable and point-of-care applications. In order to maximize performance while minimizing cost many components of such a system should ideally be designed specifically for low frequency operation. In this paper we describe recent developments in constructing and characterising a low-field portable MRI system for *in vivo* imaging at 50 mT. These developments include the design of i) high-linearity gradient coils using a modified volume-based target field approach, ii) phased-array receive coils, and iii) a battery-operated three-axis gradient amplifier for improved portability and sustainability. In addition, we report performance characterisation of the RF amplifier, the gradient amplifier, eddy currents from the gradient coils, and describe a quality control protocol for the overall system.

Keywords: low field MRI, MR hardware, halbach magnet, gradient coil design, RF coil array, RF amplifier, quality control, gradient amplifier

OPEN ACCESS

Edited by:
Sigrun Roat,
Medical University of Vienna, Austria

Reviewed by:
Robert Todd Constable,
Yale University, United States
Najat Salameh,
University of Basel, Switzerland

****Correspondence:***
Andrew G. Webb
a.webb@lumc.nl

Specialty section:
This article was submitted to Medical Physics and Imaging, a section of the journal Frontiers in Physics

Received: *27 April 2021*
Accepted: *09 July 2021*
Published: *26 July 2021*

Citation:
de Vos B, Parsa J, Abdulrazaq Z, Teeuwisse WM, Van Speybroeck CDE, de Gans DH, Remis RF, O'Reilly T and Webb AG (2021) Design, Characterisation and Performance of an Improved Portable and Sustainable Low-Field MRI System. Front. Phys. 9:701157. doi: 10.3389/fphy.2021.701157

INTRODUCTION

In the past 15 years several groups have shown significant progress in the design of low field (<100 mT) MRI systems [1–20]. Several different magnet geometries have been used, and each system contains a unique combination of custom-built and commercial components. The following paragraphs summarize the properties of systems which have been used for *in vivo* imaging in terms of their hardware design and performance. For a more detailed review, Sarracanie and Salameh have published an extensive review discussing general progress in low field MRI [21].

The Walsworth group designed a Helmholtz coil based bi-planar electromagnet which, after passive shimming creates a magnetic field of 6.5 mT [1–3]: the planes on which the conductors lie are separated by 79 cm, resulting in an open bore system which allows the subject to sit in an upright position. The maximum gradient strength of the unshielded planar gradient coils is 0.7 mTm^{-1} using 140 A of peak current. Commercial RF amplifiers (300 W), gradient amplifiers (200 A peak current) and spectrometer are used. Lurie's group in Aberdeen have designed and built a fast field cycling system which uses a 50 cm diameter custom-built resistive magnet which can be ramped to create an axial magnetic field between 50 μT and 0.2 T [4–8]. Reported gradient efficiencies are between 0.17 and 0.18 $mTm^{-1}A^{-1}$. In addition, the system uses eleven shim coils resulting in 40 ppm B_0

homogeneity, measured over a 15 cm long cylindrical volume with a diameter of 30 cm. Commercial RF amplifiers (2 kW), gradient amplifiers (107 A peak current) and multi-channel spectrometer are used.

In terms of systems which have been designed with portability and point-of-care in mind, He et al. have designed an H-shaped dipolar magnet system for cerebral stroke imaging [9]. The system has a clear bore of 26 cm and is designed for imaging within a 200 mm DSV. In this region they obtain a field strength of 50.9 mT with a homogeneity of 120 ppm after passive shimming. Unshielded fingerprint planar gradient coils have efficiencies between 0.13 and 0.36 $mTm^{-1}A^{-1}$. A custom-built (100 W) RF-amplifier and commercial gradient amplifier (150 A peak current) and spectrometer were used. A similar system with a higher field strength of 0.2 T was built by [10]. This 200 kg weighing system with a vertical gap of only 16 cm was mounted inside a minivan. Commercial RF amplifiers (150 W), gradient amplifiers (10 A peak current) and spectrometer are used. An H-type magnet system has been commercialized by Hyperfine creating a portable MRI for bedside imaging, which received FDA approval in February 2020. The system operates at 64 mT, has a 30 cm vertical opening and uses an 8-channel receive only head coil. Their bi-planar gradient coils create a gradient field with a maximum strength of 26 mT^1m^{-1} [11, 12].

An alternative approach to portable design is to use a system of many hundreds or thousands of permanent magnets based on a Halbach geometry [22–27]. The Halbach-array has the advantage of being lightweight and having almost no fringe fields, making it safer to handle. Such a system was built by [13–16], who have used an approach in which the magnet is designed to produce a linear gradient superimposed on the main magnetic field. In this way only two gradient coils and amplifiers are required, but specialized pulse sequences and image processing algorithms must be used. The B_0 field strength is 80 mT averaged over a 200 mm DSV with a built-in gradient strength of 7.6 mT^1m^{-1}. For the remaining two encoding directions unshielded cylindrical gradient coils with efficiencies of 0.575 and 0.815 $mTm^{-1}A^{-1}$ were designed. They use commercial RF (2 kW) and gradient amplifiers (maximum current 9 A).

O'Reilly et al. have used an approach in which the Halbach geometry was optimized to produce a magnetic field that is as homogeneous as possible, with conventional spatial encoding using three gradient coils [17, 18]. The 50.4 mT system has a homogeneity of 2,400 ppm after passive shimming, measured over a 200 mm DSV. Using an analytical target field approach [28] three single layer gradient coils were designed with coil efficiencies of 0.37 and 0.8 $mTm^{-1}A^{-1}$ for the axial and transverse coils, respectively. The linearity is within 5% for the transverse coils, however for the axial gradient this deviation is larger than 20% measured over a 200 mm DSV. The console/spectrometer used is a Kea 2 system (Magritek GmbH, Aachen, Germany). This operates over a frequency range of 1–100 MHz. Direct digital synthesis is used on the transmit side, with signal reception being at a fixed 100 MHz oversampled frequency, with 16-bit resolution, followed by decimation and digital filtering to the desired acquisition bandwidth. An inbuilt preamplifier has a gain of 37 dB and noise figure <1.5 dB: a passive duplexer is used as a transmit/receive switch. We use three of the four gradient driver modules, which have a +/−10 V output with 16-bit resolution. One of the eight TTL outputs is used to blank/unblank the RF amplifier. Imaging sequences were written in Prospa, which is a proprietary programming code very similar to C++: the timing resolution on instructions is 100 ns. All timing is controlled by a central 1 GHz clock.

In this work hardware improvements to the above system are described, namely an axial gradient coil with significantly improved linearity and field-of-view, a four-channel phased array receive coil for knee and calf muscle imaging, and a battery-operated gradient amplifier with improved filtering. Detailed characterisation of the gradient eddy currents, performance of the custom-built RF and gradient amplifiers, and a quality assurance protocol including the overall system noise are also reported for the first time.

IMPROVED AXIAL GRADIENT COIL DESIGN AND CONSTRUCTION

Mathematical Framework

In our previous work Turner's target field method [29] was adapted for transverse background fields [28] and stable wire path solutions were found by exploiting the cylindrical structure of the gradient coil configuration *via* Fourier analysis and high-frequency filtering: an open-source gradient design tool was made available using this method.[1] The transverse y, z-gradient coils designed with this method yield linear performance within 5% for a 200 mm DSV. However, the axial gradient has a significantly reduced region of linearity with a deviation more than 20% over this DSV. This is due to the locations of the target fields, which can only be specified on a concentric cylinder and not in the entire volume of the cylinder. Another reason is that small length/DSV ratios [30] are not particularly suited to this method because the Fourier transform requires infinitely long cylindrical structures. Our aim is to produce an axial gradient coil with a higher intrinsic linearity, as well as to further increase the imaging field-of-view in the axial dimension by increasing the length of the gradient coil.

Several approaches have been proposed to deal with relatively short finite length cylinders [31, 32], though these are not structural solutions. Carlson et al. first showed that a set of sinusoidal basis functions can be used when considering finite length cylindrical structures [33]. Later Forbes and Crozier showed that using such a series, asymmetric target field shim coils could be designed, specifically for zonal modes [34], which are constant in the azimuthal and vary along the axis of the cylinder. They showed that asymmetric target fields can be prescribed and that the ill-conditioned coil design problem can be solved in a stable manner with the help of Tikhonov regularisation [35]. The same group created a more general method to include all tesseral components [36], which are modes with variations in both the φ- and *z*-direction.

[1]Gradient design Tool: https://github.com/LUMC-LowFieldMRI/GradientDesignTool

In this work we adapt Forbes and Crozier's method for the transverse magnetic field of a Halbach-array magnet. In addition, we specify target fields within a volume, use different basis functions, and optimize with respect to power rather than current direction stability. The following finite length cylindrical surface is considered

$$\mathbb{S} = \{(r, \varphi, z); r = a, 0 \le \varphi \le 2\pi, -L \le z \le L\},$$

and a weighted sum of sinusoidal basis functions is introduced to describe the surface current density. Specifically, the φ- and z-components of the surface current density are written as

$$J_\varphi^s(\varphi, z) = \sum_{n=1}^{N}\sum_{m=1}^{M}[P_{nm}\cos(m\varphi) + Q_{nm}\sin(m\varphi)]\cos\left(\frac{n\pi(z+L)}{2L}\right),$$

$$J_z^s(\varphi, z) = \sum_{n=1}^{N}\sum_{m=1}^{M}\frac{2mL}{n\pi a}[P_{nm}\sin(m\varphi) - Q_{nm}\cos(m\varphi)]\sin\left(\frac{n\pi(z+L)}{2L}\right),$$

where N and M determine the number of modes that are considered. The unknown weights that need to be found are P_{nm} and Q_{nm}. The above equations satisfy the continuity equation for a current on a cylindrical surface. Note that the z-component of the current density vanishes at the boundaries $z = \pm L$ ensuring that no current flows out of the truncated cylindrical surface. As mentioned above, unlike the shim coils designed by Forbes, zonal modes do not need to be considered here, as they create a concomitant component. This decreases the number of unknowns.

For Halbach-based gradient coil design the relationship between current density and target field can be expressed by the transverse component of the Biot-Savart Law, which is written as

$$B_x(\mathbf{x}) = \frac{\mu_0}{4\pi}\int_{\mathbf{x}'\in\mathbb{S}}\frac{J_y^s(\mathbf{x}')(z-z') - J_z^s(\mathbf{x}')(y-y')}{|\mathbf{x}-\mathbf{x}'|^3}\,\mathrm{d}A.$$

Here $\mathbf{x}$ is the position vector, $\mathbf{x}'$ the integration vector, and μ_0 the permeability of vacuum. Writing J_x^s and J_z^s in cylindrical components and substituting the expansions leads to the field expansion

$$B_x(\mathbf{x}) = a\frac{\mu_0}{4\pi}\sum_{n=1}^{N}\sum_{m=1}^{M}P_{nm}\beta_{nm}(\mathbf{x}) + Q_{nm}\Gamma_{nm}(\mathbf{x}),$$

where β_{nm} and Γ_{nm} are given by

$$\beta_{nm}(\mathbf{x}) = \int_{z'=-L}^{L}\int_{\varphi'=0}^{2\pi}\frac{\cos(m\varphi')\cos\left(\frac{n\pi(z'+L)}{2L}\right)\cos\varphi'(z-z') - \frac{2mL}{n\pi a}\sin(m\varphi')\sin\left(\frac{n\pi(z'+L)}{2L}\right)(y - a\sin\varphi')}{\left[(x-a\cos\varphi')^2 + (y-a\sin\varphi')^2 + (z-z')^2\right]^{3/2}}\mathrm{d}\varphi'\mathrm{d}z',$$

$$\Gamma_{nm}(\mathbf{x}) = \int_{z'=-L}^{L}\int_{\varphi'=0}^{2\pi}\frac{\sin(m\varphi')\cos\left(\frac{n\pi(z'+L)}{2L}\right)\cos\varphi'(z-z') + \frac{2mL}{n\pi a}\cos(m\varphi')\sin\left(\frac{n\pi(z'+L)}{2L}\right)(y - a\sin\varphi')}{\left[(x-a\cos\varphi')^2 + (y-a\sin\varphi')^2 + (z-z')^2\right]^{3/2}}\mathrm{d}\varphi'\mathrm{d}z',$$

which are evaluated numerically. The equation for B_x is valid for a single target field point at a location $\mathbf{x}$. Requiring that this equation holds for all target field locations of interest leads to a system of equations $A\mathbf{x} = \mathbf{b}$, where $\mathbf{b}$ is the K × 1 data vector containing the target field values at the K different locations, $\mathbf{x}$ is the L × 1 vector containing the unknown expansion coefficients, and A is the K × L system matrix containing β_{mn} and Γ_{nm}. To obtain stable solutions in the next steps regularisation is implemented.

Minimizing the power consumption of the gradient coil is important for low resource settings. The power in terms of a surface current density [36] can be described as

$$P = \frac{1}{\sigma}\int_{\mathbf{x}'\in\mathbb{S}}\left|\left|J_s(\mathbf{x}')\right|\right|^2\mathrm{d}A$$

and substituting the sinusoidal basis functions in the above equations and evaluating the integrals over the surface $\mathbb{S}$ leads to

$$P = \sum_{n=1}^{N}\sum_{m=1}^{M}P_{nm}^2\upsilon_{nm} + Q_{nm}^2\upsilon_{nm},$$

where

$$\upsilon_{nm} = \frac{a\pi L}{\sigma}\left[1 + \left(\frac{2mL}{n\pi a}\right)^2\right].$$

This expression can be included and the total system can be treated as a regularised least squares problem. Specifically, introducing the diagonal L × L matrix G, with the coefficients υ_{nm} on its diagonal, the power $P = \mathbf{x}^T\mathrm{G}\mathbf{x}$ and the following functional can be minimized

$$\mathcal{F}(\mathbf{x}) = \frac{1}{2}||\mathrm{A}\mathbf{x} - \mathbf{b}||_2^2 + \frac{1}{2}\lambda\mathbf{x}^T\mathrm{G}\mathbf{x}.$$

The regularisation parameter λ allows weighing of the power efficiency and stabilizes the problem of finding the expansion coefficients. By taking the derivative of the functional with respect to x and setting it to zero, the weights of the basis functions can be found for a certain target field. Here the choice is made to regularise with respect to the power. However, any term can be added in this manner as long as it can be expressed in terms of the unknown coefficients. This has, for instance, been done to minimize the fluctuations in the current direction or the inductance [31, 36]. After obtaining values for the weight coefficients, the current density can be determined. Subsequently, stream function theory is used to obtain the wire patterns [37]. The expression for the corresponding stream function can be found to be

$$\psi(\varphi, z) = \sum_{n=1}^{N}\sum_{m=1}^{M}\frac{2L}{n\pi}[P_{nm}\cos(m\varphi) + Q_{nm}\sin(m\varphi)]sin\left(\frac{n\pi(z+L)}{2L}\right).$$

Wires should be placed in between contours of the stream functions, not on the contours themselves. The value of the current can be found by taking the difference between streamline levels. To increase the efficiency of the coil the number of turns is chosen to be such that the insulated wires

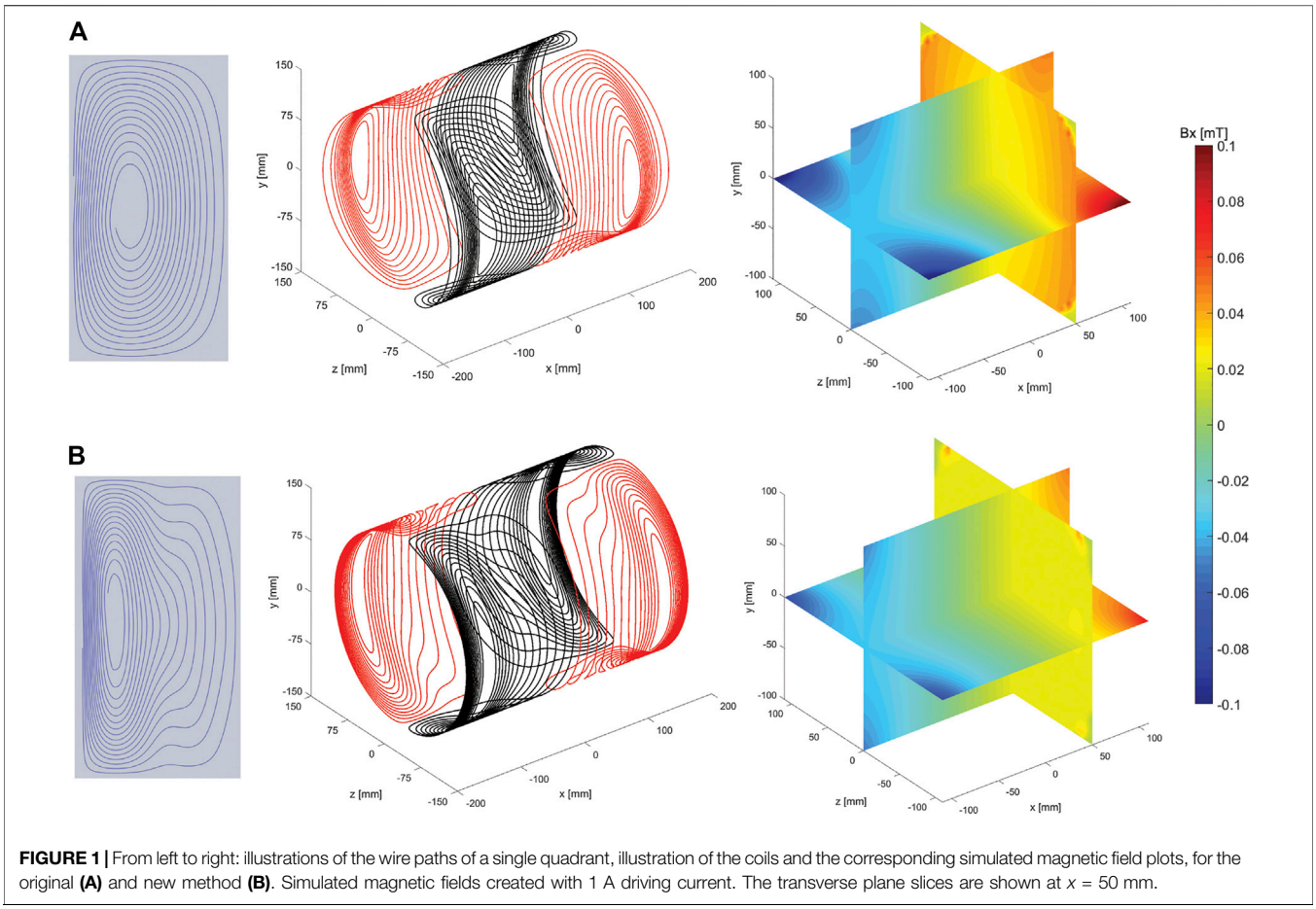

FIGURE 1 | From left to right: illustrations of the wire paths of a single quadrant, illustration of the coils and the corresponding simulated magnetic field plots, for the original **(A)** and new method **(B)**. Simulated magnetic fields created with 1 A driving current. The transverse plane slices are shown at x = 50 mm.

do not overlap, but do touch each other at the edges of the coil holder.

Gradient Coil Simulation and Construction

Two axial gradient coils are simulated for the same cylindrical geometry and optimized in terms of linearity for a 200 mm DSV. One using the original method [28] and the other uses the method described above. The diameters of both coils are 270 mm, with a length of 350 mm and 14 turns per quadrant. The results are analysed using the magnetostatic solver of CST Studio Suite 2019 (CST, Darmstadt, Germany). For the new gradient coil the highest linearity is obtained by taking 640 target field points for the defined cylindrical sub-volume with a length of 200 mm and a diameter of 200 mm. In order to take into account a sufficient number of modes, N and M, representing the axial and azimuthal modes, are both set to 8. This leads to a total of 96 modes. The optimal trade-off between coil efficiency and linearity is found using a parameters sweep, this leads to a λ of 1.5 e-12 for the simulated comparison coil.

Figure 1 shows the wire patterns of a single quadrant, the total coil and the corresponding simulated magnetic fields for the original (A) and new method (B). The yz cross sections at x = 50 mm display that there is a significant increase in uniformity using the new method. **Table 1** shows that the DSV in which the deviation from linearity along the centre line is less than 5% is increased from 50 mm for the original method to 120 mm for the new method. In previous work we found that the quasi-static simulations performed in CST were very accurate with field values varying within a few percent with respect to the field measured experimentally with a 3-axis measuring robot [28].

In order to take further advantage of the intrinsic increased linearity of coils designed using the new method, a 450 mm long gradient coil is designed and built, using the target fields, number of modes and diameter as discussed above. The optimal λ is found to be 1 e-14. As shown in **Table 1** the simulated linear DSV that falls within a 5% error is equal to 160 mm for the constructed coil.

The gradient coil is built using enamelled copper wire with a diameter of 1.5 mm pressed into a 3D printed (Raised 3D pro2 plus) cylindrical holder made from Polylactic acid (PLA) with a wall thickness of 4 mm. The holder has 1.7 × 1.7 mm^2 square slots in which the wires fit tightly. Loctite super glue-3 is used to keep the wires in place, photographs of the old and new coils can be found in the **Supplementary Figures**.

A phantom consisting of many "point-sources" is used to verify the simulation results. The phantom is cylindrically shaped, with a length of 20 cm and a diameter of 20 cm. The phantom consists of 16 vertically stacked, laser-cut, PMMA trays. Each tray holds 185 SupraD soft shell, pearl shaped, vitamin D pills. The pills have a diameter of 7 mm and a shell thickness of 0.5 mm. The core consists of sunflower oil in which the vitamins are

TABLE 1 | Characteristics of the simulated gradient coils designed using the original method and the new method (axial length 350 mm) and the actual constructed longer coil (450 mm) designed with the new method.

	Original method (simulations)	New method (simulations)	Constructed gradient coil (simulations)	Constructed gradient coil (measurements)
Coil length (mm)	350	350	450	450
Coil radius (mm)	135	135	134	134
Turns per quadrant	14	14	16	16
Wire length (simulated) (m)	36	37	46	N/A
Resistance (1.5 mm copper) wire (Ω)	N/A	N/A	N/A	0.44
Inductance (μH)	180	170	213	220
Gradient efficiency ($mTm^{-1}A^{-1}$)	0.53	0.4	0.38	0.3
Linear DSV 5% deviation (simulated) (mm)	50	120	160	143

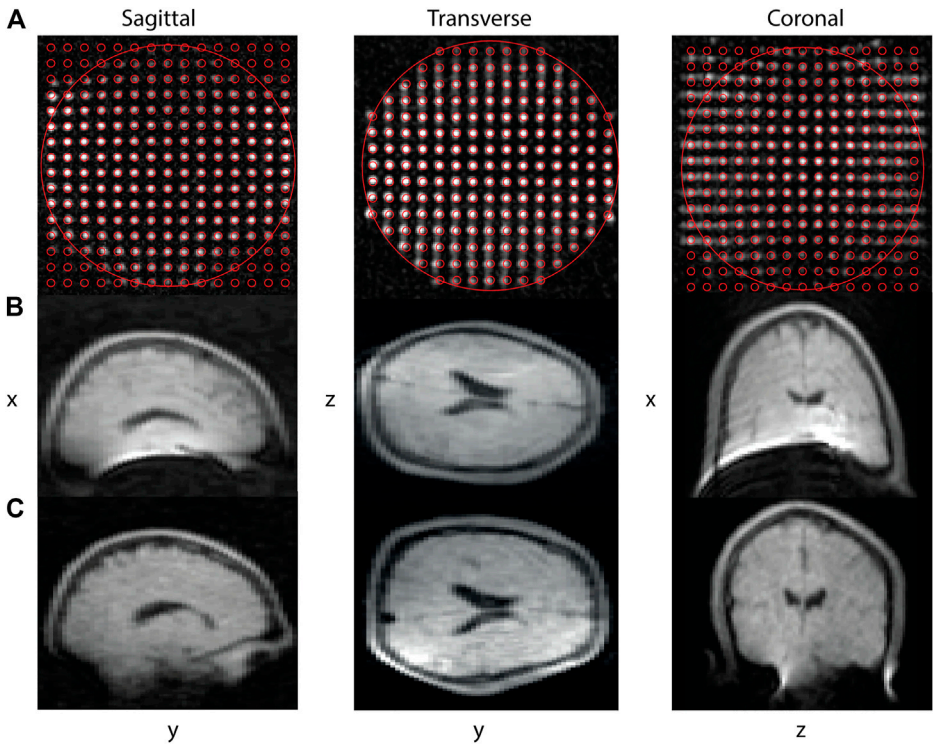

FIGURE 2 | Centre planes of a point source phantom imaged using a TSE sequence **(A)**. From left to right: Sagittal, transverse and coronal centre planes are displayed with the following acquisition parameters: 230 (*z*: right-left) × 230 (*x*: head-feet) × 230 (*y*: posterior-anterior) mm^3, data matrix: 150 × 150 × 150, TR/TE: 200/15 ms, echo train length: 6, scan duration 12 min 30 s. The small red circles denote the ground truth position of the point sources, the larger circle displays the 200 mm DSV. The lower part of the figure shows *in vivo* brain images of the same volunteer acquired with the old **(B)** and new gradient coils **(C)**. The slices are acquired using a TSE sequence with acquisition parameters: 180 (*z*: right-left) × 240 (*x*: head-feet) × 220 (*y*: posterior-anterior) mm^3, data matrix: 90 × 120 × 55, TR/TE: 400/15 ms, echo train length: 5, scan duration 9 min 36 s. For the *in vivo* and phantom images standard Fourier reconstruction with a sine bell squared filter are used.

dissolved. The centre of the pills are separated by 13 mm in all directions. The T_1 and T_2 values of the pills were measured to be 120 and 100 ms, respectively. Photographs of the phantom are shown in the **Supplementary Figures**.

The solenoid used to image the phantom has a diameter of 25 cm, a length of 25 cm and a Q-factor of 69. **Figure 2A** shows images of the centre planes of the phantom obtained using a three-dimensional turbo spin echo (TSE) sequence, with sequence parameters outlined in the figure caption. In red the "ground truth" is masked on top of the image. The outer circle denotes the 20 cm DSV. To ensure spatial distortions observed originate predominantly from the gradient non-linearities and not from B_0 in homogeneities, the double phase encoded planes are shown. These are obtained by performing three different TSE scans, each with the frequency encoding in a different direction. The phantom images show signal fading at the edges of the field of view due to the low B_1 at the extremities of the RF coil. The 5% linear DSV is determined by obtaining the displacement of the centre of each signal source with respect to the centre linear line.

In vivo brain images of a healthy volunteer were made with the old and the new gradient coil. The dimensions of the old gradient coil are those of the simulated comparison coil listed in the first column of **Table 1**. A TSE imaging sequence is used for all *in vivo* measurements: the sequence parameters are presented in the figure captions. For the reconstruction, conventional inverse Fourier transform combined with a sine bell squared k-space filter is used. **Figure 2B** shows results for the old, and **Figure 2C** for the new gradient coil.

We note that the transverse gradient coils can also be designed using the new method. However, the resulting wire patterns are essentially the same as when designed with the original method. This is because the target fields corresponding to these coils are constant in the axial direction, and the lower order harmonics proposed in the previous method are sufficient to produce these fields accurately.

DESIGN OF A FOUR-CHANNEL RADIO FREQUENCY COIL ARRAY

All of the low-field systems outlined in the introduction use a single transmit and receive coil, using a variation on a solenoid with either variable diameter or variable winding pitch. In contrast, phased array receiver coils [38] are widely used on clinical MRI systems due to their improved signal-to-noise ratio (SNR) compared to larger volume coils, and for their capability of accelerating scans by under sampling k-space [39]. Although the coil-dominated loss at lower field strengths means that the intrinsic increase in SNR is much lower than at higher fields, phased array coils can still be used to reduce the imaging time and enable lossless receive bandwidth amplification *via* preamplifier impedance mismatch. More importantly, the design of phased arrays receivers on low field systems is more challenging than at conventional fields since coil/sample coupling is much lower, loaded Q-values are higher, and as a result inter-coil coupling is higher. For the same reasons there is strong coupling between the transmit and receive array which requires high-performance detuning circuitry. Conventional PIN-diodes are not effective in the low MHz range and so other actively switching components must be used. One example of a low field array has been presented previously [15], but this used surface loops only, many of which had very low sensitivity since the B_0 and B_1 directions are coincident. The design considered here takes the transverse B_0 direction into account by choosing array elements which are different from the ones used in conventional MRI. We designed a four coil receive array for *in vivo* imaging of the knee or calf muscle with a diameter of 15 cm using a combination of loop (6×10 cm^2) and butterfly coils (15.5×13.5 cm^2) as well as an 18 cm long solenoidal transmit coil with a diameter of 20 cm which has a fast-decoupling field effect transistor (FET)-based switch.

EM simulations are performed using CST Studio Suite 2019 (CST, Darmstadt, Germany). The frequency-domain solver is used with electric boundary conditions set at 10 cm distance from the coils. The impedance matching network for each coil is implemented by simulating discrete tuning and matching capacitors. A cylindrical phantom (12 cm diameter and 15 cm length) with tissue properties ($\varepsilon = 61$, $\sigma = 0.029$ S/m, at 2.15 MHz) matching those of the knee[2] is placed at the centre of the coils. The Tx coil uses a sigmoidal function of winding pitch for the solenoid. Coupling between the adjacent butterfly and loop coils is minimized by empirically varying the distance between neighbouring elements, and finding that 10.25 mm gaps are optimal for this configuration.

The simulated B_1^+ field of the solenoid coil is shown in **Figures 3A,B**: the field is homogeneous to within 1 and 13% over a centre line of 10 cm for the radial and axial directions, respectively. **Figure 3C** shows the simulated fields of the receive array for each individual element, and the sum of squares. The left part of **Table 2** shows the simulated S parameter-matrix (in blue) for each of the Rx coils under loaded conditions. The inter-element coupling for neighbouring coils is very small, with much larger (up to −11 dB) coupling occurring between opposite butterfly elements.

Radio Frequency Coil Array Construction

The transmit solenoid coil is constructed using 31 turns of 1 mm copper wire on a 3D-printed cylinder with 20 cm diameter and 18 cm length (**Figure 4A**). The receive coils are fabricated using 0.8 mm copper wire placed on 3D-printed bases and fixed on a plexiglass cylinder with 15 cm diameter (**Figure 4B**). The loop and butterfly coils have 5 and 3 turns, respectively. For the Tx coil, capacitive segmentation into three serially-connected sections was performed using capacitors of the same value as the tuning capacitor (C_t). These values together with the Q-values of the coils unloaded and loaded with a saline phantom can be found in the right part of **Table 2**. For all coils an L-matching network was used.

Power metal oxide semiconductor field-effect transistors (MOSFETs) are appropriate counterparts for PIN diodes at low frequency [40]. The switching delay was measured to be ~10 μs at 2.15 MHz. **Figure 5** shows the circuit diagram of the MOSFET switch inserted into the impedance matching circuit of the Tx coil. A single 9-V battery is used to power the supply switch, and a voltage regulator (LM317BT, STMicroelectronics, Geneva, Switzerland) to step the voltage up to 12 V to switch the MOSFET (IRLIZ44N, Infineon Technologies AG, Germany). The TTL signal from the spectrometer is fed to an optocoupler (HCPL-2201-000E, Broadcom, United States) to switch the MOSFET gate voltage between 0 and 12 V. To detune the transmit coil an LC resonant "trap" circuit tuned to 2.15 MHz using an inductor and capacitor as well as the parasitic capacitance of the MOSFET. This is added between the drain and source of the MOSFET to detune the coil when the switch is off. An additional LC trap is placed on the ground of the MOSFET to block RF flow to the ground. The RX coils are passively detuned using crossed diodes (BAT6804E6327HTSA1, Infineon Technologies AG, Germany) and additional inductors and capacitors in parallel to the tuning capacitor to form an LC

[2]IT'IS database for thermal and electromagnetic parameters of biological tissues: https://itis.swiss/virtual-population/tissue-properties/overview/

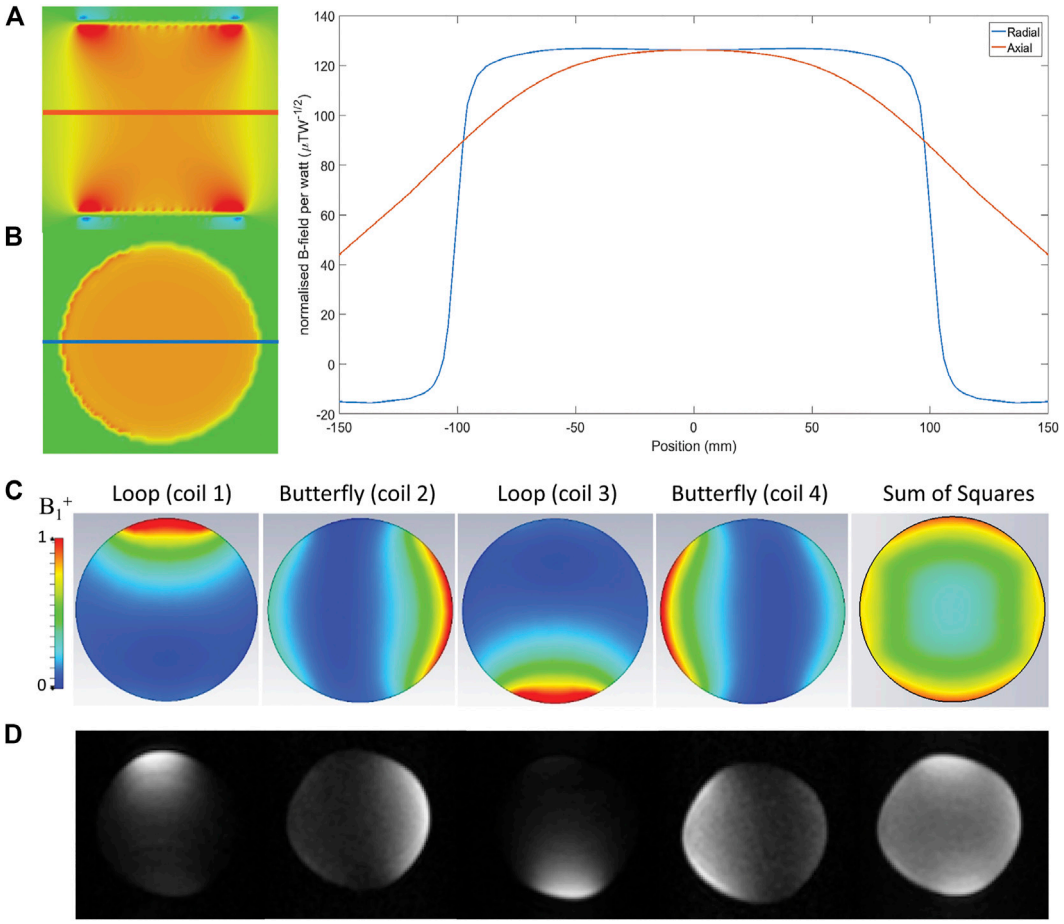

FIGURE 3 | Simulated fields of the transmit coil, axial **(A)** and transverse **(B)** slices are shown together with values of the magnetic flux density taken along the centre lines. The fields corresponding to the receive array are depicted in the bottom images **(C)**, which shows a CST model of the array loaded by a cylindrical phantom with $\varepsilon = 61$, $\sigma = 0.029$ S/m, at 2.15 MHz. The B1 is normalized to 1 W input power. **(D)** phantom measurements obtained with a cylindrical phantom of the same dimensions as the simulated phantom, the following acquisition parameters were used: 200 (*z*: right-left) × 200 (*y*: posterior-anterior) × 300 (*x*: head-feet) mm^3, data matrix: 100 × 100 × 60, TR/TE: 200/15 ms, echo train length: 6, scan duration 3 min 33 s.

TABLE 2 | Left) Simulated (blue) and measured (orange) S-parameter matrix (dB) under loaded conditions. Right) Loaded and unloaded Q values for the Tx coil and Rx coils including tuning and matching capacitor values. Variable capacitors were used in parallel with all Ct and Cm except for transmit coil where the variable capacitor is added to one of the segmentations. The numbers in the left part of the table correspond to the coils in the right part of the table.

	1.	2.	3.	4.
1.	-35	-34	-16	-38
2.		-41	-38	-11
3.			-45	-33
4.				-38
1.	-40			
2.	-25	-25		
3.	-12	-41	-42	
4.	-41	-9	-23	-26

Coils	Q Loaded	Q Unloaded	C_t [pF]	C_m [pF]
1. Loop 1	47.8	48.3	884	115
2. Butterfly 1	42.4	43	630	95
3. Loop 2	42.7	43.1	848	115
4. Butterfly 2	42.5	43.5	639	95
Transmit	96	102	162	88

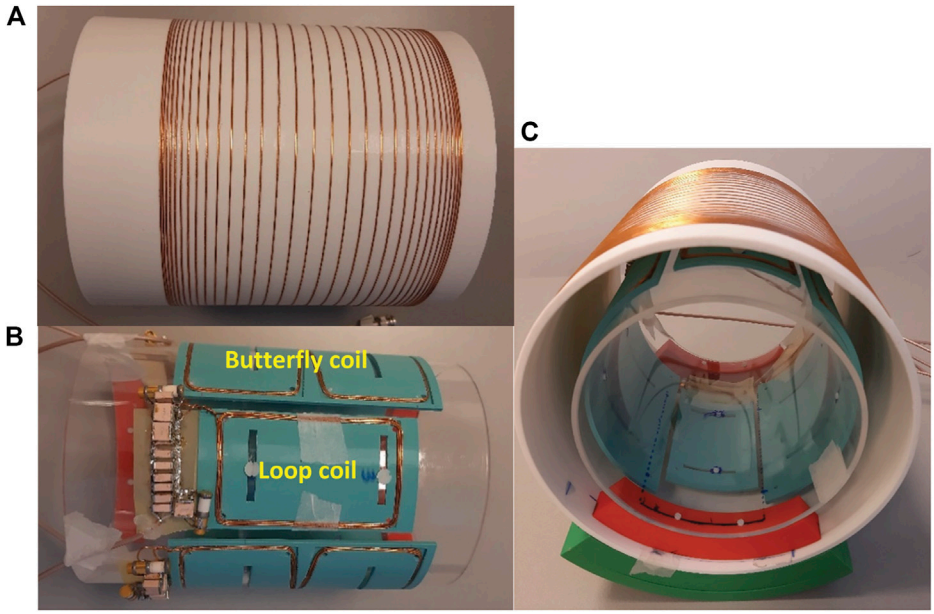

FIGURE 4 | Transmit solenoid coil **(A)**, 4-channel array coils **(B)** and the integrated assembly **(C)**.

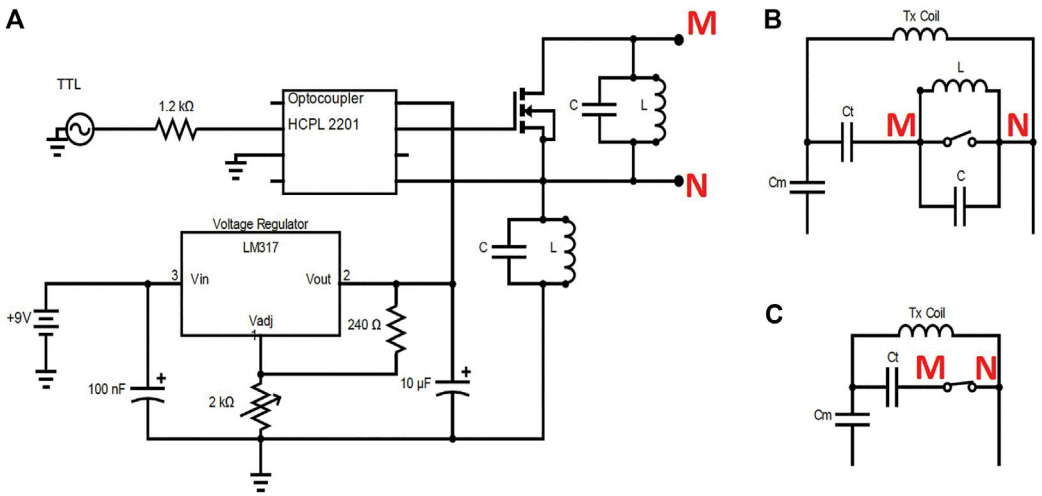

FIGURE 5 | The MOSFET switch circuit **(A)**, and Tx coil impedance matching circuit when switch is on **(B)** and off **(C)**. Note that when the TTL signal is on, the switch is off, and vice-versa.

trap at 2.15 MHz. The S-parameters obtained experimentally are shown in orange in the left part of **Table 2**.

Phantom images were performed using a TSE sequence on a 12 cm diameter 15 cm length cylindrical phantom, which is the same size as the simulated phantom. The T_1 and T_2 values of the phantom were measured to be 95 and 48 ms respectively. The results of the individual elements, sum of squares reconstruction and the sequence description can be found in **Figure 3D**. The phantom measurements are in good agreements with the coil profiles found in the simulations.

In vivo TSE knee images are acquired using the array. **Figure 6** shows the images obtained with each element, as well as a sum-of-squares reconstruction. Sequence parameters are described in the figure heading. An inverse Fourier transform combined with a sine bell squared filter was used for reconstruction. In agreement with the simulated and measured S-parameters there is very low coupling between adjacent elements because of the low mutual inductance, but signal coupling between opposite butterfly elements is apparent due to the very low loading of the sample.

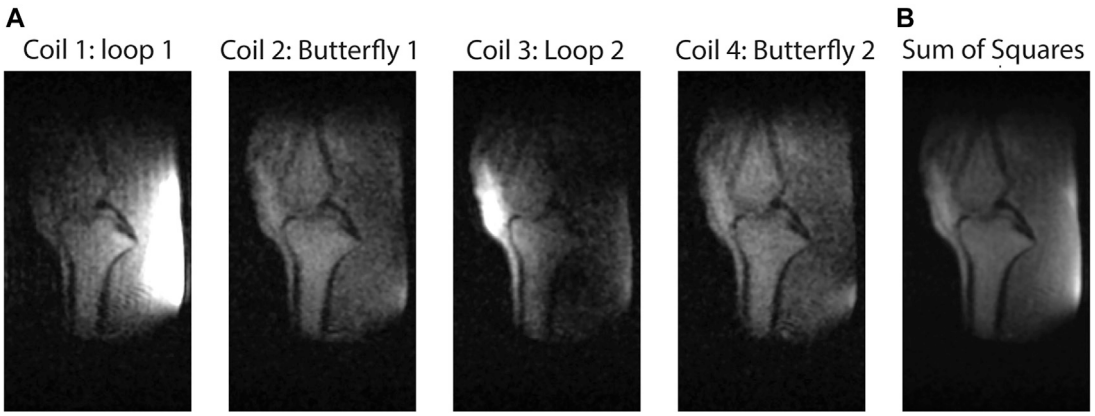

FIGURE 6 | Sagittal slice TSE images of the knee. **(A)** individual elements. **(B)** sum of squares. parameters: 150 (*z*: right-left) × 165 (*y*: posterior-anterior) × 150 (*x*: head-feet) mm^3, data matrix: 200 × 110 × 50, TR/TE: 300/15 ms, echo train length: 4, scan duration 6 min 53 s.

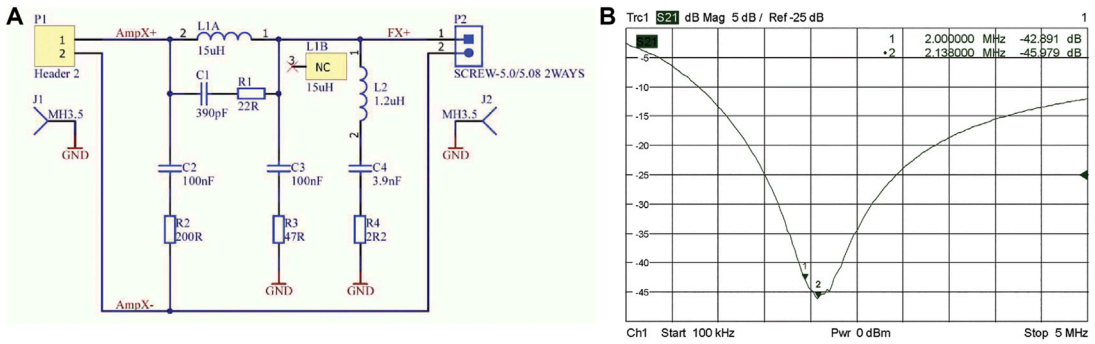

FIGURE 7 | Filter design for gradient amplifier output on each channel **(A)**, S_{21} plot of the output filters on each channel of the gradient amplifier **(B)**.

DESIGN OF A BATTERY-POWERED GRADIENT AMPLIFIER

As part of making low-field systems sustainable, the electronics should be as robust as possible with respect to operating conditions, be easily repairable, and ideally be able to run off battery power for operation in remote regions. This section describes an improved version of a three-axis current-output gradient amplifier [17] (designed and built by the Technical University of Delft) which makes it more robust and sustainable. Design specifications for the new amplifier were: maximum current to the load +/−15 Amps, maximum duty cycle 30% per channel, inductance of the gradient coil between 20 and 300 μH, a rise time 50 μs which results in a bandwidth of 7 kHz, overload protection, driving a coil with equivalent series resistance of 0.4 Ω and a parasitic parallel capacitance between the gradient coils estimated at 130 pF. The amplifier is designed to run off an external power source with a supply voltage between +/−10.5 and +/−15 V. To facilitate the use of batteries, where the voltage drops as the battery discharges, the biasing of the amplifier is made relative to the relevant power supply rails. When the batteries are drained an under-voltage lock-out disables the amplifiers at a threshold voltage of 10.5 V. Two 20 Amp car fuses (ATO Blade) are used for protection at the positive and negative terminals.

A schematic of one of the channels of the battery-operated gradient amplifier (each channel is identical) and a photograph of the gradient amplifier can be found in the **Supplementary Material**. At a 3 A average discharge current, which is typical for an imaging session, the batteries last 5–6 h.

A four-layer PCB configuration was designed with each layer designed for a specific purpose: the upper layer 1 has most of the components for easy access, replacement and routing, layer 2 is a ground layer for thermal stability and optimal heat spreading which is separated per channel to prevent cross coupling, layer three routes the power and layer four contains the high power components with wide copper tracks.

SYSTEM CHARACTERISATION

Having described in detail the improvements in the current setup for the 50 mT low-field imaging system, the final section outlines

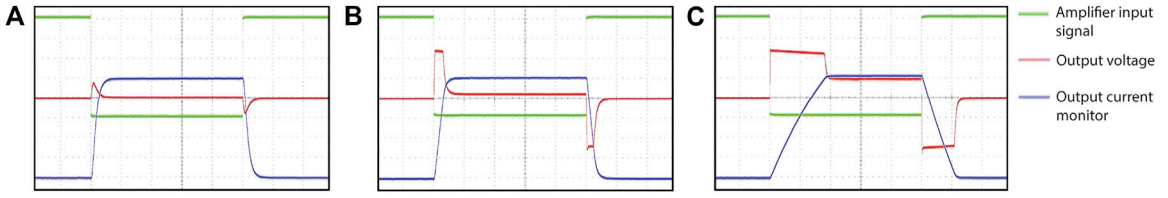

FIGURE 8 | Step response of the amplifier as a function of driving current for a gradient coil with resistance 0.32 Ω and inductance 213 μH. The ramp time is 5 μs and the plateau duration 500 μs. The amplifier input signal is shown in green, the output voltage is shown in red, and blue shows the output of the current monitor for a targeted output current of 5 A **(A)**, 10 A **(B)** and 15 A **(C)**. At 15 A the output starts to significantly limit the slew rate because of clipping to the supply rail.

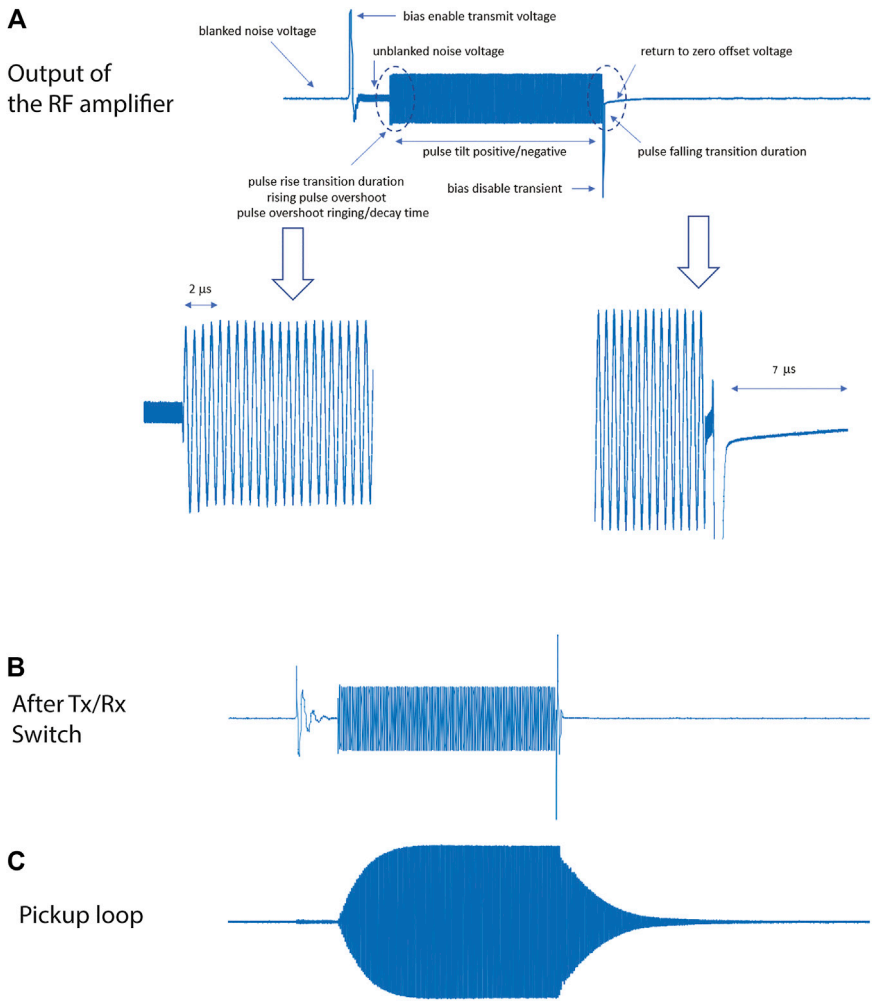

FIGURE 9 | Digital traces of a 100 μs pulse at different stages of the transmit chain. The expanded views **(A)** show different features of the amplified pulse shape. The 2.15 MHz square pulse is 100 μs long, preceded by a 5 V TTL un-blanking trigger signal 20 μs prior to the RF pulse. The same signal is shown after the Tx/Rx switch **(B)** and received by a un-tuned pickup loop **(C)**.

detailed measurements of the performance of individual components of the system, as well as that of the integrated system.

Gradient Amplifier Performance

At 2.15 MHz the measured output noise is measured to be −123 dBm/Hz, which is roughly 50 dB above thermal noise. Although an RF shield is placed between the gradient coils and the RF coil, this does not provide sufficient attenuation without it becoming so thick that eddy currents become dominant. Therefore, notch filters, see **Figures 7A,B**, were designed at the gradient amplifier outputs which give over 40 dB extra attenuation. Noise measurements performed at

TABLE 3 | Measured pulse characteristics at 2.15 MHz at the output of the RF amplifier.

Blanked noise voltage	0.0066 ± 0.0021 V
Bias enable transmit voltage	1.84 V
Unblanked noise voltage	0.0096 ± 0.004 V
Pulse rise transition duration (10–90% of peak output voltage)	<1 μs
Rising pulse overshoot	<1%
Pulse overshoot ringing/decay time	<1 μs
Pulse tilt positive/negative	<1%
Pulse falling transition duration (90–10% of peak output voltage)	<1 μs

2.15 MHz using an RF coil placed at the center of the system show no increase in the measured noise by the spectrometer after the gradient amplifiers were switched on (Section *Quality Assurance protocol and overall system noise characterisation and measurement over time*).

Figure 8 shows the step response of one of the channels when driving an inductance of 213 μH with an ESR of 0.32 Ω, which corresponds to the values of a typical gradient coil for our application. The waveforms show high fidelity at lower driving currents, whereas it is clearly seen that at 15 A the output starts to limit the slew rate because of clipping to the supply rail.

Radiofrequency Amplifier Performance

Schematics and details of the 1 kW RF amplifier used on the Halbach-based system have been provided as supplementary material to a previous publication [17], but no system performance was reported. Here, testing was performed using a four-channel digital oscilloscope (Teledyne LeCroy HDO 4034A 350 MHz). A sequence of 100 μs pulses were output from the Magritek Kea-2 spectrometer, with an unblanking 5 V TTL pulse applied 20 μs before each RF pulse, and returning to 0 V immediately after each RF pulse. Measurements were performed at: i) the input of the RF amplifier, ii) the output of the RF amplifier, iii) the output of the internal transmit/receive switch, and iv) at the RF coil *via* a loosely-coupled unmatched pick up loop.

Figure 9 shows digital traces of a 100 μs pulse at different stages of the transmit chain. **Figure 9A** shows the output of the RF amplifier, where several features of the amplified pulse are labelled with their values listed in **Table 3**. **Figure 9B** shows the pulse after the internal transmit/receive switch of the spectrometer. Lastly, **Figure 9C** shows the signal measured by an un-tuned pick up loop placed inside a tuned solenoidal coil with a Q value of ~90. The low frequency transients after the transmit/receive switch are filtered out by the tuned RF coil. The long rise-time and fall-time of the RF pulse caused by the high Q of the coil are apparent. There is a delay (400 μs) to allow pulse ringdown after each of the 100 μs pulses before the gradient pulses are applied in the 3D sequences: since the interpulse delays are on the order of 5–10 ms for *in vivo* imaging experiments this delay is not significant.

In addition, the voltage gain of the amplifier was measured across a frequency range 1–5 MHz. This was performed using the four-channel digital oscilloscope by comparing the amplitude of the 100 μs pulse before and after it went through the RF amplifier. The results are shown in **Figure 10A**, which shows a flat response with only ~2 dB variation across the entire frequency range. The linearity of the response at 2.15 MHz was measured as a function of input power from −50 to −2 dBm: as shown in **Figure 10B** the gain is within 2.8 dB for values from −50 to −10 dBm, with only substantial variations from uniformity for powers greater than −5 dBm.

Eddy Current Characterisation

In conventional superconducting MRI systems, eddy currents are created primarily by the interaction of the pulsed gradient fields with the metallic bore of the magnet. These interactions are minimized by actively shielding the gradients [33]. The quantification and correction of these effects are well documented in conventional systems [41–45]. In Halbach-based systems eddy currents produced by this interaction

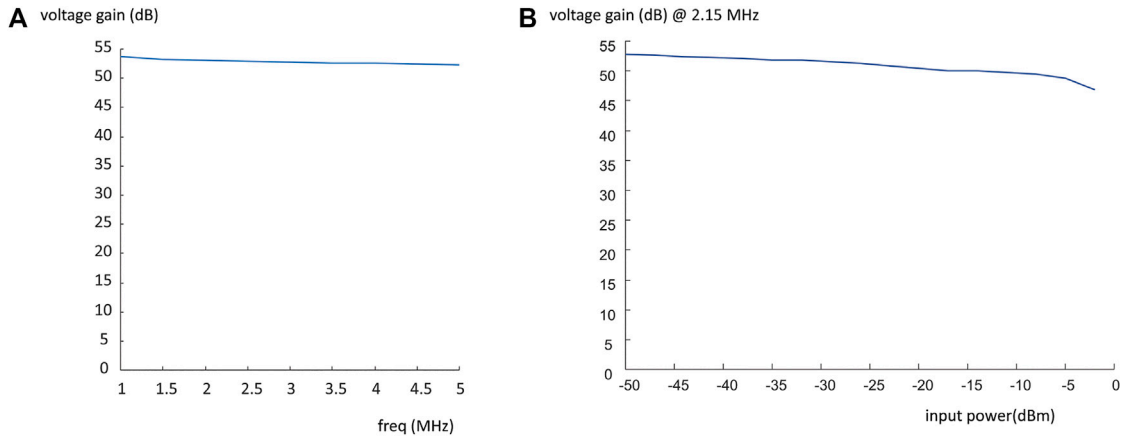

FIGURE 10 | Plot of voltage gain vs. frequency **(A)**, and the voltage gain at the operating frequency of 2.15 MHz vs. input power from the Kea spectrometer **(B)**.

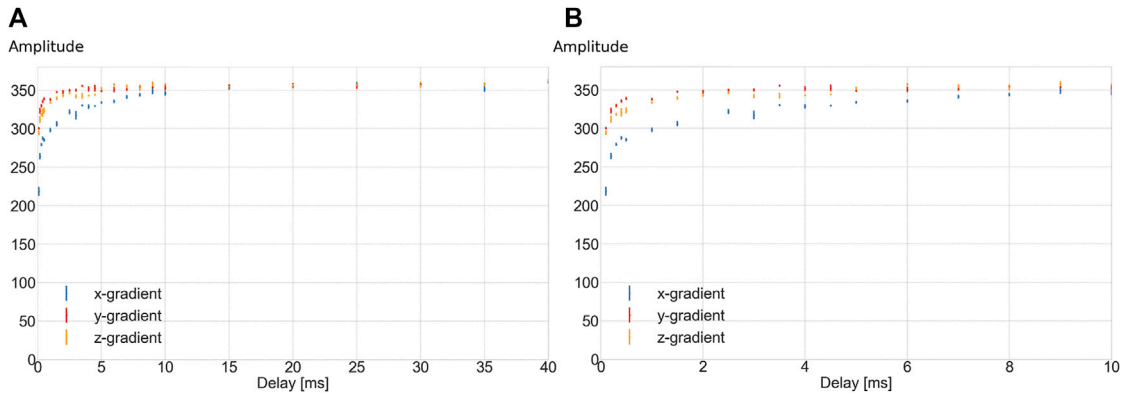

FIGURE 11 | Signal amplitudes (arbitrary units) of the magnitude spectrum as a function of the delay time after the gradient has been turned off, before the spectrum is acquired. Full extent of delay times up to 40 ms **(A)**, and zoomed view of the first 10 ms of the data **(B)**. The average and standard deviation of four measurements per delay time are displayed. Blue: *x*-gradient, red: *y*-gradient, yellow: *z*-gradient.

might be expected to be much lower, since the magnetic material is discretized into small elements, and the copper RF shield placed between the RF coil and gradient coils is much thinner than the skin depth at low frequencies.

The effects of the eddy currents were measured using a standard spectroscopic method. A 4 mT/m, 20 ms square gradient pulse is applied. The length of the gradient pulse is chosen so that the eddy current measurements were dominated by the falling edge of the gradient pulse rather than a combined effect of the rising edge and falling edge, which is the case if a shorter gradient pulse is applied. The value of 4 mT/m is ~90% of the maximum gradient strength obtainable with the system described here. The pulse is followed by a variable delay time, before an RF pulse is applied to produce a free induction decay. The peak intensity of the spectrum is recorded as a function of this delay. Three readings were made for each value to estimate the standard deviation of each measurement. Measurements were performed for the three gradient coils separately. **Figure 11** shows the measured peak amplitudes for each gradient coil. The eddy current effects are approximately the same for the y- and z-gradient which have the same geometry but are rotated by 90° with respect to one another. The x-gradient, has a different shape and shows longer time-constant eddy currents, possibly due to it being the closest to the shield.

Quality Assurance Protocol and Overall System Noise Characterisation and Measurement Over Time

Since portable systems are intended to operate in conditions outside those characterised by tightly controlled temperature and humidity, as well as an RF shielded environment, it is important to have a rapid assessment of the performance of each of the individual components of the system. In addition, it is very useful to check over a longer period of time whether system performance degrades, and which component(s) is/are responsible for this. To this end a simple 30-min quality control protocol is set up which consists of:

i) Checking the impedance matching of the coil at 2.15 MHz: the S_{11} should be less than -20 dB or the coil should be retuned.
ii) Determination of the resonance frequency with all shims set to zero. The resonance frequency is highly dependent upon the time after a previous *in vivo* scan has been acquired, since the magnets heat up in such experiments due to passive thermal emission from the body, and so the resonance frequency decreases (our estimate for the maximum shift is about 1 kHz immediately after a 45 min scan, and one measurement immediately after an *in vivo* scan was included to demonstrate this effect). For this reason, the quality control measurement is performed a significant time after *in vivo* measurements, as it is intended to monitor the very long-term stability of the magnet, since it is known that NdBFe slowly demagnetizes over time.
iii) Averaging five noise measurements with only the spectrometer turned on and the output/input of the Tx/Rx switch connected to the coil. This determines whether the coil picks up noise signals which means that any shielding or noise reduction in place is not functioning sufficiently. The Magritek console outputs a reference 1 μV signal, and measures the noise voltage with respect to this internal standard. The precision of the reference voltage is 0.01 μV. The noise is measured with the maximum receiver gain and so any quantization noise is much less than the noise level.
iv) Averaging five noise measurements with the spectrometer and the RF amplifier turned on and the output/input of the Tx/Rx switch connected to the coil. This determines whether the RF amplifier contributes to the noise.
v) Averaging five noise measurements with the spectrometer, the RF amplifier and the gradient amplifier turned on and the output/input of the Tx/Rx switch connected to the coil. This determines whether the gradient amplifier contributes noise, i.e., there may be a problem with the gradient filters.

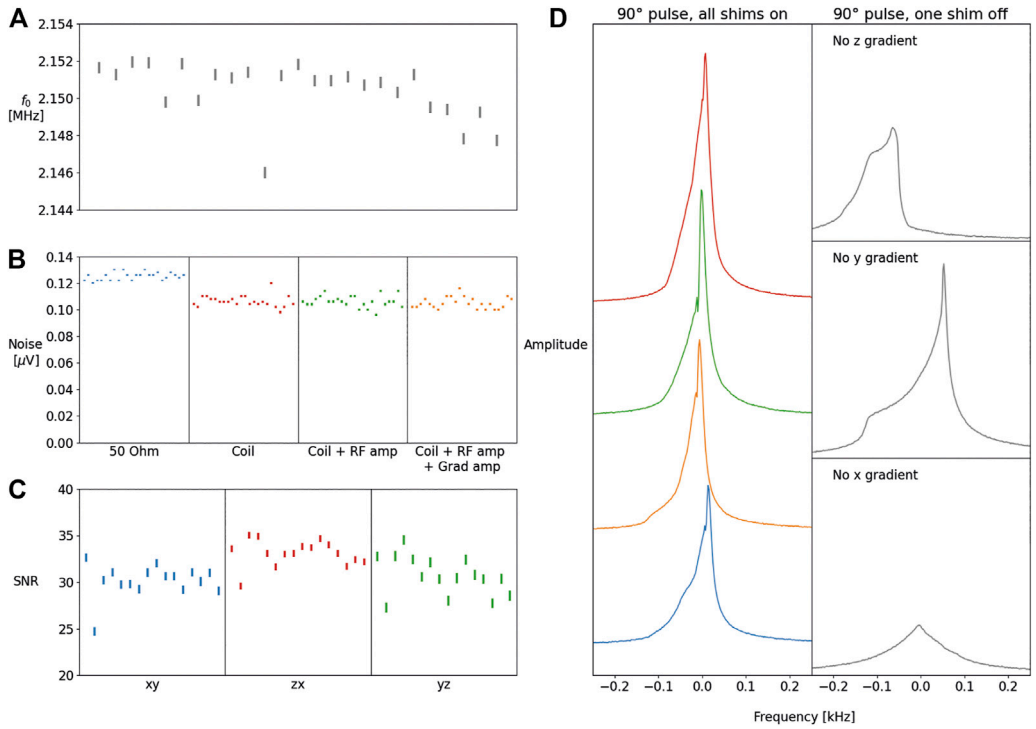

FIGURE 12 | The f_0 frequency measurements measured in the course of 6 weeks with an average of one scan per day **(A)**. Noise measured using five averages obtained in the course of 6 weeks with the coil connected, and the coil connected with respectively only the RF amplifier on and both the RF and gradient amplifiers turned on **(B)**. SNR measurements obtained over a period of 2 weeks for the three encoding directions **(C)** (frequency/phase encoding). The magnitude spectrum on different occasions measured over the course of a 3 days, with all shims on (left), and the effects on the magnitude spectrum when one of the shims is not functioning correctly **(D)**.

vi) Calibration of the power required for a 90° pulse to ensure that coil components have not degraded over time. For the 90° pulse the variation from day-to-day is less than 0.3 dB, so anything consistently outside this range indicates that the coil Q has degraded.

vii) Measuring the SNR in 2D projection spin echo images using three different combinations of the gradient coils: frequency encoding gradient x and phase encoding gradient y, frequency encoding gradient z and phase encoding gradient x, and frequency encoding gradient y and phase encoding gradient z. The spectrometer has a specific protocol for measuring the noise level with respect to an internal 1 μV standard signal. For the SNR measurements regions-of-interest were defined within the object (signal) and outside the object (noise). The measurements have a variation of ~7% which indicated that anything outside of this range should be checked further.

viii) Obtaining a simple spectrum after application of a 90° pulse in order to measure the lineshape. This measurement is made after first order shimming *via* the linear gradients. To estimate the effect of a malfunctioning gradient coil we performed one set of measurements with each of the coils disconnected in turn.

A 3D phantom holder is designed to make positioning inside the RF coil and magnet highly reproducible. The phantom is a sphere of 74 mm diameter containing a copper sulphate doped (3 mM) agar mixture (0.5%) and has a T_1 value of 227 ms and T_2 of 224 ms. It is placed inside a transmit/receive solenoidal coil (inner diameter of 147 mm, outer diameter of 155 mm, length 170 mm, 1 mm copper wire, Q value 89), which can be positioned accurately *via* markings inside the scanner. Photographs of the solenoid, phantom and holder are shown in the **Supplementary Figures**. The protocol discussed above has been run over the course of several weeks and the results are discussed below.

Figure 12A shows the frequency is stable over a longer period of time with the measurements taken once a day on average, over a course of six weeks, a significant time after *in vivo* experiments have been performed. A decrease in frequency can be observed in the last week, the likely cause is that this week was particularly warm. The increase in the temperature is likely to be the cause of this field drift. One outlier can be observed which was obtained after an entire day of *in vivo* scanning: the field drift was caused by an increase of temperature caused by the human body, as expected. This type of field drift can be corrected for when performing *in vivo* experiments as described by [18]. **Figure 12B** shows the RMS

noise measured over a bandwidth of 50 kHz, with no RF pulses applied, the data are obtained over the course of 6 weeks. No significant differences are observed when switching on the RF and gradient amplifiers. The noise measurement appears to have a variation of less than 10% (which is also limited by the resolution of the measurement on the system), and so anything beyond 20% is indicative of either very broadband interference or some problem with the preamplifier or receiving chain. **Figure 12C** shows the SNR measured from imaging data over the period of 4 weeks. The left side of **Figure 12D** shows four spectra acquired on three different days: the right side of the figure shows the effects when one of the gradients were disconnected showing a very obvious deterioration in performance.

DISCUSSION

In this paper on-going developments of a 50 mT Halbach-based portable MRI system for *in vivo* imaging have been discussed. In addition to specific hardware improvements including a gradient coil with increased region of linearity, a four-element phased array receive coil, and a battery-operated gradient amplifier, detailed system characterisations of eddy currents, RF transmitter performance, and quality control protocol have been shown.

The comparison of two axial gradient coils simulated for the same target DSV, but designed using two different target field methods, demonstrated that for fixed dimensions, in simulations, the new method increases the 5% linear DSV by ~150%, traded against a decrease in efficiency of ~25%. The improvement in linearity is confirmed with phantom measurements. This home-made inexpensive point source phantom proved to be a powerful tool for displaying the current capabilities and limits of the system. In the future the phantom can be used to calibrate new low field systems. The linearity measured differed slightly from the simulations, one reason for this is that the pills introduce a relatively large discretisation error with respect to the smoother simulated data. The increase in axial linearity allows the whole adult brain to be imaged with little geometric distortion, at a spatial resolution of ~2 mm using the maximum output of 4 Amps from the gradient amplifier. The reduced gradient efficiency comes about primarily due to the large number of very closely spaced turns at the ends of the gradient coils, which are used to increase the linearity. The trade-off between linearity and efficiency will be further investigated, particularly given that for spatial resolutions on the millimetre scale the distortions created by small non-linearities can be relatively easily corrected *via* post-processing [46]. Another area which will be investigated is the design of asymmetric axial gradient coils [47, 48]. Due to the relatively small magnet bore positioning of the subject's head at the centre of the magnet/gradient is restricted by the shoulders. This means that for all of the images currently acquired, the centre of the brain lies towards the front of the magnet, and if the subject has a relatively short neck the lower part of the brain may coincide with an area of poor B_0 homogeneity and close to the region where the axial gradient coil linearity begins to deteriorate. Cooley et al. have used boundary element methods to design an asymmetric axial gradient coil with variable diameter and the zero gradient point towards the bore entrance [13]. Such a design is also possible using asymmetrical target fields and the approach outlined in this paper.

Although not common at the moment, receive arrays could be used to reduce the time required for image acquisition, if the SNR is sufficient, by utilizing parallel imaging reconstruction of under-sampled data. In this paper we showed a basic four-element array comprised of two surface coils and two butterfly-shaped coils. The coils were reasonably decoupled from each other geometrically, but the decoupling could be increased by the use of low input impedance preamplifiers. Since coil loss is dominant at low frequency, and inter-coil coupling therefore much higher, the input impedance of such preamplifiers must be much lower than for commercial systems, so <<1 Ohm, which would require a custom design. Multiple low loss transmit/receive switches would also be required to be designed and constructed for these low frequency systems.

Designing the gradient amplifier to be battery powered demonstrated the first steps in making the system independent of the power grid, and thus well suited for low resource and remote settings. The maximum current output of ~15 Amps is much lower than that of ones used in commercial scanners, and may need to be increased if applications in musculoskeletal MRI, for example, are to be targeted, in which case sub-millimetre resolution is required. Currently we do not use any pre-emphasis in the system to compensate for eddy currents, this would require the capability to provide a large over-voltage, which might compromise the desire to have only air-cooling of the amplifier.

Finally, we presented some very simple quality checks of the noise and SNR levels when different components of the system are turned on. Since all designs are available open-source, this information allows interested researchers to construct systems based on all or a subset of the hardware described. Additionally, the system characterisation gives a baseline for future studies to compare the performance obtained with different custom-built or commercial low-field systems.

DATA AVAILABILITY STATEMENT

The raw data supporting the conclusion of this article will be made available by the authors, without undue reservation.

ETHICS STATEMENT

Ethical review and approval was not required for the study on human participants in accordance with the local legislation and institutional requirements. Written informed consent from the participants OR participants legal guardian/next of kin was not

required to participate in this study in accordance with the national legislation and the institutional requirements.

AUTHOR CONTRIBUTIONS

BV designed and built the gradient coils, performed measurements. Collected and reformatted the data and figures from other project members, wrote a part of the manuscript and did the formatting. JP designed and built the RF (radio frequency) coil array, wrote the draft text for this part and supplied the corresponding figures. ZA designed and built the transmit receive (TR)-switches and pre-amplifiers used during image acquisition. WT contributed to the practical design of the gradient coils and magnet, and assisted with the installation of the new gradient coil. DG designed and built the gradient amplifiers and supplied the documentation. CV designed and performed the quality control protocol, delivered the corresponding figures and text. RR helped with the mathematical framework and the design of the newly proposed gradient design method and proofread part of the manuscript. TO'R created the magnet system, contributed to the design of the RF-array, specified the design parameters for the new gradient amplifier and acquired the *in vivo* images. AW performed measurements, wrote part of the manuscript, proofread manuscript, produced figures.

FUNDING

Partial funding for this project was provided by Horizon 2020 European Research Grant FET-OPEN 737180 Histo MRI (TO'R), Horizon 2020 ERC Advanced NOMA-MRI 670629 (AW), and a Simon Stevin Meester Prize (BV, AW), H2020-MSCA-ITN-ETN 859908 (JP) and NWO WOTRO award (DG).

SUPPLEMENTARY MATERIAL

The Supplementary Material for this article can be found online at: https://www.frontiersin.org/articles/10.3389/fphy.2021.701157/full#supplementary-material

Supplement Figure 1 | Photographs of the constructed gradient coils where 1.5 mm diameter enameled copper wire is pressed into the grooves of a 3D printed cylindrical mold, shown for the old **(A)** and new method **(B)**.

Supplement Figure 2 | Photograph of point source phantom together with a single layer.

Supplement Figure 3 | A schematic of one of the channels of the battery-operated gradient amplifier.

Supplement Figure 4 | Photograph of the Gradient amplifier.

Supplement Figure 5 | Photograph of the quality assurance phantom, inside the solenoidal coil.

REFERENCES

1. Tsai LL, Mair RW, Rosen MS, Patz S, and Walsworth RL. An Open-Access, Very-Low-Field MRI System for Posture-dependent 3He Human Lung Imaging. *J Magn Reson* (2008) 193:274–85. doi:10.1016/j.jmr.2008.05.016
2. Tsai LL, Mair RW, Li C-H, Rosen MS, Patz S, and Walsworth RL. Posture-dependent Human 3He Lung Imaging in an Open-Access MRI System. *Acad Radiol* (2008) 15:728–39. doi:10.1016/j.acra.2007.10.010
3. Sarracanie M, LaPierre CD, Salameh N, Waddington DEJ, Witzel T, and Rosen MS. Low-cost High-Performance MRI. *Sci Rep* (2015) 5:5. doi:10.1038/srep15177
4. Choi C-H, Hutchison JMS, and Lurie DJ. Design and Construction of an Actively Frequency-Switchable RF Coil for Field-dependent Magnetisation Transfer Contrast MRI with Fast Field-Cycling. *J Magn Reson* (2010) 207: 134–9. doi:10.1016/j.jmr.2010.08.018
5. Ross PJ, Broche LM, and Lurie DJ. Rapid Field-Cycling MRI Using Fast Spin-echo. *Magn Reson Med* (2014) 73:1120–4. doi:10.1002/mrm.25233
6. Macleod MJ, Broche L, Ross J, Guzman-Guttierez G, and Lurie D. A Novel Imaging Modality (Fast Field-Cycling MRI) Identifies Ischaemic Stroke at Ultra-low Magnetic Field Strength. *Int J Stroke* (2018) 13:62–3. doi:10.1177/1747493018801108
7. Bödenler M, de Rochefort L, Ross PJ, Chanet N, Guillot G, Davies GR, et al. Comparison of Fast Field-Cycling Magnetic Resonance Imaging Methods and Future Perspectives. *Mol Phys* (2018) 117:832–48. doi:10.1080/00268976.2018.1557349
8. Broche LM, Ross PJ, Davies GR, MacLeod M-J, and Lurie DJ. A Whole-Body Fast Field-Cycling Scanner for Clinical Molecular Imaging Studies. *Sci Rep* (2019) 9:9. doi:10.1038/s41598-019-46648-0
9. He Y, He W, Tan L, Chen F, Meng F, Feng H, et al. Use of 2.1 MHz MRI Scanner for Brain Imaging and its Preliminary Results in Stroke. *J Magn Reson* (2020) 319:106829. doi:10.1016/j.jmr.2020.106829
10. Nakagomi M, Kajiwara M, Matsuzaki J, Tanabe K, Hoshiai S, Okamoto Y, et al. Development of a Small Car-Mounted Magnetic Resonance Imaging System for Human Elbows Using a 0.2 T Permanent Magnet. *J Magn Reson* (2019) 304:1–6. doi:10.1016/j.jmr.2019.04.017
11. Sheth KN, Mazurek MH, Yuen MM, Cahn BA, Shah JT, Ward A, et al. Assessment of Brain Injury Using Portable, Low-Field Magnetic Resonance Imaging at the Bedside of Critically Ill Patients. *JAMA Neurol* (2021) 78:41. doi:10.1001/jamaneurol.2020.3263
12. Turpin J, Unadkat P, Thomas J, Kleiner N, Khazanehdari S, Wanchoo S, et al. Portable Magnetic Resonance Imaging for ICU Patients. *Crit Care Explorations* (2020) 2:e0306. doi:10.1097/cce.0000000000000306
13. Cooley CZ, McDaniel PC, Stockmann JP, Srinivas SA, Cauley SF, Śliwiak M, et al. A Portable Scanner for Magnetic Resonance Imaging of the Brain. *Nat Biomed Eng* (2020) 5:229–39. doi:10.1038/s41551-020-00641-5
14. McDaniel PC. *Computational Design and Fabrication of Portable MRI Systems*. Massachusetts: Dissertation Massachusetts Institute of Technology (2020).
15. Cooley CZ, Stockmann JP, Armstrong BD, Sarracanie M, Lev MH, Rosen MS, et al. Two-dimensional Imaging in a Lightweight Portable MRI Scanner without Gradient Coils. *Magn Reson Med* (2014) 73:872–83. doi:10.1002/mrm.25147
16. Cooley CZ, Haskell MW, Cauley SF, Sappo C, Lapierre CD, Ha CG, et al. Design of Sparse Halbach Magnet Arrays for Portable MRI Using a Genetic Algorithm. *IEEE Trans Magn* (2018) 54:1–12. doi:10.1109/tmag.2017.2751001
17. O'Reilly T, Teeuwisse WM, and Webb AG. Three-dimensional MRI in a Homogenous 27 cm Diameter Bore Halbach Array Magnet. *J Magn Reson* (2019) 307:106578. doi:10.1016/j.jmr.2019.106578
18. O'Reilly T, Teeuwisse WM, Gans D, Koolstra K, and Webb AG. *In Vivo* 3D Brain and Extremity MRI at 50 mT Using a Permanent Magnet Halbach Array. *Magn Reson Med* (2020) 85:495–505. doi:10.1002/mrm.28396
19. Obungoloch J, Harper JR, Consevage S, Savukov IM, Neuberger T, Tadigadapa S, et al. Design of a Sustainable Prepolarizing Magnetic Resonance Imaging System for Infant Hydrocephalus. *Magn Reson Mater Phy* (2018) 31:665–76. doi:10.1007/s10334-018-0683-y
20. Ren ZH, Obruchkov S, Lu DW, Dykstra R, and Huang SY. A Low-Field Portable Magnetic Resonance Imaging System for Head Imaging. In: Progress in Electromagnetics Research Symposium - Fall; 2017 Nov 19–22; Singapore. PIERS - FALL (2017). doi:10.1109/piers-fall.2017.8293655
21. Sarracanie M, and Salameh N. Low-Field MRI: How Low Can We Go? A Fresh View on an Old Debate. *Front Phys* (2020) 8:127. doi:10.3389/fphy.2020.00172
22. Raich H, and Blümler P. Design and Construction of a Dipolar Halbach Array with a Homogeneous Field from Identical Bar Magnets: NMR Mandhalas. *Concepts Magn Reson* (2004) 23B:16–25. doi:10.1002/cmr.b.20018

23. Bauer C, Raich H, Jeschke G, and Blümler P. Design of a Permanent Magnet with a Mechanical Sweep Suitable for Variable-Temperature Continuous-Wave and Pulsed EPR Spectroscopy. *J Magn Reson* (2009) 198:222–7. doi:10.1016/j.jmr.2009.02.010
24. Soltner H, and Blümler P. Dipolar Halbach Magnet Stacks Made from Identically Shaped Permanent Magnets for Magnetic Resonance. *Concepts Magn Reson* (2010) 36A:211–22. doi:10.1002/cmr.a.20165
25. Windt CW, Soltner H, Dusschoten Dv., and Blümler P. A Portable Halbach Magnet that Can Be Opened and Closed without Force: The NMR-CUFF. *J Magn Reson* (2011) 208:27–33. doi:10.1016/j.jmr.2010.09.020
26. Blümler P, and Casanova F. Chapter 5. Hardware Developments: Halbach Magnet Arrays. In: *Mobile NMR and MRI: Developments and Applications*. London, United Kingdom: The Royal Society of Chemistry (2015). 133–57. doi:10.1039/9781782628095-00133
27. BlüMler P. Proposal for a Permanent Magnet System with a Constant Gradient Mechanically Adjustable in Direction and Strength. *Concepts Magn Reson* (2016) 46:41–8. doi:10.1002/cmr.b.21320
28. de Vos B, Fuchs P, O'Reilly T, Webb A, and Remis R. Gradient Coil Design and Realization for a Halbach-Based MRI System. *IEEE Trans Magn* (2020) 56:1–8. doi:10.1109/tmag.2019.2958561
29. Turner R. A Target Field Approach to Optimal Coil Design. *J Phys D: Appl Phys* (1986) 19:L147–L151. doi:10.1088/0022-3727/19/8/001
30. Zhang B, Gazdzinski C, Chronik BA, Xu H, Conolly SM, and Rutt BK. Simple Design Guidelines for Short MRI Systems. *Concepts Magn Reson* (2005) 25B: 53–9. doi:10.1002/cmr.b.20033
31. Turner R. Minimum Inductance Coils. *J Phys E Sci Instrum* (1988) 21:948–52. doi:10.1088/0022-3735/21/10/008
32. Chronik EA, and Rutt BK. Constrained Length Minimum Inductance Gradient Coil Design. *Magn Reson Med* (1998) 39:270–8. doi:10.1002/mrm.1910390214
33. Carlson JW, Derby KA, Hawryszko KC, and Weideman M. Design and Evaluation of Shielded Gradient Coils. *Magn Reson Med* (1992) 26: 191–206. doi:10.1002/mrm.1910260202
34. Forbes LK, and Crozier S. Asymmetric Zonal Shim Coils for Magnetic Resonance Applications. *Med Phys* (2001) 28:1644–51. doi:10.1118/1.1388538
35. Forbes LK, and Crozier S. A Novel Target-Field Method for Finite-Length Magnetic Resonance Shim Coils: I. Zonal Shims. *J Phys D: Appl Phys* (2001) 34: 3447–55. doi:10.1088/0022-3727/34/24/305
36. Forbes LK, and Crozier S. A Novel Target-Field Method for Finite-Length Magnetic Resonance Shim Coils: II. Tesseral Shims. *J Phys D: Appl Phys* (2002) 35:839–49. doi:10.1088/0022-3727/35/9/303
37. Brideson MA, Forbes LK, and Crozier S. Determining Complicated Winding Patterns for Shim Coils Using Stream Functions and the Target-Field Method. *Concepts Magn Reson* (2001) 14:9–18. doi:10.1002/cmr.10000
38. Roemer PB, Edelstein WA, Hayes CE, Souza SP, and Mueller OM. The NMR Phased Array. *Magn Reson Med* (1990) 16:192–225. doi:10.1002/mrm.1910160203
39. Hamilton J, Franson D, and Seiberlich N. Recent Advances in Parallel Imaging for MRI. *Prog Nucl Magn Reson Spectrosc* (2017) 101:71–95. doi:10.1016/j.pnmrs.2017.04.002
40. Nacher P-J, Kumaragamage S, Tastevin G, and Bidinosti CP. A Fast MOSFET RF Switch for Low-Field NMR and MRI. *J Magn Reson* (2020) 310:106638. doi:10.1016/j.jmr.2019.106638
41. Kim YS, and Cho ZH. Eddy-current-compensated Field-Inhomogeneity Mapping in NMR Imaging. *J Magn Reson (1969)* (1988) 78:459–71. doi:10.1016/0022-2364(88)90132-1
42. Boesch C, Gruetter R, and Martin E. Temporal and Spatial Analysis of fields Generated by Eddy Currents in Superconducting Magnets: Optimization of Corrections and Quantitative Characterization of Magnet/gradient Systems. *Magn Reson Med* (1991) 20:268–84. doi:10.1002/mrm.1910200209
43. Papadakis NG, Martin KM, Pickard JD, Hall LD, Carpenter TA, and Huang CL-H. Gradient Preemphasis Calibration in Diffusion-Weighted echo-planar Imaging. *Magn Reson Med* (2000) 44:616–24. doi:10.1002/1522-2594(200010)44:4<616::aid-mrm16>3.0.co;2-t
44. Spees WM, Buhl N, Sun P, Ackerman JJH, Neil JJ, and Garbow JR. Quantification and Compensation of Eddy-Current-Induced Magnetic-Field Gradients. *J Magn Reson* (2011) 212:116–23. doi:10.1016/j.jmr.2011.06.016
45. Niederländer B, and Blümler P. Simple Eddy Current Compensation by Additional Gradient Pulses. *Concepts Magn Reson A* (2018) 47A:e21469. doi:10.1002/cmr.a.21469
46. Koolstra K, O'Reilly T, Börnert P, and Webb A. Image Distortion Correction for MRI in Low Field Permanent Magnet Systems with strong B0 Inhomogeneity and Gradient Field Nonlinearities. *Magn Reson Mater Phy* (2021). doi:10.1007/s10334-021-00907-2
47. Tomasi D, Xavier RF, Foerster B, Panepucci H, Tannús A, and Vidoto EL. Asymmetrical Gradient Coil for Head Imaging. *Magn Reson Med* (2002) 48: 707–14. doi:10.1002/mrm.10263
48. Wang Y, Liu F, Li Y, Tang F, and Crozier S. Asymmetric Gradient Coil Design for Use in a Short, Open Bore Magnetic Resonance Imaging Scanner. *J Magn Reson* (2016) 269:203–12. doi:10.1016/j.jmr.2016.06.015

Conflict of Interest: JP was employed by Percuros BV

The remaining authors declare that the research was conducted in the absence of any commercial or financial relationships that could be construed as a potential conflict of interest..

Publisher's Note: All claims expressed in this article are solely those of the authors and do not necessarily represent those of their affiliated organizations, or those of the publisher, the editors and the reviewers. Any product that may be evaluated in this article, or claim that may be made by its manufacturer, is not guaranteed or endorsed by the publisher.

frontiers in Physics

ORIGINAL RESEARCH
published: 27 July 2021
doi: 10.3389/fphy.2021.701330

A Nested Eight-Channel Transmit Array With Open-Face Concept for Human Brain Imaging at 7 Tesla

*Sydney N. Williams[1], Sarah Allwood-Spiers[2†], Paul McElhinney[1†], Gavin Paterson[1], Jürgen Herrler[3], Patrick Liebig[4], Armin M. Nagel[5], John E. Foster[2], David A. Porter[1] and Shajan Gunamony[1,6]**

[1]Imaging Centre of Excellence, University of Glasgow, Glasgow, United Kingdom, [2]MRI Physics, NHS Greater Glasgow & Clyde, Glasgow, United Kingdom, [3]Department of Neuroradiology, University Hospital Erlangen, Erlangen, Germany, [4]Siemens Healthineers, Erlangen, Germany, [5]Institute of Radiology, University Hospital Erlangen, Erlangen, Germany, [6]MR CoilTech Limited, Glasgow, United Kingdom

Purpose: Parallel transmit technology for MRI at 7 tesla will significantly benefit from high performance transmit arrays that offer high transmit efficiency and low mutual coupling between the individual array elements. A novel dual-mode transmit array with nested array elements has been developed to support imaging the human brain in both the single-channel (sTx) and parallel-transmit (pTx) excitation modes of a 7 tesla MRI scanner. In this work, the design, implementation, validation, specific absorption rate (SAR) management, and performance of the head coil is presented.

Methods: The transmit array consisted of a nested arrangement to improve decoupling between the second-neighboring elements. Two large cut-outs were introduced in the RF shield for an open-face design to reduce claustrophobia and to allow patient monitoring. A hardware interface allows the coil to be used in both the sTx and pTx modes. SAR monitoring is done with virtual observation points (VOP) derived from human body models. The transmit efficiency and coverage is compared with the commercial single-channel and parallel-transmit head coils.

Results: Decoupling inductors between the second-neighboring coil elements reduced the coupling to less than −20 dB. Local SAR estimates from the electromagnetic (EM) simulations were always less than the EM-based VOPs, which in turn were always less than scanner predictions and measurements for static and dynamic pTx waveforms. In sTx mode, we demonstrate improved coverage of the brain compared to the commercial sTx coil. The transmit efficiency is within 10% of the commercial pTx coil despite the two large cut-outs in the RF shield. In pTx mode, improved signal homogeneity was shown when the Universal Pulse was used for acquisition *in vivo*.

Conclusion: A novel head coil which includes a nested eight-channel transmit array has been presented. The large cut-outs improve patient monitoring and reduce claustrophobia. For pTx mode, the EM simulation and VOP-based SAR management provided greater flexibility to apply pTx methods without the limitations of SAR constraints. For scanning *in vivo*, the coil was shown to provide an improved coverage in sTx mode compared to a standard commercial head coil.

Keywords: RF coil, B1 homogeneity, 7 Tesla, parallel-transmit (pTx), specific absorption rate (SAR), virtual observation points (VOPs), ultra-high field, transmit array

OPEN ACCESS

Edited by:
Sigrun Roat,
Medical University of Vienna, Austria

Reviewed by:
Özlem Ipek,
King's College London,
United Kingdom
Isabelle Saniour,
Weill Cornell Medicine, United States

****Correspondence:***
Shajan Gunamony
shajan.gunamony@glasgow.ac.uk

[†]These authors have contributed equally to this work

Specialty section:
This article was submitted to Medical Physics and Imaging, a section of the journal Frontiers in Physics

Received: *27 April 2021*
Accepted: *09 July 2021*
Published: *27 July 2021*

Citation:
Williams SN, Allwood-Spiers S, McElhinney P, Paterson G, Herrler J, Liebig P, Nagel AM, Foster JE, Porter DA and Gunamony S (2021) A Nested Eight-Channel Transmit Array With Open-Face Concept for Human Brain Imaging at 7 Tesla. Front. Phys. 9:701330. doi: 10.3389/fphy.2021.701330

INTRODUCTION

MRI at 7 tesla (7T) has the potential to improve diagnostic imaging due to the clinical capabilities in high resolution anatomical as well as functional and metabolic imaging [1]. This has provided motivation for integrating MRI at 7T into clinical workflows and initial regulatory approval [2, 3] has now been granted for brain and knee imaging using single-transmit (sTx) radiofrequency (RF) coils.

The benefits of 7T brain MRI are offset by an inhomogeneous transmit field which causes signal loss in the posterior and temporal fossae, and in the skull base. A transmit array coil together with parallel transmit (pTx) methods is essential to mitigate the image heterogeneity caused by the shorter wavelength in brain tissue [4, 5]. PTx technology will significantly benefit from the performance of the transmit array coil if the coil design offers high transmit efficiency as well as low mutual coupling between the array elements. Several transmit array designs and array decoupling methods can be found in the literature. The fundamental transmit element is designed using conventional loops [6–12], microstrip transmission lines [13–15], dipoles [16–19] or a combination of loops and dipoles [20–22]. The coupling between the adjacent elements is minimized using various decoupling methods such as geometric overlap [23], counter-wound inductors [9], resonant inductive decoupling (RID) [24], capacitors [8, 13, 14] in the gap between adjacent elements, self-decoupled coils [25] and by shielding [26]. These coil arrays are built as close-fitting transceiver arrays (TxRx) or as transmit-only receive-only arrays (ToRo), in which a large transmit array and a tight receive array is used in combination to achieve high signal-to-noise-ratio (SNR) [27, 28].

Conventional loop-based transmit arrays are well suited for high power applications because the voltage is distributed along the loop capacitors, and their tuning is less subject-dependent compared to other RF coil designs. In a ToRo head coil, the transmit array is typically built on 280–300 mm diameter cylinders to allow sufficient space for the receive array and a rear-projection mirror system for fMRI studies. Hence the size of the overlapped individual loops in an eight-channel transmit array is large enough to cause substantial coupling between the second-neighbouring elements. This results in split resonance, increased reflected power due to mismatch and coupling, and loss in transmit efficiency.

While gapped designs can reduce the coupling between the second-neighbouring elements, they also reduce the sample loading due to the smaller element size. The commonly used preamplifier decoupling technique is not applicable for transmit arrays. Chen et al. [29] have proposed triangular shaped transmit elements as a way to bring the next-neighbouring elements closer to install a decoupling inductor. We have developed a novel eight-channel transmit array in which the adjacent elements are overlapped to maintain sample loading, and the second-neighbouring elements are nested to implement decoupling inductors and minimise coupling. Although loop arrays have been extensively investigated [6–12], a nested transmit array for MRI of the brain at 7T has not been presented to the best of our knowledge. The nested-loop transmit array is combined with a 32-channel receive array and configured for use in both sTx and pTx-modes of a 7T scanner.

Self-built RF coils can improve transmit field (B_1^+) homogeneity at ultra-high fields (UHF) while allowing full access to the electromagnetic (EM) model of the coil. A wide range of UHF applications will benefit from efficient specific absorption rate (SAR) management by enabling the use of realistic virtual observation points (VOP) [30] derived from human body models. For pTx in particular, SAR can be produced in localized tissue regions by superimposed RF fields so requires accurate prediction and control. We provide extensive details of the checks we conducted for time-resolved SAR monitoring using offline calculations and experimental measurements in a phantom and *in vivo*.

In this article, we present the design, evaluation, and SAR management of our custom-built dual-mode head coil as well as a comparison with both sTx and pTx commercial head coils.

METHODS AND MATERIALS

All MR measurements were performed on a MAGNETOM Terra 7T whole body scanner (Siemens Healthcare GmbH, Erlangen Germany), fitted with a whole body gradient (amplitude 80 mT/m, slew rate 200 T/m/s). The scanner is equipped with 32 receive channels and eight transmit channels and operates in two acquisition modes, supporting sTx and pTx operation, respectively. The commercial single- and parallel-transmit head coils (1Tx32Rx and 8Tx32Rx, Nova Medical Inc., MA, United States) were used as the reference coil in the comparison studies.

We imaged healthy volunteers who had signed a written consent form approved by a delegated ethics committee with a remit from the West of Scotland Research Ethics Committee and NHS Greater Glasgow and Clyde (NHS-GGC) Research and Development Department.

Transmit Array Design

Single Transmit Element

For a transmit coil housing with inner diameter 280 mm, the width of the individual loop in the transverse plane will be about 140 mm if two adjacent elements are critically overlapped to reduce mutual coupling. The width of the loop will be about 100 mm for a gapped design with 10 mm between two adjacent loops.

Two test loops were built on a rapid prototyped fiberglass tube (inner diameter: 280 mm; wall thickness: 3 mm; length: 355 mm; manufacturer: Klaus Hoppe Werbetechnik, Ofterdingen, Germany) and the Q-ratio was measured in different positions around the cylinder. The length of the loop along the head/foot direction was chosen to be 210 mm to achieve whole brain excitation. Solder pads to assemble the capacitors were manufactured using flexible circuit board material (PW Circuits, Wigston, United Kingdom) and the pads were attached on to the surface of the tube using double sided tape (3M, Bracknell, United Kingdom).

The loop position and the corresponding coil Q-factors are shown in **Figure 1**. The Q-factor was measured by placing the

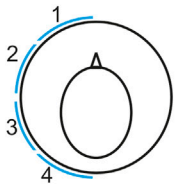

	Gapped Design Loop size: 100 mm x 210 mm Q_{UL} = 286				Overlapped Design Loop size: 140 mm x 210 mm Q_{UL} = 262			
Position	1	2	3	4	1	2	3	4
Loaded Q (Q_L)	160	150	122	64	132	122	80	42
Q ratio	1.79	1.91	2.34	4.47	1.98	2.15	3.28	6.24

FIGURE 1 | Coil Q-ratio measurements demonstrate higher sample loading for the larger loop. The larger loop has the dimensions of a single-transmit element in an overlapped 8-channel transmit array.

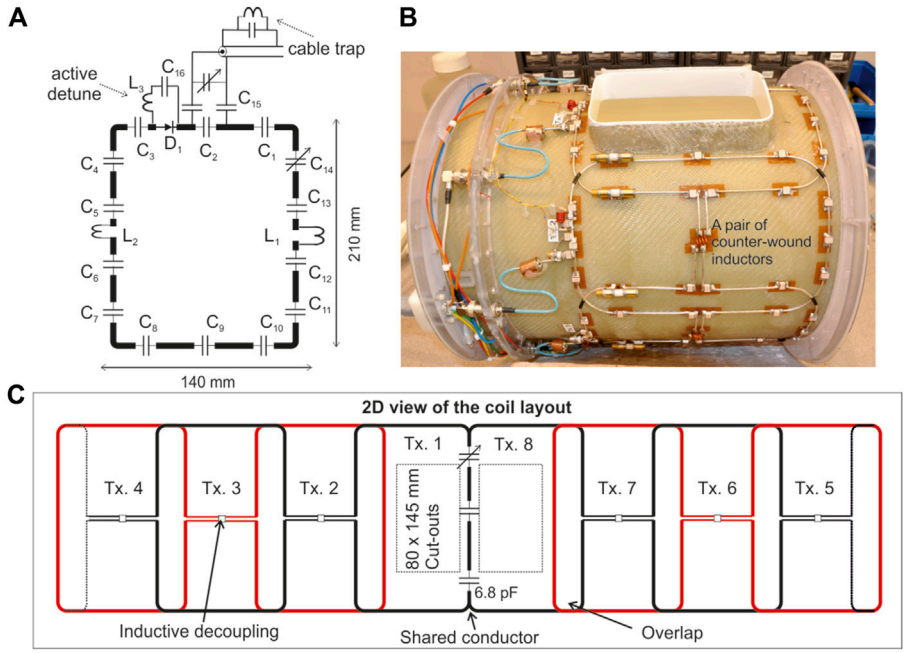

FIGURE 2 | (A) Equivalent circuit of a single element of the transmit array consisting of 13 × 6.8 pF fixed capacitors (C_1 to C_{13}) and a trimmer capacitor C_{14} to fine-tune the coil resonance frequency to 297.2 MHz. **(B)** Picture of the completed transmit array. **(C)** A two dimensional view of the transmit array configuration. The capacitor distribution in the shared conductor is also provided.

single loop inside a local RF shield at a distance of 24 mm from the loop, which was then positioned inside a dummy shield mimicking the scanner bore. The larger loop provided higher sample loading across different positions, and the overlapped configuration was chosen over gapped design.

8-Channel Nested-Loop Transmit Array

The array consisted of eight overlapped loops arranged in a single row. The loop was built using 2 mm diameter silver plated copper wire (APX, Sarrians, France). A total of 13 fixed capacitors (6.8 pF; 100°C series; American Technical Ceramics, NY, United States) and one variable capacitor (5,610; 1–7.5 pF; Johanson Manufacturing Corporation, NJ, United States) were distributed in each loop. To reduce radiation loss [31], a local RF shield was concentrically placed. A double-sided flexible PCB with 9 µm copper was used to form the RF shield. To reduce gradient induced eddy currents, each layer was slotted and the copper in the second layer was offset from the first to form a continuous RF shield at high frequency [32]. The RF shield PCB was attached to the inner surface of a fiberglass tube (Outer diameter: 340 mm; wall thickness: 2 mm; length: 355 mm) using double sided tape. The distance to the RF shield was 24 mm in this design based on the standard sized tube that was available to us. However, there is scope for further improvement in transmit performance by optimizing the distance to the RF shield [6].

The equivalent circuit of a single element is shown in **Figure 2A**. A PIN diode (D_1, MA4P7446-1091T, MACOM, United States) was installed in series with the loop and a series LC circuit (C_{16}, L_3) was connected across the PIN diode and adjusted to maximize the isolation when the diode is turned OFF. A shielded cable trap tuned to 297.2 MHz was soldered across the input matching circuit.

Due to the large size of the individual loops, the coupling between the second-neighbouring elements is strong enough to cause split resonance and deteriorate the performance of the

transmit array. Furthermore, the reflected power from a coupled transmit array depends on the amplitude and phase of the RF excitation signal, making it challenging to employ such an array in parallel transmit applications [33]. Hence, it is necessary in this case to implement a decoupling mechanism between the first and the third transmit element in addition to decoupling the adjacent elements. The second-neighbouring elements are nested as shown in **Figure 2B** and a pair of inductors wound in opposite directions [9] was installed to minimize the mutual coupling between them.

Open-Face Design

The top ranked criteria in the wish list of our clinical collaborators is an open-face coil to reduce claustrophobia and to allow monitoring of the patient. To satisfy this requirement, two large cut-outs in the RF shield and the fiberglass tubes were introduced in front of the eyes, each measuring 80 mm × 145 mm. To minimize the coil structure and allow a larger cut-out, the overlap in front of the nose was replaced by a shared conductor [29, 34]. There were two fixed capacitors (6.8 pF, ATC 100°C series) and one variable capacitor (5,610; 1–7.5 pF; Johanson Manufacturing Corporation, NJ, United States) evenly distributed along the shared conductor between transmit elements 1 and 8. The variable capacitor was adjusted to minimize the coupling between the coil elements 1 and 8. Finally, the cut-outs were closed off using a fiberglass part for ingress protection.

A 2D layout of the final transmit array configuration is shown in **Figure 2C**. Also note in **Figure 2C** that there is no inductive decoupling across the second-neighbouring coil pairs (1 and 7; 2 and 8) to maintain a clear open structure. This would allow a 'look-out' mirror, which is commonly used in 1.5T/3T clinical head coils, to be fixed outside the transmit array for the subject to see the operator during the scan and reduce claustrophobic effect.

Receive Array Design

To increase the SNR, the transmit array was combined with a 32-channel receive array. The receive array design is a retuned version of the design previously presented for a 9.4T receive array [9, 11]. Briefly, the receive array consisted of 32 elements arranged in four rows. The first three rows form a complete ring around the helmet and the fourth row formed a partial ring with only four receive elements. More details about the receive array layout and circuit schematic can be found in [9]. The final setup consisting of the transmit and receive array, with the view of the open-face approach as seen by the subject being scanned, is shown in **Figure 3A**.

Interface to Single-Transmit Mode

Until CE and FDA approval for clinical use of pTx is received, MRI at 7T will continue to be performed in a hybrid environment using scanners which support imaging in sTx mode for clinical diagnosis and pTx mode for research and clinical validation. Our coil was configured to be interfaced to both pTx and sTx modes so that a single device can be used in both the scanner modes.

The scanner provides eight PIN bias lines in each 8-channel receive socket and eight more in the pTx socket to control the active detuning of the receive and transmit elements, respectively. The PIN bias lines in the pTx socket was not used as this cannot be activated when the scanner is in sTx mode. Instead, eight PIN bias lines from the receive sockets were routed to the transmit array through a multi-pin non-magnetic connector (Amphenol Alden, Chicago, IL. United States). This can be seen in the service-end view shown in **Figure 3B**. The remaining 24 PIN bias lines were shared to control the switching of the 32-channel receive array.

A 1x8 power splitter was custom built [35] and fitted with the same 8-channel high power socket (ODU GmbH, Germany) as in the scanner. To achieve a circularly polarized (CP) mode excitation, an incremental phase offset of 45° was realized by increasing the length of the coaxial cable and implemented inside the splitter housing. The total loss introduced by the splitter and the additional short connecting cable from the patient table to the splitter input was 0.8 dB. A picture of the custom-built power splitter and an internal view showing the different cable lengths can be seen in **Figure 3C**.

The transmit array cable is connected directly to the pTx socket in the patient table just like any conventional pTx coil. In sTx mode, the RF power amplifier output is connected to the input of the splitter and the transmit array cable is connected to the output of the splitter.

Bench Measurements

The S-parameters of the transmit and receive arrays were measured by loading the coil with a fiberglass head-and-shoulder phantom filled with tissue equivalent solution (ε_r = 52.1, σ = 0.41 S/m) [36]. Bench measurements were performed using a 2-port ZND series vector network analyzer (Rohde and Schwarz, Germany). Final tuning and adjustment of the transmit array was performed in the presence of the actively detuned receive array. Test jigs were custom-built to control the switching and biasing of the PIN diodes and preamplifiers.

Transmit Array Simulation

A co-simulation approach consisting of RF circuit simulation and 3D electromagnetic (EM) simulation (CST Studio Suite, Dassault Systems, France) was used to simulate the transmit array [37, 38]. Each lumped element included series resistance values obtained from the component datasheet. The local RF shield, fiberglass tubes as well as the scanner bore were also included in the model. The RF shield and coil conductors were both made from annealed copper with the following properties: $\sigma = 5.80 \times 10^7$, $\rho = 8.93 \times 10^3$ kg/m. The fiberglass is standard FR-4 from the CST database: ε = 4.3, μ = 1, electrical tand. = 0.025. However, we did not include the coaxial cables, cable traps and DC wiring in the numerical model. The variable capacitors, matching circuit and decoupling inductors were represented as ports resulting in a total of 29 ports in the 3D EM simulation. There are eight excitation ports in circuit co-simulation and each one was connected to the matching network via a 0.6 dB attenuator to represent the cable loss from the coil feed-point to the coil plug.

The transmit array elements were tuned to 297.2 MHz and matched to a 50 Ω port in circuit co-simulation whereas the electric and magnetic field components as well as the SAR maps

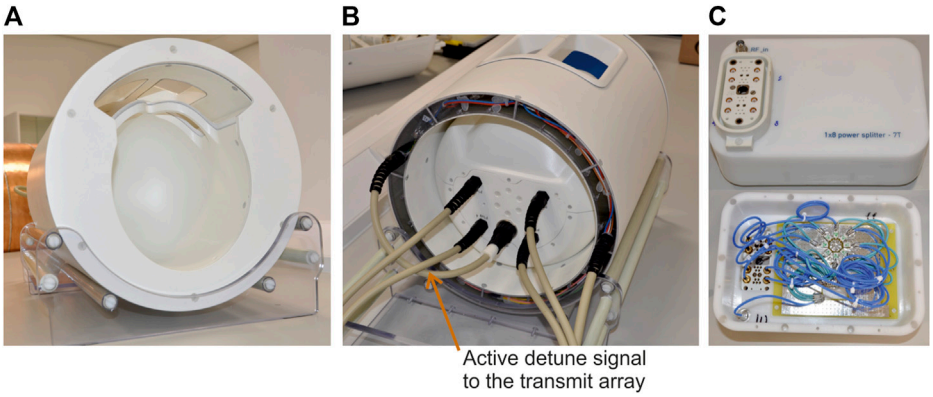

FIGURE 3 | (A) The completed coil assembly. **(B)** View of the coil from the service-end. **(C)** The custom-built 1x8 power splitter with built-in CP mode phase offsets.

were calculated in the 3D EM domain [37, 38]. A voxel model of the head-and-shoulder phantom with 1 mm isotropic resolution was imported from a CT scan. The coil was first tuned and matched to the phantom and then loaded with Duke and Ella models from the Virtual Family cohort [39] and Gustav from CST, truncated at the level of the chest. For each model, the EM field and SAR were estimated for three different positions in Z (0, −10 and −20 mm) to mimic the different possible subject positions during scans *in vivo*.

A typical mesh consisted of about 40 million cells. The frequency sweep was set from 280 to 320 MHz and a convergence criteria of −40 dB was set to obtain the RF field distribution for each discrete port. On a dual Intel Xenon workstation with 256 GB RAM and GPU acceleration using Nvidia Tesla K80, each body model simulation took approximately 1 h per 3D port, for a total simulation time of just over a day.

Virtual Observation Point Generation for Local Specific Absorption Rate Monitoring

Accuracy and control of SAR monitoring is critical for in-house UHF pTx coils [40]. The scanner used in this study uses VOPs [30] as part of its standard framework for local SAR prediction and real-time monitoring during pTx operation.

For each body model and coil position, the electromagnetic field $E(r)$ at all mesh locations r was used to average over 10 g volumes to generate a positive semi-definite "Q-matrix" [41], $Q(r) \in \mathbb{C}^{N_c \times N_c}$ for $N_c = 8$ transmit channel excitation combinations. This was achieved in CST by setting the signal of the upper matrix elements to 1 V_{rms} with a phase of 0° for both ports and in the lower matrix elements, the signal was 1 V_{rms} and 0° for the first port and 1 V_{rms} and 90° for the second port. For diagonal matrix elements signal was simply set to 1 V_{rms} for the first port. This resulted in $N_c^2 = 64$ separate post processing tasks and an $N_c \times N_c$ SAR matrix for each voxel in the simulation, from which the final three-dimensional Q-matrix array was derived. These arrays of Q-matrices were exported from CST as a text file and read into MATLAB (The MathWorks, Natick, MA). This step was validated by comparing the CST Q-matrix SAR and MATLAB SAR.

Once the MATLAB Q-matrix SAR was corroborated with CST for each body model, they were concatenated into one large Q-matrix array. The combined Q-matrix array was compressed into a set of VOPs following the method from Eichfelder and Gebhardt [30]. In an initial study [42], the effect of various overestimation factors for VOP compression on local SAR measurment online by the system was compared. In this work, time-resolved instantaneous local SAR calculations for various overestimation factors is compared with respect to the full Q-matrix array values. Ultimately, a 25% overestimation factor yielded was found to be a good compromise between local SAR and RF performance. As per the equipment manufacturer's recommendation, the VOPs were also adjusted to account for an RF supervision system error tolerance of 12% in amplitude and 5° in phase with the following calculation,

$$\mathrm{VOP}^{modified} = 1.16\,\mathrm{VOP}^{original} + 0.09\,\lambda_{max}1 \quad (1)$$

where λ_{max} is the maximum Eigenvalue from the original VOPs.

After generating the final, modified VOPs, they were validated by comparing local SAR estimates calculated offline and by the scanner for three B_1^+ shim configurations with known input power: CP (45° increments), CP^{2+} (90° increments), and the worst case mode which is the Eigenvector associated with λ_{max}. Local SAR calculated before VOP compression with the Q-matrix array was always less than the VOP-compressed SAR, which in return was always less than the scanner prediction and measurements. This test validated the coil and SAR management for B_1^+ shimming or static pTx. The entire VOP generation process is summarized in **Figure 4** below.

Coil Performance Evaluation

B_1^+ Map Simulation and Measurement Comparison

The transmit performance was evaluated by collecting B_1^+ maps with a pre-saturated Turbo-FLASH sequence [43]. For both sTx and pTx operation, a B_1^+ map combining all transmit elements was collected in CP configuration using the following parameters: number of slices 45, slice thickness 3 mm, slice gap 0.9 mm, flip angle (FA) 5°, TE 1.55 ms, TR 11010 ms, acquisition time (TA) 23 s, FOV 300 × 300 mm^2, and matrix size (MAT) 256 × 256. Results were then compared to the EM simulation qualitatively and quantitatively by comparing the peak B_1^+ field value. In pTx mode, phase-sensitive,

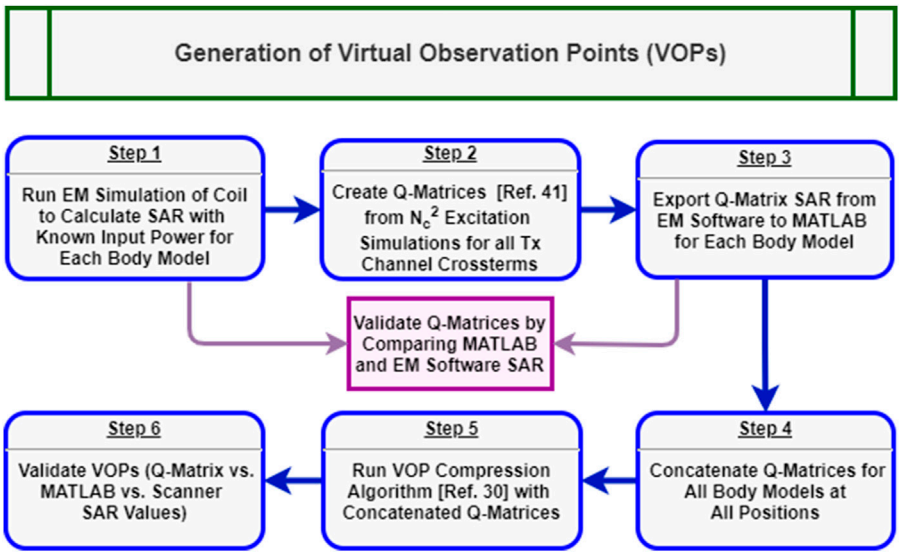

FIGURE 4 | Generalized workflow for generation and validation of the virtual observation points for local SAR monitoring in pTx. Blue boxes represent chronological steps within the procedure while, purple boxes show feedback steps for additional EM simulations.

single channel B_1^+ maps were also acquired for each transmit channel using the same scan parameters and a total measurement time of 111 s. These maps were simulated and measured in our custom-built head-and-shoulder phantom. To obtain relative phase maps between channels from the measured phase maps, a reference channel was used to remove additional residual phase components. These complex single channel B_1^+ maps were then compared qualitatively to the simulated single channel maps from the EM model.

Comparison of Self-Built Parallel-Transmit Coil and Commercial Parallel-Transmit Coil

The transmit performance of the self-built parallel-transmit array was also compared to the commercial 8Tx/32Rx coil (Nova Medical, Wilmington, MA, United States). The commercial pTx coil is not available at the Imaging Centre of Excellence at the University of Glasgow, so a second head-only phantom filled with tissue equivalent solution ($\varepsilon_r = 51.1$, $\sigma = 0.38$ S/m) was prepared. This phantom was scanned with the self-built coil in pTx mode as well as with the commercial pTx coil in another site using the pre-saturated TurboFLASH B_1^+ mapping sequence with a fixed combined voltage of 165 V (no. slices/slice thickness/slice gap/FA/TE/TR/TA/FOV/MAT = 45/4 mm/0.8 mm/10°/1.48 ms/30000 ms/61 s/240 × 240 mm^2/96 × 96). For each coil experiment, the FA maps generated from the B_1^+ mapping sequences were compared with both sagittal and axial slices for their transmit efficiency and flip angle homogeneity.

Measurement of Dynamic Parallel-Transmit Waveforms

A final validation step for our pTx coil was to verify the accuracy of the scanner's SAR estimation for time-varying RF waveforms. Four external pTx waveforms were used for this study: a conventional Shinnar-LeRoux (SLR) [44] slice-selective pulse in CP configuration with a nominal flip angle of 90°, the same SLR pulse with transmit channels 4-6 turned off, a 3D hard rectangular pulse with a nominal flip angle of 5°, and a 5° 3D Universal Pulse (UP) [45] designed with a 3D SPINS trajectory [46] using the method described in [47]. The slice-selective SLR pulses were both played out three times in a 2D FLASH sequence with a single 5 mm slice, FOV = 240 × 240 mm^2, MAT = 256 × 256, TE = 10 ms, and 3 TRs: 50, 100, and 250 ms. The 3D hard pulse and UP were both played out in a 3D GRE sequence with TE/TR/TA/FOV/MAT = 2.28 ms/1,010 ms/101 s/250 × 220 × 160 mm^3/250 × 220 × 160.

For all scans, the external RF waveforms were recorded during data measurement via the directional couplers (DICOs) of the pTx system. These measurements were compared offline to the prescribed waveforms to validate the fidelity of the dynamic pTx system. Furthermore, the time-integrated local SAR was calculated and compared to the scanner predicted and measured values. The time-varying local SAR for ith VOP at time point t the for an applied external pTx pulse $b \epsilon \mathbb{C}^{N_t \times N_c}$ was calculated as

$$SAR_{local}\ (i,t) = \tilde{b}^{H}(t) \cdot VOP(i) \cdot \tilde{b}(t) \tag{2}$$

where $\tilde{b}(t) \epsilon \mathbb{C}^{N_t N_c \times 1}$ is the pTx pulse stretched into a vector, where N_t is the total number of time points and N_c is the number of transmit channels. This instantaneous SAR was then averaged across time with respect to the RF duty cycle D, representing the fraction of RF duration for a given sequence TR. The time-averaged local SAR can be compared to scanner estimates with the following summation across each time point indexed as t_k,

$$\overline{SAR}_{local}\ (i) = \frac{D}{N_t} \sum_{k=1}^{N_t} SAR_{local}\,(i, t_k) \tag{3}$$

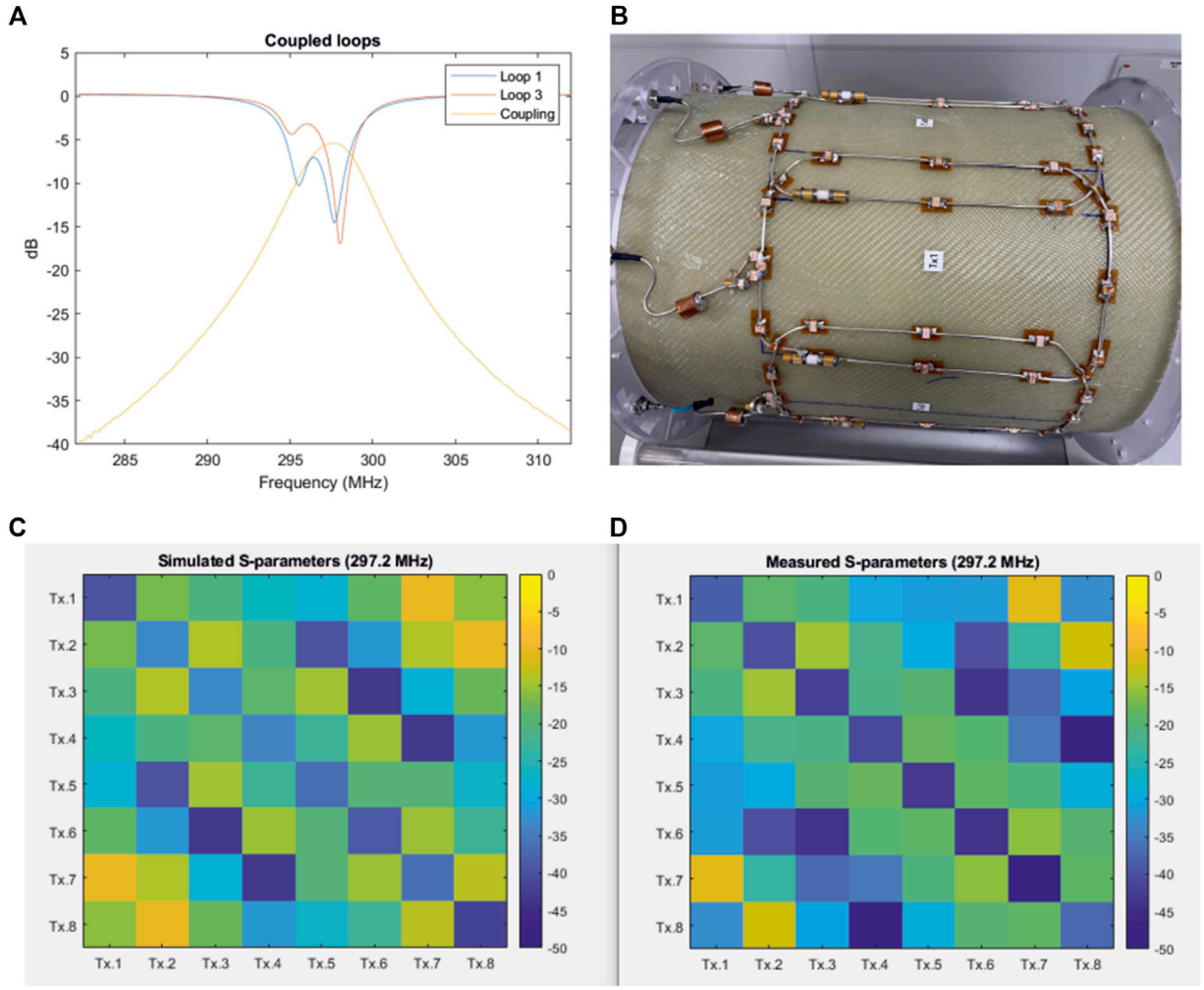

FIGURE 5 | (A) S-parameter plots of transmission and reflection demonstrating high coupling and split-resonance between second-neighbouring transmit elements in a coil without decoupling inductors. **(B)** Picture of the 8-channel loop array (140 m × 210 mm loops) with decoupled adjacent elements, but no decoupling between second neighbouring elements. **(C,D)** Simulated **(C)** and measured **(D)** S-parameter matrix of the 8-channel transmit array, respectively.

Anatomical Imaging in Single-Transmit and Parallel-Transmit Modes

After completing additional temperature mapping and simulation studies [48, 49], the coil was granted local ethics and safety approval for imaging studies of healthy subjects in pTx and sTx modes for operation in normal IEC-SAR mode in the head using local transmit coils (10 W/kg). In the first study, the longitudinal coverage of the coil was compared to the commercially available 1Tx/32Rx coil (Nova Medical, Wilmington, MA, United States). A healthy volunteer was scanned with the commercial coil and the self-built dual-mode coil in sTx operation. The same volunteer was then also scanned with the self-built coil in pTx mode using B_1^+ shimming. The three-way comparison was performed with a sagitally-oriented T2-weighted 2D RARE sequence with the following parameters: no. slices/slice thickness/slice gap/FA/TE/TR/Echo Train Length/TA/FOV/MAT = 39/3 mm/3.9 mm/140°/58 ms/9,000 ms/9/198 s/172 × 230 mm^2/768 × 1,024. When scanning in pTx mode, the vendor provided B_1^+ shimming routine was set over a volume covering the brain parenchyma.

The second *in vivo* experiment examined the performance of the self-built coil using dynamic pTx waveforms. Here, two 3D MPRAGE sequences were compared in pTx mode with the same healthy volunteer. The first acquisition used a CP hard pulse for excitation and the second used the Universal Pulse described previously in *Measurement of Dynamic Parallel-Transmit Waveforms* above. Both scans used the same vendor provided, CP mode adiabatic inversion pulse with a combined total voltage of 350 V. The remaining sequence parameters were FA/TE/TI/TR/TA/FOV/MAT = 5°/2.28 ms/1,100 ms/3,000 ms/294 s/250 × 220 × 160 mm^3/250 × 220 × 160.

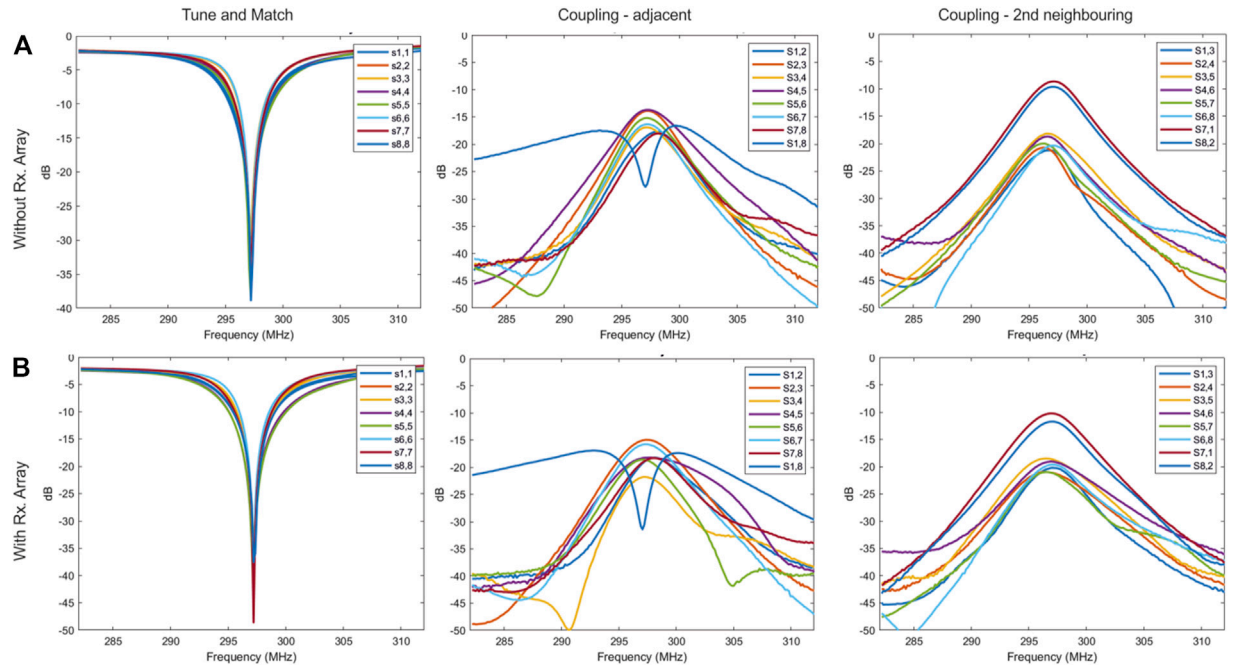

FIGURE 6 | (A,B) Measured S-parameter plots of the reflection, adjacent element and next-neighbouring element coupling of the constructed transmit array without the receive array **(A)** and with the receive array **(B)**.

RESULTS

S-Parameters

Figure 5A demonstrates the coupling between second-neighbouring elements in transmit arrays consisting of large loops. The coupling between the second-neighbouring transmit elements was more than -6 dB. During this measurement, all other loops were terminated with 50 ohms. The S11 plots also demonstrates the split resonance caused by the high mutual coupling. A picture of the 8-channel transmit array with overlapped loops constructed for these measurements is shown in **Figure 5B**.

The simulated and measured S-parameter matrices of the 8-channel transmit array are shown in **Figures 5C**,D. The measurements were performed in the presence of the actively detuned receive array, and the coil was loaded with the head-and-shoulders phantom. All channels were matched to better than −30 dB in both simulation and measurement. The average coupling between the adjacent elements in the constructed array was −19.8 dB. Nesting the second-neighbouring elements using inductors reduced the average coupling to −20.2 dB. The adjacent and second-neighbouring element coupling in the simulated model was −17.97 dB and −19.67 dB, respectively.

The measured coupling between the two pairs of second-neighbouring elements (1&7 and 2&8) across which there are no counter-wound inductors was −11 dB. The corresponding value from the simulated model was −9.83 dB. It is important to note that the size of loops 1 and 8 are reduced because the overlap between element 1 and 8 was replaced by a shared conductor. This helped to minimize the mutual coupling and maintain an acceptable decoupling. Although this will slightly reduce the overall performance of the transmit array, an open-face design with a large visual field to reduce claustrophobia was an important consideration in our design approach.

In **Figure 6**, the measured S-parameter plots of the tune and match, adjacent element, and second-neighbouring element coupling of the constructed transmit array with and without the receive array are shown. The 'm' shaped S21 curve is between the transmit elements 1 and 8 which are decoupled by the shared conductor. Only the tune and match of the transmit array was adjusted after the receive array was inserted. The decoupling inductors and the overlaps were not adjusted. The plots shown in **Figure 6** demonstrate that the transmit array coupling charecteristics are not influenced by the presence of the 32-channel receive array.

Comparison of Transmit Array Simulation and Measurements

Figure 7 compares the simulated and experimental B_1^+ maps in the head-and-shoulders phantom. **Figures 7A**,**B** show the sagittal cross section of the combined CP mode magnitude maps. The peak B_1^+ in the center of the phantom was 111 nT/V in simulation and 107 nT/V in measurement, with the voltage referenced to the coil input. Furthermore, B_1^+ maps were acquired with and without the receive array to quantify the influence of the receive array. The attenuation in the B_1^+ field

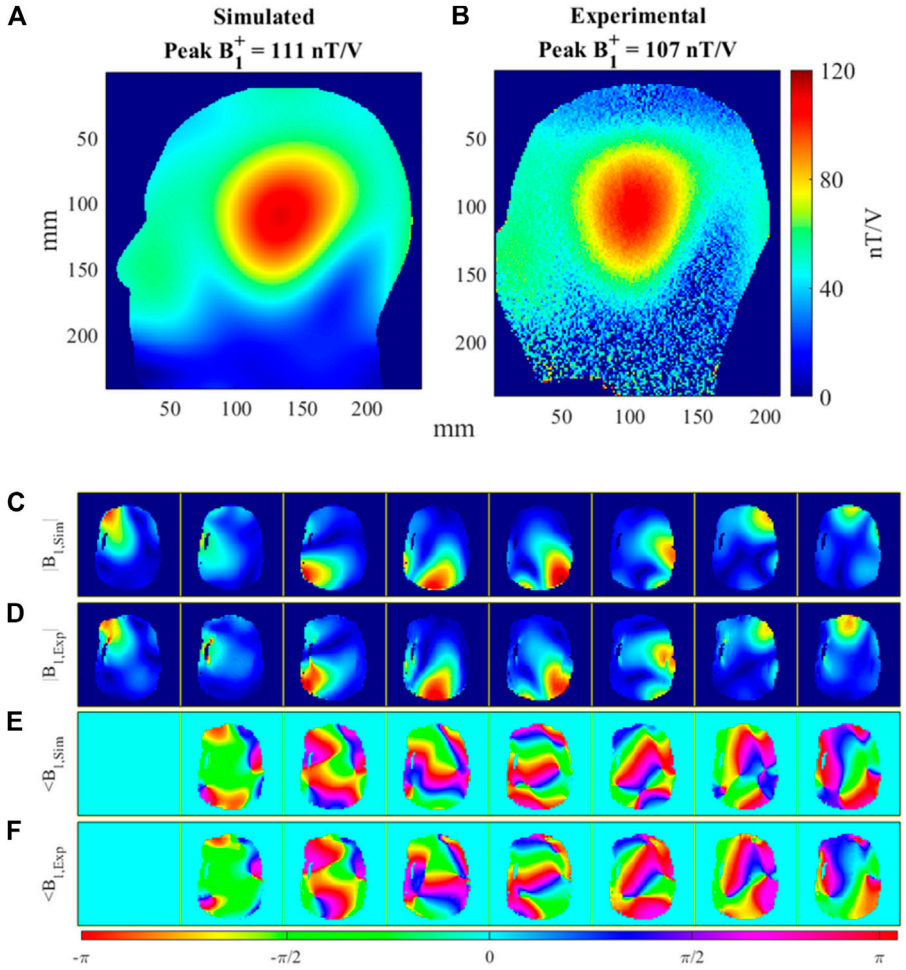

FIGURE 7 | Comparison of simulated and measured B_1^+ maps in the head-and-shoulders phantom. **(A)** Simulated, sTx (CP mode) B_1^+ map of Tx array and **(B)** matching experimental sTx B_1^+ map. **(C)** Simulated, normalized $|B_1^+|$ field magnitude and **(D)** matching experimental, normalized $|B_1^+|$ magnitude for all 8 Tx channels. **(E)** Simulated $\angle B_1^+$ field phase and **(F)** matching experimental $\angle B_1^+$ phase for all 8 Tx channels.

due to the presence of the receive array was 7%. **Figures 7C–F** show the simulated and experimental B_1^+ maps for the individual transmit channels, both magnitude and phase. The spatial distributions between simulation and their measurement match well for each individual channel, although some small phase differences do exist.

Virtual Observation Point Model Validation

Figure 8A shows the SAR simulations in the three human body models used for EM simulation (Duke, Ella, and Gustav) in CP configuration. For each model, their 10 g SAR is reported with 1W input power at the three simulated coil positions. All SAR simulations are scaled to the same windowing level for comparison. **Figure 8B** reports the local SAR for the *combined* SAR coil model (all three human body models, all three positions). The local SAR is compared for CP mode, CP^{2+} mode, and the worst case excitation vector. The values are listed for the full, combined EM simulation Q-matrices, the compressed VOPs, and the scanner prediction and measurements. The table validates the VOP models because the Q-matrix SAR is always less than the VOP compression estimate, which in return is always less than the scanner predictions and measurements.

Dynamic Parallel-Transmit Waveform Measurement and Local Specific Absorption Rate Calculations

Figure 9 demonstrates instantaneous local SAR calculations (**Eq. 2**) for the 5° 3D SPINS Universal Pulse with duration of 1 ms and explores how various VOP overestimation factors affect the local SAR estimates. **Figure 9A** plots the RF pulse magnitude waveforms for the eight transmit channels. **Figure 9B** plots the absolute instantaneous SAR of the single pulse in an MPRAGE acquisition with TR = 3,000 ms for the uncompressed Q-matrices (for visualization purposes, the Q-matrices are downsampled here). At various time points

A

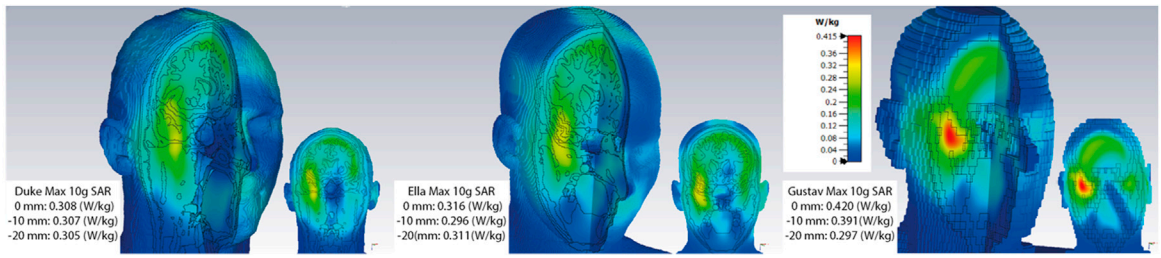

B

Shim Configuration	Input Power [W]	Q-Matrix [W/kg]	VOP Calculated [W/kg]	Scanner Predicted [W/kg]	Scanner Measured (Mean/Max) [W/kg]
CP	2.1	0.8	1.6	1.8	2.3/2.3
CP^{2+}	2.0	1.1	2.4	2.7	3.5/3.5
Worst Case	1.4	3.2	4.0	4.7	5.6/5.7

FIGURE 8 | (A) 3D CST simulations of 10 g-SAR with 1W of input power for Duke, Ella, and Gustav body models all positioned at the B_0 field isocenter with the same color scaling on each model. The max SAR value for each model for all three positions (z = 0, −10, and −20 mm) is listed in the left hand corner for each body model. **(B)** Comparison of local SAR values for concatenated body model Q-matrices, VOP compressions calculated offline, and values reported by scanner during predicition and measurement.

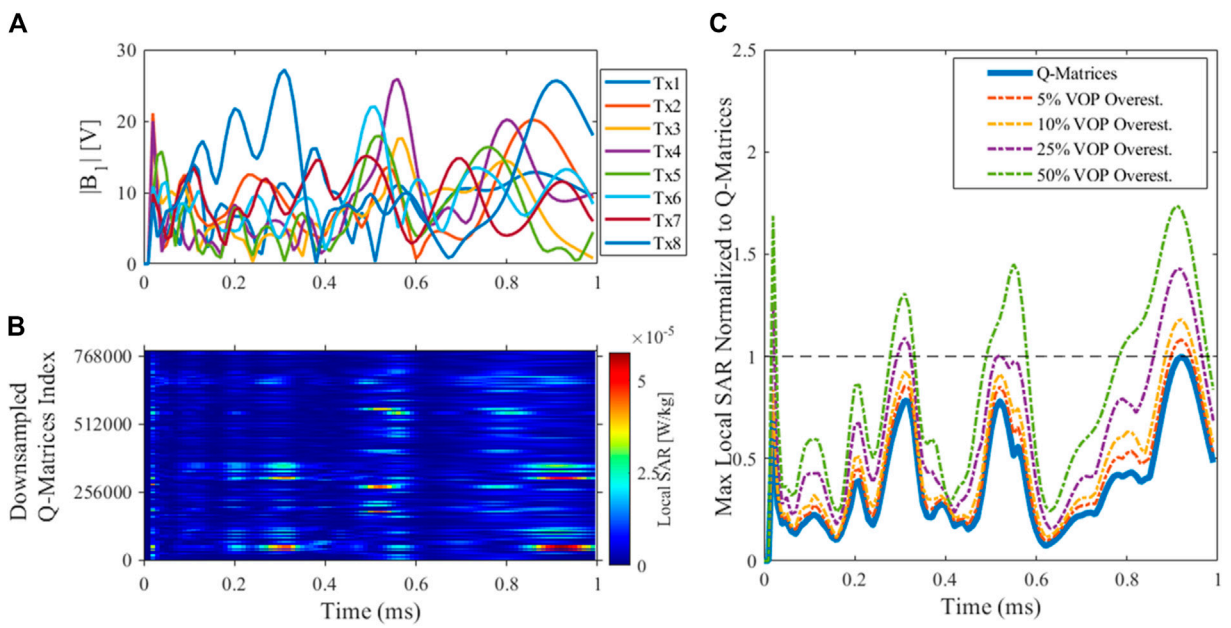

FIGURE 9 | Local SAR for a 5° excitation Universal Pulse. **(A)** UP magnitude waveform; **(B)** Instantaneous SAR for the UP excitation in MPRAGE using downsampled uncompressed Q-matrices; **(C)** Max local SAR for each time point of the UP for the Q-matrices and VOPs with 5, 10, 25, and 50% overestimation, all normalized to the maximum of the Q-matrices' SAR. Different time points of the UP (i.e., different amplitude and phase configurations) lead to varying levels of VOP overestimation relative to the Q-matrices, but importantly the VOP-derived estimate is always overestimated.

with distinct amplitude and phase configurations, different Q-matrix voxel locations deposit more local SAR. **Figure 9C** compares the normalized maximum local SAR at each time point of the UP excitation for the Q-matrices and various VOP compressions: 5, 10, 25, and 50% worst case SAR overestimation. As anticipated, the difference between max instantaneous SAR using the Q-matrices and the VOP compressions increases with overestimation factor. Higher factors also leads to smoother instantaneous SAR plots due to fewer VOPs and less possible SAR variation. In practice, the

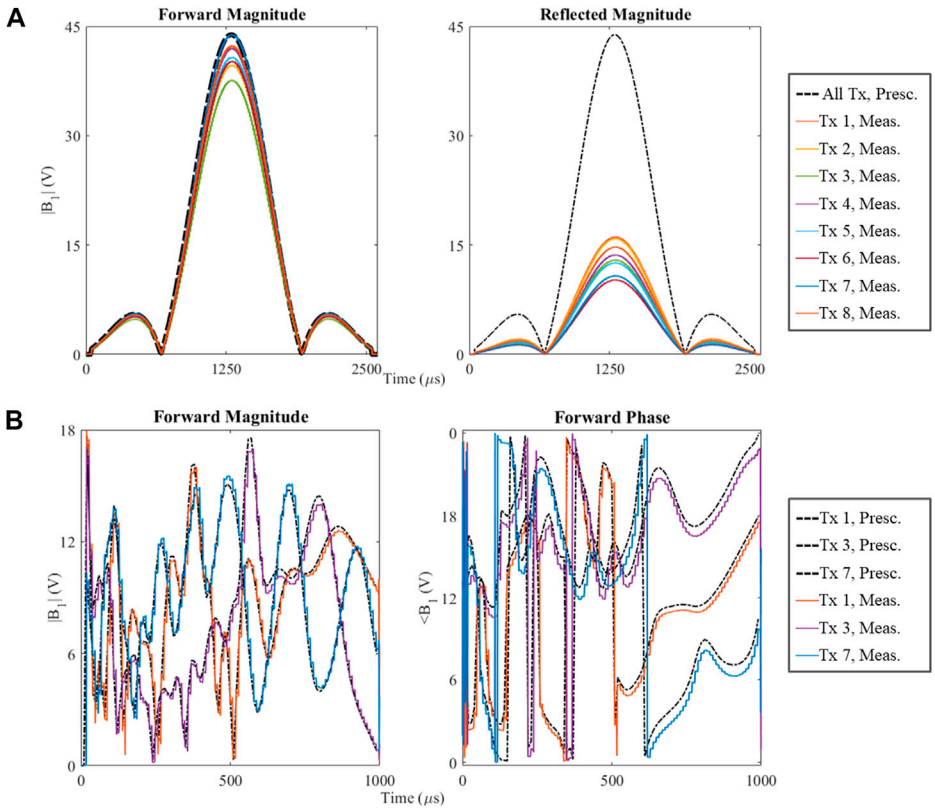

FIGURE 10 | Comparison of prescribed RF waveforms (black, dotted lines) and their measurements single transmit channels (solid, colored lines). **(A)** A conventional, circularly polarized, slice-selective SLR pulse with nominal flip angle of 90°, the left plot contains the forward measurement and the right plot contains the reflected measurement; **(B)** Dynamic, non-selective Universal Pulse pulse with nominal flip angle of 5°, the left plot shows the RF magnitude waveforms and the right plot shows RF phase waveforms for 3 out of 8 pTx channels.

dual-mode coil uses a 25% overestimation of worst case SAR. This overestimation factor was chosen empirically to provide a conservative local SAR estimate without compromising overall RF performance drastically.

Figure 10 plots test pTx waveforms and their complex-valued DICO measurements. Subplots 10A show the magnitude waveforms for forward and reflected measurements using the 2D SLR pTx pulse played in CP mode. Subplots 10B show the forward magnitude and phase waveforms for the 5° 3D SPINS Universal Pulse (for visualization simplicity, only 3 out of 8 channels are plotted here).

Table 1 compares the local SAR calculations (**Eq. 3**) for the four test 2D and 3D pTx pulses and a few different sequence TRs. The fourth column from the left shows the local SAR calculations without considering additional experimental factors. Column 5 shows these calculations including the cable loss between the RF power amplifier (RFPA) and the coil plug of the system, a fixed, measurable value roughly equal to 1.7 dB. Column 6 shows the final, true local SAR calculations that includes cable loss and the gain variation of the RFPA, a value measured for each channel that is calibrated with each new scan session. These final SAR calculations are in excellent agreement with the scanner predicted and measured values for all test pTx pulses and all TRs.

Phantom Comparison of Commercial and Self-Built Parallel-Transmit Coil

Figure 11 compares the phantom flip angle maps collected with the self-built, dual-mode parallel transmit coil and the commercially available parallel-transmit coil using the same applied 165 V. For both coils, sagittal and axial images are shown to visualize the longitudinal coverage and the FA right-left symmetry. Qualitatively, the self-built coil has similar transmit behavior to the commercial coil. Quantitatively, the maximum, mean, and standard deviation of flip angle are reported for the center slice of each acquisition orientation. The self-built coil has a decrease in peak FA and has about the same FA standard deviation despite the lower mean. These discrepancies can be attributed to the effects of the eye cut-outs not present in the commercial coil shield.

Healthy Volunteer Experiments

Figure 12 displays the T2w RARE images collected in a healthy subject using the commercial single-transmit coil and the dual-mode parallel-transmit coil operating in both sTx and pTx modes. The self-built coil has better longitudinal coverage in the inferior regions of the brain for both modes compared to the commercial sTx coil. In pTx mode, the self-built coil applied B_1^+ shimming,

TABLE 1 | Time-averaged input power (W) and SAR values (W/kg) for 4 pTx pulses: SLR, SLR w/Tx 4-6 off, CP hard excitation, and UP Excitation. For calculation and experimental measurements, each pTx pulse is associated with a specific sequence and TR. Column 4 values are from **Eq. 3** using the external pulses in volts and the electromagnetic field simulation VOPs. Column 5 values add the cable loss from the RF power amplifier (RFPA) to the coil plug, measured to be 1.7 dB. Column 6 values are the true local SAR calculations with cable loss and RFPA gain variation included. The values in column 6 are in good agreement with the scanner predicted local SAR and measured local SAR in the final two columns.

Pulse sequence/ TR [ms]	pTx pulse	Input power [W]	Calculated local SAR [W/kg] (Eq. 3)	Calculated local SAR w/cable loss [W/kg]	Calculated local SAR w/cable loss and RFPA gain variation [W/kg]	Scanner predicted local SAR [W/kg]	Scanner measured 10 s local SAR (mean/ max) [W/kg]
FLASH/50	SLR	1.72	2.55	1.72	1.75	1.88	1.76/1.80
FLASH/100	SLR	0.86	1.27	0.86	0.87	0.94	0.87/1.22
FLASH/250	SLR	0.34	0.51	0.34	0.35	0.38	0.35/0.62
FLASH/50	SLR w/Tx 4–6 off	1.08	2.46	1.66	1.69	1.95	1.86/1.91
FLASH/100	SLR w/Tx 4–6 off	0.54	1.23	0.83	0.85	0.98	0.91/0.94
FLASH/250	SLR w/Tx 4–6 off	0.22	0.49	0.33	0.34	0.39	0.37/0.65
GRE/1,010	CP hard pulse Exc.	1.01	1.52	1.03	1.04	1.11	0.89/0.95
GRE/1,010	UP Exc.	1.52	3.31	2.24	2.28	2.41	2.29/2.38

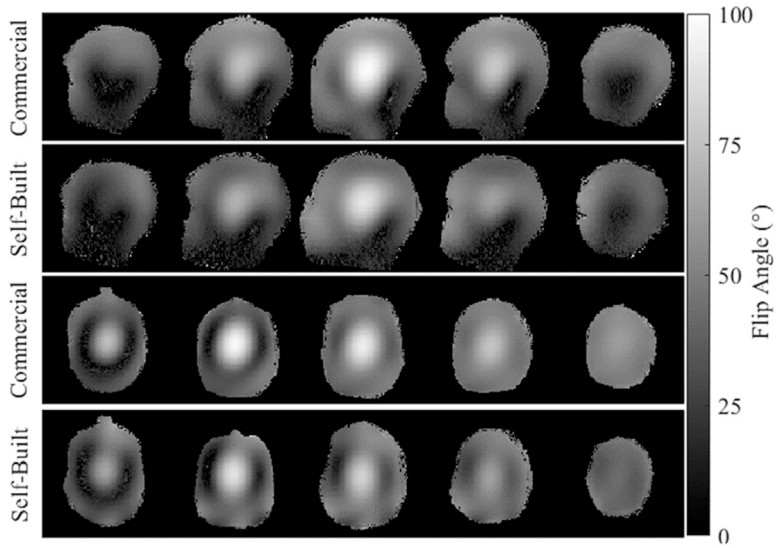

Coil/Orientation	Max. FA (°)*	Mean FA (°)*	St. Dev. FA (°)*
Commercial/Sagittal	99.1	47.5	21.0
Self-Built/Sagittal	89.7	43.0	19.7
Commercial/Axial	96.4	40.8	18.9
Self-Built/Axial	96.4	40.2	19.5

* Calculated on center slice

FIGURE 11 | Comparison of measured flip angle maps with the commercially-available pTx coil and the dual-mode self-built coil operating in pTx mode with an applied voltage of 165 V. The top two rows show sagittal images and the bottom two rows show axial images. For all flip angle maps, the max, mean, and standard deviation of flip angle in the center slice is reported in the bottom table.

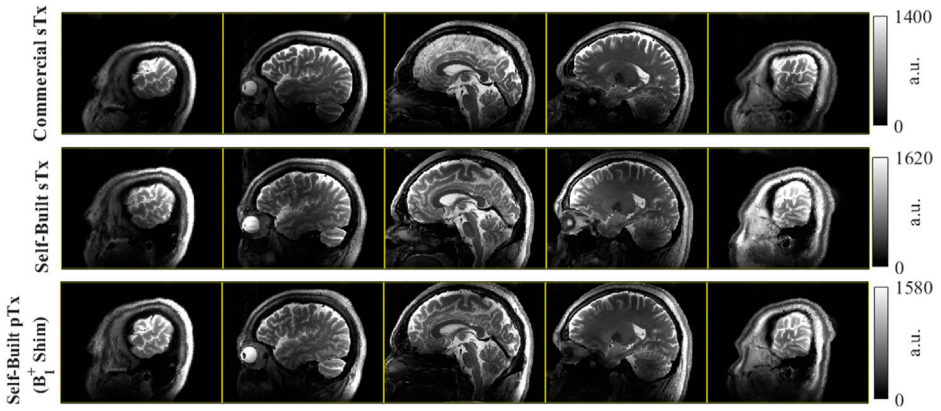

FIGURE 12 | Comparison of dual-mode head coil coverage to commercial single-transmit coil with a sagittal T2w 2D RARE acquisition in the same volunteer. Top row) Acquisition using the commercial coil at several slice locations; Middle row). The same acquisition using the dual-mode coil in single-transmit operation; Bottom row) The repeated acquisition with the dual-mode coil in parallel-transmit mode, here with complex B_1^+ shimming applied. Comparing the commercial Nova coil to the self-built dual-mode coil, there is improved coverage in the inferior regions of the brain. In this example, there are some modest improvements going from sTx to pTx in the dual-mode coil with B_1^+ shimming, particularly in the most distal slices (columns 1 and 5).

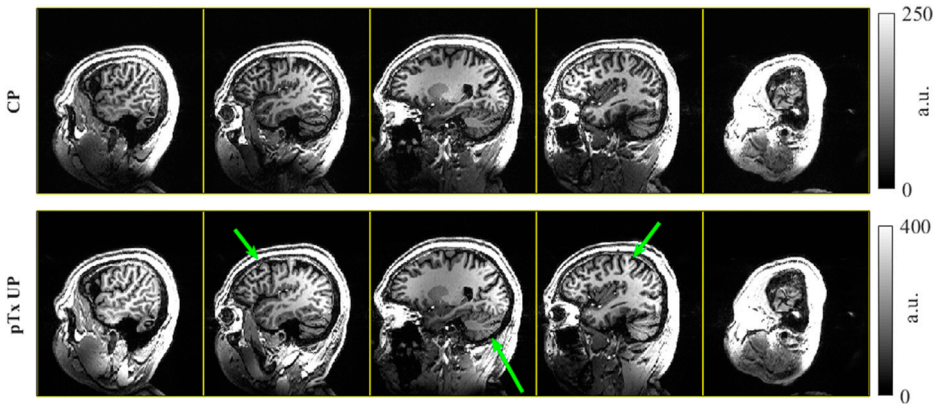

FIGURE 13 | T1w MPRAGE images collected in a healthy volunteer with the self-built coil in pTx mode. The top row shows the images acquired in CP mode, equivalent to the sTx case. The bottom row shows the images using dynamic pTx with Universal Pulses for excitation. Both images used the same CP mode 350 V adiabatic inversion and are windowed to have the same contrast. The green arrows highlight a few regions where the UP excitation improves the B_1^+ homogeneity and resulting image uniformity.

which led to improved image signal in the inferior slices of the brain.

Figure 13 shows the T1w MPRAGE images from a healthy volunteer acquired in the self-built coil operating in pTx mode. The CP pulse images have darker and less homogeneous excitation than the pTx Universal Pulse images, confirming the successful mitigation of B_1^+ field inhomogeneity of dynamic pTx with the coil.

DISCUSSION AND CONCLUSION

A dual-mode 7T head coil prototype which could be interfaced to both the excitation modes of the scanner was developed. The single device supports imaging in sTx mode for clinical diagnosis and pTx mode for research and clinical validation. MRI at 7T is expected to be performed in this hybrid environment until regulatory approval for pTx is received and the pTx workflow is simplified for non-experts.

The large cut-outs also allow a 'look-out' mirror to be fixed outside the transmit array for the subjects to see the operator, helping to reduce anxiety and claustrophobia during clinical examinations and also providing patient monitoring. Although the simulations predicted a 10% loss in transmit efficiency due to the cut-outs in the RF shield, equivalent imaging performance can be obtained by increasing the transmit power. This efficiency loss does not immediately mean increased local SAR deposition [50], because this depends on the loss mechanisms such as the radiated, reflected and absorbed power. This suggests that our approach of fully modeling the EM field of the coil and rigorously testing the SAR management experimentally is the best way to understand local SAR and safely use pTx.

The accuracy of the EM coil model was important to validate with experimental B_1^+ mapping. For sTx operation, the simulated and experimental flip angle maps are in excellent agreement both qualitatively and quantitatively (**Figures 7A**,**B**). Comparisons of the complex, single channel maps (**Figure 7C—7F**) also are qualitatively correlated yet have small phase mismatches. Further experiments to bridge these gaps could include preparing and simulating a more geometrical phantom with known electrical properties that would enable more accurate and more homogeneous field maps and also including the 32-channel receive array in our coil model simulation.

The presented transmit coil is fundamentally a transmit array in which the internal wiring enables a hardware interface through a 1x8 power splitter to the sTx mode of the scanner. We have demonstrated whole brain coverage in sTx mode, which offers a far simpler workflow similar to clinical imaging at 1.5 T/3 T. In the current implementation, a 45° phase increment was set inside the power splitter to achieve CP excitation. However, the setup allows the implementation of a non-CP phase configuration in the splitter that offers a more homogeneous excitation.

For sTx and pTx modes of the coil, SAR monitoring for CP operation uses conventional safety factor or "k-factor" supervision. The EM simulations shown in **Figure 8A** represent the range of subjects and positions that are anticipated while scanning with our coil. Here, the peak local SAR for 1 W input power and CP excitation across all body model simulations is 0.42 W/kg. The safety factor is added by listing the 1 W input SAR value as 1 W/kg in the coil file that is read by the scanner. This safety factor supervision is always active with reference to CP mode, whether the coil is driven in sTx or pTx.

In general, the more body models and positions included in local SAR estimation, the better, yet often computational and storage resources become a limiting factor with these high-resolution simulations. The overestimation factors and safety margins included in the EM field-derived VOPs ensure that the local SAR is never underestimated, even for every time point in a time-varying pTx pulse (**Figure 9**). For the initial study presented in this work, the overall safety margin was a factor of 1.7. In an ongoing work, different body models, head positions and rotations are being studied. The VOP can be created by concatenating the different Q-matrices and a higher safety factor is anticipated to account for the subject variations. Future work will also include pathological cases for use of the coil in a clinical population and will examine the influence of subject motion on local SAR [51].

Dynamic pTx operation has demonstrated the improved B_1^+ homogeneity that the additional degrees of freedom a multi-transmit can provide in the sagittal T1w MPRAGE example using Universal Pulses (**Figure 13**). With the single row transmit array design, even greater homogenization can be obtained for axially-oriented 2D acquisitions and have found this to be true in some further initial B_1^+ shimming scans.

In conclusion, a novel eight-channel nested transmit array was developed and its performance in both sTx and pTx modes was demonstrated. This work further demonstrates that a device can be hardwired to both the scanner modes. The coil setup is enhanced by incorporating two large windows which helps claustrophobic subjects as well as opens opportunities for niche applications such as motion correction. This new coil offers uniform coverage of the whole brain and is well suited for 7T clinical neuroimaging. We believe that the dual-mode coil setup is a valuable tool for both clinical diagnosis as well as research and clinical validation in pTx.

DATA AVAILABILITY STATEMENT

The datasets presented in this article are not readily available because of their proprietary nature. Requests to access the datasets should be directed to the corresponding author, Shajan Gunamony.

ETHICS STATEMENT

The studies involving human participants were reviewed and approved by West of Scotland Research Ethics Committee and NHS Greater Glasgow & Clyde (NHS-GGC) Research and Development Department. The participants provided their written informed consent to participate in this study.

AUTHOR CONTRIBUTIONS

SW collected experimental MRI data, prepared the figures, and co-wrote the manuscript. PM generated simulated coil data and prepared figures. SAS collected experimental data, provided guidance on the safety validation of the coil, and helped write the manuscript. GP helped with coil construction. JH prepared the experimental sequences and generated the Universal Pulses. PL also helped prepare experimental sequences and the experimental data collection. AN critically revised the manuscript. JF also critically revised the manuscript and provided guidance on safety validation of the coil. DP helped write the manuscript and provided key guidance on MRI experiments. SG conceived the coil concept, constructed the coil, collected bench top coil measurements, and co-wrote the manuscript. All authors participated in manuscript review.

FUNDING

This work was supported by the core funding to the Imaging Centre of Excellence, Queen Elizabeth University Hospital by the University of Glasgow.

ACKNOWLEDGMENTS

The authors most gratefully acknowledge the contributions of Tracey Hopkins, Rosemary Woodward and Natasha Fullerton of NHS-GGC R&D in helping us with the scans and formulating the study. We also thank Yuehui Tao from Siemens Healthineers, United Kingdom and Rene Gumbrecht and Robin Heidemann

from Siemens Healthineers, Erlangen for their support during the coil validation in pTx. Finally, we would like to extend our gratitude to Christopher T. Rodgers and Belinda Ding from the Wolfson Brain Imaging Centre of the University of Cambridge for their assistance with phantom scanning in the commercial pTx coil.

REFERENCES

1. Springer E, Dymerska B, Cardoso PL, Robinson SD, Weisstanner C, Wiest R, et al. Comparison of Routine Brain Imaging at 3 T and 7 T. *Invest Radiol* (2016) 51(8):469–82. doi:10.1097/RLI.0000000000000256
2. *FDA Clears First 7T Magnetic Resonance Imaging Device*, Silver Spring, MD, USA: US Food & Drug Administration. 2017. Available from: https://www.fda.gov/news-events/press-announcements/fda-clears-first-7t-magnetic-resonance-imaging-device (Accessed April 11, 2021)
3. FDA Clears Most Powerful Clinical MRI. Medgadget. 2020. Available from: https://www.medgadget.com/2020/11/fda-clears-most-powerful-clinical-mri-scanner.html (Accessed May 14, 2020)
4. Zhu Y. Parallel Excitation With an Array of Transmit Coils. *Magn Reson Med* (2004) 51(4):775–84. doi:10.1002/mrm.20011
5. Van de Moortele P-F, Akgun C, Adriany G, Moeller S, Ritter J, Collins CM, et al. B1 Destructive Interferences and Spatial Phase Patterns at 7 T with a Head Transceiver Array Coil. *Magn Reson Med* (2005) 54(6):1503–18. doi:10.1002/mrm.20708
6. Avdievich NI. Transceiver-Phased Arrays for Human Brain Studies at 7 T. *Appl Magn Reson* (2011) 41(2-4):483–506. doi:10.1007/s00723-011-0280-y
7. Gilbert KM, Belliveau J-G, Curtis AT, Gati JS, Klassen LM, and Menon RS. A Conformal Transceive Array for 7 T Neuroimaging. *Magn Reson Med* (2012) 67(5):1487–96. doi:10.1002/mrm.23124
8. Gilbert KM, Curtis AT, Gati JS, Klassen LM, and Menon RS. A Radiofrequency Coil to Facilitate B 1+ Shimming and Parallel Imaging Acceleration in Three Dimensions at 7 T. *NMR Biomed* (2011) 24(7):815–23. doi:10.1002/nbm.1627
9. Shajan G, Kozlov M, Hoffmann J, Turner R, Scheffler K, and Pohmann R. A 16-Channel Dual-Row Transmit Array in Combination With a 31-Element Receive Array for Human Brain Imaging at 9.4 T. *Magn Reson Med* (2014) 71(2):870–9. doi:10.1002/mrm.24726
10. Sengupta S, Roebroeck A, Kemper VG, Poser BA, Zimmermann J, and Goebel RA Specialized Multi-Transmit Head Coil for High Resolution FMRI of the Human Visual Cortex at 7T. *PLOS ONE* (2016). 11(12):e0165418. doi:10.1371/journal.pone.0165418
11. Gunamony S, Hoffmann J, Adriany A, Uğurbil K, and Scheffler KA 7T Head Coil With 16-Channel Dual-Row Transmit and 32-Channel Receive Array for pTx Applications and High SNR. In: *International Society for Magnetic Resonance in Medicine*, Singapore: ISMRM (2016). p. 2132.
12. Gilbert KM, Gati JS, Kho E, Klassen LM, Zeman P, and Menon RS. An Parallel-Transmit, Parallel-Receive Coil for Routine Scanning on a 7T Head Only Scanner. In: *International Society for Magnetic Resonance in Medicine* (2015). p. 0623.
13. Adriany G, Van de Moortele P-F, Wiesinger F, Moeller S, Strupp JP, Andersen P, et al. Transmit and Receive Transmission Line Arrays for 7 Tesla Parallel Imaging. *Magn Reson Med* (2005) 53(2):434–45. doi:10.1002/mrm.20321
14. Shajan G, Hoffmann J, Budde J, Adriany G, Ugurbil K, and Pohmann R. Design and Evaluation of an RF Front-End for 9.4 T Human MRI. *Magn Reson Med* (2011) 66(2):594–602. doi:10.1002/mrm.22808
15. Orzada S, Kraff O, and Schfer LC. 8-Channel Transmit/Receive Head Coil for 7 T Human Imaging Using Intrinsically Decoupled Strip Line Elements with Meanders. In: *International Society for Magnetic Resonance in Medicine*, Honolulu, HI, USA: ISMRM (2009). p. 3010.
16. Raaijmakers AJE, Ipek O, Klomp DWJ, Possanzini C, Harvey PR, Lagendijk JJW, et al. Design of a Radiative Surface Coil Array Element at 7 T: The Single-Side Adapted Dipole Antenna. *Magn Reson Med* (2011) 66(5):1488–97. doi:10.1002/mrm.22886
17. Wiggins GC, Zhang B, Lattanzi R, Chen G, and Sodickson DK. The Electric Dipole Array: An Attempt to Match the Ideal Current Pattern for Central SNR at 7 Tesla. In: *International Society for Magnetic Resonance in Medicine* (2012). p. 0541.
18. Raaijmakers AJE, Italiaander M, Voogt IJ, Luijten PR, Hoogduin JM, Klomp DWJ, et al. The Fractionated Dipole Antenna: A New Antenna for Body Imaging at 7 T Esla. *Magn Reson Med* (2016) 75(3):1366–74. doi:10.1002/mrm.25596
19. Clément JD, Gruetter R, and Ipek Ö. A Human Cerebral and Cerebellar 8-Channel Transceive RF Dipole Coil Array at 7T. *Magn Reson Med* (2019) 81(2):1447–58. doi:10.1002/mrm.27476
20. Eryaman Y, Guerin B, Kosior R, Adalsteinsson E, and Wald LL. Combined Loop + Dipole Arrays for 7 T Brain Imgaing. In: *International Society for Magnetic Resonance in Medicine*, Salt Lake City, UT, USA: ISMRM (2013). p. 0393.
21. Wiggins CJ, Zhang B, Cloos MA, et al. Mixing Loops and Electric Dipole Antennas for Increased Sensitivity at 7 Tesla. In: *International Society for Magnetic Resonance in Medicine* (2013). p. 2737.
22. Ertürk MA, Raaijmakers AJE, Adriany G, Uğurbil K, and Metzger GJ. A 16-Channel Combined Loop-Dipole Transceiver Array for 7 T Esla Body MRI. *Magn Reson Med* (2017) 77(2):884–94. doi:10.1002/mrm.26153
23. Roemer PB, Edelstein WA, Hayes CE, Souza SP, and Mueller OM. The NMR Phased Array. *Magn Reson Med* (1990) 16(2):192–225. doi:10.1002/mrm.1910160203
24. Avdievich NI, Pan JW, and Hetherington HP. Resonant Inductive Decoupling (RID) for Transceiver Arrays to Compensate for Both Reactive and Resistive Components of the Mutual Impedance. *NMR Biomed* (2013) 26(11):1547–54. doi:10.1002/nbm.2989
25. Yan X, Gore JC, and Grissom WA. Self-Decoupled Radiofrequency Coils for Magnetic Resonance Imaging. *Nat Commun* (2018) 9(1). doi:10.1038/s41467-018-05585-8
26. Gilbert KM, Curtis AT, Gati JS, Martyn Klassen L, Villemaire LE, and Menon RS. Transmit/Receive Radiofrequency Coil with Individually Shielded Elements. *Magn Reson Med* (2010) 64(6):1640–51. doi:10.1002/mrm.22574
27. Pohmann R, Speck O, and Scheffler K. Signal-to-Noise Ratio and MR Tissue Parameters in Human Brain Imaging at 3, 7, and 9.4 Tesla Using Current Receive Coil Arrays. *Magn Reson Med* (2016) 75(2):801–9. doi:10.1002/mrm.25677
28. Uğurbil K, Auerbach E, and Moeller S. Brain Imaging With Improved Acceleration and SNR at 7 Tesla Obtained With 64-Channel Receive Array. *Magn Reson Med* (2019) 82:495–509. doi:10.1002/mrm.27695
29. Chen G, Zhang B, Cloos MA, Sodickson DK, and Wiggins GC. A Highly Decoupled Transmit-Receive Array Design with Triangular Elements at 7 T. *Magn Reson Med* (2018) 80(5):2267–74. doi:10.1002/mrm.27186
30. Eichfelder G, and Gebhardt M. Local Specific Absorption Rate Control for Parallel Transmission by Virtual Observation Points. *Magn Reson Med* (2011) 66(5):1468–76. doi:10.1002/mrm.22927
31. Kozlov M, Weiskopf N, Möller HE, and Shajan G. Reverse Engineering of a 7T 16-Channel Dual-Row Transmit Array Coil. In: *International Society for Magnetic Resonance in Medicine* (2018). p. 4412.
32. Vaughan JT, Vaughan JT, Garwood M, Yacoub E, Duong T, DelaBarre L, et al. Detunable Transverse Electromagnetic (TEM) Volume Coil for High-Field NMR. *Magn Reson Med* (2002) 47(5):990–1000. doi:10.1002/mrm.10141
33. Kazemivalipour E, Sadeghi-Tarakameh A, and Atalar E. Eigenmode Analysis of the Scattering Matrix for the Design of MRI Transmit Array Coils. *Magn Reson Med* (2021) 85:1727–41. doi:10.1002/mrm.28533
34. Lanz T, Müller M, Barnes H, Neubauer S, and Schneider JE. A High-Throughput Eight-Channel Probe Head for Murine MRI at 9.4 T. *Magn Reson Med* (2010) 64(1):80–7. doi:10.1002/mrm.22414
35. Grebennikov A. Power Combiners, Impedance Transformers and Directional Couplers: Part II. *High Freq Electron* (2008) 42–53.
36. Beck BL, Jenkins KA, Rocca JR, and Fitzsimmons JR. Tissue-Equivalent Phantoms for High Frequencies. *Concepts Magn Reson* (2004) 20B(1):30–3. doi:10.1002/cmr.b.20002
37. Hoffmann J, Shajan G, Scheffler K, and Pohmann R. Numerical and Experimental Evaluation of RF Shimming in the Human Brain at 9.4 T Using a Dual-Row Transmit Array. *Magn Reson Mater Phy* (2014) 27(5):373–86. doi:10.1007/s10334-013-0419-y

38. Kozlov M, and Turner R. Fast MRI Coil Analysis Based on 3-D Electromagnetic and RF Circuit Co-Simulation. *J Magn Reson* (2009) 200(1):147–52. doi:10.1016/j.jmr.2009.06.005
39. Christ A, Kainz W, Hahn EG, Honegger K, Zefferer M, Neufeld E, et al. The Virtual Family-Development of Surface-Based Anatomical Models of Two Adults and Two Children for Dosimetric Simulations. *Phys Med Biol* (2010) 55(2):N23–N38. doi:10.1088/0031-9155/55/2/N01
40. Hoffmann J, Henning A, Giapitzakis IA, Scheffler K, Shajan G, Pohmann R, et al. Safety Testing and Operational Procedures for Self-Developed Radiofrequency Coils. *NMR Biomed* (2016) 29(9):1131–44. doi:10.1002/nbm.3290
41. Graesslin I, Homann H, Biederer S, Börnert P, Nehrke K, and Vernickel PA Specific Absorption Rate Prediction Concept for Parallel Transmission MR*Magn Reson Med* (2012). 68(5):1664–74. doi:10.1002/mrm.24138
42. Williams SN, McElhinney P, Porter DA, and Gunamony S. Comparing the Practical Effects of VOP Compressions for SAR Monitoring at 7 Tesla. In: *Minnesota Workshop on High and Ultra-high Field Imaging and Training Courses* (2019).
43. Chung S, Kim D, Breton E, and Axel L. Rapid B 1 + Mapping Using a Preconditioning RF Pulse With TurboFLASH Readout. *Magn Reson Med* (2010) 64:439–46. doi:10.1002/mrm.22423
44. Pauly J, Le Roux P, Nishimura D, and Macovski A. Parameter Relations for the Shinnar-Le Roux Selective Excitation Pulse Design Algorithm (NMR Imaging). *IEEE Trans Med Imaging* (1991) 10(1):53–65. doi:10.1109/42.75611
45. Gras V, Vignaud A, Amadon A, Bihan D, and Boulant N. Universal Pulses: A New Concept for Calibration-Free Parallel Transmission. *Magn Reson Med* (2017) 77(2):635–43. doi:10.1002/mrm.26148
46. Malik SJ, Keihaninejad S, Hammers A, and Hajnal JV. Tailored Excitation in 3D with Spiral Nonselective (SPINS) RF Pulses. *Magn Reson Med* (2012) 67(5): 1303–15. doi:10.1002/mrm.23118
47. Herrler J, Liebig P, Gumbrecht R, Ritter D, Schmitter S, Maier A, et al. Fast Online-Customized (FOCUS) Parallel Transmission Pulses: A Combination of Universal Pulses and Individual Optimization. *Magn Reson Med* (2021) 85: 3140–53. doi:10.1002/mrm.28643
48. Shajan G, McElhinney P, Allwood-Spiers S, Paterson G, and Goense J. An 8-Channel Transmit 32-Channel Receive 7T Head Coil for 1Tx and pTx Scanner Modes. In: *International Society for Magnetic Resonance in Medicine* (2019). p. 0572.
49. Williams SN, Allwood-Spiers S, McElhinney P, Tao Y, Foster JE, Gunamony S, et al. Validation and Safety Approval of a Dual-Mode Head Coil for pTx Applications *In Vivo* at 7 Tesla. In: *International Society for Magnetic Resonance in Medicine* (2020). p. 4038.
50. Avdievich NI, Hoffmann J, Shajan G, Pfrommer A, Giapitzakis IA, Scheffler K, et al. Evaluation of Transmit Efficiency and SAR for a Tight Fit Transceiver Human Head Phased Array at 9.4 T. *NMR Biomed* (2017) 30(2):e3680. doi:10.1002/nbm.3680
51. Kopanoglu E, Deniz CM, Erturk MA, and Wise RG. Specific Absorption Rate Implications of Within-scan Patient Head Motion for Ultra-high Field MRI. *Magn Reson Med* (2020) 84:2724–38. doi:10.1002/mrm.28276

Conflict of Interest: The coil design is the subject of a US patent application US16857649A. PL is employed by Siemens Healthineers and SG is a shareholder in MR CoilTech Limited. These companies have commercial interest in MRI and RF coils.

The remaining authors declare that the research was conducted in the absence of any commercial or financial relationships that could be construed as a potential conflict of interest.

Publisher's Note: All claims expressed in this article are solely those of the authors and do not necessarily represent those of their affiliated organizations, or those of the publisher, the editors and the reviewers. Any product that may be evaluated in this article, or claim that may be made by its manufacturer, is not guaranteed or endorsed by the publisher.

frontiers in Physics

ORIGINAL RESEARCH
published: 28 July 2021
doi: 10.3389/fphy.2021.704566

B_0-Shimming Methodology for Affordable and Compact Low-Field Magnetic Resonance Imaging Magnets

*Konstantin Wenzel[1], Hazem Alhamwey[1], Tom O'Reilly[2], Layla Tabea Riemann[1], Berk Silemek[1] and Lukas Winter[1]**

[1]Physikalisch-Technische Bundesanstalt (PTB), Berlin and Braunschweig, Germany, [2]C.J. Gorter Center for High Field MRI, Department of Radiology, Leiden University Medical Center, Leiden, Netherlands

Low-field (B_0 < 0.2 T) magnetic resonance imaging (MRI) is emerging as a low cost, point-of-care alternative to provide access to diagnostic imaging technology even in resource scarce environments. MRI magnets can be constructed based on permanent neodymium-iron-boron (NdFeB) magnets in discretized arrangements, leading to substantially lower mass and costs. A challenge with these designs is, however, a good B_0 field homogeneity, which is needed to produce high quality images free of distortions. In this work, we describe an iterative approach to build a low-field MR magnet based on a B_0-shimming methodology using genetic algorithms. The methodology is tested by constructing a small bore (inner bore diameter = 130 mm) desktop MR magnet (<15 kg) at a field strength of B_0 = 0.1 T and a target volume of 4 cm in diameter. The configuration consists of a base magnet and shim inserts, which can be placed iteratively without modifying the base magnet assembly and without changing the inner dimensions of the bore or the outer dimensions of the MR magnet. Applying the shims, B_0 field inhomogeneity could be reduced by a factor 8 from 5,448 to 682 ppm in the target central slice of the magnet. Further improvements of these results can be achieved in a second or third iteration, using more sensitive magnetic field probes (e.g., nuclear magnetic resonance based magnetic field measurements). The presented methodology is scalable to bigger magnet designs. The MR magnet can be reproduced with off-the-shelf components and a 3D printer and no special tools are needed for construction. All design files and code to reproduce the results will be made available as open source hardware.

Keywords: magnetic resonance imaging, B_0 shimming, low field MRI, Halbach arrays, MR magnet, open source hardware

OPEN ACCESS

Edited by:
Lionel Marc Broche, University of Aberdeen, United Kingdom

Reviewed by:
Esteban Anoardo, Universidad Nacional de Córdoba, Argentina
Duarte Mesquita Sousa, University of Lisbon, Portugal

****Correspondence:***
Lukas Winter
lukas.winter@ptb.de

Specialty section:
This article was submitted to Medical Physics and Imaging, a section of the journal Frontiers in Physics

Received: *03 May 2021*
Accepted: *09 July 2021*
Published: *28 July 2021*

Citation:
Wenzel K, Alhamwey H, O'Reilly T, Riemann LT, Silemek B and Winter L (2021) B_0-Shimming Methodology for Affordable and Compact Low-Field Magnetic Resonance Imaging Magnets. Front. Phys. 9:704566. doi: 10.3389/fphy.2021.704566

INTRODUCTION

In the last decades, magnetic resonance imaging (MRI) developed to one of the most useful medical imaging techniques allowing to depict the structure and function of tissue and organs in a quality, which is unmatched by other clinical imaging modalities. Despite this technological and clinical progress, machines and operation of these machines is still very expensive and restricted to a small portion of the global population of patients [1]. Current MRI magnets mostly rely on cryogenically cooled superconductors to reach high magnetic fields of typically B_0 = 1.5–3.0 T. These high fields

drive the complexity and are mainly responsible for the high costs of an MRI [2]. Recently, several efforts emerged investigating the benefits of low field MRI (B_0 < 0.2 T) to provide a low cost, point-of-care alternative [2–7]. The MR magnet design benefits from reduced complexity and costs at lower fields. While in the past most low field MR magnets were based on permanently magnetized iron with a ferromagnetic yoke, more recently permanent magnet designs are based on a Halbach or Halbach type layout, where multiple small magnets are arranged in a specific way [8–12]. These designs have the advantage that less magnetic mass is utilized, making the magnets smaller, more mobile, and less costly. A challenge with these designs is, however, to achieve a good B_0 field homogeneity, which for commercial high field systems is typically below <10 ppm. One way to relax these requirements is to build in fixed gradients into the magnet design which are used for spatial encoding [7, 10–13]. Even for classical imaging applications using switched gradient coils along three dimensions, Halbach based low-field magnet designs were recently able to produce *in-vivo* imaging of the extremities, the brain [14] and implants [15], which benefits from lower specific absorption rate (SAR) and lower susceptibility artefacts compared to higher field systems. These encouraging results were acquired with a Halbach based permanent magnet that has an inhomogeneity of 2,400 ppm in the target field of view, demonstrating that the requirements on B_0 field homogeneity at low fields are less strict. Spin echo based imaging can be used to generate most contrasts and T_2* based contrasts utilizing gradient echo imaging techniques that require higher field homogeneities, are much lower at lower fields. Nevertheless, the B_0 homogeneity over the target volume needs to be within the bandwidth of the RF excitation and a strong B_0 inhomogeneity might lead to image distortions.

Even though MR magnets can be designed very homogeneously in numerical simulations [9], translating these results into the practice is very challenging especially in a low-cost setting. The strengths of the magnetic field from neodymium-iron-boron (NdFeB) magnets may vary up to 5% due to material imperfections and the angular variation of the magnetization vector up to 0.9° [16]. The remanence of the magnetic material is sensitive to temperature changes and the positioning and orientation of the many magnets will deviate slightly from the simulated setting e.g., due to forces that are present between the magnets [17].

B_0 shimming work for low-field permanent magnets is so far mostly limited to simulation studies [18], two pole or C-shaped magnets [18, 19] and/or for small shimming volumes focusing on the application of nuclear magnetic resonance (NMR) spectroscopy [20]. Recently low-field MR magnets are being constructed based on genetic algorithms using a dipole approximation to determine the position, orientation and material of the discrete magnets to reach a target field profile [9, 11, 12].

In this work an iterative approach in the design of a low-field MR magnet using Halbach arrays is investigated with the goal to improve B_0 homogeneity. The methodology is tested on a small bore (inner bore diameter = 130 mm) MR magnet with a B_0 field strength of 0.1 T and a target field of view of ~4 cm in diameter. The strategy is two-fold relying on a compact base magnet design, which consequently is shimmed using a genetic algorithm and shim inserts. The MR magnet can be reproduced with off-the-shelf components and a 3D printer and used e.g., for educational purposes in existing setups [21]. The evaluated shimming techniques improve B_0 homogeneity up to a factor of 8 in the first iteration and the applied methodology is scalable to bigger magnet designs. Design files and code from this work will be made available as open source hardware on opensourceimaging.org.

MATERIALS AND METHODS

The presented strategy to construct a homogeneous MR magnet consist of two parts:

1) The construction of a base magnetic field with the envisioned B_0 field strengths and inner bore diameter (**Figure 1**).
2) Shimming of the base magnet using a genetic algorithm to calculate the sizes, locations, and orientations of the shimming magnets, which are inserted in the base magnet design (**Figure 2**). A requirement of this shimming approach is that the inner or outer dimensions of the base magnet are not modified.

The proof of concept of this methodology is tested on a desktop MR magnet with a targeted inner bore diameter of 10 cm (including gradient coils). The size was chosen such that all components can be 3D printed with a standard sized 3D printer.

Simulation Environment and Mathematical Methods

For the base magnet, magnetostatic field simulations were conducted using COMSOL Multiphysics 5.4 (COMSOL AB, Stockholm, Sweden) utilizing the finite element method (FEM). The geometry of the magnets is assumed to be not chamfered. Inside the magnets, the remanent field is set to the appropriate strength, while outside it is assumed $\mu_r = \varepsilon_r = 1$.

For the B_0 shimming algorithm, the dipole approximation was used to calculate the magnetic field distribution of each shim magnet [22]:

$$\vec{B} = \frac{\mu_0}{4\pi}\left(\frac{3\vec{r}\left(\vec{m}\cdot\vec{r}\right)}{|\vec{r}|^5} - \frac{\vec{m}}{|\vec{r}|^3}\right) \tag{1}$$

with the permeability of vacuum μ_0 and the location r of the magnetic field with respect to the origin of the magnetic dipole moment (or shim magnet) m. For a shim magnet, the magnitude of the magnetic dipole moment m can be calculated by [23].

$$m = \frac{B_r V}{\mu_0} \tag{2}$$

with the remanence B_r and the magnet volume V. Only the z-component is considered, as the magnetic field to be shimmed is oriented along this axis.

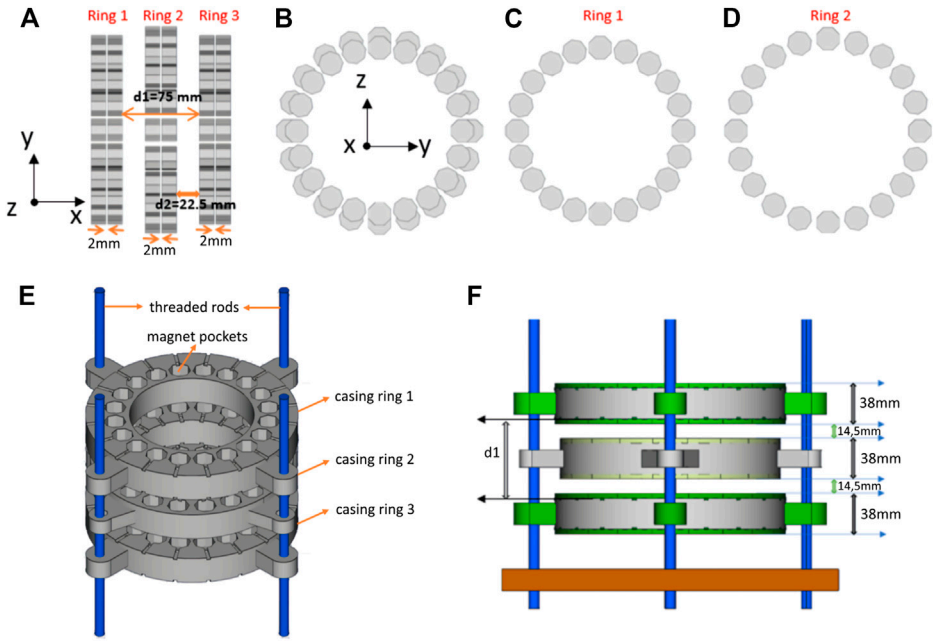

FIGURE 1 | Illustration of the base magnet before shimming. **(A)** Side and **(B)** Front view on the base magnet depicting the octagonal magnets of Ring 1–3. Front view on **(C)** Ring 1 (radius r_1 = 80.5 mm) and **(D)** Ring 2 (radius r_2 = 89.2 mm). **(E)** 3D renderings of the magnet casing showing the magnet pockets and threaded rods allowing to adjust the correct distance between the rings. **(F)** Side view of the 3D model of the base magnet including a base plate to mount the threaded rods and lids for each magnet pocket.

Using the weighted orthogonal basis set of real (orthonormalized) spherical harmonic functions Y_{lm} in spherical coordinates, the z-component of the magnetic field B_z on a sphere with radius r, polar θ and azimutal ϕ angles is described as

$$B_z(\theta, \phi) = \sum_{l=0}^{\infty} \sum_{m=-l}^{l} c_{lm} Y_{lm}(\theta, \phi) \tag{3}$$

The spherical harmonic coefficients c_{lm}, dependent on the degree l and order m, can be calculated with

$$c_{lm} = -\int_0^{2\pi} \int_{-1}^{1} B_z(\theta', \phi) Y_{lm}(\theta', \phi) d\theta' d\phi \tag{4}$$

Using this representation, coefficients of higher order and degree, can be truncated reducing the number of parameters used to represent the field and subsequently reducing the computational time of the shimming algorithm. Note that the spherical harmonic coefficients used here are not implicitly dependent on the radius contrary to standard literature, as the field is considered on a sphere with constant radius [22]. The coefficients are calculated using the module SHTOOLS [24].

Base Magnet Design

The base magnet is made from octagonal (circumradius = 11.64 mm, width = 14 mm) NdFeB magnets (N50, Ningbo Zhaobao Magnet, Ningbo Shi, China), which are arranged in three times two rings of 20 magnets each (total of 120 magnets) in a Halbach array design [16, 25] (**Figure 1**). Octagonal magnets were chosen over rectangular ones, because in terms of homogeneity they can better resemble an ideal Halbach array [16, 26, 27]. The base magnet was constructed of same sized magnets to facilitate reproducibility and the octagonal magnet size was limited to maintain reasonable forces enabling a relatively safe and easy construction by hand. Multiple dipolar Halbach magnet stacks or rings can improve field homogeneity by adjusting the distance between the rings [8]. While for two rings the distance can be determined analytically, for a higher number of stacked rings numerical calculations are required. A higher number of rings increases the overall magnet size, weight and costs substantially. Therefore, a three-ring setup is implemented in this work. Two stacks of octagonal magnets with 2 mm distance in x-direction are considered a single ring (**Figure 1**). The central ring (Ring 2) generates a field of around 50 mT in the center and shows a concave B_z profile along y-z direction (**Figure 3**). Adjusting the distance of Ring 1 and Ring 3 generates a convex magnetic field profile along the same direction (**Figure 3**). By adjusting the distance between ring 1 and ring 3, it is therefore possible to homogenize the field in the center of ring 2 to some extent (**Figure 3**). More importantly this step can be performed based on measurements (including all material imperfections or positioning errors) and does not require simulations to determine the distance. Overall a B_0 of 103 mT is reached in the center of the base magnet. For the base magnet the octagonal magnets were not individually measured and sorted beforehand so that all material imperfections influence B_0 homogeneity of the base magnet.

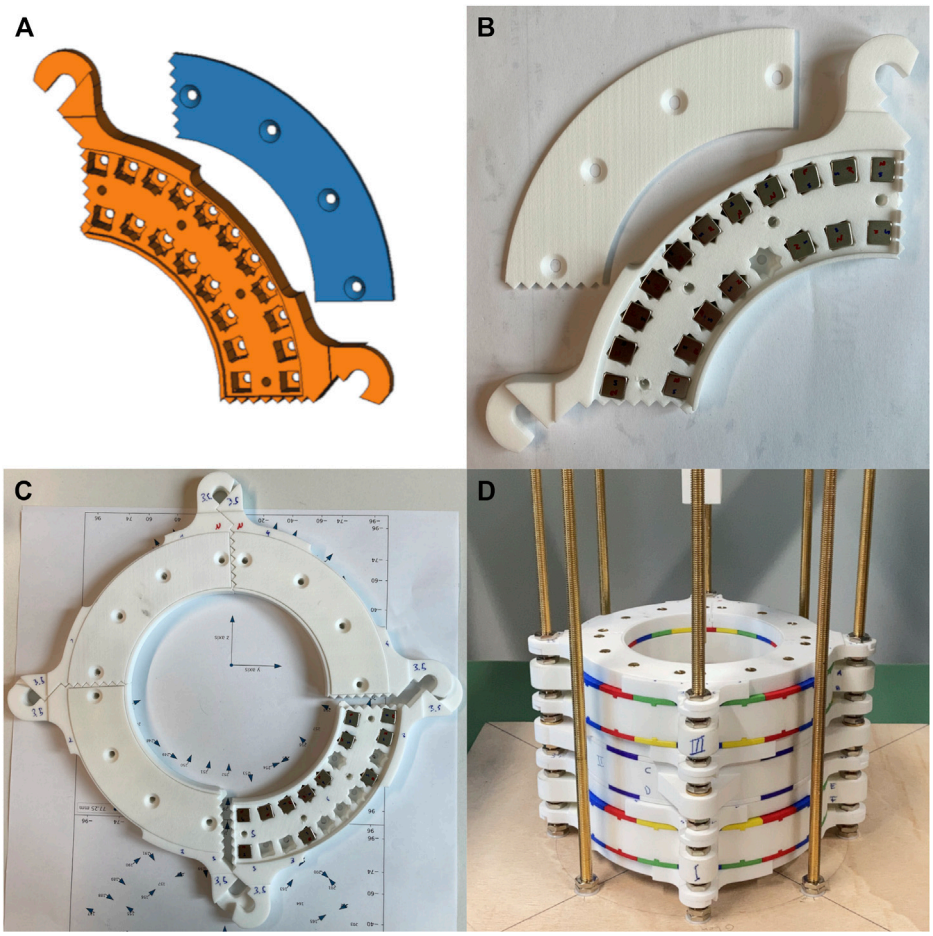

FIGURE 2 | Photographs and 3D renderings of the constructed and assembled shim pieces including the 9 mm cubic shim magnets. **(A)** CAD drawing of a single shim piece (orange) and cover (blue). Please note that the pockets are designed in a way that the shim magnets can be inserted in both radial (k = 1) and Halbach (k = 2) orientation. **(B)** 3D printed shim piece with inserted magnets and the cover removed. The poles of the magnets are marked with north (N) and south (S). **(C)** Illustration of a fully assembled shim ring constructed from four shim pieces. **(D)** Photograph of the fully assembled base magnet including all shim inserts.

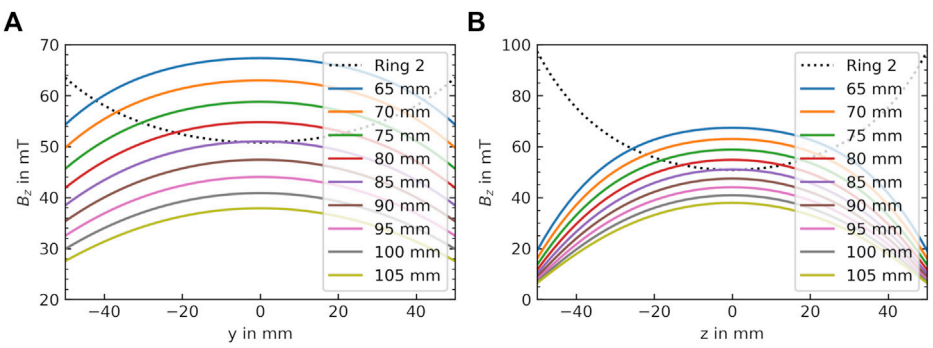

FIGURE 3 | Optimization procedure of the base magnet to determine the optimal distance between the rings. Simulations of the magnetic flux densities of Ring 1 and 3 based on the distance between the rings (d1 in **Panel 1F**) along **(A)** y-direction and **(B)** z-direction. The magnetic flux distribution from Ring 2 (central ring) is plotted as a black dotted line. The concave curvature generated by the Ring 1 and Ring 3 configuration can be compensated to some extent by the convex curvature of Ring 2 in order to homogenize B_z.

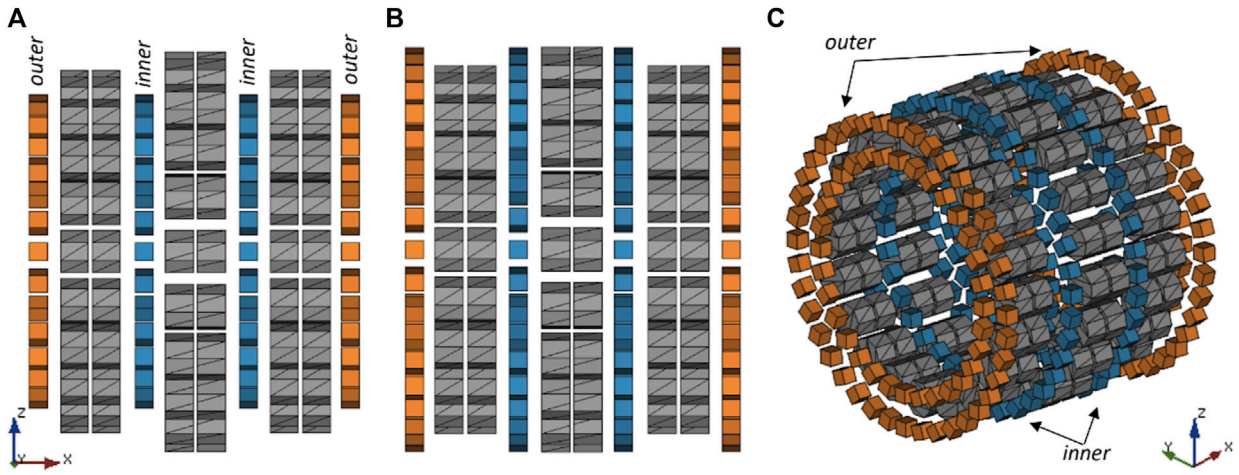

FIGURE 4 | Illustration of the shim ring positions with respect to the base magnet **(A)** Side view of the shim ring positions with respect to the base magnet rings 1–3 (grey). Smallest radius rings of the inner (blue) and outer (orange) shim rings (for 9 mm magnet size the radius is 73 mm), **(B)** Sideview of the shim ring positions of the larger radius (r = 95 mm) for the inner and outer shim rings. **(C)** 3D view of the fully assembled magnet and position of the stacked shim rings with respect to the base magnet.

Genetic Algorithm

For B_0-shimming, shim magnet placement was restricted in between and at the end of the base magnet rings (**Figure 4**), thus not reducing inner bore diameter or increasing the outer magnet dimensions. Furthermore, as the magnetic field decreases with the power of three **Eq. (1)**, placing shim magnets further away from the targeted field of view increases the magnetic mass of the shims and the overall magnet weight and costs.

After B_0 field measurements to determine the B_0 field distribution of the base magnet in the field of view, a genetic algorithm is used to determine the size, position, and orientation of the shim magnets [9, 28]. Over other algorithms typically used in shimming as linear programming or the least square method this allows for a more flexible mathematical formulation of the optimization problem [29].

In the algorithm, a population (i.e., a collection of possible arrangements of shimming magnets) is evolved to find the best individual (i.e., best arrangement to homogenize the field). Each individual has a genome composed of genes (e.g., location of a shim magnet) describing the state (e.g., the orientation of the shim magnet) of the individual. As an underlying symmetry, the magnets are placed in a ring around the bore in Halbach or radial orientation. In total for each magnet five states were considered, four rotational deviations by 0°, 90°, 180° and 270° from the Halbach or respectively radial arrangement and the fifth state indicated no magnet placement.

The algorithm starts by creating 25,000 random individuals and calculates their cost function, which is a measure of inhomogeneity created by a given individual. The best individuals of the population are selected *via* tournament selection, where three individuals are chosen by random and the best is selected as a surviving individual. This process is repeated until the new population reaches the initial population size including redundant individuals. In the next step, the two-point crossover is performed with a probability of 75%, which recombines two neighbouring individuals by interchanging one randomly chosen part of their genome. To further diversify the population, a 20% mutation chance was set. If an individual mutates, every gene of its genome is changed randomly with a 5% chance. All cost functions, which have been changed by previous procedures, are calculated and the algorithm starts again with the tournament selection. The chosen probabilities have been shown to work well within the class of problems [8, 10]. A minimum of 300 iterations is performed, the algorithm converges when the last 20% of iterations do not create new individuals with a lower cost function. For the implementation, Python 3.6 was used and the DEAP module [9].

For the target field approach, using predetermined values at given spatial positions [30], the cost function is set to the peak-to-peak B_0 difference in the investigated 2D or 3D area. Compared to inhomogeneity, this avoids calculating the mean, which is numerically costly. This is reasonable since the B_0 shim field does not change the mean field amplitude significantly.

In addition, a representation based on spherical harmonics was investigated and the results compared to the target field approach. For this spherical harmonics approach, the cost function is chosen as the sum of the absolute values of the spherical harmonic coefficients (except the 0^{th}) [31, 32]. As orthonormalized functions are used, every function contributes equally to the field inhomogeneities and no weights are applied.

2D/3D B_0-Shimming

Prior to shimming the base magnet, simulations were performed to evaluate different shim configurations. The field of the magnet is simulated using the FEM and the genetic algorithm is used to assess different shimming scenarios. The number of magnets in one ring is maximized for the given radius while considering a 2 mm distance between neighbouring magnets. A single shim ring consists of two stacked rings of magnets with $r_1 = 67\ mm + \frac{\sqrt{2}}{2} \cdot d_m$ (**Figure 4A**) and $r_2 = 95\ mm$

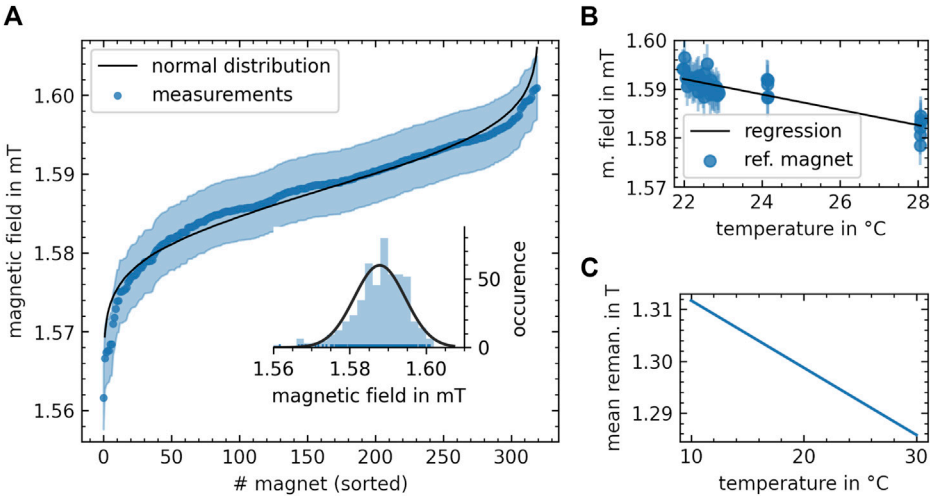

FIGURE 5 | Experimental characterization of individual shim magnets used for populating the shim inserts. **(A)** Magnetic field measurements for each individual magnet represented by a blue dot. The error is displayed with an opaque blue band. In the inset, a histogram of the distribution of the magnetic field amplitudes is displayed. Quantification of the effective remanence of the shim magnets. **(B)** Magnetic field measurements of the reference magnet at different temperatures with regression fit to determine the temperature coefficient of the magnet. **(C)** Resulting temperature dependence of the mean effective remanence of all magnets calculated based on the temperature coefficient of the reference magnet.

(**Figure 4B**), where d_m is the magnet size. Three configurations were assessed:

1. One shim ring is positioned in between Ring 1 and Ring 2 and another one in between Ring 2 and Ring 3 with an offset of 26.25 mm from the center of the magnet. These rings are referred to as *inner* shim rings (**Figure 4A**).
2. One shim ring is placed in front of Ring 1 and another one at the end of Ring 3. These rings are referred to as outer shim rings (**Figures 4A–C**). The distance of the outer shim rings to the center of the bore is ±78.75 mm.
3. A combination of *inner* and *outer* rings, which is referred to as *both*.

For all these combinations, the genetic algorithm was applied for cube-shaped shim magnets of 6, 8, 10, 12 and 14 mm edge length. Two targets to homogenize the field were investigated:

1) A 2D area of 4 cm in diameter in y-z plane at the center of the magnet (x = 0), which corresponds to a 2D slice used for imaging
2) A 3D spherical volume of 4 cm in diameter around the center of the magnet.

Each simulation took on average 2 h 35 min with a standard deviation of 43 min on an Intel Xeon Processors E5-2,690 v3 (12 cores, 24 threads in total).

For the finally applied shims, cube shaped $(9 \times 9 \times 9)$ mm^3 NdFeB magnets (N48, Otom Group GmbH, Bräunlingen, Germany) were purchased. Before installation, the magnetic field of these magnets was measured at a distance of 45.6 mm to reduce variability in between magnets. Each 10th measurement a reference magnet was used, and the temperature was monitored (**Figure 5**). Magnets with stronger variations in magnetic field were sorted out. Within the errors of the sensor, they are normally distributed with a mean of 1.587 mT and a standard deviation of 7 μT. This results in a mean effective remanence (assuming a perfect magnet volume of $(9 \times 9 \times 9)$ mm^3) of 1.296 T with standard deviation 6 mT at 20°C. This mean remanence was used for the B_0 shimming calculations.

Magnet Construction

The base magnet casing and the shim inserts were designed in FreeCAD (v018, http://www.freecadweb.org). Selective laser sintering (SLS), with a dimensional accuracy of ±0.3 mm, was used to fabricate the designs. These rings are positioned on four threaded brass rods, whereas the distance between the rings was adjusted using nuts (**Figure 2D**). Each shim ring consists of four interlockable pieces (**Figures 2A–C**), which can be inserted radially into the base magnet without modifying its assembly (**Figure 2D**). These shim inserts contain pockets that allow the placement of $(9 \times 9 \times 9)$ mm³ magnets to be positioned at various angles in radial or Halbach orientation. A maximum of 76 shim magnets can be placed in a single shim ring, leading to an overall maximum of 304 shim magnets that can be inserted into the shims.

Measurement Setup

For magnetic field measurements of B_z, a Hallprobe (Gaussmeter Model 460, LakeShore Cryotronics, Westerville, OH, United States) was used. The Hallprobe was mounted to COSI Measure [33], an open source 3-axis positioning system with submillimeter precision, to autonomously map the magnetic field of the magnet before and after shimming. Since the magnets are temperature dependent, room temperature was measured inside a water bottle using a temperature probe (P550, Dostmann

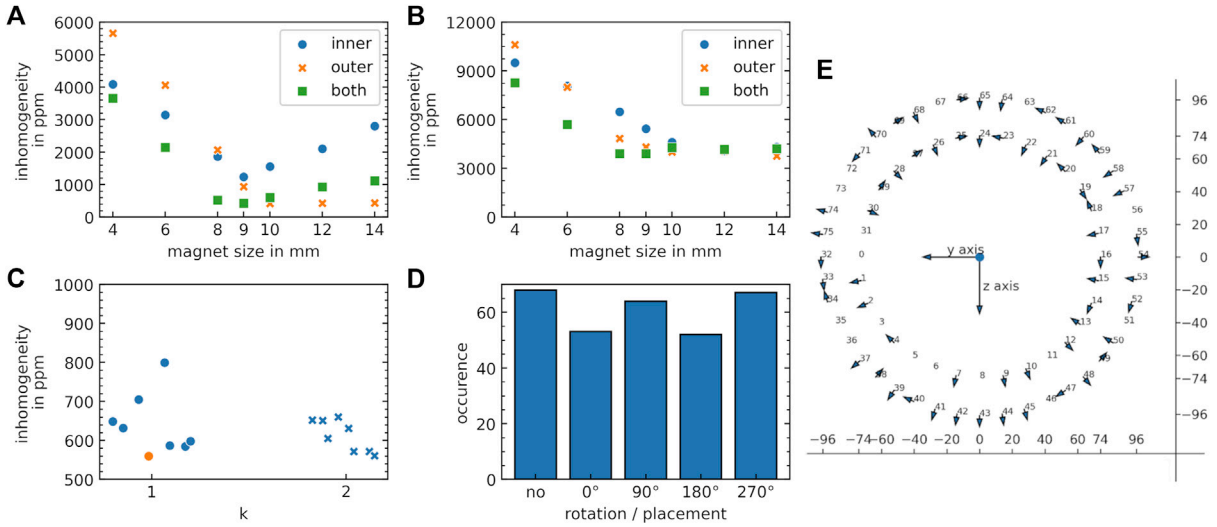

FIGURE 6 | Results calculated by the shimming algorithms. **(A)** Homogeneities achieved for different shim magnet sizes based on the simulated magnetic field distribution (FEM) for configurations inner (blue circles), outer (orange crosses), both (green boxes) for **(A)** the 2D target slice of 4 cm in diameter and **(B)** the 3D sphere of 4 cm in diameter. **(C)** Calculated B_0 homogeneities for a radial (k = 1) and Halbach (k = 2) base symmetry of the shim. The best calculation is indicated in orange. **(D)** Occurrence of the rotational orientation and placement for the best design identified in C. **(E)** Example configuration of shim magnet placement in one shim ring. The arrows indicate the orientations of the magnetic moments at the respective positions of the shim magnets.

electronic GmbH, Wertheim-Reicholzheim, Germany). The 2D magnetic field measurements were performed at 1 mm spatial resolution in all dimensions inside an area/region of 5 cm diameter around the center of the bore. A snail shell like pattern was sampled (starting at the inside and moving towards the outside) with an overall measurement time of about 80 min. The 3D sphere was sampled on 40 evenly spaced points along the azimuthal plane and 40 points along the altitude angle obeying the quadrature points. This measurement took 70 min to sample 1600 points.

RESULTS

Base Magnet

The distance d_1 between Ring 1 and Ring 3 was adjusted in measurements to 75 mm, which was the distance found giving the best compromise between compact magnet size and B_0 field homogeneity. The measured unshimmed magnetic field of the base magnet in the center of the field of view is B_0 = 102.8 (3) mT, with an inhomogeneity of 5,448 ppm in the 2D and 8,271 ppm in the 3D target region, both of 4 cm diameter.

B_0-Shimming

The results based on the simulations of the base magnet to evaluate the shim magnet size and configuration are displayed in **Figure 6**. For the 2D target the lowest B_0 inhomogeneity was 418 ppm using 10 mm magnets for the outer shim rings (**Figure 6A**). Using only the inner rings for shimming, the minimum was found for 9 mm cube magnets with an overall inhomogeneity of 1,240 ppm. A combination of inner and outer same sized magnets showed a minimum of 429 ppm using 9 mm cube shaped magnets. Like the 2D shimming results, 10 mm magnets showed the best homogeneity for the outer ring magnets with 4,015 ppm and a 3D target volume (**Figure 6B**). The magnet size for the inner ring magnets was best for 12 mm sized magnets with 4,091 ppm. Using the configuration "both" for same sized magnets, B_0 homogeneity could be improved slightly to 3,913 ppm for 9 mm magnets.

2D B_0-Shimming of the Base Magnet

Based on the simulation results, 9 mm cube shaped magnets were used to determine the shims for the base magnet. The results of the genetic algorithm for multiple runs and different magnet orientations [k = 1 (radial), k = 2 (Halbach)] are depicted in **Figure 6C**. Both show similar performance. Due to an easier construction process, a radial orientation was used for the final shim. The overall number of magnets at a certain rotational angle is displayed in **Figure 6D** and shows a balanced distribution between the different states. Overall, 236 of possible 304 magnets were placed in the shim rings and all rotational possibilities were used in the final set of shim magnets. The final shim magnet arrangement (exemplified on a single shim ring) is shown in **Figure 6E**. Implementing this shim, the simulations predicted a reduction in inhomogeneity by a factor 8 from 5,448 ppm (**Figure 7A**) to 560 ppm (**Figure 7B**). The measured field inhomogeneity was 682 ppm (**Figure 7C**). The calculated and measured field inhomogeneities over the target area are depicted in **Figure 7D**. A slight shift in the measured mean field was observed, which was 0.35 mT higher in the absolute B_0 values for the calculated shim configuration (**Figure 7E**).

Spherical Harmonics

All spherical harmonics coefficients up to the 17th degree and ±17th order of the measured B_0 field of the desktop magnet are

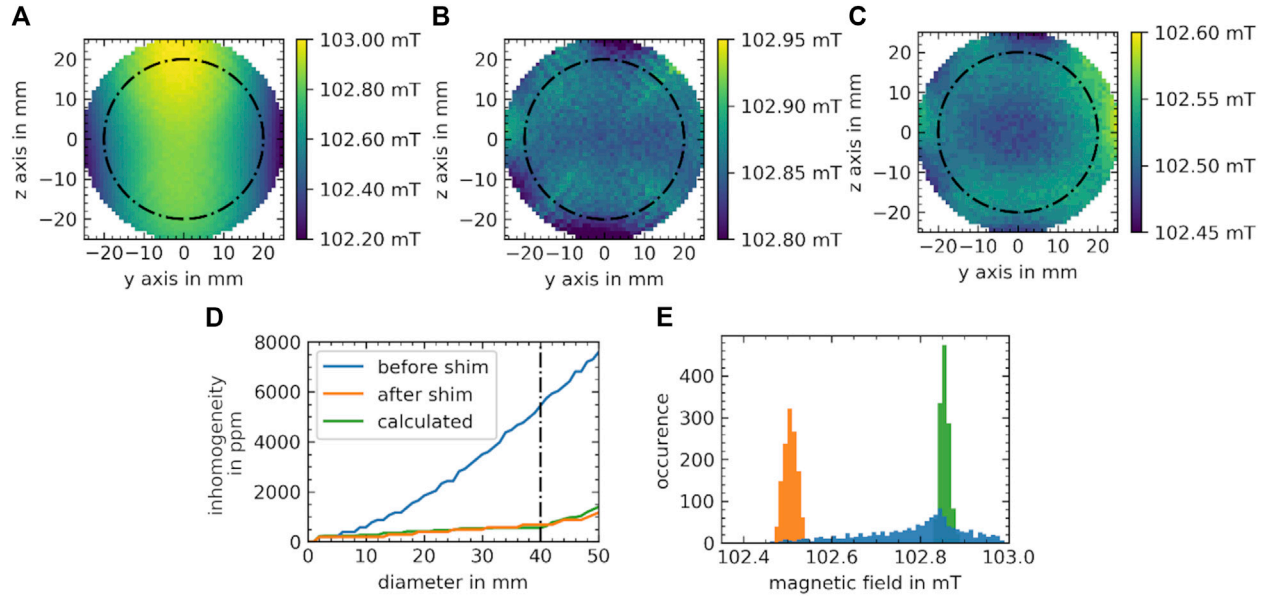

FIGURE 7 | Measured magnetic field distributions before and after shimming on a two-dimensional target slice. **(A)** Measured field distribution of the desktop MR magnet before shimming. **(B)** Predicted distribution calculated by the genetic algorithm with the dipole approximation. **(C)** Measurement after the implementation of the shim. The black dash-dotted line indicates the 4 cm target region. **(D)** Field inhomogeneities over diameter of the slice measured before (blue) and after the shim (orange), together with the prediction of the shim, as calculated by the algorithm (green). **(E)** Occurrence of field values measured before (blue) and after shimming (orange) and calculated (green) by the algorithm in the 4 cm target area (dash-dotted line in D) using the same colour representation as in D.

shown in **Figure 8A**. To determine how many coefficients are necessary to properly reconstruct the field, the pointwise difference for a truncation at a certain degree (and order in the inset) is depicted in **Figure 8B**. Above degree four and order two no improvement (deviation <100 μT) of the reconstruction from the measured field can be observed. The difference between the measured (**Figure 8C**) and the reconstructed field based on the truncated ($l \leq 4$, $m \leq 4$) spherical harmonics (**Figure 8D**) is depicted in **Figure 8E**. Overall a mean difference of 0.2 ± 17 μT was found with a maximum peak-to-peak difference of 145 μT in the overall volume. Consequently, the truncated spherical harmonics representation can be used to calculate a B_0 shim for the 3D volume, which reduced computational time substantially in particular for a larger number of shimming magnets.

3D B_0-Shimming

The calculated and measured 3D shim results are displayed in **Figure 9**. Before shimming, the 3D target sphere showed an inhomogeneity of 8,271 ppm. The calculated magnetic field distribution after shimming using the 9 mm magnets showed a inhomogeneity of 2,596 ppm (**Figure 9A**) over the target volume while the measured values were at 3,759 ppm (**Figure 9B**). The difference is displayed in **Figure 9C**. For the 3D approach, the improvement in homogeneity is less pronounced compared to the 2D target by only a factor of 2.2 (**Table 1**). Illustrating the shimming results based on spherical harmonic degree showed that all spherical harmonic coefficients except the coefficients of degree four can be shimmed efficiently (**Figure 9D**). Three coefficients are mainly contributing to the inhomogeneities. These are (l, m) = (2, −2), (l, m) = (4, 0) and (l) = (4, 2) as illustrated in **Figure 9E**. To further understand how the truncation of the field distribution is influencing the outcome of the shim, the field of the shim magnets is calculated with the dipole approximation and added to the truncated measured field before shimming. Compared to the calculation of the shim field with the truncated coefficients, the inhomogeneity reduces by 31 ppm. Consequently, the truncation of the dipole field of the shims is a good approximation and does not induce a large error. The results of the inhomogeneity per diameter of the sphere is displayed in **Figure 9F**. After a diameter of around 30 mm, B_0 inhomogeneity rapidly decreases.

DISCUSSION

In this work, B_0 shimming based methodology is investigated to construct a homogeneous, low-cost and low-field (B_0 = 0.1 T) MR magnet using permanent magnets in an Halbach array configuration. The desktop magnet can be easily constructed using 3D printers, readily available NdFeB magnets and simple tools. It is relatively lightweight (~15 kg) and has an overall material cost of ~700 €, which is mostly due to the cost of the magnetic material used. It is therefore suitable to be used for educational applications in tabletop systems [21, 34] or small volume imaging applications.

Previous work demonstrated that a homogeneity of 2,400 ppm over the target field of view is sufficient to achieve good image quality at 50 mT using turbo spin echo sequences with reasonable acquisition times [9, 14, 15]. To reach these homogeneities for

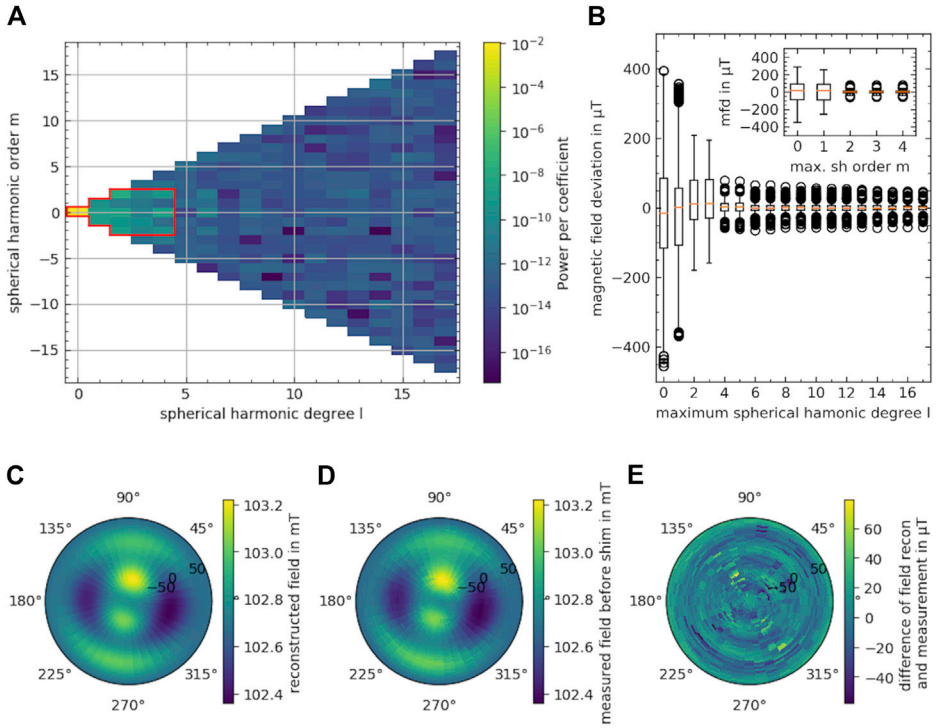

FIGURE 8 | Evaluation of the measured magnetic field distribution on the 4 cm 3D sphere of the base magnet. **(A)** Power per spherical harmonic coefficient of the measurement. In red the truncated spherical harmonic coefficients are enclosed. **(B)** Boxplot of the point wise difference between the measured data and the reconstruction truncated at a maximum spherical harmonic degree. In the inset, the point wise difference for a maximum spherical harmonic order is displayed for the truncated spherical harmonics at degree four. The box extends from the lower to the upper quartile, the orange line represents the median and the whiskers extend according to Tukey's boxplot. Outliers are indicated as circles. **(C)** Reconstruction of the measured field of the unshimmed desktop magnet with the truncated coefficients displayed in the red box in A. The field is displayed in polar projection, with the center of the depiction being at the greatest x coordinate. **(D)** Measured field without reconstruction. **(E)** Residuum of reconstruction and measurement.

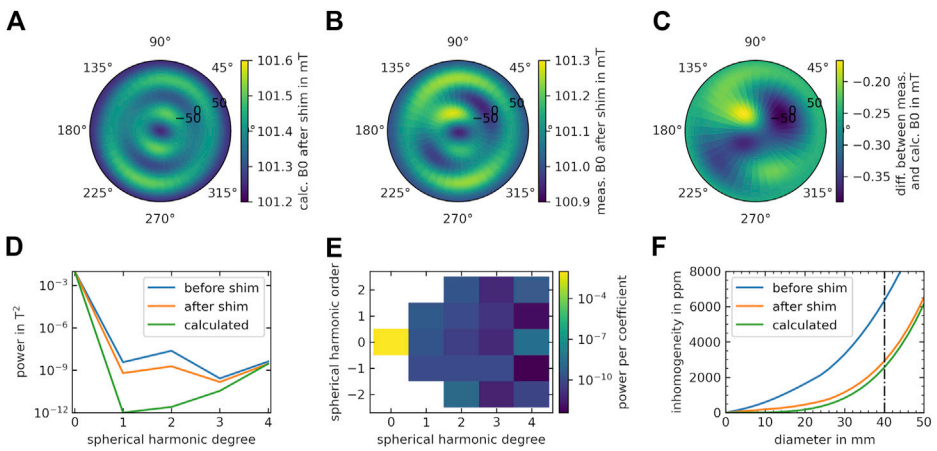

FIGURE 9 | Measured field distribution after shimming for a 3D target sphere. The magnetic field distribution is depicted in polar projection of the field. **(A)** Calculated field distribution after the shim determined by the genetic algorithm with the dipole approximation. **(B)** Measured field distribution after the shim. **(C)** Difference between the measured and predicted data. **(D)** Power per spherical harmonic degree present in the unshimmed desktop magnet (blue) and determined after the shim by measurement (orange) and by calculation with the genetic algorithm (green). **(E)** Power per spherical harmonic coefficient for the measured field after shimming. **(F)** Field inhomogeneity in the target region of the desktop MR magnet. The data is reconstructed from field data measured on a 4 cm sphere using truncated spherical harmonics and plotted along the diameter of the three-dimensional sphere for the unshimmed (blue), shimmed (orange) magnet and predicted by the algorithm (green). The dash-dotted line indicates the diameter of the measured target region.

TABLE 1 | Summary of 2D and 3D shimming results using the target field or spherical harmonics approach and the genetic algorithm.

Target	Approach	Before shim	After shim (calculated)	After shim (measured)	Improvement
2D slice	Target field	5,448 ppm	560 ppm	682 ppm	8.0
3D sphere	Target field	8,271 ppm	2,596 ppm	3,932 ppm	2.1
3D sphere	Spherical harmonics	8,271 ppm	2,515 ppm	3,759 ppm	2.2

the desktop magnet, an iterative approach is suggested to build a base magnet that mainly determines the targeted B_0 field and in a second step to iteratively position shim inserts to improve the field homogeneity. With this approach, the initial B_0-field inhomogeneity of the base magnet of 5,448 ppm in the 2D area could be reduced by a factor ~8–682 ppm in the first shimming iteration. The results are encouraging and suggest that even higher B_0 shimming homogeneities can be reached using an iterative approach. Simulation results of varying the shim magnet sizes show that the outer rings alone already improve B_0 field homogeneity substantially (**Figure 6A**). Consequently, a first shimming stage would e.g., implement the outer shim rings first and apply the genetic algorithm to determine the magnet size for the second shimming stage. Due to the more homogeneous base field, the magnets from the second stage will be much smaller (e.g., half the size) allowing space for the potential placement of another two shim rings in a third shimming stage close to the magnet center. This iterative shimming approach was not tested in this work due to limitations in the available Hall sensor sensitivity (~500 ppm), which is clearly visible in the presented data (**Figures 7B,C**). For further investigations and to improve the results, a Hall sensor with higher sensitivity is needed or an NMR based magnetic field measurement where accuracies typically are in the order of 10 ppm or less.

For the 3D shimming results the target sphere could be shimmed from initially 8,271 to 3,759 ppm. This corresponds to an improvement by a factor of 2.2. Even though such improvement is comparable to other works on passive B_0 shimming after a single iteration [35], it is relatively low compared to the 2D shim results. Calculations based on the measured spherical harmonic coefficients (**Figure 9F**) demonstrated that B_0 field inhomogeneity decreases rapidly after around 30 mm diameter from the center of Ring 2. Further calculations (**Figure 9D**) showed that the main contributor to these inhomogeneities are the spherical harmonic coefficients of fourth degree, which could not be shimmed efficiently using the investigated setup. This indicates a drawback in the presented magnet design of the base magnet, which is adjusted to perform 2D imaging of a central slice. To improve the homogeneity along the x-axis, more rings are needed in order to approach the homogeneity of a perfect Halbach cylinder [26, 36]. Adding these rings however would furthermore increase the size, weight and cost of the magnet substantially and would require numerical optimization [36].

One advantage of the presented approach is that the shims can be inserted after the base magnet assembly, without compromising the inner or outer dimensions of the magnet. Placing movable magnet blocks inside the magnet [37], could further improve B_0 field homogeneity while compromising inner bore diameter. Placing shims outside of the magnet may require bigger shimming magnets and more magnetic mass. Another advantage of the three-ring setup for the base magnet is that, in principle, it can be constructed without any magnetostatic field simulations using FEM, where dedicated software is required. The distance adjustment between Ring 1 and Ring 3 can be performed based on the measurements alone. At this stage the optimization for homogeneity is less important due to the possibility of adding the shim inserts afterwards and homogenizing B_0 in an iterative manner using the genetic algorithm and the dipole approximation. This would allow the magnets to be scaled easily to a particular application of interest where a target B_0 is chosen based on parameters such as inner/outer radius and/or cost of magnetic material used [38]. Bigger magnet sizes are likely to further improve the shimming results since more shimming magnets can be used and magnetic field fluctuations in the target area due to position, orientation and/or material errors of individual shim magnets are expected to be less severe.

Octagonal magnets were used to improve the homogeneity of the base magnet and increase the magnetic flux compared to rectangular magnets [16, 27]. However, the first shim iteration is already improving homogeneity by nearly an order of magnitude, so it might be advantageous to use rectangular magnets, which are more accessible and affordable.

The calculations based on the genetic algorithm converged within 300 ppm (**Figure 7D**), therefore the parameters are chosen well and conservative. For 3D shimming and larger overall MR magnet dimensions the number of shim magnets that could be placed would increase together with the overall calculation time. Using the spherical harmonics approach investigated in this work reduces the number of parameters used for the genetic algorithm leading to a reduction in simulation time by a factor of ~3.

From the data presented in **Figure 7E**, it is visible that the shimmed field shows lower overall B_0 values compared to the calculated shim. This may indicate a slight misalignment of the shim rings along the x-axis, which reduces the absolute field values in the target area. Improving the precision in aligning the shim rings along the x-axis may improve the shimming results in the y-z plane leading to values closer to the calculated ones.

A drawback of permanent magnets is the associated temperature drift of the magnetic field (**Figure 5**). In order to investigate the temperature dependence of B_0 field distribution of the current setup an additional experiment was performed, where the magnet was heated inhomogeneously (**Supplementary Figure 1**). This resembles a possible worst-case scenario, where both ambient temperature changes and local temperature changes are present. Heating the magnet to temperatures from 30.5–36.8°C resulted in a decrease in homogeneity from 407 to 1,095 ppm in the investigated area. Apart from the inhomogeneous temperature distribution which influences both base magnet and shim ring

field drifts, a reason for the increased inhomogeneity at different temperatures might be the use of two different magnet grades used in the setup: N50 for the octagonal magnets and N42 for the shim inserts. Ideally a single material grade is implemented for both base magnet and shim inserts to avoid different temperature dependencies, which may affect B_0 homogeneity even for global temperature changes. An interesting approach to stabilize the field at different temperatures is the use of at least two magnetic materials with different temperature coefficients, which can be positioned in a way to cancel temperature dependent field variations efficiently [39]. Another way to counteract unavoidable temperature changes and homogenize the field is the use of active B_0 shimming techniques [31, 40].

CONCLUSION

It was demonstrated that an iterative approach to construct a cost-effective, homogeneous desktop MR magnet consisting of a base magnet and B_0 shim ring inserts is feasible. The approach is scalable to bigger magnet dimensions and has the potential to improve B_0 field homogeneity even further. These findings are encouraging towards increasing the availability of MR imaging technology globally using affordable low-field MR systems.

DATA AVAILABILITY STATEMENT

The raw data supporting the conclusions of this article will be made available by the authors, without undue reservation.

AUTHOR CONTRIBUTIONS

KW and LW contributed to conception and design of the study. KW, HA, and LW constructed the magnet. KW, HA, BS, and LW performed the measurements. KW and TO implemented the genetic algorithm. KW and LR implemented the spherical harmonics approach. KW and LW wrote the manuscript. All authors contributed to manuscript revision, read, and approved the submitted version.

ACKNOWLEDGMENTS

The authors would like to acknowledge Peter Blümler, Antonia Barghoorn, Raphael Moritz and Eva Behrens for their support.

SUPPLEMENTARY MATERIAL

The Supplementary Material for this article can be found online at: https://www.frontiersin.org/articles/10.3389/fphy.2021.704566/full#supplementary-material

Supplementary Figure 1 | Temperature dependent 2D B_0 field maps at the center of the magnet measured with an NMR probe (PT2026, Metrolab Technology SA, Geneva, Switzerland). The magnet was heated from a homogeneous baseline room temperature of 24.7°C to an inhomogeneous temperature distribution of 36.8°C on one outer shim ring vs. 30.5°C on the other outer shim ring. (A) Measured B_0 at 24.7°C room temperature with a mean of 91.58 mT and an inhomogeneity of 407 ppm. (B) B_0 field measurements for an inhomogeneous temperature gradient ranging from 30.5 to 36.8°C over the desktop MR magnet. Temperatures were measured with an infrared thermometer. The mean of the corresponding magnetic field is 1.15 mT smaller with 90.43 mT with an inhomogeneity of 1,095 ppm. C) Difference map between (A) and (B).

REFERENCES

1. WHO | World Health Organization. Available from: http://gamapserver.who.int/gho/interactive_charts/health_technologies/medical_equipment/atlas.html (Accessed May 3, 2021).
2. Sarracanie M, and Salameh N. Low-Field MRI: How Low Can We Go? A Fresh View on an Old Debate. *Front Phys* (2020) 8:172. doi:10.3389/fphy.2020.00172
3. Winter L, Pellicer-Guridi R, Broche L, Winkler SA, Reimann HM, Han H, et al. Open Source Medical Devices for Innovation, Education and Global Health: Case Study of Open Source Magnetic Resonance Imaging. *Co-Creation* (2019) 147–63. doi:10.1007/978-3-319-97788-1_12
4. Wald LL, McDaniel PC, Witzel T, Stockmann JP, and Cooley CZ. Low-Cost and Portable MRI. *J Magn Reson Imaging* (2020) 52:686–96. doi:10.1002/jmri.26942
5. Marques JP, Simonis FFJ, and Webb AG. Low-Field MRI: An MR Physics Perspective. *J Magn Reson Imaging* (2019) 49:1528–42. doi:10.1002/jmri.26637
6. Shah J, Cahn B, and By S. Portable, Bedside, Low-Field Magnetic Resonance Imaging in an Intensive Care Setting for Intracranial Hemorrhage. *Neurology* (2020) 94:270.
7. Cooley CZ, McDaniel PC, Stockmann JP, Srinivas SA, Cauley SF, Śliwiak M, et al. A Portable Scanner for Magnetic Resonance Imaging of the Brain. *Nat Biomed Eng* (2020) 5:229–39. doi:10.1038/s41551-020-00641-5
8. Soltner H, and Blümler P. Dipolar Halbach Magnet Stacks Made from Identically Shaped Permanent Magnets for Magnetic Resonance. *Concepts Magn Reson* (2010) 36A:211–22. doi:10.1002/cmr.a.20165
9. O'Reilly T, Teeuwisse WM, and Webb AG. Three-Dimensional MRI in a Homogenous 27 cm Diameter Bore Halbach Array Magnet. *J Magn Reson* (2019) 307:106578. doi:10.1016/j.jmr.2019.106578
10. Cooley CZ, Stockmann JP, Armstrong BD, Sarracanie M, Lev MH, Rosen MS, et al. Two-dimensional Imaging in a Lightweight Portable MRI Scanner without Gradient Coils. *Magn Reson Med* (2015) 73:872–83. doi:10.1002/mrm.25147
11. Cooley CZ, Haskell MW, Cauley SF, Sappo C, Lapierre CD, Ha CG, et al. Design of Sparse Halbach Magnet Arrays for Portable MRI Using a Genetic Algorithm. *IEEE Trans Magn* (2018) 54:1–12. doi:10.1109/TMAG.2017.2751001
12. McDaniel PC, Cooley CZ, Stockmann JP, and Wald LL. The MR Cap: A Single-Sided MRI System Designed for Potential Point-of-Care Limited Field-Of-View Brain Imaging. *Magn Reson Med* (2019) 82:1946–60. doi:10.1002/mrm.27861
13. Vogel MW, Guridi RP, Su J, Vegh V, and Reutens DC. 3D-Spatial Encoding With Permanent Magnets for Ultra-low Field Magnetic Resonance Imaging. *Sci Rep* (2019) 9:1522. doi:10.1038/s41598-018-37953-1
14. O'Reilly T, Teeuwisse WM, Gans Dde, Koolstra K, and Webb AG. *In Vivo* 3D Brain and Extremity MRI at 50 mT Using a Permanent Magnet Halbach Array. *Magn Reson Med* (2021) 85:495–505. doi:10.1002/mrm.28396
15. Van Speybroeck CDE, O'Reilly T, Teeuwisse W, Arnold PM, and Webb AG. Characterization of Displacement Forces and Image Artifacts in the Presence of Passive Medical Implants in Low-Field (<100 mT) Permanent Magnet-Based MRI Systems, and Comparisons With Clinical MRI Systems. *Physica Med* (2021) 84:116–24. doi:10.1016/j.ejmp.2021.04.003
16. Blümler P, and Casanova F. CHAPTER 5. Hardware Developments: Halbach Magnet Arrays. In: ML Johns, EO Fridjonsson, SJ Vogt, and A Haber, editors. *New Developments in NMR*. Cambridge: Royal Society of Chemistry (2015). p. 133–57. doi:10.1039/9781782628095-00133
17. O'Reilly T, and Webb AG. The Role of Non-Random Magnet Rotations on Main Field Homogeneity of Permanent Magnet Assemblies. *Proc Intl Soc Mag Reson Med* (2021) 4042.

18. Lopez HS, Liu F, Weber E, and Crozier S. Passive Shim Design and a Shimming Approach for Biplanar Permanent Magnetic Resonance Imaging Magnets. *IEEE Trans Magn* (2008) 44:394–402. doi:10.1109/TMAG.2007.914770
19. Überrück T, and Blümich B. Variable Magnet Arrays to Passively Shim Compact Permanent-Yoke Magnets. *J Magn Reson* (2019) 298:77–84. doi:10.1016/j.jmr.2018.11.011
20. Parker AJ, Zia W, Rehorn CWG, and Blümich B. Shimming Halbach Magnets Utilizing Genetic Algorithms to Profit from Material Imperfections. *J Magn Reson* (2016) 265:83–9. doi:10.1016/j.jmr.2016.01.014
21. Cooley CZ, Stockmann JP, Witzel T, LaPierre C, Mareyam A, Jia F, et al. Design and Implementation of a Low-Cost, Tabletop MRI Scanner for Education and Research Prototyping. *J Magn Reson* (2020) 310:106625. doi:10.1016/j.jmr.2019.106625
22. Jackson JD. *Classical Electrodynamics*. 3rd ed. Berkley: John Wiley & Sons (1998).
23. Chen J, Wang D, and Cheng S. A Hysteresis Model Based on Linear Curves for NdFeB Permanent Magnet Considering Temperature Effects. *IEEE Trans Magn* (2017) 54:1–5. doi:10.1109/TMAG.2017.2763238
24. Wieczorek MA, and Meschede M. SHTools: Tools for Working with Spherical Harmonics. *Geochem Geophys Geosyst* (2018) 19:2574–92. doi:10.1029/2018GC007529
25. Moritz R. *Development and Characterization of Halbach Arrays Tailored for Magnetic Resonance at Low Magnetic Field Strengths*. Berlin, Germany: MSc Thesis TU Berl (2017).
26. Raich H, and Blümler P. Design and Construction of a Dipolar Halbach Array with a Homogeneous Field from Identical Bar Magnets: NMR Mandhalas. *Concepts Magn Reson* (2004) 23B:16–25. doi:10.1002/cmr.b.20018
27. Barghoorn A. *Halbach Magnet Array Design for Low Cost Magnetic Resonance Imaging*. Berlin, Germany: BSc Thesis TU Berl (2016).
28. Fortin F-A. DEAP: Evolutionary Algorithms Made Easy. *J Mach Learn Res* (2012) 13:2171–5.
29. Kong X, Zhu M, Xia L, Wang Q, Li Y, Zhu X, et al. Passive Shimming of a Superconducting Magnet Using the L1-Norm Regularized Least Square Algorithm. *J Magn Reson* (2016) 263:122–5. doi:10.1016/j.jmr.2015.11.019
30. Ye B, Wang Q, Yu Y, and Kim K. Target Field Approach for Spherical Coordinates. *IEEE Trans Appl Supercond* (2004) 14:1317–21. doi:10.1109/TASC.2004.830565
31. Wachowicz K. Evaluation of Active and Passive Shimming in Magnetic Resonance Imaging. *Res Rep Nucl Med* (2014) 4:1–12. doi:10.2147/RRNM.S46526
32. Roméo F, and Hoult DI. Magnet Field Profiling: Analysis and Correcting Coil Design. *Magn Reson Med* (1984) 1:44–65. doi:10.1002/mrm.1910010107
33. Han H, Moritz R, Oberacker E, Waiczies H, Niendorf T, and Winter L. Open Source 3D Multipurpose Measurement System with Submillimetre Fidelity and First Application in Magnetic Resonance. *Sci Rep* (2017) 7:13452. doi:10.1038/s41598-017-13824-z
34. OCRA – Open-Source Console for Real-Time Acquisition. Available from: https://zeugmatographix.org/ocra/ (Accessed May 3, 2021).
35. Zhang Y, Xie D, Bai B, Yoon HS, and Koh CS. A Novel Optimal Design Method of Passive Shimming for Permanent MRI Magnet. *IEEE Trans Magn* (2008) 44:1058–61. doi:10.1109/TMAG.2007.916267
36. Turek K, and Liszkowski P. Magnetic Field Homogeneity Perturbations in Finite Halbach Dipole Magnets. *J Magn Reson* (2014) 238:52–62. doi:10.1016/j.jmr.2013.10.026
37. Danieli E, Mauler J, Perlo J, Blümich B, and Casanova F. Mobile Sensor for High Resolution NMR Spectroscopy and Imaging. *J Magn Reson* (2009) 198:80–7. doi:10.1016/j.jmr.2009.01.022
38. Winter L, Barghoorn A, Blümler P, and Niendorf T. COSI Magnet: Halbach Magnet and Halbach Gradient Designs for Open Source Low Cost MRI. *Proc Intl Soc Mag Reson Med.* (2016). p. 3568.
39. Danieli E, Perlo J, Blümich B, and Casanova F. Highly Stable and Finely Tuned Magnetic Fields Generated by Permanent Magnet Assemblies. *Phys Rev Lett* (2013) 110:180801. doi:10.1103/PhysRevLett.110.180801
40. Stockmann JP, and Wald LL. *In Vivo* B 0 Field Shimming Methods for MRI at 7 T. *NeuroImage* (2018) 168:71–87. doi:10.1016/j.neuroimage.2017.06.013

Conflict of Interest: The authors declare that the research was conducted in the absence of any commercial or financial relationships that could be construed as a potential conflict of interest.

Publisher's Note: All claims expressed in this article are solely those of the authors and do not necessarily represent those of their affiliated organizations, or those of the publisher, the editors and the reviewers. Any product that may be evaluated in this article, or claim that may be made by its manufacturer, is not guaranteed or endorsed by the publisher.

frontiers in Physics

ORIGINAL RESEARCH
published: 03 August 2021
doi: 10.3389/fphy.2021.697104

Network and Field Analysis of Koch Snowflake Fractal Geometry Radiofrequency Coils for Sodium MRI

Cameron E. Nowikow[1,2], *Paul Polak*[1,2], *Norman B. Konyer*[2], *Natalia K. Nikolova*[3] *and Michael D. Noseworthy*[1,2,3,4]*

[1]School of Biomedical Engineering, McMaster University, Hamilton, ON, Canada, [2]Imaging Research Centre, St. Joseph's Healthcare, Hamilton, ON, Canada, [3]Electrical and Computer Engineering, McMaster University, Hamilton, ON, Canada, [4]Department of Radiology, McMaster University, Hamilton, ON, Canada

Sodium is one of the most abundant physiological cations and is a key element in many cellular processes. It has been shown that several pathologies, including degenerative brain disorders, cancers, and brain traumas, express sodium deviations from normal. Therefore, sodium magnetic resonance imaging (MRI) can prove to be valuable for physicians. However, sodium MRI has its limitations, the most significant being a signal-to-noise ratio (SNR) thousands of times lower than a typical proton MRI. Radiofrequency coils are the components of the MRI system directly responsible for signal generation and acquisition. This paper explores the intrinsic properties of a Koch snowflake fractal radiofrequency surface coil compared to that of a standard circular surface coil to investigate a fractal geometry's role in increasing SNR of sodium MRI scans. By first analyzing the network parameters of the two coils, it was found that the fractal coil had a better impedance match than the circular coil when loaded by various anatomical regions. Although this maximizes signal transfer between the coil and the system, this is at the expense of a lower Q, indicating greater signal loss between the tissue and coil. A second version of each coil was constructed to test the mutual inductance between the coils of the same geometry to see how they would behave as a phased array. It was found that the fractal coils were less sensitive to each other than the two circular coils, which would be beneficial when constructing and using phased array systems. The performance of each coil was then assessed for B_1^+ field homogeneity and signal. A sodium phantom was imaged using a B_1^+ mapping sequence, and a 3D radial acquisition was performed to determine SNR and image quality. The results indicated that the circular coil had a more homogeneous field and higher SNR. Overall while the circular coil proved to generate a higher signal-to-noise ratio than the fractal, the Koch coil showed higher versatility when in a multichannel network which could prove to be a benefit when designing, constructing, and using a phased array coil.

Keywords: radiofrequency coils, fractals, sodium-23, magnetic resonance imaging, koch, B1+ mapping

OPEN ACCESS

Edited by:
Simone Angela S. Winkler, Cornell University, United States

Reviewed by:
Elizaveta Motovilova, Department of Radiology, United States
Joseph Vincent Rispoli, Purdue University, United States

***Correspondence:**
Michael D. Noseworthy
nosewor@mcmaster.ca

Specialty section:
This article was submitted to Medical Physics and Imaging, a section of the journal Frontiers in Physics

Received: *18 April 2021*
Accepted: *21 July 2021*
Published: *03 August 2021*

Citation:
Nowikow CE, Polak P, Konyer NB, Nikolova NK and Noseworthy MD (2021) Network and Field Analysis of Koch Snowflake Fractal Geometry Radiofrequency Coils for Sodium MRI. Front. Phys. 9:697104. doi: 10.3389/fphy.2021.697104

1 INTRODUCTION

Sodium magnetic resonance imaging (^{23}Na-MRI) has the potential to become a valuable tool in the clinical setting, by assisting physicians through the diagnosis, prognosis, and monitoring of a variety of pathologies including cancers, degenerative brain disorders, concussion, and osteoarthritis [1, 2]. However, due to quantum mechanical limitations such as rapid spin dephasing and a small gyromagnetic ratio, and biological restrictions including low *in vivo* sodium concentrations, the signal-to-noise ratio (SNR) of the resultant ^{23}Na-MRI images can be up to thousands of times lower than traditional clinical proton MRI images [2, 3]. The point-of-source in MRI signal generation and acquisition is the radiofrequency (RF) coil, and the quality of coil performance will propagate throughout the remainder of the system. The quality of the performance of an MRI RF coil is based on the contribution of several factors intrinsic to the coil such as the tune and match of the coil, the quality factor (Q), the homogeneity of the produced RF field (B_1^+), and the homogeneity of the induced RF signal (B_1^-) [4, 5].

The simplest RF coil is a one element transmit/receive (Tx/Rx) surface coil, consisting usually of a single conductive loop with capacitors for tuning and matching [4, 5]. The Tx/Rx surface coil has great signal sensitivity in a local area; however, it produces an inherently heterogeneous B_1^+ field (and due to reciprocity, the B_1^-) because the field strength decreases with distance from the coil. Multiple surface coils can be arranged together to form a multi-channel phased array coil. Phased array coils can produce a more homogeneous $B_1^{+,-}$ field over a larger volume than a single surface coil; however, the multiple elements interact with each other, which creates challenges when designing and constructing the coil. This study looks to see if a fractal geometry can play a role in improving the SNR of ^{23}Na-MRI by overcoming some of the shortcomings of traditional RF coils.

The term fractal originated from Benoit Mandelbrot's *Fractal Geometry of Nature* published in 1983 [6], however these structures have been studied by mathematicians since the early 1900's. Fractal geometries are patterns that can be decomposed into self-similar elements. As such, they do not conform to standard Euclidean geometry and instead behave idiosyncratically. These patterns can exist in non integer dimensions and have unique space filling ability [7, 8]. Fractal geometries have been explored before in electromagnetic applications [9], as fractal antennas have been used in telecommunication systems for years, with the common benefit being compact size which allows for a greater effective antenna length within a smaller space. This is not the only benefit to having a fractal (or fractal-like) shape, as it has been shown that these so-called "shaped antennas" can produce higher gain, directivity, and field strength than a standard loop or monopole/dipole antenna of a comparable size [8, 10].

Telecommunication systems are generally focused on far field applications, however most MRI RF coils exist in the near field region, so the question arises: how do far field fractal antennas translate to near field MRI applications? A single fractal antenna can act as though it is comprised of multiple elements due to each self-similar subsection of the coil radiating as a single antenna [8]. This may produce some interesting constructive and destructive interference patterns more locally around the antenna and could more evenly distribute the radiated energy. The aforementioned space filling ability of a fractal antenna has been shown to result in higher Q values and better impedance matching than standard antennas that take up the same amount of space, which would benefit MRI by maximizing the signal transfer [11, 12]. It has also been shown that a multi-loop fractal-like surface coil geometry in proton MRI applications produces higher sensitivity [13].

There exist thousands of fractal and fractal-like geometries and a smaller subset are the focus of most antenna research and applications, but here only one pattern was studied: the Koch snowflake (**Figure 1**). This geometry was one of the fractals that was explored in [11, 12] and showed a higher Q, better impedance match, and less mutual inductance when in arrays. In proton MRI applications, it has been shown that multiple Koch snowflake fractal elements when in an overlapping array have higher sensitivity, Q values, and SNR along with reduced mutual inductance than circular elements in a similar array [14]. Previous simulations of a Koch snowflake coil performed by Dona Lemus et al. [15] and Nowikow et al. [16] have shown that physical construction and implementation is warranted.

This leads to the hypothesis that a Koch snowflake fractal geometry surface coil can improve the quality of ^{23}Na-MRI images by increasing the resultant SNR due to a more homogeneous B_1^+ (and B_1^-) field, a superior filling factor, and more robust impedance matching than a typical circular geometry surface coil. In addition, the lower mutual inductance for the Koch snowflake geometry will facilitate implementation in phased array coils.

2 MATERIALS AND METHODS

2.1 Coil Design

Design parameters for the initial simulations were set with fabrication in mind. Due to the complex geometry of the Koch snowflake fractal, it was decided that the coils would be manufactured on a printed circuit board (PCB) to allow for consistency and accuracy. This restricted the size of the coil designs to fit within a 100 mm by 100 mm area. As such, the coil diameter chosen was 90 mm (~3.5″) which falls within the 3–6″ size of many standard commercial surface coils. The choice of conductor was copper as it is a standard etching material. The width of the copper was selected to be 3 mm as it was narrow enough to allow for a Koch design but wide enough for ease of capacitor soldering for the eventual construction. With restrictions on coil diameter and copper width, it was determined early on that the only viable Koch snowflake fractal generation that could be manufactured with a level of practicality was a third-generation Koch. Thus, two different Tx/Rx surface coils were simulated and constructed, the first was circular in geometry to act as a reference for a standard "typical" surface coil and the second was a third-generation Koch snowflake fractal geometry (**Figure 2**).

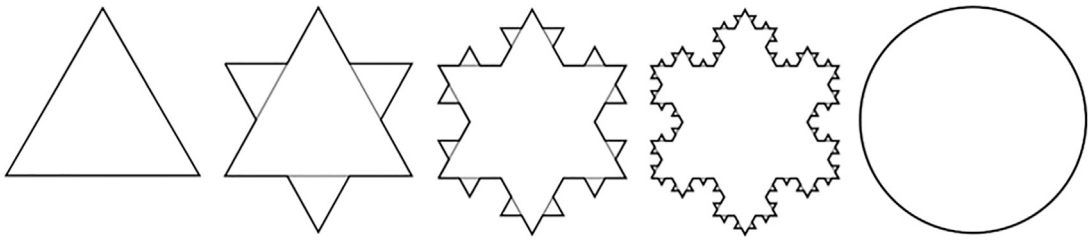

FIGURE 1 | The first four generations of a Koch snowflake fractal compared to a circle of the same radius (image modified from https://en.wikipedia.org/wiki/Koch_snowflake, which is licensed for free use under: https://creativecommons.org/licenses/by-sa/3.0/deed.en).

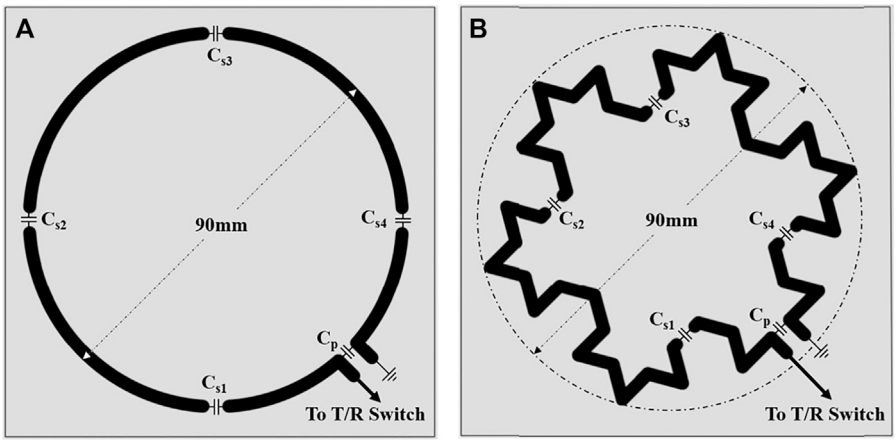

FIGURE 2 | The geometry of the **(A)** circular, and **(B)** fractal coil. Each were copper etched on a 100 × 100 mm FR4 substrate with breaks in loop for the tuning capacitors (C_{s1-4}) and the matching capacitor (C_p). One end of the loop for both coils was connected to the T/R switch via a coaxial cable while the other end of the loop was grounded using the same coaxial cable to form a one port network.

2.2 Simulations

The two coils were simulated using ANSYS HFSS (Ansys Inc., Canonsburg, PA, United States), using the design constraints laid out previously. The coils were simulated as copper sheet conductor (infintesimally thin) on a 1 mm thick FR4 substrate. Each design incorporated five breaks, four in the main loop for tuning capacitors and one in between the legs for a matching capacitor. These were used to tune the coils to 33.8 MHz, the Larmor frequency of sodium at 3 Tesla (T), and to match the coils to 50Ω. The coils were loaded by a rectangular box of 0.9% wt/v saline to mimic a standard ^{23}Na-MRI phantom.

Two sets of fields data were acquired via simulation. The first set included the electric (E) and magnetic (H) fields, as well as the surface current density (J), obtained at unity power, where both coils were fed with the same power level to act as a direct comparison between the fields. The second set of fields were acquired at an adjusted power level such that the coils would produce a magnetic field that would cause a 90° tip in the sodium spins in the phantom directly below the coil. At this power level the now denoted B1 fields were acquired, as well as the E fields and surface J fields.

The H and B1 fields were analyzed in MATLAB (Mathworks, Natick, MA, United States) to determine their homogeneity with two main methods. First the homogeneity of the field was measured by calculating the mean and standard deviation of the signal over various regions of interest (ROIs) selected to be located in the sensitive region of the coil [4, 5], where the standard deviation of the field in each ROI was used as a representation of the homogeneity. The selected ROIs were two cylindrical regions of different radii (25 and 45 mm) situated with their circular faces parallel to the coil plane with a height between a half radius and a radius away from the coil plane. Six spherical ROIs were also selected, with varying radii (6, 8, 10, 12, 14, and 18 mm). All ROIs are shown in **Figure 3**. It was also of interest to see how the magnetic fields behaved as distance from the coil increased, and so a set of plots were made of the mean signal strength as a circular ROI (of two radii, 25 and 45 mm) moved away from the coil plane.

The E and J fields were used as a way to see if the safety measures between the two coils would need to be modified. As the fractal coil has a greater effective length of conductor in the same area it was thought it may require more capacitive breaks to help disperse the E field and current density.

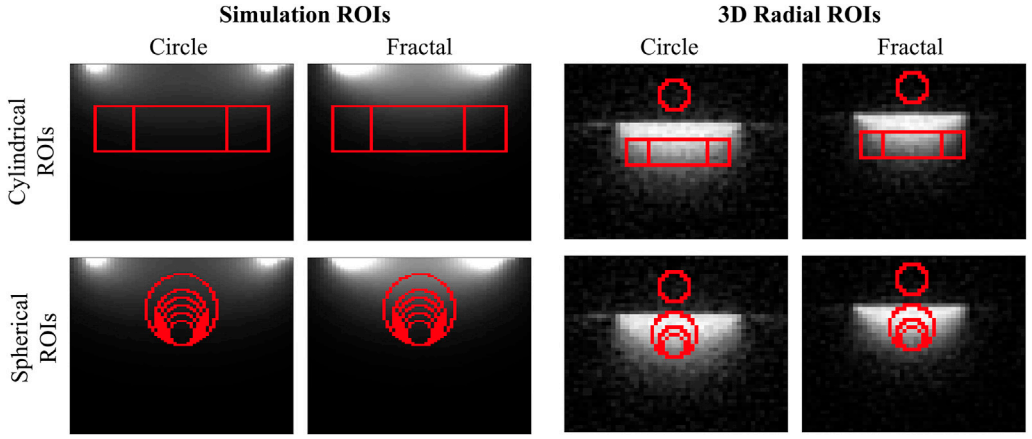

FIGURE 3 | The ROIs used for the homogeneity measurements of the simulated fields and the 3D radial volume data, as well as the SNR calculations from the 3D radial data of both the circular and fractal coils. The cylindrical ROIs are of radius 25 mm and ~45 mm and are used to represent the coil's optimal sensitivity region between r/2 and r deep into the phantom [4]. The simulations also used six spherical ROIs of radii 6, 8, 10, 12, 14, and 18 mm, whereas the measured 3D radial data used only three spherical ROIs of radii 9, 12.5, and 18.75 mm. The noise ROI for SNR calculations using the measured data is shown as the spherical ROI above the coil plane for the 3D radial data.

2.3 Coil Construction and Bench Measurements

After simulation the two coils were then constructed. The coils were manufactured on a PCB, as copper etching on an FR4 substrate by Elecrow (https://www.elecrow.com/). The etched copper was 3 mm in width and 35 um in thickness, and the coils themselves replicated the simulated designs: 90 mm in diameter to fit on the 100 × 100 mm substrate. The same number of breaks in each loop as the simulations were incorporated into the design to allow for tuning and matching capacitors (American Technical Ceramics, NY) with values ranging between 10 and 470 pF. Ideally, the coils would be fed by a $\lambda/2$ coaxial cable; however, due to sodium resonating at such a low frequency at 3T, the coaxial cable required would have to be 4.45 m in length which would not be feasible to implement in the MRI without introducing loops and bends. Instead, a 0.4 m coaxial cable was used to feed the two coils, the shortest length that allowed the coil to reach both the phantom and transmit/receive (T/R) switch.

All S-parameter and Q measurements of the fabricated coils were performed using an Agilent 4395A network analyzer and an Agilent 87511A S-parameter test set. Both the circular and fractal surface coil were tuned and matched, while being loaded by a saline phantom, to 33.8 MHz, the Larmor frequency of sodium at 3 T. To explore how effective each geometry was at matching to various parts of anatomy, once their original tune and match (to the phantom) were set, the coils were loaded with different parts of the body and the respective S_{11} parameters were recorded and reported in decibels (dB): $20 \log_{10}(|S_{11}|)$. The chosen regions of anatomy were the right knee, abdomen (slightly right from midline, below the ribcage to emulate a possible liver scan), and the back of the head as these are three potential clinically relevant regions for ^{23}Na-MRI scans. 11 subjects were used for the knee, abdomen, and head loading experiment. A ratio of unloaded to loaded Q (Q_U and Q_L) was calculated for each bodily load [denoted as (Q_{ratio})].

Additional circular and fractal coils were constructed, and tuned and matched to the phantom, to explore how the coil geometry affected their mutual inductance. The S_{21} of each coil pair while loaded by the phantom were measured as $20 \log_{10}(|S_{21}|)$ (dB) using the aforementioned network analyzer and *S*-parameter test set at multiple separation distances between 4 and 9 cm (measured center to center), as well as at the optimal separation for a single, not split, S_{21} peak. As two coils interact with each other their resonant frequency splits into two modes which can be visualized as a split in S_{21} curve. The geometry of the coil dictates at what degree of coil separation geometric decoupling occurs (i.e. where the mutual inductance is eliminated, or at least minimized) which can be visualized as this split S_{21} curve merges back into a single resonant peak. The fractal coil's S_{21} for each distance was measured in three configurations: overlap on the long axis (denoted LA), overlap on the short axis (denoted SA), and overlap between the long axis of one fractal and the short axis of the other (denoted MA, for "mixed axis"). The Q_U and Q_L were measured for the coils at their optimal distance of separation/overlap.

2.4 Experimental Setup

The remaining experiments were performed using a GE MR750 3 T magnet (General Electric Healthcare, WI). The phantom was elevated on the bed of the MRI by a foam riser such that when the selected coil was placed atop, the field-of-view (FOV) of the coil was at magnet isocenter. The coil in use was connected to the scanner *via* a single-channel sodium T/R switch. The coil that was being used was positioned on top of the phantom, substrate down, such that the coaxial feed was aligned down the bore of the magnet. The coil was secured in place using a weighted bag. Each coil had a vitamin E capsule taped to the center of the coil to allow for localization with a

generic proton three-plane localizing scan using the body coil. The phantom used to load the coils during their tune and match was the phantom that was used for imaging. The phantom was a rectangular plastic box of dimensions 160 × 270 mm with a depth of 90 mm containing 0.9% wt/v saline (aqueous NaCl). The size of the phantom was chosen to allow for a B_1^+ map of the full FOV of each coil if a 90° tip angle was applied directly below the coil plane.

2.5 MNS Prescan

To determine the power required to achieve a 90°tip angle, a GE Healthcare sequence, implemented by Schulte et al. [17] called the MNS prescan, was used. The power was calibrated to a 10 mm thick plane at the surface of the phantom, directly below, and parallel to the plane of the coil, and the lid of the phantom. Before the MNS prescan was run, an initial 10dB attenuation was applied to the RF power, so that the transmit gain (TG) could be effectively chosen (no initial attenuation would result in too much power for a 90°tip, even if the TG was 0).

2.6 B_1^+ Mapping

The Bloch-Siegert shift method, as outlined by Sacolick et al. [18], was selected as the way to map the B_1^+ fields of the two coils. Four maps of the B_1^+ field were calculated for each coil: one perpendicular to the coil plane and through the center of the coil, and three maps parallel to the coil plane, at differing depths (15, 25, 35 mm) from the coil. The data was acquired using a 2D, four-arm spiral sequence over a 150 mm FOV. The tip angle of the 10 mm thick slice selective pulse was 90°. The repetition time (TR) of the sequence was 84 ms, and 50 signal averages (NEX) were used. K-space was reconstructed using the algorithm described by Beatty et al. [19] into an 80 × 80 matrix. The mean and standard deviation of the field strength over each map's FOV was calculated to determine the homogeneity of the field in that slice.

2.7 Homogeneity and Signal-to-Noise Ratio Measurements

A 3D radial sequence was used to obtain a 48 × 48 × 48 image matrix of the phantom. A 90°hard pulse was used to excite a 150 × 150 × 150 mm volume, and 7,333 spokes were sampled—one per every 23 ms TR.

Two NEX were used, and k-space was reconstructed using the previously stated algorithm [19]. The volume selected was centered on the coil in the transverse plane, and encompassed the entire depth of the phantom below the coil, and an additional air space above the coil. This volume was chosen such that the entire FOV of the coil would be imaged while leaving enough "empty space" available for a noise measurement.

The B_1^+ mapping sequence acquired the data in a 10 mm thick slice, and as such did not allow for reliable measurements of field homogeneity over a volume. However, since the acquired signal is proportional to the sine of the flip angle, and the flip angle is proportional to the magnitude of the B_1^+ field, the signal acquired by the 3D radial imaging sequence over its 15 cm FOV is representative of the field strength over that same volume. The homogeneity of the field was then measured using this 3D volume, by calculating the mean and standard deviation of the signal over various ROIs selected to be as similar as possible to the ROIs used to analyze the simulation results. The cylindrical ROIs for the experimental data were situated in the same coil sensitivity region with radii of 25 and 45 mm. Due to a reduction in resolution of the experimental data versus the simulated fields, only three spherical ROIs could be obtained with radii of 9, 12.5 and 18.75 mm. The ROIs used for this 3D radial data can be found alongside the simulated fields' ROIs in **Figure 3** (Note the FOV of the simulated data is 11 cm as opposed to the 15 cm FOV of the experimental data which explains the size discrepancy in the figure). As with the simulations it was of interest to see how the B_1^+ field behaved as distance from the coil increased. Thus, plots were made of the mean signal strength as a circular ROI (of two radii, 25 and 44 mm) moved away from the coil plane. Much like the analysis of the simulated data, all experimental data was analyzed using MATLAB.

The 3D volume acquired by the radial sequence was also used for SNR measurements. To allow for a homogeneity/SNR comparison, multiple SNR values were calculated, using the five ROIs described previously (**Figure 3**) as the signal region in the SNR calculation. The noise region used in the calculations was kept constant and can be seen in **Figure 3** (spherical region above the coil). SNR was calculated as $\mu_{signalROI}/\sigma_{noiseROI}$.

TABLE 1 | The S_{11} values (in dB), the Q values (unitless), and the ratio of unloaded to loaded Q are reported in this table for both the circular and fractal coil over various loads. A mean and standard deviation are reported for the values calculated over the 11 subjects.

Load		Circular	Fractal
Unloaded	S_{11} (dB)	−2.50	−4.00
	Q_U	199	178
Phantom	S_{11} (dB)	−28.26	−29.59
	Q_L	31	43
	Q_{ratio}	6.48	4.14
Knee	S_{11} (dB)	−4.62 ± 0.51	−7.06 ± 0.68
	Q_L	111 ± 12	105 ± 9
	Q_{ratio}	1.82 ± 0.19	1.70 ± 0.15
Abdomen	S_{11} (dB)	−6.97 ± 1.56	−8.60 ± 1.71
	Q_L	78 ± 16	91 ± 14
	Q_{ratio}	2.65 ± 0.53	2.01 ± 0.33
Head	S_{11} (dB)	−4.76 ± 0.67	−7.18 ± 0.76
	Q_L	108 ± 14	104 ± 9
	Q_{ratio}	1.87 ± 0.25	1.73 ± 0.16

3 RESULTS

3.1 Coil Loading and Matching

The S_{11} and Q values of the two coils when unloaded, loaded by the phantom, and loaded by the varying anatomical regions are given in **Table 1**. The values associated with anatomical

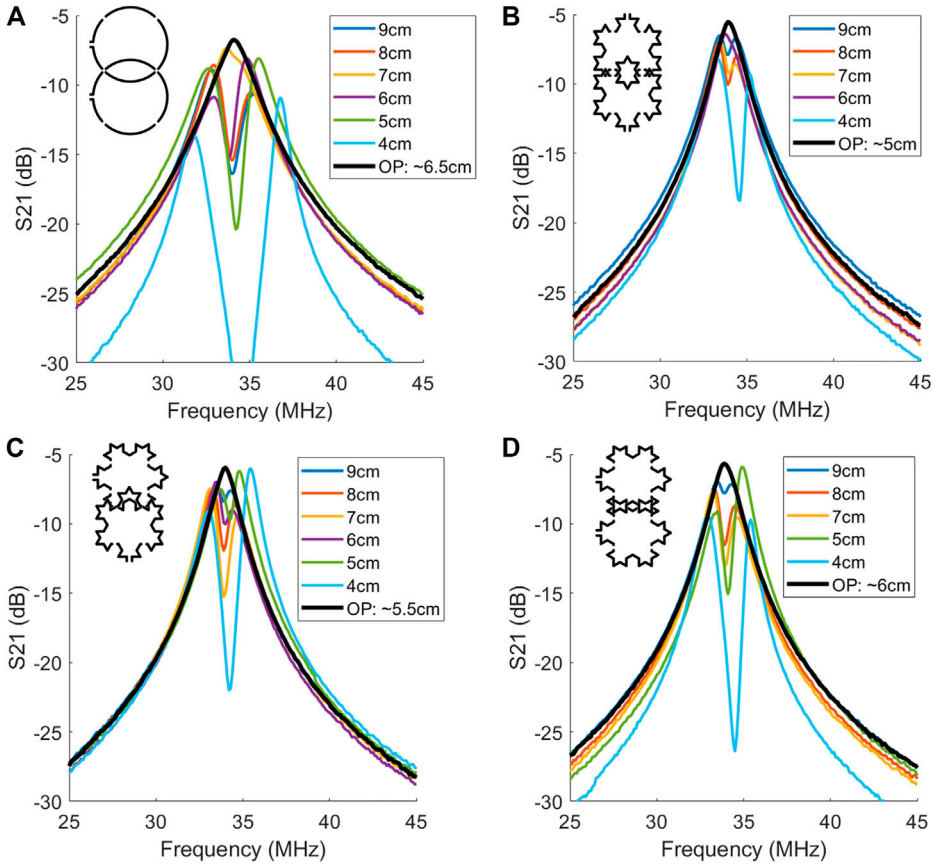

FIGURE 4 | The S_{21} curves (in dB) of **(A)** the circular coil pair, **(B)** long axis (LA) overlap of the fractal pair, **(C)** mixed axis (MA) overlap of the fractal pair, and **(D)** short axis (SA) overlap of the fractal pair. The coil diagrams in the top left corner of each plot show the coil configurations. The black "OP" curve is the curve at an optimal distance of separation where the mutual inductance goes to zero and the curve merges into one singular peak.

regions (n = 11 subjects) are reported as a mean ± standard deviation. The Q_{ratio} (Q_U/Q_L) is also reported in the table. The coils were tuned and matched while being loaded by the phantom, and as such the respective S_{11} (at 33.8 MHz) of both are below a respectable −28 dB. There are three notable differences between the two coils when it comes to coil match and tissue coupling. First, the Koch coil has a significantly better match than the circular coil when being loaded by the anatomical regions, which can be observed in the lower S_{11} values. The second notable difference is the measured values when the coils are unloaded. The circular coil "unmatches" more so than the Koch coil (i.e. a higher S_{11}) which results in a higher Q_U. These combine for a notable difference in Q_{ratio} when loaded by the phantom, and less notable difference in Q_{ratio} when loaded by human subjects.

3.2 Mutual Inductance

The S_{21} curves of the circular coil pair, and three configurations of the fractal coil pair, are shown in **Figure 4** over a 20 MHz bandwidth. At a separation distance of 9 cm both coil pairs had a split S_{21} peak, and as coils began to overlap, the peaks merged into one, each at a unique distance. It can be seen that depending on the rotational orientation of the fractal pair, the optimal distance to eliminate mutual inductance was varied, ranging between 5 and 6 cm, whereas the circular pair only had one optimal distance of 6.5 cm. It can be noted as well that the fractal coil pairs, regardless of orientation, were less responsive in terms of an S_{21} split peak as a function of distance, which could lead to the assumption that the interaction between the two fractal coils is less than the interaction between the two circular coils. The Q_L and the Q_U values are reported in **Table 2** for the different coil pair configurations. There were two instances, when the coil pair was unloaded, that the S_{21} peak split and the Q_U was not measurable—and is indicated as "n/a" in the table.

3.3 B_1^+ Field Homogeneity and Signal-to-Noise Ratio

The four B_1^+ maps made for each coil are shown in **Figure 5**, alongside their simulated counterparts. The experimentally determined maps were overlayed onto their respective slices taken from the 3D volume acquired using the radial sequence.

TABLE 2 | The Q values for each coil pair when arranged at their optimal distance to eliminate mutual inductance. Those distances are respectively 6.5, 5, 5.5, and 6 cm. The Q_U was reported as "n/a" for the configurations where the S_{21} peak was split at the optimal distance when unloaded.

Q values	Circular pair	Fractal LA pair	Fractal MA pair	Fractal SA pair
Q_U	n/a	107.2	109.5	n/a
Q_L	28.2	42.8	42.2	40.8

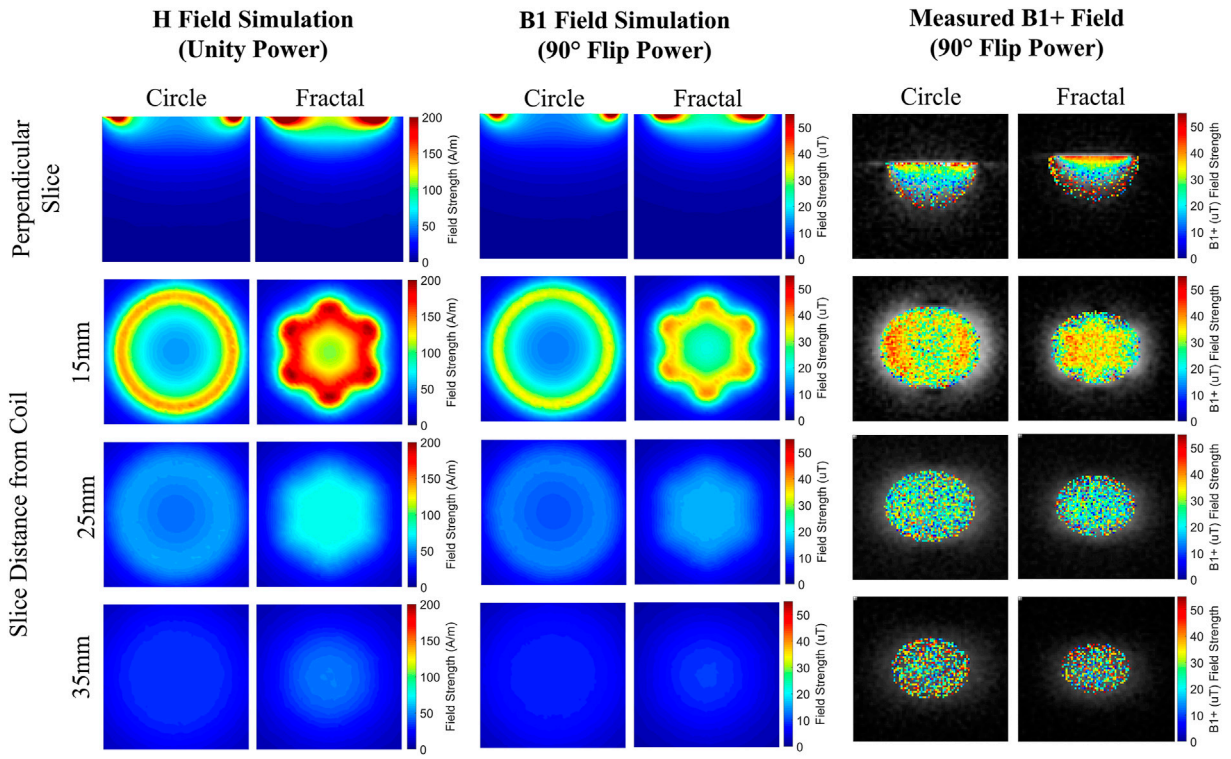

FIGURE 5 | The experimental B_1^+ field maps of the circular and fractal coil, alongside each maps simulated counterpart at the same slice location. The simulated B1 field maps and the measured B_1^+ field maps are given in μT and the simulated H field maps are given in A/m.

TABLE 3 | The mean and standard deviation of each of the measured B_1^+ maps shown in **Figure 5**, given in μT over the FOV shown in the map. The three parallel slices are listed in order of depth from the coil: 15, 25, and 35 mm respectively.

Coil	Perpendicular slice	Parallel slice 1	Parallel slice 2	Parallel slice 3
Circular	26.91 ± 10.99	33.37 ± 7.15	25.96 ± 9.30	29.73 ± 12.19
Fractal	31.37 ± 11.80	31.82 ± 7.61	25.64 ± 9.72	30.00 ± 13.18

The mean and standard deviation of the B_1^+ maps are given in **Table 3**. The acquired maps were quite noisy, especially the third parallel slice 35 mm from the coil, which explains why the field strength appeared to increase at a larger depth. However, the standard deviation of the circular coil's B_1^+ field for each map was consistently lower.

The signal strength and homogeneity calculated over the various ROIs from the 3D volume are given in **Figure 6**, again, alongside their simulated counterparts. In the simulations the field strength of the fractal coil over the ROIs was consistantly higher, whereas experimentally the coil with the higher signal for each ROI fluctuated; however, the standard deviation of the signal acquired by the circular coil is consistently lower than that of the Koch coil, over all ROIs—simulated and measured. The plots of signal behaviour with distance from the coil are shown in **Figure 7**. The signal from the Koch coil decays (in space) more rapidly than that from the circular coil, with signal variation of the latter being less as well. The SNR, calculated over various ROIs (**Figure 3** and **Table 4**) shows the circular coil consistently had greater SNR than the fractal coil.

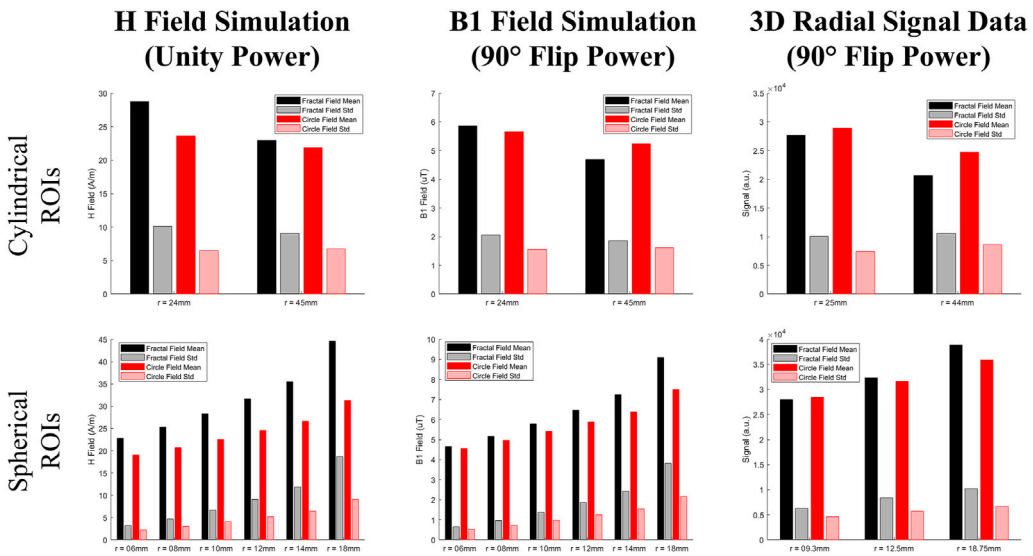

FIGURE 6 | The means and standard deviations over various ROIs shown in **Figure 3** for the simulated H field (given in A/m), the power compensated simulated B_1 field (given in μT), and the measured signal from the 3D radial volume data (given in a.u.) for both the circular and fractal coil. As the standard deviation of the ROIs was used as the main metric for determining a given coil's homogeneity, the standard deviations are shown for comparison as their own bar in the plot. The radii of each ROI is the label for each set of bars.

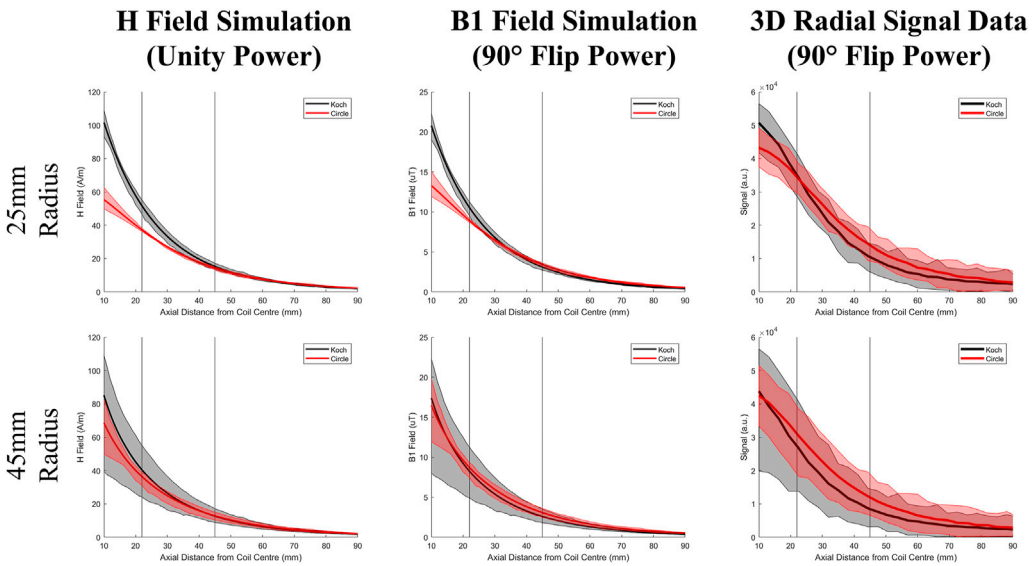

FIGURE 7 | The plots of field strength and variation of the simulated H field (given in A/m), the power compensated simulated B_1 field (given in μT), and the measured signal from the 3D radial volume data (given in a.u.) over a circular ROI (of radii 25 and 45 mm) as the ROI moves away from the coil and deeper into the phantom for both the circular and fractal coils. The mean of the field strength is given by the bold curves in red and black, and the lighter bands in grey and pink that encompass the bold curves represent the range of signal values over the ROI at each distance from the coil.

3.4 Coil Safety

The simulated coil surface current densities, coil surface electric fields, and the simulated electric fields in the phantom can be found in **Figure 8**. It can be seen that the fractal coil's conductive surface had both a lower current density and electric field than that of the circular coil at both power levels. The E fields deposited in the phantom are quite similar for both coils, however the circular coil's E field appears to penetrate deeper into the phantom, whereas the fractal coil's E field is more concentrated into a smaller area (on a slice per slice basis).

TABLE 4 | The SNR values for each 3D radial experimental data ROI shown in **Figure 3**. The first three ROIs in the table are the spherical ROIs, and the last two are the cylindrical ROIs. The noise ROI used for calculations is also given in **Figure 3** as the spherical ROI above the coil plane.

Coil/ROI radius (mm)	9.0	12.5	19.0	25.0	44.0
Circular	17.39	19.31	21.90	17.66	15.09
Fractal	15.46	17.87	21.45	15.30	11.43

matching, mutual inductance, RF field homogeneity and SNR was evaluated. However, the fractal design only excelled in being less prone to object-induced match variability and in reducing mutual inductance between loops, as compared to circular coils of the same diameter.

Impedance matching is important when designing, constructing, and tuning an MRI RF coil—the better the match, the optimal the power transfer between the coil and

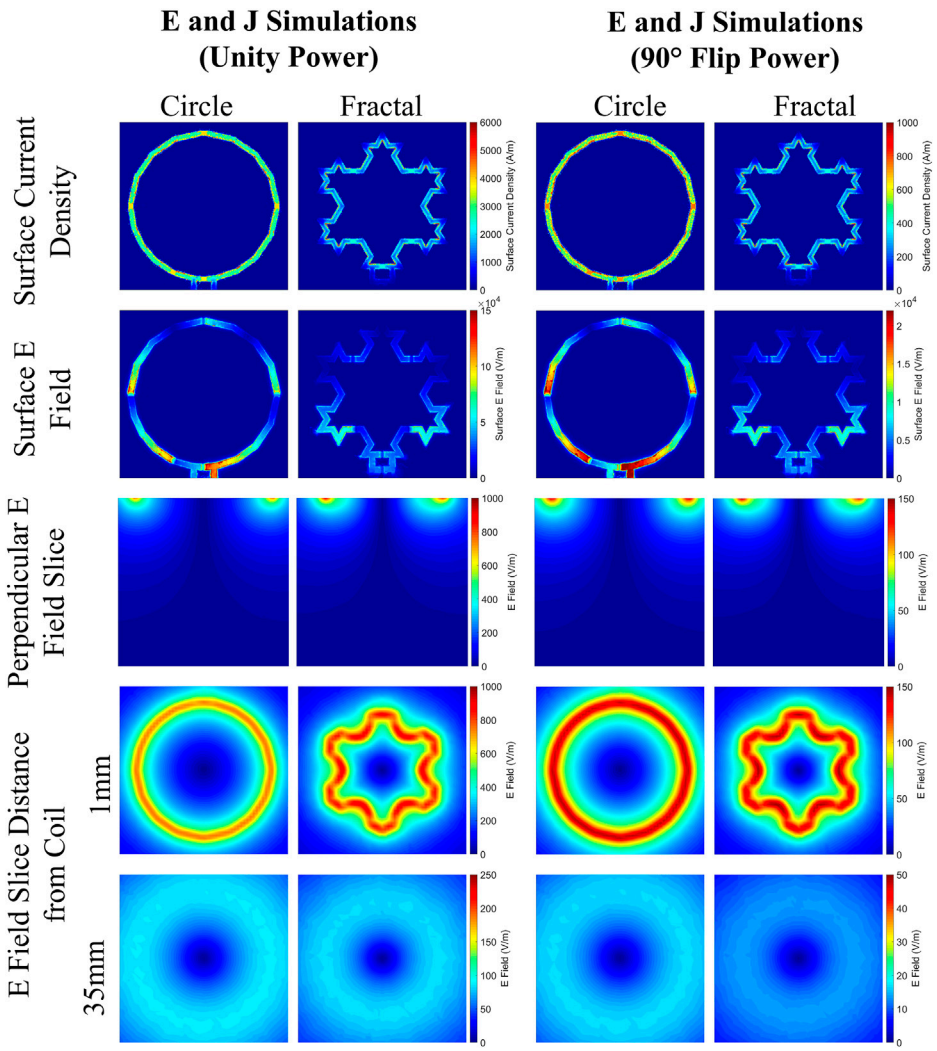

FIGURE 8 | The simulated surface current density, the surface electric field, and the electric field depositied in the phantom for both the circular and fractal coil.

4 DISCUSSION

This study explored the network parameter and B_1^+ field characteristics of a Koch snowflake fractal geometry RF surface coil compared to that of a standard circular surface coil for sodium MRI. The hypothesis was that the fractal coil would provide increased SNR in sodium MRI. Coil loading and the system, and hence a higher resultant SNR [20]. Most coils are tuned and matched once to a standardized phantom or specific region of anatomy. Some in house manufactured surface coils may include a variable capacitor that can be adjusted based on the load, however most commercial coils lack this feature, and furthermore, would be impractical for phased arrays. There has been work in tuning circuits for

single and multi coil applications however they are limited [5, 21, 22]. The coil impedance match is ideal when loaded by the phantom/body part to be probed. Once the coil is loaded by something else, whether it be a different phantom or different region of the body, or a different person altogether, the match will suffer for it. The S_{11} parameter is a measure of the coil match, where the lower the S_{11} (in dB) the better. Based on S_{11} measurements (**Table 1**) the fractal coil was more robust and insensitive to anatomical region compared to the circular coil. However, this advantage came at the cost of a reduced Q_{ratio}. Thus, fractal-based coils may offer a robust solution to impedance matching (at a cost) for varied anatomy when manual matching is not an option (i.e. phased array configurations). The S_{11} values would need to be explored further in a larger phased array configuration.

When surface coils are arranged in arrays they begin to interact and interfere with each other via geometric coupling, resulting in an equivalent mutual inductance between coils. It is not possible to eliminate between-coil mutual inductance in phased arrays. However, a goal is to ideally minimize this problem in order to maximize SNR [5]. As individual coil elements are moved towards each other and begin to overlap, the mutual inductance effect worsens. As the overlap continues the coils will reach an optimal overlap that eliminates the mutual inductance, where this optimal configuration varies based on geometry [23]. Optimal overlaps are well documented for coil array elements for standard geometries, however it can be a challenge to adhere to those restrictions when trying to optimize coil coverage over a set area. The S_{21} network parameter of a coil network indicates the mutual inductance between two coils. When two coils experience coupling it appears as a split S_{21} peak and the peaks will merge into one when the mutual inductance is minimized. The S_{21} measurements made (**Figure 4**) between the pair of circular coils, and the pair of fractal coils, revealed that the fractal pair allowed for more configurations and spacings, such that the mutual inductance between coils could be minimized or ideally eliminated. It was also observed that the fractal pair was less sensitive to coil overlap as seen by less profound S_{21} peak splitting which could allow for increased error when arranging large numbers of coils in array configurations.

The homogeneity of the coil's B_1^+ field is also essential in maximizing image SNR. The SNR is related to the sine of the flip angle, and the flip angle is related directly to the B_1^+ field strength. In order to maximize signal from a sample, the flip angle needs to be 90°, assuming adequate T1 recovery time is permitted. This also requires a spatially homogeneous B_1^+ field across the sample as well. It is well known that surface coils produce inherently heterogeneous fields, and any increase in homogeneity would be beneficial to increasing SNR [4]. Measured B_1^+ field maps were created (**Figure 5**) for both circular and fractal coils, and field homogeneity was compared. The standard deviation of the field strength over each map was used as a metric for homogeneity, where the lower the standard deviation the higher the homogeneity (**Table 3**). Over all the maps of the circular coil had a lower standard deviation, indicating a more homogeneous field compared to the fractal coil. However, these maps were noisy even after averaging over a 10 mm thick slice. This made homogeneity assessment over a volume challenging. Thus, a 3D volume was imaged and signal intensity variation across several ROIs inside the coil FOV were used as a B_1^+ field homogeneity metric (**Figure 6**). For the experimentally determined data, across all five ROIs selected, the circular coil had lower signal variation compared to the fractal coil, based on ROI standard deviation measurements. Again, lower standard deviation within an ROI indicates a more homogeneous field, corroborating the B_1^+ field map findings. The 3D volume was also used to create a plot of signal intensity versus distance from the coil plane, to visualize axial homogeneity (**Figure 7**). Surface coils have reasonable homogeneity at approximately one radius from the coil plane after which the signal uniformity decreases rapidly (with distance). The fractal coil signal drops faster with distance which also supports the same conclusion as the perpendicularly sliced B_1^+ map that the circular coil produces a more homogeneous field compared to the same diameter fractal coil.

When comparing the simulation results to the experimental there are some differences that should be noted. Interestingly in the simulations, the fractal coil produced a higher mean field over the ROIs (**Figure 6**) and this discrepancy was reduced when power was compensated for. This can be explained by the fact that the fractal's field, as can be seen in **Figure 5**, is more concentrated into a smaller FOV, whereas the circular coil's field is more dispersed over a larger area. And so experimentally due to the MNS prescan (the fractal coil required less power than the circular coil), the coils produced the same field strength at the surface of the phantom and so the mean field strength's experimentally are quite similar. This same phenomenon can be seen in **Figure 7** as well, where in simulation the fractal coil produces a stronger field closer to the coil. As the ROI increases from 25 to 45 mm, the means of the coils at shallower depths converge, again confirming that the fractal coil's FOV is smaller with a field that is more concentrated to the center of the slice. And then again since the MNS Prescan calibrates the power such that the coils give equal field strength, the curves for the experimental data in **Figure 7** are essentially the same mean value.

The main similarity between the simulated magnetic fields and the experimental data is that the circular coil consistently had a lower standard deviation meaning higher homogeneity. However, it is important to note that since it's been determined that the FOV's of the two coils are different, it may be of some interest to investigate other ROI's of different shapes and sizes to more accurately deduce if the circular coil has a more homogeneous field for all applications.

SNR was calculated from the same 3D volume, over the same five ROIs as described above. Aligning with expectations that the coil with the more homogeneous B_1^+ field would provide a higher SNR, the circular coil produced a higher SNR measurement across all ROIs used. While this result is the opposite to our hypothesis there are still potential benefits to a fractal surface coil that deserve exploration. Sodium has only one resonance peak *in vivo*, but homogeneity over a wider excitation bandwidth was not explored as it is not necessary for sodium. As a fractal geometry consists of self-similar elements, each individual element of the whole can radiate as its own antenna, metaphorically. In

practicality what this means is the single element fractal antenna can have a wider bandwidth than a non-fractal antenna, or even be multi-band [8, 10, 12]. A wider bandwidth could improve the spectral homogeneity of the generated B_1^+ field. Improved transmit homogeneity would be beneficial for imaging nuclei with wide spectral bandwidths such as ^{13}C, ^{19}F and ^{31}P, especially when chemical shift imaging of these nuclei is being attempted.

In conclusion we found that, although a Koch snowflake shaped surface coil did not provide improved SNR or spatial homogeneity, the largest potential benefit is with reduced mutual inductance and robust impedance matching if implemented in phased array configurations. Phased array coils almost always provide higher SNR than their surface coil counterparts [24–26]. They can accelerate acquisitions via parallel imaging [27, 28] or compressed sensing techniques [29]. Multi-element arrays are a challenge to design and construct as geometric coupling plays a large role in the ability of the coil to function properly. There have been attempts to create unique geometries of elements to reduce this cross-talk and mutual inductance [30], but we believe the Koch snowflake would offer a more robust solution. As shown by the measured S_{21} parameters, the fractal design allows for more latitude when it comes to positioning individual elements over a surface, and provides minimal mutual inductance between a pair of coils. Another challenge facing phased array coils is that they are a challenge to manually rematch with each scan, and is seldom, if ever, done. The ability of a fractal design RF coil to provided a lower S_{11} over varying loads could also improve the signal transfer to the system, boosting SNR. Thus, further exploration into larger array fractal-based phased configurations, compared to arrays of circular coils, is warranted.

DATA AVAILABILITY STATEMENT

The raw data supporting the conclusion of this article will be made available by the authors, without undue reservation.

AUTHOR CONTRIBUTIONS

All authors listed have made a substantial, direct, and intellectual contribution to the work and approved it for publication.

FUNDING

Funding was provided through a Natural Sciences and Engineering Research Council (NSERC) Canada NSERC Discovery Grant (RGPIN-2017-06318) to MN.

REFERENCES

1. Burnier M. *Sodium in Health and Disease*. New York, NY: Informa Healthcare (2008).
2. Madelin G, and Regatte RR. Biomedical Applications of Sodium Mri *In Vivo*. *J Magn Reson Imaging* (2013) 38:511–29. doi:10.1002/jmri.24168
3. Berendsen HJC, and Edzes HT. The Observation and General Interpretation of Sodium Magnetic Resonance in Biological Material. *Ann NY Acad Sci* (1973) 204:459–85. doi:10.1111/j.1749-6632.1973.tb30799.x
4. Mispelter J, Lupu M, and Briguet A. *NMR Probeheads for Biophysical and Biomedical Applications*. London, UK: Imperial College Press (2015).
5. Gruber B, Froeling M, Leiner T, and Klomp DWJ. Rf Coils: A Practical Guide for Nonphysicists. *J Magn Reson Imaging* (2018) 48:590–604. doi:10.1002/jmri.26187
6. Mandelbrot BB. *Fractal Geometry of Nature*. New York, NY: W. H. Freeman (1983).
7. Lauwerier H, and Gill-Hoffstadt S. *Fractals: Endless Repeated Geometrical Figures*. Princeton, NJ: Princeton University Press (1991).
8. Cohen N. Fractal Antenna Applications in Wireless Telecommunications. In: Professional Program Proceedings: Electronic Industries Forum of New England. IEEE (1997). p. 43–9.
9. Werner DH, and Mittra R. *Frontiers in Electromagnetics*. New York, NY: IEEE Press (2000).
10. Cohen N. *Tuning Fractal Antennas and Fractal Resonators*. United States of America: US6104349 (2000).
11. Gianvittorio JP, and Rahmat-Samii Y. Fractal Antennas: A Novel Antenna Miniaturization Technique, and Applications. *IEEE Antennas Propag Mag* (2002) 44:20–36. doi:10.1109/74.997888
12. Gianvittorio JP, and Rahmat-Samii Y. Fractal Element Antennas: a Compilation of Configurations with Novel Characteristics. In: *IEEE Antennas and Propagation Society International Symposium. Transmitting Waves of Progress to the Next Millennium. 2000 Digest. Held in Conjunction with: USNC/URSI National Radio Science Meeting (Cat. No.00CH37118)*. IEEE (2000). p. 1688–91.
13. Frass-Kriegl R, Hosseinnezhadian S, Poirier-Quinot M, Laistler E, and Ginefri J-C. Multi-loop Radio Frequency Coil Elements for Magnetic Resonance Imaging: Theory, Simulation, and Experimental Investigation. *Front Phys* (2020) 7:16. doi:10.3389/fphy.2019.00237
14. Ha S, Nalcioglu O, and Roeck WW. *Fractal RF Coils for Magnetic Resonance Imaging*. United States of America: US20150048828A1 (2015).
15. Lemus OMD, Konyer NB, and Noseworthy MD. Micro-strip Surface Coils Using Fractal Geometry for 129Xe Lung Imaging Applications. In: Proceedings of the Joint Annual Meeting of ISMRM-ESMRMB; Paris, France. Concord, CA; ISMRM (2018).
16. Nowikow CE, Konyer NB, Yazdanbakhsh P, and Noseworthy MD. Koch snowflake Fractal Rf Surface Coils to Improve 23na-Magnetic Resonance Imaging at 3t. In: Proceedings of the 36th Annual Scientific Meeting of ESMRMB; Rotterdam, Netherlands. Vienna, Austria; ESMRMB (2019).
17. Schulte RF, Sacolick L, Deppe MH, Janich MA, Schwaiger M, Wild JM, et al. Transmit Gain Calibration for Nonproton Mr Using the Bloch-Siegert Shift. *NMR Biomed* (2011) 24:1068–72. doi:10.1002/nbm.1657
18. Sacolick LI, Wiesinger F, Hancu I, and Vogel MW. B1 Mapping by Bloch-Siegert Shift. *Magn Reson Med* (2010) 63:1315–22. doi:10.1002/mrm.22357
19. Beatty PJ, Nishimura DG, and Pauly JM. Rapid Gridding Reconstruction with a Minimal Oversampling Ratio. *IEEE Trans Med Imaging* (2005) 24:799–808. doi:10.1109/TMI.2005.848376
20. Fujita H, Zheng T, Yang X, Finnerty MJ, and Handa S. Rf Surface Receive Array Coils: The Art of an Lc Circuit. *J Magn Reson Imaging* (2013) 38:12–25. doi:10.1002/jmri.24159
21. Venook RD, Hargreaves BA, Gold GE, Conolly SM, and Scott GC. Automatic Tuning of Flexible Interventional Rf Receiver Coils. *Magn Reson Med* (2005) 54:983–93. doi:10.1002/mrm.20616
22. Reykowski A, and Duensing R. A Wireless Digital Capacitor Module for Tuning Receive Coil Arrays. In: Proceedings of the 23rd Annual Meeting of ISMRM; Milan, Italy. Concord, CA; ISMRM (2014).
23. Keil B, and Wald LL. Massively Parallel Mri Detector Arrays. *J Magn Reson* (2013) 229:75–89. doi:10.1016/j.jmr.2013.02.001
24. Bangerter NK, Kaggie JD, Taylor MD, and Hadley JR. Sodium MRI Radiofrequency Coils for Body Imaging. *NMR Biomed* (2016) 29:107–18. doi:10.1002/nbm.3392

25. Roemer PB, Edelstein WA, Hayes CE, Souza SP, and Mueller OM. The Nmr Phased Array. *Magn Reson Med* (1990) 16:192–225. doi:10.1002/mrm.1910160203
26. Hayes CE, Hattes N, and Roemer PB. Volume Imaging with Mr Phased Arrays. *Magn Reson Med* (1991) 18:309–19. doi:10.1002/mrm.1910180206
27. Ohliger MA, and Sodickson DK. An Introduction to Coil Array Design for Parallel Mri. *Magn Reson Med* (1999) 42:952–62. doi:10.1002/nbm.1046
28. Pruessmann KP, Weiger M, Scheidegger MB, and Boesiger P. Sense: Sensitivity Encoding for Fast Mri. *NMR Biomed* (2006) 19:300–15. doi:10.1002/nbm.1042
29. Blunck Y, Kolbe SC, Moffat BA, Ordidge RJ, Cleary JO, and Johnston LA. Compressed Sensing Effects on Quantitative Analysis of Undersampled Human Brain Sodium Mri. *Magn Reson Med* (2020) 83:1025–33. doi:10.1002/mrm.27993
30. Lakshmanan K, Brown R, Madelin G, Qian Y, Boada F, and Wiggins GC. An Eight-Channel Sodium/proton Coil for Brain Mri at 3 T. *NMR Biomed* (2018) 31:e3867. doi:10.1002/nbm.3867

Conflict of Interest: The authors declare that the research was conducted in the absence of any commercial or financial relationships that could be construed as a potential conflict of interest.

frontiers in Physics

TECHNOLOGY AND CODE
published: 28 September 2021
doi: 10.3389/fphy.2021.699468

Methods: Of Stream Functions and Thin Wires: An Intuitive Approach to Gradient Coil Design

Sebastian Littin[1]*, *Feng Jia*[1], *Philipp Amrein*[1] and *Maxim Zaitsev*[1,2]

[1]Medical Physics, Department of Radiology, Faculty of Medicine, University Freiburg, Freiburg, Germany, [2]High Field MR Center, Center for Medical Physics and Biomedical Engineering, Medical University of Vienna, Lazarettgasse, Austria

The design of gradient coils is sometimes perceived as complex and counterintuitive. However, a current density is connected to a stream function in fact by a simple relation. Here we present an intuitive open source code collection to derive stream functions from current densities on simple surface geometries. Discrete thin wires, oriented orthogonally to the main magnetic field direction are used to describe a surface current density. An inverse problem is solved and stream functions are derived to find coil designs in the current and stream function domains. The flexibility of the design method is demonstrated by deriving gradient coil designs on several different surface topologies. This collection is primarily intended for teaching, as well as for demonstrating all gradient coil design steps with openly available software tools.

Keywords: magnetic resonance imaging, gradient coil design, MRI hardware, boundary element method, stream function, open source

OPEN ACCESS

Edited by:
Simone Angela S. Winkler, Cornell University, United States

Reviewed by:
Isabelle Saniour, Weill Cornell Medicine, United States
Feng Liu, The University of Queensland, Australia

***Correspondence:**
Sebastian Littin
sebastian.littin@uniklinik-freiburg.de

Specialty section:
This article was submitted to Medical Physics and Imaging, a section of the journal Frontiers in Physics

Received: *23 April 2021*
Accepted: *31 August 2021*
Published: *28 September 2021*

Citation:
Littin S, Jia F, Amrein P and Zaitsev M (2021) Methods: Of Stream Functions and Thin Wires: An Intuitive Approach to Gradient Coil Design. Front. Phys. 9:699468. doi: 10.3389/fphy.2021.699468

1 INTRODUCTION

Gradient coils are the key component to enable imaging using **n**uclear **m**agnetic **r**esonance (NMR). Spatially varying magnetic fields are switched in a time dependent manner to achieve spatial encoding of the NMR signals. Different approaches to gradient coil design have been proposed over the past decades to derive very sophisticated designs compared to initially implemented Maxwell and Golay type coils [1,2].

Most approaches to gradient coil design today are based on boundary element methods [3,4]. These approaches are based on representing the actual electrical current density by its stream function discretized on a surface mesh. Due to the counterintuitive approximation of a surface current density by equidistant iso-contour lines of the stream function the coil design problem is oftentimes perceived as complex. However, the relation between the current density and stream function is oftentimes perceived as complex. For educational purposes the level of complexity of the boundary element method can be reduced to understand and design simple gradient coils. The coil design problem can be derived intuitively with an intermediate step which represents the current density. In addition it can be simplified by reducing its dimensionality if the current carrying surface is oriented in parallel to the main magnetic field. This is done by neglecting currents which flow in parallel to B_0 and therefore do not generate a B_z component relevant for encoding. Therefore we propose the most simple framework for coil design based on thin wires oriented orthogonally to the main magnetic field. This paper aims at providing an intuitive access to gradient coil design.

Abbreviations: FEM, finite element method; MRI, magnetic resonance imaging; NMR, nuclear magnetic resonance.

Additionally, Stream functions are derived from an intermediate representation of current densities and by a direct solution. The straight-forward, yet powerful approach presented here is suitable for simple, regular surface geometries such as cylinders or planes.

Most coil designs are derived by deploying commercially available closed source software, e.g. [5,6]. To the knowledge of the authors there is no code openly available which includes the surface mesh definition for gradient coil design, as well. One repository available on GitHub by Bringout et al. [7]. needs a predefined triangular surface mesh. Here, the mesh definition is included within the code that accompanies this paper and the complete sources are available on GitHub.

2 THEORY AND METHODS

All scripts to demonstrate this method were designed to run with GNU Octave and MatLab (The Mathworks, Nattick, MA, United States). Images in this manuscript were plotted with GNU Octave on a laptop computer.

Gradient coils for spatial encoding are usually operated with frequencies below $10kHz$, therefore the coil design may be treated as a magneto-static problem. The relation between the magnetic field of the gradient coil, $\mathbf{B}(\boldsymbol{r})$, and a free current density, $\mathbf{J}(\boldsymbol{r})$, is given by Ampere's law:

$$\nabla \times \mathbf{B}(\mathbf{r}) = \mu_0 \mathbf{J}(\mathbf{r}), \tag{1}$$

where μ_0 is the permeability of free space.

Conventional **m**agnetic **r**esonance **i**maging (MRI) usually deploys a main magnetic field which is highly uniform, unidirectional and very strong to achieve a sufficient spin polarization. Due to its historic origin from NMR, direction of the main field B_0 is by convention chosen along the z-axis. The local Larmor precession frequency only depends on the absolute value of the superposition of the main magnetic field and the field induced by the gradient coil. A Taylor expansion of this magnitude of the superposition field yields

$$\left|B_{0,z}\hat{\mathbf{z}} + \mathbf{B}(\mathbf{r})\right| \approx B_{0,z} + B_z(\mathbf{r}) + \frac{B_{xy}^2}{2 \cdot B_0} + \ldots, \tag{2}$$

where $\hat{\mathbf{z}}$ is a unit vector along z. For high field systems the magnitude of the main magnetic field, B_0, exceeds the magnitude of the gradient encoding fields typically about two orders of magnitude. Therefore, the expansion in **Eq. 2** can typically be terminated after the first order term, corresponding to the z-component $B_z(\mathbf{r})$, and the transverse field components $B_{xy}(\mathbf{r})$ can usually be neglected.

Thin-Wire Approximation

For simple, regular surface geometries such as planar or cylindrical, a current density, $\mathbf{J}(\boldsymbol{r})$, may be approximated by discrete thin wire segments. As only B_z is considered relevant for spatial encoding and due to the curl operation as in **Eq. 1** between the current and the generated magnetic field, the orientation of each current carrying element, m, is chosen to be orthogonal to the z-axis. Wires running parallel to B_0 produce no B_z component and can be used in this model to feed the orthogonal current segments. All feeding wires are allowed to overlap in space, as wire thickness is ignored in the basic thin-wire approximation.

Each orthogonal thin-wire segment m with a current I_m contributes to each target point n, which results in a spatially dependent magnetic field $B_{z,n}$, at point n, depicted in **Figure 1A**. The relation between the current in each thin-wire segment and the field of each point in space is described by the Biot-Savart law:

$$d\mathbf{B} = \frac{\mu_0 I d\mathbf{l} \times \mathbf{r}}{4\pi r^3} \tag{3}$$

Combining these relations defines the sensitivity matrix S_{nm}. By representing the currents in each thin wire segment as a vector, I_m, and extracting only the B_z component of the field vector, simple algebraic expressions become possible. The resulting gradient field is defined by the column vector, $B_{z,n}$, according to

$$B_{z,n} = S_{nm} \cdot I_m. \tag{4}$$

A corresponding current distribution for a given target field B_z^{target} may be calculated by deploying the pseudoinverse S_{nm}^{+} of S_{nm}. However, depending on the number of current elements m and number of target points n, the resulting system of linear equations may be under-determined. In addition, this inverse problem is ill-conditioned, as most inverse problems in magnetostatics. A direct inversion of such problems typically leads to impractical solutions such as depicted in **Figure 2A**.

Power Optimization

A Tikhonov regularization may be used to find solutions with smaller norms, which penalizes high opposing currents according to the following minimization problem

$$min\left(\left\|S_{nm} \cdot I_m - B_z^{target}\right\|_2^2 + \left\|\Gamma \cdot I_m\right\|_2^2\right). \tag{5}$$

Here, $\|\cdot\|_2$ is the Euclidean norm and Γ describes the Tikhonov matrix which is in this case chosen as the identity matrix multiplied by a regularization parameter λ:

$$\Gamma = \lambda 1. \tag{6}$$

The identity matrix in the Tikhonov regularization penalizes the sum of squares of the currents in each of the elements. This is proportional to the power dissipated by all elements and therefore acts to limit the total required electrical power. From a physics point of view the coefficient λ is related to the resistance of the wire segments. An appropriate choice of the weighting factor is balancing efficiency against accuracy of the resulting field. This free design parameter has to be chosen by the coil designer. Different approaches, e.g. the L-curve method [8] may be used to choose practical values. An exemplary regularized current distribution is shown in **Figure 2B**.

The Stream Function Representation and Discretization

Discrete wire layouts of gradient coil designs are usually derived from a stream function representation of surface currents. The stream function is then used to plot equidistant iso-contours, so

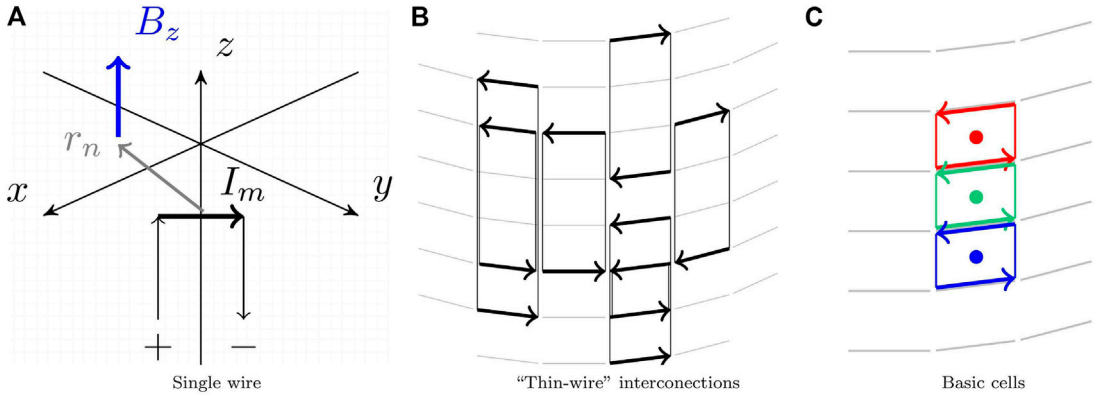

FIGURE 1 | (A) One current carrying element which hosts a current I_m generates a magnetic field component B_z at position r_n. Multiple discrete thin wires which are oriented orthogonal to the direction of the main magnetic field, z, may be used to approximate a current density, J, on a regular surface. **(B)** A coil design may be realized with closed loops if there is a return path for each current flowing along z. **(C)** A basic rectangular cell of a boundary element is defined by combining two neighboring thin-wire elements with opposite current directions. Each color depicts one basic cell. If only B_z is considered this cell is composed of two parallel wires.

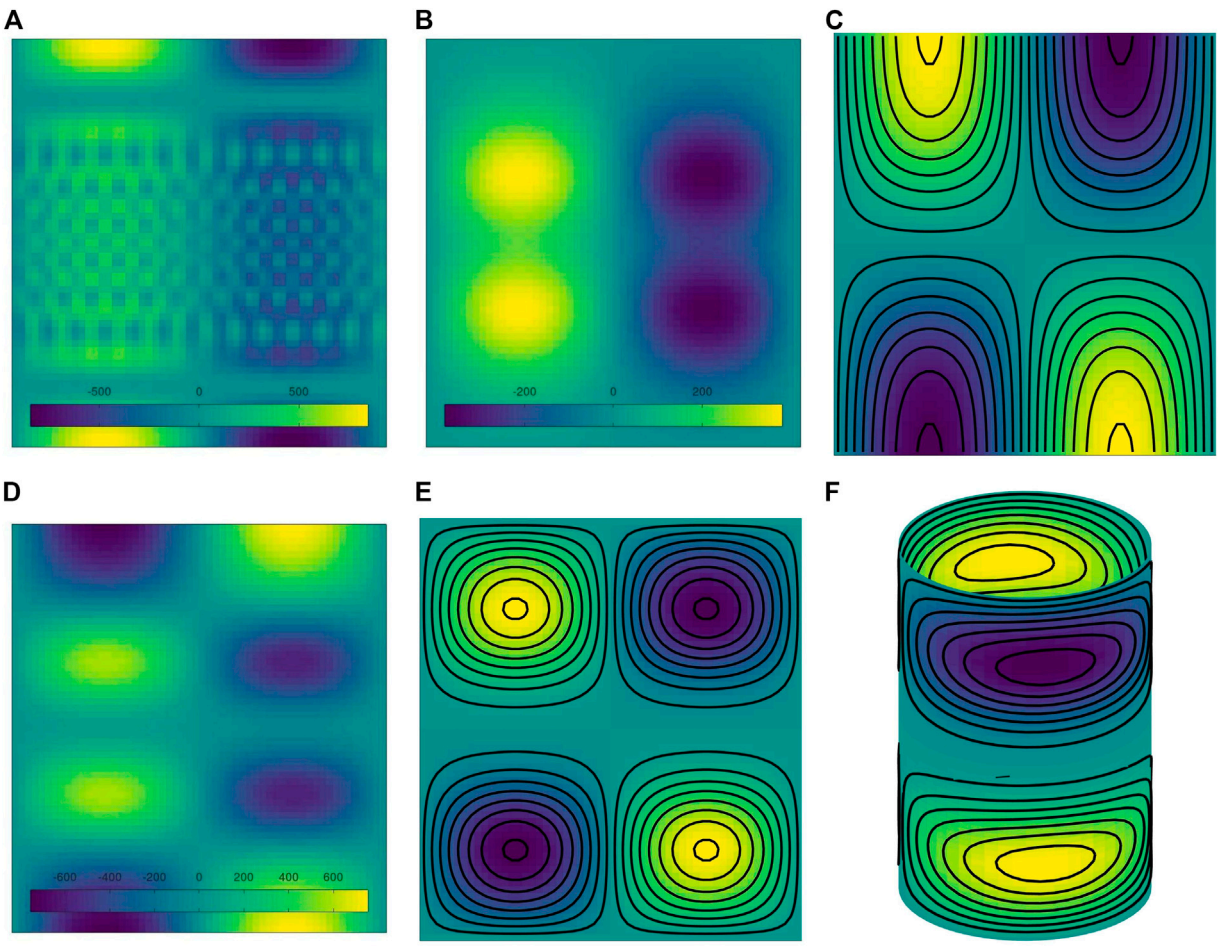

FIGURE 2 | Different steps to illustrate gradient coil design based on a surface current density. Scales are in [A]. **(A)** An un-regularized current density results in high opposing currents and is therefore very inefficient. **(B)** Regularization penalizes opposing currents. **(C)** Integration along the z yields the stream function. However, the discrete wire paths which are given by streamlines are not realizable by closed loops. **(D)** An additional constraint is added to ensure that the sum of currents along z equals zero. **(E)** The corresponding wire paths are now realizable as closed loops. **(F)** A 3D-rendering may be plotted by the supplied code.

called streamlines, representing trajectories of equally spaced steady flow of current. The number of streamlines is chosen according to engineering constraints, e.g. wire thickness, minimum wire spacing or maximum inductance.

The stream function is related to the current density by its integral. An integration of the previously regularized current density is depicted in **Figure 2C**. In matrix form, the integration may be directly acquired from the current density by calculating the cumulative sum along the z-direction according to

$$[a, b, c, \ldots] = [a, a + b, a + b + c, \ldots]. \tag{7}$$

Here, it should be noted that the depicted discrete coil layout may not be realized by closed loops, leading to a gradient coil requiring many current terminals on each side. The example shown in **Figure 2C** would require current terminals and sinks of twice the number of iso-contours on each side, which is impractical.

Realizing Closed Loops

As depicted in **Figure 2C**, even the regularized current distribution may not be realizable in a straight-forward manner due to a high number of feeding ports. An additional constraint, enforcing the sum of currents along the z-axis to be zero along the surface boundaries, ensures for a design with closed loops. This constraint is given by

$$\sum_z I_{ij,z} = 0. \tag{8}$$

In this equation the index m is replaced by two indices, corresponding to the position of represented segments in the 2D matrix. Effectively, this is equivalent to Kirchhoff's current law, which states the principle of the electric charge conservation. If this condition is fulfilled, for each current flowing along the direction orthogonal to z there is an opposing current, or currents with the same ij coordinate, present elsewhere along the z axis. Closed loops, including their feeding wires running in parallel to B_0 needed to fulfill **Eq. 8** are sketched in **Figure 1B**. Such interconnections along z might even be realized without altering the resulting target field B_z. On continuous surfaces of simple topologies this ensures a design which is realizable with closed current loops on this surface. In the practical implementation **Eq. 8** can be converted to a matrix form and appended to **Eq. 5** before solving the regularization problem.

Closed loop iso-contours derived from the stream function requires some manual interaction to get realizable gradient coil design, which can be manufactured by a single wire. Manual addition of connections between neighboring iso-contour lines transforms each quadrant into a spiral. Connections are usually chosen along the z-direction while return paths are positioned on top to mitigate effects from the introduced changes [9]. An automated process to interconnect multiple groups of streamlines has been proposed recently [10]. However, such an automatic approach is beyond the scope of this work.

Additional constraints may be added to enforce further design requirements. Exemplary mentioned here is the balance of force or torque which may be expressed by simple matrix operations, as well. Assuming thin wires which host currents I_n orthogonal to a strong and unidirectional main magnetic field B_z the force on each discrete element, n, is given by

$$\overrightarrow{F_n} = I_n \cdot \vec{l} \times \vec{B}. \tag{9}$$

To account for field inhomogeneities, the main magnetic field B needs to be defined at each wire location. Accordingly, the excess torque may now be calculated by summation over all moments from force F at position r. The resulting term

$$\overrightarrow{M} = \sum_n r_n \times \overrightarrow{F_n}, \tag{10}$$

may be added and minimized during the optimization. A regularization parameter has to be added for an adequate weighting of the constraints. Balancing multiple regularization parameters is the art of coil design and usually requires a comparison of multiple designs within a reasonable parameter space [11].

From Current Distributions to Stream Functions

The thin-wire approximation provides an already powerful approach to find realizable gradient coil designs. However, the coil layout is not directly derived, but requires and intermediate step in the current domain.

For calculating stream functions, the boundary element method is usually deployed. Most methods are based on triangular meshes, each triangle describing one boundary element. However, **f**inite **e**lement **m**ethods (FEMs) in general are not limited to triangular meshes. Boundary elements with a rectangular mesh may be used, as well (e.g. [12,13]). Considering only the z-component of the magnetic field, a simplified rectangular element may be derived from two neighboring thin wires, as used in the thin-wire approach. Since connecting paths along the z-axis do not contribute to B_z, they may be neglected. A basic cell from wire elements is sketched in **Figure 1C**.

Corresponding to the sensitivity matrix S (**Eq. 4**) a similar sensitivity matrix in the stream function domain S_{stream} may be derived. Size of the original sensitivity matrix S is given by the number of target points, n, the number of circumferential segments, m_c, and number of segments along z, m_z, S_{n,m_c,m_z}. The stream function sensitivity S_{stream} is given by spatial derivative along z of the sensitivity S. In a matrix-like notation the stream function sensitivity is defined as

$$S_{stream} = S_{n,m}(:, 1{:}\ end - 1) - S_{n,m}(:, 2{:}\ end). \tag{11}$$

In analogy to the inverse problem stated in **Eq. 5** a corresponding current value may be calculated. For regularizing this equation an effective current has to be used which consists of the combination from currents of two neighboring cells at the same location which can be achieved by an appropriate modification of the matrix Γ.

As previously shown, closed loops were enforced in the current domain by a constraint which was defined in a global manner (see **Eq. 8**). Due to the definition of the stream-function as spatial difference between two neighboring current carrying

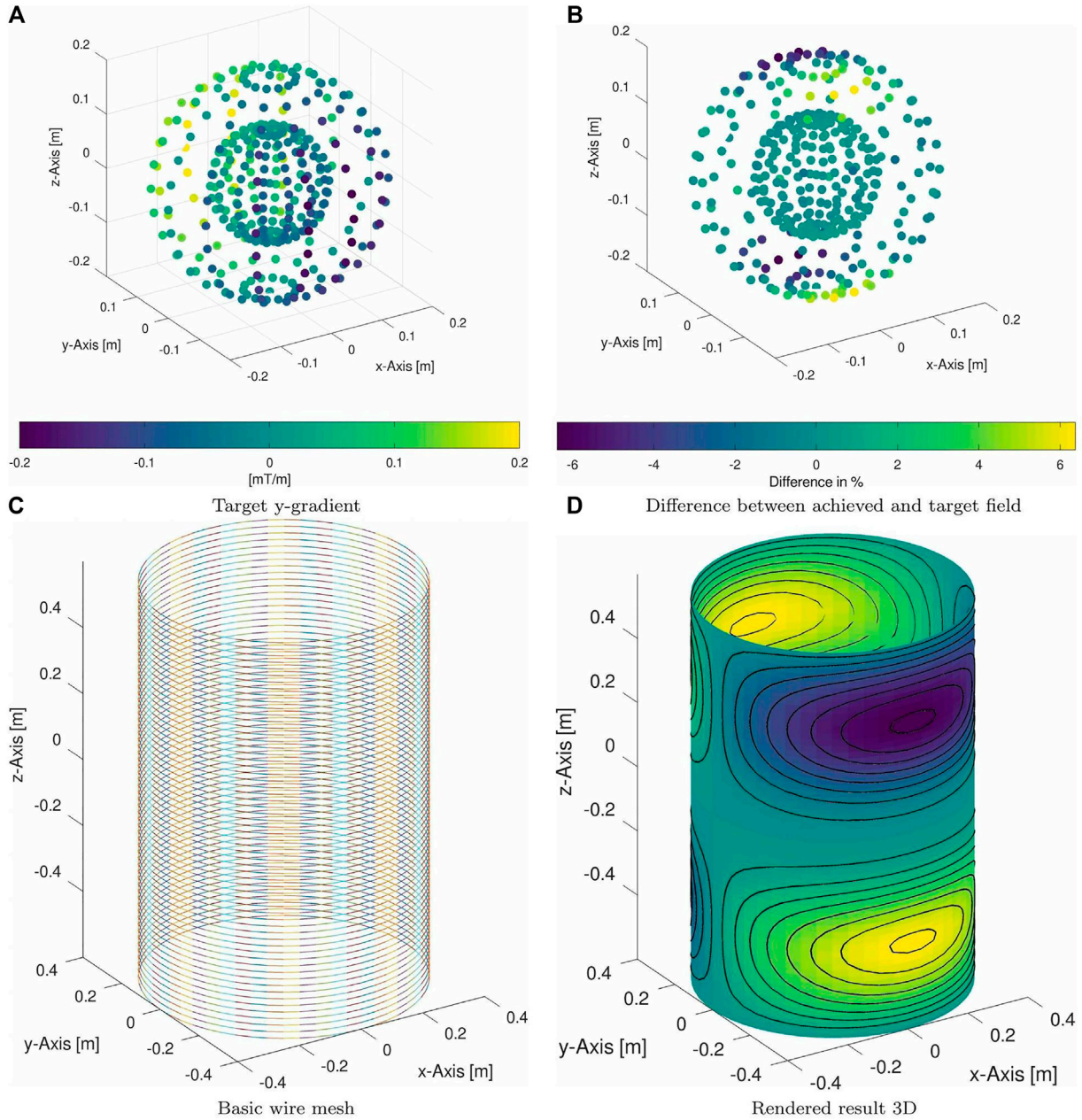

FIGURE 3 | (A) A spherical y-gradient target with 1 [mT/m] was used for the cylindrical coil design. **(B)** The difference between target and generated field is depicted. **(C)** The mesh for the optimization consists of single individual wires which are oriented orthogonal to the main field direction. **(D)** 3D-rendering with dimensions of the resulting cylindrical whole-body gradient design.

elements the same constraint does not lead to a meaningful result. Therefore closed loops have to be enforced using a different strategy. The approach chosen here was to demand the peripheral elements to carry zero current. This requires the addition of further terms to the inverse problem. Same currents of all outer elements, in this case zero, ensures closed stream lines. In analogy to the closed loops, further constraints may be added similarly. As stated above, this may include balance of force and torque, maximum current density or others.

The basic idea of the coil design method is demonstrated using the dimensions of a cylindrical whole-body gradient setup with a radius of 0.4 [m], a length of 1.2 [m], a mesh density of 56 angular by 61 longitudinal elements. A y-gradient with a 1 [mT/m] spherical target field with a radius of 0.2 [m] was chosen.

Besides a simple cylinder other geometries were simulated to demonstrate the variability of the method. This includes a shielded setup which consists of two independent cylindrical surfaces with radii of 0.4 [m] and 0.5 [m] and a length of 1.2 [m]. A thin-wire

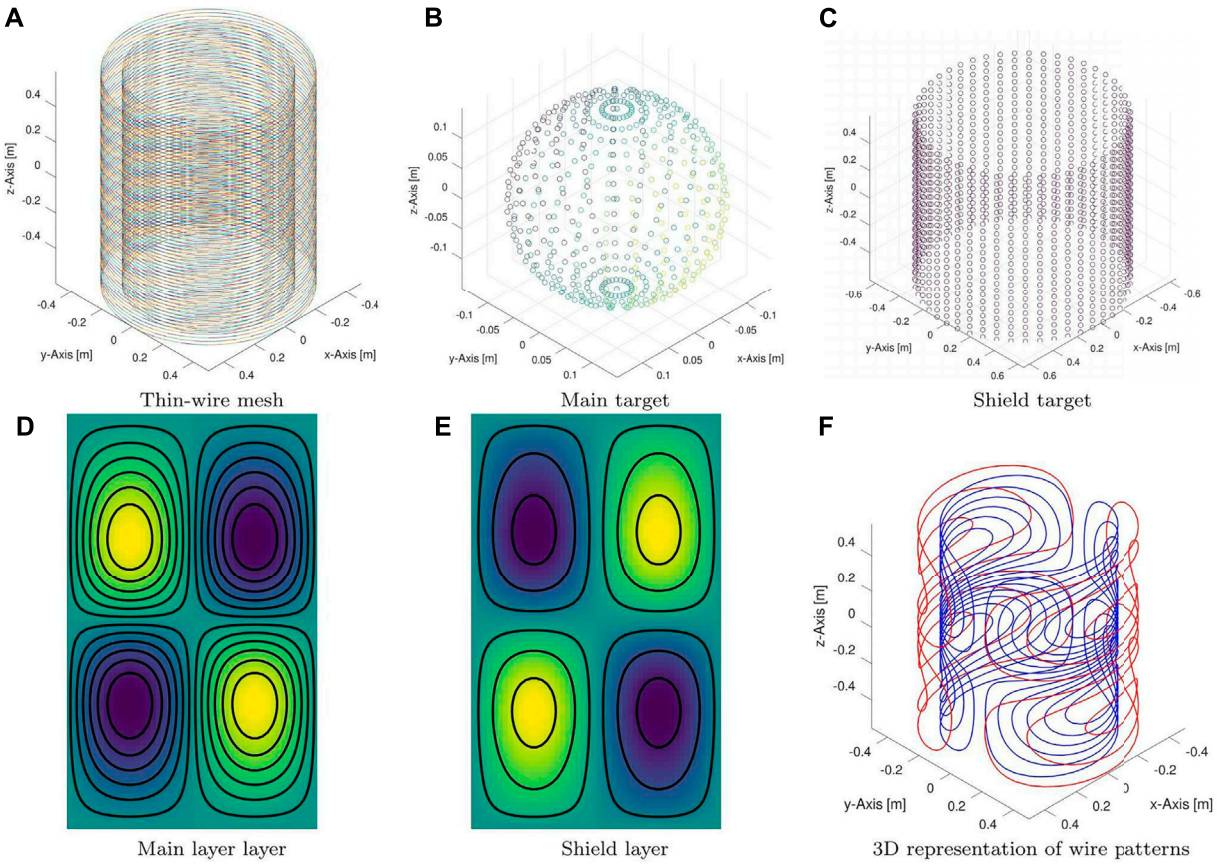

FIGURE 4 | (A) The design of a shielded gradient coil hosts currents on two independent surfaces. In such a design the goal is to achieve a target field in center **(B)**, while suppressing fields outside the coil. **(C)** The magnetic field on an additional cylindrical target surface, representing the cryostat, was set to zero. Depicted are **(D)** the main layer, **(E)** the shielding layer and **(F)** a combined representation of the resulting coil design.

mesh of 48 angular by 61 longitudinal elements was chosen on each cylinder along with a spherical target with a radius of 0.15 $[m]$.

A biplanar coil setup with two flat surfaces of 0.6 $[m] \times 0.6$ $[m]$ separated by 0.4 $[m]$ with a mesh of 61×61 elements was used to demonstrate the feasibility of flat surfaces. The target region was chosen to be spherical with a radius of 0.15 $[m]$.

An additional level of complexity is added for split gradient coils e.g. for multi-modality or combined MR-Linac systems [14,15]. Such coils in a shielded arrangement consist of four independent current carrying surfaces. Dimensions of the cylindrical shielded coil were used as a basis to simulate such a setup with radii of 0.4 $[m]$ and 0.5 $[m]$, a length of 0.6 $[m]$ and a separation along z of 0.2 $[m]$. A thin-wire mesh of 48 angular by 61 longitudinal elements was chosen on each cylinder along with a spherical target with a radius of 0.15 $[m]$. Plots of each surface mesh are included in the code supplied with this paper.

The strength for each target field was set to 1 $[mT/m]$ and the number of iso-contours was chosen to allow for a good visualization for plotting. It should be noted that the actual number of iso-contours is usually chosen based on constraints given by the overall system design. For larger coils the choice is a trade-off between efficiency and possible switching speed which is limited by the available maximum current and voltage. For smaller coils the number of iso-contours is mostly limited by the available space which is needed for a finite wire thickness.

3 RESULTS

To demonstrate the versatility of the proposed method, stream functions based on discrete current distributions have been calculated for multiple different numbers of independent current carrying surfaces and different coil geometries. A gradient coil design on a single surface is given by the cylindrical design shown in **Figure 2**. The original target field along with the deviation of the resulting field is depicted in **Figure 3**. The regularization chosen here results in a deviation of about ±6%. This deviation may be controlled by the relation between the regularization and the chosen dimensions.

Cylindrical shielded gradient coils are usually used in high-field MRI scanners to suppress eddy currents in the cryostat [16–18]. Therefore, a second target region is defined on a cylindrical surface at the position of the cold radiation shield. A wire mesh along with the main and shield target is shown in **Figure 4**. Compared to the main layer, the shield exhibits opposite polarity which corresponds to opposite direction of currents.

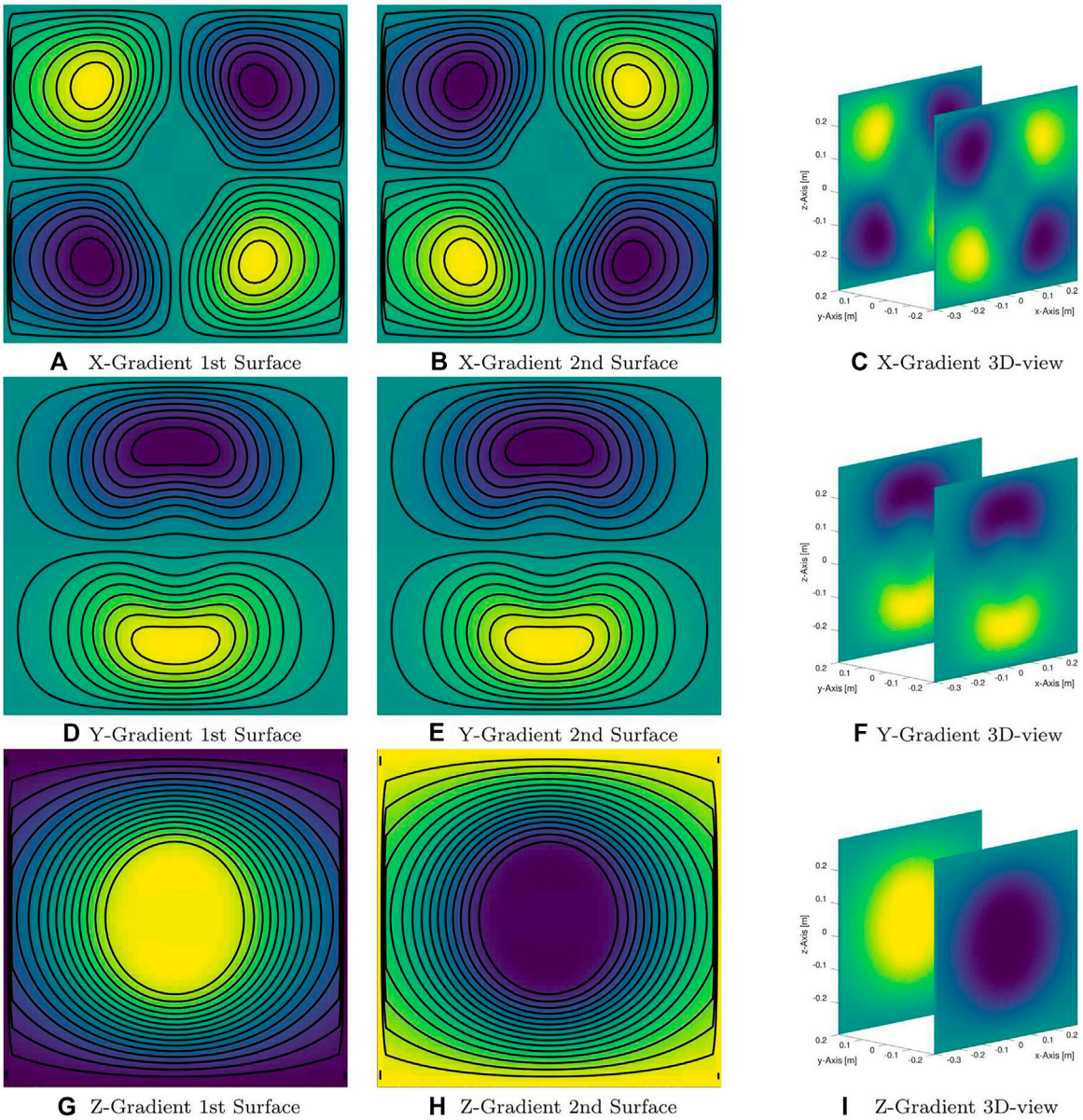

FIGURE 5 | Bi-planar design to demonstrate the feasibility of using flat surface geometries. Direction of the main magnetic field is along the *z*-axis. Both surfaces (first and second row) along with a 3D visualization are shown for three different gradient fields. Currents on all edges of both surfaces had to be forced to zero for achieving closed loops.

A biplanar set of coils deploys two independent current carrying surfaces and is depicted in **Figure 5**. One should keep in mind that most biplanar setups in the literature are designed for a main magnetic field which is oriented along the vertical axis. However, this is not the case in the example shown here.

An additional level of complexity is added in the design of split coils e.g. for multi-modality or combined MR-Linac systems [14,15]. Such coils in a shielded arrangement consist of four independent current carrying surfaces. Resulting wire layouts are shown in **Figure 6**. Same dimensions as for the previous shielded design and a gap of 0.2 m was chosen.

One of the main results is the code which was used to generate the rectangular thin-wire mesh and all designs within this manuscript. The full code is available as supporting material and under[1].

4 DISCUSSION

One of the main motivations for this work is the educational aspect, introducing gradient coil design in a straight-forward, intuitive and

[1]https://github.com/Sebastian-MR/ThinWire_MRIGradientCoilDesign

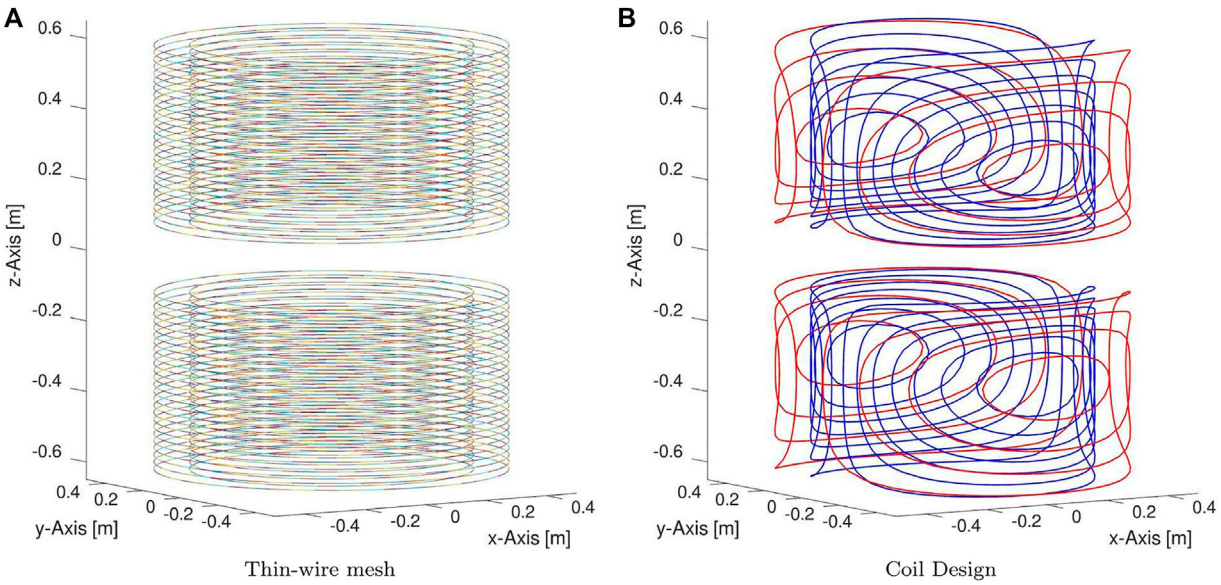

FIGURE 6 | A shielded split coil design with four independent current carrying surfaces. Depicted are **(A)** the thin-wire mesh and **(B)** the resulting wire layout. Such designs are usually deployed in systems which combine linear accelerators for cancer treatment with MRI for imaging.

easy to understand way. To do so, we approach the gradient coil design from a current-density perspective. If the magnitude of the encoding field is much smaller than the main field strength a simplified representation becomes possible by considering the z-component of the magnetic field, only. Hence one field component instead of all three has to be calculated while significantly reducing the computational effort. Versatility of the proposed method is demonstrated by coil designs on flat and cylindrical surfaces. Coil designs on multiple independent current carrying surfaces are demonstrated by a shielded and a split shielded design.

The coil design methods shown are closely related to previously shown boundary element approaches, e.g. [3,4] which have been maximally reduced. Due to the reduction to B_z only, the optimization may not be usable directly for all magnet types. For classical and superconducting electromagnets the current carrying surface(s) are usually orthogonal to the main magnetic field, regardless of field strength. MRI systems based on rare Earth magnets are usually orientated such, that the current carrying surfaces of the gradient coils are not perpendicular to the direction of the main magnetic field. This includes u-shaped and Hallbach array type magnets [19–22] and others. However, the reduced form presented here may be easily adapted by adding longitudinal thin-wires to consider all field components, including B_{xy}, and closing the boundary element loops. Such a possible addition comes with an increased computational effort.

Due to the simplification using only wires orthogonal to the z-axis, the current method is limited to regular surface geometries. Methods for arbitrary surfaces have been shown e.g. in [5,23]. It should be noted that for manufacturing reasons most gradient coils are realized in fact on simple surfaces. However, with new manufacturing techniques based on 3D printed materials, such as shown in [24] other shapes might be used more often in the future. For such cases a full description of all components of the current density is also possible. For instance in the literature on the FEM methodology, approaches to shear and deform rectangular elements are usually covered, e.g. [12,13]. In the context of gradient coil design non-triangular mesh elements have been used, as well [25,26].

Minimum wire distance is one of the engineering constraints which has to be considered during the design. This has not been considered in the designs presented here and the associated problems are most apparent in the bi-planar designs in **Figure 5**. One approach is to choose the number of coil turns according to spatial constraints. More sophisticated approaches constrain the gradient of the stream function, the current density, using a minimax design or a p-norm [6,27]. Alternatively, an explicit constraint could be relatively trivially added directly to the thin-wire solver.

As a further step the iso-contour lines of the stream function have to be interconnected. A automatized interconnection algorithm has been demonstrated recently [10]. We hope that a combination of the intuitive approach to coil design shown here with an easy to use interconnection algorithm lowers the boundary for making experimental gradient coils.

A further goal of this publication was to make gradient coil design code which covers main aspects of the coil design problem, including surface mesh definition, available to the public. In addition to the supplemented materials, the code is available on GitHub under[1]. We hope that additional adaptations of the code are available in the future, including extensions to arbitrary orientations of the main magnetic field, e.g. for systems based on Halbach type magnets.

[1]https://github.com/Sebastian-MR/ThinWire_MRIGradientCoilDesign

DATA AVAILABILITY STATEMENT

The datasets presented in this study can be found in the **Supplementary Material** and on github: https://github.com/Sebastian-MR/ThinWire_MRIGradientCoilDesign.

AUTHOR CONTRIBUTIONS

SL: Wrote code and manuscript FJ: Support with Code gradient design questions PA: Support with Code gradient design questions MZ: Initial code idea, supervision and guidance.

FUNDING

The article processing charge was funded by the Baden-Wuerttemberg Ministry of Science, Research and Art and the University of Freiburg in the funding program Open Access Publishing.

SUPPLEMENTARY MATERIAL

The Supplementary Material for this article can be found online at: https://www.frontiersin.org/articles/10.3389/fphy.2021.699468/full#supplementary-material

REFERENCES

1. Turner R. Gradient Coil Design: A Review of Methods. *Magn Reson Imaging* (1993) 11:903–20. doi:10.1016/0730-725X(93)90209-V
2. Hidalgo-Tobon SS. Theory of Gradient Coil Design Methods for Magnetic Resonance Imaging. *Concepts Magn Reson* (2010) 36A:223–42. doi:10.1002/cmr.a.20163
3. Lemdiasov RA, and Ludwig R. A Stream Function Method for Gradient Coil Design. *Concepts Magn Reson* (2005) 26B:67–80. doi:10.1002/cmr.b.20040
4. Poole M, and Bowtell R. Novel Gradient Coils Designed Using a Boundary Element Method. *Concepts Magn Reson* (2007) 31B:162–75. doi:10.1002/cmr.b.20091
5. Handler WB, Harris CT, Scholl TJ, Parker DL, Goodrich KC, Dalrymple B, et al. New Head Gradient Coil Design and Construction Techniques. *J Magn Reson Imaging* (2014) 39:1088–95. doi:10.1002/jmri.24254
6. Jia F, Littin S, Layton KJ, Kroboth S, Yu H, and Zaitsev M. Design of a Shielded Coil Element of a Matrix Gradient Coil. *J Magn Reson* (2017) 281:217–28. doi:10.1016/j.jmr.2017.06.006
7. Bringout G, and Buzug TM. Coil Design for Magnetic Particle Imaging: Application for a Preclinical Scanner. *IEEE Trans Magn* (2015) 51:1–8. doi:10.1109/tmag.2014.2344917
8. Hansen PC The L-Curve and its Use in the Numerical Treatment of Inverse Problems In P. Johnston, editor *Computational Inverse Problems in Electrocardiology Advances in Computational Bioengineering*. Ashurst, UK: WIT Press (2000). p. 119–142.
9. Peeren GN. Stream Function Approach for Determining Optimal Surface Currents. *J Comput Phys* (2003) 191:305–21. doi:10.1016/s0021-9991(03)00320-6
10. Jia F, Littin S, and Zaitsev M. Routing Algorithm for the Interconnection of Closed Wire Loops for Mr Gradient and Mr Shim Coils. Proceedings of the 2020 ISMRM and SMRT Virtual Conference and Exhibition (2020), 4070.
11. Cobos Sanchez C, Fernandez Pantoja M, Poole M, and Rubio Bretones A. Gradient-coil Design: A Multi-Objective Problem. Conference Name: IEEE Transactions on Magnetics. *IEEE Trans Magn* (2012) 48:1967–75. doi:10.1109/TMAG.2011.2179943
12. Jin JM. *The Finite Element Method in Electromagnetics*, Vol. 3. Wiley-IEEE Press (2014).
13. Brenner SC, and Scott LR. *The Mathematical Theory of Finite Element Methods*, 15. New York, NY: Springer (2008). doi:10.1007/978-0-387-75934-0
14. Poole M, Bowtell R, Green D, Pittard S, Lucas A, Hawkes R, et al. Split Gradient Coils for Simultaneous Pet-Mri. *Magn Reson Med* (2009) 62:1106–11. doi:10.1002/mrm.22143
15. Tang F, Freschi F, Sanchez Lopez H, Repetto M, Liu F, and Crozier S. Intra-coil Interactions in Split Gradient Coils in a Hybrid MRI-LINAC System. *J Magn Reson* (2016) 265:52–8. doi:10.1016/j.jmr.2016.01.013
16. Mansfield P, and Chapman B. Active Magnetic Screening of Coils for Static and Time-dependent Magnetic Field Generation in NMR Imaging. *J Phys E: Sci Instrum* (1986) 19:540–5. doi:10.1088/0022-3735/19/7/008
17. Roemer PB, and Hickey JS. Self-shielded Gradient Coils for Nuclear Magnetic Resonance Imaging. *Magn Reson Imaging* (1986) 1986:1038–94. doi:10.1002/mrmp.22419860310
18. Bowtell R, and Mansfield P. Gradient Coil Design Using Active Magnetic Screening. *Magn Reson Med* (1991) 17:15–21. doi:10.1002/mrm.1910170105
19. Halbach K. Strong Rare Earth Cobalt Quadrupoles. *IEEE Trans Nucl Sci* (1979) 26:3882–4. doi:10.1109/tns.1979.4330638
20. Halbach K. Design of Permanent Multipole Magnets with Oriented Rare Earth Cobalt Material. *Nucl Instr Methods* (1980) 169:1–10. doi:10.1016/0029-554X(80)90094-4
21. Raich H, and Blümler P. Design and Construction of a Dipolar Halbach Array with a Homogeneous Field from Identical Bar Magnets: Nmr Mandhalas. *Concepts Magn Reson* (2004) 23B:16–25. doi:10.1002/cmr.b.20018
22. Cooley CZ, Haskell MW, Cauley SF, Sappo C, Lapierre CD, Ha CG, et al. Design of Sparse Halbach Magnet Arrays for Portable Mri Using a Genetic Algorithm. *IEEE Trans Magn* (2018) 54:1–12. doi:10.1109/tmag.2017.2751001
23. Lemdiasov RA, and Ludwig R. A Stream Function Method for Gradient Coil Design. *Concepts Magn Reson* (2005) 26B:67–80. doi:10.1002/cmr.b.20040
24. Littin S, Jia F, Layton KJ, Kroboth S, Yu H, Hennig J, et al. Development and Implementation of an 84-channel Matrix Gradient Coil. *Magn Reson Med* (2018) 79:1181–91. doi:10.1002/mrm.26700
25. Zhu M, Xia L, Liu F, Zhu J, Kang L, and Crozier S. A Finite Difference Method for the Design of Gradient Coils in MRI-An Initial Framework. *IEEE Trans Biomed Eng* (2012) 59:2412–21. doi:10.1109/TBME.2012.2188290
26. Kang L, Xia L, Wang Q, Wang Y, Tang F, and Liu F. A Volumetric Finite-Difference Method for the Design of Three-Dimensional, Arbitrary-Structured Mri Gradient Coil. *Rev Scientific Instr* (2021) 92:034712. doi:10.1063/5.0035118
27. Poole MS, While PT, Lopez HS, and Crozier S. Minimax Current Density Gradient Coils: Analysis of Coil Performance and Heating. *Magn Reson Med* (2012) 68:639–48. doi:10.1002/mrm.23248

Conflict of Interest: The authors declare that the research was conducted in the absence of any commercial or financial relationships that could be construed as a potential conflict of interest.

Publisher's Note: All claims expressed in this article are solely those of the authors and do not necessarily represent those of their affiliated organizations, or those of the publisher, the editors and the reviewers. Any product that may be evaluated in this article, or claim that may be made by its manufacturer, is not guaranteed or endorsed by the publisher.

frontiers in Physics

ORIGINAL RESEARCH
published: 08 October 2021
doi: 10.3389/fphy.2021.716521

Potential Reduction of Peripheral Local SAR for a Birdcage Body Coil at 3Tesla Using a Magnetic Shield

C.C. van Leeuwen[1], B.R. Steensma[1], S.B. Glybovski[2], M.F.J. Lunenburg[3], C. Simovski[4], D.W.J. Klomp[1], C.A.T. van den Berg[1] and A.J.E. Raaijmakers[1,5]*

[1]Department of Radiology, University Medical Center Utrecht, Utrecht, Netherlands, [2]Faculty of Physics and Engineering, ITMO University, St. Petersburg, Russia, [3]Tesla Dynamic Coils, Zaltbommel, Netherlands, [4]Department of Electronics and Nanoengineering, Aalto University, Espoo, Finland, [5]Biomedical Engineering Department, Eindhoven University of Technology, Eindhoven, Netherlands

The birdcage body coil, the standard transmit coil in clinical MRI systems, is typically a shielded coil. The shield avoids interaction with other system components, but Eddy Currents induced in the shield have an opposite direction with respect to the currents in the birdcage coil. Therefore, the fields are partly counteracted by the Eddy currents, and large coil currents are required to reach the desired B_1^+ level in the subject. These large currents can create SAR hotspots in body regions close to the coil. Complex periodic structures known as metamaterials enable the realization of a magnetic shield with magnetic rather than electric conductivity. A magnetic shield will have Eddy currents in the same direction as the coil currents. It will allow generating the same B_1^+ with lower current amplitude, which is expected to reduce SAR hotspots and improve homogeneity. This work explores the feasibility of a birdcage body coil at 3 T with a magnetic shield. Initially, we investigate the feasibility by designing a scale model of a birdcage coil with an anisotropic implementation of a magnetic shield at 7 T using flattened split ring resonators. It is shown that the magnetic shield destroys the desired resonance mode because of increased coil loading. To enforce the right mode, a design is investigated where each birdcage rung is driven individually. This design is implemented in a custom built birdcage at 7 T, successfully demonstrating the feasibility of the proposed concept. Finally, we investigate the potential improvements of a 3 T birdcage body coil through simulations using an idealized magnetic shield consisting of a perfect magnetic conductor (PMC). The PMC shield is shown to eliminate the peripheral regions of high local SAR, increasing the B_1^+ per unit maximum local SAR by 27% in a scenario where tissue is present close to the coil. However, the magnetic shield increases the longitudinal field of view, which reduces the transmit efficiency by 25%.

Keywords: birdcage (BC) coil, SAR, metamaterial, split ring resonator (SRR), MRI, RF, antenna, magnetic shield

OPEN ACCESS

Edited by:
Sigrun Roat,
Medical University of Vienna, Austria

Reviewed by:
Daniel Wenz,
École Polytechnique Fédérale de Lausanne, Switzerland
Angelo Galante,
University of L'Aquila, Italy

****Correspondence:***
C.C. van Leeuwen
C.C.vanleeuwen-11@umcutrecht.nl

Specialty section:
This article was submitted to Medical Physics and Imaging, a section of the journal Frontiers in Physics

Received: *28 May 2021*
Accepted: *31 August 2021*
Published: *08 October 2021*

Citation:
van Leeuwen CC, Steensma BR, Glybovski SB, Lunenburg MFJ, Simovski C, Klomp DWJ, van den Berg CAT and Raaijmakers AJE (2021) Potential Reduction of Peripheral Local SAR for a Birdcage Body Coil at 3 Tesla Using a Magnetic Shield. Front. Phys. 9:716521. doi: 10.3389/fphy.2021.716521

INTRODUCTION

The birdcage body coil [1] has been the standard transmit coil in almost all MRI systems for well over 30 years. With two ports, it allows for quadrature excitation and reception and provides excellent homogeneity. Birdcage body coils are surrounded by a shield, which screens external radio frequency (RF) signals and prevents unwanted interactions with other parts of the scanner. Typically, such an RF shield consists of copper foil, in which some precaution has been made to reduce low frequency eddy currents (e.g., [2, 3]) due to switching of the gradients. A downside of such a shield is that the

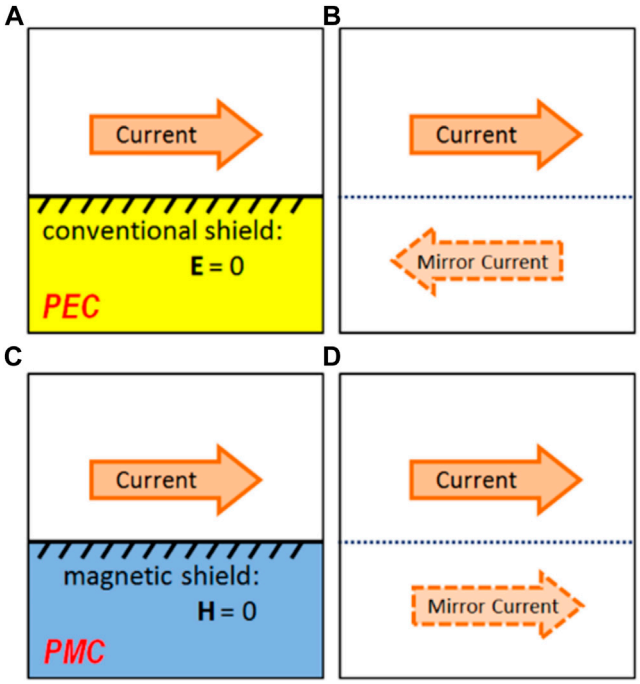

FIGURE 1 | Illustration of how the method of mirror currents can be used to describe shielded currents. **(A)** A conventional shield with high electric conductivity (modeled as a perfect electric conductor) does not allow electric fields to penetrate. As a result, the tangential component of the electric field is zero at the boundary. **(B)** An out-of-phase mirror current at the opposite side of the shield (dotted line) satisfies the same boundary condition on the shield and realizes the same field distributions. **(C)** A magnetic shield (modeled as a perfect magnetic conductor) does not allow magnetic fields to penetrate. As a result, the tangential component of the magnetic field is zero at the boundary. **(D)** An in-phase mirror current at the opposite side of the shield (dotted line) satisfies the same boundary condition on the shield and realizes the same field distributions.

currents in the birdcage coil induce eddy currents in the shield, which are described by out-of-phase mirror currents. The B_1 field produced by these eddy currents in the shield interferes destructively with the field produced by the coil. This reduces the B_1 field strength per unit current. For this reason, larger currents are required to reach a desired B_1 level. These strong currents are associated with large amounts of reactive energy [4], which can dramatically increase Specific Absorption Rate (SAR) levels in close proximity to the coil.

To prevent tissue damage due to high SAR, the International Electrotechnical Commission (IEC) provides guidelines that limit the amount of power that may be deposited in patients. For whole body coils, the limit is set to 4 W/kg of global SAR at the first level controlled operation mode, averaged over 6 min [5]. No limits are set for local SAR when a whole body birdcage coil is used for transmission. However, recent studies [6–12] indicate that SAR hotspots can cause local temperatures to exceed 40°C without exceeding the global SAR limit. Although the extensive history of safe use of current clinical MRI scanners provides strong confidence in its safety, it is still with some unease that these local temperature levels are regarded. In this work, we explore the potential reduction of local SAR by adapting the RF shield of the birdcage body coil using a magnetically conducting shield.

A conventional copper shield imposes a boundary condition ($\mathbf{E}_{tan} = 0$) at the metal surface due to its high conductivity. To satisfy this boundary condition, the currents in the shield (described by mirror currents) must have opposite phase with respect to the source currents (**Figures 1A,B**). The destructive interference can be alleviated by placing the shield at further distance. In the extreme case, the shield could be placed at a distance of one-quarter wavelength at which the mirror currents constructively interfere due to phase retardation over the distance. However, such an approach requires very large bore diameters, which is not feasible. In practice, every inch of bore diameter is precious and the body coil should be realized as thin as possible. Some hybrid approach is to have the birdcage's rungs bend slightly inward. This increases the distance between the shield and the rungs, reducing destructive interference [13]. As an alternative, Foo et al. [14] have explored analytically the possibility of filling the space between the coil and the shield with dielectric material but only considered the idealized case where the coil, shield, and phantom have infinite length. Liu et al. [15] have investigated various ways of adapting the birdcage and shield to provide different return paths for the current. They found small improvements in terms of homogeneity and Signal-to-Noise Ratio (SNR) but did not evaluate SAR. However, recent advances in electromagnetics of complex periodic structures known as metamaterials have opened up new routes for improving the RF shield. In this work, we propose the use of a magnetic shield for a birdcage body coil.

A magnetic shield [16, 17] is a shield that exhibits *magnetic* conductivity (instead of "normal" electric conductivity), which implies that the tangential component of the magnetic field is zero at the boundary. Eddy currents in a magnetic shield are described by in-phase mirror currents (see **Figures 1C,D**), which interfere constructively with the field produced by the coil. This increases the amount of field generated per unit current.

While true magnetic conductors do not exist in nature, they can easily be simulated with the Finite Difference Time Domain (FDTD) method [18]. Moreover, current RF technology is able to physically realize magnetic conductivity using metasurfaces. These two-dimensional structures with engineered electromagnetic boundary conditions consist of many periodically arranged passive circuits. Macroscopically, this results in extraordinary interactions with incident electromagnetic fields. A range of metasurfaces exist, known as artificial magnetic conductors (AMCs) or high-impedance surfaces (HISs), which exhibit high effective magnetic conductivity and surface impedance over a particular bandwidth [19–21]. These surfaces are often applied in the GHz range but can be adapted to operate at lower frequencies. Saleh et al. [22] have successfully applied such a structure to improve the B_1^+ efficiency of a stripline antenna at 7 T. Chen Zhichao et al. have used a HIS to improve the SAR efficiency of a loop antenna at 7 T [23]. They also report an increased SAR efficiency and homogeneity for a single dipole antenna backed by a HIS [24], compared to a copper shield. These improvements match closely the expected improvements when the HIS shield is

replaced with a Perfect Magnetic Conductor (PMC) shield in a FDTD simulation. For an 8-channel dipole array at 7 T, the HIS results in only modest improvements on a homogeneous phantom, and on a heterogeneous head model, no improved SAR efficiency is reported [25]. Additionally, Chen Haiwei et al. [26] reported an increased SAR efficiency at 9.4 T when comparing a loop coil shielded by a magnetically conducting metasurface to the one with a plain copper shield.

Lezhennikova et al. [27] have investigated potential improvement of a birdcage head coil at 7 T using a slot resonator, which makes a section of the shield magnetically conductive. Using a 400 mm diameter birdcage, they found significant improvement in transmit efficiency using their slot resonator. However, a smaller conventional birdcage with 300 mm diameter still performed better, and the authors were unable to apply their slot resonator to this smaller coil. In other work, Lezhennikova et al. [28] described potential improvement of birdcage coils with RF shields of arbitrary impedance, and they designed an artificial magnetic shield for use in a small animal coil (Ø 70 mm) for 7 T. However, their resonant structure has a significant thickness, increasing the diameter of the total coil + shield to 140 mm, thus resulting in a solution that would not be practical to implement at 3 T, where bore space is precious.

This work explores the feasibility and potential improvements of a birdcage body coil at 3 T with a magnetic shield. For practical reasons, the final result at 3 T contains simulated results only, and various measurements at 7 T are performed to demonstrate the feasibility of our proposed solutions at 3 T. This work consists of three sections: The first section outlines the development of a magnetic shield at 7 T using flattened split ring resonators. Bench measurements and simulations are used to assess whether this shield is working as intended. The second section uses 3 T simulations to show that the birdcage needs to be adapted for use with a magnetic shield. This adaptation is implemented in a custom built birdcage at 7 T with 300 mm diameter. This birdcage is a scaled down version (by a factor of 7/3rd) of a birdcage body coil at 3 T and is used to demonstrate the feasibility of the required adaptation. Finally the third section compares simulated results of a birdcage body coil with magnetic shield to a conventionally shielded birdcage body coil at 3 T.

THEORY

Figure 1 illustrates how the Eddy currents in a shield can be described using mirror currents for both Perfect Electric Conductor (PEC) and Perfect Magnetic Conductor (PMC) boundary conditions. The fields generated in the scanning subject (or phantom) are a superposition of the fields generated by the source current and the mirror current. Of course, in a practical situation, the amplitude of the mirror current will be lower than that of the source due to losses. Additionally, phase retardation due to the distance between the antenna and the shield must be taken into account. However, in general, the fields generated by an antenna with a PEC shield are caused by the difference (superposition with 180 phase difference) of two currents. Therefore, they will decay more rapidly with an increasing distance from the antenna, compared to those generated by unshielded or PMC-shielded antennas. **Figure 2** shows the effect this has on the field of a birdcage coil: to reach a target B_1 level in the center of the coil with a PEC shield, a strong current is required which results in strong electric fields in close proximity to the birdcage rungs. Note that a PEC shield reduces the amount of field generated per unit current, but not necessarily per unit power. Since the PEC shield reduces both B-fields and E-fields per unit current, the loading to the current decreases. As a result, generating 1 A of shielded current requires less power than 1 A of unshielded current.

To define what magnetic conductivity is, let us first review how electric conductivity is described using Ampère's circuital law (in differential form and SI units),

$$\nabla \times \mathbf{B} = \mu_0 \left(\mathbf{J} + \varepsilon_0 \frac{\partial \mathbf{E}}{\partial t} \right). \tag{1}$$

Here, μ_0 and ε_0 refer to the vacuum permeability and permittivity, respectively. **B** and **E** refer to the magnetic and electric fields, and **J** is the electrical current density, describing the movement of electric charges. Analogously, we could write Faraday's law of induction as

$$\nabla \times \mathbf{E} = \left(\mathbf{J}_m - \frac{\partial \mathbf{B}}{\partial t} \right), \tag{2}$$

where we have introduced a "magnetic current" $\mathbf{J}_m$ that is normally absent in typical formulations of Faraday's law. This magnetic current is entirely fictional: It describes the movement of magnetic monopoles, which do not exist, and therefore it is always zero. However, the second term $\partial \mathbf{B}/\partial t$ can definitely exist, and a material is said to exhibit "magnetic conductivity" when this time-varying magnetic field behaves in such a way that it effectively functions as a magnetic conductivity. Metamaterials with this property are called Artificial Magnetic Conductors (AMCs) and typically consist of periodic structures, which are tuned to capture this time-varying magnetic field in local currents, resulting in magnetic conductivity within a certain bandwidth [19–21]. A metasurface (2D metamaterial) with this property is also known as an HIS as opposed to a PEC surface whose surface impedance is zero. In this study, we will refer to them simply as a "magnetic shield".

METHODS

The Split Ring Shield

This section outlines the development and validation of the split ring shield, a magnetic shield suitable for MRI purposes at 7 T. Since the final application is a birdcage coil shield, uni-directional magnetic conductivity is considered sufficient where the magnetic conductivity will be oriented along the azimuthal direction following the circumference of the birdcage coil.

Designing the Split Ring Shield

Figure 3 illustrates the design process of our magnetic shield, designed to operate at 300 MHz. Split ring resonators were

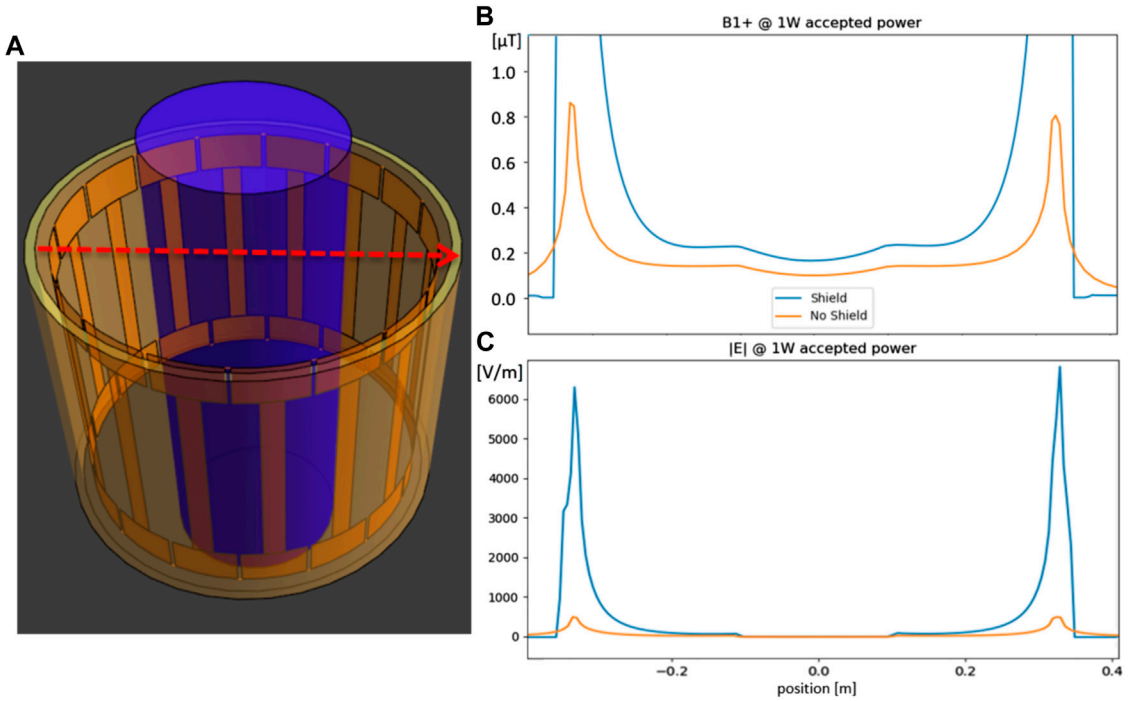

FIGURE 2 | (A) example geometry of birdcage using FDTD simulation. Dotted red line indicates position of the profiles of **(B)** and **(C)**. The loading phantom (blue cylinder) was given tissue-like properties. Birdcage dimensions are radius: 352 mm, rung length: 420 mm, endring width: 80 mm, rung width: 40 mm, and shield radius: 372 mm. **(B)** B_1^+ field strength profile with and without PEC shield. Since the fields are normalized to 1 W accepted power, the shield actually increases B_1 because without a shield, more power is radiated away. **(C)** Electric field strength profile with and without shield.

flattened and arranged in a periodic array and combined with a copper backplate to produce the Split Ring Shield (SRS). The dimensions of the rings (length: 360 mm, height: 4 mm) were determined via exploratory FDTD simulations: a plain dipole (length: 300 mm, width: 12 mm) is placed in front of a SRS design (oriented parallel to the resonator elements; see **Figure 4**), and the B_1 field distribution is compared to a simulated dipole setup with an ideal magnetic shield (PMC). It was expected that beneficial reflective properties would occur in a bandwidth below the self-resonance frequency of the rings, which is around 380–400 MHz with these dimensions. Ideally, a somewhat longer length of around 420 mm would be preferred, bringing the resonance closer to (but still safely above) 300 MHz. However, the split ring resonator elements carry current, which causes the transmitted field to extend further in the z-direction than that of the dipole alone. Typical UHF MRI arrays are designed to generate fields over lengths up to 300 mm for body imaging (head imaging: ~200 mm), and generating fields outside of a target region is inefficient. The length of 360 mm was chosen as a tradeoff between 300 and 420 mm.

Measuring the Field of a Dipole Antenna With Magnetic Shield

Figure 4 shows photographs of the measurement setup. Reflective properties were measured by positioning a dipole antenna (length: 300 mm, width: 12 mm) close to the SRS (10 mm distance from the backplate) and parallel to the rings. A tank of salt water was positioned at 20 mm distance from the antenna. The dipole antenna was connected to the first port of a vector network analyzer (VNA). A pickup loop was positioned in the water and connected to the second port of the VNA, and transmission was measured at varying distance from the antenna by measuring S12 from 250 to 450 MHz. The distance between the antenna and the pickup loop was varied from 20 to 140 mm. The same measurements were performed with a conventional copper shield (at 10 mm distance from the antenna) and without a shield. Each measurement was performed multiple times. (without shield: 3 times, conventional shield: 5 times, SRS: 7 times)

To characterize how quickly the field decays with increasing distance from the antenna, we fit the following function to the data:

$$Transmission(x) = A \cdot \frac{\exp(-\beta \cdot x)}{x^q}, \tag{3}$$

where x is the distance between the pickup loop and the antenna, and the exponential factor encompasses the reduction in field strength due to conductivity of the salt water, with β being the imaginary part of the wave propagation vector, computed using $\sigma = 0.5$ S/m and $\varepsilon_r = 78$ [29]. A and q are the free parameters, A representing the amplitude and q representing how rapidly the field falls off with distance, with higher q signifying a more rapid decay. For each measurement, this fit is performed at each frequency, and the q values of different measurements are averaged.

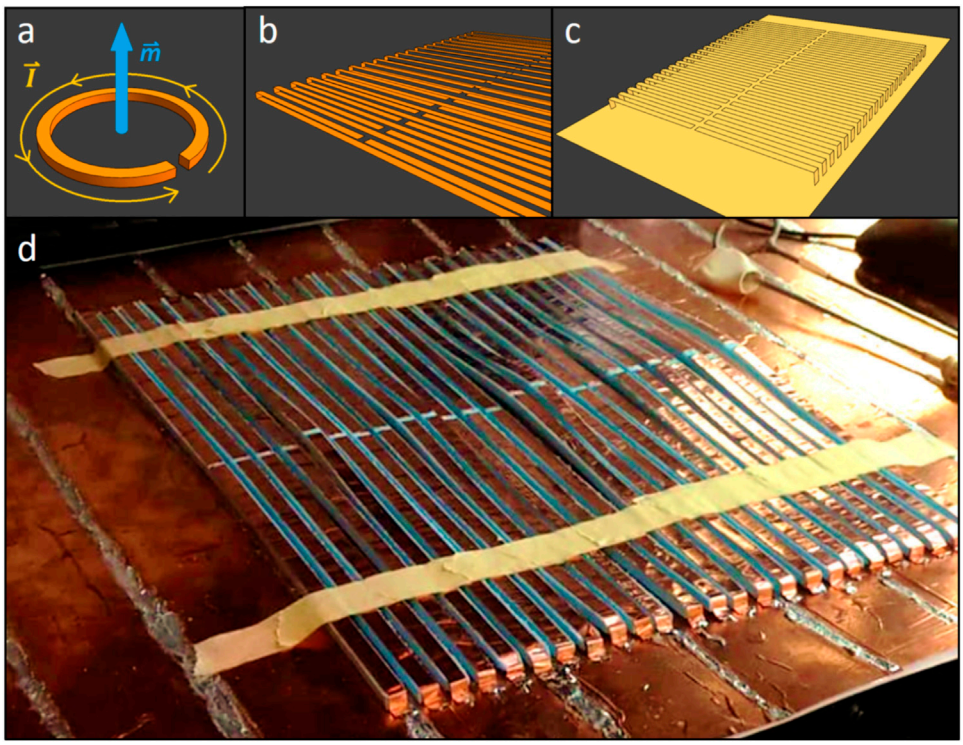

FIGURE 3 | (A) A split ring resonator, which carries current and thus is able to capture a time-varying magnetic field. **(B)** Split ring resonators are flattened and arranged into a period array. **(C)** The split ring resonators are merged with a backplate and dubbed the "Split Ring Shield" (SRS). **(D)** Photograph of the SRS under construction. The rings are made by applying copper tape to foam spacers and soldered to a copper backplate. The dimensions are as follows: ring length: 360 mm, width: 6 mm, height: 4 mm, gap size: 2 mm, and ring spacing period: 10 mm.

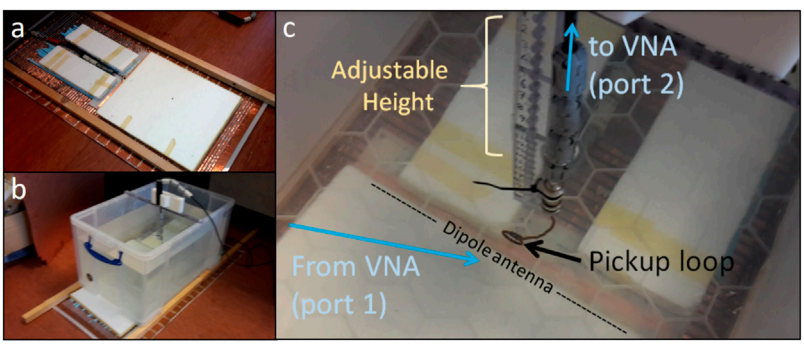

FIGURE 4 | (A) Photograph of split ring shield with foam spacers and dipole antenna (length = 300 mm). **(B)** Measurement setup with SRS, dipole antenna, foam spacers, salt water tank (σ = 0.5 S/m), and pickup loop inside the water. **(C)** Close-up of the pickup loop positioned inside the water. The dipole is oriented in the *z*-direction, the loop position varies in the *x*-direction, and the loop is oriented in the xz-plane.

The measurement setup was also simulated using FDTD (Sim4Life, Zurich Medtech, Switzerland), where 6.6 MCells were used to model the dipole antenna, water tank (σ = 0.5 S/m, ε_r = 78), and shield. Each simulation was performed on the same grid. In addition to the SRS, conventional shield, and unshielded simulation, a simulation with a PMC shield was also performed. Again, in-depth B_1 profiles were fitted to **Eq. 3**to arrive at a decay constant q as a function of frequency. Additionally, the source current magnitude was computed from the simulated fields and the B_1 amplitude was taken at a point located 100 mm deep in the phantom on the central axis

above the antenna to compute the current-efficiency in terms of B_1 per unit current.

The Loading Problem and Multi Transmit Birdcages

This section outlines how the resonant mode of a birdcage coil gets disrupted if the conventional shield is replaced by a magnetic shield and presents a solution. To demonstrate the feasibility of this solution, it is implemented in an eight-channel (8Tx) birdcage shielded with the SRS at 7 T and used for *in vivo* imaging.

Simulations of Unloaded Birdcage Coils at 3 T

Initially, we will compare FDTD simulations of two unloaded high-pass birdcages at 3 T (128 MHz) with a conventional shield (modeled as a perfect electrical conductor, PEC) or a PMC shield. Both shields have a length of 600 mm and a radius of 372 mm. Initial tests showed that the setup with the PMC shield radiated energy (~50% of input power in loaded condition) in the axial (±z) direction. To reduce these radiation losses, both shields were extended with 400 mm PEC sections on both sides, reducing radiation losses to <5% of input power for both setups in loaded condition. In the unloaded condition, there are no other losses (all copper is simulated as PEC and the shield as PEC or PMC) than radiation, which prevents the simulations from converging properly. To remedy this, the background medium (i.e., the "air") of the simulation environment was given a small conductivity of 10^{-6} S/m. For both setups, the birdcage geometric properties are 16 rungs, radius: 352 mm, rung length: 420 mm, endring width: 80 mm, rung width: 40 mm, and shield radius: 372 mm. Both birdcage setups are tuned to 128 MHz and are simulated on the same grid (nvoxels = 153 * 153 * 69 = 1.615 MCells). Both simulations are run until a convergence level of −40 dB is reached. We will evaluate the B_1^+ and |E| field, with the two ports driven in quadrature (without any matching circuits) and normalized to accepted power (forward power−reflected power). Additionally, we will calculate the birdcage's current efficiency in terms of B_1^+ in the isocenter per unit current in the rungs.

Simulations of Loaded Birdcage Coils at 3 T

To evaluate the performance of the birdcages in a more realistic situation, we load the birdcages with a cylindrical phantom (σ = 0.5 S/m, ε_r = 46, length: 1 m, and radius: 200 mm). As shown by the results, this severely dampens the required resonant mode of the birdcage with PMC shield due to increased resistance. Our solution to enforce the correct mode is to place a port in each of the birdcage's rungs, yielding a 16Tx bandpass birdcage with PMC shield. This allows us to enforce the desired current pattern in the rungs regardless of the load. Subsequently, the capacitors in the endrings need to be optimized to make sure that the currents in the endrings are in the correct phase to contribute maximally to the B_1^+ field, when the rungs are driven in quadrature.

Construction of the 8Tx Birdcage at 7 T

We aim to investigate the potential improvements at 3 T via a downscaled model of a birdcage at 7 T. With the frequency increased by 7/3rd and all length scales reduced by the same factor, the two birdcages are described by the same physics. The reason behind this detour is merely practical: Adapting the shield of a 3 T birdcage body coil would require dismantling the MR system, severely hindering clinical operation and possibly voiding warranty. At the 7 T scanner, the smaller birdcage coil can be inserted, connected, and tested while leaving the scanner itself intact.

The SRS presented in *Introduction* (built on a flexible backplate) is curved into a cylindrical shape (diameter: 320 mm, total length: 500 mm). A birdcage coil with eight rungs (diameter: 300 mm, length: 250 mm, rung and endring width: 12 mm) is constructed on a Plexiglass former. Plastic spacers are attached to the shield to hold the birdcage in place. A port is inserted in every rung of the birdcage using SMB connectors, the female part of which was soldered onto a small PCB in the rung containing matching elements. Small holes were drilled in the shield through which the male part of the SMB connector was connected, allowing us to feed each rung individually using coaxial lines. Extra insulation was applied to prevent the connectors and matching elements from touching the SRS.

Tuning the 8Tx Birdcage

To find the optimal value of capacitors in the endrings of the birdcage, a series of FDTD simulations with a realistic human model ("Duke", ITIS Foundation [30]) is performed with capacitance values ranging from 3 to 10 pF. The legs are chosen as an imaging target, mostly because the shoulders do not fit to enable head imaging. Also, the chosen setup has tissue in close proximity to the antenna, which poses a risk of creating SAR hotspots if a conventional birdcage were used, whereas a PMC shield birdcage would not have this problem. The rungs are driven in quadrature (45° phase increments between neighboring channels). Average B_1, B_1 homogeneity (σ/μ), and SAR efficiency (average $B_1/\sqrt{\text{peak SAR}}$) are computed over the voxels containing tissue over a 180 mm FoV. The capacitance value that maximizes these metrics in simulations is considered optimal and will be used in the constructed 8Tx birdcage. For reference, the same setup is simulated using a conventional 2Tx birdcage (with the same dimensions) with PEC shield.

In-Vivo Measurements

The legs of a healthy volunteer are scanned by a 7 T scanner (Philips Achieva). Eight channels, corresponding to the eight birdcage rungs, are used for both transmission and reception. Transmit phases are determined by phase shimming on a dumbbell-shaped target region containing both legs. Anatomical scans are performed with the following parameters: Gradient echo, TE/TR = 4.935/11 ms; FA:10°, and voxelsize: $1 \times 2 \times 1$ mm^3. DREAM B_1 amplitude maps are recorded with the following parameters: TE/TR = 1.97/14 ms, FA: 10°, steam FA: 60°, and voxelsize: 4.7x4.7x30 mm^3. Local SAR was assessed based on simulated fields. The validity of simulated fields was assessed by comparing measured and simulated B_1 maps.

The Simulated 16Tx Birdcage With PMC Shield at 3 Tesla

This section compares the performance of a sixteen-channel (16Tx) birdcage body coil with PMC shield to a conventional 2Tx birdcage with copper shield at 3 T (128 MHz) using FDTD simulations with a realistic human model.

For the 16Tx birdcage, the lumped elements in the endring do not necessarily have to be capacitive but may also need to be inductive for optimal performance. It is therefore referred to as endring reactance X_{ER}. To determine the optimal value of the endring reactance, a series of simulations is performed. In each simulation, a value of X_{ER} ranging from –j 12,433 Ω (0.1 pF) to + j 80 Ω (100 nH), as well as shorted and open connections, was assigned to all endring lumped elements. The rung currents are forced to produce a CP-mode by driving them with corresponding fixed phases using current sources, mimicking perfect matching. The birdcage is loaded with the cylindrical phantom mentioned in the section titled *Simulations of loaded Birdcage coils at 3 T*. Transmit efficiency ($B_1^+/\sqrt{P_{acc}}$) is evaluated by averaging over voxels contained in a spherical volume with 300 mm diameter around the origin. The value of X_{ER}, which yields the highest transmit efficiency, is considered optimal. By this procedure, we are effectively "tuning" the 16Tx birdcage with PMC shield.

In order to make a fair comparison of the transmit efficiency of the 16Tx birdcage with magnetic (PMC) shield versus a conventional 2Tx birdcage with conventional (PEC) shield, we will consider only fixed quadrature drive settings, i.e., 2Tx-PEC: [0, 90°], 16Tx-PMC: [0, 22.5, 45, . . . , 315, 337.5°]. This allows us to isolate the benefits of a magnetic shield from the inherent gains (and added complexity) that are associated with an increased number of transmit channels. Additionally, the fixed quadrature drive setting represents a more realistic use case of a 16Tx-PMC birdcage than using 16 channels in parallel transmit. If we allow the 16Tx coil to be driven with any phase setting, coupling will cause a significant portion of the forward power to be reflected, drastically increasing the amount of forward power required to reach the desired B_1 level. With carefully designed matching circuits, it is possible to cancel all reflections for one particular drive setting, e.g., quadrature. In our simulations, we mimicked these perfect matching conditions by using current sources and normalizing to accepted power.

We compare the birdcages with PMC and PEC shields using FDTD simulations loaded with a realistic human model. The model is positioned for abdominal imaging with the isocenter of the coil coinciding with lumbar vertebra L4. The birdcage and shield dimensions and simulation parameters are the same as mentioned in the section titled *Simulations of unloaded Birdcage coils at 3 T*, except for the grid that is made finer (n_{voxels} = 285 * 383 * 334 = 36.46 MCells) to allow for accurate assessment of local SAR. Additionally, we will perform the same comparison in a "tissue-near-coil scenario" where Duke's wrist is positioned close (~8 mm) to the coil.

The various simulation setups that were outlined in the preceding paragraphs will be evaluated by a couple of metrics. First, the B_1 field per unit current is extracted. This figure is expected to increase for PMC shielded coils. For the same B_1 field, currents will be lower, and therefore, lower peak SAR levels are expected close to the coil structures. Transmit efficiency is defined as the B_1^+ field per unit power ($|B_1^+|/\sqrt{P_{acc}}$). This ultimately determines how much B_1 is achieved for a given amount of deposited power. This metric also determines the global SAR; for larger transmit efficiency, the global SAR levels will be lower. Transmit homogeneity is defined as the average B_1^+ divided by the standard deviation. The final metric is the SAR efficiency, which is defined as the average B_1^+ divided by the square root of peak local SAR (average $|B_1^+|/\sqrt{}$ peak SAR_{10g}). Average and standard deviation of B_1^+ are evaluated over all tissue within a 300 mm diameter sphere centered at the isocenter.

RESULTS

Split Ring Shield

Figure 5A shows two examples of measured depth profiles, one obtained with a conventional shield (red) and one without a shield (blue). Fitted parameters *A* and *q* are also shown, and we see that with the conventional shield the value of *q* is higher, signifying a more rapid decay. **Figure 5B** shows the average values of *q* over the entire bandwidth, where we see that at each frequency, the conventional shield results in a more rapid decay than without a shield. The SRS is seen to exhibit resonant behavior around 380–400 MHz. Above the resonance frequencies, it functions poorly, showing rapid decay. Below the resonance frequencies, a large bandwidth exists where the *q* values measured with the SRS are lowest. **Figure 5C** shows *q* values resulting from fitting simulated data, which are in agreement with the measured values. A simulation with PMC shield is also included, which shows that decay profiles with PMC are very similar to the unshielded situation. All this shows that the SRS is working properly as a magnetic shield. The current-efficiency, computed from the simulated fields, was 0.39 μT/A with the PEC shield. With the SRS, the PMC shield, and no shield, the current efficiencies were 0.77, 1.35, and 1.05 μT/A, respectively. This shows that the SRS successfully increases the current-efficiency of the dipole antenna.

The Loading Problem and Multi-Transmit Birdcages

Simulations of Unloaded Birdcage Coils at 3 Tesla

Figure 6 shows simulated fields for two unloaded birdcages: one with a conventional shield and one with a magnetic shield. Both are high-pass birdcages, tuned to 128 MHz (3 T) and driven in quadrature by two ports located in the endrings. The lumped elements required to obtain the correct mode were 29.9 pF and 18.4 nH for the PEC and PMC birdcages, respectively. The simulation geometry is shown in **Figure 6A**, along with arrows indicating the positions of the transverse slices. The depicted transverse slices showing the B_1^+ distributions (**Figures 6C,E**) are located in the mid plane, but the electric field slices (**Figures 6I,K**) are located just above the bottom

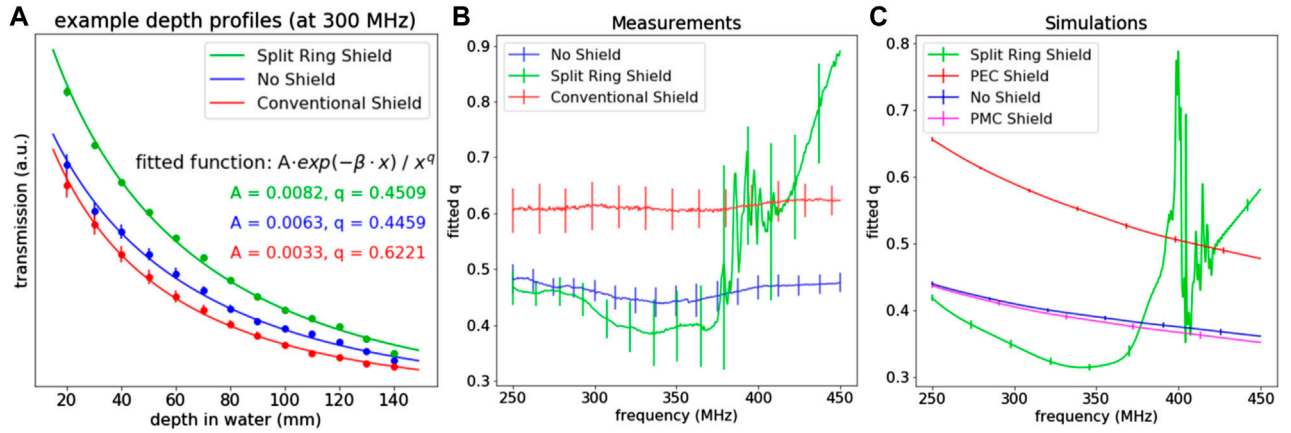

FIGURE 5 | (A) Three example depth profiles of measured transmission at 300 Mhz with SRS (green), without shield (blue) and with conventional copper shield (red). Parameters A and q resulting from fitting **Eq. 3** to these depth profiles are also shown. The numerical value of β is around 10.5 m^{-1} at 300 MHz. **(B)** Averages of fitted q from measured data as a function of frequency. **(C)** Fitted q from simulated data. Vertical bars signify 1σ error margins.

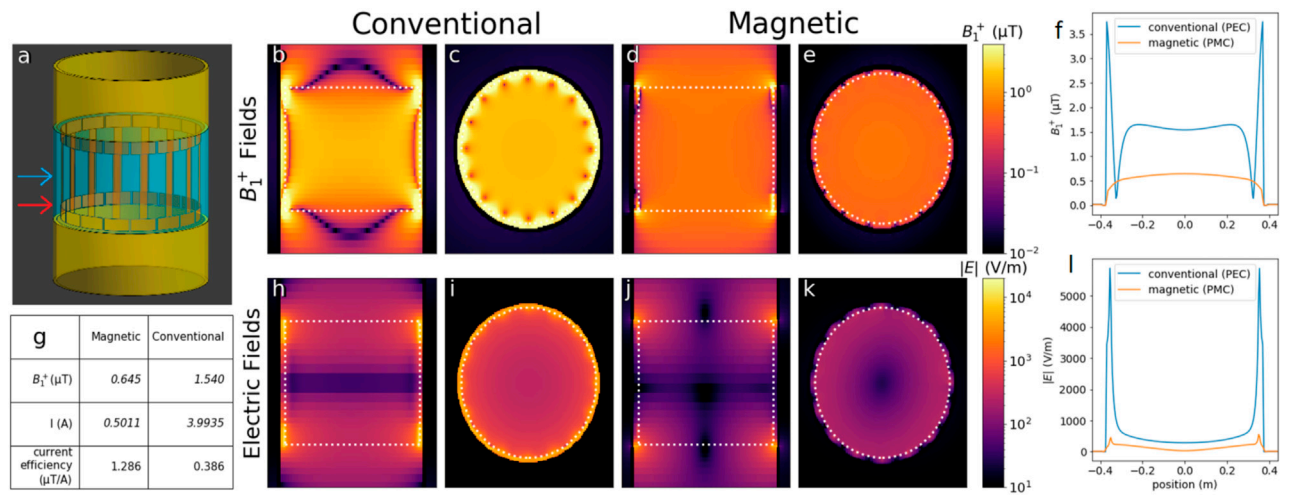

g	Magnetic	Conventional
B_1^+ (μT)	*0.645*	*1.540*
I (A)	*0.5011*	*3.9935*
current efficiency (μT/A)	1.286	0.386

FIGURE 6 | Unloaded birdcage coil field distributions with the conventional (PEC) or magnetic (PMC) shield at 128 MHz. **(A)** Simulation geometry. The part of the shield simulated as either the conventional or magnetic shield is depicted in blue. The yellow part was PEC for both scenarios. The red arrow indicates the position (z = 200 mm) of the transverse slices **(I,K)** and profile (L) of the electric fields. The blue arrow indicates the position (z = 0) of the transverse slices **(C,E)** and profile **(F)** of the B_1 fields. **(B–E)** Mid-sagittal and transverse slices of the B_1^+ fields of the birdcages with conventional **(B,C)** and magnetic shield **(D,E)**. **(H–K)** Mid-sagittal and transverse slices of the electric fields of the birdcages with conventional **(H,I)** and magnetic shield **(J,K)**. The white dashed line denotes the birdcage outline. **(F,L)** Transverse profiles of B_1 and electric fields, respectively, at height indicated by the arrow in **(A)**. **(G)** Table summarizing the B_1^+ field strength in the center and required current, as well as their ratio. Currents are computed by numerically integrating the Ampère–Maxwell equation. The value listed here is the maximum of the magnitude of the currents in the rungs. All results are normalized to 1 W of accepted power.

endring where the largest E-field components are located. In all slices, we see that the conventional birdcage generates stronger fields (normalized to accepted power) than the birdcage with magnetic shield, but from the table (**Figure 6G**), we see that the conventional birdcage requires disproportionally more current. This makes the birdcage with magnetic shield more efficient in terms of B_1^+ per unit current. Note that the choice to stabilize the unloaded simulations using slightly elevated air conductivity may cause an unknown bias in the italic values presented in the table (**Figure 6G**). However, the resulting current-efficiency does not depend on the type of losses that are included. The reasons for presenting these results are to show that the PMC-birdcage can be made to resonate in the correct mode and to compare the shape of the resulting field distributions. Another notable difference between the PEC and PMC cases lies in the homogeneity. From **Figures 6C,H** as well as the profiles shown in **Figures 6F,L**, we see that the field generated by the PEC-birdcage is homogeneous in the center but increases substantially in close

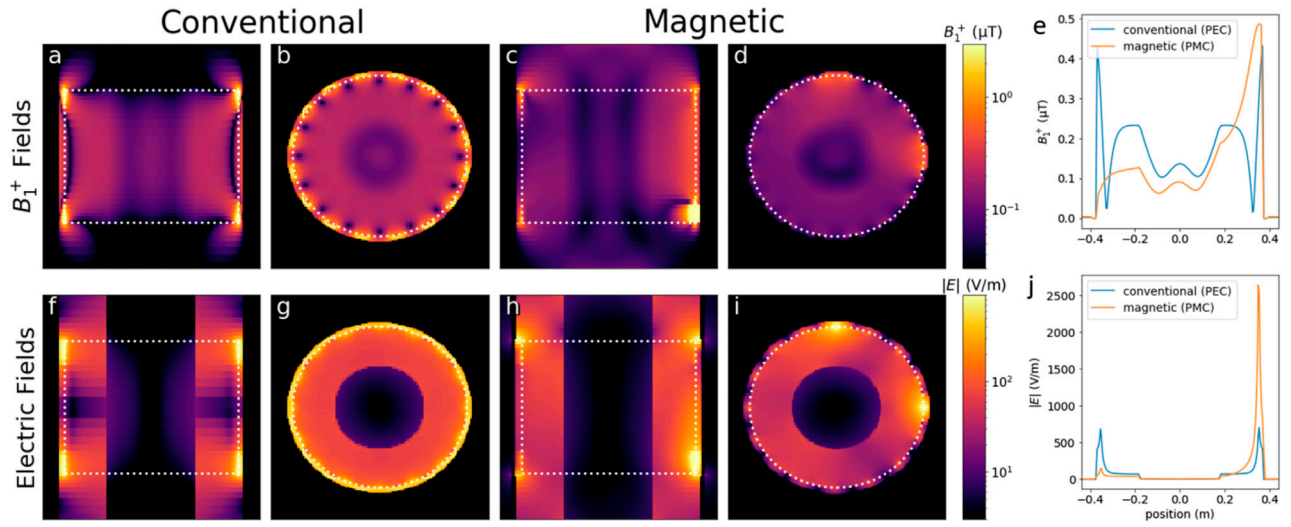

FIGURE 7 | Loaded birdcage coil field distributions with the conventional [PEC, **(A,B,F,G)**] or magnetic [PMC, **(C,D,H,I)**] shield. **(A–D)** B_1^+ field distributions. **(F–I)** electric field distributions. **(A,C,F,H)** Sagittal slices. **(B,D,G,I)** transverse slices. For the B_1^+ distributions, both the sagittal and transverse slices are positioned at the origin (x = 0 or y = 0). The transverse slices of the electric fields are positioned at z = 200 mm (see **Figure 6A**). The white dashed line denotes the birdcage outline. **(E,J)** transverse profiles of B_1 and electric fields, respectively, at the same height as the transverse slices. All results are normalized to 1 W of accepted power.

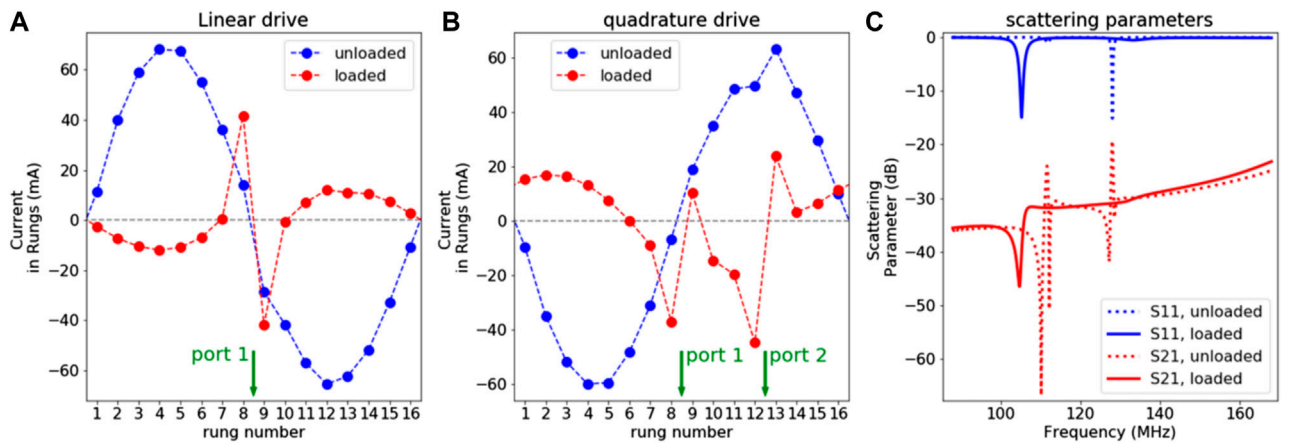

FIGURE 8 | (A) Current distributions in the rungs of the birdcage with magnetic (PMC) shield in loaded (frequency = 133 MHz) and unloaded (frequency = 128 MHz) conditions, with one port active. **(B)** Idem with two ports active, driven in quadrature. The currents were calculated from the electric and magnetic fields by numerically integrating the Ampère–Maxwell equation over a rectangular path (in the central transverse plane) enclosing the rung. Here shown is the real part of the phasor. All results are normalized to 1 W of accepted power. **(C)** Scattering parameters of the birdcage with magnetic shield in loaded and unloaded situations.

proximity to the rungs. The fields of the PMC-birdcage are more uniform toward the edges. From **Figure 6D**, we see that the volume where the PMC-birdcage generates a homogeneous B_1^+ field extends further in the *z*-direction than with the PEC-birdcage.

Simulations of Loaded Birdcage Coils at 3 Tesla

Figure 7 shows simulated B_1^+ and electric fields similar to **Figure 6**, but now the birdcages are loaded with a phantom. The conventional birdcage (**Figures 7A,B,F,G**) still has a homogeneous field, but the birdcage with magnetic shield (**Figures 7C,D,H,I**) does not. In **Figures 7C,H**, we see a strong field in the bottom right corner, close to where the port is located. In **Figures 7D,I**, we see that only the rungs next to the ports produce a significant B_1^+ field. The profiles of **Figures 7E,J** also show asymmetric field distributions for the birdcage with magnetic shield. This is caused by increased resistance due to the larger current efficiency, as illustrated by **Figure 8**. **Figures 8A,B** show current distributions over the 16 rungs of the birdcage with magnetic shield in loaded and unloaded conditions. In **Figure 8A**, only one port is active, and in **Figure 8B**, two ports are active and driven with a 90° phase difference. The characteristic sinusoidal

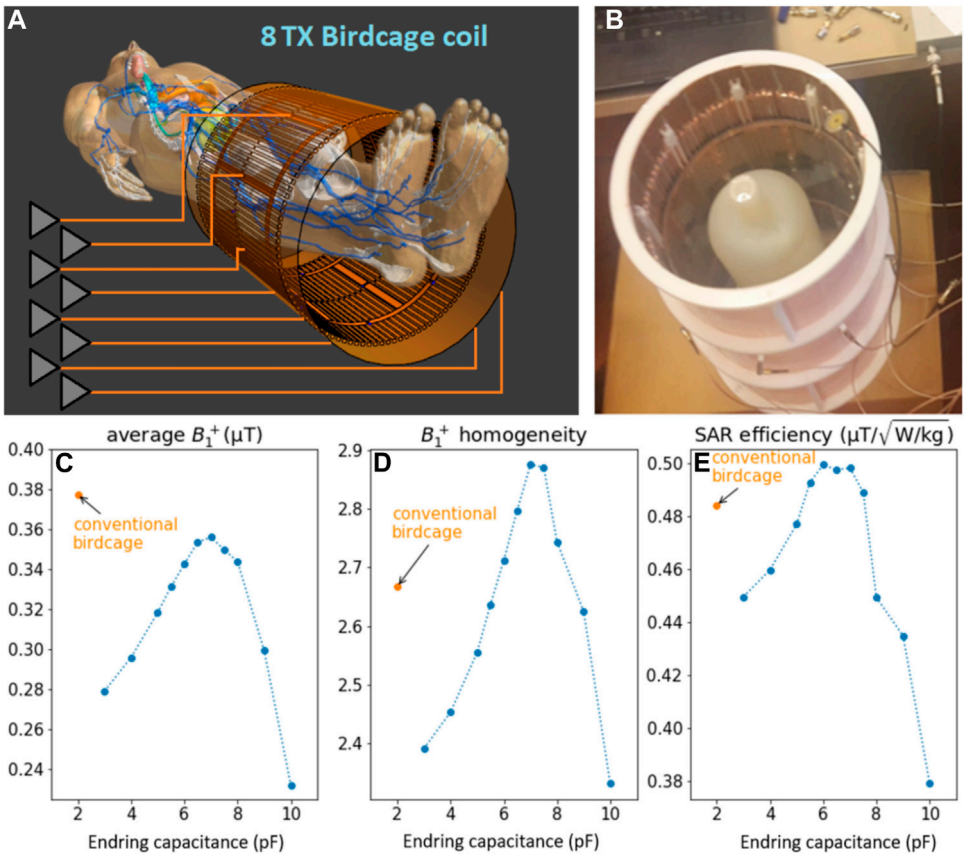

FIGURE 9 | (A) 8Tx birdcage coil with SRS in FDTD simulation environment (Sim4Life) with a feeding port located in each rung. **(B)** photograph of the 8Tx birdcage coil with SRS and a loading phantom. The ports are connected through small holes in the shield. **(C–E)** "Tuning" the 8Tx birdcage. Simulated (at 300 MHz) values of average B_1^+ **(C)**, homogeneity **(D)** and SAR efficiency **(E)** are shown as a function of endring capacitance value. Values obtained with a conventional birdcage (with the same dimensions as the 8Tx birdcage) are also shown for reference. All results are normalized to 1 W accepted power.

pattern, used to construct the CP-mode, can still be seen but the amplitude is much lower. In fact, the current only has high amplitudes in the rungs adjacent to the feeding port(s). **Figure 8C** shows the reflection coefficients S_{11} and S_{12} at one of the ports of the birdcage with magnetic shield in loaded and unloaded situations. In the unloaded situation, a resonant mode is observed at 128 MHz. In the loaded situation, the mode is shifted to 133 MHz, but the increased resistance lowers the Q-factor such that it can hardly be observed.

The 8Tx Birdcage at 7 Tesla

The bottom row of **Figure 9** shows results of the tuning process, plotting various metrics versus endring capacitance value. We see that all metrics have their maximum value around a capacitance of 7 pF, so this is the value that was used in the constructed birdcage. The left part of **Figure 10** compares the performance of the 8Tx birdcage with SRS to a conventional 2Tx birdcage with the same dimensions. Overall, the two coils showed similar performance. We see that the conventional birdcage produces a slightly higher average B_1 but much higher peak SAR values, resulting in a marginally better SAR efficiency for the birdcage with SRS. These metrics are summarized in the table (**Figure 10G**), which also shows the maximum current amplitudes found in both the rungs and endrings of the birdcage. The right part of **Figure 10** shows *in vivo* results, demonstrating the feasibility of the concept of a multi-transmit birdcage. The scattering matrix of the 8Tx birdcage with SRS can be found in the supplementary material as **Supplementary Figure S1**.

The 16Tx Birdcage With PMC Shield at 3 Tesla

Figure 11A depicts the model of the 16Tx birdcage at 3 T with a phantom load used for tuning and the locations of the ports indicated by red dots. **Figure 11B** shows the result of the tuning process, similar to **Figure 9**. The average B_1^+ magnitude is plotted for various values of endring reactance. The optimal values are those where the absolute magnitude of the reactance is high: small capacitance, high inductance, or open connections. For symmetry and stability reasons, we decided to use a lumped capacitance of 1 pF in the endring gaps.

Figure 12 shows field distributions for the conventional 2-port birdcage with conventional shield (left) and 16-port birdcage with magnetic shield (right). Both birdcages are driven in quadrature.

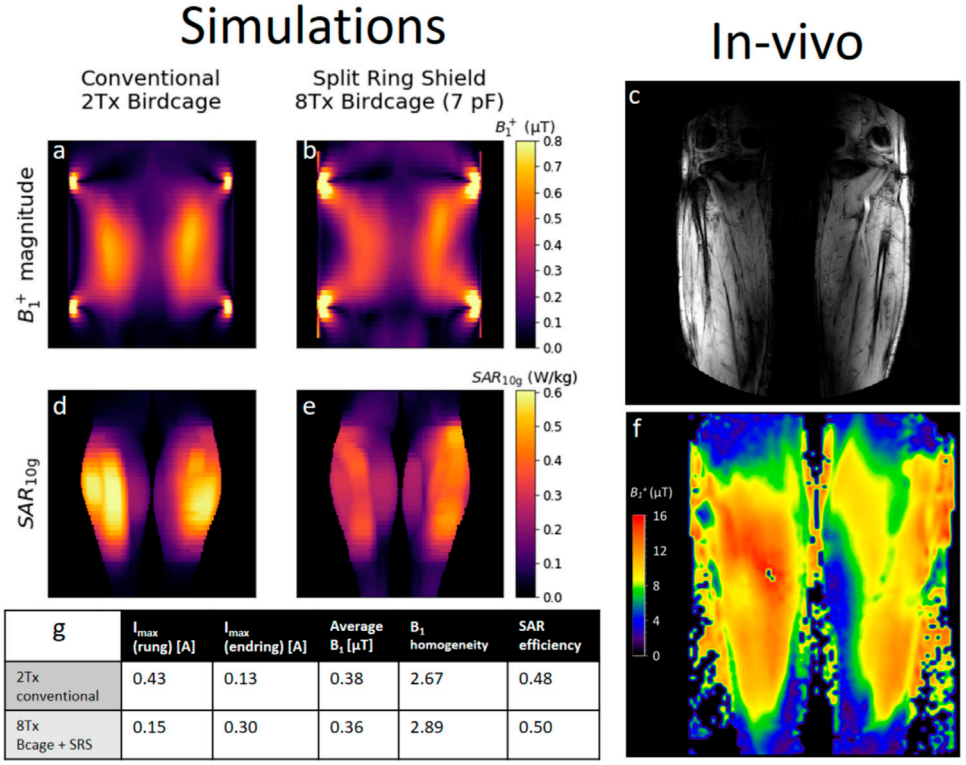

g	I_{max} (rung) [A]	I_{max} (endring) [A]	Average B_1 [μT]	B_1 homogeneity	SAR efficiency
2Tx conventional	0.43	0.13	0.38	2.67	0.48
8Tx Bcage + SRS	0.15	0.30	0.36	2.89	0.50

FIGURE 10 | Overview of results obtained using 8Tx birdcage with SRS. **Left:** simulated B_1 distributions **(A,B)** and 10-g averaged SAR distributions **(D,E)** comparing the 8Tx birdcage with SRS to a conventional 2Tx birdcage with PEC shield. **(G)** Table summarizing metrics computed from simulated fields. All simulated fields are normalized to 1 W accepted power. **Right:** *In-vivo* results obtained using 8Tx birdcage with SRS. **(C)** Anatomical image. **(F)** DREAM-B_1 map obtained with 1,257 W of accepted power.

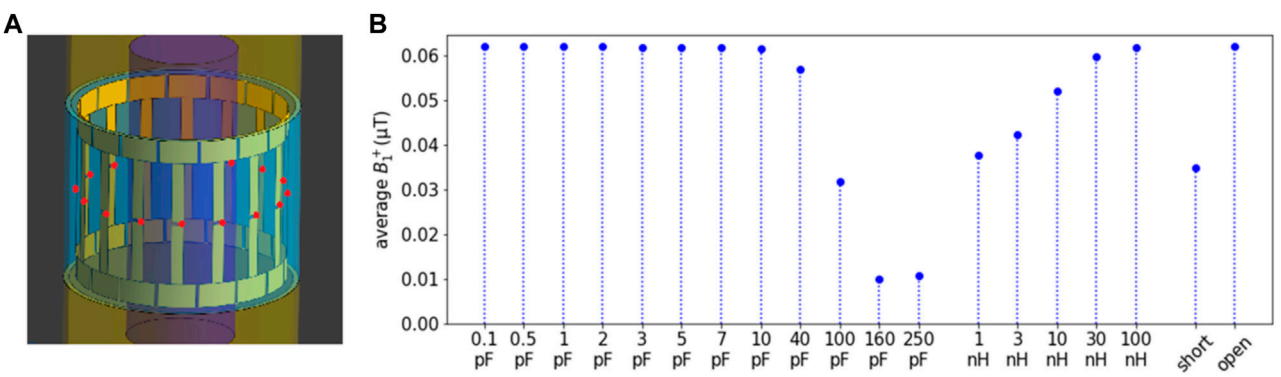

FIGURE 11 | 16Tx PMC-birdcage. **(A)** Simulation geometry. The locations of the ports are denoted by red dots in the rungs. The magnetically conducting part of the shield is shown in blue, and the yellow part is modeled as PEC. The cylindrical phantom (ε_r = 46, σ = 0.5 S/m) is shown in purple. **(B)** Average B_1^+ as a function of endring reactance. The ports were simulated as harmonic current sources, driven in quadrature. The field was evaluated in a spherical volume of 300 mm diameter about the isocenter and normalized to 1 W of accepted power.

The top row shows B_1^+ distributions in transverse and coronal slices. The bottom row shows maximum intensity projections of the 10-g-averaged SAR distributions in coronal and transverse planes. The table (**Figure 12I**) summarizes the relevant metrics. The birdcage with magnetic shield has 27% lower B_1^+ magnitude and 33% lower peak local SAR resulting in a SAR efficiency (*average* $B_1^+/\sqrt{peak\ SAR}$) that is 11% lower. However, the magnetic shield does increase homogeneity by 13%.

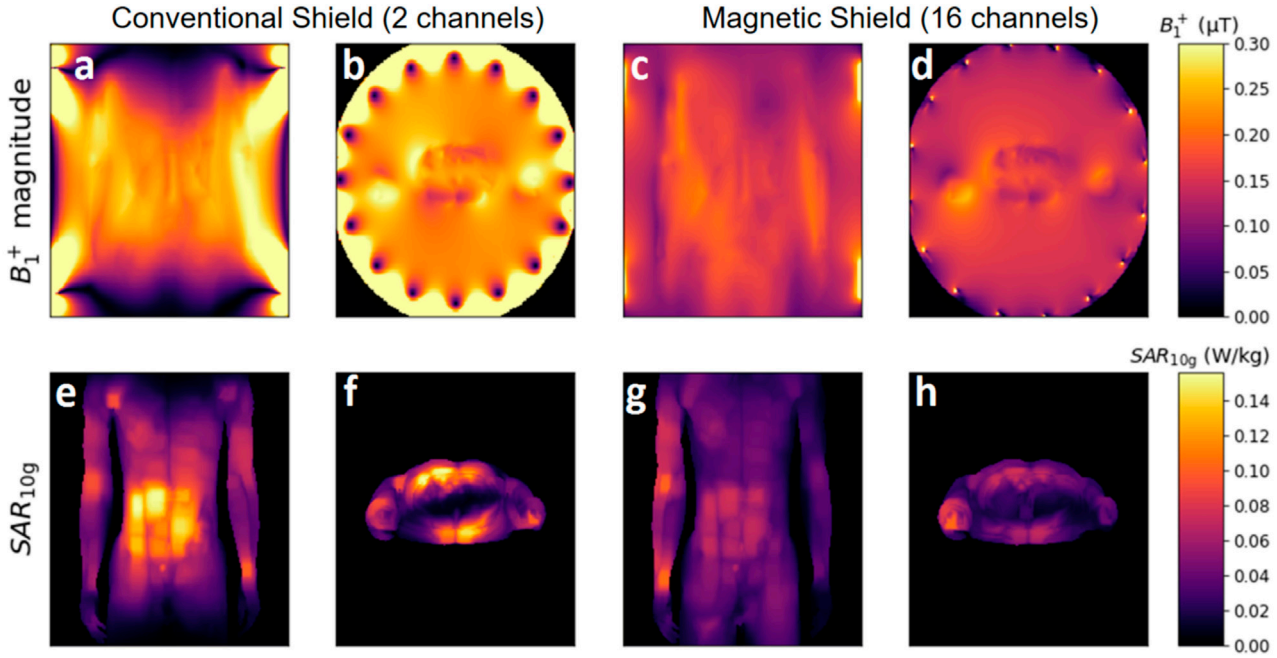

i	Max current (mA)	Average B_1^+ (μT)	Homogeneity (CoV^{-1})	Max SAR_{10g} (W/kg)	SAR efficiency (μT / $\sqrt{W/kg}$)
Conventional	651.5	0.21	5.96	0.16	0.52
Magnetic	8.5	0.15	6.74	0.11	0.47

FIGURE 12 | Field distribution in the birdcage coils with conventional [PEC, **(A,B,E,F)**] and magnetic [PMC, **(C,D,G,H)**] shield. The top row shows coronal **(A,C)** and transverse **(B,D)** slices of the B_1^+ distribution. The bottom row shows maximum intensity projections of the 10-g averaged local SAR distributions projected to the coronal **(E,G)** and transverse **(F,H)** plane. The table **(I)** summarizes important metrics calculated from the fields. Maximum current values are found in the endrings of the PEC-birdcage but in the rungs of the PMC-birdcage. All fields are normalized to 1 W of accepted power.

Figure 13 shows field distributions similar to **Figure 12**, but this time, the model's arm has been repositioned such that it is close (8 mm) to one of the endrings. The bottom row shows that this causes a local SAR hotspot to appear in the lower arm when a conventional shield is used but not with a magnetic shield. The birdcage with magnetic shield again yields lower (25% less) B_1^+ per unit power, but the peak local SAR is almost three times higher with the conventional shield. This results in the birdcage with magnetic shield having a 27% higher SAR efficiency, as can be seen in table (**Figure 13I**). Additionally, the magnetic shield again results in a slightly more homogeneous (6%) transmit field.

DISCUSSION

The Split Ring Shield

The resonator length of 360 mm was chosen as a tradeoff between 300 and 420 mm. Of course, various strategies can be employed to reduce the resonance frequency of the resonators without increasing their total length, and there exist MRI applications where a 420 mm FOV is desired, but these are outside the scope of this proof-of-concept study. However, note that scaling these dimensions by 7/3rd results in 840 mm long resonators (and fields extending equally far in *z*-direction) at 3 T, so if applied at 3 T, the current implementation would have to be adapted to reduce resonator length.

In both bench measurements and simulations, the SRS significantly reduces the rate at which the field of a dipole antenna decays. However, its behavior somewhat differs from that of a PMC. The field of the dipole with PMC closely resembles that of the unshielded dipole antenna. This is expected, as the field produced by two closely located in-phase current sources is essentially the same as the field produced by a single current source. More surprising is that the SRS outperforms the unshielded situation over a large bandwidth. This may be caused by the fact that the SRS is longer than the dipole, and the resonators of the SRS carry current over their total length. Thus, the spatial extent of the current that generates the field is larger, resulting in less rapid decay.

Overall, the SRS behaves like a magnetic shield at 300 MHz in the sense that it reduces the decay rate of the field produced by a dipole antenna, when compared to a conventional copper shield. Additionally, the SRS reduces the current of the dipole antenna, increasing the amount of field generated per unit current. However, by design, the magnetic conductivity of the SRS is anisotropic: if the source current is not oriented parallel to the resonators of the shield, no magnetic conductivity is seen.

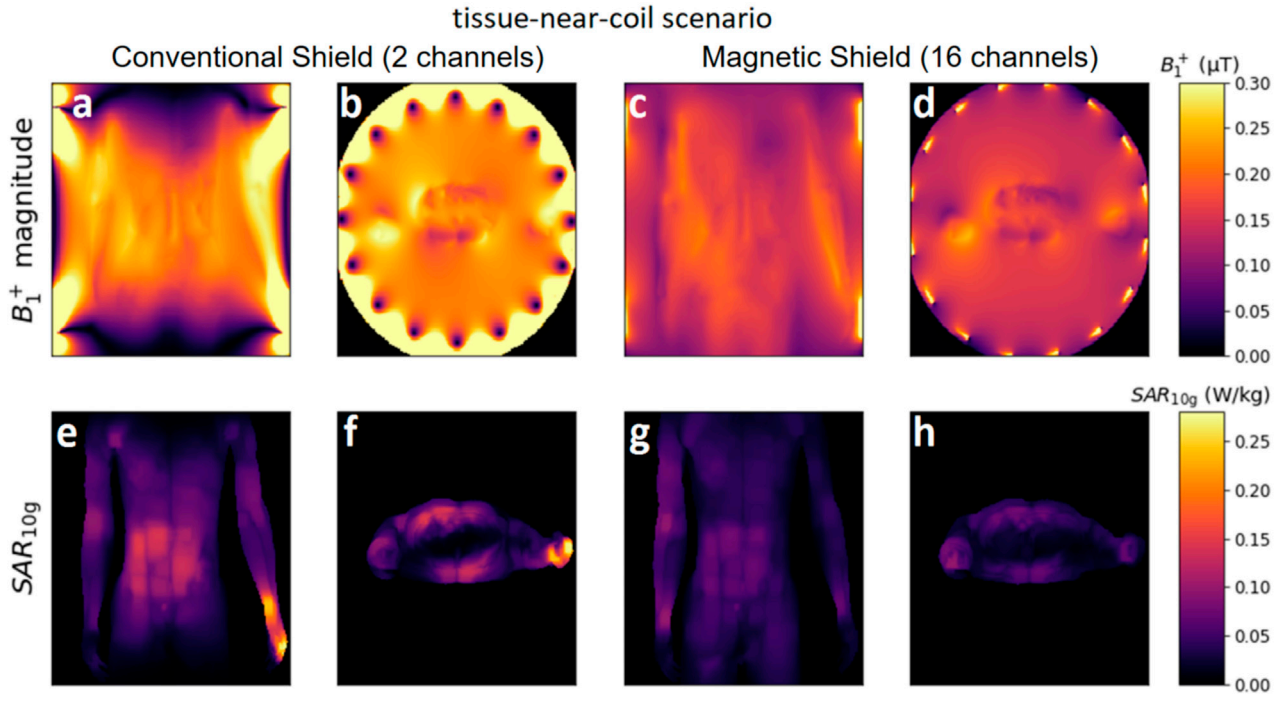

i	Max current (mA)	Average B_1^+ (μT)	Homogeneity (CoV^{-1})	Max SAR_{10g} (W/kg)	SAR efficiency (μT / $\sqrt{W/kg}$)
Conventional	622.6	0.20	6.06	0.28	0.38
Magnetic	8.6	0.15	6.44	0.10	0.48

FIGURE 13 | Same as **Figure 12**, except for the fact that the model now has his hand close (~8 mm) to one of the endrings. Field distribution in the birdcage coils with conventional [PEC, **(A,B,E,F)**] and magnetic [PMC, **(C,D,G,H)**] shield. The top row shows coronal **(A,C)** and transverse **(B,D)** slices of the B_1^+ distribution. The bottom row shows maximum intensity projections of the 10-g averaged local SAR distributions projected to the coronal **(E,G)** and transverse **(F,H)** plane. The table **(I)** summarizes important metrics calculated from the fields. Maximum current values are found in the endrings of the PEC-birdcage but in the rungs of the PMC-birdcage. All fields are normalized to 1 W of accepted power.

The Loading Problem and Multi-Transmit Birdcages

A drawback of the magnetic shield is that the resistance due to loading is increased. In a birdcage coil with conventional shield, the energy delivered by the port is allowed to propagate around the birdcage in the azimuthal direction with little loss due to loading. The propagating waves form a distinct resonance mode setting up the desired sinusoidal current pattern. With a magnetic shield but without loading, this is still the case, as shown in **Figures 6**, **8**. However, when the birdcage with magnetic shield is loaded, the resistance increases dramatically. This follows from the definition of resistance as $R = \frac{deposited\ power}{|I_{coil}|^2} = \frac{\iiint \sigma |E|^2 dV}{|I_{coil}|^2} = \iiint \sigma \left|\frac{E}{I_{coil}}\right|^2 dV$. With a magnetic shield, the birdcage coil becomes much more efficient in terms of RF field magnitude per unit current. This applies to the B_1^+ field but also to the electric field. For a coil with magnetic shield, the term E/I in this definition of resistance increases and therefore the resistance increases. This results in stronger losses as the energy propagates in the azimuthal direction. With a magnetic shield in the loaded situation, the losses are so severe that the desired sinusoidal current pattern nearly disappears and instead the current tends to take the shortest path: a local loop-like current that flows through the rungs adjacent to the port. This loop-like current also generates B_1 but only very locally. Moreover, it is ~90° out of phase with what is left of the desired sinusoidal current. This results in an inhomogeneous B_1 field. Thus, a birdcage with PMC shield driven in quadrature with two ports performs poorly because the desired resonance mode with sinusoidal current pattern cannot be achieved.

In situations with weaker loading than described in this work (e.g., children in a 3 T scanner whole body birdcage, a head in a 400 mm birdcage at 7 T or small animal scanners [28]), this loading problem will be less severe. The energy can propagate in the azimuthal direction without too much losses, which results in a sinusoidal current pattern over the rungs. An

example is provided by Lezhennikova et al. [27] where a 400 mm diameter birdcage coil with magnetic shield loaded by a human head at 7 T did not severely disrupt the sinusoidal current pattern.

As a solution, we propose a multi-transmit birdcage with one port in each rung, which allows us to enforce the CP-mode, regardless of loading. An eight-channel birdcage with 300 mm diameter, shielded with the SRS, has been constructed and successfully used for imaging at 7 T. Simulations show this 8Tx birdcage with SRS has similar performance as a conventional birdcage of the same dimensions. It achieves slightly lower average B_1 with a lower peak SAR value, resulting in a slightly higher SAR efficiency, but the differences are small. Both in simulations and *in vivo*, the 8Tx birdcage with SRS achieved B_1 amplitudes ranging from 0.23 to 0.45 μT (normalized to 1 W accepted power), providing confidence in the validity of the simulated fields. Due to the anisotropic magnetic conductivity of the SRS, it exhibits a different surface impedance for the z-oriented currents in the rungs than for the azimuthally oriented currents in the endrings. For this reason, the table (**Figure 10G**) vshows the maximum values of rung and endring currents separately. Compared to the conventional birdcage, the current in the rungs is much lower, but the current in the endrings is actually higher with the SRS. This strongly mitigates the benefit of the magnetic shield in this specific case: in **Figure 10E**, we see the peak SAR value occurs in the leg close to the endring. This implementation of a birdcage with magnetic shield is therefore suboptimal for reducing SAR hotspots. However, it does successfully demonstrate the feasibility of a birdcage with magnetic shield using a multi-transmit drive configuration to enforce the CP mode with a sinusoidal current pattern over the rungs.

The 16Tx Birdcage With PMC Shield at 3 Tesla

This work explored the use of a magnetic shield to improve the performance of a birdcage body coil at 3 T. The main advantage provided by a magnetic shield is an increased efficiency in terms of B_1^+ per unit current. A conventional birdcage can create SAR hotspots close to the endrings due to strong currents. With a magnetic shield, the currents are lower, which eliminates these SAR hotspots near the rungs and endrings. The magnetic shield reduces B_1^+ efficiency but substantially reduces peak local SAR if tissue is present in close proximity to the coil, increasing the SAR efficiency by 27%. This tissue-near-coil scenario is a potentially realistic situation since patients are, in principle, free to place their arms in a position that is comfortable (as long as they do not create current loops), possibly on the bore lining and close to the birdcage coil.

The current IEC guidelines [5] only limit global SAR when a volume coil, such as a birdcage body coil, is used. However, our results confirm the findings from other studies [6–12] that local SAR can reach considerably high levels although global SAR levels are kept within the limits. Results show that, in particular, a posture with the hand of the patient close to the birdcage ring may result in excessively high SAR levels. The same may hold for obese patients where parts of the body will inherently be close to the rings. Results have shown that a 16Tx birdcage body coil with magnetic shield requires much lower currents to reach the same B_1 level, which translates into much more lenient SAR levels in body parts close to the coil conductors. However, the reduced transmit efficiency of ~25% indicates that in order to reach the same B_1^+ level with a magnetic shield, the whole-body SAR will be ~1.8 times higher.

To investigate the potential benefit of a magnetic shield for a 3 T birdcage body coil, we chose to perform the comparison in an idealized situation with a PMC shield. No copper losses were included in any of the simulations. Of course, a physical implementation of an artificial magnetic conductor is associated with losses, but the exact loss performance depends very much on the specific implementation. However, the lower currents in the birdcage (as a result of field-per-current efficiency) with a magnetic shield indicate that ohmic losses in the birdcage coil will be lower if a magnetic shield is used. Furthermore, a PMC reflects incoming electromagnetic waves from all incident angles and polarizations with perfect 0° phase, whereas AMCs have a reflection coefficient of which the magnitude and phase depend on the incident angle and polarization. Often times, a tradeoff exists between losses, angle independence, and thickness of the structure. Based on AMC implementations at higher field strengths [23–26], we suggest a patch-based approach with vias, but more research is needed to determine which AMC structure would be most suitable for MRI. For example, the implementation by Chen Zhichao [23–25] uses a thicker structure, but the implementation by Chen Haiwei [26] might be more lossy due to the presence of lumped capacitors.

The practical realization of a 16Tx birdcage body coil with magnetic shield is first of all impeded by the clinical workflow, which does not allow the adaptation of any of our scanners. Without this obstacle, it would still pose a considerable engineering challenge. The 16Tx drive could be achieved using a Butler matrix to distribute the power over the rungs. Note that while the coupling between ports is relatively low due to the increased load with magnetic shield, still coupling levels of up to −6 dB are present (see **Supplementary Figure S2**). Therefore, the matching circuits in each rung need to be designed such that they negate all reflections caused by coupling for one particular drive setting (CP-mode). By employing current sources driven with fixed phases, this simulation study essentially mimics perfect matching conditions and considers only the effect of the magnetic shield itself.

By using a PMC as a magnetic shield and assuming perfect matching conditions for the 16Tx setup, we have assumed two "best case" scenarios for our birdcage with magnetic shield. Still the final result is ambiguous: Though the 16Tx PMC-birdcage successfully reduces SAR hotspots in the periphery, the reduced transmit efficiency makes the coil inferior for most applications. Note that imperfections in realistic magnetic shield implementations may further deteriorate the efficiency as reported here.

The birdcage coil dimensions used in this work were derived from an actual 3 T system. Dimensions with the conventional and magnetic shield were kept the same to study the effect of the

magnetic shield only. However, the 16Tx birdcage coil with magnetic shield yields a remarkably large field-of view in the *z*-direction of almost 1 m. This explains the lower B_1^+ efficiency for the birdcage coil with magnetic shield. Subsequent efforts will focus on adaptations of the system such that more field focusing is achieved with a magnetic shield. However, preliminary findings (shown in the supplementary material under "Additional Setups") indicate that this is not trivial. Reduction of the birdcage dimension and/or the shield length do not suffice (see **Supplementary Figure S3**). There are situations where this longer B_1 field is advantageous, such as whole-body imaging. At higher field strengths, the "long" transmit field of a magnetically shielded coil becomes comparable to the FOV of the scanner, and similar transmit efficiencies can be achieved with a magnetic or conventional shield, as shown in *The loading problem and multi-transmit birdcages* (**Figure 10**). However, for a typical 3 T birdcage, the FOV is maximally 500 mm, and a B_1 field that extends for almost 1 m in *z*-direction is not efficient.

One might argue that the investigated 16Tx birdcage is similar to a phased array of dipoles and that similar performance gains (improved SAR efficiency and homogeneity) can be achieved in a simpler way using dipoles and a magnetic shield. However, in our 16Tx birdcage, the endrings do carry some current (albeit much less than with a conventional 2Tx birdcage), which adds to the produced B_1 field. Simulations show that plain dipoles with a magnetic shield perform worse than our 16Tx birdcage with a magnetic shield, which can be seen in **Supplementary Table S1**. This indicates that some capacitive coupling between the rungs through the endrings still adds to the B_1^+ efficiency.

Since a conventional birdcage is shown to exhibit SAR hotspots close to the endrings, one might argue that removing the ports from the endrings and placing a port in each rung is already enough to remove these hotspots, without the need for a magnetic shield. We have performed additional simulations to show that this is not the case. As can be seen in **Supplementary Table S1**, a 16Tx birdcage with conventional shield and a port in each rung performs worse than a regular 2Tx birdcage.

Maximum current values are found in the endrings of the PEC-birdcage but in the rungs of the PMC-birdcage. We realize that the model's hand is positioned close (<1 cm) to one of the endrings and not necessarily close to the rungs (~4.5 cm), possibly resulting in a bias towards the PMC-birdcage where the rungs carry most current. To test this, we have performed the same simulations again but with *Duke* rotated such that his hand is now close to the rung as well. The results (shown in **Supplementary Figure S4**) were slightly different but did not change the significance of our results.

The purpose of this study was to investigate whether the application of a magnetically conducting shield could improve the performance of a birdcage coil. Other studies [22–26] have demonstrated improved performance for local transmit antennas by using a magnetically conducting shield, but for the birdcage coil at 3 T, this has not been investigated. Lezhennikova et al. [27, 28] have investigated potential improvements of birdcage coils with a magnetic shield under weaker loading conditions, where no adaptation to the driving scheme is required. However, they have not investigated potential SAR hotspots in any scenario where tissue is present close to one of the conductors, which was the focus of this work. Our results indicate that the magnetic shield substantially reduces the current required to produce B_1^+ field, which reduces the strong electric fields near the coil. However, birdcage coils traditionally use a resonant mode to set up the desired current pattern efficiently. The improved current efficiency of the magnetically shielded birdcage associated with increased load resistance severely dampens the resonant mode. Therefore an alternative driving scheme is employed to restore the CP mode. The magnetic shield reduces peak local SAR by a factor of three in a tissue-near-coil scenario. However, in both the standard scenario and the tissue-near-coil scenario, the magnetic shield reduces the B_1^+ efficiency from 0.20 to 0.21 to 0.15 $\mu T/\sqrt{W}$. Thus, using a magnetic shield reduces the SAR efficiency ($B_1^+/\sqrt{}$ peak local SAR) from 0.52 to 0.47 $\mu T/\sqrt{(W/kg)}$ in the standard scenario, but it increases the SAR efficiency from 0.38 to 0.48 $\mu T/\sqrt{(W/kg)}$ in the tissue-near-coil scenario. Nevertheless, for general applications where a large field of view is not required, the magnetically shielded birdcage body coil is still inferior to a conventional birdcage body coil because of the reduced B_1^+ efficiency and concomitant increased global SAR levels.

CONCLUSION

The birdcage body coil with a conventional (electric) shield requires large currents to reach sufficient B_1^+ inside the patient. These large currents may cause severe SAR hotspots in parts of the patient that are close to the birdcage endrings. This study explores the possibility of improving a birdcage body coil using a magnetic shield. A magnetic shield using split ring resonators, suitable for MRI at 7 T, is developed and tested. Magnetic shields make antennas much more current-efficient, which reduces the required current amplitudes. However, this larger efficiency also results in severely increased loading of the coil. In the case of a birdcage coil, this dampens the required operation mode. This can be addressed by driving the birdcage coil at each rung separately, resulting in a multi-transmit birdcage coil. The feasibility of this concept is demonstrated by constructing an 8Tx birdcage with magnetic shield at 7 T. Its feasibility is demonstrated by *in vivo* leg imaging while FDTD simulations show that the magnetic shield birdcage has similar B_1^+ efficiency and larger SAR efficiency than a conventional birdcage counterpart. At 3 T, a simulation study comparing a 16Tx birdcage coil with magnetic shield to a conventional 2Tx birdcage coil has been conducted for a standard imaging posture and a posture where the hand of the patient model is positioned close to the endring (tissue-near-coil scenario). Results show that local SAR hotspots in extremities close to the endrings can be avoided using a birdcage with magnetic shield. However, the increased longitudinal field of view results in reduced transmit efficiency, which effectively renders the magnetically shielded birdcage coil as presented in this study still inferior to the current state-of-the-art for general application.

DATA AVAILABILITY STATEMENT

The raw data supporting the conclusions of this article will be made available by the authors, without undue reservation.

ETHICS STATEMENT

Ethical review and approval was not required for the study on human participants in accordance with the local legislation and institutional requirements. The patients/participants provided their written informed consent to participate in this study.

AUTHOR CONTRIBUTIONS

CvL performed the simulations, with help of BS. CvL wrote the article, with help of BS and AR. CvL and ML performed the bench measurements with the shielded antennas. CvL, BS, and AR performed the *in vivo* measurements. SG and KS contributed to the conception of the idea and helped interpret the results. CvdB and DK aided in data acquisition and interpretation. All authors contributed to revising the article.

FUNDING

This project has received funding from the European Union's Horizon 2020 research and innovation program under grant agreement No 736937.

SUPPLEMENTARY MATERIAL

The supplementary material for this article can be found online at: https://www.frontiersin.org/articles/10.3389/fphy.2021.716521/full#supplementary-material

REFERENCES

1. Hayes CE, Edelstein WA, Schenck JF, Mueller OM, and Eash M. An Efficient, Highly Homogeneous Radiofrequency Coil for Whole-Body NMR Imaging at 1.5 T. *J Magn Reson (1969)* (1985) 63:622–8. doi:10.1016/0022-2364(85)90257-4
2. Hayes CE, and Eash MG. Shield for Decoupling RF and Gradient Coils in an NMR Apparatus. *US Patent* (1987) 4:642.
3. Roemer PB, and Edelstein WA. Double-sided RF Shield for RF Coil Contained within Gradient Coils of NMR Device. *US Patent* (1989) 4:879.
4. Jin J. *Electromagnetic Analysis and Design in Magnetic Resonance Imaging*. Boca Raton, Florida: CRC Press (1998):164–90.
5. IEC 60601-2-33:2010+AMD1:2013+AMD2:2015. *Medical Electrical Equipment - Part 2-33: Particular Requirements for the Basic Safety and Essential Performance of Magnetic Resonance Equipment for Medical Diagnosis*. Geneva, Switzerland: International Electrotechnical Commission (IEC) (2015).
6. Shrivastava D, Utecht L, Tian J, Hughes J, and Vaughan JT. *In Vivo* radiofrequency Heating in Swine in a 3T (123.2-MHz) Birdcage Whole Body Coil. *Magn Reson Med* (2013) 72(4):1141–50. doi:10.1002/mrm.24999
7. Nadobny J, Klopfleisch R, Brinker G, and Stoltenburg-Didinger G. Experimental Investigation and Histopathological Identification of Acute thermal Damage in Skeletal Porcine Muscle in Relation to Whole-Body SAR, Maximum Temperature, and CEM43 °C Due to RF Irradiation in an MR Body Coil of Birdcage Type at 123 MHz. *Int J Hyperthermia* (2015) 31(4):409–20. doi:10.3109/02656736.2015.1007537
8. Murbach M, Neufeld E, Cabot E, Zastrow E, Córcoles J, Kainz W, et al. Virtual Population-based Assessment of the Impact of 3 Tesla Radiofrequency Shimming and Thermoregulation on Safety and B_1+ Uniformity. *Magn Reson Med* (2015) 76:986–97. doi:10.1002/mrm.25986
9. Murbach M, Zastrow E, Neufeld E, Cabot E, Kainz W, and Kuster N. Heating and Safety Concerns of the Radio-Frequency Field in MRI. *Curr Radiol Rep* (2015) 3:45. doi:10.1007/s40134-015-0128-6
10. Fiedler TM, Ladd ME, and Bitz AK. SAR Simulations & Safety Neuroimage. *Neuroimage* (2018) 168:33–58. doi:10.1016/j.neuroimage.2017.03.035
11. Murbach M, Cabot E, Neufeld E, Gosselin M-C, Christ A, Pruessmann KP, et al. Local SAR Enhancements in Anatomically Correct Children and Adult Models as a Function of Position within 1.5 T MR Body Coil. *Prog Biophys Mol Biol* (2011) 107(3):428–33. doi:10.1016/j.pbiomolbio.2011.09.017
12. Seifert F, Wübbeler G, Junge S, Ittermann B, and Rinneberg H. Patient Safety Concept for Multichannel Transmit Coils. *J Magn Reson Imaging* 26:1315–21. doi:10.1002/jmri.21149
13. Foo TK, Hayes CE, and Kang Y. An Analytical Model for the Design of RF Resonators for MR Body Imaging. *Magn Reson Med* (1991) 21:165–77. doi:10.1002/mrm.1910210202
14. Foo TK, Hayes CE, and Kang Y. Reduction of RF Penetration Effects in High Field Imaging. *Magn Reson Med* (1992) 23:287–301. doi:10.1002/mrm.1910230209
15. Liu W, Zhang S, Collins CM, Wang J, and Smith MB. Comparison of Four Different Shields for Birdcage-type Coils with Experiments and Numerical Calculations. *Concepts Magn Reson B Magn Reson Eng* (2006) 29B(4):176–84. doi:10.1002/cmr.b.20073
16. Engheta N, and Ziolkowski R. *Metamaterials Physics and Engineering Explorations*. chapters 2.8, 11.3. Hoboken, New Jersey: John Wiley & Sons (2006).
17. Capolino F. *Theory and Phenomena of Metamaterials*. chapter 4. Milton Park, Oxfordshire: Taylor & Francis Group (2009).
18. Gedney S. *Introduction to the Finite-Difference Time-Domain (FDTD) Method for Electromagnetics*. an Rafael, CA: Morgan & Claypool Publishers (2011):63.
19. Sievenpiper D, Zhang L, Broas RFJ, Alexopolous NG, and Yablonovitch E. High-impedance Electromagnetic Surfaces with a Forbidden Frequency Band. *IEEE Trans Microwave Theor Tech* (1999) 47(11):2059–74. Nov. doi:10.1109/22.798001
20. Simovski CR, and Sochava AA. High-impedance Surfaces Based on Self-Resonant Grids. Analytical Modelling and Numerical Simulations. *Prog Electromagnetics Res PIER* (2003) 43:239–56. doi:10.2528/pier03042801
21. Goussetis G, Feresidis AP, and Vardaxoglou JC. Tailoring the AMC and EBG Characteristics of Periodic Metallic Arrays Printed on Grounded Dielectric Substrate. *IEEE Trans Antennas Propagation* (2006) 54(1):82–9. doi:10.1109/tap.2005.861575
22. Saleh G, Solbach K, and Rennings A. EBG Structure to Improve the B1 Efficiency of Stripline Coil for 7 Tesla MRI. In: 2012 6th European Conference on Antennas and Propagation (EUCAP); 2012 26–30 march; Brussels, Belgium (2012) p. 1399–401. doi:10.1109/EuCAP.2012.6206267
23. Chen Z, Solbach K, Erni D, and Rennings A. Improving B_1 Efficiency and Signal-To-Noise-Ratio of a Surface Coil by a High-Impedance-Surface RF Shield for 7-T Magnetic Resonance Imaging. *IEEE Trans Microwave Theor Tech* (2017) 65(3):988–97. doi:10.1109/tmtt.2016.2631169
24. Chen Z, Solbach K, Erni D, and Rennings A. Improved B1 Distribution of an MRI RF Coil Element Using a High-Impedance-Surface Shield. In: 2015 German Microwave Conference; 2015 16–18 march; Erlangen, Germany (2015) p. 111–4. doi:10.1109/gemic.2015.7107765
25. Chen Z, Solbach K, Erni D, and Rennings A. Electromagnetic Field Analysis of a Dipole Coil Element with Surface Impedance Characterized Shielding Plate

for 7-T MRI. *IEEE Trans Microwave Theor Tech* (2016) 64(3):972–81. doi:10.1109/tmtt.2016.2518168
26. Chen H, Guo L, Li M, Liu C, Shan S, Wang Y, Weber E, Liu F, and Crozier S. Metamaterial RF Shield with Reduced Specific Absorption Rate and Improved Transmit Efficiency for 9.4 T MRI. In: Proceedings of ISMRM; 2018 16–21 june; Concord, California (2018).
27. Lezhennikova K, Simovski C, Abdeddaim R, Balafendiev R, and Glybovski S. Extending a Birdcage Coil for Magnetic Resonance Imaging of a Human Head with an Artificial Magnetic Shield. *Photon Nanostructures - Fundamentals Appl* (2021) 43:100890. doi:10.1016/j.photonics.2020.100890
28. Lezhennikova K, Abdeddaim R, Hurshkainen A, Vignaud A, Dubois M, Jomin P, et al. Constructive Near-Field Interference Effect in a Birdcage MRI Coil with an Artificial Magnetic Shield. *Phys Rev Appl* (2020) 13:064004. doi:10.1103/physrevapplied.13.064004
29. Jackson JD. *Classical Electrodynamics*. 1st ed Hoboken, New Jersey: John Wiley & Sons (1962):223–4.
30. Gosselin MC, Neufeld E, Moser H, Huber E, Farcito S, Gerber L, et al. Development of a New Generation of High-Resolution Anatomical Models for Medical Device Evaluation: the Virtual Population 3.0. *Phys Med Biol* (2014) 59(18):5287–303. doi:10.1088/0031-9155/59/18/5287

Conflict of Interest: ML was employed by the company Tesla Dynamic Coils.

The remaining authors declare that the research was conducted in the absence of any commercial or financial relationships that could be construed as a potential conflict of interest.

frontiers in Physics

MINI REVIEW
published: 27 October 2021
doi: 10.3389/fphy.2021.717369

Interelement Decoupling Strategies at UHF MRI

Irena Zivkovic *

Electrical Engineering Department, Technical University of Eindhoven, Eindhoven, Netherlands

Moving to the ultrahigh field magnetic resonance imaging (UHF MRI) brought many benefits such as potentially higher signal-to-noise ratio, contrast-to-noise ratio, and improved spectral resolution. The UHF MRI regime also introduced some challenges which could prevent full exploitation of mentioned advantages. A higher static magnetic field means increase in Larmor frequency, which further implies the shorter wavelength in a tissue. The shorter wavelength causes interferences of the RF signal and inhomogeneous excitation, which can be partially resolved by the introduction of the multichannel coil arrays. The biggest problem in UHF multichannel densely populated arrays is the existence of the interelement coupling, which should be minimized as much as possible. This article presents the nonconventional, recently developed decoupling techniques used in UHF MRI.

Keywords: decoupling, UHF MRI, RF coils, MRI arrays, interelement decoupling

OPEN ACCESS

Edited by:
Roberta Frass-Kriegl,
Medical University of Vienna, Austria

Reviewed by:
Stephan Orzada,
German Cancer Research Center (DKFZ), Germany
Lucia Isabel Navarro De Lara,
Massachusetts General Hospital and Harvard Medical School, United States

****Correspondence:***
Irena Zivkovic
i.zivkovic@tue.nl

Specialty section:
This article was submitted to Medical Physics and Imaging, a section of the journal Frontiers in Physics

Received: *30 May 2021*
Accepted: *24 September 2021*
Published: *27 October 2021*

Citation:
Zivkovic I (2021) Interelement Decoupling Strategies at UHF MRI. Front. Phys. 9:717369. doi: 10.3389/fphy.2021.717369

INTRODUCTION

Moving to the ultrahigh field regime brought many benefits such as increased signal-to-noise ratio (SNR), contrast-to-noise ratio (CNR), and spectral resolution [1–8]. With a higher static magnetic field, the Larmor frequency increases and wavelength in a tissue decreases. Shorter wavelength in a tissue causes constructive and destructive interferences which cause inhomogeneous excitation, lower SNR, and even signal voids. Introduction of parallel transmit (pTx) systems with individually controllable amplitudes and phases of each channel helped in solving the interference problems [4, 9–12]. Multichannel arrays allowed homogeneity shimming of the transmit field in a region of interest and accelerated acquisition. Very often, the individual elements in multichannel arrays are closely spaced, and due to the magnetic flux linkage and stray capacitance emanating from the coils, the problem of interelement coupling arises. The coupling manifests as induced voltage across the terminals of input ports of individual elements in the array. This produces an unwanted tertiary magnetic field, and as a result, the corresponding reflection coefficient measured at the input of the coupled terminals shows "mode splitting." The coupling of more than two coils will produce additional modes in the frequency spectrum which will manifest in both reflection and transmission coefficients. The coupling is a big issue for transmit-only or transmit-and-receive (transcieve) systems because it dramatically reduces the efficiency and influences the shimming capabilities of pTx systems. However, for receive-only coils, the increased coupling increases noise correlations and has an effect on the g-factor.

The most common coil elements in MRI but also at UHF are loop coils. Widely used decoupling techniques of loop elements are partial overlapping [13], preamplifier decoupling [14], and introduction of the inductive [15] and capacitive networks [16, 17] between the elements. In the work in reference [18], it was demonstrated that at 9.4T, it is possible to decouple an eight-channel loop array only by partial overlap of the elements. It is shown that at 9.4T and for a given size of a loop

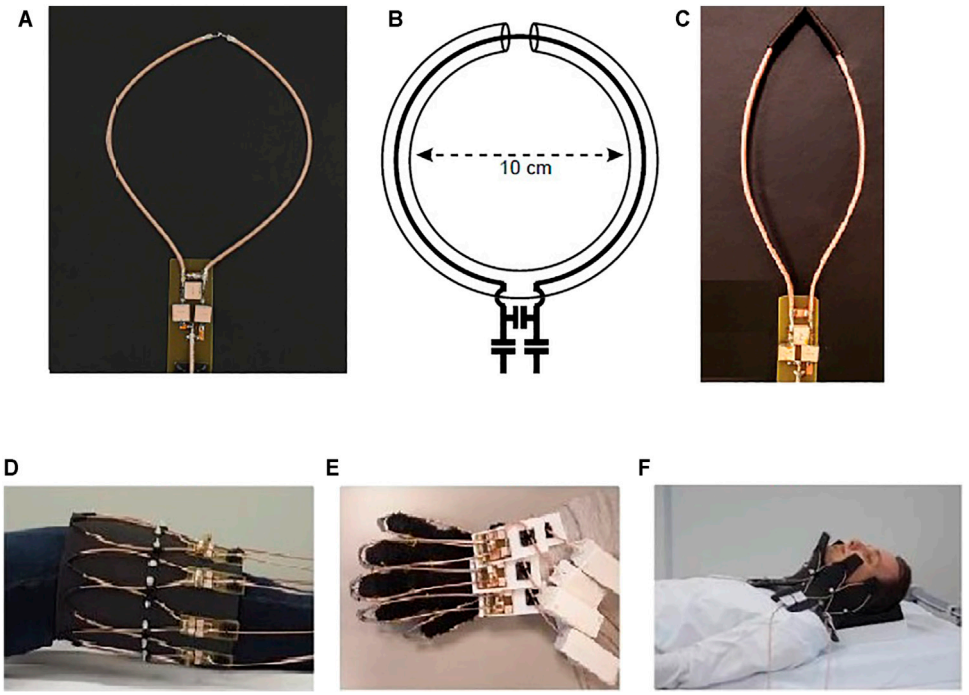

FIGURE 1 | Fabricated SCC coils and arrays with SCC coil elements. **(A)** Round SCC coil, **(B)** schematics of the SCC element, **(C)** elongated SCC coil, **(D)** 8-channel knee array, **(E)** 5-channel hand array, and **(F)** 5-channel neck array. This Figure was partially adapted from [19].

element, there is an optimal overlap which minimizes both resistive and reactive couplings at the same time. Overlapping of loops allows using of loops with increased diameter. Overlapped loops with increased diameters have increased penetration depth compared to the gapped loops. Overlapping also eliminates a signal void present in the gaps of nonoverlapped loops which improves peripheral SNR (which is associated with a greater loop size). On the receive side, overlapped loops have reduced g-factor but only for higher accelerations [18].

Beside loops, other common elements used in UHF multichannel arrays are dipole and monopole antennas, microstrip elements, and recently proposed shielded-coaxial-cable (SCC) coils. Decoupling strategies developed for loop coils do not easily translate to nonlooped elements; thus, some novel techniques have been introduced.

In this review article, the latest developments in interelement decoupling techniques of the mentioned array elements at UHF will be described.

INDIVIDUAL COIL DESIGN FOR IMPROVED INTERELEMENT DECOUPLING

Shielded-Coaxial-Cable Coils—Decoupled Elements Per Se

The shielded-coaxial-cable (SCC) coil has recently been proposed for use at UHF [19, 20]. The SCC coil is made of a coaxial cable with the shield interrupted at one point and with the central conductor interrupted at the opposite point of the shield interruption. The SCC coil design is very similar to that of the high impedance coil [21]. The main difference is in the matching circuit; in the high impedance coil [21], there is a parallel inductor across the feed port, while in the SCC coil design [19, 20], there is a parallel capacitor (the matching circuit contains only capacitors). The use of a matching capacitor versus an inductor influences the coupling properties of the coil. The high impedance coil [21] needs preamplifiers for additional decoupling and for that reason is proposed for use as a receive-only element for hand imaging. The SCC coil is a highly decoupled element, and there is no need for any additional decoupling. Multichannel arrays built with SCC coils are shown in **Figure 1**. The SCC array elements can be used as both transmit and/or receive elements since their decoupling property does not depend on pre-amplifiers or partial overlapping. Those elements are flexible—the coils can be bent, elongated (**Figure 1A,C**), and overlapped while maintaining the high interelement decoupling without compromising the performance of the coil. A constructed neck array, for example, consists of five SCC elements placed on flexible foam [20] and can conform to different neck sizes without elements being detuned. Likewise, a five-channel array was constructed for hand imaging [19]. SCC elements were attached to the glove. Due to the hand geometry, every SCC element was elongated, and in a final setup, when the glove with the attached SCC elements was placed on a hand, individual elements, besides being elongated, were also partially overlapped. Even in this extreme case, the tuning and matching were not

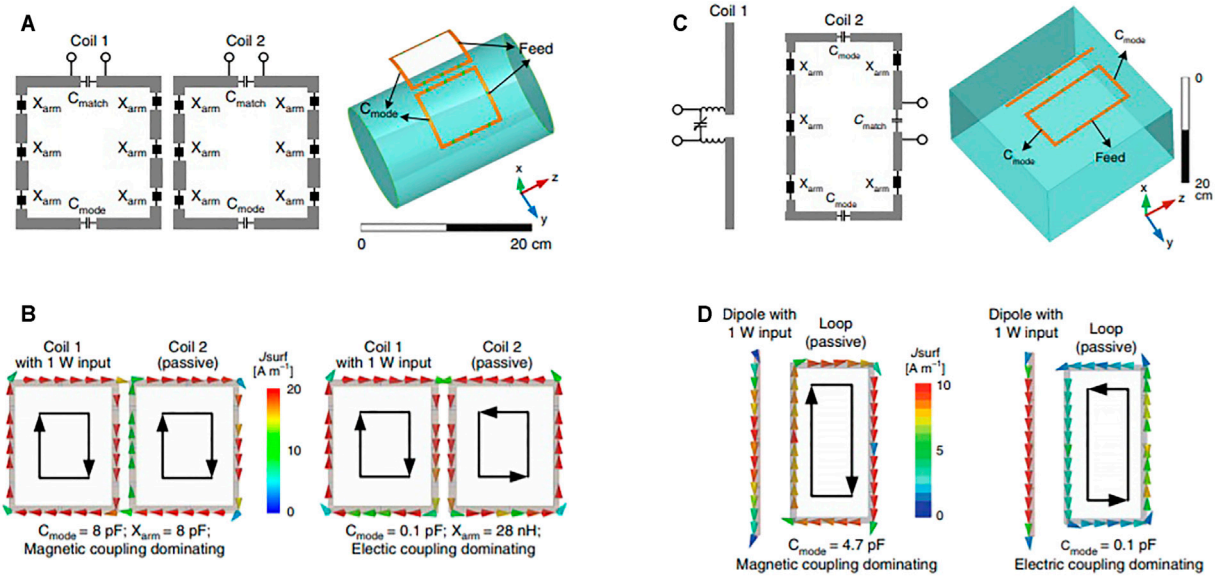

FIGURE 2 | (A) Schematics of a pair of decoupled coils. **(B)** Simulated vector current distribution of magnetic-dominant and electric-dominant coupling. **(C)** Schematics of a loop–dipole decoupling array. **(D)** Simulated vector current distribution of a loop-mode and dipole-mode coupling achieved by adjusting the two C-mode capacitors in a loop. This Figure was reproduced from [24].

altered. The diameter of the proposed SCC coil was around 10 cm in all presented examples of arrays operating at 7T. That size of the SCC coil seems to be optimal for different imaging regions (knee, head, neck, hand, etc.). The diameter of the SCC coil cannot be arbitrary. It can vary from around 8 to 12 cm for operation at 7T, and there is a need for using techniques for increasing/decreasing the coil diameter. In the work in reference [22], it is proposed to introduce multiple gaps on the shield and/or inner conductor to obtain the desired coil size. Similarly, in the work in reference [23], different combinations of multiple gaps and multiple turns were proposed for optimal operations at different frequencies. Introduction of the multiple gaps influenced the coupling properties of the coil, which in turn introduced the need for partial overlap for further improvement of decoupling [22]. The coupling properties of the coils proposed in the work in reference [23] were not investigated.

Self-Decoupled Coils

Recently the self-decoupled coil principle was introduced, based on the intentional nonuniform distribution of impedances along a rectangular coil [24]. Relatively large impedance is positioned opposite the coil feed port, and the rectangular coil behaves as a hybrid of a dipole and a loop element (**Figure 2**); thus, the coupling between the adjacent coils is both electric and magnetic in nature (they are of the same magnitude but opposite signs). The current density on a coil's conductor depends on the impedance of the corresponding arm, and the current's magnitude defines the coupling nature. The concept can be used for decoupling rectangular coil elements and decoupling between dipoles and loops (**Figure 2**). The drawback of this method is in the required number of lumped elements, the values of which must be precisely calculated. Also, the relative orientation of the coils with respect to each other is fixed, and therefore is not appropriate for flexible arrays.

Microstrip Elements With Meander Endings

In the work in reference [25], microstrip elements are ended with meandered structures. It is demonstrated that the size of the meandered structure influences interelement coupling, that is, it is possible to optimize the size and geometry of the meander for the best decoupling between the elements. In the optimized case, no additional decoupling is needed. There are some additional parameters that can be optimized at the same time as the meander size, such as distance between the antennas in the array and the distance from the phantom, for both RF efficiency and coupling properties. After parametric study, it was concluded that the medium meander size produces maximum central H-field strength and optimum decoupling between the elements. This work shows that alteration of the electrical length of the microstrip elements changes current distribution along the element, which influences its coupling properties. Similar strategies can be applied on linear coils such as dipole and monopole antennas.

PASSIVE STRUCTURES AND METASURFACES FOR IMPROVED DECOUPLING

Induced Current Elimination or Magnetic Wall Decoupling Method

The use of induced current elimination or magnetic walls has been proposed as a decoupling method for transmission lines [26], loops

[27], and monopole [28] and dipole [29, 30] elements. To reduce the mutual coupling, a magnetic wall is inserted between elements in the form of a passive element. The magnetic wall operates as a stopband between the terminals of the coils and eliminates the transmission of energy between the two individual channels. This technique is especially attractive for elements that cannot be partially overlapped or decoupled by using inductive or capacitive networks. In the example of two monopole elements [28], the decoupling element is inserted between the active elements. The decoupling element is a passive monopole element connected through the capacitor to the common ground plane of the two active elements. A similar strategy is also used for loop and microstrip elements [26, 27]. The passive loops and microstrip elements are placed between the two active elements. The electromagnetic field from the active elements induces current into the inserted passive element, and in that way, the coupling between the active elements is reduced. In the work in reference [30], decoupling of two or three active dipoles by insertion of one passive (parasitic) dipole between them has been demonstrated. For a dense array where the distance between the elements is less than one tenth of a wavelength, the decoupling condition differs. This method of decoupling shrinks the operational bandwidth of dipoles. The drawback of this method is in affecting the primary RF field. An additional RF field produced by the inserted passive elements interferes with the primary RF field and reduces the efficiency of the array and/or decreases the primary field homogeneity.

As another example [31], decoupling of meander microstrip line elements with parasitic elements is shown. Conductivity of the sample creates common current paths within the sample, and coupling has resistive (real) and reactive (imaginary) components. The common impedance should be equal to 0 for the completely decoupled case. It must be mentioned that the RF array [31] is surrounded by the RF shield (to be isolated from the gradients and the outside environment), which also has the effect of reducing coupling.

Decoupling of Dipole Antennas—EBG Structures, Stacked Resonators, and Metasurfaces

Dipole antennas are very popular antennas at UHF MRI, especially for use as array elements for body imaging. Dipole elements are linear elements, and therefore, decoupling techniques such as geometrical decoupling cannot be applied. There have been several dipole decoupling techniques proposed recently: decoupling with the electromagnetic bandgap (EBG) structures [32], decoupling with stacked resonators [33], and decoupling with metasurfaces [34].

The EBG structures are periodic structures with subwavelength periodicity. The EBG effect prevents all surface modes in a certain frequency band from propagating. In the work in reference [32], the finite EBG structure containing mushroom-type metasurface elements has been designed and positioned between dipole antenna elements. The position of the EBG structure was optimized for the best decoupling between the two elements. With this technique, the interelement decoupling is improved while the biggest drawback is reduced transmit efficiency.

As a decoupling strategy of dipole-type antennas, passive stacked magnetic resonators (SMRs) have been proposed [33]. The design of the SMR structure was inspired by metamaterial structures and consists of several open loops which end with capacitive gaps. Improved decoupling is achieved when more layers are positioned between the coils.

Decoupling of dipole antennas using metasurfaces without distortion of the transmit field has been proposed in the work in reference [34]. The metasurface is a periodic structure which consists of five parallel resonant wires and is a continuation of the work presented in reference [30]. Compared to decoupling with a single resonant wire [29], in the proposed metasurface, it is possible to excite higher-order coupled modes. The single wire acts as a scatterer and produces a strong parasitic resonance. In the work in reference [34], the transmit field of the coil has been studied in the cases without decoupling elements and with one and five resonant decoupling elements. It is shown that adding more resonant elements improves the isolation between the channels without distorting the transmit RF field.

Another decoupling technique applied to dipole and monopole types of antennas is cloaking. In the work in reference [35], the dipole antennas were cloaked with two metasurfaces consisting of N vertical metallic strips. In the work in reference [36], two monopole-type antennas operating at different frequencies were cloaked with two embedded elliptically shaped metasurfaces. The efficiency depends on the number of linear elements in the array, as this constrains the distance between them. For distances less than 1/30th of lambda, the proposed techniques do not work.

Similar to the use of meandered structures at the end of microstrip elements [25] to alter electrical length and current distribution, it is proposed [37] to fold dipole antennas. The eight-element array consisting of folded dipole-type antennas for head imaging has been proposed. It was shown that folding of the dipole element and use of the RF shield close to the folded part can decouple the array elements sufficiently. The mutual inductance is defined by the distance of the dipoles to the RF shield and the length of a folded portion of the dipole element. The optimal decoupling value, S_{12}, can be achieved for various combinations of height and the portion of the folded dipole. The bending and folding of the dipole element "takes away" the current on the element which directly influences coupling between the elements. Different array configurations with different elements were examined, such as bent dipole, straight dipole, 10-mm folded bent dipole, 30-mm folded bent dipole, and 10-mm straight folded dipole. All those arrays were simulated with and without the RF shield. The parameters such as SAR and transmit efficiency and averaged coupling coefficients over all eight elements were observed, and the most optimal array configuration was the one with the 30-mm bent folded dipole.

DISCUSSIONS

In this review, we presented the most recent developments in interelement decoupling strategies for application in multichannel array design for operation at UHF MRI. The loop element is one of the most used coils in MRI, but at UHF, other elements, such as dipole and monopole antennas,

TABLE 1 | Summary of the coil type in the array and the decoupling method.

Coil type	References	Decoupling method	Advantages/disadvantages
Loop	[13, 18]	Partial overlapping	At 9.4T, head array sufficient for decoupling of all elements/cannot be applied to nonadjacent elements
Loop	[14]	Pre-amplifier decoupling/high and low input impedance preamplifiers	Decoupling of nonadjacent elements/receive-only arrays
Loop, microstrip	[15–17]	Inductive and capacitive networks	Maximized isolation between the adjacent elements/networks become complex for nonadjacent elements
SCC coils	[19, 20]	The coil is made of shielded-coaxial cable	Coils are decoupled and not sensitive to bending, elongation, and amount of overlap/diameter of the coil cannot be arbitrary
Self-decoupled coils	[24]	Intentional uneven impedance distribution along the conductor	High degree of interelement isolation is achieved/relative orientation between the elements is fixed
Microstrip	[25]	Elements are ended with meandered structures	High degree of interelement isolation is achieved/meandered structure should be optimized vs. distance between the coils
Microstrip, loop, monopole, dipole	[26–30]	Insertion of a single passive element	Maximized isolation between the adjacent elements/the primary RF field's efficiency and homogeneity could be affected
Dipole	[32–34]	Insertion of periodic passive structures with multiple unit cells	Can be applied also to microstrip, monopole, and loop coils; the interaction with the primary RF field is eliminated/the effect disappears for densely populated unit cells
Dipole	[37]	Folding of the end of the dipole	High degree of interelement isolation is achieved/the presence of the RF shield significantly affects performance

microstrip coils, and shielded-coaxial-cable coils, were proposed. For newly proposed elements, traditional decoupling techniques cannot be applied. To improve decoupling between the elements at UHF, two strategies could be recognized: 1) use of advanced element design (a shielded-coaxial-cable SCC coil, self-decoupled elements, microstrip elements with a meandered structure at the end, etc.) and 2) development of new decoupling techniques (inclusion of the passive elements, metasurfaces, RF shields, etc.). The advanced element design reduces coupling between the elements by adjusting the geometry and the design concept of the element itself. The shielded-coaxial-cable coil has been proposed as a highly decoupled element, and operation of several arrays at 7T were demonstrated. The optimal coil diameter at 7T is around 10 cm and cannot be increased/decreased arbitrarily. Self-decoupled coils use intentionally nonequal impedance distribution along the coil's conductor, which defines the current distribution which dictates a coupling between the neighboring elements. The decoupling between the neighboring elements is improved while nonadjacent elements are not solved. The example of a microstrip element terminated by meanders demonstrates the possibility of decoupling between the elements by altering the electrical length of the elements, which further alters the current distribution and influences coupling.

As a second direction in reducing the coupling between the elements in an array is the use of passive structures. The basic principle is the following: the energy that would be transferred between the active elements is captured by the passive element/structure placed close to the active elements. The active elements become isolated from each other. The drawback of this technique is the existence of the secondary RF field produced by the passive element/structure which can reduce the radiation efficiency of the active array. In the work in reference [34], it is shown that the higher number of passive elements and their proper spacing can reduce interaction with the transmit RF field. Passive decoupling structures could also interfere with the receive array elements (in transmit-only receive-only (ToRo) configurations) since the passive elements are not detuned.

Some of the latest developments in the interelement decoupling at UHF were mentioned and discussed. **Table 1** summarizes the mentioned coil types and related decoupling methods with the main advantages and disadvantages. There is still room for improvement in designing both elements for the lowest coupling and optimal passive structures to reduce interelement coupling.

AUTHOR CONTRIBUTIONS

The author confirms being the sole contributor of this work and has approved it for publication.

REFERENCES

1. Vaughan JT, Garwood M, Collins CM, Liu W, DelaBarre L, Adriany G, et al. 7T vs. 4T: RF Power, Homogeneity, and Signal-To-Noise Comparison in Head Images. *Magn Reson Med* (2001) 46:24–30. doi:10.1002/mrm.1156
2. Yacoub E, Shmuel A, Pfeuffer J, Van De Moortele P-F, Adriany G, Andersen P, et al. Imaging Brain Function in Humans at 7 Tesla. *Magn Reson Med* (2001) 45:588–94. doi:10.1002/mrm.1080
3. Wiggins GC, Potthast A, Triantafyllou C, Wiggins CJ, and Wald LL. Eight-channel Phased Array Coil and Detunable TEM Volume Coil for 7 T Brain Imaging. *Magn Reson Med* (2005) 54:235–40. doi:10.1002/mrm.20547
4. Adriany G, Van de Moortele P-F, Wiesinger F, Moeller S, Strupp JP, Andersen P, et al. Transmit and Receive Transmission Line Arrays for 7 Tesla Parallel Imaging. *Magn Reson Med* (2005) 53:434–45. doi:10.1002/mrm.20321
5. Ibrahim TS, Mitchell C, Schmalbrock P, Lee R, and Chakeres DW. Electromagnetic Perspective on the Operation of RF Coils at 1.5-11.7 Tesla. *Magn Reson Med* (2005) 54:683–90. doi:10.1002/mrm.20596

6. Zhu X-H, Zhang Y, Tian R-X, Lei H, Zhang N, Zhang X, et al. Development of 17O NMR Approach for Fast Imaging of Cerebral Metabolic Rate of Oxygen in Rat Brain at High Field. *Proc Natl Acad Sci* (2002) 99:13194–9. doi:10.1073/pnas.202471399
7. Lei H, Zhu X-H, Zhang X-L, Ugurbil K, and Chen W. *In Vivo*31P Magnetic Resonance Spectroscopy of Human Brain at 7 T: An Initial Experience. *Magn Reson Med* (2003) 49:199–205. doi:10.1002/mrm.10379
8. Zhang X, Ugurbil K, and Chen W. Microstrip RF Surface Coil Design for Extremely High-Field MRI and Spectroscopy. *Magn Reson Med* (2001) 46: 443–50. doi:10.1002/mrm.1212
9. Webb A, and Collins C. Parallel Transmit and Receive Technology in High-field Magnetic Resonance Neuroimaging. *Int J Imaging Syst Technol* (2010) 20: 2-13. doi:10.1002/ima.20219
10. Katscher U, and Börnert P. Parallel RF Transmission in MRI. *NMR Biomed* (2006) 19:393–400. doi:10.1002/nbm.1049
11. Abraham R, and Ibrahim TS. Proposed Radiofrequency Phased-Array Excitation Scheme for Homogenous and Localized 7-Tesla Whole-Body Imaging Based on Full-Wave Numerical Simulations. *Magn Reson Med* (2007) 57:235–42. doi:10.1002/mrm.21139
12. Graessl A, Renz W, Hezel F, Dieringer MA, Winter L, Oezerdem C, et al.Modular 32-channel Transceiver Coil Array for Cardiac MRI at 7.0T. *Magn Reson Med* (2014) 72:276–90. doi:10.1002/mrm.24903
13. Avdievich NI, Giapitzakis IA, Pfrommer A, Shajan G, Scheffler K, and Henning A. Decoupling of a Double-Row 16-element Tight-Fit Transceiver Phased Array for Human Whole-Brain Imaging at 9.4 T. *NMR Biomed* (2018) 31(9):e3964. doi:10.1002/nbm.3964
14. Shajan G, Kozlov M, Hoffmann J, Turner R, Scheffler K, and Pohmann R. A 16-channel Dual-Row Transmit Array in Combination with a 31-element Receive Array for Human Brain Imaging at 9.4 T. *Magn Reson Med* (2014) 71(2):870–9. doi:10.1002/mrm.24726
15. Wu B, Zhang X, Qu P, and Shen GX. Design of an Inductively Decoupled Microstrip Array at 9.4T. *J Magn Reson* (2006) 182:126–32. doi:10.1016/j.jmr.2006.04.013
16. Zhang X, and Webb A. Design of a Capacitively Decoupled Transmit/receive NMR Phased Array for High Field Microscopy at 14.1T. *J Magn Reson* (2004) 170:149–55. doi:10.1016/j.jmr.2004.05.004
17. Lee RF, Giaquinto RO, and Hardy CJ. Coupling and Decoupling Theory and its Application to the MRI Phased Array. *Magn Reson Med* (2002) 48:203–13. doi:10.1002/mrm.10186
18. Avdievich NI, Giapitzakis I-A, Pfrommer A, and Henning A. Decoupling of a Tight-Fit Transceiver Phased Array for Human Brain Imaging at 9.4T: Loop Overlapping Rediscovered. *Magn Reson Med* (2018) 79(2):1200–11. doi:10.1002/mrm.26754
19. Ruytenberg T, Webb A, and Zivkovic I. Shielded-coaxial-cable Coils as Receive and Transceive Array Elements for 7T Human MRI. *Magn Reson Med* (2019) 83(3):1135–46. doi:10.1002/mrm.27964
20. Ruytenberg T, Webb A, and Zivkovic I. A Flexible Five-channel Shielded-coaxial-cable (SCC) Transceive Neck Coil for High-resolution Carotid Imaging at 7T. *Magn Reson Med* (2020) 84(3):1672–7. doi:10.1002/mrm.28215
21. Zhang B, Sodickson DK, and Cloos MA. A High-Impedance Detector-Array Glove for Magnetic Resonance Imaging of the Hand. *Nat Biomed Eng* (2018) 2(8):570–7. doi:10.1038/s41551-018-0233-y
22. Mollaei MSM, Van Leeuwen CC, Raaijmakers AJE, and Simovski CR. Analysis of High Impedance Coils Both in Transmission and Reception Regimes. *IEEE Access* (2020) 8:129754–62. doi:10.1109/access.2020.3009367
23. Nohava L, Czerny R, Roat S, Obermann M, Kuehne A, Frass-Kriegl R, et al.Flexible Multi-Turn Multi-Gap Coaxial RF Coils: Design Concept and Implementation for Magnetic Resonance Imaging at 3 and 7 Tesla. *IEEE Trans Med Imaging* (2021) 40(4):1267–78. doi:10.1109/tmi.2021.3051390
24. Yan X, Gore JC, and Grissom WA. Self-decoupled Radiofrequency Coils for Magnetic Resonance Imaging. *Nat Commun* (2018) 9:3481. doi:10.1038/s41467-018-05585-8
25. Rietsch SHG, Quick HH, and Orzada S. Impact of Different Meander Sizes on the RF Transmit Performance and Coupling of Microstrip Line Elements at 7 T. *Med Phys* (2015) 42(8):4542–52. doi:10.1118/1.4923177
26. Yan X, Ole Pedersen J, Wei L, Zhang X, and Xue R. Multichannel Double-Row Transmission Line Array for Human MR Imaging at Ultrahigh Fields. *IEEE Trans Biomed Eng* (2015) 62(6):1652–9. doi:10.1109/tbme.2015.2401976
27. Yan X, Zhang X, Feng B, Ma C, Wei L, and Xue R. 7T Transmit/Receive Arrays Using ICE Decoupling for Human Head MR Imaging. *IEEE Trans Med Imaging* (2014) 33(9):1781–7. doi:10.1109/tmi.2014.2313879
28. Yan X, Zhang X, Wei L, and Xue R. Magnetic wall Decoupling Method for Monopole Coil Array in Ultrahigh Field MRI: A Feasibility Test. *Quant Imaging Med Surg* (2014) 4(2):79–86. doi:10.3978/j.issn.2223-4292.2014.04.10
29. Yan X, Zhang X, Wei L, and Xue R. Design and Test of Magnetic Wall Decoupling for Dipole Transmit/Receive Array for MR Imaging at the Ultrahigh Field of 7T. *Appl Magn Reson* (2015) 46:59–66. doi:10.1007/s00723-014-0612-9
30. S.M. Mollaei M, Hurshkainen A, Kurdjumov S, Glybovski S, and Simovski C. Passive Electromagnetic Decoupling in an Active Metasurface of Dipoles. *Photon Nanostructures - Fundamentals Appl* (2018) 32:53–61. doi:10.1016/j.photonics.2018.10.001
31. Abuelhaija A, Orzada S, and Solbach K. Parasitic Element Based Decoupling of 7 Tesla MRI Coil Array. In: Loughborough Antennas and Propagation Conference LAPC 2015 (2015).
32. Hurshkainen AA, Derzhavskaya TA, Glybovski SB, Voogt IJ, Melchakova IV, Van Den Berg CAT, et al. Element Decoupling of 7 T Dipole Body Arrays by EBG Metasurface Structures: Experimental Verification. *J Magn Reson* (2016) 269:87–96. doi:10.1016/j.jmr.2016.05.017
33. Georget E, Luong M, Vignaud A, Giacomini E, Chazel E, Ferrand G, et al. Stacked Magnetic Resonators for MRI RF Coils Decoupling. *J Magn Reson* (2017) 275:11–8. doi:10.1016/j.jmr.2016.11.012
34. Hurshkainen A, Mollaei MSM, Dubois M, Kurdjumov S, Abdeddaim R, Enoch S, et al. Decoupling of Closely Spaced Dipole Antennas for Ultrahigh Field MRI with Metasurfaces. *IEEE Trans Antennas Propagat* (2021) 69:1094–106. doi:10.1109/tap.2020.3016495
35. Monti A, Soric J, Alu A, Bilotti F, Toscano A, and Vegni L. Overcoming Mutual Blockage between Neighboring Dipole Antennas Using a Low-Profile Patterned Metasurface. *Antennas Wirel Propag Lett* (2012) 11:1414–7. doi:10.1109/lawp.2012.2229102
36. Moreno G, Yakovlev AB, Bernety HM, Werner DH, Xin H, Monti A, et al. Wideband Elliptical Metasurface Cloaks in Printed Antenna Technology. *IEEE Trans Antennas Propagat* (2018) 66(7):3512–25. doi:10.1109/tap.2018.2829809
37. Avdievich NI, Solomakha G, Ruhm L, Scheffler K, and Henning A. Decoupling of Folded-End Dipole Antenna Elements of a 9.4 T Human Head Array Using an RF Shield. *NMR Biomed* (2020) 33(9):e4351. doi:10.1002/nbm.4351

Conflict of Interest: The author declares that the research was conducted in the absence of any commercial or financial relationships that could be construed as a potential conflict of interest.

frontiers in Physics

ORIGINAL RESEARCH
published: 09 February 2022
doi: 10.3389/fphy.2021.727536

An Unmatched Radio Frequency Chain for Low-Field Magnetic Resonance Imaging

Joshua R. Harper[1], Cristhian Zárate[2†], Federico Krauch[2†], Ivan Muhumuza[3], Jorge Molina[2], Johnes Obungoloch[3] and Steven J. Schiff[1,4,5]*

[1]Center for Neural Engineering, Department of Engineering Science and Mechanics, The Pennsylvania State University, University Park, PA, United States, [2]Laboratory of Mechanics and Energy, Department of Engineering, National University of Asunción, Asunción, Paraguay, [3]Low Field MRI Lab, Department of Biomedical Engineering, Mbarara University of Science and Technology, Mbarara, Uganda, [4]Department of Neurosurgery, The Pennsylvania State University, University Park, PA, United States, [5]Department of Physics, The Pennsylvania State University, University Park, PA, United States

Magnetic Resonance Imaging (MRI) is a safe and versatile diagnostic tool for intracranial imaging, however it is also one of the most expensive and specialized making it scarce in low- to middle-income countries (LMIC). The affordability and portability of low-field MRI offers the potential for increased access to brain imaging for diseases like Hydrocephalus in LMIC. In this tutorial style work, we show the design of a low powered and low cost radio frequency chain of electronics to be paired with a previously reported prepolarized low-field MRI for childhood hydrocephalus imaging in sub-Saharan Africa where the incidence of this condition is high. Since the Larmor frequency for this system is as low as 180 kHz, we are able to minimize the impedance of the transmit coil to 5 ohms rather than match to 50 ohms as is traditionally the case. This reduces transmit power consumption by a factor of 10. We also show the use of inexpensive and commonly available animal enclosure fencing ("chicken wire") as a shield material at this frequency and compare to more traditional shield designs. These preliminary results show that highly portable and affordable low-field MRI systems could provide image resolution and signal-to-noise sufficient for planning hydrocephalus treatment in areas of the world with substantial resource limitations. Employment of these technologies in sub-Saharan Africa offers a cost-effective, sustainable approach to neurological diagnosis and treatment planning in this disease burdened region.

Keywords: low field MRI, low cost, low power, prepolarization MRI, low- to middle-income countries, radiofrequency, sustainable MRI, portable

Edited by:
Simone Angela S. Winkler, Cornell University, United States

Reviewed by:
Shaoying Huang, Singapore University of Technology and Design, Singapore
Joseph Vincent Rispoli, Purdue University, United States

****Correspondence:***
Joshua R. Harper
jrh69@psu.edu

[†]These authors have contributed equally to this work

Specialty section:
This article was submitted to Medical Physics and Imaging, a section of the journal Frontiers in Physics

Received: *18 June 2021*
Accepted: *17 December 2021*
Published: *09 February 2022*

Citation:
Harper JR, Zárate C, Krauch F, Muhumuza I, Molina J, Obungoloch J and Schiff SJ (2022) An Unmatched Radio Frequency Chain for Low-Field Magnetic Resonance Imaging. Front. Phys. 9:727536. doi: 10.3389/fphy.2021.727536

1 INTRODUCTION

Magnetic Resonance Imaging (MRI) is one of the safest and most versatile biomedical imaging methods available. Higher field strength systems (> 1.5 tesla) can produce increased signal-to-noise pushing voxel size as low as hundreds of micrometers [1]. However, this capability comes at a cost of at least $1M per tesla [2] making these high-field systems inaccessible to those in low-to-middle income countries (LMIC). The unequal distribution of MRI and other medical technologies throughout the world has been well documented [3]. Even when technology such as MRI is introduced into LMIC through donation or purchase, more than half typically falls into disrepair and more than a quarter may never even be operational [4]. This is due to the lack of spare parts,

consumables, trained technical staff, or reliable power in addition to the high initial cost of acquisition [5]. A sustainable solution is necessary if diagnostic imaging is to be a useful tool for clinical practice in LMIC.

The term "sustainability" has been used in many different contexts, even as it relates to medical care. Following a review of the uses of "sustainability" in medical research in which the authors attempted to aggregate the most common definitions used, this work most closely matches the category of "Continued program activities" [6]. Here we invoke "sustainability" in the most literal sense—we need technology that can operate in LMIC in the long term.

A condition representing high clinical need in LMIC is childhood hydrocephalus. Globally there are an estimated 400,000 new cases of pediatric hydrocephalus per year with over 90% in LMIC [7]. In sub-Saharan Africa where post-infectious hydrocephalus is most common, there are approximately 180,000 new cases per year [8]. These infants require treatment to survive. In Hydrocephalus there is a buildup of cerebrospinal fluid around the brain and within the ventricles, creating excess intracranial pressure. It is treated with either ventriculoperitoneal shunting [9, 10] or endoscopic third ventriculostomy (with or without choroid plexus cauterization, ETV-CPC) [11, 12]. For treatment planning, computed tomography is often employed in LMIC since it provides good spatial resolution and contrast between brain and CSF, and is less costly than high-field MRI, however the ionizing radiation associated with this technology has been shown to be a high risk especially for infants [13]. Ultrasound can be a useful tool, but only before the first year of life when the skull begins to fuse [14]. Fortunately, the imaging needs for hydrocephalus treatment planning are relatively straightforward—clinicians must visually separate CSF from brain with enough confidence to plan surgery. While typical high-field images can provide sub-millimeter voxel spacing, we have suggested that considerably larger voxels ($3 \times 3 \times 10\,\mathrm{mm}^3$) could be sufficient for treatment planning [15] opening the door for the use of low-field MRI technology.

There has been recently renewed interest in clinical low-field MRI as an affordable and portable alternative to high-field imaging. Permanent magnet systems with main field strengths of 50 milli-tesla [16], 80 milli-tesla [17], and 64 milli-tesla [18] have all shown capability for clinically relevant brain imaging at varying levels of portability and cost. The system described by O'Reilley et al. (2020) has been made available in an open source forum for an estimated cost of 10,000 euros (https://www.opensourceimaging.org/project/halbach-array-magnet-for-in-vivo-imaging/). Coil-based low-field MRI offers another potential route to sustainable clinical imaging at even lower field strength. Work by Ref. [19] has shown impressive images of brain using a large Helmoltz coil design (220 cm diameter) with field strength of 6.5 milli-tesla. Although this system produces quality human brain images with a coil-based low-field MRI, it is not portable and consumes more than 4 kW of energy to generate the main, static field. Previous work from our group has described a pre-polarized low-field MRI (PMRI) specifically designed to assist with treatment planning for infant hydrocephalus in Uganda [15]. Details of this specific magnet design are discussed in Ref. [15] and in further general detail in Refs [20–22].

While the work in Ref. [15] described the magnet design and testing for the PMRI system, the present work focuses on the radio frequency chain (RF chain) of electronics required to operate the PMRI system. The motivation behind this work was to design a rugged and low power option for sustainable operation in low resource countries like Uganda and provide documentation that can serve as a basic tutorial on how to implement the RF system. The RF chain is powered using two 12 volt tractor-style lead-acid batteries. We take advantage of the relatively low operating frequency of 180 kHz to allow components in our RF chain to remain unmatched to 50 ohm impedance. This allows the transmit (Tx) coil to be tuned to a minimum impedance, maximizing the current delivered to the coil. In addition, we employ commonly available animal enclosure fencing (chicken wire) as a Faraday shield and compare the effectiveness over more traditional shielding options. Finally, we show imaging capability using basic geometrical phantoms filled with water.

2 MATERIALS AND METHODS

The Drive-L spectrometer developed by PureDevices was used for our PMRI system. **Figure 1A** shows the block diagram of the RF chain which includes a Transmit (Tx) amplifier, a Tx coil, a tuning network for the Tx coil, a receive coil (Rx), a tuning network for the Rx coil, a low noise amplifier for the Rx coil (LNA), and a shield surrounding the system. All analog-to-digital conversion takes place within the spectrometer.**Figure 1B** shows the RF characteristics of the Tx amplifier and LNA. The main magnet in this system generates a center field of 4.23 milli-tesla which corresponds to a Larmor frequency of 180.1 kHz.

2.1 Transmit and Receive Coils

Two separate RF coils were used for transmit and receive (Tx and Rx respectively). A saddle design was chosen for both since these coils are straightforward to build with copper wire and have a relatively uniform field. **Table 1** shows the parameters of the two coils used. An initial calibration step is necessary to ensure the Tx and Rx coil are decoupled. For a two-coil system, decoupling can be achieved by rotating the coils so that their field directions are orthogonal to each other. This was done by connecting the Rx coil to an oscilloscope and passing a 180 kHz signal through the Tx coil at 5 mV_{pp} with a function generator. When the coils are strongly coupled the signal amplitude will approach 5 mV_{pp} as measured by the oscilloscope. Decoupling is achieved by rotating the Rx coil until a signal amplitude less than a microvolt is visible on the oscilloscope.

Litz wire has been suggested to be a more efficient wire for low frequency RF signals since it reduces the loss in current density along the wire produced by the skin effect. It has also has been shown to be useful in low field MRI applications [23]. In a circular conductor, current density is pushed toward the outside edge as frequency increases due to the changing internal magnetic fields caused by the alternating signal. This increases the effective

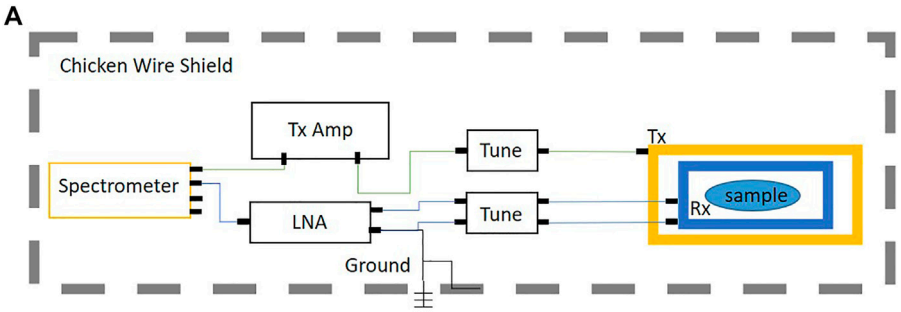

B

RF characteristics of custom electronics

	Tx Amplifier		LNA	
	Input	Output	Input	Output
Capacitance	50.6 pF	19.3 pF	7.2 pF	210 nF
Impedance	190 kΩ	537 Ω	1 kΩ	8 Ω

FIGURE 1 | (A) Block diagram of the RF chain in the PMRI system; **(B)** RF characteristics of the Tx amplifier and LNA.

TABLE 1 | RF coil properties.

Coil	Wire Type	Diameter (cm)	Length (cm)	Turns	Impedance (ohms) @ 180 kHz
Rx	100/36 Litz	10	12	10	1,508
Tx	100/36 Litz	24	25	20	10

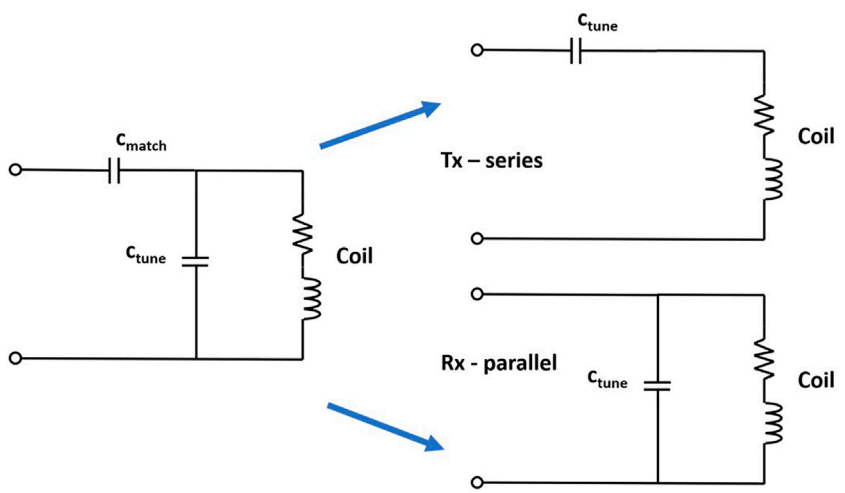

FIGURE 2 | RCL circuit. Typical tuning of the RF coil uses a tuning capacitor in parallel (c_{tune}) and a matching capacitor in series (c_{match}). In the low-field design, Tx can be tuned in series, providing minimum impedance, and Rx can be tuned in parallel, providing a higher Q.

resistance of the conductor. The optimal wire diameter should be twice the skin-depth of the wire material at the frequency of operation. A smaller wire also has increasingly small current carrying capacity, but if many small wires are soldered in parallel, the current can be split between them reducing the impedance. The Litz wire used in our PMRI system has 100 strands of AWG 36 wire.

2.2 Tuning Circuits

Both the Tx and Rx coil can be modeled as a resonant resistor-capacitor-inductor (RCL) circuit. For PMRI, the coil should be resonant at the Larmor frequency in order to detect the small signals (μV) resulting from low static magnetic field. A tuning capacitor is added in parallel with the coil to shift the natural resonant frequency to the Larmor frequency, as shown in **Figure 2**. A matching capacitor is typically added in series to match the impedance of the coil to 50 ohms. Addition of this capacitor alters the tuned frequency and one must use an iterative process to tune and match. In the low-field system at 180 kHz, matching is not a requirement and it may be desirable to have minimum impedance in the Tx coil while maintaining a higher impedance in the Rx coil.

It is a well-established principle in RF engineering that an impedance mismatch between input and output ports of two connected RF components leads to reduction in power transmission efficiency. It has also been shown that matching impedance of source and load between each component in a chain of RF electronics provides the most optimal power transfer efficiency [24]. For historical reasons, most RF electronic components and cables are impedance matched to 50 ohms.

There are specialized cases where ports and cables are not matched to 50 ohms. Test equipment that is sensitive to small voltages may have high impedance (100 Mohm or more) so that voltage drops preferentially on the input port of the measurement device. In some audio/video applications 75 ohm transmission cables and impedance matching is used. For most mid- to short-wave frequency applications, 50 ohm matching is the standard.

The power attenuation from impedance mismatch comes from the reflection of the transmitted wave at the input back to the source or to the surrounding space. When the reflected wave combines with the incident wave to create standing waves, peaks and nodes occur along the transmission line. The measurement of this phenomenon is often called the Standing Wave Ratio (SWR) [25].

The effect of SWR on efficiency is dependent on transmission frequency and the length of the transmission cable [25]. Significant reflections can be avoided if the cable is much less than one-quarter of the frequency wavelength. This rule of thumb makes impedance mismatch possible at low RF frequencies without sacrificing much efficiency. For example, at our typical operating frequency of 180 kHz, the wavelength is around 1,600 m. Since the cables used in the PMRI system rarely exceed 1 m they are not considered "long," and therefore energy loss at the load due to reflection at this frequency is virtually non-existent. This means an impedance mismatch will not lead to significant power inefficiencies.

Relaxation of the impedance matching principle provides more flexibility in designing electronics that are cost-effective and low power. For example, if the transmit amplifier is not driving 50 ohms, it could be low voltage and still deliver a useful amount of current. Since the impedance of a series RCL circuit has a frequency dependent minimum at resonance, a series capacitor is used to tune the Tx coil, as shown in **Figure 2**. Conversely, the impedance of a parallel RCL circuit has a frequency dependent maximum at resonance, so the parallel resonant circuit is used to tune the Rx coil as shown in **Figure 2**. By creating a series resonant RCL circuit at the desired frequency, impedance can be shifted to a minimum approaching the DC resistance of the Tx coil. Inefficiencies in passive electronic components and residual skin effect in the wire of the Tx coil make the impedance higher than DC resistance, but we were able to tune our coil to 180 kHz at an impedance of 5 ohms, providing a >5X current increase per signal voltage over the 50 ohm, impedance matched case.

In our low-field system, a 1 milli-second pulse with a 1 A_{pp} current delivers the desired $\pi/2$ flip angle. For a coil tuned to 180 kHz with an impedance of 5 ohms, this requires a 5 V_{pp} signal, or 25 W, compared to the 50 ohm impedance matched case, which would require 25 V_{pp} and over 125 W. In addition to an increase in power, the required voltages and increased power dissipation does carry significant design implications for the Tx amplifier—namely number of standard op-amps required to drive the load and number and type of required power sources for the op-amps.

2.3 Transmit Amplifier

The Tx amplifier was designed to operate with a minimum impedance Tx coil. The key aspect in designing an RF amplifier is choice of the correct operational amplifier (op-amp). For the specific aims of this project the op-amp should meet the voltage and current requirements of the application, maintain signal integrity, be as readily available throughout the world as possible, be of the appropriate size to work without specialized equipment, and be affordable in low quantities. The circuit design should also be as simple as possible to allow for fewer components and low-tech construction or repair.

Texas Instruments (TI) op-amp OPA-549 was chosen to drive the voltage amplifier. The op-amp data sheet is available on the Texas Instruments website (www.ti.com) and the circuit design for the Tx amplifier can be found in the supplemental data. The op-amp is capable of 8 A continuous output and can be driven by up to ±30 volt. Open loop gain is linear at the frequency of intended use and noise voltage density is at a minimum of 70 nV/$\sqrt{Hz}$.

Power supply requirements are important to consider in terms of heat dissipation and rail-to-rail voltage. Consider the case where one might want to drive a 50 ohm impedance matched RF coil at 180 kHz with an OPA-549 amplifier. If we want to drive 0.5 A of current we need a 50 V_{pp} swing (25 volts in each direction). The rail-to-rail voltage of a differential amplifier (i.e. the voltage limit in the positive and negative direction before the signal is clipped) is typically slightly less than the supply voltage, and is often specified in the op-amp

documentation. This means, for a single OPA-549, we could supply this desired signal amplification with a ±30 volt power supply, but we would need to consider a good cooling strategy for the op-amp. We would also be utilizing a very small amount of the available current output for the maximum voltage supply.

Alternatively, we chose to build a bridged amplifier with two OPA-549 op-amps—one per supply pole. This allows us to divide the heat dissipation across two op-amps and reduces our need for cooling. It also maintains the current driving capability while essentially doubling the rail-to-rail voltage of the amplifier. This means that we could supply 60 volts to each side (roughly 120 volts rail-to-rail) and even drive the coil with 1 A of current. If more current is desired, op-amps can be added in series to each polar side of the design. This design meets the amplification needs of our system without requiring forced cooling strategies.

Since the Tx coil in our system was tuned to 5 ohms instead of 50 ohms the power supply strategy can be simplified to two 12 volt supplies. We can supply the OPA-549 with ±12 volt to produce a rail-to-rail of 20 V_{pp}, or we can bridge two amplifiers and supply each with 12 volt and drive a little over 1 A of current without excessive heat dissipation. This method has a few other advantages. Many other electronic components in the system are driven with 12 volt power supplies, which means we can couple them all to two 12 volt linear power supplies, or power the entire RF chain using two 12 volt car or tractor batteries. This has many sustainability advantages when it comes to use in LMIC.

The Tx amplifier is capable of 8 A continuous (10 A peak) output with a rail-to-rail voltage of around 20 volts before clipping. The Tx coil was tuned to 5 ohm impedance which allows for a maximum of 4 A delivered to the coil. For the spin-echo imaging used in the PMRI system, minimum pulse widths of between 0.5 ms and 1 ms are typically used for the $\pi/2$ pulse with 1 A current. shorter pulse widths could be desirable, in which case supply voltage can be increased or the amplifier can be bridged to increase the rail-to-rail voltage.

2.4 Low Noise Amplifier

One of the most important components of the RF chain is the low noise amplifier (LNA). The LNA is used to amplify the small signal coming from the receive coil, which can be as low as μV for PMRI. A good LNA design will add the appropriate amount of gain over the bandwidth of interest without adding a significant amount of noise. Unfortunately, it is difficult to tune all of these parameters simultaneously. A small amount of noise is unavoidable, since these are active electronic devices constructed using transistors. For RF signals, transistor performance depends on source impedance, frequency, and amplifier gain [26]. In order to optimize noise performance, matching networks are often used to transform the source impedance from 50 ohms to the optimal impedance at the target frequency, often at the expense of gain. For most applications, the target source impedance is much more than 50 ohms and has been suggested to be closer to 1 kohm [26].

Placement of the LNA within the system can also be important. Long cables connecting the coil to the input of the LNA can attenuate signal, add thermal noise, and introduce other types of noise artifact such as interference from other systems or movement of wires. The LNA is often placed as close to the coil as possible, bearing in mind that the strong magnetic fields can induce unwanted currents through the Hall effect [27].

Lastly, in many receive chains there are other components after the LNA which could also contribute to the amount of noise added to signal after reception. This is often referred to as the noise figure (NF) which is a measure of the noise added to the signal by a circuit element. As the first electronic component in the chain, the NF of the LNA dominates that of the other components and so greatest care must be taken in its design [27]. For our low-field system, many of these design restrictions can be relaxed. For example, at 180 kHz a 1 m cable connecting the Rx coil to the LNA will add very little attenuation and minimal resistance. Lower frequency also reduces the likelihood of parasitic capacitance within the board layout, and so a more relaxed construction approach can be realized. Unfortunately, most out-of-the-box LNAs are usually optimized for higher frequency applications and can be quite expensive.

We designed an LNA to meet the specifications outlined in **Table 2**. The actual build specifications are also listed for comparison. The circuit diagram of the LNA can be found in **Figure 3A**. The LNA is an instrumentation amplifier with a 60 kHz bandwidth Butterworth filter centered at 180 kHz on the output.

The choice of op-amp for the LNA is the most important aspect of the design architecture. A single-ended op-amp has a single input and output, both referenced to ground. This creates a simple architecture, but does not reject common mode signals arising from interference on signal lines. A differential amplifier has differential input and output. The output becomes the gain times the subtraction of the two input lines. This means any signal common to both lines will be removed from the output, which is useful in high external noise scenarios [28].

Instrumentation amplifiers have all the benefits of a differential amplifier with the added benefit of single-ended output and, often, lower noise [29]. An instrumentation amplifier op-amp (INA-103) from Texas Instruments (TI) was chosen for the LNA design. The instrumentation amplifier has three internal op-amps. The two input amplifiers act as differential input rejecting common mode at a common-mode rejection ratio (CMRR) of 100 dB. The third stage combines these signals and delivers a single ended output referenced to ground. Another useful feature is that gain is set by adding a single external resistor at pin 14, while the internal feedback resistors are laser-trimmed ($3\,k\Omega \pm 0.1\%$) which provides excellent gain balance between the internal differential stages. INA-103 has excellent noise performance for source impedance below $10\,k\Omega$. In addition, the amplifier acts as low-pass filter for frequencies above 1 MHz. This is useful for eliminating high frequency noise, but with an operating frequency at 180 kHz we chose to add a bandpass filter as well.

An active fourth-order Butterworth bandpass filter with two stages was designed and added to the output of the LNA, as can be seen in the circuit diagram in **Figure 3B**. At high frequencies, passive filters are often designed using reactive elements such as inductors and capacitors. At low frequency, the inductor values can become too large to be practical, adding unwanted time

TABLE 2 | LNA Design Spec vs. Actual.

Spec	Gain (dB)	CMRR (dB)	NF	Settling Time (μs)	Center Frequency (kHz)	Bandpass BW (kHz)
Design	50	100	1	10	180	60
Actual	50	100	1.2	1.47	180	60

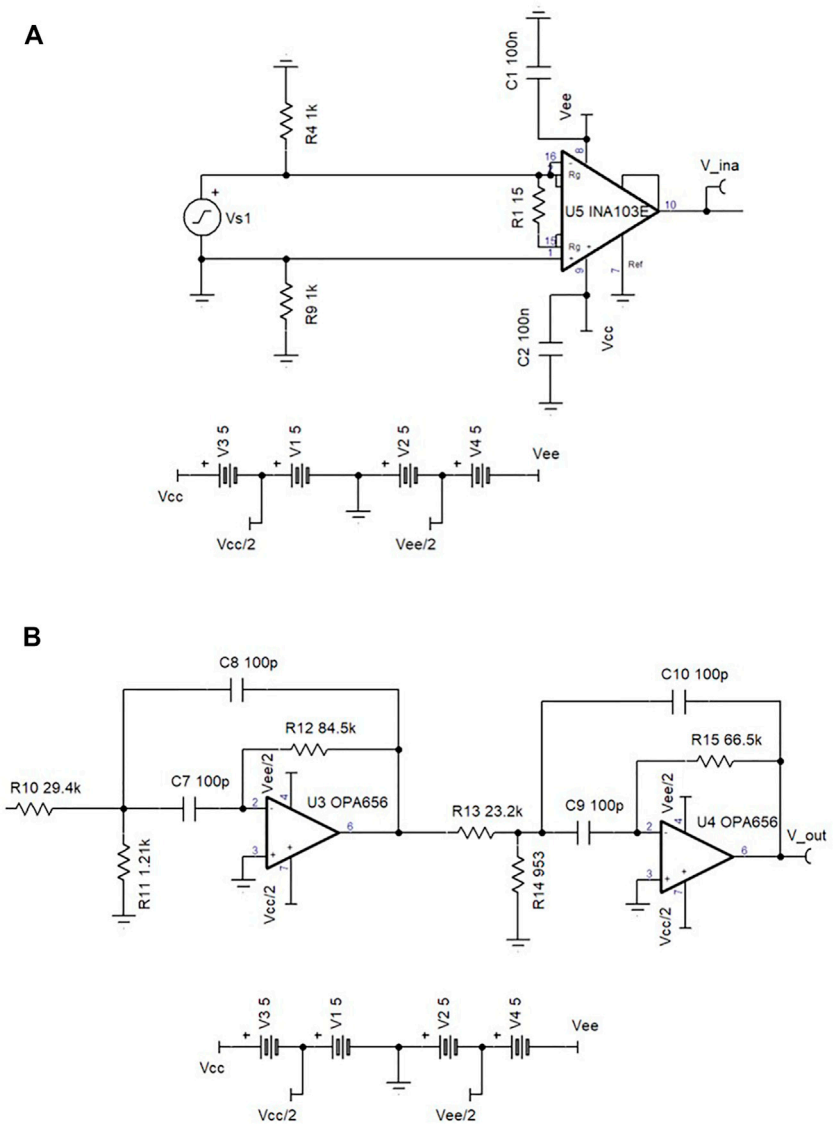

FIGURE 3 | (A) The circuit diagram for the custom LNA design using TINA software from Texas Instruments. **(B)** The circuit diagram for the 4th order butterworth filter used at the output of the LNA.

delays in the circuit, and so active circuits are preferred. The bandpass filter was constructed with two OPA-656 op-amps. It has a unity gain bandwidth of 500 MHz, 7 $nV/\sqrt{Hz}$ input noise voltage, and a 60 kHz bandwidth around the 3 dB attenuation points. **Table 3** shows the specifications of each stage in the bandpass filter. While the 500 MHz bandwidth was not an important aspect of the design consideration and is considerably wider than required, unity gain stability in the bandpass filter avoids amplification of noise added in the filter stage.

This amplifier was designed to replace a high end LNA made by Stanford Research Systems (SR560). While the SR560

TABLE 3 | Bandpass filter specifications.

Spec	First Stage	Second Stage
Center Freq (kHz)	160	202
Min. GBW (MHz)	68.3	86.6
Stage Gain (V/V)	1	1
Stage Q-factor	4.272	4.272
Topology	Multi-feedback	Multi-feedback

is an excellent LNA, it has a high NF (24 dB) at the frequency and source impedance of the PMRI application. An experiment was designed to compare the LNA designed in this work to the SR560. A 1 mV_{rms} signal was sent to the Tx coil, received by the Rx coil tuned at 180 kHz, and amplified with both the LNA and SR560. The output of the LNA or the SR560 was measured by a spectrum analyzer and the noise floor around the signal was recorded. **Figure 4** shows the comparison. The LNA shows an improvement of 24 dBm over the SR560 in this application. This is an illustration of how simple, purpose built electronics can outperform bench-top solutions at a fraction of the cost. The LNA developed in this work costs around $100, while the SR560 costs around $5,000. It should be noted that the SR560 was not designed to be a low noise amplifier at frequencies or source impedances as low as this application requires and we should not expect high performance for our application. This example is intended to illustrate the cost-savings that can be achieved through simple, custom built designs.

The LNA is powered by two 12 volt linear power supplies or two 12 volt batteries. An internal circuit is used to step down the power voltage to the filter op-amps to ±5 volt.

2.5 Shielding

The last component of the RF chain to discuss is the shield for the system. For high-field MRI systems, a well shielded room is an expensive and necessary component in order to achieve the high SNR these systems are designed to exhibit. Although shielding for low-field systems can be much simpler and more affordable, it is still an important component of maximizing available SNR that must be addressed.

The first consideration is the size of the shield. An excellent solution for reducing cost with good shielding effect is to build an aluminum Faraday cage around the system alone, leaving the room unshielded. This also allows for portability of the system, an important component to sustainable design. This design was used in [16] to great effect, producing good quality low-field brain images *in vivo*. One potential risk with this method is that one side of the shield must be left open for the patient to enter the machine. The patient also acts as an antenna as he or she couples with the RF receive coil. In [16], a conductive aluminum cloth grounded to the shield was used to cover most of the patient's body, which reduced noise by a factor of 10. The downside of such a shield is that the conductive cloth is quite expensive and could be hard to acquire in the developing world. The small shielded enclosure is also hard to see inside and may not be ergonomically designed for infant imaging.

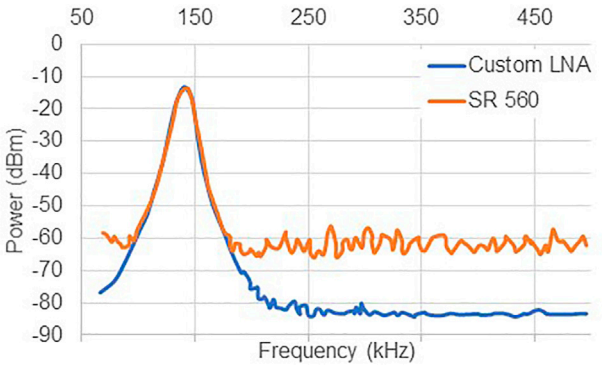

FIGURE 4 | A comparison of the noise floor and signal level between the custom LNA and the SR560. The custom LNA shows a 20 dB improvement in noise floor over the SR560. Data points were extracted and plotted from an analog spectrum analyzer.

Another option is to construct a room sized enclosure, large enough to seat at least two adults (parent and technician) and image an infant. One potential advantage of such a system is that, with low-field MRI, ferric material that is relatively far from the system will not distort the magnetic field or turn into a dangerous projectile. This means there is the potential to use ferric metal as the shield material, such as an alloy of steel. In our experience, steel is typically less expensive and more readily available (especially in LMIC) than aluminum or copper and would be a preferred option for sustainability reasons. A drawback of this design is that it is not portable, unless built around a truck-bed or in a trailer, and the larger size could incur more cost. The use of inexpensive steel materials may be able to offset the cost of larger size.

Another fortuitous aspect of shielding at low frequency, such as 180 kHz, is that it is much easier to construct an ergonomic enclosure with a focus on patient comfort without embedding the shield in the walls of the room. This can be achieved by using perforated material as a shield. If designed properly, perforated material can be as effective as solid material and it allows for good airflow and reduces claustrophobia.

In electromagnetic interference (EMI) shielding theory, there are three main aspects of the shield design that should be considered as it relates to the target frequencies to be shielded: 1) the shield material, 2) the thickness of the shield, and 3) the size of any gaps in the shield. In some applications, shields are designed to be effective for electric and magnetic fields, however for the PMRI system we focused on shielding electric fields. Electrical interference interacts with the shield by reflection, absorption, and transmission [30].

Figure 5 shows a cross-section of an EMI shield interacting with a noise signal outside the shield. Depending on the shield material and frequency of the noise signal, some of the incident wave will be reflected and some will be absorbed. The amount of the incident wave absorbed depends on the shield material and frequency of the wave, but also on the thickness of the shield material. To understand this, we need to look at how AC current is carried in conductors.

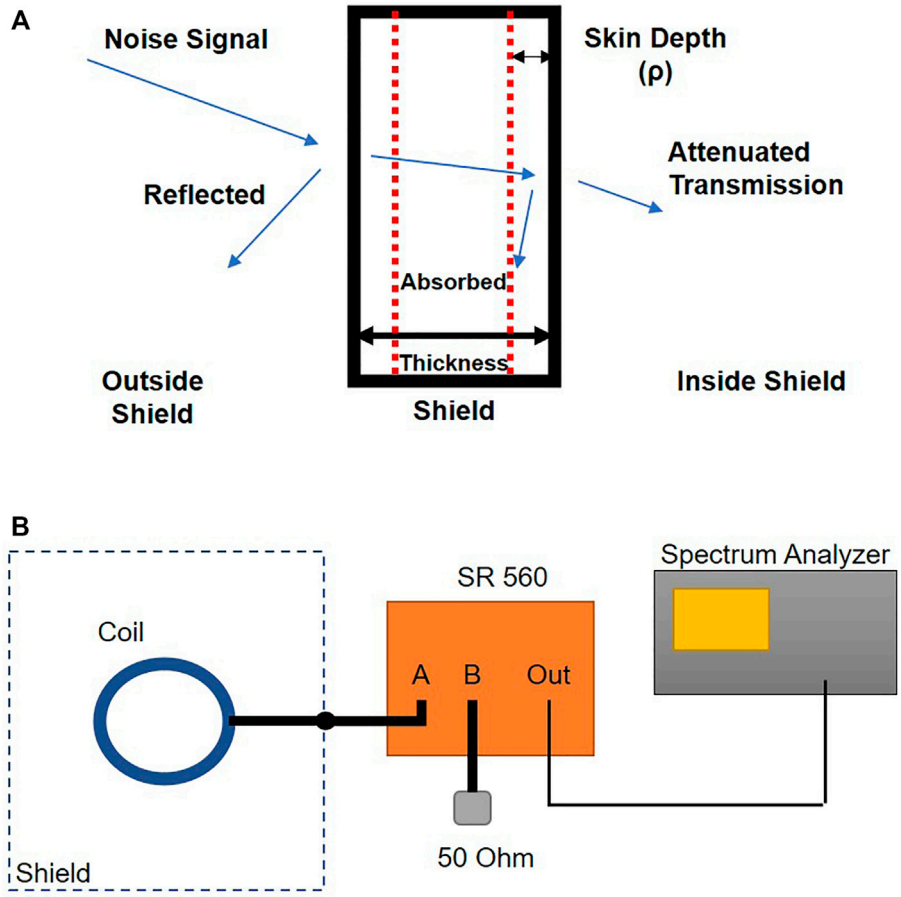

FIGURE 5 | (A) Cross-section of an EMI shield. Interference signals are shielded by external reflection or absorption of RF energy. Depending on the efficiency of the shield, an attenuated interference signal is re-transmitted into the shielded space. **(B)** Shield test setup. The coil was placed inside each shield with coil cable grounded to the shield and connected to input A of the SR 560 low noise amplifier. A 50 ohm resistor was connected to input B of the amplifier. Output was measured by a spectrum analyzer.

A DC current uses the entire cross-section of a conductor to move charge. As frequency increases in an AC current, a back-EMF is generated the by the alternating charge through increasing magnetic field at the center of the conductor. This increased magnetic field looks like higher and higher impedance to the current, and charge density is pushed toward the edge of the conductor. This effect also increases the resistance of the conductor as frequency increases. This phenomenon is called the skin-effect. The cross-sectional area in which more than 37% of the charge is being carried is called the skin-depth, as measured from the surface of the conductor. The equation for skin depth is [31].

$$\delta = \sqrt{\frac{2}{\omega \mu_o \sigma}} \tag{1}$$

where ω is the angular frequency of the AC signal, μ_o is the permeability of a vacuum, and σ is the conductivity of the material. From **Eq. 1** we see that as frequency increases skin depth decreases. This is important for the design of the thickness of the shield because it will determine the upper limit frequency that can be effectively absorbed by the shield. If the shield thickness approaches the skin depth of the target frequency, the shield will not behave as an effective conductor and most of the energy that is not reflected will be re-transmitted into the enclosure. As a rule of thumb, the shield should be more than five times the thickness of the skin depth [30]. Comparisons between frequency, material, and thickness can be made using the shielding effectiveness nomograms printed in Ref. [30].

TABLE 4 | Shield effectiveness comparison.

Condition	Noise Power at 180 kHz (dBm)
No Shield	–76.6
50 Ω	–89.6
Chicken Wire	–85.1
Perforated Al	–89.6
Solid Al	–89.6

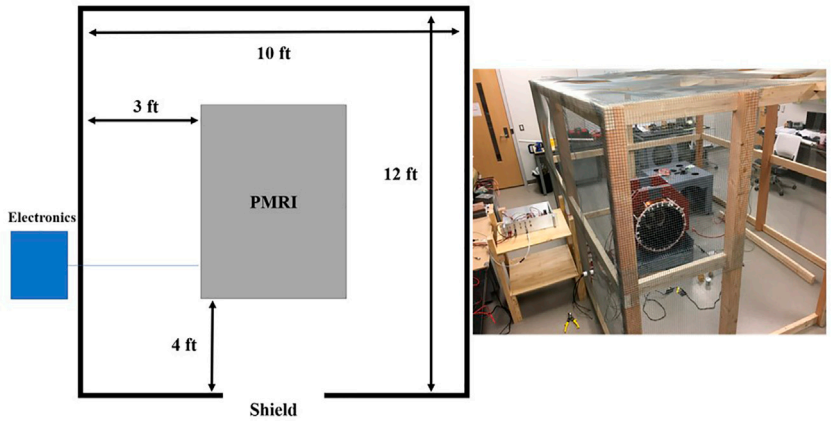

FIGURE 6 | Footprint of the shield enclosure (left) with image of constructed shield (right). The shield was constructed using 2 × 4 s and chicken wire.

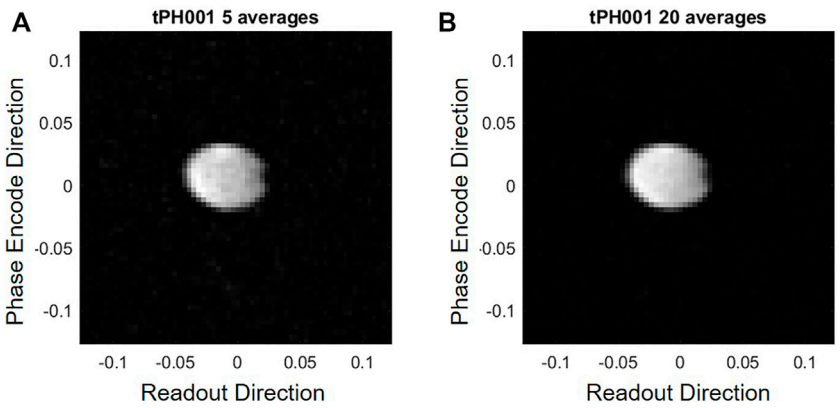

FIGURE 7 | Comparison between 5 averages (SNR = 23) **(A)** and an 20 averages (SNR = 39) **(B)** for a turbo spin echo sequence of image the cylindrical water phantom.

For the PMRI signal, we want to shield frequencies around 180 kHz. Since the Low Noise Amplifier has a 60 kHz bandwidth filter on the output, we at least must shield frequencies that will be passed by this filter. In practice, this is an easy case to design for. If we take the highest important frequency to be 240 kHz (a full filter bandwidth above center), the wavelength of this frequency is over 1,200 m. This means that, although the best case scenario shield is a solid box with no gaps, we should be able to use a perforated material to allow for better airflow. When choosing material, an obvious choice is aluminum or copper. The skin depth of 240 kHz in these materials is $\delta_{Al} = 0.2\ mm$ and $\delta_{Cu} = 0.15\ mm$. Since the PMRI system has such a low field and we plan to build an enclosure that is much larger than the 5 Gauss line, we might also consider steel with a skin depth of $\delta_{Steel} = 1\ mm$.

Three small enclosures were constructed to test the best case to worst case scenario for shielding for comparison. Each box was $1 \times 1 \times 1$ ft^3 in size. Box 1 was made of 10 mm thick solid aluminum, box 2 was made of 10 mm thick perforated aluminum with 10 mm diameter perforations, and box 3 was made of steel chicken wire with a 12.7 mm square grid pattern.

The tests were performed using a 50 ohm impedance matched single-ended saddle coil resonating at 180 kHz. Coil location in the room was consistent across tests. The coil was placed in each shield with the coaxial cable grounded to the shield. The SR 560 low noise amplifier made by Stanford Research Systems was used to amplify the signal with a gain of 100x. The noise spectrum was analyzed with a spectrum analyzer. Each shield case was compared to the baseline noise of a 50 ohm resistor connected to port B of the amplifier. A fourth scenario was tested without any shield to establish the maximum noise picked up by the coil in the environment.

It can be seen from **Table 4** that perforated and solid aluminum are the best performers, at least to the noise floor of the spectrum analyzer, since they both match the noise power of the 50 ohm resistor. Interestingly, the chicken wire shows a 10 dBm improvement over no shield, and only lags the aluminum options by 5 dBm. If we consider patient comfort, then the perforated aluminum option is better than the solid aluminum since it allows for air flow. The cost of the perforated aluminum is roughly 10 times that of the chicken wire and so chicken wire

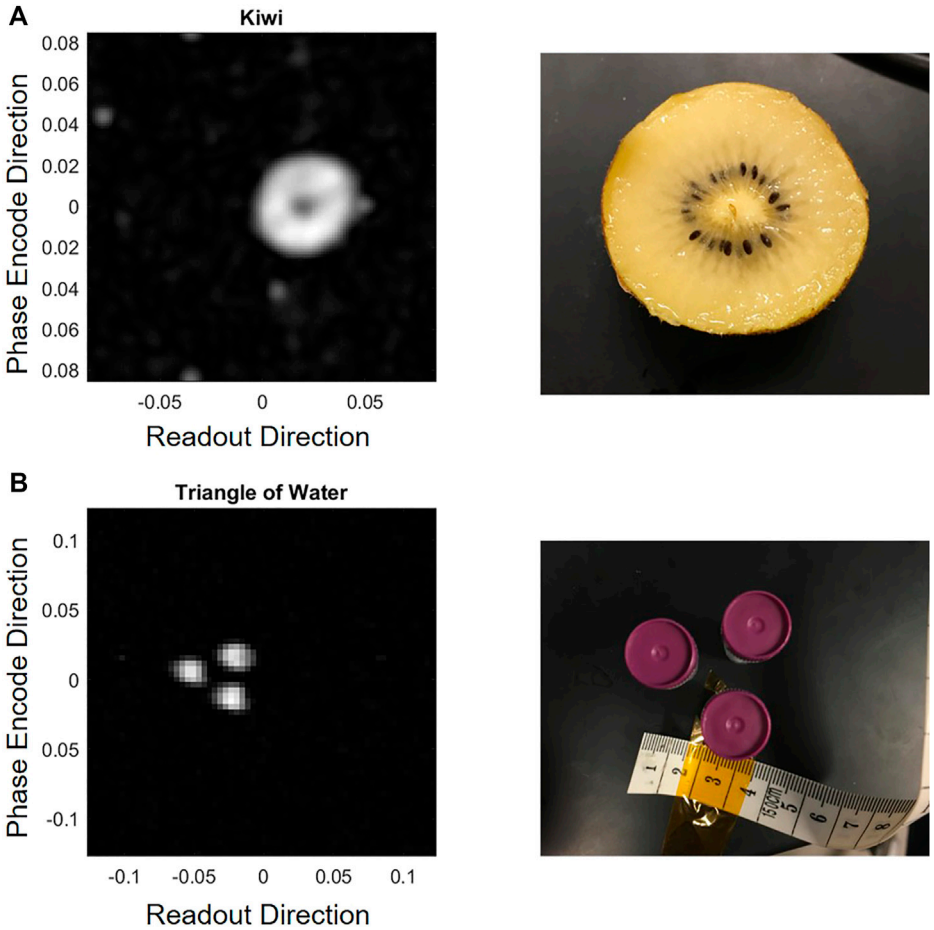

FIGURE 8 | Images of a kiwi **(A)** and three small bottles of water arranged in a triangle **(B)**.

could be an excellent option for a shielded enclosure on a sustainable system targeted to the developing world.

The shielded enclosure for the PMRI system was designed to be large enough for two adults to freely move inside the enclosure during imaging. **Figure 6** shows the footprint of the shield enclosure. There is at least 1 m between the PMRI system and the shield to allow for a technician to access any part of the system with ample space. The enclosure is 188 cm tall—large enough to accommodate a tall adult. The shield frame is made from common lumber used for framing small structures (in this case, 2 × 4 inch lumber) and brass screws. The shield material is chicken wire as described above. The total material cost of the shield was $300 USD, a 10X cost reduction over a shielded enclosure with perforated aluminum.

3 RESULTS

The PMRI system can achieve an SNR of 10 for the cylindrical water phantom with a 64 × 64 resolution FOV of 25 cm^2 and using 5 averages with 50 mT Bp field (20 Amp, 75 volt battery power). **Figure 7** shows the cylindrical water phantom measured with 5 averages (A) and 20 averages (B). Although the SNR roughly doubles by using 20 averages instead of 5 averages, the imaging time increases by 4. **Figure 8** shows images of a kiwi (A) and three small water bottles arranged in a triangle (B).

Imaging experiments were performed in order to show the capability of the designed electronics. To determine SNR capability, a phantom was constructed using a plastic cylinder 5 cm long and 6.5 cm in diameter and filled with distilled water. This phantom is ideal for testing since it fills most of the Rx coil described in this work and is not long in the z direction. This helps to minimize inhomogeneity effects caused by unwanted Bm gradients in the z direction but still allows for a significant amount of signal for imaging in the x-y plane. A turbo spin-echo (TSE) sequence was used with a turbo factor of 16 on a 64 × 64 matrix image. The turbo factor defines the number of TR blocks that will be used in the TSE sequence. A turbo factor of 16 for a 64 × 64 image means there will be 4 TR blocks. The Bp was on for 4 s prior to imaging and there was a 550 ms wait time between turning off the Bp and starting the imaging sequence. This wait time causes a 27% loss in SNR due to T1 decay. The receiver bandwidth was 50 Hz per pixel with a $\pi/2$ pulse of 1 ms. The effective echo time was 80 ms.

Although this basic phantom is useful for troubleshooting, more complex phantoms were also imaged. To show capability of imaging a phantom with more complex internal structure, a kiwi was imaged using a TSE sequence with a turbo factor of 32 and with echo time of 50 ms, and Bp duration of 3 s with a wait time after Bp before imaging of 450 ms. The Bp was powered to 50 mT by batteries. Image resolution was set to 32×32 with a 17 cm^2 square FOV. A 75 Hz/pixel bandwidth was used with a 1 ms $\pi/2$ pulse. The image of the kiwi can be found in **Figure 8**.

In addition, three small water-filled tubes arranged in a triangle were also imaged as can be seen in **Figure 8**. The water tubes were each 5 cm long with a diameter of 1 cm. The triangle was imaged with the 50 mT Bp field and 20 averages using the same imaging sequence as the cylindrical phantom.

4 DISCUSSION

Components of the RF chained designed in this work were successfully paired without the need for 50 ohm impedance matching. Not only did this reduce the complexity of the circuit design and construction, it more importantly reduced the energy required to power these circuits. Our goal was to design an electronic system that could be paired with the magnet described in [15] and which had the potential for use in hydrocephalus imaging. At the time of this writing, our colleagues at the Mbararra University of Science and Technology in Mbararra, Uganda have reproduced the coil-based PMRI system and electronics.

Despite this success, there is a drawback to the un-matched RF chain. When matching to 50 ohms, a component such as a coil can be replaced or changed without altering the experimental parameters or power efficiency of the RF chain. When the RF chain is unmatched, adding of a new component with different RF characteristics from the old component will require adjustment and calibration. For example, switching a Tx or Rx coil in the system will require recalibration of Rx pulse width and amplitude to achieve the optimal flip angle. This could be a significant drawback considering SNR is improved when coil size closely matches the object it is measuring. Further investigation should explore whether the power and simplicity gained in the unmatched case prove beneficial even in systems that are permanent magnet based. These systems already have a power advantage over coil based systems and an SNR advantage since they tend to produce larger static fields.

The imaging experiments in **Figures 7**, **8** demonstrate the capability of this affordable and low-power MRI system. The water phantoms show that with proper shielding and common post-processing techniques even low-voltage signals have enough SNR to accurately image collections of water. The image of the kiwi in **Figure 8A** further illustrates the ability of this system to show contrast between regions of the kiwi with high water content and low water content. Other details, such as seeds, would be hard to see at this resolution. **Figure 8B** shows that our system accurately captures the spacing and size of the water bottles, suggesting the possibility of 4 mm resolution with a 64×64 image.

In the context of hydrocephalus treatment planning, these are promising results, where we are most interested in accurately imaging large fluid collections and distinguishing them from brain. The water triangle phantom in **Figure 8B** demonstrates resolution accuracy that is on the verge of our target resolution for hydrocephalus imaging, as discussed in [15]. While the Rx coil used in this study is too small for infant head imaging, the rest of the system is appropriately sized and future work could likely provide similar results with a larger coil.

Another important aspect of this system is that these images were generated using very affordable and common electronic components such as tractor batteries, hand soldered electronics, and chicken wire. We demonstrate that low-field MRI opens the door to system design that does not require the strict tolerancing and high-end fabrication techniques common to the field of MRI technology. In this way, systems that can be built and maintained in low-resource regions of the world have the potential to aid in clinical decision making as with the example of infant hydrocephalus treatment planning in countries like Uganda. To that end, the MRI system employing both the PMRI coil described in [15] and accompanying electronics are actively being reproduced by our collaborators at the Mbarara University of Science and Technology in Mbarara, Uganda.

5 CONCLUSION

RF chain design is an important aspect of an MRI system, especially at low magnetic field where SNR is also typically low. Despite this, simple electronics and affordable shield materials, such as chicken wire, can provide high enough SNR to visualize internal structures at a low resolution. By leaving RF chain components unmatched to 50 ohms, we further simply the design and reduce RF power requirements during transmit. The design strategy for the RF chain compliments our efforts to develop a sustainable low-field MRI for use in the developing world.

While advanced low-field MRI solutions are becoming available that offer exciting clinical possibilities for a variety of diseases, we have demonstrated the capability of a low-powered RF chain for our portable PMRI system which was designed for treatment planning of hydrocephalus in low-resource settings. The power efficiency and simplicity, and low cost of the RF chain design offer the potential for a system that can be sustained in LMIC with primarily local resources. Further development and adoption of this technology will allow for access to diagnostics in rural populations where there are few current options that could have substantial clinical impact throughout the world.

DATA AVAILABILITY STATEMENT

The raw data supporting the conclusion of this article will be made available by the authors, without undue reservation.

AUTHOR CONTRIBUTIONS

JH—Design, construction, and testing of the electronics and experiments described in this work. Primary author of the

text. CZ—Design, construction, and testing of the LNA and authorship of the section on the LNA.

FK—Design, construction, and testing of the LNA and authorship of the section on the LNA.

IM—Construction and testing of select electronics and experiments.

JM—Advisor to CZ and FK during design and construction of LNA.

JO—Design, construction, and testing of coil-based magnet used in this work.

SS—Advisor to main author during this work.

FUNDING

Supported by US National Institutes of Health grant R01HD085853. ClinicalTrials.gov registration number NCT01936272. Design and construction of the LNA supported by CONACYT-Paraguay.

ACKNOWLEDGMENTS

We would like to acknowledge the fabrication support provided by the Learning Factory at Penn State and Bob Crable at the Electronics Research Instrumentation Facility at Penn State. We also acknowledge Rod Kreuter for his design, fabrication, and testing support on the electronics outlined in this work. Finally, Kristen Crable who worked on fabrication of electronics and shielding.

SUPPLEMENTARY MATERIAL

The Supplementary Material for this article can be found online at: https://www.frontiersin.org/articles/10.3389/fphy.2021.727536/full#supplementary-material

Supplementary Figure S1 | The circuit diagram for the Transmit amplifier.

REFERENCES

1. Rutland JW, Delman BN, Gill CM, Zhu C, Shrivastava RK, Balchandani P. Emerging Use of Ultra-high-field 7t Mri in the Study of Intracranial Vascularity: State of the Field and Future Directions. *AJNR Am J Neuroradiol* (2020) 41:2–9. doi:10.3174/ajnr.a6344
2. Klein HM. *Clinical Low Field Strength Magnetic Resonance Imaging: A Practical Guide to Accessible MRI*. Cham, Heidelberg, New York, Dordrecht, London: Springer (2015).
3. World Health Organization. *Baseline Country Survey on Medical Devices 2010*. Tech. rep. Geneva: World Health Organization (2011).
4. Gatrad AR, Gatrad S, Gatrad A. Equipment Donation to Developing Countries. *Anaesthesia* (2007) 62:90–5. doi:10.1111/j.1365-2044.2007.05309.x
5. Malkin RA. Design of Health Care Technologies for the Developing World. *Annu Rev Biomed Eng* (2007) 9:567–87. doi:10.1146/annurev.bioeng.9.060906.151913
6. Lennox L, Maher L, Reed J. Navigating the Sustainability Landscape: a Systematic Review of Sustainability Approaches in Healthcare. *Implement Sci* (2018) 13:27–17. doi:10.1186/s13012-017-0707-4
7. Dewan MC, Rattani A, Mekary R, Glancz LJ, Yunusa I, Baticulon RE, et al. Global Hydrocephalus Epidemiology and Incidence: Systematic Review and Meta-Analysis. *J Neurosurg* (2018) 130:1–15. doi:10.3171/2017.10.JNS17439
8. Warf BC. Educate One to Save a Few. Educate a Few to Save many. *World Neurosurg* (2013) 79:S15–8. doi:10.1016/j.wneu.2010.09.021
9. Warf BC. Comparison of 1-year Outcomes for the Chhabra and Codman-Hakim Micro Precision Shunt Systems in uganda: a Prospective Study in 195 Children. *J Neurosurg Pediatr* (2005) 102:358–62. doi:10.3171/ped.2005.102.4.0358
10. Lane JD, Mugamba J, Ssenyonga P, Warf BC. Effectiveness of the Bactiseal Universal Shunt for Reducing Shunt Infection in a Sub-saharan African Context: a Retrospective Cohort Study in 160 Ugandan Children. *Ped* (2014) 13:140–4. doi:10.3171/2013.11.peds13394
11. Warf BC. Comparison of Endoscopic Third Ventriculostomy Alone and Combined with Choroid Plexus Cauterization in Infants Younger Than 1 Year of Age: a Prospective Study in 550 African Children. *J Neurosurg Pediatr* (2005) 103:475–81. doi:10.3171/ped.2005.103.6.0475
12. Warf BC, Campbell JW. Combined Endoscopic Third Ventriculostomy and Choroid Plexus Cauterization as Primary Treatment of Hydrocephalus for Infants with Myelomeningocele: Long-Term Results of a Prospective Intent-To-Treat Study in 115 East African Infants. *Ped* (2008) 2:310–6. doi:10.3171/ped.2008.2.11.310
13. Frush DP, Donnelly LF, Rosen NS. Computed Tomography and Radiation Risks: what Pediatric Health Care Providers Should Know. *Pediatrics* (2003) 112:951–7. doi:10.1542/peds.112.4.951
14. Cinalli G, Maixner WJ, Sainte-Rose C. *Pediatric Hydrocephalus*. Milano: Springer Science & Business Media (2012).
15. Obungoloch J, Harper JR, Consevage S, Savukov IM, Neuberger T, Tadigadapa S, et al. Design of a Sustainable Prepolarizing Magnetic Resonance Imaging System for Infant Hydrocephalus. *Magn Reson Mater Phy* (2018) 31:665–76. doi:10.1007/s10334-018-0683-y
16. O'Reilly T, Teeuwisse WM, de Gans D, Koolstra K, Webb AG. *In Vivo* 3d Brain and Extremity Mri at 50 Mt Using a Permanent Magnet Halbach Array. *Magn Reson Med* (2020) 85:495–505. doi:10.1002/mrm.28396
17. Cooley CZ, McDaniel PC, Stockmann JP, Srinivas SA, Cauley SF, Śliwiak M, et al. A Portable Scanner for Magnetic Resonance Imaging of the Brain. *Nat Biomed Eng* (2021) 5:229–39. doi:10.1038/s41551-020-00641-5
18. Sheth KN, Mazurek MH, Yuen MM, Cahn BA, Shah JT, Ward A, et al. Assessment of Brain Injury Using Portable, Low-Field Magnetic Resonance Imaging at the Bedside of Critically Ill Patients. *JAMA Neurol* (2021) 78 (1):41–47. doi:10.1001/jamaneurol.2020.3263
19. Sarracanie M, LaPierre CD, Salameh N, Waddington DEJ, Witzel T, Rosen MS. Low-cost High-Performance Mri. *Sci Rep* (2015) 5:15177–9. doi:10.1038/srep15177
20. Macovski A, Conolly S. Novel Approaches to Low-Cost Mri. *Magn Reson Med* (1993) 30:221–30. doi:10.1002/mrm.1910300211
21. Macovski A. *A Low-Cost, High Quality Mri Breast Scanner Using Prepolarization*. Tech. rep. Stanford, CA: Stanford University (1999).
22. Matter NI, Scott GC, Grafendorfer T, Macovski A, Conolly SM. Rapid Polarizing Field Cycling in Magnetic Resonance Imaging. *IEEE Trans Med Imaging* (2005) 25:84–93. doi:10.1109/TMI.2005.861014
23. Grafendorfer T, Conolly S, Matter N, Pauly J, Scott G. Optimized Litz Coil Design for Prepolarized Extremity Mri. In: Proceedings of the 14th Annual Meeting of ISMRM; May 6–12, 2006; Seattle, WA (2006). p. 2613.
24. Bowick C. *RF Circuit Design*. Amsterdam: Elsevier (2011).
25. Eskelinen P. *Introduction to RF Equipment and System Design*. Boston: Artech House (2004).
26. Middlebrook R. Optimum Noise Performance of Transistor Input Circuits. In: 1958 IEEE International Solid-State Circuits Conference. Digest of Technical Papers; February 20–21, 1958; Philadelphia, PA, 1. IEEE (1958). p. 43–4.
27. Klomp DWJ, Webb AG. The Mr Receiver Chain. In: AG Webb, editor. *Magnetic Resonance Technology: Hardware and System Component Design*. Cambridge: Royal Society of Chemistry (2002). p. 308–30. chap. 7.
28. Carter B, Brown TR. *Handbook of Operational Amplifier Applications*. Dallas, TX: Texas Instruments (2001).
29. Kitchin C, Counts L. *A Designer's Guide to Instrumentation Amplifiers*. Norwood, MA: Analog Devices (2006).

30. Gnecco LT. *Design of Shielded Enclosures: Cost-Effective Methods to Prevent EMI*. Boston: Elsevier (2000).
31. Wheeler HA. Formulas for the Skin Effect. *Proc IRE* (1942) 30:412–24. doi:10.1109/jrproc.1942.232015

Conflict of Interest: The authors declare that the research was conducted in the absence of any commercial or financial relationships that could be construed as a potential conflict of interest.

Publisher's Note: All claims expressed in this article are solely those of the authors and do not necessarily represent those of their affiliated organizations, or those of the publisher, the editors and the reviewers. Any product that may be evaluated in this article, or claim that may be made by its manufacturer, is not guaranteed or endorsed by the publisher.

frontiers | Frontiers in Physics

ORIGINAL RESEARCH
published: 08 July 2022
doi: 10.3389/fphy.2022.907619

Overview of Methods for Noise and Heat Reduction in MRI Gradient Coils

Elizaveta Motovilova[1,2] *and Simone Angela Winkler*[1]*

[1]*Department of Radiology, Weill Cornell Medicine, New York, NY, United States,* [2]*Department of Radiology, Hospital for Special Surgery, New York, NY, United States*

Magnetic resonance imaging (MRI) gradient coils produce acoustic noise due to coil conductor vibrations caused by large Lorentz forces. Accurate sound pressure levels and modeling of heating are essential for the assessment of gradient coil safety. This work reviews the state-of-the-art numerical methods used in accurate gradient coil modeling and prediction of sound pressure levels (SPLs) and temperature rise. We review several approaches proposed for noise level reduction of high-performance gradient coils, with a maximum noise reduction of 20 decibels (dB) demonstrated. An efficient gradient cooling technique is also presented.

Keywords: MRI, gradient coil, vibroacoustics, acoustic noise, sound pressure level, MR safety, heating

OPEN ACCESS

Edited by:
Federico Giove, Centro Fermi—Museo storico della Fisica e Centro Studi e Ricerche Enrico Fermi, Italy

Reviewed by:
Nansha Gao, Northwestern Polytechnical University, China
Marco Miniaci, UMR8520 Institut d'Électronique, de Microélectronique et de Nanotechnologie (IEMN), France

***Correspondence:**
Simone Angela Winkler
ssw4001@med.cornell.edu

Specialty section:
This article was submitted to Medical Physics and Imaging, a section of the journal Frontiers in Physics

Received: *29 March 2022*
Accepted: *20 June 2022*
Published: *08 July 2022*

Citation:
Motovilova E and Winkler SA (2022) Overview of Methods for Noise and Heat Reduction in MRI Gradient Coils. Front. Phys. 10:907619. doi: 10.3389/fphy.2022.907619

1 INTRODUCTION

Gradient coils of magnetic resonance imaging (MRI) scanners undergo large Lorentz forces as rapidly switched electrical currents are passing through them in the presence of the static magnetic field B_0. Due to these forces, the gradient coil conductors vibrate, and these vibrations radiate into the air as acoustic pressure waves and sound radiation. The acoustic noise pattern depends on the gradient form and thus is different for each pulse sequence. The sound pressure levels (SPL) produced by gradient coils can exceed safety limits set by the National Institute of Occupational Safety (NIOSH) of 85 dB. For example, the echo-planar imaging (EPI) sequence, one of the loudest sequences, produces SPLs in the range of 110–120 dB. Exposure to such noise levels creates patient discomfort, anxiety, and could even result in a temporary hearing loss, thus requiring hearing protection for patients—and sometimes for operators [1]. High SPLs were also reported to cause other unwanted side effects, such as spectral line shape distortions, anti-symmetrical sidebands, and signal loss [2, 3].

High-performance gradient coil designs that improve spatial/diffusion encoding and speed up data acquisition have been the focus of research in recent years [4–17]. However, these designs may further increase noise levels, as such systems are designed to produce stronger gradient fields and sharper slew rates. Moreover, the resulting gradient coil heating becomes an additional concern, as the surfaces of smaller insert coils are now much closer to the patients' ears.

Therefore, accurate numerical modeling of gradient coil acoustics is essential for realistic noise estimates and safety analysis. Over the last two decades, many analytical, numerical, and experimental studies have been published to improve our understanding of vibrational properties of gradient coils. Several comprehensive review articles on the topic were published by McJury et al. in 2000 [18], Mechefske in 2008 [19], Takkar et al. in 2017 [20], Winkler et al. in 2018 [21], and most recently McJury provided a narrative/descriptive review in 2022 [22]. A summary of the analytical studies and noise reduction techniques is presented in **Figure 1** in chronological order.

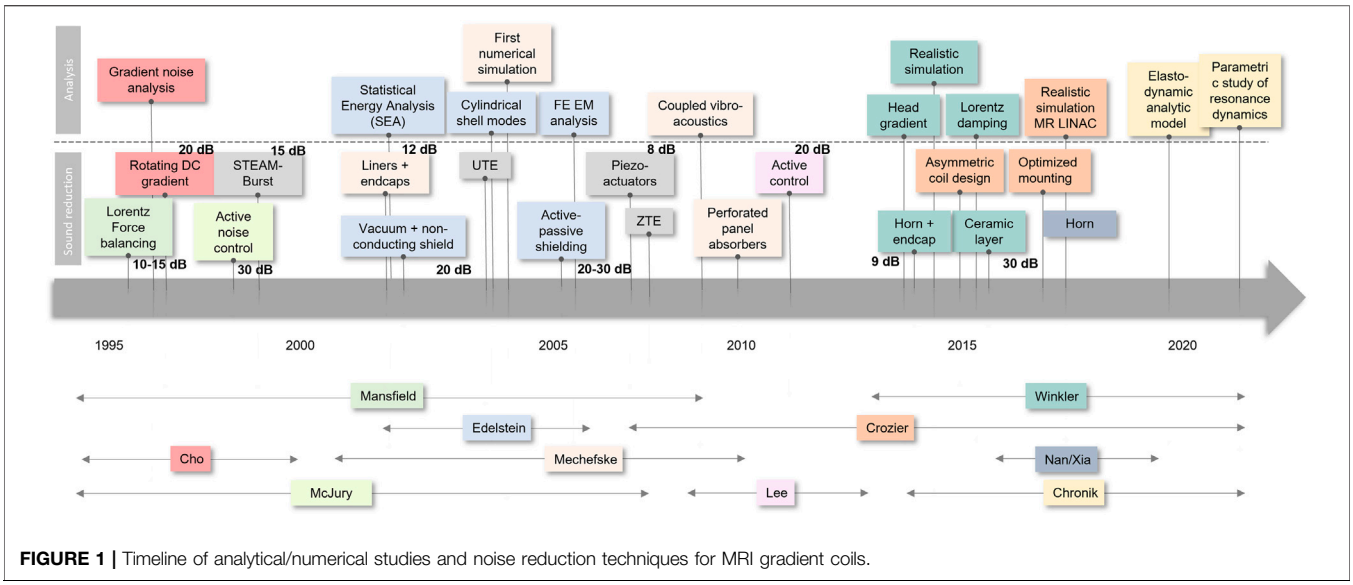

FIGURE 1 | Timeline of analytical/numerical studies and noise reduction techniques for MRI gradient coils.

1.1 Analytical Models

The first analytical model to be used for gradient coil vibrations analysis was a thin-walled shell theory [23]. Taracila et al. calculated vibrational shell modes [24] and analyzed finite length cylindrical ducts with open end termination [25, 26]. In their comprehensive analysis [27, 28], Li and Mechefske combined both vibrational shell modes and acoustic wave propagation in open-ended cylindrical ducts. They were also the first to describe the coupling between the vibrational and acoustic modes.

1.2 Numerical Models

The first numerical model used to describe gradient coil acoustics was implemented using statistical energy analysis (SEA) by Edelstein et al. [1], which solves complex acoustic systems as an energy balance problem with a highly reduced computational cost compared to more detailed methods such as the finite element method (FEM). Mechefske et al. performed the first FEM numerical modeling of gradient coil acoustics, where both vibrational analysis and acoustics of a stand-alone thick-walled gradient cylinder were analyzed [27, 29–31]. FEM analysis was also used in a recent study for a split MRI-LINAC system [32, 33].

The computational resources of earlier studies were limited, and thus the first numerical models included assumptions and simplifications, such as neglecting certain physical effects. In [34] Winkler et al. proposed a new vibroacoustic model, which includes previously neglected but essential Lorentz damping along with additional previously neglected detail such as accurate wire patterns, the bore shape, patient bridge, and the air outside the bore. This realistic multiphysics simulation platform improves our understanding of the underlying principles of vibroacoustics in head gradient coils. Moreover, this simulation platform can help improve existing gradient coils and guide the design of novel gradient coils with lower SPLs.

Recently, Sakhr and Chronik proposed an exact linear analytical elastodynamic model for shielded longitudinal gradient coils [35]. This model demonstrates that the frequency response depends on a dimensionless "profile function" that specifies how the current density varies along the cylinder axis of the gradient coil. The model was then used to study the resonance dynamics of a gradient coil with respect to cylinder geometry parameters such as length, mean radius, and radial thickness [36].

1.3 Acoustic Noise Measurements

High acoustic noise levels in MRI have always been a source of safety concerns [18, 22, 37] and various noise reduction techniques have been proposed over the years. In 1995, McJury [37] measured the acoustic noise levels experienced during typical MRI sequences in 1.0 Tesla (T) and 1.5 T systems and found that many sequences produce noise levels above the regulatory safety thresholds. In 1997, Cho et al. [38] systematically studied the acoustic noise behavior of a commercial 1.5 T and a research-type 2.0 T systems using typical sequences such as Prescan, Spin-Echo (SE), Gradient-Echo (GE), Echo-Planar Imaging (EPI), and Inversion Recovery (IR). They found that the noise profile is not only dependent on the sequence parameters, but also on the gradient coil structure and support. They suggested two possible solutions to reduce the acoustic noise: 1) develop quieter imaging sequences, and/or 2) modify gradient coil structure. In [39], Mechefske measured the actual sound radiation experienced by patients at 4 T and proposed to use acoustic lining for noise reduction.

1.4 Silent Gradient Sequences

Among other methods, the acoustic noise in MRI can be reduced by optimizing pulse sequence parameters, e.g., the gradient slew-rate and amplitude. Cho et al. [40] developed an MRI technique based on projection reconstruction variation and using a mechanically rotating direct current (DC) gradient coil, which minimized gradient pulsing and resulted in a 20.7 dB noise attenuation. Another quiet gradient sequence called

stimulated-echo acquisition mode (STEAM)-Burst was developed by Cremillieux et al. in 1997 and was 15 dB quieter than a typical EPI sequence [41]. Ultra-short time to echo (UTE) [42] and zero TE (ZTE) [43] sequences use radial sampling of k-space, and given the short repetition times (TRs) the gradients can remain active instead of requiring repeated switching, which results largely reduced acoustic noise in imaging procedures.

1.5 Active noise control

Several active noise cancellation (also called 'antinoise') techniques have been proposed over the years [44–49]. McJury et al. proposed an active noise control (ANC) system [45], in which the acoustic reduction of noise is achieved by introducing an antiphase acoustic wave to create a zone of destructive interference at a particular area in space. On average, 10–15 dB of noise was removed over the frequency range of 100–350 Hz, with a maximum noise reduction of 30 dB. Chen et al. [46] used a similar adaptive technique and achieved a noise reduction of 18.8 dB for frequencies below 4 kHz. Li et al. used an improved ANC system [47, 48] that works in a wide range of frequencies up to 5kHz, and allows the covering of most frequencies used in a typical MRI scanner. Chambers et al. [49] developed an opto-acoustical transducer that operates on the principal of light modulation and does not create electro-magnetic interference (EMI), which is important for functional MRI.

1.6 Quiet Gradient Coils

Despite these methods that show varied success, the ideal approach to reduce acoustic noise in MRI is still the tackling of the source of the problem by designing "quiet" gradient coils. Gradient coils can be designed such that the Lorentz forces produced by the pulsing currents are balanced. Mansfield was the first to propose Lorentz force balancing [50–52] in 1994 with a 10 dB reduction achievable at 1.0 kHz. Active acoustic control [53, 54] operating at spot frequencies within a narrow band offered an average reduction in measured acoustic output of 30 dB.

Edelstein et al. used a combination of 1) a vacuum enclosure for gradient assembly isolation, 2) a radiofrequency (RF) coil with a low-eddy-current profile, and 3) an inner bore cryostat made of non-conducting material for acoustic noise reduction [1]. In the proposed active-passive shielding technique, it was also demonstrated numerically that the mechanical power deposition in the warm bore can be effectively decreased by wrapping a thin copper layer around the *Z*-gradient coil, which resulted in acoustic noise reduction of about 25 dB [55].

Roozen et al. [56] developed an active vibration noise control technique based on seismic mass piezo actuators, that reduced the spatially averaged acoustic noise of the Y-gradient coil vibrations by 3–8 dB at the dominant frequencies.

Wang et al. [57] proposed an asymmetric half-connected gradient coil design that improves the electromagnetic performance of the coil and provides higher efficiency, lower inductance, lower resistance, a higher figure of merit, and more acoustic radiation attenuation compared to the non-connected coils.

1.7 Passive Solutions

The mechanical vibrations of gradient coils can be attenuated by surrounding the coil with special noise absorbing materials for acoustic noise dampening.

Li and Mechefske showed that micro-perforated panel (MPP) acoustic absorbers, when properly designed, can reduce acoustic noise [58]. It was demonstrated experimentally that MPPs have multiple absorption frequency bands as well as wider frequency bands at higher frequency ranges [58].

Nan et al. proposed a technique for acoustic noise reduction in a split gradient coil [59], where 1) an asymmetric coil design was used to avoid vibrations of some resonant modes, and 2) horn structures were attached to the outer ends of the split main magnet such that they guided acoustic waves away from patient region.

While there are excellent review articles offering a comprehensive survey of the numerical methods for gradient coil analysis [21], as well as active acoustic control solutions such as ANC, "quiet" gradient coils, and "silent" pulse sequences [18, 22], other passive acoustic noise reduction methods are not well described in the literature. The purpose of this review is to summarize recent progress on acoustic noise reduction techniques with a focus on those using passive absorbing linings, and acoustic guiding structures. We also briefly discuss improved coil cooling strategies. The pursuit of quieter gradient coil technology remains a challenging area in MRI research and can potentially revolutionize medical imaging practice.

2 ACCURATE NUMERICAL MODELLING OF GRADIENT COILS

Accurate numerical modeling of gradient coils is essential for producing realistic predictions of SPLs. We numerically study and analyze gradient coils using a comprehensive numerical modeling approach where gradient-induced acoustics and vibrations are analyzed together with previously neglected but essential Lorentz damping. SPLs incurred by body and head gradient coils are compared. We also study how the strength of the main field B_0 affects acoustic noise and vibration levels. We then focus on SPL reduction and efficient gradient cooling methods. To justify the numerical analysis, SPLs were also measured experimentally.

All numerical simulations were done using the finite-element package COMSOL. A folded shielded gradient head coil design intended for high performance human brain imaging was used as the base model [10]. The coil support structure was modeled as a cylinder with the following dimensions: inner diameter = 338 mm, outer diameter = 490 mm, length = 450 mm), and linear elastic material properties (E = 13 GPa, density ρ = 1,600 kg/m^3, ν = 0.4). Conductor wire patterns were designed to accurately represent the spatial excitation distribution (**Figures 2A–C**). The air inside and outside the bore was modeled as a pressure acoustic fluid domain (speed of sound c_0 = 343 m/s, ρ =

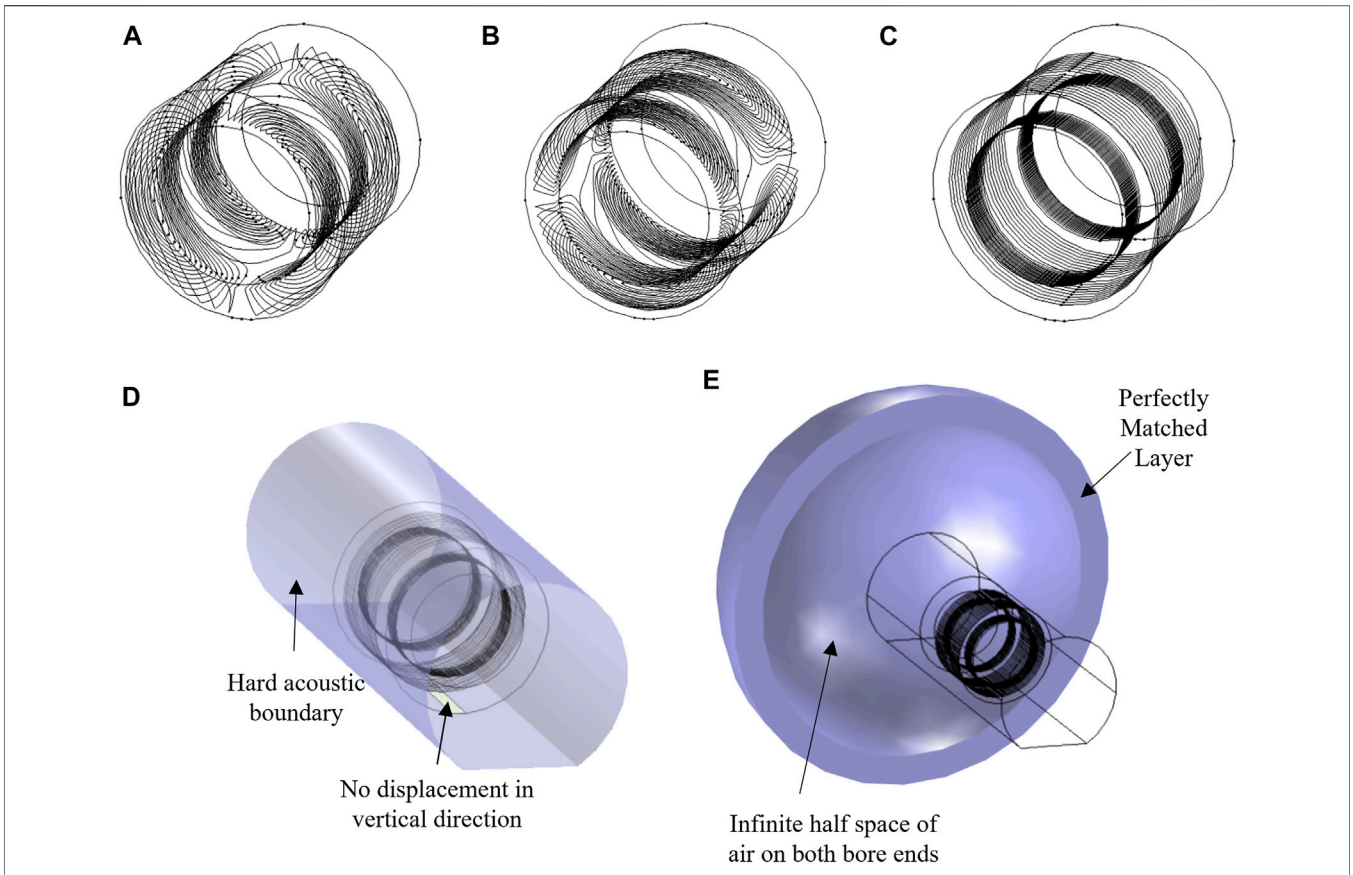

FIGURE 2 | Simulation model. **(A)** X-, **(B)** Y-, and **(C)** Z-axis gradient coils. **(D,E)** Applied boundary conditions.

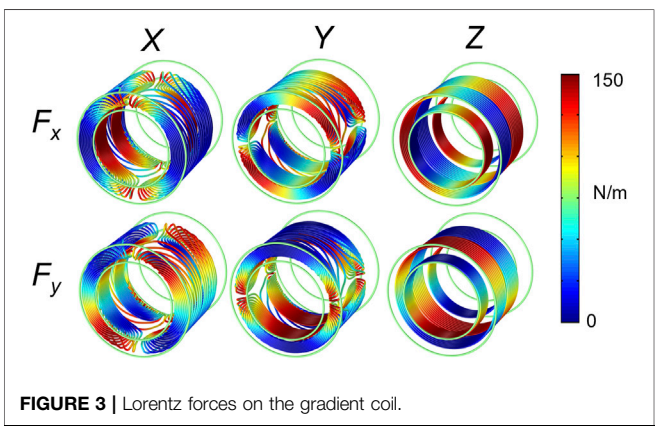

FIGURE 3 | Lorentz forces on the gradient coil.

1.2 kg/m^3). Full coupling between acoustics and structural vibrations was implemented in the simulation model. The MRI bore duct was modelled as a 60 cm diameter cylinder with a flat bottom (to represent the patient table support) with hard sound wall conditions (**Figure 2D**). At both ends of the bore, a hemispherical air volume of radius 1 m was added to simulate the sound waves propagation outside the bore. A perfectly matched layer (PML) of 20 cm was added to the model to mimic infinite size simulation domain (**Figure 2E**). A harmonic excitation with an alternating current (AC) of amplitude 50 A was used to drive the gradient coil. The frequency range of 0–3 kHz was chosen to cover the most pulse sequences used in MRI scanners. The performance of this head gradient coil was evaluated in comparison to the existing body gradient coil along the *X*-axis. Moreover, the head coil performance was evaluated and compared at three field strengths:–3, 7, and 10.5 T. **Figure 3** shows the Lorentz forces **Fx** and **Fy** induced on all three gradient coils.

Figure 4 compares SPL spectra of the head and body gradient coils performed using (a) a standalone analysis and (b) the complete realistic analysis. From the standalone analysis it appears that the body coil is louder as it has more excited modes in the spectra. However, the full analysis shows similar acoustic SPLs of the head and body gradients, with the average SPLs of 97.6 and 90.5 dB for the head and body gradient coils, respectively.

3 LORENTZ DAMPING AND MAGNETIC FIELD DEPENDENCE

One of the interesting predictions of the vibroacoustic model described in [34] is related to the dependence of the SPL on the

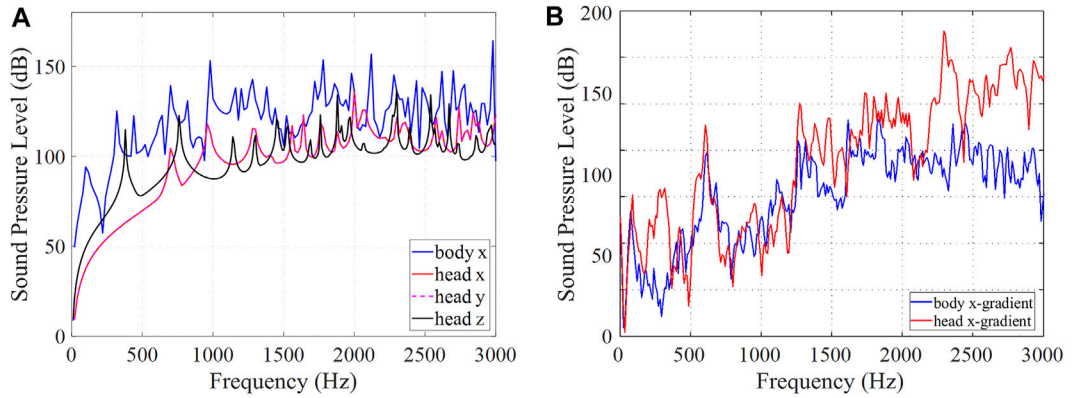

FIGURE 4 | Comparison of head and body gradient coil spectra. **(A)** Standalone and **(B)** complete analysis.

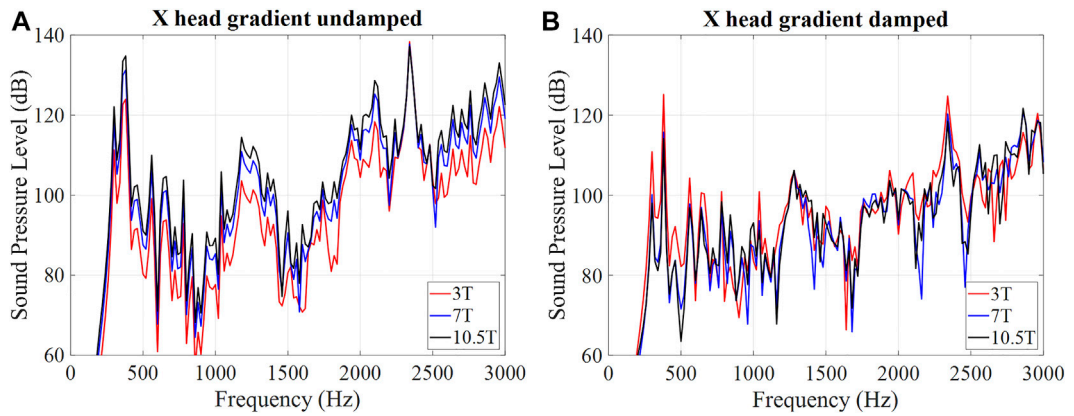

FIGURE 5 | SPL spectra **(A)** without and **(B)** with Lorentz damping at different field strengths.

main magnetic field B_0. In [34], a motion equation for an incremental section of a conductor was derived with the secondary Lorentz force (a counter-EMF) taken into account. From there it follows that while the primary Lorentz force term depends linearly on the main magnetic field B_0, the Lorentz damping term depends quadratically on B_0. It indicates that the SPLs do not scale linearly with B_0, as previously thought. In fact, if the damping term becomes large enough, the SPLs will decrease with B_0.

Figure 5 shows the simulated SPL spectra of the head gradient coil (X-axis only) (a) without and (b) with the added Lorentz damping term, respectively. If the Lorentz damping effect is not taken into account (a), the spectrally averaged SPLs were calculated to be 91.2, 97.5, and 100.8 dB, for 3, 7 and 10.5 T, respectively, confirming the expected linear scaling with the main field strength B_0. However, some frequency points do not obey the linear relationship due to suspected structural-acoustic coupling. If the Lorentz damping is taken into account (b), the spectra behaves quite differently, with the calculated spectrally averaged SPLs of 92.1, 89.8, and 90.5 dB for 3, 7, and 10.5 T, respectively, demonstrating the reduction of the SPL values with the main magnetic field B_0, as predicted by our improved numerical model.

4 NOISE REDUCTION METHODS

This section presents several methods for acoustic noise reduction in the MRI head gradient coil, including those using an absorbing foam and ceramic layer in various geometries, a horn sound guide, and endcap absorbers.

4.1 Absorbing Foam

Acoustic noise can be reduced with a layer of absorbing foam lining the inner bore wall as illustrated in **Figure 6A**; for example, with B-QUiet by VComp, foam layer thickness 20 mm, which provides a transmission loss of 15–37 dB in the range of frequencies from 125Hz to 4 kHz. Simulated bore volume average SPL spectra are shown in **Figure 6B**, with an average noise reduction of 12.5 dB (from 100.7 to 94.9 dB).

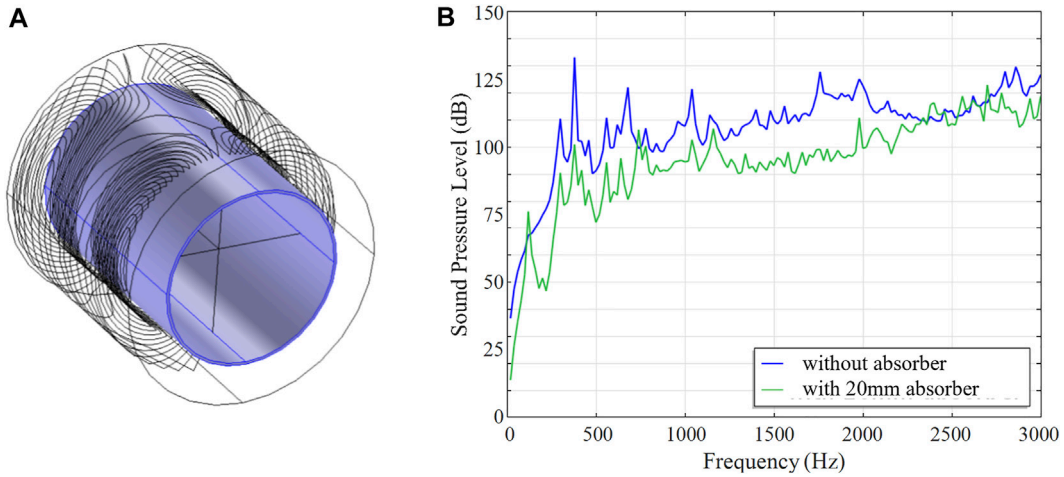

FIGURE 6 | Noise reduction with an absorbing foam. **(A)** 3D model of the gradient coil and the absorber. **(B)** Simulated SPL results with and without the absorber.

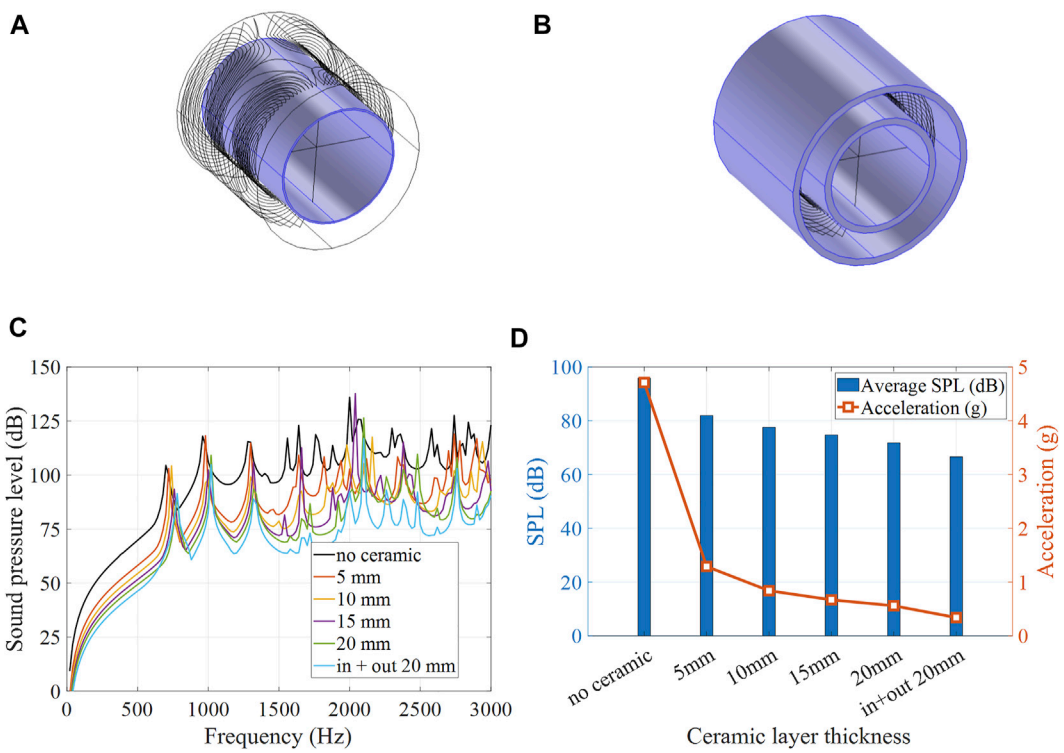

FIGURE 7 | Noise reduction with an absorbing ceramic. 3D models of the gradient coil with **(A)** a single inner layer absorber and **(B)** inner and outer layer absorbers. **(C)** Simulated SPL spectra at various absorbing layer thicknesses. **(D)** Simulated average SPL and acceleration at various absorbing layer thicknesses.

4.2 Ceramic Absorber

Further, acoustic noise can be significantly reduced with a ceramic absorbing layer. A cylindrical ceramic layer (98% alumina, E = 300 GPa, density ρ = 3900 kg/m^3, Poisson ratio ν = 0.22) of various thicknesses ranging from 5 to 20 mm was placed along the inner bore lining, as illustrated in **Figure 7A**. Moreover, a double layer configuration with two ceramic absorbers lining the inside and outside of the gradient coil was also considered, as illustrated in **Figure 7B**. Simulated bore volume averaged SPL spectra at various ceramic absorber thicknesses are shown in **Figure 7C**. Simulated averaged SPLs and acceleration at various ceramic absorbing layer

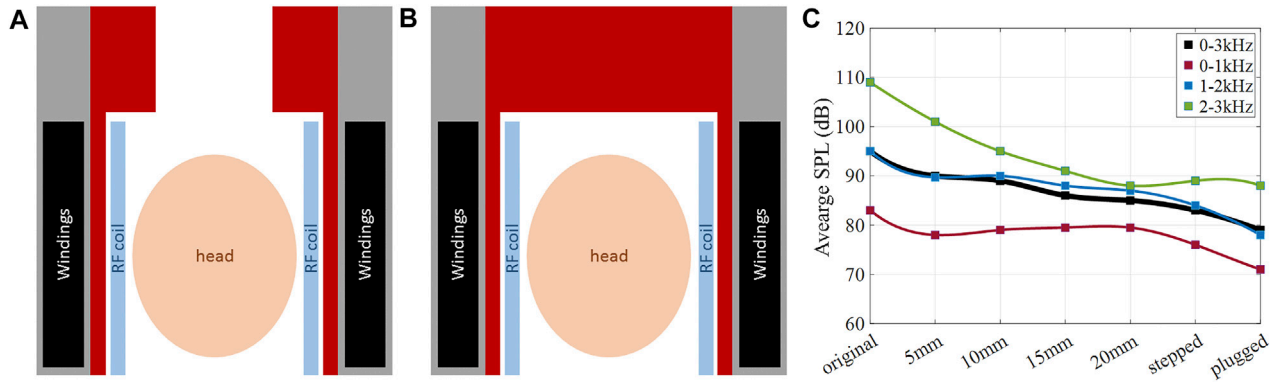

FIGURE 8 | Noise reduction with ceramic layer of various shapes. 2D sketch of the head gradient coils setup with **(A)** a stepped ceramic insert, **(B)** a ceramic endcap. **(C)** Simulated average SPLs for the studied configurations.

thicknesses are shown in **Figure 7D**. It is demonstrated that frequency-averaged SPL reduction of 10.9 dB can be achieved with the help of a 20 mm ceramic layer insert alone, with the majority of noise reduction (10 dB) completed by the first 15 mm. With the addition of the outer ceramic layer, the average noise level is reduced by approximately 30 dB, from 95.8 to 66.6 dB.

4.3 Stepped Ceramic Absorber

Other ceramic layer configurations were considered as well. **Figure 8** shows a 2D sketch of the head gradient coil with (a) a 20 mm ceramic absorber that includes an additional stepped section of 50 mm thickness extending over 200 mm at the service end of the gradient coil, and (b) a 20 mm thick cylinder in combination with a 200 mm thick "end-cap" completely filling the bore at the service end. Both designs (a) and (b) leave an adequate room to place the head and center the brain at the isocenter of the gradient coil. **Figure 8C** shows the frequency-averaged SPL reductions (black curve) due to the ceramic insert, with the maximum SPL reduction of 16.8 dB achieved with the plug insert. Moreover, frequency-averaged SPLs are shown for three separate frequency bands (red curve: 0–1 kHz, blue curve: 1–2 kHz, green curve: 2–3 kHz). The greatest SPL reductions are achieved in the high frequency band (green curve), with a maximum SPL reduction of 20.7 dB, the majority of which was reached by adding the first 15 mm of ceramic inner layer. This high frequency regime benefits the most from a ceramic layer alone without the need for stepped or plugged insert. In contrast, the lower frequency bands (blue and red curves) benefit the most from the added stepped or plugged ceramic insert, with SPL reduction in the range of 8 dB contributed by these features.

4.4 Horn and End Caps

The MRI bore acts as an acoustic waveguide for sound waves. The bore ends introduce discontinuity in the sound wave propagation due to the change in the acoustic impedance at the interface of bore ends/outside air. In order to reduce acoustic SPLs inside the scanner bore, a horn structure could be used which flares out sound waves to better match the characteristic acoustic impedance of the MRI bore to the free space acoustic impedance of the outside air. The sound energy will then be better carried from the interior of the resonator toward the outside world, thereby reducing the acoustic energy resonating inside the bore. The horn model was studied in simulations using COMSOL. The horn shape was chosen to follow an exponential outline r (Z) = $r_i \cdot e^{bz}$, which provides large impedance-matching bandwidth. **Figure 9A** illustrates this concept, where a horn is attached to one end of the bore and helps to guide the sound energy outward.

Another solution to minimize impedance discontinuity is to use an absorbing end cap at the bore end to absorb reflected energy. The absorbing end cap was studied in simulations using COMSOL. The end cap was modeled as a 5 cm thick cylinder with an absorption coefficient of 7 Np/m. **Figure 9B** illustrates this concept, where an end cap is attached to the other (service) end of the bore and absorbs the sound energy.

We used the same head gradient coil described in **Section 2**. The individual gradient axes were excited with a sinusoidal current waveform of 60 s sweep duration.

To confirm the simulation, experimental measurement of SPLs and vibration levels were performed. Sound pressure levels (SPLs) were measured using a Behringer ECM800 condenser microphone at various spatial positions in the bore. Vibration levels were measured using a single-axis Analog Devices ADX001-70Z accelerometer, sensitive to acceleration amplitudes of ±70 g. The accelerometer was positioned on the inner bore surface at various positions along the bore Z-axis.

Figure 9C shows the simulated SPLs averaged over the bore volume at each frequency point. The black curve corresponds to the unmodified gradient coil and shows an average of 77 dB over the band of interest (0–3,000 Hz). For the horn structure, it was found that the following parameters give the best impedance matching: $b = 2$, $h = 10$ cm. The simulated SPLs of the gradient coil with this horn structure are shown in red, with a calculated mean noise reduction of 2 dB. The simulated SPLs of the gradient coil with the end cap are shown in blue, with a calculated mean noise reduction of 2 dB. When the horn and end cap are used in

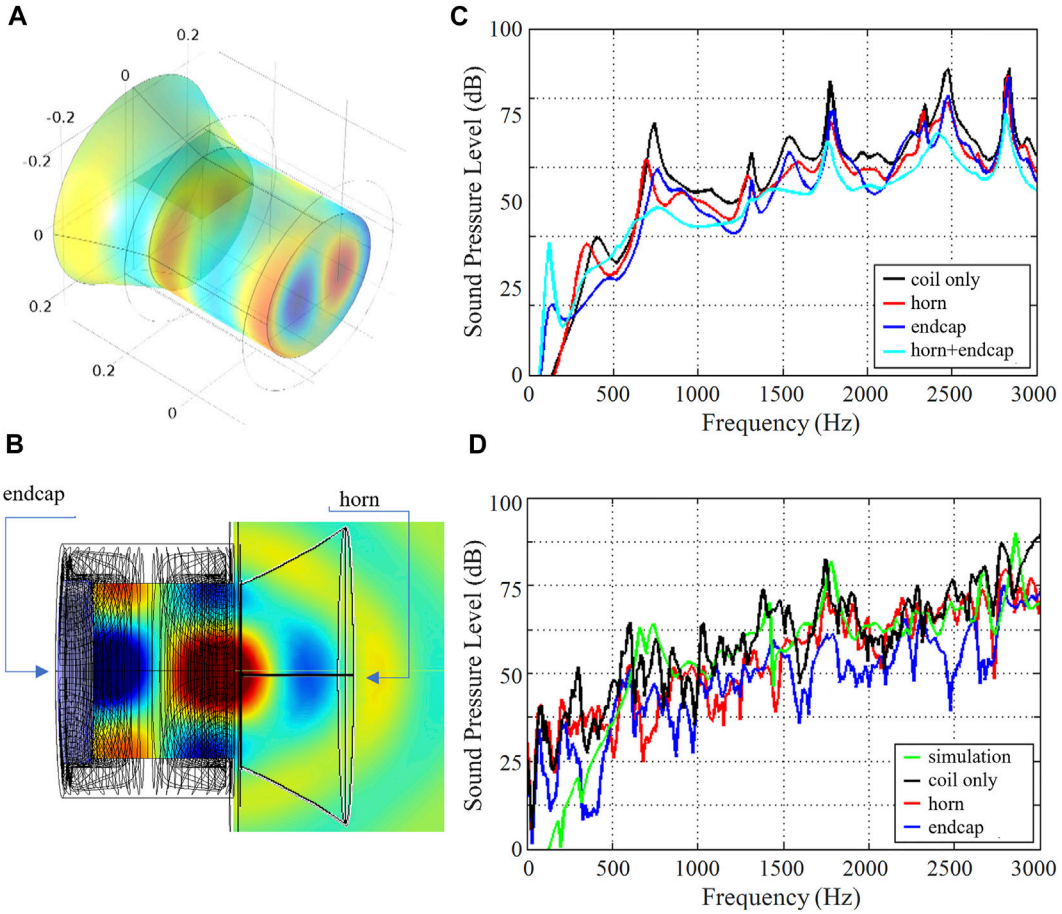

FIGURE 9 | Noise reduction using a horn and endcaps. **(A)** 3D representation of a gradient coil with an additional horn structure for noise guidance and suppression. **(B)** 2D representation of the gradient coil with a horn and an end cap. **(C)** Simulated SPL spectrum. **(D)** Measured SPL spectra.

combination (cyan curve), the mean noise reduction is 3 dB. Both techniques help to smooth out the peaks in the acoustic spectrum. The maximal noise reduction of 8, 10, and 13 dB was found at a frequency of 740 Hz for the horn, the end cap, and both of them used together, respectively. **Figure 9D** shows experimentally measured SPLs at a point +10 cm to the right of isocenter, for *X*-gradient excitation. The measured spectrum (black curve) agrees well with the simulation (green curve), with an average SPL of 76 dB. When the horn structure is used (red curve), the maximum recorded noise reduction is 28 dB with the average noise reduction of 4 dB across the whole frequency range. When the end cap is used (blue curve), the maximum recorded noise reduction is 27 dB, with the average noise reduction of 9 dB across the entire spectrum.

5 EFFICIENT GRADIENT COIL COOLING

High-performance MR gradient coils are subject to strong resistive heating due to the large electrical currents passing through them. For reasons of patient safety and system stability, it is important to limit the temperature rise inside the gradient coil and on the bore surfaces. In their recent work, Wade et al. [9, 10] demonstrated a novel insertable folded head gradient design for human brain imaging that uses hollow copper conductors to allow substantially higher thermal performance. To fully evaluate gradient coil safety, we require a tool for accurate thermal analysis, including the ability to model gradient axes built from either solid or hollow copper. Here we 1) model gradient configurations that use two hollow copper gradient axes and one solid copper axis in comparison with configurations that use all hollow copper axes, and 2) obtain spatially and temporally dependent temperature distributions to study and optimize the key design parameters of such gradient coils.

Realistic numerical modeling simulations were performed using COMSOL. The head gradient coil design described in **Section 2** was used with the following modifications. Epoxy was modeled as a solid heat transfer domain (ρ = 1,600 kg/m^3, k = 2.16 W/m.K, C = 1200J/kg.K). Accurate 3D hollow conductor paths were embedded in epoxy, with resistive heating modeled as a tubular heat source using the calculated copper resistive power dissipated per unit length

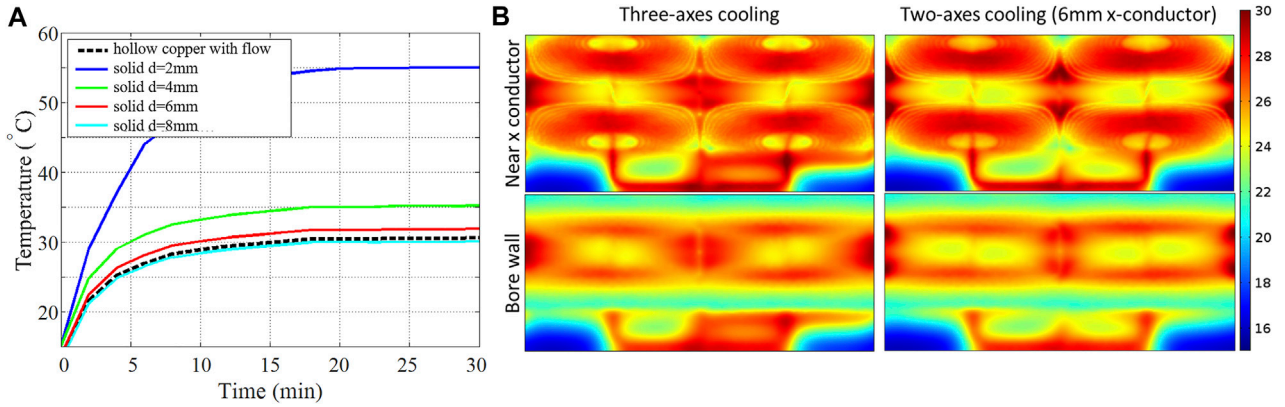

FIGURE 10 | Efficient gradient cooling. **(A)** Temperature as a function of time. **(B)** Temperature distribution on the inner bore.

in W/m, and with hollow conductor coolant flow modeled as a Newtonian fluid with inlet water temperature 16°C and flow rates of 1.74 L/min (*Y*) and 1 L/min (*Z*). We used conductor dimensions representative of one of the recently proposed head gradient prototypes (circular *Y*-conductor with inner diameter/wall thickness 3.5 mm/0.75 mm, rectangular *Z*-conductor with inner dimensions w = 2 mm and h = 4.5 mm and wall thickness of 0.75 mm) [9, 10]. Thermal performance was analyzed for two different scenarios: (a) full three-axis cooling with a flow rate on the *X*-axis of 0.72 L/min and a hollow copper conductor of inner diameter/wall thickness of 2.3 mm/1 mm, as well as (b) two-axis cooling with a solid *X*-axis conductor of varying diameters from 2 to 8 mm. All simulations were carried out using a DC excitation of 150 A on all three axes simultaneously over a transient period from 0 to 30 min.

Figure 10A shows temperature as a function of time (t = 0–30 min) at a position embedded in the epoxy, close to the *X*-gradient conductors, at the top side, patient end of the head gradient (x = 0 mm, y = 189 mm, z = 157 mm). This position was estimated in advance to be among the hottest spatial locations. The black dashed line corresponds to full three-axis cooling and shows that a steady-state temperature of 30.5°C is reached. The colored lines correspond to two-axis cooling with solid *X*-conductors of diameters 2, 4, 6, and 8 mm, showing maximum steady-state temperature rise of 55.0, 35.1, 31.9, and 30.3°C, respectively. This result suggests that a two-axis (*Y*, *Z*) hollow conductor configuration with solid *X*-conductor of ≥6 mm diameter performs nearly as well as an all-hollow conductor coil of otherwise similar design. To further evaluate this equivalency, we show spatial temperature maps for the two configurations in **Figure 10B**; these maps show temperature distributions on cylindrical surfaces located at the inner bore wall (r = 165 mm) and near the *X*-conductor (r = 182 mm). The two maps show negligible differences, with r.m.s/maximum ΔT (temperature rise from the initial temperature of 15°C) of 9.5/15.8°C and 10.6/16.2°C for the three- and two-axis configurations, respectively.

6 DISCUSSION

In this paper, we show that numerical analysis of gradient coils can accurately predict vibroacoustics and temperature increase, which can further be used to reduce sound pressure levels and vibrations, ultimately leading to the safe operation of MR gradient coils. It was demonstrated that the Lorentz damping effect depends on the conductor cross section. At higher frequencies, when the skin depth is reduced, the amount of damping effect may reduce as well. Moreover, based on this realistic vibroacoustic modeling, the mechanical stress, vibrations, and SPLs of gradient coils might be much more manageable at ultra high fields (UHFs) than previously thought.

It was demonstrated that ceramic inserts provide significant SPL reduction in gradient coils. However, it should be noted that ceramic materials are relatively heavy, and the added weight has to be considered in any practical application. In particular, a 5 mm thick ceramic cylinder would add 20.4 kg to the gradient coil, while a 20 mm thick ceramic cylinder will add 35.1 kg. If the stepped ceramic absorber is used, the extra added weight goes up to 61.5 kg. The maximum added weight is for the plugged ceramic absorber design, with 89.5 kg extra weight added to the gradient coil. In terms of the most benefit per frequency, the additional plugged/stepped inserts show more noise reduction in the low-/intermediate-frequency bands, with the acoustic levels being 10–25 dB lower than in the high-frequency band. For the high frequency band, using a 15 mm straight ceramic layer will provide significant noise reduction, with an only moderately increase in weight. Moreover, the ceramic layer can improve thermal heat conduction and therefore minimize thermal hotspots.

It was shown that an end cap attached at the service end of gradient coil sound waves can absorb the acoustic noise while a horn structure attached to the other end can effectively guide the sound wave away from the bore into the free space. The combined effect of these two strategies applied together allows for a significant sound reduction.

We have presented a framework for the accurate thermal analysis of gradient coils. We demonstrate the feasibility of moving from an all-hollow copper (three cooled gradient axes)

coil concept to a two-axis-only cooling concept that uses a 6 mm solid conductor for the third axis. The r.m.s/maximum temperature rise for the three- and two-axis configurations show negligible differences and are 9.5/15.8°C and 10.6/16.2°C, respectively.

Various acoustic noise reduction methods have been reported here and in the literature. From an engineering point of view, the best solution for tackling the acoustic noise problem is to redesign the gradient coil structure such that it does not produce unwanted noise; for example, by balancing out the Lorentz forces generated by the moving currents [50–52]. However, in practice, their installation into existing MRI systems could prove very expensive compared to other alternative noise mitigation strategies. Recent advances in "silent" MRI sequence developments such as UTE [42] and ZTE [43] are very encouraging with gradient noise levels of only 2.6 dBA above the in-bore background noise [60] and improved pediatric scan success rates [61]. However, some comparative reports indicate image blurring and reduced SNR for these sequences [62]. Modern ANC systems can achieve average SPL attenuation of 20 dB [63]. However, for optimal performance, such ANC systems have to be positioned very close to the patient's ear, i.e., integrated into headphones. This creates a system limitation, as headphones are often incompatible with head coils. Passive acoustic noise reduction solutions, such as noise absorbing bore linings and end caps, can provide a considerable noise attenuation of up to 30 dB; however, their additional weight could become a design concern. The search for an elegant solution to gradient noise reduction is still active and on-going, as a truly silent MRI system could potentially revolutionize medical imaging practice.

7 CONCLUSION

In this paper, we reviewed state-of-the-art numerical methods and practical solutions for acoustic noise reduction in MRI gradient coils. We provided a timeline outlining the major milestones in this research area, with the focus on passive noise reduction solutions using absorbing bore liners, endcaps, and other methods. We also discussed efficient cooling strategies. We highlight the importance of accurate and realistic multi-physics computational methods that include the previously neglected but essential Lorentz damping effect. Our analysis of the dependence of gradient vibroacoustics on the main magnetic field strength suggests that gradient acoustics and vibrations are more manageable at UHF MRI field strengths than previously thought. Experimental measurements of SPLs and acceleration levels agree well with the simulations. It was shown that a uniform 15 mm thick cylindrical ceramic insert is a practical design that provides a considerable acoustic noise reduction of 10.9 dB averaged over the frequency range of 0-3 kHz., with a substantially higher reduction of 20.7 dB in the high frequency range (2–3 kHz). Using horn and/or endcap results in only moderate noise reduction of 4 dB/9 dB averaged over 0–3 kHz.

DATA AVAILABILITY STATEMENT

The raw data supporting the conclusions of this article will be made available by the authors, without undue reservation.

AUTHOR CONTRIBUTIONS

EM: writing, extraction of results, collection of data. SW: simulations, design methods, writing, supervision.

ACKNOWLEDGMENTS

The authors would like to acknowledge the following funding sources: NSERC fellowship, GE Healthcare, Burroughs Wellcome Fund, NIH K99/NIH R00 R00EB024341. The authors would like to acknowledge the gradient team at Robarts Research who contributed to the original conference abstracts and publication mentioned as part of this review paper. The content of this manuscript has been presented in part at the ISMRM 2014 [14], ISMRM 2015 [13, 15] and ISMRM 2016 [16].

REFERENCES

1. Edelstein WA, Hedeen RA, Mallozzi RP, El-Hamamsy S-A, Ackermann RA, Havens TJ. Making MRI Quieter. *Magn Reson Imaging* (2002) 20(2):155–63. doi:10.1016/s0730-725x(02)00475-7
2. Clayton DB, Elliott MA, Leigh JS, Lenkinski RE. 1H Spectroscopy without Solvent Suppression: Characterization of Signal Modulations at Short echo Times. *J Magn Reson* (2001) 153(2):203–9. doi:10.1006/jmre.2001.2442
3. Nixon TW, McIntyre S, Rothman DL, de Graaf RA. Compensation of Gradient-Induced Magnetic Field Perturbations. *J Magn Reson* (2008) 192(2):209–17. doi:10.1016/j.jmr.2008.02.016
4. Handler WB, Harris CT, Scholl TJ, Parker DL, Goodrich KC, Dalrymple B, et al. New Head Gradient Coil Design and Construction Techniques. *J Magn Reson Imaging* (2014) 39(5):1088–95. doi:10.1002/jmri.24254
5. Wong EC. Local Head Gradient Coils: Window(s) of Opportunity. *Neuroimage* (2012) 62(2):660–4. doi:10.1016/j.neuroimage.2012.01.025
6. Chronik BA, Alejski A, Rutt BK. Design and Fabrication of a Three-axis Edge ROU Head and Neck Gradient Coil. *Magn Reson Med* (2000) 44(6):955–63. doi:10.1002/1522-2594(200012)44:6<955::aid-mrm18>3.0.co;2-1
7. Chronik EA, Rutt BK. Constrained Length Minimum Inductance Gradient Coil Design. *Magn Reson Med* (1998) 39(2):270–8. doi:10.1002/mrm.1910390214
8. While PT, Forbes LK, Crozier S. 3D Gradient Coil Design - Toroidal Surfaces. *J Magn Reson* (2009) 198(1):31–40. doi:10.1016/j.jmr.2009.01.006
9. Wade T, Alejski A, Bartha J, Tsarapkina D, Rutt B, McKenzie C. Thermal Characterization of an All Hollow Copper Insertable Head Gradient Coil. *Proc Intl Soc Mag Reson Med* (2015). https://archive.ismrm.org/2015/1021.html.
10. Wade T, Alejski A, Bartha J, Tsarapkina D, Hinks R, McKinnon G, et al. editors. Design, Construction and Initial Evaluation of a Folded Insertable Head Gradient Coil. Proceedings of the 22nd Annual Meeting of ISMRM Milano; 2014.
11. Vom Endt A, Riegler J, Eberlein E, Schmitt F, Dorbert U, Krüger G, et al. A High-Performance Head Gradient Coil for 7T Systems. *Proc Intl Soc Magn Reson Med* (2007). https://archive.ismrm.org/2006/1370.html.

12. Tomasi D, Xavier RF, Foerster B, Panepucci H, Tannús A, Vidoto EL. Asymmetrical Gradient Coil for Head Imaging. *Magn Reson Med* (2002) 48(4):707–14. doi:10.1002/mrm.10263
13. Winkler S, Wade T, McKenzie C, Rutt B. Lorentz Damping and the Field Dependence of Gradient Coil Vibroacoustics. *Proc Intl Soc Mag Reson Med* (2015).
14. Winkler S, Wade T, McKenzie C, Rutt B. Accurate Vibroacoustic Simulations in High Performance Gradient Coils. *Proc Int Soc Magn Res* (2014) 22:3089. https://archive.ismrm.org/2015/3089.html.
15. Winkler SA, Alejski A, Wade T, McKenzie C, Rutt BK. A Traveling-Wave Approach to Acoustic Noise Reduction in MR Gradient Coils. *Proc Intl Soc Mag Reson Med* (2014). https://archive.ismrm.org/2014/4852.html.
16. SA Winkler, A Alejski, T Wade, C McKenzie, BK Rutt, editors. *Vibroacoustic Noise Reduction in High Performance Head Gradient Coils Using Ceramic Inserts*. Concord, CA, USA: ISMRM (2016).
17. Wade T, Alejski A, McKenzie C, Rutt B. Peripheral Nerve Stimulation Thresholds of a High Performance Insertable Head Gradient Coil, Proceedings of the 24th Annual Meeting of ISMRM, Singapore (2016).
18. McJury PhD M, Shellock PhD FG. Auditory Noise Associated with MR Procedures: a Review. *J Magn Reson Imaging* (2000) 12(1):37–45. doi:10.1002/1522-2586(200007)12:1<37::aid-jmri5>3.0.co;2-i
19. Mechefske C. Vibration in MRI Scanners. In: A Al-Jumaily A Alizad, editors. *Biomedical Applications of Vibration and Acoustics in Therapy, Bioeffects, and Modeling*. New York: ASME Press (2008).
20. Takkar MS, Sharma MK, Pal R, A Review on Evolution of Acoustic Noise Reduction in MRI. 2017*Recent Dev Control Automation Power Eng (Rdcape)*; 2017: IEEE.
21. Winkler SA, Schmitt F, Landes H, de Bever J, Wade T, Alejski A, et al. Gradient and Shim Technologies for Ultra High Field MRI. *NeuroImage* (2018) 168:59–70. doi:10.1016/j.neuroimage.2016.11.033
22. McJury MJ. Acoustic Noise and Magnetic Resonance Imaging : A Narrative/Descriptive Review. *Magn Reson Imaging* (2022) 55(2):337–46. doi:10.1002/jmri.27525
23. Soedel W. *Vibrations of Shells and Plates*. Concord, CA, USA: CRC Press (2004).
24. Taracila V, Edelstein WA, Kidane TK, Eagan TP, Baig TN, Brown RW. Analytical Calculation of Cylindrical Shell Modes: Implications for MRI Acoustic Noise. *Concepts Magn Reson* (2005) 25B(1):60–4. doi:10.1002/cmr.b.20031
25. Shao W, Mechefske CK. Analysis of the Sound Field in Finite Length Infinite Baffled Cylindrical Ducts with Vibrating walls of Finite Impedance. *The J Acoust Soc America* (2005) 117(4):1728–36. doi:10.1121/1.1867832
26. Zorumski WE. Generalized Radiation Impedances and Reflection Coefficients of Circular and Annular Ducts. *J Acoust Soc America* (1973) 54(6):1667–73. doi:10.1121/1.1914466
27. Li G, Mechefske CK. Structural-acoustic Modal Analysis of Cylindrical Shells: Application to MRI Scanner Systems. *Magn Reson Mater Phy* (2009) 22(6):353–64. doi:10.1007/s10334-009-0185-z
28. Mechefske CK, Wang F. Theoretical, Numerical, and Experimental Modal Analysis of a Single-Winding Gradient Coil Insert cylinder. *Magn Reson Mater Phy* (2006) 19(3):152–66. doi:10.1007/s10334-006-0038-y
29. Mechefske CK, Wu Y, Rutt BK. MRI Gradient Coil cylinder Sound Field Simulation and Measurement. *J Biomech Eng* (2002) 124(4):450–5. doi:10.1115/1.1488169
30. Mechefske CK, Yao G, Li W, Gazdzinski C, Rutt BK. Modal Analysis and Acoustic Noise Characterization of a 4T MRI Gradient Coil Insert. *Concepts Magn Reson* (2004) 22B(1):37–49. doi:10.1002/cmr.b.20013
31. Yao GZ, Mechefske CK, Rutt BK. Characterization of Vibration and Acoustic Noise in a Gradient-Coil Insert. *Magma* (2004) 17(1):12–27. doi:10.1007/s10334-004-0041-0
32. Wang Y, Liu F, Crozier S. Simulation Study of Noise Reduction Methods for a Split MRI System Using a Finite Element Method. *Med Phys* (2015) 42(12):7122–31. doi:10.1118/1.4935864
33. Wang Y, Liu F, Weber E, Tang F, Jin J, Tesiram Y, et al. Acoustic Analysis for a Split MRI System Using FE Method. *Concepts Magn Reson* (2015) 45(2):85–96. doi:10.1002/cmr.b.21283
34. Winkler SA, Alejski A, Wade T, McKenzie CA, Rutt BK. On the Accurate Analysis of Vibroacoustics in Head Insert Gradient Coils. *Magn Reson Med* (2017) 78(4):1635–45. doi:10.1002/mrm.26543
35. Sakhr J, Chronik BA. Vibrational Response of a MRI Gradient Coil cylinder to Time-Harmonic Lorentz-Force Excitations: An Exact Linear Elastodynamic Model for Shielded Longitudinal Gradient Coils. *Appl Math Model* (2019) 74:350–72. doi:10.1016/j.apm.2019.04.054
36. Sakhr J, Chronik BA. Parametric Modeling of Steady-State Gradient Coil Vibration: Resonance Dynamics under Variations in cylinder Geometry. *Magn Reson Imaging* (2021) 82:91–103. doi:10.1016/j.mri.2021.06.007
37. McJury MJ. Acoustic Noise Levels Generated during High Field MR Imaging. *Clin Radiol* (1995) 50(5):331–4. doi:10.1016/s0009-9260(05)83427-0
38. Cho ZH, Park SH, Kim JH, Chung SC, Chung ST, Chung JY, et al. Analysis of Acoustic Noise in MRI. *Magn Reson Imaging* (1997) 15(7):815–22. doi:10.1016/s0730-725x(97)00090-8
39. Mechefske CK, Geris R, Gati JS, Rutt BK. Acoustic Noise Reduction in a 4 T MRI Scanner. *Magma* (2001) 13(3):172–6. doi:10.1007/bf02678593
40. Cho ZH, Chung ST, Chung JY, Park SH, Kim JS, Moon CH, et al. A New Silent Magnetic Resonance Imaging Using a Rotating DC Gradient. *Magn Reson Med* (1998) 39(2):317–21. doi:10.1002/mrm.1910390221
41. Crémillieux Y, Wheeler-Kingshott CA, Briguet A, Doran SJ. STEAM-Burst: a Single-shot, Multi-slice Imaging Sequence without Rapid Gradient Switching. *Magn Reson Med* (1997) 38(4):645–52.
42. Gatehouse PD, Bydder GM. Magnetic Resonance Imaging of Short T2 Components in Tissue. *Clin Radiol* (2003) 58(1):1–19. doi:10.1053/crad.2003.1157
43. Weiger M, Brunner DO, Dietrich BE, Müller CF, Pruessmann KP. ZTE Imaging in Humans. *Magn Reson Med* (2013) 70(2):328–32. doi:10.1002/mrm.24816
44. Goldman AM, Gossman WE, Friedlander PC. Reduction of Sound Levels with Antinoise in MR Imaging. *Radiology* (1989) 173(2):549–50. doi:10.1148/radiology.173.2.2798889
45. McJury M, Stewart RW, Crawford D, Toma E. The Use of Active Noise Control (ANC) to Reduce Acoustic Noise Generated during MRI Scanning: Some Initial Results. *Magn Reson Imaging* (1997) 15(3):319–22. doi:10.1016/s0730-725x(96)00337-2
46. Chen CK, Tzi-Dar Chiueh T-D, Jyh-Horng Chen J-H. Active Cancellation System of Acoustic Noise in MR Imaging. *IEEE Trans Biomed Eng* (1999) 46(2):186–91. doi:10.1109/10.740881
47. Li M, Lim TC, Lee J-H. Simulation Study on Active Noise Control for a 4-T MRI Scanner. *Magn Reson Imaging* (2008) 26(3):393–400. doi:10.1016/j.mri.2007.08.003
48. Li M, Rudd B, Lim TC, Lee J-H. *In Situ* active Control of Noise in a 4 T MRI Scanner. *J Magn Reson Imaging* (2011) 34(3):662–9. doi:10.1002/jmri.22694
49. Chambers J, Bullock D, Kahana Y, Kots A, Palmer A. Developments in Active Noise Control Sound Systems for Magnetic Resonance Imaging. *Appl Acoust* (2007) 68(3):281–95. doi:10.1016/j.apacoust.2005.10.008
50. Mansfield P, Glover P, Bowtell R. Active Acoustic Screening: Design Principles for Quiet Gradient Coils in MRI. *Meas Sci Technol* (1994) 5(8):1021–5. doi:10.1088/0957-0233/5/8/026
51. Mansfield P, Chapman BLW, Bowtell R, Glover P, Coxon R, Harvey PR. Active Acoustic Screening: Reduction of Noise in Gradient Coils by Lorentz Force Balancing. *Magn Reson Med* (1995) 33(2):276–81. doi:10.1002/mrm.1910330220
52. Bowtell RW, Mansfield P. Quite Transverse Gradiant Coils: Lorentz Force Balanced Designs Using Geometrical Similitude. *Magn Reson Med* (1995) 34(3):494–7. doi:10.1002/mrm.1910340331
53. Mansfield P, Haywood B. Principles of Active Acoustic Control in Gradient Coil Design. *Magma* (2000) 10(2):147–51. doi:10.1007/bf02601849
54. Mansfield P, Haywood B, Coxon R. Active Acoustic Control in Gradient Coils for MRI. *Magn Reson Med* (2001) 46(4):807–18. doi:10.1002/mrm.1261
55. Edelstein WA, Kidane TK, Taracila V, Baig TN, Eagan TP, Cheng Y-CN, et al. Active-passive Gradient Shielding for MRI Acoustic Noise Reduction. *Magn Reson Med* (2005) 53(5):1013–7. doi:10.1002/mrm.20472

56. Roozen NB, Koevoets AH, Den Hamer AJ. Active Vibration Control of Gradient Coils to Reduce Acoustic Noise of MRI Systems. *Ieee/asme Trans Mechatron* (2008) 13(3):325–34. doi:10.1109/tmech.2008.924111
57. Wang Y, Liu F, Li Y, Tang F, Crozier S. Asymmetric Gradient Coil Design for Use in a Short, Open Bore Magnetic Resonance Imaging Scanner. *J Magn Reson* (2016) 269:203–12. doi:10.1016/j.jmr.2016.06.015
58. Li G, Mechefske CK. A Comprehensive Experimental Study of Micro-perforated Panel Acoustic Absorbers in MRI Scanners. *Magn Reson Mater Phy* (2010) 23(3):177–85. doi:10.1007/s10334-010-0216-9
59. Nan J, Zong N, Chen Q, Zhang L, Zheng Q, Xia Y. A Structure Design Method for Reduction of MRI Acoustic Noise. *Comput Math Methods Med* (2017) 2017:6253428. doi:10.1155/2017/6253428
60. Liu X, Gómez PA, Solana AB, Wiesinger F, Menzel MI, Menze BH. Silent 3D MR Sequence for Quantitative and Multicontrast T1 and Proton Density Imaging. *Phys Med Biol* (2020) 65(18):185010. doi:10.1088/1361-6560/aba5e8
61. Zhu X, Ye J, Bao Z, Luo X, Zhu Q, Shang S, et al. Benefits of Silent DWI MRI in Success Rate, Image Quality, and the Need for Secondary Sedation during Brain Imaging of Children of 3-36 Months of Age. *Acad Radiol* (2020) 27(4):543–9. doi:10.1016/j.acra.2019.09.022
62. Holdsworth SJ, Macpherson SJ, Yeom KW, Wintermark M, Zaharchuk G. Clinical Evaluation of Silent T1-Weighted MRI and Silent MR Angiography of the Brain. *Am J Roentgenology* (2018) 210(2):404–11. doi:10.2214/ajr.17.18247
63. Lee N, Park Y, Lee GW. Frequency-domain Active Noise Control for Magnetic Resonance Imaging Acoustic Noise. *Appl Acoust* (2017) 118:30–8. doi:10.1016/j.apacoust.2016.11.003

Conflict of Interest: The authors declare that the research was conducted in the absence of any commercial or financial relationships that could be construed as a potential conflict of interest.

Advantages of publishing in Frontiers

OPEN ACCESS
Articles are free to read for greatest visibility and readership

FAST PUBLICATION
Around 90 days from submission to decision

HIGH QUALITY PEER-REVIEW
Rigorous, collaborative, and constructive peer-review

TRANSPARENT PEER-REVIEW
Editors and reviewers acknowledged by name on published articles

Frontiers
Avenue du Tribunal-Fédéral 34
1005 Lausanne | Switzerland

Visit us: www.frontiersin.org
Contact us: frontiersin.org/about/contact

REPRODUCIBILITY OF RESEARCH
Support open data and methods to enhance research reproducibility

DIGITAL PUBLISHING
Articles designed for optimal readership across devices

FOLLOW US
@frontiersin

IMPACT METRICS
Advanced article metrics track visibility across digital media

EXTENSIVE PROMOTION
Marketing and promotion of impactful research

LOOP RESEARCH NETWORK
Our network increases your article's readership